Designing spatiotemporally tunable viscoelastic hyaluronic acid hydrogels to study cell mechanobiology during fibrosis

---

A dissertation presented to the faculty of the School of Engineering and Applied Science
University of Virginia

In partial fulfillment of the requirements for the degree of
Doctor of Philosophy in Chemical Engineering

by
Erica Hui
October 2021

Doctoral Committee:

Assistant Professor Steven Caliari, Advisor
Associate Professor Matt Lazzara, Chair
Professor Thomas Barker
Assistant Professor Rachel Letteri
Assistant Professor Chris Highley

APPROVAL SHEET

This

Dissertation

is submitted in partial fulfillment of the requirements
for the degree of

Doctor of Philosophy

Author: Erica Hui

This Dissertation has been read and approved by the examing committee:

Advisor: Steven Caliari

Advisor:

Committee Member: Matthew Lazzara

Committee Member: Rachel Letteri

Committee Member: Christopher Highley

Committee Member: Thomas Barker

Committee Member:

Committee Member:

Accepted for the School of Engineering and Applied Science:

Jennifer L. West, School of Engineering and Applied Science

October 2021

Abstract

The ECM is highly dynamic and is constantly regulated through cell-cell and cell-matrix interactions. ECM dysregulation can trigger various signaling cascades and promote deviant cell behaviors and disease progression. Fibrosis is a heterogeneous pathological scarring outcome of many diseases that is characterized by progressive matrix stiffening and decreasing viscoelasticity. Treatments have been largely unsuccessful due to a lack of suitable test systems for probing molecular mechanisms involved in fibrogenesis. Additionally, most hydrogel models fail to display tissue-relevant time-dependent properties such as stress relaxation, which has shown to be a critical regulator of cell phenotype. Engineered hydrogels with tunable properties has become a powerful method to study the mechanoregulatory role of mechanical and biochemical cues on cell behaviors. Overall, the goal of this thesis is to develop a class of mechanically dynamic and spatiotemporally heterogeneous hydrogels with precise control over cell-instructive inputs, allowing recapitulation of both normal and diseased microenvironments.

For this work, we used phototunable hyaluronic acid (HA)-based hydrogels that enable independent tuning of stiffness, viscoelasticity, and adhesive ligand presentation to understand how physical and chemical cues collectively influence cell behaviors in fibrosis. Chapter 3 characterizes the time-dependent properties of *ex vivo* tissue, such as stress relaxation and frequency-dependent behavior, to direct the design of ECM-mimetic biomaterials. Chapter 4 illustrates the development of an *in vitro* fibrosis model to study how stiffness, viscoelasticity, and heterogeneity influences fibroblast response. Chapter 5 uses engineered fibronectin adhesive fragments to understand the individual and combined roles of stiffness, viscoelasticity, and adhesion on cell spreading, actin stress fiber formation, and focal adhesion maturation. Finally,

Chapter 6 explores how viscoelastic cues impact cell behaviors in 3D cultures. Altogether, these studies present a framework for engineering instructive hydrogel platforms that offer greater insight into the role that complex matrix properties play in regulating cell mechanobiology in the context of fibrosis progression.

Acknowledgements

First and foremost, I would like to thank my advisor, Dr. Steven Caliari, for taking a chance on me five years ago. It has been quite a unique and exciting journey starting up the lab and watching it grow over the years. I am forever grateful for the kindness, support, and patience you showed me from the very beginning. You taught me to think more critically, learn to accept failure and move forward, and to be confident in myself and my abilities. I have also appreciated your love for food, especially all things chocolate. Thank you to my committee members Dr. Matt Lazzara, Dr. Tom Barker, Dr. Rachel Letteri, and Dr. Chris Highley for all the insightful discussions, guidance, and mentorship, without which this thesis would not have been possible.

I would also like to thank my undergraduate advisor, Dr. Prajnaparamita Dhar, and graduate mentor, Dr. Aishik Chakraborty, for introducing me to research and supporting me throughout my undergraduate career. Your guidance and encouragement did not go unnoticed. I would not have pursued a graduate degree without having such strong examples of what good mentors look like.

Inevitably, the Caliari lab has grown and changed over the past several years. I feel lucky to have worked and interacted alongside so many intelligent, funny, creative, and kind individuals who have helped create such a welcoming and supportive lab atmosphere – Beverly Miller, Ivan Basurto, Deniz Unal, Jenna Sumey, Mackenzie Grubb, Kelly Bukovic, Leilani Astrab, James Gentry, and undergraduate researchers Rebecca, Oliver, Priyanshi, Sarah, Mark, Erin, Audrey, Gregg, Austin, Abigail, Samir, and Emily. All of you have been vital towards my growth as a researcher, scientist, and person overall, and I cannot thank you enough for helping me with troubleshooting experiments, coming up with new ideas, providing feedback on countless practice

presentations, being my rocks throughout the struggles of graduate school, always making time for food and coffee outings, and making work a fun place to be. Special thanks to the undergraduates who I have had a pleasure of mentoring and learning from – Grant Guan, Kathryn Gimeno, and Kathryn Smith. Thank you all for always being curious, motivated, and patient with me as I was learning how to be a mentor. A large portion of my research success is attributed to your hard work and I am so appreciative.

I journeyed through graduate school with the best classmates and colleagues I could ever ask for. I am especially grateful to know that I will leave with lifelong friends. I want to thank Kate Dagnall for being such a great roommate and friend for over 5 years; I am so glad to have had you by my side for everything from co-organizing department recruitment weekends and research symposia to planning birthday celebrations. I also want to thank Naomi Miyake and Devanshi Gupta for their unwavering support and friendship and for always pushing me to be a better researcher and person. I also want to acknowledge Dr. Lucy Yoon, Xueying Zhao, Dr. Saringi Agata, Dr. Lucas Kimerer, Joey Roberts, Dr. Kevin Chang, Dr. Kevin Gu, Dr. Luke Huelsenbeck, Dr. Hongxi Luo, and Dr. Evan Day for being constant sources of friendship and for making my time at UVA some of the very best. The countless bonfires, birthday celebrations, secret Santa exchanges, trips to Richmond, and more are some of my absolute favorite memories.

One of the biggest reasons that I gravitated toward UVA was because of the people. For the past five years, I have been able to lean on so many people as we faced the many excitements and challenges of graduate school. Stephanie Guthrie, Arch Creasy, Jason Reck, James Tang, Gordon Brezicki, James Kammert, Sabra Hanspal, Eric Dybeck, Lauren Russell, Natalie Smith, Madison

Mann, Greg Grewal, Natalia Diaz, Tracy Kuper, Colby Whitcomb, Miranda Miller, Makenzie Kimerer, Brian Dregne, Sam Crowl – thank you for all the great times at wineries and breweries, trivia nights, dinners, board games, TV show binging, and hangouts in general. I am also so thankful to have such a great support system outside of UVA. I especially want to thank Stephanie Walker, Brooke Lohman, Sarah Graves, Addison Schauer, Anna Schauer, and Danielle Neighbour for your friendships over the many years and always being there for me in all capacities – whether it is sitting at home or traveling across the world, I am so grateful to have you all in my life.

Finally, I want to thank my family for their unconditional love and unwavering support in all my endeavors. They have always been my biggest cheerleaders and role models and I would not be who I am and where I am today without them. Mom, thank you for your constant love and support for everything I've wanted to do. You have always been so selfless and I can only hope that one day I will be like you. Dad, thank you for inspiring me to pursue degree(s) and a career in science and engineering. You worked so hard to give us the best life and I am eternally grateful. Andy, you are such a talented and intelligent person and I am lucky to be your sister. Thanks for joining me in Charlottesville for a few years and I'm so excited to continue watching you grow. I also want to thank my grandparents, aunts, uncles, and cousins for continuing to encourage and support me throughout my life. Last but not least, to my fiancé Zack, thank you for being by my side throughout this journey. There have been countless plane rides, dinner dates (a special shout out to Bebedero), Netflix binges, trivia nights, board games, concerts, and lots and lots of laughter. I am forever grateful for you and I can't wait to spend the rest of our lives together.

Table of Contents

List of Symbols and Abbreviations

Symbol/Abbreviation	Meaning
2D	Two-dimensional
3D	Three-dimensional
α-SMA	α-smooth muscle actin
A	Area
A_0	Surface area
ACTA2	Alpha actin 2
Ad	Adamantane
AFM	Atomic force microscopy
aHz	Alkyl aldehyde
ALD	Aldehyde
ALP	Alkaline phosphatase
ANOVA	Analysis of variance
AR	Aspect ratio
β-CD-HDA	6-(6-aminohexyl)amino-6-deoxy-βcyclodextrin
BCN	Bicyclononyne
bFGF	Basic fibroblast growth factor
bHz	Benzylaldehyde
BLD	Benzyl
BOP	Benzotriazole-1-yloxytris-(dimethylamino)phosphonium hexaflorophosphate
BSA	Bovine serum albumin
CD-HA	β-cyclodextrin-modified hyaluronic acid
CE-ESI-MS	Capillary electrophoresis-electrospray ionization-mass spectrometry
ChABC	Chondroitinase ABC
Col2a1	Type II collagen
CSI	Cell shape index
Ctgf	Connective tissue growth factor

CuAAC	Copper-catalyzed azide-alkyne cycloaddition
δ	Phase lag
d	Depth
d_0	Displacement amplitude
DA	Diels-Alder
DAPI	4',6-diamidino-2-phenylindole
DBCO (or DIBO)	Dibenzocyclooctyne
DCC	Dynamic covalent chemistry
DIFO	Difluorinated cyclooctyne
DMA	Dynamic mechanical analysis
DMEM	Dulbecco's Modified Eagle Medium
DMF	N,N-dimethylformamide
DMSO	Dimethylsulfoxide
DNA	Deoxyribonucleic acid
DODT	2,2'-(ethylenedioxy) diethanethiol
DTT	Dithiothreitol
E	Young's modulus (elastic modulus)
E(t)	Time-dependent Young's modulus
E(0)	Instantaneous Young's modulus
E'	Storage modulus
E"	Loss modulus
E_{eff}	Effective Young's modulus
ECM	Extracellular matrix
EDC	1-ethyl-3(3-dimethylaminopropyl)carbodiimide
EDG	Electron donating group
EGF	Epidermal growth factor
EGFP	Enhanced green fluorescent protein
ELP	Elastin-like protein
EMT	Epithelial-to-mesenchymal transition
EWG	Electron withdrawing group
F	Applied force

F_0	Load amplitude or initial force
F_{inf}	Equilibrium force
F-actin	Filamentous actin
FA	Focal adhesion
FAK	Focal adhesion kinase
FBS	Fetal bovine serum
FITC	Fluorescein isothiocyanate
Fn	Fibronectin
λ	Wavelength
G	Shear modulus
G’	Shear storage modulus
G”	Shear loss modulus
G-actin	Globular actin
GAG	Glycosaminoglycans
GHHA	Glycidyl methacrylated 3,3’-dithiobis(propionic hydrazide)
GPa	Gigapascal
HA	Hyaluronic acid
HA-TBA	Hyaluronic acid *tert*-butyl ammonium salt
hMSC	Human mesenchymal stem cell
HOMO	Highest occupied molecular orbital
HRP	Horseradish peroxidase
HSC	Hepatic stellate cell
HSD	Honestly significant difference
Hz	Hertz
I2959	Irgacure 2959
IEDDA	Inverse electron demand Diels-Alder
IL-13	Interleukin-13
IPN	Interpenetrating network
IPTG	Isopropyl β-d-1-thiogalactopyranoside
K_a	Binding association constant
K_D	Binding dissociation constant

kPa	Kilopascal
LAP	Lithium phenyl(2,4,6-trimethylbenzoyl)phosphinate
LOX	Lysyl oxidase
LUMO	Lowest unoccupied molecular orbital
LX-2	Human hepatic stellate cell line
MALDI	Matrix-assisted laser desorption/ionization
MeHA	Methyacrylated hyaluronic acid
MMP	Matrix metalloproteinase
mpT	Methylphenyltetrazine
MRTF-A	Myocardin-related transcription factor A
MSC	Mesenchymal stem cell
NHS	*N*-hydroxysuccinimide
NMR	Nuclear magnetic resonance
NorHA	Norbornene-modified hyaluronic acid
o-NB	*Ortho*-nitrobenzyl
OC	Osteocalcin
OD_{600}	Optical density at 600 nm
P(NiPAAM-*co*-GMA)	Poly(N-isopropylacrylamide-*co*-glycidyl methacrylate)
P	Perimeter
Pa	Pascal
PA	Polyacrylamide
PBS	Phosphate-buffered saline
PDAC	Pancreatic ductal adenocarcinoma
PDD	Poly(dimethylacrylamide-*co*-diacetoneacrylamide)
PDGFR	Platelet-derived growth factor
PEG	Poly(ethylene) glycol
PVA	Poly(vinyl alcohol)
R	Radius
R_i	Radius of the spherical tip
RGD	Arginine-glycine-aspartate
ROCK	Rho-associated protein kinase

RUNX2	Runt-related transcription factor 2
Sox9	SRY (sex determining region Y)-box 9
SPAAC	Strain-promoted azide-alkyne cycloaddition
SRF	Serum response factor
SrtA	Sortase A
TCO	*Trans*-cyclooctene
TCP	Tissue culture plastic
TEAD	Transcriptional enhanced associate domain
TGF-β	Transforming growth factor-beta
TosCl	p-Toluenesulfonyl chloride
TNF-α	Tumor necrosis factor-alpha
UV	Ultraviolet
v	Poisson's ratio
V	Volume
VE	Viscoelastic
VEGF	Vascular endothelial growth factor
VIC	Valvular interstitial cell
YAP/TAZ	Yes-associated protein/transcriptional co-activator with PDZ-binding motif

List of Figures

CHAPTER 1

CHAPTER 2

CHAPTER 3

CHAPTER 4

CHAPTER 5

CHAPTER 6

APPENDIX A

List of Tables

CHAPTER 2

List of Schemes

CHAPTER 2

CHAPTER 1: INTRODUCTION AND BACKGROUND

1.1 Overview

The ECM is highly complex and is constantly regulated by cells through cell-cell and cell-matrix interactions. Dysregulation in ECM dynamics can trigger various signaling cascades and promote aberrant cell behaviors and disease progression. Fibrosis is a heterogeneous pathological scarring outcome of many diseases that is characterized by progressive matrix stiffening and decreasing viscoelasticity. Treatments have been largely unsuccessful due to a lack of suitable test systems for probing molecular mechanisms involved in fibrogenesis. Additionally, most hydrogel models fail to display tissue-relevant time-dependent properties such as stress relaxation. Engineered biomaterials with tunable properties offers a promising method to study the mechanoregulatory role of mechanical and biochemical cues on cell behaviors, particularly during disease progression and fibrosis. This thesis focuses on the design and development of phototunable viscoelastic hyaluronic acid (HA) hydrogels with independently tunable stiffness, viscoelasticity, and ligand presentation to study cell mechanobiology during fibrosis.

1.2 The extracellular matrix (ECM)

The extracellular matrix (ECM) serves important structural and functional roles for tissue organization and cellular activities. The ECM is composed of several fibrous proteins, including collagen, elastin, fibronectin, and laminin, that provide physical structure, mediate cell adhesion, and guide tissue development[1–5], as well as hydrophilic proteoglycans and glycosaminoglycans (GAGs) that support tissue hydration and modulate the presentation of signaling molecules such as growth factors[6–8]. Tissue ECMs are heterogeneous and dynamic structures that undergo constant remodeling through cell-cell and cell-matrix interactions. The physical and chemical makeup of

the ECM is unique to each tissue – mechanical and chemical properties vary greatly between tissues (e.g., brain versus liver versus bone[9,10]) (**Figure 1.1**) and even within a single tissue such as tissue-dense versus cell-dense composition[11–15] or normal versus pathophysiological states[9,16–18].

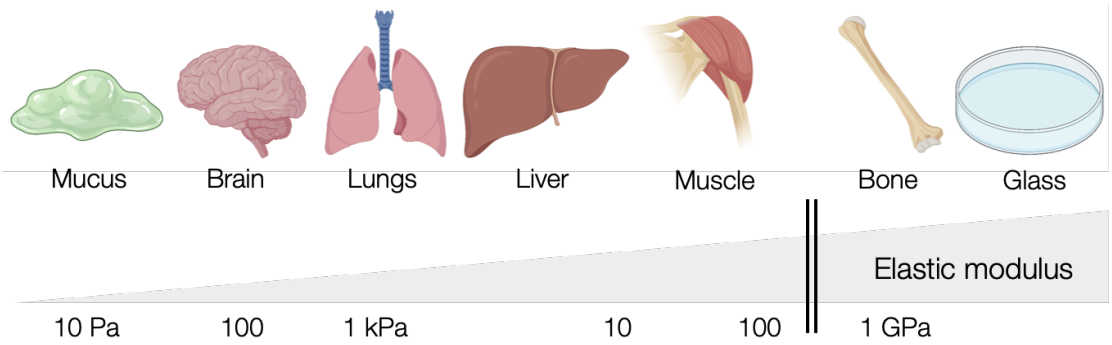

Figure 1.1. Tissue mechanical properties. Each tissue has a unique structure and function that impacts ECM composition and stiffness based on its physiological needs. Bone, whose primary function is to provide structure and protect internal organs, has an elastic modulus or stiffness on the order of gigapascals (GPa). In contrast, brain tissue is more compliant and flexible and is on the order of 100 pascals (Pa). Tissue stiffness will vary spatially and also during development and disease processes. Figure adapted from[10].

The idea of dynamic reciprocity, or the bidirectional crosstalk between cells and their microenvironment, has been recognized as a critical driver of a multitude of cellular responses[19–21]. As cells sense and respond to mechanical and biochemical cues (e.g., stiffness, topography, adhesive ligand presentation, growth factors) from the surrounding ECM via cell surface receptors, signal transduction from the cytoplasm to the nucleus can impact gene expression and cell behaviors including growth, migration, and differentiation in a process known as mechanotransduction[22–24]. Cell-matrix interactions are important for maintaining mechanical homeostasis and tissue function. Dysregulation in ECM composition, such as the

overaccumulation of matrix proteins and decreased tissue viscoelasticity observed during fibrosis, has shown to play a role in the persistence of mechanotransduction signaling dynamics[25–28].

1.2.1 The ECM during development

The maintenance of ECM structure and function during homeostasis supports tissue health, and involves constant matrix mechanoregulation by cells. In general, the ECM is made up of an array of proteins and sugars[3,23]. For most solid tissues, tissue mechanics are supported by fibrillar collagen, elastic fibers, and GAG-containing glycoproteins. Elastic fibers provide connective tissues like lungs and skin with flexibility and resilience[29]. Age-induced changes in tissue properties, such as stiffening, lead to compromised function of elastic fibers[30]. Fibrous collagen is the most abundant protein of the ECM, providing tissue structure and strength, and is subjected to high turnover rates[1,3,23]. GAG-containing glycoproteins enable tissue compression due to their ability to sequester water. Cells are the primary regulator of the ECM from development to proper tissue function and response to insults[23]. Fibroblasts, one of the main cell types that maintains ECM homeostasis, synthesize ECM proteins as well as proteases to break down matrices[31].

1.2.2 The ECM during fibrosis

Fibrosis is a common pathological scarring outcome that occurs when the normal tissue repair response becomes dysregulated as a result of infectious or chronic triggers, including exposure to toxins, chronic inflammation, genetic disorders, and persistent infections[9,18]. Fibrosis contributes to almost half of the deaths in the developed world due to its prevalence in nearly every tissue in the body[18,32,33]. During fibrosis, fibroblasts can become activated into myofibroblasts and begin to exhibit profibrotic behaviors such as the excessive production of ECM proteins (e.g., collagen,

fibronectin) that contribute to progressive matrix stiffening and decreased viscoelasticity. Fibrosis is further complicated by significant spatial and temporal heterogeneity, where areas of dense and fibrous collagen representing mature fibrosis alternate with active fibroblast foci, indicative of early-stage fibrosis[34–37].

In the case of pulmonary fibrosis, the accumulation of highly contractive collagen-producing myofibroblasts around the alveoli and bronchioles leads to areas of normal lung tissue alternating with fibrotic foci, observed as hallmark lesions of active fibrogenesis, and cystic "honeycomb" features[38–43]. In many tissues, including the lung, these phenotypic changes facilitate the transition of normal tissue mechanics from soft and viscoelastic (rich in elastin) to stiffer and more elastic (richer in fibrillar collagen) depending on the degree of fibrosis[9,38]. Normal and fibrotic lung tissue stiffness has been reported in the range of 0.5-5 kPa and 5-100 kPa, respectively[39,40].

1.3 Mechanotransduction

The process of mechanotransduction occurs at the interface between the cell membrane and the ECM where cells are able to convert mechanical forces into biochemical signaling pathways[23,24,44,45]. This signal transduction plays an important role in regulating behaviors such as cell spreading, contraction, migration, and differentiation[46,47]. The interplay between cells and the surrounding ECM is well orchestrated, and disruptions can result in aberrant signaling and disease pathologies[9,44]. In particular, changing mechanics in the local microenvironment during fibrosis progression can cause a cascade of biochemical and biophysical signaling events. Increases in global or local physical forces and strain can impact cell cytoskeletal tension, including focal

adhesion formation and contractility, causing rapid responses in fibroblast-mediated ECM remodeling and long-term alterations in downstream gene expression[48–51].

1.3.1 Integrin-based adhesions

Integrins are transmembrane proteins composed of α and β subunits that link the cell cytoskeleton to the surrounding ECM[52]. Integrin-based adhesion sites are primary mediators of bidirectional cell-matrix interactions and play a large mechanosensing role during force transmission (**Figure 1.2A**)[53–55]. There are 18 α and 8 β subunits that give rise to 24 integrin heterodimers that can then bind to various ECM ligands. The strength of integrin-ECM bonds is regulated by integrin pair, density, and presentation. Formation of integrin clusters due to cell-matrix signaling or force mechanotransduction events can heavily influence actin cytoskeletal dynamics and cell morphologies (**Figure 1.2B**)[56,57]. Importantly, integrin-based adhesions facilitate the conversion of complex biophysical cues into chemical signals, playing a major role in regulating mechanotransduction and subsequent downstream changes in gene expression, cytoskeletal organization, and cell adhesivity[58,59].

1.3.1.1 Focal adhesion formation

Focal adhesions are clusters of integrins and proteins that enable force transmission from the cytoskeleton to the nucleus and regulate cell mechanobiology[23,44,51,60]. As cell-matrix contacts are formed, external forces (e.g., matrix stiffness) and actomyosin contractility within the cell cytoskeleton can promote integrin activation and the recruitment of adaptor and signaling proteins such as talin, kindlin, paxillin, and vinculin to the cytoplasmic tail[59]. Increased integrin-ligand binding lifetimes can cause adhesion structures, or integrin clusters, to mature from nascent

adhesions (< 0.25 μm) into stable focal adhesions (1-5 μm)[56,61–63]. Larger focal adhesions and increased cell contractility can play a key role in cell spreading, migration, proliferation, and altered gene expression[64–66].

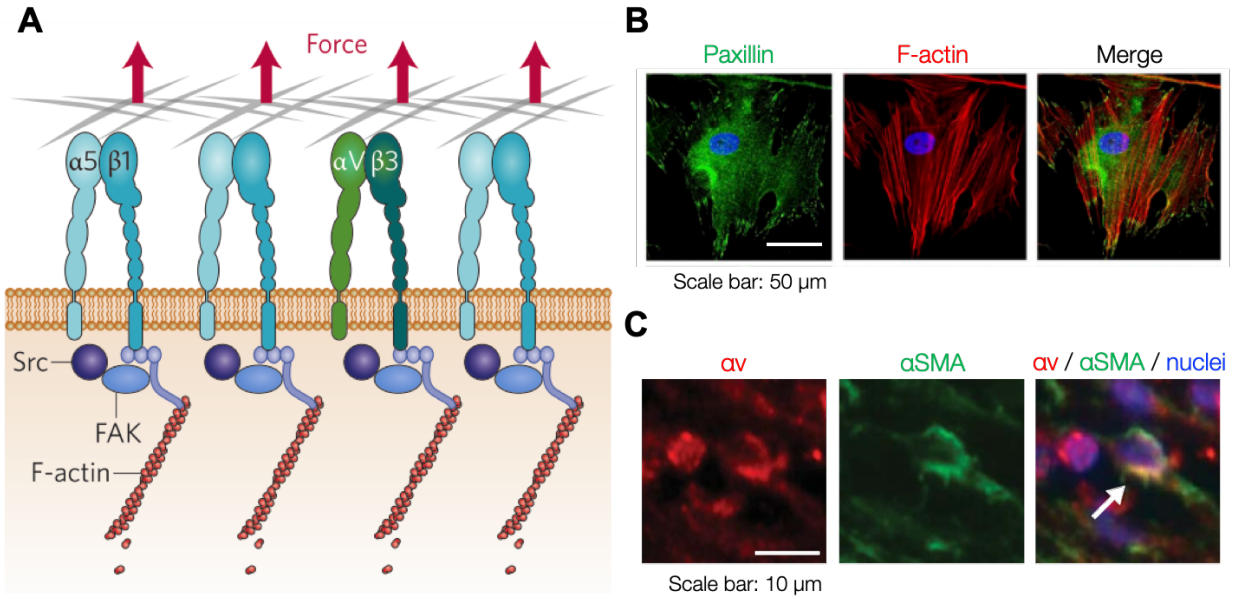

Figure 1.2. Integrin-mediated cell adhesion can influence pathological behaviors. (A) In response to force, integrins become activated and strengthen their adhesion to the substrate. The recruitment of intracellular proteins such as talin enable integrin anchoring to the actin cytoskeleton and influences downstream signaling pathways via signaling proteins such as Src and focal adhesion kinase (FAK). Figure adapted from[54]. (B) Increasing stiffness of 2D polyacrylamide hydrogels (E ~ 25 kPa) correlated with increased cell spreading, F-actin stress fiber organization, and focal adhesion formation. Scale bar: 50 μm. Figure adapted from[27]. (C) Provisional matrix proteins such as fibronectin are upregulated during early stages of tissue remodeling and engagement of specific fibronectin-associated integrins such as αv has shown to correlate with myofibroblast activation. Immunofluorescent images of myofibroblasts on human fibrotic liver tissue shows co-localization of αv with α-SMA (white arrow). Scale bar: 10 μm. Figure adapted from[67].

1.3.1.2 Integrins as regulators of fibrosis

Integrin-based adhesions play a prominent role in directing cell behaviors, especially in the context of disease processes. Recent work as shown that provisional matrix proteins such as fibronectin are upregulated during early stages of tissue remodeling (**Figure 1.2C**). Integrin-specific

fibronectin engagement (e.g., αvβ3 versus α5β1) can influence mechanoregulation in mechanics-driven outcomes such as fibrosis[41,53,68]. In particular, preferential αvβ3 engagement promotes the mechanoactivation of latent transforming growth factor-beta 1 (TGF-β1), which plays a role in myofibroblast activation, fibroblast recruitment, and proliferation in disease pathologies and fibrosis[41,58,68–71]. In addition, the formation and organization of α-smooth muscle actin (α-SMA) stress fibers further increases cell contractility. Integrin clustering is also responsive to chemical and physical cues provided by the ECM, including matrix stiffness and ligand density[59,65,72]. The clustering of these transmembrane proteins enhances mechanotransmission of force and can lead to the formation of stress fibers and focal adhesions, which in turn regulates the activity of transcriptional regulators to drive gene expression.

1.3.2 Roles of the actin cytoskeleton and nucleus in mechanotransduction

Actin is a major component of the cell cytoskeleton and is responsible for maintaining structural stability and supporting dynamic processes such as cell migration, proliferation, morphogenesis, and intracellular protein transport[22,73–75]. The actin cytoskeleton is a dynamic structure consisting of monomeric, globular actin (G-actin), which can polymerize into filamentous actin (F-actin), and actin binding proteins that regulate actin polymerization[75,76]. Importantly, the actin cytoskeleton plays a key mechanosensing role by linking the ECM to the nucleus and enabling force transmission and signal transduction to occur[24,44,77]. In particular, external stresses and tensile forces applied to adherent cells can strengthen cell-matrix connections and increase actomyosin contractility via the formation of higher order actin bundles, or stress fibers, leading to the activation of mechanotransduction pathways[78–80].

The RhoA/Rho-associated protein kinase (ROCK) signaling pathway has been demonstrated as a key regulator of cytoskeletal dynamics[77,81–85]. The activation of RhoA can be triggered by mechanical forces and leads to the stimulation and stabilization of F-actin polymers (and subsequent decrease in free G-actin). In the case of the mechanosensitive myocardin-related transcription factor (MRTF)/serum response factor (SRF) (MRTF/SRF) signaling axis, activated RhoA reduces the concentration of G-actin that is available to sequester MRTF, resulting in dissociation of MRTF from G-actin and activates SRF in the nucleus[75,86,87]. The nuclear localization of MRTF and subsequent binding to SRF promotes the expression and upregulation of target genes such as alpha actin 2 (*ACTA2*), which is the gene encoding myofibroblast activation marker α-SMA[28,88,89]. MRTF activity has been implicated in several physiological and pathological processes, including fibrosis[41,90–92]. Another mechanoresponsive signaling axis, Yes-associated protein and transcriptional co-activator with PDZ-binding domain (YAP/TAZ)/transcriptional enhanced associate domain (TEAD) (YAP/TEAD), also responds to mechanical forces and RhoA activation via dysregulation of the Hippo signaling pathway[88,93–95]. Similar to MRTF shuttling mechanisms, dysregulation or inactivation of the Hippo pathway can be triggered by external stresses or forces and lead to the de-phosphorylation and nuclear translocation of YAP/TAZ[94–96]. In the nucleus, YAP/TAZ interacts with TEAD transcription factor to promote the expression of genes such as connective tissue growth factor (*Ctgf*), which is associated with TGF-β and is a central mediator of tissue remodeling and fibrosis[97–99]. Nuclear YAP activity has been associated with disease outcomes such as fibrosis[96,100–102].

Overall, an increased appreciation of the force-mediated external and internal regulators involved in mechanotransduction has provided insight toward disease processes and the development of

novel therapies. Moving forward, approaches to better understand the extent of mechanosensing by the cell cytoskeleton and nucleus, crosstalk between signaling pathways, and integrative approaches using genomics, biophysical assays, and spatiotemporal cell analyses will increase our knowledge of the complex cell-matrix dynamics at play.

1.4 Hydrogel systems to study cell mechanobiology

It has been recognized that cell-matrix interactions play an important role during tissue remodeling and repair processes. However, the multifaceted and intricate relationship between cells and the ECM complicates the ability to mimic the biological milieu. ECM mimetic biomaterials, such as hydrogels, are particularly attractive model systems to gain a better understanding of cell behaviors *in vivo* due to their ability to mimic natural tissue properties such as high water content and soft tissue mechanics[103,104].

Hydrogels systems are highly versatile and can exhibit a wide range of physical, chemical, and biological properties such as biocompatibility, mechanical integrity, and degradability that make them attractive for mimicking soft biological tissues (**Figure 1.3**)[105,106]. Typically, hydrogels are formed under mild, cytocompatible conditions and allow the transport of oxygen, nutrients, and other soluble factors that is essential for cell culture, especially in 3D systems[107–109]. Many hydrogels formed from natural materials such as collagen, hyaluronic acid (HA), or alginate offer inherent biocompatibility and bioactivity, enabling cell adhesion, viability, proliferation, and migration[110–112]. However, the innate complexity of natural polymers, decreased tunability of mechanical and biochemical properties (which can be particularly attractive for studying changes in tissue properties over time), and higher batch-to-batch variability may lead to confounding

factors when studying cell-matrix interactions. Synthetic polymers such as poly(ethylene) glycol (PEG) and polyacrylamide (PA) are classified as inert, "blank slate" materials that can be functionalized with crosslinking-related molecules, cell adhesive ligands, and degradable sites[113–118]. While most synthetic materials enable greater tunability and user-control of mechanical and biochemical properties, they must be modified for cell culture. Hybrid hydrogel systems that combine natural and synthetic elements such as chemically modified HA can also be used to impart both biocompatibility and high crosslinking tunability for studying cell mechanobiology[119–121].

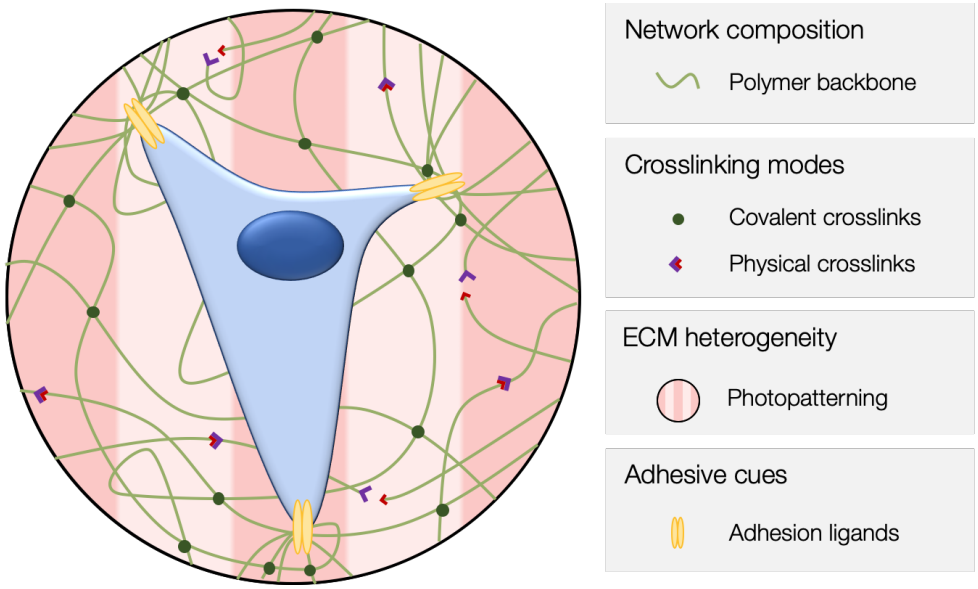

Figure 1.3. Hydrogels as cell culture systems. Hydrogels can be designed to model the complex cellular microenvironment to improve our understanding of how cells interact with the extracellular matrix (ECM). The network composition and concentration can be varied through polymer type. Different crosslinking modes can be used to control over mechanics via crosslink density and viscoelasticity using a combination of interactions. ECM heterogeneity, found in normal and diseased tissues, can be engineered through techniques such as photolithography, which offers spatiotemporal control. Adhesive cues are important in hydrogel systems to control integrin-mediated cell attachment.

In addition to the polymer backbone, hydrogel fabrication is also influenced by the presentation of various instructional cues. Hydrogel network formation can occur through chemical (covalent) or

physical (noncovalent) crosslinking of individual polymer chains[103,122–124]. Common chemical crosslinks include chain-growth polymerization[125,126], photoenzyme-catalyzed reactions[127], and step-growth polymerization (e.g., Michael-type addition)[128–130]. A popular method of forming crosslinks is via photopolymerization[131–134]. Physical crosslinks – polymer entanglements[135], ionic/electrostatic bonds[110,136–138], hydrogen bonds[139,140], protein/peptide interactions, hydrophobic interactions[141,142], and supramolecular interactions[143–146] – exhibit shear-thinning properties and are typically stimuli-responsive (e.g., pH, temperature). By tuning the crosslinking density as well as incorporating multiple crosslinking modes, mechanical properties such as stiffness and viscoelasticity can be controlled. Covalent bonds and physical reactions can also be used to engineer complexity by introducing various signaling molecules such as adhesive ligands or growth factors in a tethered or soluble format, respectively.

Hydrogel system tunability can also be influenced by dimensionality; both 2D (cells atop substrates) and 3D (cells encapsulated within substrates) cultures have revealed the complex relationships of cell adhesion, matrix mechanics, and biochemical cues on cell fate. Traditional studies on 2D cultures established the fundamental relationship between cells and their surrounding microenvironment; notably, seminal work by Discher and co-workers demonstrated that increased substrate stiffness led to increased cell spreading and differentiation[47,147]. Subsequent work has since identified the influence of 2D matrix mechanics on cell morphology[121,136,148,149], migration[150–152], proliferation[135,153,154], and gene expression[27,155,156]. Recently, 3D cell culture studies have been gaining momentum for more closely mimicking native tissue geometry. Changes in hydrogel dimensionality inherently influences factors such as the presentation of adhesive ligands, network mesh size, and nutrient and oxygen diffusion[104,108]. As

such, many studies have shown opposing cell behaviors in 3D compared to 2D. Matrix interactions on 2D cultures that caused pro-fibrotic behaviors (e.g., increased cell spread area, stress fiber organization, nuclear localization of transcriptional co-activators) actually hindered the same outcomes within 3D systems – cells were unable to rearrange and reorganize highly dense covalently crosslinked networks and exhibited more rounded morphologies, decreased contractility, and reduced nuclear localization of transcriptional co-activators[121,157,158]. Other factors such as time-dependent viscoelasticity[110,159] and degradability[160,161] can also influence how cells sense and interpret mechanical cues in 3D. In viscoelastic liquid, or viscoplastic, systems that enable plastic deformation, cells have demonstrated greater spreading and protrusions in faster stress relaxing substrates, similar to what has been observed on equivalent 2D cultures[110,162]. Viscoelastic solid hydrogels that do not allow irrecoverable plastic deformation have shown decreased cell spread area and more rounded morphologies atop hydrogels due to energy dissipation into the matrix. Similarly, degradability is important in 3D systems, particularly in covalently crosslinked networks in which cells would need to degrade the local environment to pull on the surrounding matrix and spread[121,163]. In general, these trends emphasize the need to develop 3D biomimetic hydrogels that can identify critical regulators of cell fate and understand how microenvironmental cues affect cell function differently in different cell culture systems[104].

1.4.1 Incorporation of tissue-relevant mechanical and biochemical cues

In order to gain a better understanding of how cells sense and interpret complex signaling dynamics from the microenvironment, researchers have sought to design instructive hydrogel systems with tunable presentation of mechanical and biochemical cues. Here, we highlight several parameters

that have been identified as important regulators of cell mechanobiology, particularly during development and disease.

1.4.1.1 Stiffness

Tissue stiffness has become one of the most well-established mechanical cues that affects cell behavior and not only varies between different tissue types but also during development, homeostasis, and wound healing processes[9,90]. As highlighted in Section 1.4, Engler *et al*. first demonstrated the ability for substrate stiffness to dictate mesenchymal stem cell (MSC) lineage specification[47]. MSCs on compliant collagen-coated polyacrylamide hydrogels (E ~ 0.1-1 kPa) resulted in neuronal differentiation with branched, filopodia-rich cell morphologies, whereas stiffer substrates mimicking muscle (E ~ 8-17 kPa) and collagenous bone (E ~ 25-40 kPa) induced differentiation of MSCs into spindle-shaped myoblasts and polygonally-shaped osteoblasts, respectively (**Figure 1.4A**).

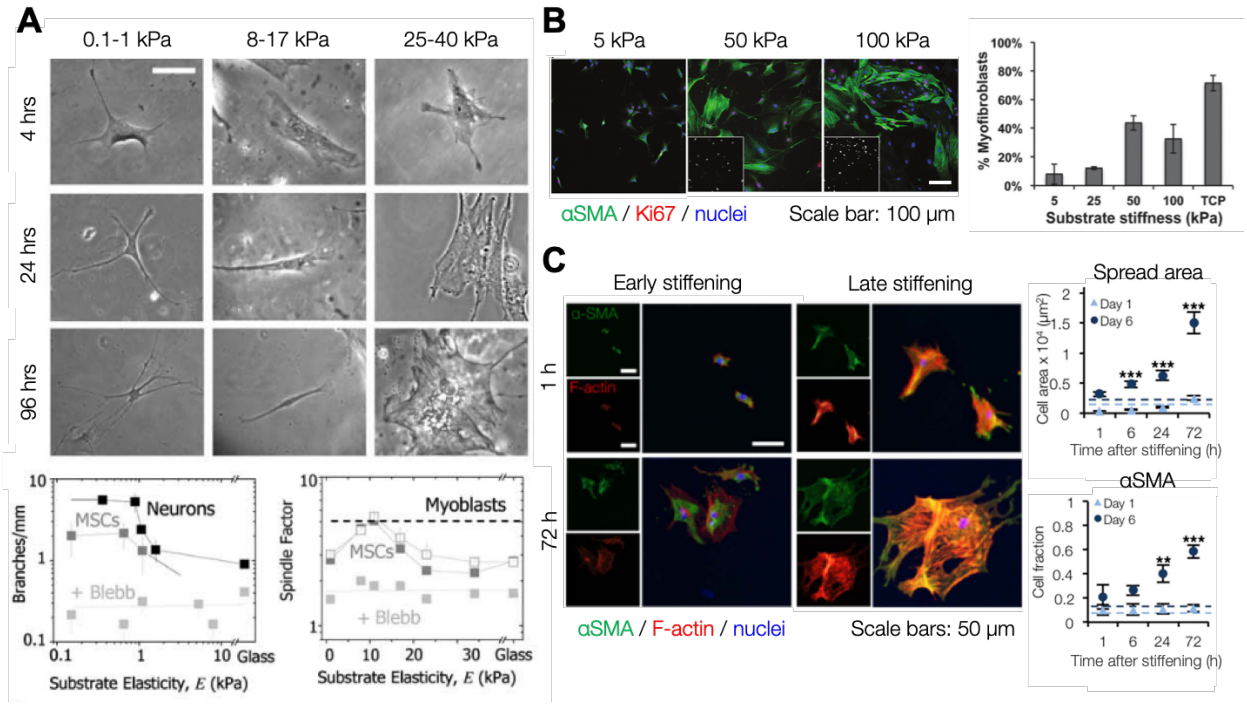

Figure 1.4. Substrate stiffness influences cell behavior. (A) Phase images show changes in cell shape and spreading over time depending on hydrogel stiffness. Cells exhibited branching, spindles, and polygonal morphologies when cultured on hydrogels mimicking brain, muscle, and collagenous bone, respectively. Cell branching per length of neurons, MSCs, and blebbistatin-treated MSCs and spindle morphology of MSCs compared to myoblasts show lineage specification. Scale bar: 20 μm. Figure adapted from[47]. (B) Lung myofibroblast percentage and proliferation increased as a function of stiffness on collagen-coated silicone substrates ranging from 5 kPa to tissue culture plastic (TCP). Scale bar: 100 μm. Figure adapted from[164]. (C) Hepatic stellate cells (HSCs) on soft hyaluronic acid hydrogels that were stiffened later in the culture period exhibited more rapid spreading and α-SMA stress fiber organization compared to HSCs that were stiffened after 1 day. Immunofluorescent images are at 1 hour and 72 hours following stiffening. Scale bars: 50 μm. Figure adapted from[165].

More recently, evidence pointing to increasing matrix stiffness as a contributing factor of pathological outcomes such as fibrosis reveals the importance of mechanical inputs toward disease progression. On 2D cultures, increasing matrix stiffness has directly correlated with increased cell spread area stress fiber formation and organization, and nuclear localization of transcriptional co-activators involved in disease[133,154,166]. Balestrini *et al*. showed increasing lung fibroblast activation on stiffer 2D cultures (E > 25 kPa), characterized by greater cell spread area, contractility, α-SMA organization, TGF-β1 expression, and proliferation (**Figure 1.4B**)[164]. Increased nuclear localization of YAP/TAZ has also been shown for MSCs on stiffer elastic 2D hydrogels[93,121]. Nuclear YAP/TAZ trends have also been correlated with increased cell spreading and elongation on 2D cultures. Conversely, decreased YAP/TAZ nuclear translocation has been reported in stiffer 3D substrates, along with more rounded morphologies and decreased contractility[121].

Mechanically dynamic substrates have also been developed to explore time-dependent mechanotransduction events. *In situ* photostiffening of 2D hydrogels (E ~ 3 to 37 kPa), mimicking fibrosis, increased cardiac fibroblast spread area and promoted myofibroblast activation, as

measured by the increase in α-SMA staining[133]. Caliari *et al.* demonstrated temporal effects of substrate stiffening; hepatic stellate cells (HSCs) cultured on compliant HA hydrogels (E ~ 2 kPa) that were subjected to later substrate stiffening (E ~ 33 kPa) within the first week of culture exhibited quicker cell spreading and α-SMA stress fiber formation compared to HSCs that were exposed to stiffening earlier in the culture period (**Figure 1.4C**)[165].

1.4.1.2 Viscoelasticity

Viscoelasticity has recently emerged as an important parameter for probing cell behaviors and functions – most biological tissues display viscoelastic behaviors such as time-dependent stress relaxation, corresponding to a decreased resistance to deformation over time[110,136,167–170]. Soft tissues such as brain, liver, and lung report loss moduli (G") within an order of magnitude of their storage moduli (G'), typically 10% to 20%[170–172]. The rate of stress relaxation can also vary depending on tissue type; most biological tissues will experience partial relaxation within seconds to minutes (**Figure 1.5A**)[110,173,174]. Notably, viscoelasticity has been shown to alter disease-relevant behaviors such as cell spreading, actin stress fiber formation, and nuclear localization of transcriptional co-activators involved in mechanotransduction[27,41]. Therefore, it has been of interest to develop viscoelastic hydrogel systems to study the effect of time-dependent parameters such as stress relaxation on cellular outcomes.

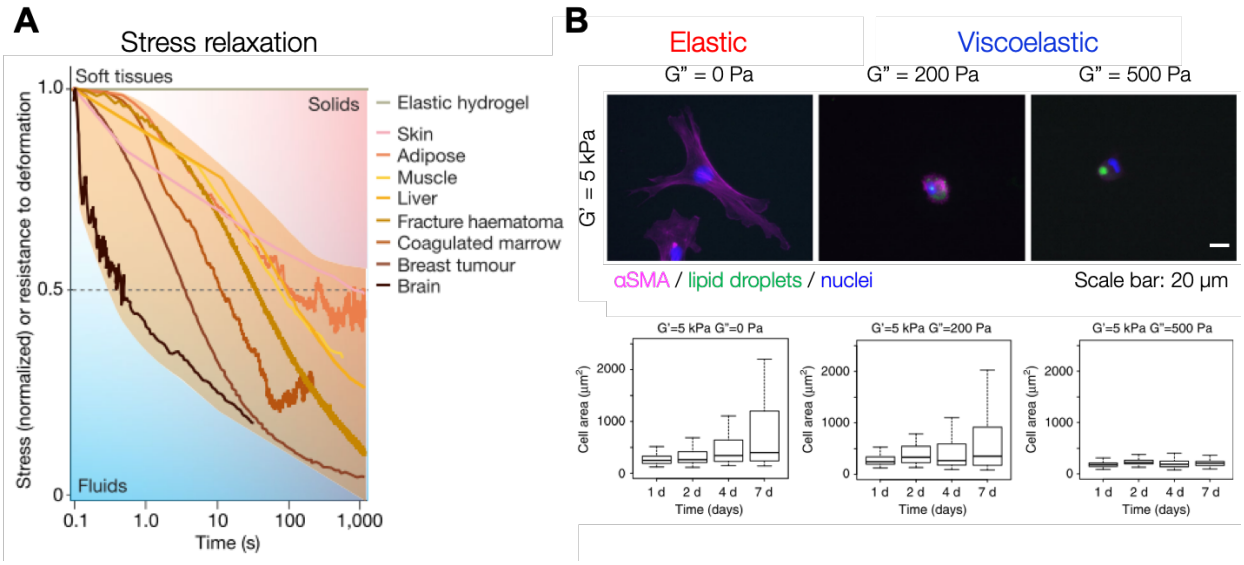

Figure 1.5. Biological tissues are viscoelastic and exhibit stress relaxation. (A) At a constant strain, most soft tissues exhibit time-dependent stress relaxation, and the extent of relaxation varies based on tissue type, region, and physiological state. Figure adapted from[17]. (B) Primed myofibroblasts showed increased spreading and the expression of α-SMA. As hydrogel viscoelasticity increased (greater G" while G' was constant), myofibroblasts reduced in area and de-differentiated, as characterized by lipid droplet restoration. Scale bar: 20 μm. Figure adapted from[135].

Recent work utilizing solid viscoelastic substrates has highlighted changes in cell morphologies and gene expression correlating with increasing loss modulus (G")[135,175]. Charrier *et al*. designed a viscoelastic hydrogel system consisting of high molecular weight linear polyacrylamide (PA) sterically trapped within a covalently crosslinked PA matrix, enabling energy dissipation into the matrix from the slowly relaxing linear PA chains[135]. Fibroblasts on viscoelastic hydrogels with greater G" displayed smaller cell areas compared to on purely elastic hydrogels due to viscous dissipation inhibiting integrin clustering, large focal adhesion formation, and cell spreading (**Figure 1.5B**). Differentiation of hepatic stellate cells into myofibroblasts decreased as G" increased even as G' remained constant, suggesting that viscous interactions play an important

role in cell fate and viscoelastic hydrogel systems can be used to understand normal and pathological cell behaviors.

1.4.1.3 Adhesive ligand presentation

The functionalization and presentation of adhesive ligands is important for various tissue engineering and biomaterials applications, including as hydrogel scaffolds, biomolecule delivery systems, and for developing *in vitro* models to study cell-matrix interactions[176–178]. The majority of adhesions are through integrins that allow bidirectional signaling to occur between the cell and ECM (Section 1.3.1). The most common method of mediating cell adhesion to hydrogel substrates is using the synthetic arginine-glycine-aspartic acid (RGD) tripeptide[179,180]. The native RGD sequence is found in several ECM proteins, most notably fibronectin, and can bind to multiple integrin heterodimers. The RGD peptide can be easily synthesized and incorporated into biomaterials at controlled densities, making it advantageous for regulating cell adhesion. It can also promote attachment of multiple cell types. An important parameter to consider is substrate bioactivity, which can be regulated by adhesive ligand density. Several studies have explored the influence of ligand density on differential cell behaviors. Wen *et al.* decoupled substrate stiffness, porosity, and adhesion, and observed that stem cell differentiation occurred independent of adhesive ligand density[154]. Interestingly, Ye *et al*. observed stiffness-dependent increases in MSC count, spread area, and F-actin organization as a function of decreased RGD nanospacing (47 nm versus 135 nm) (**Figure 1.6A**)[181]. In a breast cancer model, Fisher *et al.* showed that an increase in RGD density correlated with breast cancer cell proliferation but did not influence invasion into the hydrogel[182].

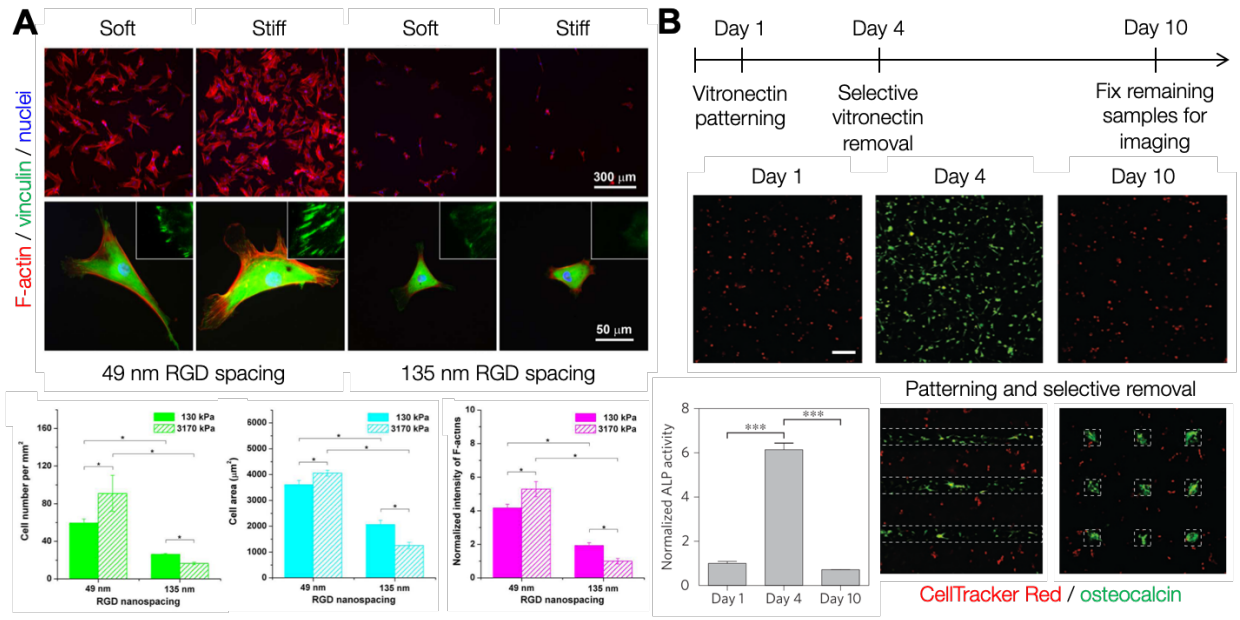

Figure 1.6. Adhesive ligand presentation influences cell behaviors. (A) Mesenchymal stem cells on RGD-patterned PEG hydrogels with lower ligand spacing demonstrated increased proliferation, spread area, F-actin organization, and focal adhesion maturation. Scale bars: 300 μm *(top),* 50 μm *(bottom).* Figure adapted from[181]. (B) Fluorescently labeled hMSCs encapsulated within PEG hydrogels were homogeneously or spatially patterned with vitronectin on day 1. On day 4, hMSCs displayed spread morphologies and stained positive for osteocalcin (OC), a marker of osteogenic differentiation. Subsequent removal of vitronectin on day 4 led to cell detachment and more rounded morphologies coupled with decreased OC staining. Alkaline phosphatase (ALP) activity correlated with OC trends. For patterned substrates, patterned removal of vitronectin resulted in OC staining only in the vitronectin-positive regions. Scale bar: 200 μm. Figure adapted from[183].

A confounding factor of the RGD sequence is that it engages in multiple integrin heterodimers and has a lower binding affinity compared to larger peptide or protein domains – the GRGDSP hexapeptide is around 1000 times less effective in cell attachment compared to fibronectin itself[179,184]. Alternate studies have functionalized protein domains such as collagen[153,185], laminin[186,187], vitronectin[183,188], and fibronectin[189,190] for cell adhesion to hydrogel systems. Expanding on previous efforts[191,192], DeForest *et al.* used a photoreversible patterning approach to spatially introduce vitronectin in a 3D culture system (**Figure 1.6B**)[183]. MSCs encapsulated in hydrogels with tethered vitronectin ligands exhibited spreading and osteogenic lineage

specification, measured by osteocalcin (OC) immunostaining and alkaline phosphatase (ALP) activity. After vitronectin was photoreleased, both OC staining and ALP activity reduced to pre-differentiation levels, demonstrating independent and spatiotemporal control over the presentation of bioactive molecules. Integrin specificity can also be modulated through engineered protein fragments to understand how preferential integrin engagement may influence cell behaviors during disease progression. Cao *et al.* designed engineering fibronectin fragments spanning the 9th and 10th type III repeats to include both the RGD and PHSRN synergy sequences[190]. By inserting leucine to proline point mutation, the spatial and angular orientation of PHSRN was stabilized with respect to RGD, increasing selectivity to β1 integrins. In contrast, insertion of a four glycine linker between the 9th and 10th type III repeats increased the distance between the PHSRN and RGD sites, leading to preferential αvβ3 engagement.

1.4.1.4 Tissue mechanical heterogeneity

Biological tissues are inherently heterogeneous, particularly during disease progression (**Figure 1.7A**). For example, during fibrosis, activated fibroblasts will begin to deposit excessive ECM proteins such as collagen and fibronectin, leading to nodules of nonfunctional scar tissue[44,193]. As such, there have been efforts to recapitulate spatiotemporally heterogeneous mechanics in a well-controlled manner to model the dynamic behavior and investigate cell phenomena. Recent work using light-based chemistries to spatially pattern mechanics has shown that cells responded according to their local environment[148,194–198]. Commonly, the use of a photomask transparency over a hydrogel has enabled the introduction of secondary crosslinking in the exposed regions, resulting in well-defined areas of increased mechanics (e.g., stiffness)[148,196]. Cells cultured on patterned substrates have demonstrated increased cell spread area and α-SMA stress fibers.

Interestingly, feature size also played a role in cell morphology; HSCs cultured on elastic hydrogels with smaller stiff circular regions (diameter ≤ 100 μm) led to smaller and more quiescent HSCs due to cell crowding (**Figure 1.7B**)[196]. Similarly, Lueckgen *et al.* developed a hydrogel system capable of spatially patterning stiffness as well as biomolecule presentation and degradation[199]. On stiffness-patterned hydrogels, fibroblasts assumed an adipogenic and osteogenic lineage on soft and stiff regions, respectively. Fibroblasts on stiffer striped regions also aligned in the direction of the striped pattern while also increasing in both spread area and elongation. Spatiotemporal control over ligand presentation (e.g., adhesive cues and bioactive molecules) has also shown utility in several hydrogel systems, illustrating the ability to design instructive hydrogels for cell mechanobiology investigations[178].

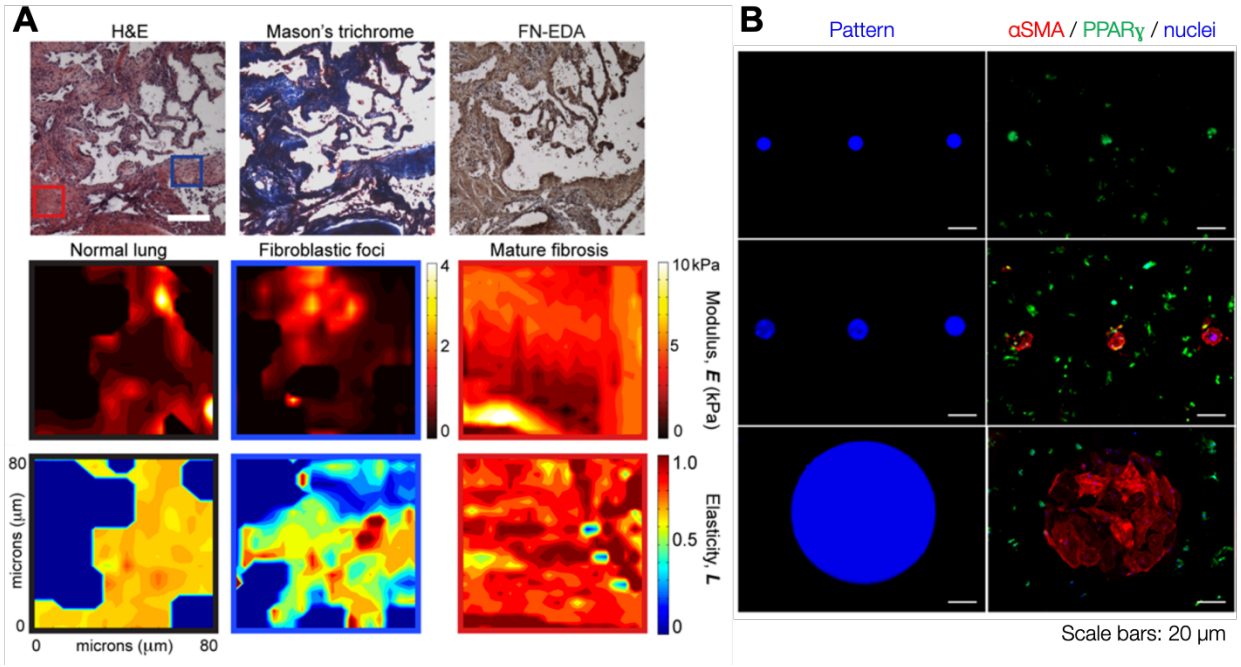

Figure 1.7. Spatiotemporal tissue and hydrogel heterogeneity. (A) *Top*: Fibrotic lung tissue stained for hematoxylin & eosin (H&E), Masson's trichrome, and fibronectin-EDA (Fn-EDA) reveal significant heterogeneity. *Middle*: Atomic force microscopy (AFM) maps of Young's moduli, E, for normal lung, fibroblastic foci, and mature fibrosis regions are more compliant compared to mature fibrotic tissue. *Bottom*: AFM maps of elasticity, L, show that during fibrosis progression, tissue mechanics transition from soft and nonlinearly elastic to stiff and linearly elastic. Interestingly, both normal lung and fibroblast foci tissue regions show nonlinear elasticity, but

spatial gradients are more prominent for fibroblastic foci. Scale bar: 100 μm. Figure adapted from[41]. (B) Hepatic stellate cells (HSCs) on hyaluronic acid hydrogels with patterned stiffness show feature size-dependent changes in cell morphologies. Outside of stiff patterns, cells stained positive for PPARɣ, characteristic of quiescent HSCs. Cells on smaller pattern sizes retained smaller cell areas and stained positive for PPARɣ. In contrast, HSCs on larger stiff patterns were able to spread and activate into myofibroblasts, indicated by α-SMA expression and organization. Scale bars: 20 μm. Figure adapted from[196].

1.4.2 Characterization of substrate mechanics

As discussed in Section 1.4, hydrogels are valuable cell culture models that can recapitulate the mechanical and biochemical properties of soft biological tissues. Specifically, the mechanical environment of tissue states has been recognized as a critical regulator of cell behaviors[9,19,22]. As such, it is important to be able to precisely characterize the mechanical properties of tissues and hydrogel to develop accurate and reproducible *in vitro* models for understanding cell-matrix interactions. Two common hydrogel (and tissue) characterization techniques, rheology and nanoindentation, are emphasized here.

1.4.1.1 Rheology

A common technique that has been used to mechanically characterize hydrogels (and tissues) is through oscillatory shear rheology, which measures the flow and deformation of a bulk material. Rheology can be done quickly, requires small sample sizes, and can help elucidate the influence of hydrogel parameters such as crosslinking density and polymer molecular weight on bulk mechanics[200]. For *in situ* characterization, a precursor solution can be pipetted between a fixed bottom plate and a top (cone) plate with a specified gap and angle. The top rotating plate then shears the material at a specific speed and the resulting shear stress from the resistance to the rotation can be determined. The shear storage (G') and loss (G") modulus, which is the ratio between the applied strain and resulting stress, can be used to calculate the stiffness and

viscoelasticity of the material, respectively. Typical G' and G" units are in Pascals (or N/m^2). Substrate viscoelasticity can be determined by the ratio between G" and G' – a greater ratio is indicative of increasing viscous character. Frequency sweeps, which measure G' and G" over a range of frequencies, can be used to understand frequency-dependent behavior of hydrogels and how they respond to increasing oscillations. Stress relaxation and recovery tests provide a measure of the extent and rate of relaxation at a constant applied strain; stress relaxation is a key characteristic of soft viscoelastic tissues. Similarly, creep tests can be used to determine the amount of deformation, or strain, a material experiences at a constant applied stress. Many of these rheological characterization methods have been utilized in characterizing bulk hydrogel properties prior to cell culture studies but are limited in characterizing heterogeneous materials at the micro- or nano-scales.

1.4.1.2 Indentation

Indentation techniques such as nanoindentation and atomic force microscopy (AFM) have been used to spatially characterize local hydrogel (and tissue) mechanics in physiologically-relevant environments[170,201–207]. Typically, a probe of known diameter and stiffness will be used to deform a material surface at a controlled force or distance. As a result, the indentation (loading) and removal (unloading) of the probe from the material can be used to calculate substrate stiffness, or Young's modulus (E), through relevant contact models such as the Hertz and Ogden models[208–210].

The use of indentation has been most powerful in characterizing heterogeneous materials at the local level, relevant to cell sensing[148,211,212]. Probe sizes can range from nanometers to millimeters

in diameter and probe stiffness spans orders of magnitude and can indent from soft, mucus-like materials to bone-relevant stiffnesses[208]. AFM, a type of scanning probe microscopy, can be coupled with indentation techniques to spatially characterize the mechanics of biological substrates and cells with high resolution[202,204,213]. Traditional AFM-based indentation involves measuring deflection changes due to cantilever bending through the reflection of a laser light into a photodiode. However, some limitations of using AFM include increased operation complexity, limited cantilever working range, and incompatibility with higher throughput set-ups (e.g., 96-well plates)[214,215]. Small scale indentation, or nanoindentation, has recently emerged as a user-friendly method for mechanical testing of hydrogels, tissues, and cells[100,208,216–218]. Nanoindentation methods have utilized capacitance gauges, speaker coils, and optical interferometry to output mechanical measurements of biological samples[170,214]. In particular, recent work using optical-based nanoindentation has demonstrated the ability to study mechanical properties on a larger testing scale, in high throughput modalities such as well plates, and in a semi-automatic capacity[214,219].

Another feature of indentation is the ability to characterize time-dependent properties such as viscoelasticity. By indenting the probe to a constant depth (or force) and holding, force relaxation metrics can reveal substrate viscoelasticity[204]. Additionally, some nanoindentation approaches have evolved to include dynamic mechanical analysis (DMA)-like tests that enable frequency-dependent behavior to be measured via mechanical oscillations in the z-direction during indentation. Young's modulus (E), or elastic modulus, can be related to shear storage (G') and loss (G") moduli through the Poisson's ratio, which typically falls around 0.5 for most hydrogels and soft tissues[202,204,220].

1.5 Research objectives

Overall, the goal of this thesis is to develop a class of mechanically dynamic and spatiotemporally heterogeneous hyaluronic acid hydrogels with independent tuning of stiffness, viscoelasticity, and adhesive ligand presentation to understand how physical and chemical cues collectively influence cell behaviors in fibrosis.

Chapter 2 reviews the advancement of click-based hydrogel models as cell culture systems for studying mechanobiology. Chapter 3 illustrates the characterization of time-dependent parameters such as stress relaxation and frequency-dependent behavior of *ex vivo* rat lung tissues using nanoindentation to inform biomaterial design. Chapter 4 covers the development of a phototunable hyaluronic acid hydrogel system offering spatiotemporal control over stiffness and viscoelasticity to investigate the role of matrix mechanical properties in regulating fibrosis-relevant cell behaviors. Chapter 5 describes the individual and combined roles of viscoelastic and adhesive cues in fibroblast-activating behaviors such as cell spread area, stress fiber organization, and focal adhesion formation. Chapter 6 investigates the impact of viscoelasticity on fibroblast and mesenchymal stem cell behavior in 3D hydrogel models. Chapter 7 concludes the thesis with a summary of the presented work and expands on potential avenues for ongoing and future work in the biomaterials field.

1.6 References

(1) Frantz, C.; Stewart, K. M.; Weaver, V. M. The Extracellular Matrix at a Glance. *J. Cell Sci.* **2010**, *123* (24), 4195–4200. https://doi.org/10.1242/jcs.023820.

(2) Hynes, R. O. The Extracellular Matrix: Not Just Pretty Fibrils. *Science (80-.).* **2009**, *326* (5957), 1216–1219. https://doi.org/10.1126/science.1176009.

(3) Kular, J. K.; Basu, S.; Sharma, R. I. The Extracellular Matrix: Structure, Composition, Age-Related Differences, Tools for Analysis and Applications for Tissue Engineering. *J. Tissue Eng.* **2014**, *5*. https://doi.org/10.1177/2041731414557112.

(4) Theocharis, A. D.; Skandalis, S. S.; Gialeli, C.; Karamanos, N. K. Extracellular Matrix Structure. *Adv. Drug Deliv. Rev.* **2016**, *97*, 4–27. https://doi.org/10.1016/j.addr.2015.11.001.

(5) Kusindarta, D. L.; Wihadmadyatami, H. The Role of Extracellular Matrix in Tissue Regeneration. In *Tissue Regeneration*; 2018.

(6) Lander, A. D.; Selleck, S. B. The Elusive Functions of Proteoglycans: In Vivo Veritas. *J. Cell Biol.* **2000**, *148* (2), 227–232. https://doi.org/10.1083/jcb.148.2.227.

(7) Walimbe, T.; Panitch, A. Proteoglycans in Biomedicine: Resurgence of an Underexploited Class of ECM Molecules. *Front. Pharmacol.* **2020**, *10* (January), 1–13. https://doi.org/10.3389/fphar.2019.01661.

(8) Yue, B. Biology of the Extracellular Matrix: An Overview. *J. Glaucoma* **2014**, *23* (8), S20–S23. https://doi.org/10.1097/IJG.0000000000000108.

(9) Wells, R. G. Tissue Mechanics and Fibrosis. *Biochim. Biophys. Acta - Mol. Basis Dis.* **2013**, *1832* (7), 884–890. https://doi.org/10.1016/j.bbadis.2013.02.007.

(10) Barnes, J. M.; Przybyla, L.; Weaver, V. M. Tissue Mechanics Regulate Brain Development, Homeostasis and Disease. *J. Cell Sci.* **2017**, *130* (1), 71–82. https://doi.org/10.1242/jcs.191742.

(11) Guimarães, C. F.; Gasperini, L.; Marques, A. P.; Reis, R. L. The Stiffness of Living Tissues and Its Implications for Tissue Engineering. *Nat. Rev. Mater.* **2020**, *5* (5), 351–370. https://doi.org/10.1038/s41578-019-0169-1.

(12) Camasão, D. B.; Pezzoli, D.; Loy, C.; Kumra, H.; Levesque, L.; Reinhardt, D. P.; Candiani, G.; Mantovani, D. Increasing Cell Seeding Density Improves Elastin Expression and Mechanical Properties in Collagen Gel-Based Scaffolds Cellularized with Smooth Muscle

Cells. *Biotechnol. J.* **2019**, *14* (3), 1–12. https://doi.org/10.1002/biot.201700768.

(13) Zhang, C.; Qian, L.; Zhao, H. Elucidation of Regional Mechanical Properties of Brain Tissues Based on Cell Density. *J. Bionic Eng.* **2021**, *18* (3), 611–622. https://doi.org/10.1007/s42235-021-0047-6.

(14) Blumlein, A.; Williams, N.; McManus, J. J. The Mechanical Properties of Individual Cell Spheroids. *Sci. Rep.* **2017**, *7* (1), 1–10. https://doi.org/10.1038/s41598-017-07813-5.

(15) Zhang, J.; Wehrle, E.; Adamek, P.; Paul, G. R.; Qin, X. H.; Rubert, M.; Müller, R. Optimization of Mechanical Stiffness and Cell Density of 3D Bioprinted Cell-Laden Scaffolds Improves Extracellular Matrix Mineralization and Cellular Organization for Bone Tissue Engineering. *Acta Biomater.* **2020**, *114*, 307–322. https://doi.org/10.1016/j.actbio.2020.07.016.

(16) Handorf, A. M.; Zhou, Y.; Halanski, M. A.; Li, W. J. Tissue Stiffness Dictates Development, Homeostasis, and Disease Progression. *Organogenesis* **2015**, *11* (1), 1–15. https://doi.org/10.1080/15476278.2015.1019687.

(17) Chaudhuri, O.; Cooper-White, J.; Janmey, P. A.; Mooney, D. J.; Shenoy, V. B. Effects of Extracellular Matrix Viscoelasticity on Cellular Behaviour. *Nature* **2020**, *584* (7822), 535–546. https://doi.org/10.1038/s41586-020-2612-2.

(18) Wynn, T. Cellular and Molecular Mechanisms of Fibrosis. *J. Pathol.* **2008**, *214*, 199–210.

(19) Thorne, J. T.; Segal, T. R.; Chang, S.; Jorge, S.; Segars, J. H.; Leppert, P. C. Dynamic Reciprocity between Cells and Their Microenvironment in Reproduction. *Biol. Reprod.* **2015**, *92* (1), 1–10. https://doi.org/10.1095/biolreprod.114.121368.

(20) Xu, R.; Boudreau, A.; Bissell, M. J. Tissue Architecture and Function: Dynamic Reciprocity via Extra- and Intra-Cellular Matrices. *Cancer Metastasis Rev.* **2009**, *28* (1–2), 167–176. https://doi.org/10.1007/s10555-008-9178-z.

(21) Schultz, G. S.; Davidson, J. M.; Kirsner, R. S.; Bornstein, P.; Herman, I. M. Dynamic Reciprocity in the Wound Microenvironment. *Wound Repair Regen.* **2011**, *19* (2), 134–148. https://doi.org/10.1111/j.1524-475X.2011.00673.x.

(22) Lim, C. T.; Bershadsky, A.; Sheetz, M. P. Mechanobiology. *J. R. Soc. Interface* **2010**, *7*, S291–S293. https://doi.org/10.1098/rsif.2010.0150.focus.

(23) Humphrey, J. D.; Dufresne, E. R.; Schwartz, M. A. Mechanotransduction and Extracellular Matrix Homeostasis. *Nat. Rev. Mol. Cell Biol.* **2014**, *15* (12), 802–812.

https://doi.org/10.1038/nrm3896.

(24) Jansen, K. A.; Atherton, P.; Ballestrem, C. Mechanotransduction at the Cell-Matrix Interface. *Semin. Cell Dev. Biol.* **2017**, *71*, 75–83. https://doi.org/10.1016/j.semcdb.2017.07.027.

(25) Santos, A.; Lagares, D. Matrix Stiffness: The Conductor of Organ Fibrosis. *Current Rheumatology Reports*. Current Rheumatology Reports 2018. https://doi.org/10.1007/s11926-018-0710-z.

(26) Klingberg, F.; Hinz, B.; White, E. S. The Myofibroblast Matrix: Implications for Tissue Repair and Fibrosis. *Journal of Pathology*. 2013, pp 298–309. https://doi.org/10.1002/path.4104.

(27) Liu, F.; Mih, J. D.; Shea, B. S.; Kho, A. T.; Sharif, A. S.; Tager, A. M.; Tschumperlin, D. J. Feedback Amplification of Fibrosis through Matrix Stiffening and COX-2 Suppression. *J. Cell Biol.* **2010**, *190* (4), 693–706. https://doi.org/10.1083/jcb.201004082.

(28) Zhao, X. H.; Laschinger, C.; Arora, P.; Szászi, K.; Kapus, A.; McCulloch, C. A. Force Activates Smooth Muscle α-Actin Promoter Activity through the Rho Signaling Pathway. *J. Cell Sci.* **2007**, *120* (10), 1801–1809. https://doi.org/10.1242/jcs.001586.

(29) Midwood, K. S.; Schwarzbauer, J. E. Elastic Fibers : Building Bridges Between Cells and Their Matrix. *Curr. Biol.* **2002**, *12* (02), 279–281.

(30) Sherratt, M. J. Tissue Elasticity and the Ageing Elastic Fibre. *Age (Omaha).* **2009**, *31* (4), 305–325. https://doi.org/10.1007/s11357-009-9103-6.

(31) Cox, T. R.; Erler, J. T. Remodeling and Homeostasis of the Extracellular Matrix: Implications for Fibrotic Diseases and Cancer. *DMM Dis. Model. Mech.* **2011**, *4* (2), 165–178. https://doi.org/10.1242/dmm.004077.

(32) Tomasek, J. J.; Gabbiani, G.; Hinz, B.; Chaponnier, C.; Brown, R. A. Myofibroblasts and Mechano: Regulation of Connective Tissue Remodelling. *Nat. Rev. Mol. Cell Biol.* **2002**, *3* (5), 349–363. https://doi.org/10.1038/nrm809.

(33) Wynn, T. A.; Ramalingam, T. R. Mechanisms of Fibrosis: Therapeutic Translation for Fibrotic Disease. *Nat. Med.* **2012**, *18* (7), 1028–1040. https://doi.org/10.1038/nm.2807.

(34) Wynn, T. A. Integrating Mechanisms of Pulmonary Fibrosis. *J. Exp. Med.* **2011**, *208* (7), 1339–1350. https://doi.org/10.1084/jem.20110551.

(35) Smith, M.; Dalurzo, M.; Panse, P.; Parish, J.; Leslie, K. Usual Interstitial Pneumonia-Pattern

Fibrosis in Surgical Lung Biopsies. Clinical, Radiological and Histopathological Clues to Aetiology. *J. Clin. Pathol.* **2013**, *66* (10), 896–903. https://doi.org/10.1136/jclinpath-2013-201442.

(36) Chin, L. K.; Xia, Y.; Discher, D. E.; Janmey, P. A. Mechanotransduction in Cancer. *Curr. Opin. Chem. Eng.* **2016**, *11*, 77–84. https://doi.org/10.1016/j.coche.2016.01.011.

(37) Pakshir, P.; Hinz, B. The Big Five in Fibrosis: Macrophages, Myofibroblasts, Matrix, Mechanics, and Miscommunication. *Matrix Biol.* **2018**, *68–69* (2017), 81–93. https://doi.org/10.1016/j.matbio.2018.01.019.

(38) Plantier, L.; Cazes, A.; Dinh-Xuan, A. T.; Bancal, C.; Marchand-Adam, S.; Crestani, B. Physiology of the Lung in Idiopathic Pulmonary Fibrosis. *Eur. Respir. Rev.* **2018**, *27* (147), 1–14. https://doi.org/10.1183/16000617.0062-2017.

(39) Booth, A. J.; Hadley, R.; Cornett, A. M.; Dreffs, A. A.; Matthes, S. A.; Tsui, J. L.; Weiss, K.; Horowitz, J. C.; Fiore, V. F.; Barker, T. H.; et al. Acellular Normal and Fibrotic Human Lung Matrices as a Culture System for in Vitro Investigation. *Am. J. Respir. Crit. Care Med.* **2012**, *186* (9), 866–876. https://doi.org/10.1164/rccm.201204-0754OC.

(40) Sundarakrishnan, A.; Chen, Y.; Black, L. D.; Aldridge, B. B.; Kaplan, D. L. Engineered Cell and Tissue Models of Pulmonary Fibrosis. *Adv. Drug Deliv. Rev.* **2018**, *129*, 78–94. https://doi.org/10.1016/j.addr.2017.12.013.

(41) Fiore, V. F.; Wong, S. S.; Tran, C.; Tan, C.; Xu, W.; Sulchek, T.; White, E. S.; Hagood, J. S.; Barker, T. H. Avβ3 Integrin Drives Fibroblast Contraction and Strain Stiffening of Soft Provisional Matrix during Progressive Fibrosis. *JCI insight* **2018**, *3* (20), 1–35. https://doi.org/10.1172/jci.insight.97597.

(42) Cool, C. D.; Groshong, S. D.; Rai, P. R.; Henson, P. M.; Stewart, J. S.; Brown, K. K. Fibroblast Foci Are Not Discrete Sites of Lung Injury or Repair: The Fibroblast Reticulum. *Am. J. Respir. Crit. Care Med.* **2006**, *174* (6), 654–658. https://doi.org/10.1164/rccm.200602-205OC.

(43) Jones, M. G.; Fabre, A.; Schneider, P.; Cinetto, F.; Sgalla, G.; Mavrogordato, M.; Jogai, S.; Alzetani, A.; Marshall, B. G.; O'Reilly, K. M. A.; et al. Three-Dimensional Characterization of Fibroblast Foci in Idiopathic Pulmonary Fibrosis. *JCI Insight* **2016**, *1* (5), 1–11. https://doi.org/10.1172/JCI.INSIGHT.86375.

(44) Duscher, D.; Maan, Z. N.; Wong, V. W.; Rennert, R. C.; Januszyk, M.; Rodrigues, M.; Hu,

M.; Whitmore, A. J.; Whittam, A. J.; Longaker, M. T.; et al. Mechanotransduction and Fibrosis. *J. Biomech.* **2014**, *47* (9), 1997–2005. https://doi.org/10.1016/j.jbiomech.2014.03.031.

(45) Van Helvert, S.; Storm, C.; Friedl, P. Mechanoreciprocity in Cell Migration. *Nat. Cell Biol.* **2018**, *20* (1), 8–20. https://doi.org/10.1038/s41556-017-0012-0.

(46) Wang, N.; Tytell, J. D.; Ingber, D. E. Mechanotransduction at a Distance: Mechanically Coupling the Extracellular Matrix with the Nucleus. *Nat. Rev. Mol. Cell Biol.* **2009**, *10* (1), 75–82. https://doi.org/10.1038/nrm2594.

(47) Engler, A. J.; Sen, S.; Sweeney, H. L.; Discher, D. E. Matrix Elasticity Directs Stem Cell Lineage Specification. *Cell* **2006**, *126* (4), 677–689. https://doi.org/10.1016/j.cell.2006.06.044.

(48) Wells, R. G. The Role of Matrix Stiffness in Regulating Cell Behavior. *Hepatology* **2008**, *47* (4), 1394–1400. https://doi.org/10.1002/hep.22193.

(49) Nam, S.; Lee, J.; Brownfield, D. G.; Chaudhuri, O. Viscoplasticity Enables Mechanical Remodeling of Matrix by Cells. *Biophys. J.* **2016**, *111* (10), 2296–2308. https://doi.org/10.1016/j.bpj.2016.10.002.

(50) Oria, R.; Wiegand, T.; Escribano, J.; Elosegui-Artola, A.; Uriarte, J. J.; Moreno-Pulido, C.; Platzman, I.; Delcanale, P.; Albertazzi, L.; Navajas, D.; et al. Force Loading Explains Spatial Sensing of Ligands by Cells. *Nature* **2017**, *552* (7684), 219–224. https://doi.org/10.1038/nature24662.

(51) Burridge, K.; Guilluy, C. Focal Adhesions, Stress Fibers and Mechanical Tension. *Exp. Cell Res.* **2016**, *343* (1), 14–20. https://doi.org/10.1016/j.yexcr.2015.10.029.

(52) Kechagia, J. Z.; Ivaska, J.; Roca-Cusachs, P. Integrins as Biomechanical Sensors of the Microenvironment. *Nat. Rev. Mol. Cell Biol.* **2019**, *20* (8), 457–473. https://doi.org/10.1038/s41580-019-0134-2.

(53) Roca-Cusachs, P.; Iskratsch, T.; Sheetz, M. P. Finding the Weakest Link-Exploring Integrin-Mediated Mechanical Molecular Pathways. *J. Cell Sci.* **2012**, *125* (13), 3025–3038. https://doi.org/10.1242/jcs.095794.

(54) Wang, N. Instant Integrin Mechanosensing. *Nat. Mater.* **2017**, *16* (12), 1173–1174. https://doi.org/10.1038/nmat5041.

(55) Driscoll, T. P.; Ahn, S. J.; Huang, B.; Kumar, A.; Schwartz, M. A. Actin Flow-Dependent

and -Independent Force Transmission through Integrins. *Proc. Natl. Acad. Sci. U. S. A.* **2020**, *117* (51), 32413–32422. https://doi.org/10.1073/pnas.2010292117.

(56) Gardel, M. L.; Schneider, I. C.; Aratyn-Schaus, Y.; Waterman, C. M. Mechanical Integration of Actin and Adhesion Dynamics in Cell Migration. *Annu. Rev. Cell Dev. Biol.* **2010**, *26* (1), 315–333. https://doi.org/10.1146/annurev.cellbio.011209.122036.

(57) Mohammed, D.; Versaevel, M.; Bruyère, C.; Alaimo, L.; Luciano, M.; Vercruysse, E.; Procès, A.; Gabriele, S. Innovative Tools for Mechanobiology: Unraveling Outside-In and Inside-Out Mechanotransduction. *Frontiers in Bioengineering and Biotechnology*. 2019.

(58) Henderson, N. C.; Sheppard, D. Integrin-Mediated Regulation of TGFβ in Fibrosis. *Biochim. Biophys. Acta - Mol. Basis Dis.* **2013**, *1832* (7), 891–896. https://doi.org/10.1016/j.bbadis.2012.10.005.

(59) Sun, Z.; Guo, S. S.; Fässler, R. Integrin-Mediated Mechanotransduction. **2016**, *215* (4).

(60) Ingber, D. E. Cellular Mechanotransduction: Putting All the Pieces Together Again. *FASEB J.* **2006**, *20* (7), 811–827. https://doi.org/10.1096/fj.05-5424rev.

(61) Choi, C. K.; Vicente-Manzanares, M.; Zareno, J.; Whitmore, L. A.; Mogilner, A.; Horwitz, A. R. Actin and α-Actinin Orchestrate the Assembly and Maturation of Nascent Adhesions in a Myosin II Motor-Independent Manner. *Nat. Cell Biol.* **2008**, *10* (9), 1039–1050. https://doi.org/10.1038/ncb1763.

(62) Kim, M. C.; Neal, D. M.; Kamm, R. D.; Asada, H. H. Dynamic Modeling of Cell Migration and Spreading Behaviors on Fibronectin Coated Planar Substrates and Micropatterned Geometries. *PLoS Comput. Biol.* **2013**, *9* (2). https://doi.org/10.1371/journal.pcbi.1002926.

(63) Maziveyi, M.; Alahari, S. K. Cell Matrix Adhesions in Cancer: The Proteins That Form the Glue. *Oncotarget* **2017**, *8* (29), 48471–48487. https://doi.org/10.18632/oncotarget.17265.

(64) Seong, J.; Wang, N.; Wang, Y. Mechanotransduction at Focal Adhesions: From Physiology to Cancer Development. *J. Cell. Mol. Med.* **2013**, *17* (5), 597–604. https://doi.org/10.1111/jcmm.12045.

(65) Paszek, M. J.; Boettiger, D.; Weaver, V. M.; Hammer, D. A. Integrin Clustering Is Driven by Mechanical Resistance from the Glycocalyx and the Substrate. *PLoS Comput. Biol.* **2009**, *5* (12). https://doi.org/10.1371/journal.pcbi.1000604.

(66) Elosegui-Artola, A.; Trepat, X.; Roca-Cusachs, P. Control of Mechanotransduction by Molecular Clutch Dynamics. *Trends Cell Biol.* **2018**, *28* (5), 356–367.

https://doi.org/10.1016/j.tcb.2018.01.008.

(67) Henderson, N. C.; Arnold, T. D.; Katamura, Y.; Giacomini, M. M.; Rodriguez, J. D.; McCarty, J. H.; Pellicoro, A.; Raschperger, E.; Betsholtz, C.; Ruminski, P. G.; et al. Targeting of Av Integrin Identifies a Core Molecular Pathway That Regulates Fibrosis in Several Organs. *Nat. Med.* **2013**, *19* (12), 1617–1624. https://doi.org/10.1038/nm.3282.

(68) Conroy, K. P.; Kitto, L. J.; Henderson, N. C. Av Integrins: Key Regulators of Tissue Fibrosis. *Cell Tissue Res.* **2016**, *365* (3), 511–519. https://doi.org/10.1007/s00441-016-2407-9.

(69) Fernandez, I. E.; Eickelberg, O. The Impact of TGF-β on Lung Fibrosis: From Targeting to Biomarkers. *Proc. Am. Thorac. Soc.* **2012**, *9* (3), 111–116. https://doi.org/10.1513/pats.201203-023AW.

(70) Leiphart, R. J.; Chen, D.; Peredo, A. P.; Loneker, A. E.; Janmey, P. A. Mechanosensing at Cellular Interfaces. *Langmuir* **2019**, *35* (23), 7509–7519. https://doi.org/10.1021/acs.langmuir.8b02841.

(71) Deng, X.; Jin, K.; Li, Y.; Gu, W.; Liu, M.; Zhou, L. Platelet-Derived Growth Factor and Transforming Growth Factor B1 Regulate ARDS-Associated Lung Fibrosis Through Distinct Signaling Pathways. *Cell. Physiol. Biochem.* **2015**, *36* (3), 937–946. https://doi.org/10.1159/000430268.

(72) Janmey, P. A.; Miller, R. T. Mechanisms of Mechanical Signaling in Development and Disease. *J. Cell Sci.* **2011**, *124* (1), 9–18. https://doi.org/10.1242/jcs.071001.

(73) Dominguez, R.; Holmes, K. C. Actin Structure and Function. *Annu. Rev. Biophys.* **2011**, *40* (1), 169–186. https://doi.org/10.1146/annurev-biophys-042910-155359.

(74) Cingolani, L. A.; Goda, Y. Actin in Action: The Interplay between the Actin Cytoskeleton and Synaptic Efficacy. *Nat. Rev. Neurosci.* **2008**, *9* (5), 344–356. https://doi.org/10.1038/nrn2373.

(75) Ohashi, K.; Fujiwara, S.; Mizuno, K. Roles of the Cytoskeleton, Cell Adhesion and Rho Signalling in Mechanosensing and Mechanotransduction. *J. Biochem.* **2017**, *161* (3), 245–254. https://doi.org/10.1093/jb/mvw082.

(76) Winder, S. J.; Ayscough, K. R. Actin-Binding Proteins. *J. Cell Sci.* **2005**, *118* (4), 651–654. https://doi.org/10.1242/jcs.01670.

(77) Martino, F.; Perestrelo, A. R.; Vinarský, V.; Pagliari, S.; Forte, G. Cellular

Mechanotransduction: From Tension to Function. *Front. Physiol.* **2018**, *9* (JUL), 1–21. https://doi.org/10.3389/fphys.2018.00824.

(78) Tojkander, S.; Gateva, G.; Lappalainen, P. Actin Stress Fibers - Assembly, Dynamics and Biological Roles. *J. Cell Sci.* **2012**, *125* (8), 1855–1864. https://doi.org/10.1242/jcs.098087.

(79) Lehtimäki, J. I.; Rajakylä, E. K.; Tojkander, S.; Lappalainen, P. Generation of Stress Fibers through Myosin-Driven Reorganization of the Actin Cortex. *Elife* **2021**, *10*, 1–43. https://doi.org/10.7554/eLife.60710.

(80) Kassianidou, E.; Kumar, S. A Biomechanical Perspective on Stress Fiber Structure and Function. *Biochim. Biophys. Acta - Mol. Cell Res.* **2015**, *1853* (11), 3065–3074. https://doi.org/10.1016/j.bbamcr.2015.04.006.

(81) McBeath, R.; Pirone, D. M.; Nelson, C. M.; Bhadriraju, K.; Chen, C. S. Cell Shape, Cytoskeletal Tension, and RhoA Regulate Stem Cell Lineage Commitment. *Dev. Cell* **2004**, *6*, 483–495.

(82) Deng, Z.; Jia, Y.; Liu, H.; He, M.; Yang, Y.; Xiao, W.; Li, Y. RhoA/ROCK Pathway: Implication in Osteoarthritis and Therapeutic Targets. *Am. J. Transl. Res.* **2019**, *11* (9), 5324–5331.

(83) Yuan, Y.; Li, M.; To, C. H.; Lam, T. C.; Wang, P.; Yu, Y.; Hu, X.; Ke, B. The Role of the RhoA / ROCK Signaling Pathway in Differentiation. *Biochem. Mol. Biol.* **2018**, *59*, 3619–3629.

(84) Knipe, R. S.; Probst, C. K.; Lagares, D.; Franklin, A.; Spinney, J. J.; Brazee, P. L.; Grasberger, P.; Zhang, L.; Black, K. E.; Sakai, N.; et al. The Rho Kinase Isoforms ROCK1 and ROCK2 Each Contribute to the Development of Experimental Pulmonary Fibrosis. *Am. J. Respir. Cell Mol. Biol.* **2018**, *58* (4), 471–481. https://doi.org/10.1165/rcmb.2017-0075OC.

(85) Marjoram, R. J.; Lessey, E. C.; Burridge, K. Regulation of RhoA Activity by Adhesion Molecules and Mechanotransduction. *Curr. Mol. Med.* **2014**, *14* (2), 199–208. https://doi.org/10.2174/1566524014666140128104541.

(86) Miralles, F.; Posern, G.; Zaromytidou, A. I.; Treisman, R. Actin Dynamics Control SRF Activity by Regulation of Its Coactivator MAL. *Cell* **2003**, *113* (3), 329–342. https://doi.org/10.1016/S0092-8674(03)00278-2.

(87) Gau, D.; Roy, P. SRF'ing and SAP'ing - The Role of MRTF Proteins in Cell Migration. *J.*

Cell Sci. **2018**, *131* (19), 1–11. https://doi.org/10.1242/jcs.218222.

(88) Foster, C. T.; Gualdrini, F.; Treisman, R. Mutual Dependence of the MRTF-SRF and YAP-TEAD Pathways in Cancer-Associated Fibroblasts Is Indirect and Mediated by Cytoskeletal Dynamics. *Genes Dev.* **2017**, *31* (23–24), 2361–2375. https://doi.org/10.1101/gad.304501.117.

(89) Hinson, J. S.; Medlin, M. D.; Lockman, K.; Taylor, J. M.; Mack, C. P. Smooth Muscle Cell-Specific Transcription Is Regulated by Nuclear Localization of the Myocardin-Related Transcription Factors. *Am. J. Physiol. - Hear. Circ. Physiol.* **2007**, *292* (2), H1170–H1180. https://doi.org/10.1152/ajpheart.00864.2006.

(90) Janmey, P. A.; Fletcher, D. A.; Reinhart-King, C. A. Stiffness Sensing by Cells. *Physiol. Rev.* **2020**, *100* (2), 695–724. https://doi.org/10.1152/physrev.00013.2019.

(91) Gupta, M.; Korol, A.; West-Mays, J. A. Nuclear Translocation of Myocardin-Related Transcription Factor-A during Transforming Growth Factor Beta-Induced Epithelial to Mesenchymal Transition of Lens Epithelial Cells. *Mol. Vis.* **2013**, *19* (May), 1017–1028.

(92) O'Connor, J. W.; Gomez, E. W. Cell Adhesion and Shape Regulate TGF-Beta1-Induced Epithelial-Myofibroblast Transition via MRTF-A Signaling. *PLoS One* **2013**, *8* (12), 1–11. https://doi.org/10.1371/journal.pone.0083188.

(93) Dupont, S.; Morsut, L.; Aragona, M.; Enzo, E.; Giulitti, S.; Cordenonsi, M.; Zanconato, F.; Le Digabel, J.; Forcato, M.; Bicciato, S.; et al. Role of YAP/TAZ in Mechanotransduction. *Nature* **2011**, *474* (7350), 179–184. https://doi.org/10.1038/nature10137.

(94) Dey, A.; Varelas, X.; Guan, K. L. Targeting the Hippo Pathway in Cancer, Fibrosis, Wound Healing and Regenerative Medicine. *Nat. Rev. Drug Discov.* **2020**, *19* (7), 480–494. https://doi.org/10.1038/s41573-020-0070-z.

(95) Piersma, B.; Bank, R. A.; Boersema, M. Signaling in Fibrosis: TGF-β, WNT, and YAP/TAZ Converge. *Front. Med.* **2015**, *2* (SEP), 1–14. https://doi.org/10.3389/fmed.2015.00059.

(96) Noguchi, S.; Saito, A.; Nagase, T. YAP/TAZ Signaling as a Molecular Link between Fibrosis and Cancer. *Int. J. Mol. Sci.* **2018**, *19* (11). https://doi.org/10.3390/ijms19113674.

(97) Boopathy, G. T. K.; Hong, W. Role of Hippo Pathway-YAP/TAZ Signaling in Angiogenesis. *Front. Cell Dev. Biol.* **2019**, *7* (APR), 1–12. https://doi.org/10.3389/fcell.2019.00049.

(98) Huh, H. D.; Kim, D. H.; Jeong, H.-S.; Park, H. W. Regulation of TEAD Transcription

Factors in Cancer Biology. *Cells* **2019**, *8* (600), 1–22.

(99) Lipson, K. E.; Wong, C.; Teng, Y.; Spong, S. CTGF Is a Central Mediator of Tissue Remodeling and Fibrosis and Its Inhibition Can Reverse the Process of Fibrosis. *Fibrogenesis Tissue Repair* **2012**, *5* (S1), 2–9. https://doi.org/10.1186/1755-1536-5-s1-s24.

(100) Mason, D. E.; Collins, J. M.; Dawahare, J. H.; Nguyen, T. D.; Lin, Y.; Voytik-Harbin, S. L.; Zorlutuna, P.; Yoder, M. C.; Boerckel, J. D. YAP and TAZ Limit Cytoskeletal and Focal Adhesion Maturation to Enable Persistent Cell Motility. *J. Cell Biol.* **2019**, *218* (4), 1369–1389. https://doi.org/10.1083/jcb.201806065.

(101) Matera, D.; DiLillo, K.; Smith, M.; Davidson, C.; Parikh, R.; Said, M.; Wilke, C.; Lombaert, I.; Arnold, K.; Moore, B.; et al. Microengineered 3D Pulmonary Interstitial Mimetics Highlight a Critical Role for Matrix Degradation in Idiopathic Pulmonary Fibrosis. *Sci. Adv.* **2020**, No. September, 2020.06.02.129718. https://doi.org/10.1101/2020.06.02.129718.

(102) Elosegui-Artola, A.; Andreu, I.; Beedle, A. E. M.; Lezamiz, A.; Uroz, M.; Kosmalska, A. J.; Oria, R.; Kechagia, J. Z.; Rico-Lastres, P.; Le Roux, A. L.; et al. Force Triggers YAP Nuclear Entry by Regulating Transport across Nuclear Pores. *Cell* **2017**, *171* (6), 1397-1410.e14. https://doi.org/10.1016/j.cell.2017.10.008.

(103) Caliari, S. R.; Burdick, J. A. A Practical Guide to Hydrogels for Cell Culture. *Nat. Methods* **2016**, *13* (5), 405–414. https://doi.org/10.1038/nmeth.3839.

(104) Baker, B. M.; Chen, C. S. Deconstructing the Third Dimension-How 3D Culture Microenvironments Alter Cellular Cues. *J. Cell Sci.* **2012**, *125* (13), 3015–3024. https://doi.org/10.1242/jcs.079509.

(105) Li, X.; Sun, Q.; Li, Q.; Kawazoe, N.; Chen, G. Functional Hydrogels with Tunable Structures and Properties for Tissue Engineering Applications. *Front. Chem.* **2018**, *6* (OCT), 1–20. https://doi.org/10.3389/fchem.2018.00499.

(106) Spicer, C. D. Hydrogel Scaffolds for Tissue Engineering: The Importance of Polymer Choice. *Polym. Chem.* **2020**, *11* (2), 184–219. https://doi.org/10.1039/c9py01021a.

(107) Cushing, M. C.; Anseth, K. S. Hydrogel Cell Cultures. *Science (80-.).* **2007**, *316* (5828), 1133–1134. https://doi.org/10.1126/science.1140171.

(108) Tibbitt, M. W.; Anseth, K. S. Hydrogels as Extracellular Matrix Mimics for 3D Cell Culture. *Biotechnol. Bioeng.* **2009**, *103* (4), 655–663. https://doi.org/10.1002/bit.22361.

(109) Liu, J.; Zheng, H.; Poh, P. S. P.; Machens, H. G.; Schilling, A. F. Hydrogels for Engineering

of Perfusable Vascular Networks. *Int. J. Mol. Sci.* **2015**, *16* (7), 15997–16016. https://doi.org/10.3390/ijms160715997.

(110) Chaudhuri, O.; Gu, L.; Klumpers, D.; Darnell, M.; Bencherif, S. A.; Weaver, J. C.; Huebsch, N.; Lee, H. P.; Lippens, E.; Duda, G. N.; et al. Hydrogels with Tunable Stress Relaxation Regulate Stem Cell Fate and Activity. *Nat. Mater.* **2016**, *15* (3), 326–334. https://doi.org/10.1038/nmat4489.

(111) Nguyen, B. N. B.; Moriarty, R. A.; Kamalitdinov, T.; Etheridge, J. M.; Fisher, J. P. Collagen Hydrogel Scaffold Promotes Mesenchymal Stem Cell and Endothelial Cell Coculture for Bone Tissue Engineering. *J. Biomed. Mater. Res. - Part A* **2017**, *105* (4), 1123–1131. https://doi.org/10.1002/jbm.a.36008.

(112) Dahlmann, J.; Krause, A.; Möller, L.; Kensah, G.; Möwes, M.; Diekmann, A.; Martin, U.; Kirschning, A.; Gruh, I.; Dräger, G. Fully Defined in Situ Cross-Linkable Alginate and Hyaluronic Acid Hydrogels for Myocardial Tissue Engineering. *Biomaterials* **2013**, *34* (4), 940–951. https://doi.org/10.1016/j.biomaterials.2012.10.008.

(113) Zhu, J. Bioactive Modification of Poly(Ethylene Glycol) Hydrogels for Tissue Engineering. *Biomaterials* **2010**, *31* (17), 4639–4656. https://doi.org/10.1016/j.biomaterials.2010.02.044.

(114) Lin, C. C.; Raza, A.; Shih, H. PEG Hydrogels Formed by Thiol-Ene Photo-Click Chemistry and Their Effect on the Formation and Recovery of Insulin-Secreting Cell Spheroids. *Biomaterials* **2011**, *32* (36), 9685–9695. https://doi.org/10.1016/j.biomaterials.2011.08.083.

(115) Madduma-Bandarage, U. S. K.; Madihally, S. V. Synthetic Hydrogels: Synthesis, Novel Trends, and Applications. *J. Appl. Polym. Sci.* **2021**, *138* (19), 1–23. https://doi.org/10.1002/app.50376.

(116) Díaz-Bello, B.; Monroy-Romero, A. X.; Pérez-Calixto, D.; Zamarrón-Hernández, D.; Serna-Marquez, N.; Vázquez-Victorio, G.; Hautefeuille, M. Method for the Direct Fabrication of Polyacrylamide Hydrogels with Controlled Stiffness in Polystyrene Multiwell Plates for Mechanobiology Assays. *ACS Biomater. Sci. Eng.* **2019**, *5* (9), 4219–4227. https://doi.org/10.1021/acsbiomaterials.9b00988.

(117) Papavasiliou, G.; Sokic, S.; Turturro, M. Synthetic PEG Hydrogels as Extracellular Matrix Mimics for Tissue Engineering Applications. In *Biotechnology - Molecular Studies and*

Novel Applications for Improved Quality of Human Life; 2012.

(118) Liu, S. Q.; Rachel Ee, P. L.; Ke, C. Y.; Hedrick, J. L.; Yang, Y. Y. Biodegradable Poly(Ethylene Glycol)-Peptide Hydrogels with Well-Defined Structure and Properties for Cell Delivery. *Biomaterials* **2009**, *30* (8), 1453–1461. https://doi.org/10.1016/j.biomaterials.2008.11.023.

(119) Highley, C. B.; Prestwich, G. D.; Burdick, J. A. Recent Advances in Hyaluronic Acid Hydrogels for Biomedical Applications. *Curr. Opin. Biotechnol.* **2016**, *40*, 35–40. https://doi.org/10.1016/j.copbio.2016.02.008.

(120) Cosgrove, B. D.; Mui, K. L.; Driscoll, T. P.; Caliari, S. R.; Mehta, K. D.; Assoian, R. K.; Burdick, J. A.; Mauck, R. L. N-Cadherin Adhesive Interactions Modulate Matrix Mechanosensing and Fate Commitment of Mesenchymal Stem Cells. *Nat. Mater.* **2016**, *15* (12), 1297–1306. https://doi.org/10.1038/nmat4725.

(121) Caliari, S. R.; Vega, S. L.; Kwon, M.; Soulas, E. M.; Burdick, J. A. Dimensionality and Spreading Influence MSC YAP/TAZ Signaling in Hydrogel Environments. *Biomaterials* **2016**, *103*, 314–323. https://doi.org/10.1016/j.biomaterials.2016.06.061.

(122) Hu, W.; Wang, Z.; Xiao, Y.; Zhang, S.; Wang, J. Advances in Crosslinking Strategies of Biomedical Hydrogels. *Biomater. Sci.* **2019**, *7* (3), 843–855. https://doi.org/10.1039/c8bm01246f.

(123) Khunmanee, S.; Jeong, Y.; Park, H. Crosslinking Method of Hyaluronic-Based Hydrogel for Biomedical Applications. *J. Tissue Eng.* **2017**, *8*, 1–16. https://doi.org/10.1177/2041731417726464.

(124) Hui, E.; Sumey, J. L.; Caliari, S. R.; Hui, E. Click-Functionalized Hydrogel Design for Mechanobiology Investigations. *Mol. Syst. Des. Eng.* **2021**. https://doi.org/10.1039/d1me00049g.

(125) Lin, C. C.; Anseth, K. S. PEG Hydrogels for the Controlled Release of Biomolecules in Regenerative Medicine. *Pharmaceutical Research*. 2009, pp 631–643. https://doi.org/10.1007/s11095-008-9801-2.

(126) Mũnoz, Z.; Shih, H.; Lin, C. C. Gelatin Hydrogels Formed by Orthogonal Thiol-Norbornene Photochemistry for Cell Encapsulation. *Biomater. Sci.* **2014**, *2* (8), 1063–1072. https://doi.org/10.1039/c4bm00070f.

(127) Liu, H. Y.; Greene, T.; Lin, T. Y.; Dawes, C. S.; Korc, M.; Lin, C. C. Enzyme-Mediated

Stiffening Hydrogels for Probing Activation of Pancreatic Stellate Cells. *Acta Biomater.* **2017**, *48*, 258–269. https://doi.org/10.1016/j.actbio.2016.10.027.

(128) Metters, A.; Hubbell, J. Network Formation and Degradation Behavior of Hydrogels Formed by Michael-Type Addition Reactions. *Biomacromolecules* **2005**, *6* (1), 290–301. https://doi.org/10.1021/bm049607o.

(129) Dong, Y.; Sigen, A.; Rodrigues, M.; Li, X.; Kwon, S. H.; Kosaric, N.; Khong, S.; Gao, Y.; Wang, W.; Gurtner, G. C. Injectable and Tunable Gelatin Hydrogels Enhance Stem Cell Retention and Improve Cutaneous Wound Healing. *Adv. Funct. Mater.* **2017**, *27* (24), 1–12. https://doi.org/10.1002/adfm.201606619.

(130) Caliari, S. R.; Perepelyuk, M.; Soulas, E. M.; Lee, G. Y.; Wells, R. G.; Burdick, J. A. Gradually Softening Hydrogels for Modeling Hepatic Stellate Cell Behavior during Fibrosis Regression. *Integr. Biol.* **2016**, *8* (6), 720–728. https://doi.org/10.1039/c6ib00027d.

(131) Lin, C. C.; Ki, C. S.; Shih, H. Thiol-Norbornene Photoclick Hydrogels for Tissue Engineering Applications. *J. Appl. Polym. Sci.* **2015**, *132* (8). https://doi.org/10.1002/app.41563.

(132) Fairbanks, B. D.; Schwartz, M. P.; Bowman, C. N.; Anseth, K. S. Photoinitiated Polymerization of PEG-Diacrylate with Lithium Phenyl-2,4,6-Trimethylbenzoylphosphinate: Polymerization Rate and Cytocompatibility. *Biomaterials* **2009**, *30* (35), 6702–6707. https://doi.org/10.1016/j.biomaterials.2009.08.055.

(133) Yeh, Y. C.; Corbin, E. A.; Caliari, S. R.; Ouyang, L.; Vega, S. L.; Truitt, R.; Han, L.; Margulies, K. B.; Burdick, J. A. Mechanically Dynamic PDMS Substrates to Investigate Changing Cell Environments. *Biomaterials* **2017**, *145*, 23–32. https://doi.org/10.1016/j.biomaterials.2017.08.033.

(134) Hao, Y.; Lin, C. C. Degradable Thiol-Acrylate Hydrogels as Tunable Matrices for Three-Dimensional Hepatic Culture. *J. Biomed. Mater. Res. - Part A* **2014**, *102* (11), 3813–3827. https://doi.org/10.1002/jbm.a.35044.

(135) Charrier, E. E.; Pogoda, K.; Wells, R. G.; Janmey, P. A. Control of Cell Morphology and Differentiation by Substrates with Independently Tunable Elasticity and Viscous Dissipation. *Nat. Commun.* **2018**, *9* (1), 1–13. https://doi.org/10.1038/s41467-018-02906-9.

(136) Chaudhuri, O.; Gu, L.; Darnell, M.; Klumpers, D.; Bencherif, S. A.; Weaver, J. C.; Huebsch,

N.; Mooney, D. J. Substrate Stress Relaxation Regulates Cell Spreading. *Nat. Commun.* **2015**, *6*, 1–7. https://doi.org/10.1038/ncomms7365.

(137) Vorvolakos, K.; Isayeva, I. S.; do Luu, H. M.; Patwardhan, D. V.; Pollack, S. K. Ionically Cross-Linked Hyaluronic Acid: Wetting, Lubrication, and Viscoelasticity of a Modified Adhesion Barrier Gel. *Med. Devices Evid. Res.* **2011**, *4* (1), 1–10. https://doi.org/10.2147/MDER.S13962.

(138) Tamilmani, V.; Daul, C. A.; Venuvanalingam, P. Electrostatic Control on Endo/Exo Selectivity in Ionic Cycloaddition. *Chem. Phys. Lett.* **2005**, *416* (4–6), 354–357. https://doi.org/10.1016/j.cplett.2005.09.120.

(139) Tan, Y.; Huang, H.; Ayers, D. C.; Song, J. Modulating Viscoelasticity, Stiffness, and Degradation of Synthetic Cellular Niches via Stoichiometric Tuning of Covalent versus Dynamic Noncovalent Cross-Linking. *ACS Cent. Sci.* **2018**, *4* (8), 971–981. https://doi.org/10.1021/acscentsci.8b00170.

(140) Wijnen, J. W.; Zavarise, S.; Engberts, J. B. F. N.; Charton, M. Substituent Effects on an Inverse Electron Demand Hetero Diels-Alder Reaction in Aqueous Solution and Organic Solvents: Cycloaddition of Substituted Styrenes to Di(2-Pyridyl)-1,2,4,5-Tetrazine. *J. Org. Chem.* **1996**, *61* (6), 2001–2005. https://doi.org/10.1021/jo9518563.

(141) Meijer, A.; Otto, S.; Engberts, J. B. F. N. Effects of the Hydrophobicity of the Reactants on Dieis-Alder Reactions in Water. *J. Org. Chem.* **1998**, *63* (24), 8989–8994. https://doi.org/10.1021/jo981359x.

(142) Taylor, M. T.; Blackman, M. L.; Dmitrenko, O.; Fox, J. M. Design and Synthesis of Highly Reactive Dienophiles for the Tetrazine-Trans-Cyclooctene Ligation. *J. Am. Chem. Soc.* **2011**, *133* (25), 9646–9649. https://doi.org/10.1021/ja201844c.

(143) Rodell, C. B.; Kaminski, A. L.; Burdick, J. A. Rational Design of Network Properties in Guest-Host Assembled and Shear-Thinning Hyaluronic Acid Hydrogels. *Biomacromolecules* **2013**, *14* (11), 4125–4134. https://doi.org/10.1021/bm401280z.

(144) Highley, C. B.; Rodell, C. B.; Burdick, J. A. Direct 3D Printing of Shear-Thinning Hydrogels into Self-Healing Hydrogels. *Adv. Mater.* **2015**, *27* (34), 5075–5079. https://doi.org/10.1002/adma.201501234.

(145) Miller, B.; Hansrisuk, A.; Highley, C. B.; Caliari, S. R. Guest-Host Supramolecular Assembly of Injectable Hydrogel Nanofibers for Cell Encapsulation. *ACS Biomater. Sci.*

Eng. **2021**. https://doi.org/10.1021/acsbiomaterials.1c00275.

(146) Wang, L. L.; Highley, C. B.; Yeh, Y. C.; Galarraga, J. H.; Uman, S.; Burdick, J. A. Three-Dimensional Extrusion Bioprinting of Single- and Double-Network Hydrogels Containing Dynamic Covalent Crosslinks. *J. Biomed. Mater. Res. - Part A* **2018**, *106* (4), 865–875. https://doi.org/10.1002/jbm.a.36323.

(147) Discher, D. E.; Janmey, P.; Wang, Y. L. Tissue Cells Feel and Respond to the Stiffness of Their Substrate. *Science (80-.).* **2005**, *310* (5751), 1139–1143.

(148) Hui, E.; Gimeno, K. I.; Guan, G.; Caliari, S. R. Spatiotemporal Control of Viscoelasticity in Phototunable Hyaluronic Acid Hydrogels. *Biomacromolecules* **2019**, *20* (11), 4126–4134. https://doi.org/10.1021/acs.biomac.9b00965.

(149) Bauer, A.; Gu, L.; Kwee, B.; Li, W. A.; Dellacherie, M.; Celiz, A. D.; Mooney, D. J. Hydrogel Substrate Stress-Relaxation Regulates the Spreading and Proliferation of Mouse Myoblasts. *Acta Biomater.* **2017**, *62*, 82–90. https://doi.org/10.1016/j.actbio.2017.08.041.

(150) Hadden, W. J.; Young, J. L.; Holle, A. W.; McFetridge, M. L.; Kim, D. Y.; Wijesinghe, P.; Taylor-Weiner, H.; Wen, J. H.; Lee, A. R.; Bieback, K.; et al. Stem Cell Migration and Mechanotransduction on Linear Stiffness Gradient Hydrogels. *Proc. Natl. Acad. Sci. U. S. A.* **2017**, *114* (22), 5647–5652. https://doi.org/10.1073/pnas.1618239114.

(151) Adebowale, K.; Gong, Z.; Hou, J. C.; Wisdom, K. M.; Garbett, D.; Lee, H. pyo; Nam, S.; Meyer, T.; Odde, D. J.; Shenoy, V. B.; et al. Enhanced Substrate Stress Relaxation Promotes Filopodia-Mediated Cell Migration. *Nat. Mater.* **2021**. https://doi.org/10.1038/s41563-021-00981-w.

(152) Mascharak, S.; Benitez, P. L.; Proctor, A. C.; Madl, C. M.; Hu, K. H.; Dewi, R. E.; Butte, M. J.; Heilshorn, S. C. YAP-Dependent Mechanotransduction Is Required for Proliferation and Migration on Native-like Substrate Topography. *Biomaterials* **2017**, *115*, 155–166. https://doi.org/10.1016/j.biomaterials.2016.11.019.

(153) Rowlands, A. S.; George, P. A.; Cooper-White, J. J. Directing Osteogenic and Myogenic Differentiation of MSCs: Interplay of Stiffness and Adhesive Ligand Presentation. *Am. J. Physiol. - Cell Physiol.* **2008**, *295* (4), C1037–C1044. https://doi.org/10.1152/ajpcell.67.2008.

(154) Wen, J. H.; Vincent, L. G.; Fuhrmann, A.; Choi, Y. S.; Hribar, K. C.; Taylor-Weiner, H.; Chen, S.; Engler, A. J. Interplay of Matrix Stiffness and Protein Tethering in Stem Cell

Differentiation. *Nat. Mater.* **2014**, *13* (10), 979–987. https://doi.org/10.1038/nmat4051.

(155) Killaars, A. R.; Walker, C. J.; Anseth, K. S. Nuclear Mechanosensing Controls MSC Osteogenic Potential through HDAC Epigenetic Remodeling. *Proc. Natl. Acad. Sci. U. S. A.* **2020**, *117* (35), 21258–21266. https://doi.org/10.1073/pnas.2006765117.

(156) Lee, J. Y.; Dominguez, A. A.; Nam, S.; Stowers, R. S.; Qi, L. S.; Chaudhuri, O. Identification of Cell Context-Dependent YAP-Associated Proteins Reveals B1 and B4 Integrin Mediate YAP Translocation Independently of Cell Spreading. *Sci. Rep.* **2019**, *9* (1), 1–11. https://doi.org/10.1038/s41598-019-53659-4.

(157) Stowers, R. S.; Allen, S. C.; Suggs, L. J.; Anseth, K. S. Dynamic Phototuning of 3D Hydrogel Stiffness. *Proc. Natl. Acad. Sci. U. S. A.* **2015**, *112* (7), 1953–1958. https://doi.org/10.1073/pnas.1421897112.

(158) Alge, D. L.; Azagarsamy, M. A.; Donohue, D. F.; Anseth, K. S. Synthetically Tractable Click Hydrogels for Three-Dimensional Cell Culture Formed Using Tetrazine-Norbornene Chemistry. *Biomacromolecules* **2013**, *14* (4), 949–953. https://doi.org/10.1021/bm4000508.

(159) Lee, H. pyo; Stowers, R.; Chaudhuri, O. Volume Expansion and TRPV4 Activation Regulate Stem Cell Fate in Three-Dimensional Microenvironments. *Nat. Commun.* **2019**, *10* (1). https://doi.org/10.1038/s41467-019-08465-x.

(160) Lueckgen, A.; Garske, D. S.; Ellinghaus, A.; Desai, R. M.; Stafford, A. G.; Mooney, D. J.; Duda, G. N.; Cipitria, A. Hydrolytically-Degradable Click-Crosslinked Alginate Hydrogels. *Biomaterials* **2018**, *181*, 189–198. https://doi.org/10.1016/j.biomaterials.2018.07.031.

(161) Suo, A.; Xu, W.; Wang, Y.; Sun, T.; Ji, L.; Qian, J. Dual-Degradable and Injectable Hyaluronic Acid Hydrogel Mimicking Extracellular Matrix for 3D Culture of Breast Cancer MCF-7 Cells. *Carbohydr. Polym.* **2019**, *211* (October 2018), 336–348. https://doi.org/10.1016/j.carbpol.2019.01.115.

(162) Chaudhuri, O. Viscoelastic Hydrogels for 3D Cell Culture. *Biomater. Sci.* **2017**, *5* (8), 1480–1490. https://doi.org/10.1039/c7bm00261k.

(163) Khetan, S.; Guvendiren, M.; Legant, W. R.; Cohen, D. M.; Chen, C. S.; Burdick, J. A. Degradation-Mediated Cellular Traction Directs Stem Cell Fate in Covalently Crosslinked Three-Dimensional Hydrogels. *Nat. Mater.* **2013**, *12* (5), 458–465. https://doi.org/10.1038/nmat3586.

(164) Balestrini, J. L.; Chaudhry, S.; Sarrazy, V.; Koehler, A.; Hinz, B. The Mechanical Memory of Lung Myofibroblasts. *Integr. Biol.* **2012**, *4* (4), 410–421. https://doi.org/10.1039/c2ib00149g.

(165) Caliari, S. R.; Perepelyuk, M.; Cosgrove, B. D.; Tsai, S. J.; Lee, G. Y.; Mauck, R. L.; Wells, R. G.; Burdick, J. A. Stiffening Hydrogels for Investigating the Dynamics of Hepatic Stellate Cell Mechanotransduction during Myofibroblast Activation. *Sci. Rep.* **2016**, *6*, 1–10. https://doi.org/10.1038/srep21387.

(166) Olsen, A. L.; Bloomer, S. A.; Chan, E. P.; Gaça, M. D. A.; Georges, P. C.; Sackey, B.; Uemura, M.; Janmey, P. A.; Wells, R. G. Hepatic Stellate Cells Require a Stiff Environment for Myofibroblastic Differentiation. *Am. J. Physiol. - Gastrointest. Liver Physiol.* **2011**, *301* (1), 110–118. https://doi.org/10.1152/ajpgi.00412.2010.

(167) Cacopardo, L.; Guazzelli, N.; Nossa, R.; Mattei, G.; Ahluwalia, A. Engineering Hydrogel Viscoelasticity. *J. Mech. Behav. Biomed. Mater.* **2019**, *89* (May 2018), 162–167. https://doi.org/10.1016/j.jmbbm.2018.09.031.

(168) Liu, F. D.; Pishesha, N.; Poon, Z.; Kaushik, T.; Van Vliet, K. J. Material Viscoelastic Properties Modulate the Mesenchymal Stem Cell Secretome for Applications in Hematopoietic Recovery. *ACS Biomater. Sci. Eng.* **2017**, *3* (12), 3292–3306. https://doi.org/10.1021/acsbiomaterials.7b00644.

(169) Gong, Z.; Szczesny, S. E.; Caliari, S. R.; Charrier, E. E.; Chaudhuri, O.; Cao, X.; Lin, Y.; Mauck, R. L.; Janmey, P. A.; Burdick, J. A.; et al. Matching Material and Cellular Timescales Maximizes Cell Spreading on Viscoelastic Substrates. *Proc. Natl. Acad. Sci. U. S. A.* **2018**, *115* (12), E2686–E2695. https://doi.org/10.1073/pnas.1716620115.

(170) Islam, M. R.; Virag, J.; Oyen, M. L. Micromechanical Poroelastic and Viscoelastic Properties of Ex-Vivo Soft Tissues. *J. Biomech.* **2020**, *113*, 110090. https://doi.org/10.1016/j.jbiomech.2020.110090.

(171) Budday, S.; Sommer, G.; Holzapfel, G. A.; Steinmann, P.; Kuhl, E. Viscoelastic Parameter Identification of Human Brain Tissue. *J. Mech. Behav. Biomed. Mater.* **2017**, *74* (May), 463–476. https://doi.org/10.1016/j.jmbbm.2017.07.014.

(172) Perepelyuk, M.; Chin, L.; Cao, X.; Van Oosten, A.; Shenoy, V. B.; Janmey, P. A.; Wells, R. G. Normal and Fibrotic Rat Livers Demonstrate Shear Strain Softening and Compression Stiffening: A Model for Soft Tissue Mechanics. *PLoS One* **2016**, *11* (1), 1–18.

https://doi.org/10.1371/journal.pone.0146588.

(173) Geerligs, M.; Peters, G. W. M.; Ackermans, P. A. J.; Oomens, C. W. J.; Baaijens, F. P. T. Linear Viscoelastic Behavior of Subcutaneous Adipose Tissue. *Biorheology* **2008**, *45* (6), 677–688. https://doi.org/10.3233/BIR-2008-0517.

(174) Liu, Z.; Bilston, L. On the Viscoelastic Character of Liver Tissue: Experiments and Modelling of the Linear Behaviour. *Biorheology* **2000**, *37* (3), 191–201.

(175) Hui, E.; Moretti, L.; Barker, T. H.; Caliari, S. R. The Combined Influence of Viscoelastic and Adhesive Cues on Fibroblast Spreading and Focal Adhesion Organization. *Cell. Mol. Bioeng.* **2021**. https://doi.org/10.1007/s12195-021-00672-1.

(176) Mantha, S.; Pillai, S.; Khayambashi, P.; Upadhyay, A.; Zhang, Y. Smart Hydrogels in Tissue Engineering and Regenerative Medicine. *Materials (Basel).* **2019**, *12* (3323), 33.

(177) Madl, C. M.; Heilshorn, S. C. Engineering Hydrogel Microenvironments to Recapitulate the Stem Cell Niche. *Annu. Rev. Biomed. Eng.* **2018**, *20* (1), 21–47. https://doi.org/10.1146/annurev-bioeng-062117-120954.

(178) Ekerdt, B. L.; Segalman, R. A.; Schaffer, D. V. Spatial Organization of Cell-Adhesive Ligands for Advanced Cell Culture. *Biotechnol. J.* **2013**, *8* (12), 1411–1423. https://doi.org/10.1002/biot.201300302.

(179) Ruoslahti, E. RGD and Other Recognition Sequences for Integrins. *Annu. Rev. Cell Dev. Biol.* **1996**, *12* (1), 697–715. https://doi.org/10.1146/annurev.cellbio.12.1.697.

(180) Bellis, S. L. Advantages of RGD Peptides for Directing Cell Association with Biomaterials. *Biomaterials* **2011**, *32* (18), 4205–4210. https://doi.org/10.1016/j.biomaterials.2011.02.029.

(181) Ye, K.; Wang, X.; Cao, L.; Li, S.; Li, Z.; Yu, L.; Ding, J. Matrix Stiffness and Nanoscale Spatial Organization of Cell-Adhesive Ligands Direct Stem Cell Fate. *Nano Lett.* **2015**, *15* (7), 4720–4729. https://doi.org/10.1021/acs.nanolett.5b01619.

(182) Fisher, S. A.; Anandakumaran, P. N.; Owen, S. C.; Shoichet, M. S. Tuning the Microenvironment: Click-Crosslinked Hyaluronic Acid-Based Hydrogels Provide a Platform for Studying Breast Cancer Cell Invasion. *Adv. Funct. Mater.* **2015**, *25* (46), 7163–7172. https://doi.org/10.1002/adfm.201502778.

(183) Deforest, C. A.; Tirrell, D. A. A Photoreversible Protein-Patterning Approach for Guiding Stem Cell Fate in Three-Dimensional Gels. *Nat. Mater.* **2015**, *14* (5), 523–531.

https://doi.org/10.1038/nmat4219.

(184) Hautanen, A.; Gailit, J.; Mann, D. M.; Ruoslahti, E. Effects of Modifications of the RGD Sequence and Its Context on Recognition by the Fibronectin Receptor. *J. Biol. Chem.* **1989**, *264* (3), 1437–1442. https://doi.org/10.1016/s0021-9258(18)94206-7.

(185) Lou, J.; Stowers, R.; Nam, S.; Xia, Y.; Chaudhuri, O. Stress Relaxing Hyaluronic Acid-Collagen Hydrogels Promote Cell Spreading, Fiber Remodeling, and Focal Adhesion Formation in 3D Cell Culture. *Biomaterials* **2018**, *154*, 213–222. https://doi.org/10.1016/j.biomaterials.2017.11.004.

(186) Li, H.; Zheng, J.; Wang, H.; Becker, M. L.; Leipzig, N. D. Neural Stem Cell Encapsulation and Differentiation in Strain Promoted Crosslinked Polyethylene Glycol-Based Hydrogels. *J. Biomater. Appl.* **2018**, *32* (9), 1222–1230. https://doi.org/10.1177/0885328218755711.

(187) Spearman, B. S.; Agrawal, N. K.; Rubiano, A.; Simmons, C. S.; Mobini, S.; Schmidt, C. E. Tunable Methacrylated Hyaluronic Acid-Based Hydrogels as Scaffolds for Soft Tissue Engineering Applications. *J. Biomed. Mater. Res. - Part A* **2020**, *108* (2), 279–291. https://doi.org/10.1002/jbm.a.36814.

(188) Scaffidi, A. K.; Moodley, Y. P.; Weichselbaum, M.; Thompson, P. J.; Knight, D. A. Regulation of Human Lung Fibroblast Phenotype and Function by Vitronectin and Vitronectin Integrins. *J. Cell Sci.* **2001**, *114* (19), 3507–3516. https://doi.org/10.1242/jcs.114.19.3507.

(189) Missirlis, D.; Haraszti, T.; Scheele, C. V. C.; Wiegand, T.; Diaz, C.; Neubauer, S.; Rechenmacher, F.; Kessler, H.; Spatz, J. P. Substrate Engagement of Integrins A5 B1 and Av B3 Is Necessary, but Not Sufficient, for High Directional Persistence in Migration on Fibronectin. *Sci. Rep.* **2016**, *6* (March), 1–18. https://doi.org/10.1038/srep23258.

(190) Cao, L.; Nicosia, J.; Larouche, J.; Zhang, Y.; Bachman, H.; Brown, A. C.; Holmgren, L.; Barker, T. H. Detection of an Integrin-Binding Mechanoswitch within Fibronectin during Tissue Formation and Fibrosis. *ACS Nano* **2017**, *11* (7), 7110–7117. https://doi.org/10.1021/acsnano.7b02755.

(191) DeForest, C. A.; Anseth, K. S. Cytocompatible Click-Based Hydrogels with Dynamically Tunable Properties through Orthogonal Photoconjugation and Photocleavage Reactions. *Nat. Chem.* **2011**, *3* (12), 925–931. https://doi.org/10.1038/nchem.1174.

(192) DeForest, C. A.; Anseth, K. S. Photoreversible Patterning of Biomolecules within Click-

Based Hydrogels. *Angew. Chemie - Int. Ed.* **2012**, *51* (8), 1816–1819. https://doi.org/10.1002/anie.201106463.

(193) Gurtner, G. C.; Werner, S.; Barrandon, Y.; Longaker, M. T. Wound Repair and Regeneration. *Nature* **2008**, *453* (7193), 314–321. https://doi.org/10.1038/nature07039.

(194) Gramlich, W. M.; Kim, I. L.; Burdick, J. A. Synthesis and Orthogonal Photopatterning of Hyaluronic Acid Hydrogels with Thiol-Norbornene Chemistry. *Biomaterials* **2013**, *34* (38), 9803–9811. https://doi.org/10.1016/j.biomaterials.2013.08.089.

(195) Khetan, S.; Burdick, J. A. Patterning Network Structure to Spatially Control Cellular Remodeling and Stem Cell Fate within 3-Dimensional Hydrogels. *Biomaterials* **2010**, *31* (32), 8228–8234. https://doi.org/10.1016/j.biomaterials.2010.07.035.

(196) Guvendiren, M.; Perepelyuk, M.; Wells, R. G.; Burdick, J. A. Hydrogels with Differential and Patterned Mechanics to Study Stiffness-Mediated Myofibroblastic Differentiation of Hepatic Stellate Cells. *J. Mech. Behav. Biomed. Mater.* **2014**, *38*, 198–208. https://doi.org/10.1016/j.jmbbm.2013.11.008.

(197) Lampi, M. C.; Guvendiren, M.; Burdick, J. A.; Reinhart-King, C. A. Photopatterned Hydrogels to Investigate the Endothelial Cell Response to Matrix Stiffness Heterogeneity. *ACS Biomater. Sci. Eng.* **2017**, *3* (11), 3007–3016. https://doi.org/10.1021/acsbiomaterials.6b00633.

(198) Leijten, J.; Seo, J.; Yue, K.; Trujillo-de Santiago, G.; Tamayol, A.; Ruiz-Esparza, G. U.; Shin, S. R.; Sharifi, R.; Noshadi, I.; Álvarez, M. M.; et al. Spatially and Temporally Controlled Hydrogels for Tissue Engineering. *Mater. Sci. Eng. R Reports* **2017**, *119*, 1–35. https://doi.org/10.1016/j.mser.2017.07.001.

(199) Lueckgen, A.; Garske, D. S.; Ellinghaus, A.; Mooney, D. J.; Duda, G. N.; Cipitria, A. Dual Alginate Crosslinking for Local Patterning of Biophysical and Biochemical Properties. *Acta Biomater.* **2020**, *115*, 185–196. https://doi.org/10.1016/j.actbio.2020.07.047.

(200) Zuidema, J. M.; Rivet, C. J.; Gilbert, R. J.; Morrison, F. A. A Protocol for Rheological Characterization of Hydrogels for Tissue Engineering Strategies. *J. Biomed. Mater. Res. - Part B Appl. Biomater.* **2014**, *102* (5), 1063–1073. https://doi.org/10.1002/jbm.b.33088.

(201) Norman, M. D. A.; Ferreira, S. A.; Jowett, G. M.; Bozec, L.; Gentleman, E. Measuring the Elastic Modulus of Soft Culture Surfaces and Three-Dimensional Hydrogels Using Atomic Force Microscopy. *Nat. Protoc.* **2021**, *16* (5), 2418–2449. https://doi.org/10.1038/s41596-

021-00495-4.

(202) Jorba, I.; Uriarte, J. J.; Campillo, N.; Farré, R.; Navajas, D. Probing Micromechanical Properties of the Extracellular Matrix of Soft Tissues by Atomic Force Microscopy. *J. Cell. Physiol.* **2017**, *232* (1), 19–26. https://doi.org/10.1002/jcp.25420.

(203) Efremov, Y. M.; Wang, W. H.; Hardy, S. D.; Geahlen, R. L.; Raman, A. Measuring Nanoscale Viscoelastic Parameters of Cells Directly from AFM Force-Displacement Curves. *Sci. Rep.* **2017**, *7* (1), 1–14. https://doi.org/10.1038/s41598-017-01784-3.

(204) Efremov, Y. M.; Okajima, T.; Raman, A. Measuring Viscoelasticity of Soft Biological Samples Using Atomic Force Microscopy. *Soft Matter* **2019**, *16* (1), 64–81. https://doi.org/10.1039/c9sm01020c.

(205) Bouchonville, N.; Meyer, M.; Gaude, C.; Gay, E.; Ratel, D.; Nicolas, A. AFM Mapping of the Elastic Properties of Brain Tissue Reveals KPa Mm-1 Gradients of Rigidity. *Soft Matter* **2016**, *12* (29), 6232–6239. https://doi.org/10.1039/c6sm00582a.

(206) Grant, C. A.; Twigg, P. C.; Tobin, D. J. Static and Dynamic Nanomechanical Properties of Human Skin Tissue Using Atomic Force Microscopy: Effect of Scarring in the Upper Dermis. *Acta Biomater.* **2012**, *8* (11), 4123–4129. https://doi.org/10.1016/j.actbio.2012.06.042.

(207) Chen, X.; Hughes, R.; Mullin, N.; Hawkins, R. J.; Holen, I.; Brown, N. J.; Hobbs, J. K. Mechanical Heterogeneity in the Bone Microenvironment as Characterized by Atomic Force Microscopy. *Biophys. J.* **2020**, *119* (3), 502–513. https://doi.org/10.1016/j.bpj.2020.06.026.

(208) Ebenstein, D. M.; Pruitt, L. A. Nanoindentation of Biological Materials. *Nano Today* **2006**, *1* (3), 26–33. https://doi.org/10.1016/S1748-0132(06)70077-9.

(209) Lin, D. C.; Shreiber, D. I.; Dimitriadis, E. K.; Horkay, F. Spherical Indentation of Soft Matter beyond the Hertzian Regime: Numerical and Experimental Validation of Hyperelastic Models. *Biomech. Model. Mechanobiol.* **2009**, *8* (5), 345–358. https://doi.org/10.1007/s10237-008-0139-9.

(210) Rubiano, A.; Galitz, C.; Simmons, C. S. Mechanical Characterization by Mesoscale Indentation: Advantages and Pitfalls for Tissue and Scaffolds. *Tissue Eng. - Part C Methods* **2019**, *25* (10), 619–629. https://doi.org/10.1089/ten.tec.2018.0372.

(211) Li, Q.; Qu, F.; Han, B.; Wang, C.; Li, H.; Mauck, R. L.; Han, L. Micromechanical

Anisotropy and Heterogeneity of the Meniscus Extracellular Matrix. *Acta Biomater.* **2017**, *54*, 356–366. https://doi.org/10.1016/j.actbio.2017.02.043.

(212) Elkin, B. S.; Azeloglu, E. U.; Costa, K. D.; Morrison, B. Mechanical Heterogeneity of the Rat Hippocampus Measured by Atomic Force Microscope Indentation. *J. Neurotrauma* **2007**, *24* (5), 812–822. https://doi.org/10.1089/neu.2006.0169.

(213) Chang, Y. R.; Raghunathan, V. K.; Garland, S. P.; Morgan, J. T.; Russell, P.; Murphy, C. J. Automated AFM Force Curve Analysis for Determining Elastic Modulus of Biomaterials and Biological Samples. *J. Mech. Behav. Biomed. Mater.* **2014**, *37*, 209–218. https://doi.org/10.1016/j.jmbbm.2014.05.027.

(214) Oyen, M. L. Mechanical Characterisation of Hydrogel Materials. *Int. Mater. Rev.* **2014**, *59* (1), 44–59. https://doi.org/10.1179/1743280413Y.0000000022.

(215) Dujardin, A.; De Wolf, P.; Lafont, F.; Dupres, V. Automated Multi-Sample Acquisition and Analysis Using Atomic Force Microscopy for Biomedical Applications. *PLoS One* **2019**, *14* (3), 1–19. https://doi.org/10.1371/journal.pone.0213853.

(216) Ebenstein, D. M.; Pruitt, L. A. Nanoindentation of Soft Hydrated Materials for Application to Vascular Tissues. *J. Biomed. Mater. Res. - Part A* **2004**, *69* (2), 222–232. https://doi.org/10.1002/jbm.a.20096.

(217) Herbert, E. G.; Oliver, W. C.; Pharr, G. M. Nanoindentation and the Dynamic Characterization of Viscoelastic Solids. *J. Phys. D. Appl. Phys.* **2008**, *41* (7). https://doi.org/10.1088/0022-3727/41/7/074021.

(218) Wu, G.; Gotthardt, M.; Gollasch, M. Assessment of Nanoindentation in Stiffness Measurement of Soft Biomaterials: Kidney, Liver, Spleen and Uterus. *Sci. Rep.* **2020**, *10* (1), 1–11. https://doi.org/10.1038/s41598-020-75738-7.

(219) Casey, J.; Yue, X.; Nguyen, T. D.; Acun, A.; Zellmer, V. R.; Zhang, S.; Zorlutuna, P. 3D Hydrogel-Based Microwell Arrays as a Tumor Microenvironment Model to Study Breast Cancer Growth. *Biomed. Mater.* **2017**, *12* (2). https://doi.org/10.1088/1748-605X/aa5d5c.

(220) Ahearne, M.; Yang, Y.; El Haj, A. J.; Then, K. Y.; Liu, K. K. Characterizing the Viscoelastic Properties of Thin Hydrogel-Based Constructs for Tissue Engineering Applications. *J. R. Soc. Interface* **2005**, *2* (5), 455–463. https://doi.org/10.1098/rsif.2005.0065.

CHAPTER 2: CLICK-FUNCTIONALIZED HYDROGEL DESIGN FOR MECHANOBIOLOGY INVESTIGATIONS

This chapter has been adapted from the following publication: Hui, E., Sumey, J.L., Caliari, S.R. "Click-functionalized hydrogel design for mechanobiology investigations." *Molecular Systems Design & Engineering* **2021**.

2.1 Abstract

The advancement of click-functionalized hydrogels in recent years has coincided with rapid growth in the fields of mechanobiology, tissue engineering, and regenerative medicine. Click chemistries represent a group of reactions that possess high reactivity and specificity, are cytocompatible, and generally proceed under physiologic conditions. Most notably, the high level of tunability afforded by these reactions enables the design of user-controlled and tissue-mimicking hydrogels in which the influence of important physical and biochemical cues on normal and aberrant cellular behaviors can be independently assessed. Several critical tissue properties, including stiffness, viscoelasticity, and biomolecule presentation, are known to regulate cell mechanobiology in the context of development, wound repair, and disease. However, many questions still remain about how the individual and combined effects of these instructive properties regulate the cellular and molecular mechanisms governing physiologic and pathologic processes. In this review, we discuss several click chemistries that have been adopted to design dynamic and instructive hydrogels for mechanobiology investigations. We also chart a path forward for how click hydrogels can help reveal important insights about complex tissue microenvironments.

2.2 Introduction

Biomaterials designed to mimic and exploit native tissue signals, such as mechanical and chemical cues, allow improved understanding of a diverse range of physiologic and pathologic conditions from development to wound healing and disease processes[1,2]. In particular, biomaterials have become instrumental in studying how biophysical factors, namely mechanics, influence cell and tissue function, also known as mechanobiology[3–6]. Hydrogels are versatile water-swollen polymeric biomaterials that can be designed to recapitulate key attributes of the native microenvironment, enabling further understanding of the interplay between cells and their surrounding extracellular matrix (ECM)[7–10]. Many of the key elements that comprise an ideal hydrogel testbed to study mechanobiology can be found within the click chemistry toolbox. The utilization of click chemistries has become a powerful approach to easily and rapidly form hydrogel networks due to their simplicity, high reactivity and reaction specificity, and ability to be carried out under mild reaction conditions without harsh byproducts[11]. From a biomaterials perspective, click reactions are particularly useful in directing material properties through incorporation of mechanical and biochemical cues in a highly specific and bioorthogonal manner (**Figure 2.1**). The ability to independently tune network composition by modulating features such as crosslinker content/concentration and degree of degradation to control a wide range of cell-instructive properties (e.g., stiffness, viscoelasticity, ligand presentation) makes click chemistries specifically advantageous for studying mechanobiology (**Table 2.1**). Within the last decade, significant advances have been made in the design of click-based systems to probe mechanistic features of cell-matrix interactions and for various tissue engineering applications[10,12–19].

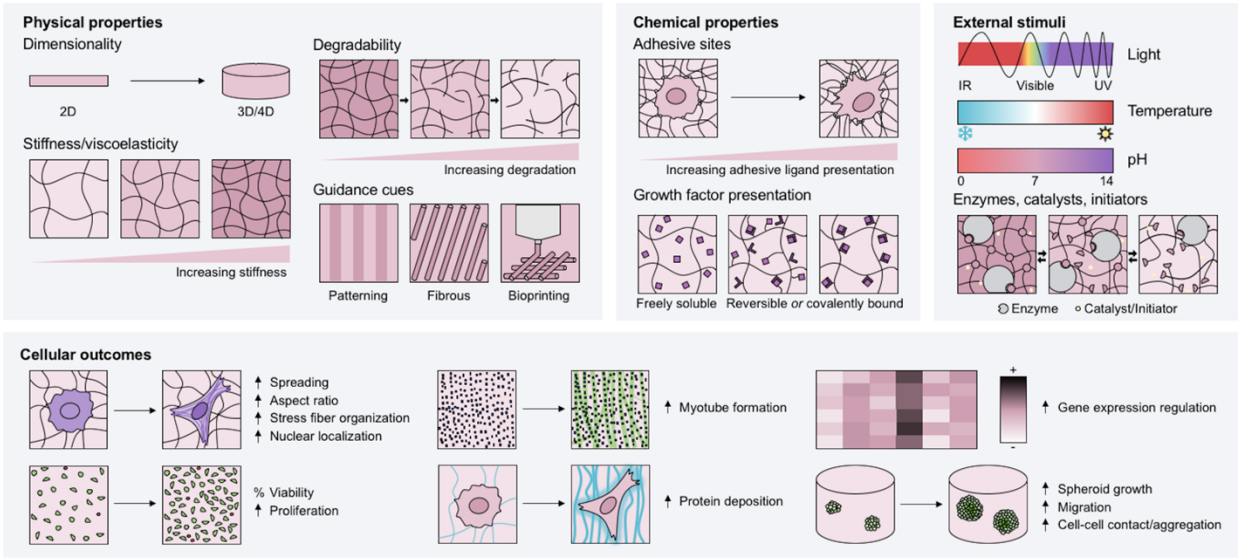

Figure 2.1. The click chemistry toolbox enables tuning of tissue-relevant physical (e.g., dimensionality, degradability, stiffness, viscoelasticity, architectural cues) and chemical (e.g., adhesion, growth factor presentation) properties to understand mechanobiological cell responses. Many click reactions are responsive to stimuli such as light, temperature, and pH. This can be exploited to control hydrogel properties including gelation kinetics, secondary crosslinking, and/or degradation. Application of click-functionalized hydrogels can help reveal how individual and combined biophysical factors regulate and influence cell mechanobiology in the context of development, wound healing, and disease processes.

Click chemistry is particularly useful in the design and synthesis of hydrogels that mimic salient features of the ECM. The ECM is a highly complex macromolecular network that not only acts as a support structure for cells, but also contains myriad physical, chemical, and mechanical cues that are dynamic in nature, including external and cell-mediated forces, growth factors and other signaling molecules, and changes in tissue architecture and compliance[20–24]. Cells sense mechanical signaling cues provided by the heterogeneous ECM from cell surface receptors (e.g., integrins) that facilitate signal transduction between cells and their surroundings in a process known as mechanotransduction. Integrin-mediated adhesions can initiate conformational changes within the cell body, leading to translocation of relevant proteins and cytoplasmic molecules and activation of downstream signaling pathways[22,25–27]. The bidirectional relationship between ECM

mechanics and growth factor presentation, also known as dynamic reciprocity, also plays a significant role in regulating and activating disease-relevant signaling pathways[28,29]. For example, matrix remodeling can result in transforming growth factor-β (TGF-β) activation from its latent state and new ECM cytoskeletal and contractile protein expression, which can lead to subsequent promotion of pro-tumorigenic responses such as cellular migration, invasion, and epithelial-to-mesenchymal transition (EMT)[30–33]. Similarly, platelet-derived growth factor (PDGFR) isoforms are important in tissue development and homeostasis; overexpression has been linked to fibrosis and cancer, influencing cell proliferation and migration[34–37].

More recently, mechanical properties such as stiffness[38–46], topography[39,47–52], and viscoelasticity[53–61] have been highlighted as critical regulators of cell behavior. For example, during fibrosis, a pathologic scarring process that occurs in most major organs in response to a range of diseases, events such as exposure to toxins, chronic inflammation, and persistent infections trigger the activation of ECM-producing myofibroblasts[62–64]. The contractility of active stress fiber-containing myofibroblasts directly affects the physical ECM via continuous profibrotic feed-forward mechanisms driving ECM deposition and dynamic remodeling[65–68]. In turn, aberrant changes in tissue mechanics – declines in tissue viscoelasticity and increases in tissue stiffness via lysyl oxidase (LOX)-mediated collagen crosslinking, play a key role in the persistence of mechanotransduction signaling dynamics[41,46,63,69–71]. Importantly, these extracellular cues collectively influence and regulate many cell processes such as growth[25,60,72,73], migration[74–76], and differentiation[56,77,78] during normal and disease processes. The ability to decouple mechanical and biochemical cues has allowed researchers to investigate cell-matrix interactions in a controlled manner. As progress continues to be made toward using click chemistry to design biomimetic

systems capable of recapitulating dynamic tissue mechanics, these models will enable more nuanced investigations of mechanobiology-influenced complex biological phenomena.

In this review, we highlight the promising applications of click-functionalized hydrogels as cell culture systems for studying mechanobiology. We cover several bioconjugation reactions that have specifically been used for hydrogel fabrication such as thiol-based chemistries, azide-alkyne cycloadditions, Diels-Alder, inverse electron demand Diels-Alder, oxime, hydrazone, and bio-orthogonal platforms combining multiple click reactions. We also discuss the influence of physical (e.g., topography, dimensionality), mechanical (e.g., stiffness, degradability, viscoelasticity), and chemical (e.g., adhesive sites, growth factor presentation) properties on cell mechanobiology, as well as provide commentary on future directions of click-based biomaterial cell culture models.

Click chemistry	**Rate constant k (M^{-1} s^{-1})**	**Pros**	**Cons**	**Common base polymers**	**Common reactive group 1**	**Common reactive group 2**	**Tunable biophysical properties**	**Reaction method**
CuAAC	10 - 100 [79]	Fast kinetics, high yield, and bioorthogonal Limited side product formation (azides/alkynes are not present in nature)	Potential catalyst toxicity Mammalian cells can only survive low copper concentrations Catalyst is unstable	Alginate, HA, PEG	Azide	Alkyne	Stiffness	Catalyst Occurs at physiologic conditions
SPAAC	10^{-2} - 1 [80]	No initiator or catalyst required High reactivity to allow rapid cell encapsulation	Complex synthesis of cyclooctynes Cyclooctyne reagents may undergo side reactions with nucleophiles (e.g., sulfhydryl side chain of free cysteines)	Chitosan, dextran, HA, NiPAAm, PEG	Cycloalkyne (DIFO, DBCO, BCN)	Azide	Stiffness, viscoelasticity Degradation Adhesion	Occurs at physiologic conditions
Diels-Alder	10^{-2} - 1 [81,82]	No toxic catalyst required Thermal reversibility	Slow gelation kinetics	Alginate, chitosan, gelatin, HA, PEG	Furan Furyl Fulvene	Maleimide Dichloro-maleic	Stiffness Gelation rate Degradation	Tempera-ture

		No reaction byproducts						
IEDDA	1 - 10^6 [83]	Rapid gelation kinetics at physiologic conditions No initiator or catalyst required 10,000 times faster than CuAAC	Trade-off between reactivity and stability	Alginate, gelatin, HA, PEG	Tetrazine	Norbornene Trans-cyclooctene (TCO)	Stiffness, viscoelasticity Gelation rate Adhesion	Occurs at physiologic conditions
Oxime	10^{-3} - 10 [84,85]	More stable than hydrazone bonds	Slow gelation kinetics	Alginate, HA, PEG, poly(DMA-co-DAAM)	Aldehyde Ketone	Hydroxyl-amine Aminooxy	Stiffness Gelation rate	pH
Hydrazone	10^{-2} - 100 [84–86]	pH reversibility	More likely to undergo hydrolysis compared to oximes Slow gelation kinetics	Alginate, ELP, HA, PEG	Aldehyde Ketone	Hydrazine	Viscoelasticity Degradation	Occurs at physiologic conditions pH Tempera-ture
Thiol-ene/-yne (radical-mediated)	N/A	Rapid gelation kinetics Spatiotemporal control	Toxicity of photoinitiators and radicals Cross-reactivity of thiols	Alginate, gelatin, HA, PDMS, PEG	Norbornene	Thiol	Stiffness, viscoelasticity Gelation rate Ligand presentation	Light
Thiol-Michael addition	10^{-6} - 100 [87,88]	No photoinitiator needed	Can't as easily control gelation; less spatiotemporal control Cross-reactivity of thiols Often requires basic conditions	Dextran, gelatin, HA, PEG	(Meth)acrylate, vinyl sulfone, maleimide	Thiol	Stiffness, viscoelasticity Gelation rate	pH

Table 2.1. Summary of click chemistries covered in this review.

2.3 Copper-catalyzed azide-alkyne cycloaddition (CuAAC)

Copper(I)-catalyzed azide-alkyne (CuAAC) reactions were published in 2002 by Meldal and Sharpless, who defined the term “click” chemistry the previous year, making it one of the first categorized click reactions[89,90]. The CuAAC reaction is able to proceed in aqueous solutions and

at physiologic temperatures, has fast kinetics, high yield, and is bioorthogonal[91]. The reaction itself involves reacting a terminal alkyne with an organic azide, creating a triazole ring, similar to uncatalyzed Huisgen cycloadditions (**Scheme 2.1**). This catalyzed version, however, proceeds much faster and with greater efficiency than the uncatalyzed cycloaddition.

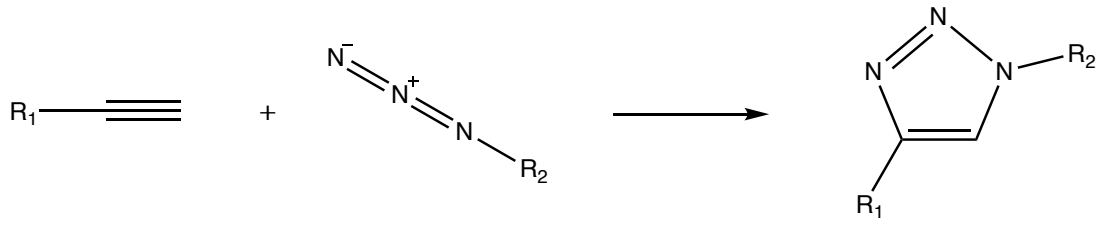

Scheme 2.1. Mechanism for copper(I)-catalyzed azide-alkyne cycloaddition.

Ossipov *et al.* published the first use of CuAAC to create azide and alkyne functionalized poly(vinyl alcohol) (PVA) hydrogels[92]. These hydrogels could reach stiffnesses (elastic moduli) from ~ 2-20 kPa depending on the density of the crosslinker and reactive groups available. Other researchers have reported using CuAAC to make hydrogels from other commonly used polymers in the biomaterials field, such as poly(ethylene glycol) (PEG)[93] and hyaluronic acid (HA)[94]. This mechanism yields quick gelation times, from 2-30 min, depending on the concentrations of the catalyst and polymer, as well as temperature[95].

CuAAC reactions, although fast and efficient, are limited in many biological applications due to the presence of copper ions as well as reactive oxygen species formed by the copper ions, which may be toxic to cells and destroy proteins, polysaccharides, and nucleic acids[96]. For many *in situ* cell cultures or *in vivo* analyses, click chemistries that do not require a metal catalyst are more favorable. For more extensive reviews on CuAAC chemistries, including its history and in-depth descriptions of the mechanism, the reader is referred to the following discussions[97–102]. Another

disadvantage of the CuAAC mechanism is that the addition of Cu(I) salt or the reduction of Cu(II) to the Cu(I) catalyst typically provides little to no spatiotemporal control over the reaction, which is often important in tissue engineering and cell culture applications. However, efforts to reduce Cu(II) to the Cu(I) catalyst using photochemical techniques (pCuAAC) resulted in better spatiotemporal control in the crosslinking of alkyne- and azide-functionalized PEG hydrogels. Following initial hydrogel formation through using thiol-yne chemistry, fluorescent patterns could be created in the hydrogel using photomasks where the pCuAAC reaction occurred in the regions exposed to light[103].

New efforts in designing degradable hydrogels for controlled drug delivery make use of the CuAAC reaction to enable enzymatic[104] or light-mediated hydrogel degradation. For example, Azagarsamy *et al.* reacted visible light degradable azide-functionalized coumarin onto an alkyne-functionalized PEG backbone using the copper catalyzed cycloaddition. The authors reported that higher copper concentration resulted in faster gelation, but with lower shear elastic moduli likely caused by heterogeneous network formation. While this report highlights the ability to engineer user-controlled photodegradable hydrogels, for cytocompatible platforms the authors suggest copper-free click mechanisms[105].

2.3.1 CuAAC hydrogels for cell culture

While the CuAAC mechanism often involves using cytotoxic amounts of copper catalysts, researchers have still been able to study cellular responses on hydrogels developed with this chemistry as long as cells were incorporated after hydrogel formation[106,107]. Liu *et al.* demonstrated that fibroblasts could attach and proliferate over a period of 7 days when seeded onto tetraacetylene

PEG hydrogels functionalized with RGD-containing diazide and formed by the CuAAC mechanism[95]. To better mimic the native ECM, Hu *et al.* developed a hydrogel system consisting of azide-functionalized HA and chondroitin sulfate that underwent crosslinking with alkyne-functionalized gelatin[108]. Following 7 days of culture, they found no significant difference in chondrocyte cell viability on the CuAAC crosslinked hydrogel versus standard TCPS, indicating that their system supported cell adhesion and viability. To introduce hydrazone interactions, Lou *et al.* functionalized azide-modified hydrazines onto HA using CuAAC[61]. They subsequently developed interpenetrating networks (IPNs) to create a two-step stress relaxing network that mimicked properties of the native ECM; more details can be found in Section 6 on hydrazone-based hydrogels.

In another study, Seelbach *et al.* used CuAAC to decorate propargylamine-derived hyaluronic acid with either a dendrimer containing an RGDS peptide and one azide, or a thermoresponsive poly(N-isopropylacrylamide) with a terminal azide group[109]. This enabled creation of an injectable, thermoresponsive hyaluronic acid hydrogel with controlled presentation of bioactive features. The authors encapsulated bone marrow-derived human mesenchymal stromal cells (hMSCs) by suspending them in the combined polymer solution and forming hydrogel beads following exposure to warm (37°C) culture media. Cell viability was maintained over a 21 day culture period; however, because this hydrogel did not incorporate degradability – for example, with a matrix metalloproteinase (MMP)-sensitive peptide – the cells did not show significant spreading and maintained spherical morphologies.

2.3.2 Gradient and photopatterned CuAAC hydrogels

Since the reporting of spatiotemporal control of CuAAC using photopatterning, researchers have used this to their advantage to create tailored hydrogels. Chen *et al.* engineered a micropatterned hydrogel consisting of alkyne-functionalized PEG and azide-functionalized bromine plasma polymer using photochemical Cu(II) reduction to Cu(I) to yield the azide-alkyne cycloaddition[110]. The photoinitiator radicals also led to the radical crosslinking of PEG, so using a photomask, the authors could spatially control hydrogel properties with regions of either the PEG hydrogel (patterned) or an azide-functionalized plasma polymer (unpatterned). The authors demonstrated the spatial control of mouse fibroblast attachment on the patterned regions of PEG compared to unpatterned samples.

The controlled presentation of biomolecules using CuAAC has also been explored, predominantly by Becker and colleagues. After developing a method for conjugating azide-functionalized peptides, like RGD, that could undergo CuAAC onto an alkyne gradient containing a self-assembled monolayer (SAM), Gallant *et al.* reported that increasing RGD concentration led to more smooth muscle cell adherence on their gradient system[111]. The conjugation of azide-functionalized RGD was also used to show increased attachment of rabbit corneal epithelial cells onto self-assembled poly(2-methyl-2-carboxytrimethylene carbonate-co-D, L-lactide) nanoparticles[112]. An alternative method of conjugating RGD to SAMs was used to investigate hMSC adhesion and focal adhesion formation, which increased with increasing RGD[113]. This same method was also applied to the conjugation of azide-functionalized osteogenic growth peptide (OGP) to an alkyne gradient to probe preosteoblast adhesion and proliferation. Cell adhesion increased with decreasing OGP concentration over the course of 3 days[114].

Following the discovery of the first known click chemistry - the CuAAC reaction - advancements in click-based systems rapidly developed. While the CuAAC reaction is amenable to quick crosslinking in aqueous solutions at physiologic conditions, the need for a copper catalyst proved to be cytotoxic for many cell experiments within the biomaterials field. The authors found no reports of CuAAC in the context of mammalian cell encapsulation and only one publication describing the proliferation of encapsulated yeast cells within CuAAC-crosslinked HA[94]. In this study, Crescenzi *et al*. reported 80% cell proliferation 24 hours after encapsulation within these hydrogels, which they formed *in situ* within a few minutes. Although this provides some preliminary evidence to support the use of CuAAC-based systems for tissue engineering applications, the lack of published studies is likely due to the toxicity of the copper ions generated[94]. While more cytocompatible catalysts are in development for use with this rapid crosslinking mechanism, the authors found no report of these different catalysts to create hydrogels for tissue engineering applications[115]. At this time, copper-free click reactions provide more cytocompatible platforms for investigating cell behaviors, including mechanobiology. Although CuAAC is not commonly used in biomaterial design for cell culture, this discovery was crucial to the advancement of more popular click chemistries used today, such as strain-promoted azide-alkyne cycloaddition (SPAAC) or thiol-ene click reactions.

2.4 Strain-promoted azide-alkyne cycloaddition (SPAAC)

Strain-promoted azide-alkyne cycloaddition (SPAAC) reactions were developed in the early 2000s by Bertozzi and coworkers to address cytotoxicity concerns associated with traditional copper-catalyzed click reactions[116]. SPAAC is bioorthogonal, can occur efficiently under physiologically-relevant conditions without additional reagents (e.g., catalysts, initiators), and results in products

with high stability[117–119]. Compared to previous copper-based reactions, SPAAC has more favorable gelation kinetics (second order rate constant, k ~ 0.1 $M^{-1}s^{-1}$) in aqueous conditions, permitting efficient cell encapsulation without significantly impacting cell viability[117,120,121].

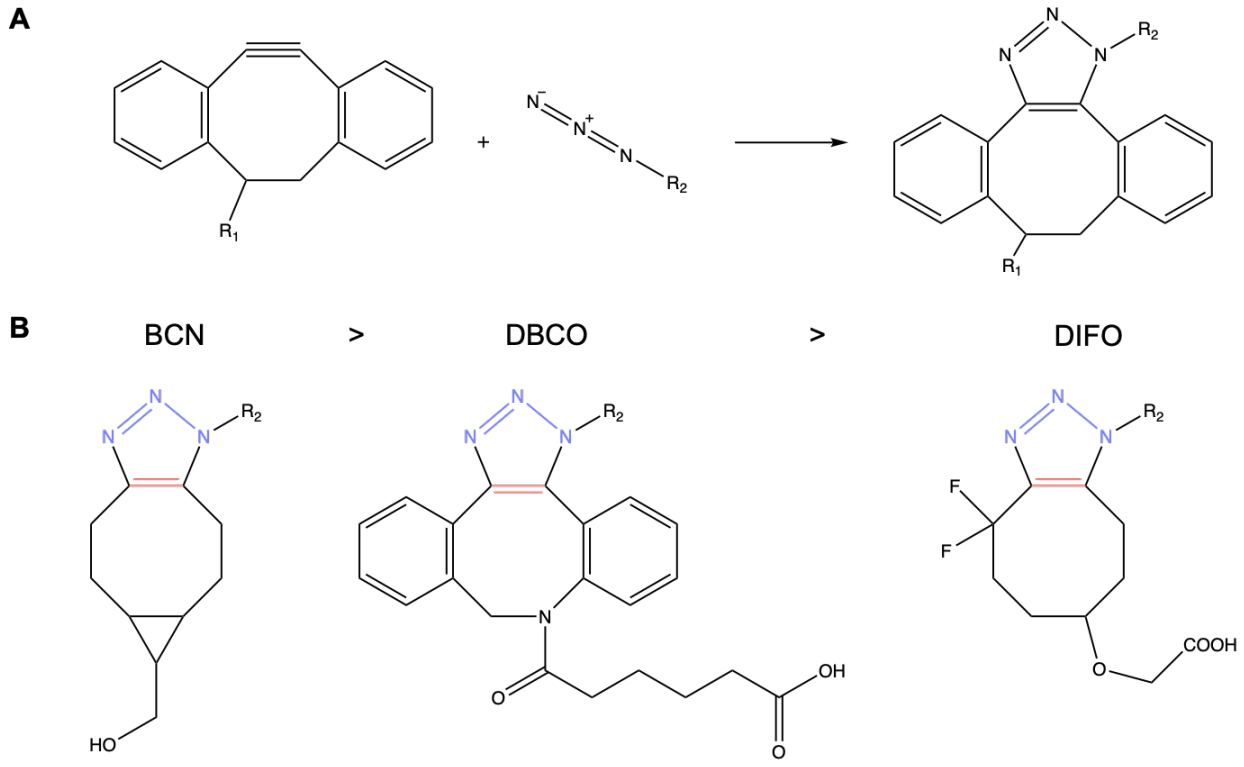

Scheme 2.2. Strain-promoted azide alkyne cycloaddition (SPAAC). (A) Dibenzylcyclooctyne (DBCO) reacts with a simple aliphatic azide to form the triazole product without the presence of a catalyst or initiator. (B) SPAAC products of common cycloalkynes (listed from most to least reactive), bicyclononyne (BCN), dibenzocyclooctyne (DBCO), and difluorinated cyclooctyne (DIFO), with an azide.

In general, SPAAC proceeds as a (3 + 2) dipolar cycloaddition of a strained cycloalkyne with an organic azide, generating a triazole[80,117]. The reaction is fast and spontaneous due to the release of the strained ring into a fused ring system, as shown in **Scheme 2.2A**. Similar to other click chemistries, the balance between reactivity and stability can be influenced by the reactant. Studies

have mainly focused on altering the cycloalkyne ring structure to increase reactivity, which can be beneficial for rapid 3D cell encapsulation.

Commonly used cycloalkynes used for hydrogel fabrication include difluorinated cyclooctyne (DIFO)[122,123], dibenzocyclooctyne (DBCO or DIBO)[13,124–127], and bicyclononyne (BCN)[13,128–130]. The order of reactant reactivity, BCN > DBCO > DIFO, can be explained by the increasing ring strain imposed onto the carbon atoms (**Scheme 2.2B**). Specifically, increased sp^2-hybridized carbons in the cyclooctyne results in increasing ring strain and reactivity[80,117]. Introduction of electron-withdrawing substituents such as fluorine on DIFO can lead to enhanced reactivity. DBCO falls within the class of (di)benzoannulated cyclooctynes, which impart increased reactivity compared to electron-withdrawing groups – the introduction of two adjacent benzene rings increases ring strain and ultimately, reactivity. For BCN, the fusion of cyclooctyne to cyclopropane produces a reactive bicyclo[6.1.0]non-4-yne that outweighs benzoannulated structures[131]. However, a significant limitation to SPAAC is that cyclooctyne synthesis involves several steps (many cyclooctyne derivative syntheses contain around 10 steps) with low overall yield, hindering scale-up. Fortunately, synthesis of BCN and DBCO is relatively simple, requiring only 4-5 steps. Compared to the growing body of literature surrounding the development of various cycloalkynes, modifications to the azide reactant have not been studied as extensively[80,132,133]. The majority of azides that participate in SPAAC reactions for hydrogel synthesis are simple aliphatic azides.

Depending on the reactive functional groups and application, polymerization can take anywhere from 90 seconds to an hour under physiologic conditions. Varying the relative macromer concentrations and degree of functionalization can produce hydrogels with variable stiffness,

viscoelasticity, degradation modes, and ligand presentation[134,135]. For example, early SPAAC work by Anseth and co-workers utilized difluorinated cyclooctyne (DIFO3) and azide moieties to quickly form 3D hydrogels within 5 minutes[122,123]. Material degradability can be tuned with pH, where slightly more basic conditions correlate with faster hydrolysis, presenting a promising approach for tissue engineering applications that require quick degradation and material clearance[136]. Increased stability and secondary incorporation of biomolecules can also be achieved by employing orthogonal click chemistries such as photopolymerizable thiol-ene addition, enabling researchers to independently study how variables such as mechanics and ligand presentation affect cell behavior over longer culture periods[123,135,137].

SPAAC has also been used to tether both adhesive ligands and growth factors to promote migration[122], stem cell lineage specification[138,139], and cell release[140]. Arakawa *et al.* demonstrated rapid hydrogel formation using PEG-tetraBCN and a di-azide crosslinker decorated with an adhesive RGD sequence, MMP-degradable sequence, and an *ortho*-nitrobenzyl (*o*NB) group[130]. Hydrogels formed through SPAAC were stable and supported both customizable microvessel generation and long-term viability of encapsulated human umbilical vein endothelial cells (HUVECs). High-resolution spatiotemporal control over vessel formation allowed for a wide range of tunable physical properties such as geometry, thickness, and flow, critical for studying blood vessel function and hemodynamics. Using a similar approach, Shadish *et al.* demonstrated the ability to spatiotemporally immobilize proteins via BCN-azide SPAAC chemistry as well as trigger protein photocleavage with potential applications in directing dynamic cellular behaviors[129]. HeLa cells encapsulated within SPAAC hydrogels were subjected to patterned violet light (λ = 400 nm), releasing tethered epidermal growth factor (EGF) from specific regions. Over

two weeks, presentation of retained EGF promoted increased cell density and spheroid growth compared to regions without immobilized EGF, highlighting the ability to tether and release bioactive molecules in a spatiotemporal manner to guide cell fate.

2.4.1 Thermoresponsive SPAAC hydrogels

Thermally-responsive hydrogels have also been developed using SPAAC chemistry. Truong *et al.* fabricated chitosan-based hydrogels that were stable at physiologically-relevant conditions[141]. Gelation of azide-functionalized chitosan and propiolic acid ester-functionalized PEG crosslinker occurred within 15 minutes at 37°C. Increasing polymer concentrations and greater alkyne-azide ratios resulted in faster gelation times (from 55 minutes to 4 minutes) and increased stiffness (up to storage modulus, G' ~ 44 kPa). MSCs seeded atop hydrogels for seven days exhibited fibroblastic morphologies typically seen on tissue culture polystyrene, with defined F-actin filaments and vinculin staining, important for adhesion and spreading. In contrast, cell spreading was more restricted in 3D cultures and cells remained rounded.

To promote tissue-specific repair, Guo *et al.* formed thermoresponsive poly(N-isopropylacrylamide-*co*-glycidyl methacrylate) (P(NiPAAM-*co*-GMA)) hydrogels capable of biomolecule conjugation via SPAAC[142]. The alkyne-containing PEG crosslinker was modified with azide-modified biomolecules designed to promote either chondrogenesis, such as chondroitin sulfate and N-cadherin-mimicking peptide, or osteogenesis, including bone marrow homing peptide 1 and glycine-histidine-lysine. Advantageously, SPAAC-based conjugation of cartilage- and bone-specific biomolecules to the crosslinker occurred through simple mixing at room temperature in water, and presentation of biochemical cues was varied by changing the crosslinker

concentration. MSCs encapsulated within cartilage-promoting hydrogels led to cartilage-like matrix synthesis (sulfated glycosaminoglycans) and maintained viability over a month. In contrast, MSCs exposed to bone-specific molecules promoted osteogenesis through expression of osteogenic markers Runt-related transcription factor 2 (RUNX2) and osteopontin.

2.4.2 Viscoelastic SPAAC hydrogels

There is tremendous interest in generating hydrogels that recapitulate the viscoelastic stress relaxing nature of tissues. One method to tune viscoelastic properties is through secondary physical interactions introduced via dibenzylcyclooctyne (DBCO) groups. By varying the ratio of covalent DBCO-azide interactions, physical DBCO-DBCO interactions (i.e., hydrophobic and hydrogen bonding interactions), and degradable macromer (i.e., incorporation of a labile ester linkage in PEG-azide), Tan *et al.* was able to match cartilage stiffness, viscoelasticity, and degradability, respectively[125]. Hydrogels formed with an excess of PEG-DBCO exhibited increased stiffness and decreased swelling compared to hydrogels formed with an excess of PEG-azide due to the physical DBCO-DBCO interactions. The increase in non-covalent interactions resulted in faster stress relaxation (stress relaxation time $\tau_{1/2}$ of ~ 132 min compared to 291-320 min). Stiffer and more viscoelastic hydrogels supported increased chondrocyte proliferation and deposition of type II collagen and glycosaminoglycans, both of which are chondrogenic markers. Degradation also played a key role in maintaining the chondrocyte phenotype; chondrocytes encapsulated in faster-degrading groups showed greater proliferation and more robust deposition of type II collagen.

Combining boronate ester and SPAAC chemistries, Tang *et al.* further demonstrated the importance of stress relaxation timescales on cell-matrix interactions[127]. Viscoelasticity was

introduced via boronate ester bonds and hydrogels were stabilized through SPAAC chemistry between DBCO and azide groups (**Figure 2.2A,B**), with all hydrogel groups experiencing stress relaxation times of one second or less. In comparison to the previous viscoelastic hydrogel system, this study targeted relaxation timescales to match those of biological processes (e.g., propagation of mechanical signals from the cytoplasm to the nucleus). In comparison to elastic hydrogels, encapsulated hMSCs in stress relaxing substrates displayed increased spreading, larger cell and nuclear volume, and increased nuclear localization of the transcriptional mechanoregulators YAP/TAZ, extending the ability to easily tune complex mechanics to study cell morphology (**Figure 2.2C-G**).

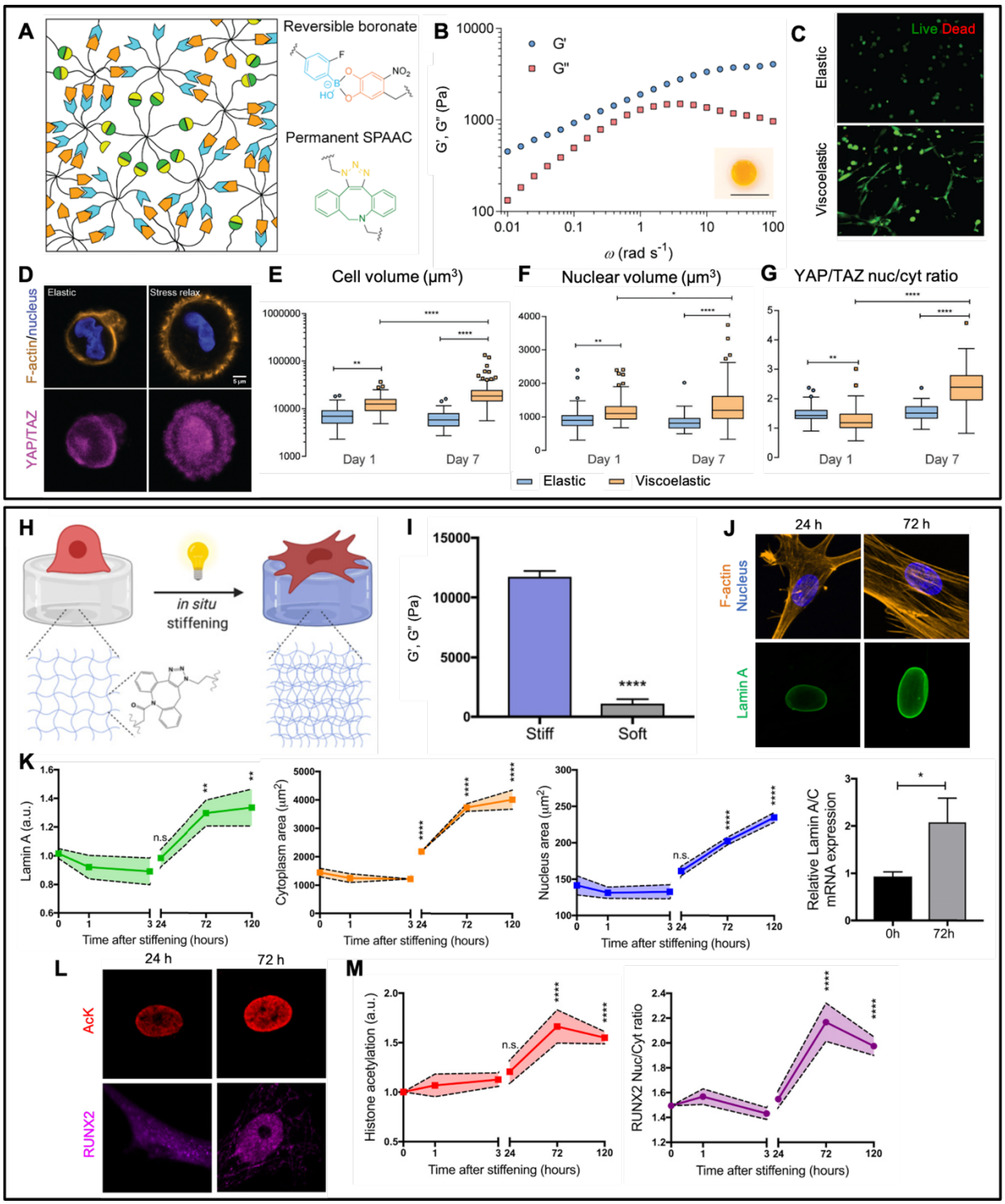

Figure 2.2. SPAAC chemistry can be used in combination with secondary crosslinking mechanisms to create dynamic and complex hydrogel networks useful for studying mechanotransduction. (A) A hybrid network containing reversible boronate ester bonds and permanent SPAAC interactions allowed for the fabrication of a stable hydrogel with stress relaxing properties. (B) Frequency sweep of a swollen hydrogel after 7 days (shown in inset photograph,

scale bar = 1 cm) demonstrated viscoelasticity and mechanical stability. (C) Cells in viscoelastic (stress relaxing) hydrogels displayed increased cell spread area after 7 days. (D) Immunofluorescent staining for YAP/TAZ (magenta), F-actin (orange), and nuclei (blue) in hMSCs encapsulated for 7 days. Scale bar = 5 μm. (E-G) Quantification of cell volume, nuclear volume, and nuclear localization of YAP/TAZ showed significant increases in all categories for cells in viscoelastic hydrogels. (A-G) adapted with permission from[127]. Copyright 2018 Wiley-VCH. (H) Initially formed SPAAC hydrogels can undergo photostiffening in the presence of excess DBCO groups. (I) Average storage moduli, G', of the compliant (G' ~ 1 kPa) and stiff (G' ~ 12 kPa) hydrogel groups, n = 3 hydrogels. (J) Immunofluorescent staining for lamin A (green), F-actin (yellow), and nuclei (blue) in hMSCs 24 and 72 hours after stiffening. (K) Quantification of lamin A intensity and cell areas show gradual increases between 0 and 120 hours after stiffening. (L) Representative hMSCs stained for RUNX2 (purple) and histone acetylation, AcK (red) 24 and 72 hours after stiffening. (M) Quantification of histone acetylation and RUNX2 nuclear localization shows increased levels in hMSCs post-stiffening. (H-M) adapted with permission from[143]. Copyright 2020 National Academy of Sciences.

2.4.3 Dual-crosslinking SPAAC hydrogel systems

Several groups have combined orthogonal click chemistries to achieve spatiotemporally tunable mechanics. After synthesizing initially compliant hydrogels (G' ~ 700 Pa) via a SPAAC reaction between DBCO and azide groups, Brown *et al.* then further stiffened the network through secondary photopolymerization of excess DBCO groups (G' ~ 5 kPa)[126]. The on-demand stiffening capabilities of this system enabled a rapid and stable increase in stiffness of hydrogels to between 200-700% of their initial values (given an alkyne:azide ratio of 2-3:1), relevant to changes in stiffness related to muscle disease. Indeed, C2C12 myoblasts encapsulated in initially compliant networks (G' ~ 700 Pa) showed decreased cell spreading and lower nuclear localization of YAP after immediate photostiffening (G' ~ 5 kPa). In contrast, encapsulated myoblasts that underwent photostiffening after seven days were able to spread prior to the delayed stiffening and interestingly, exhibited an overall increase in cell elongation and YAP nuclear localization by day 15. The dual crosslinking modes provide a high level of control over mechanics to recapitulate dynamic disease processes.

One emerging application of tunable hydrogel systems is the ability to study how mechanical cues directly influence cell epigenetic programming and gene expression. Similar to the previous study, Killaars *et al*. formed a PEG-based hydrogel through DBCO-azide interactions that could undergo a secondary photocrosslinking step to enable *in situ* stiffening of excess DBCO groups (**Figure 2.2H,I**)[143]. The dynamic nature of this hydrogel platform enables direct analysis of how evolving mechanics can affect epigenetic remodeling as a function of time. hMSCs were seeded atop initially compliant hydrogels (G' = 1 kPa) that were stiffened (G' = 12 kPa) after one day and analyzed at several timepoints after stiffening (0, 1, 3, 24, 72, and 120 hours). While nuclear localization of YAP occurred within 24 hours, F-actin stress fiber organization was only evident after 72 hours, suggesting that sustained cytoskeletal tension occurs after nuclear localization of mechanosensitive transcriptional co-activators (**Figure 2.2J,K**). The timescale of Lamin A intensity, which plays a role in force transmission via the LINC complex, correlated with F-actin stress fiber formation. Interestingly, *in situ* stiffening resulted in increased histone acetylation and RUNX2 nuclear localization within the same 72-hour timeframe, suggesting its connection to nuclear tension (**Figure 2.2L,M**). Additionally, increased nuclear tension, caused by stiffening, led to decreased activity of epigenetic modulators histone deacetylases (HDAC)1, 2, and 3 as well as reduced osteogenic fate.

Photochemistry can also be used to introduce biomolecular regulators of cell fate with spatiotemporal control. DeForest *et al.* designed a 3D hydrogel system where initial cell encapsulation occurred via SPAAC between azide-functionalized PEG and bis(DIFO3)-functionalized crosslinker and secondary thiol-ene addition enabled biomolecule patterning[123]. The crosslinker contained a photoreactive alkene group and an MMP-cleavable sequence to allow

independent control over chemical and mechanical properties, respectively. Specifically, the photoreactive alkene participates in thiol-ene addition to introduce biomolecule patterning and the enzymatically degradable sequence allows cell-mediated remodeling. Fibroblast morphology was assessed in hydrogels with photopatterned regions of thiol-functionalized RGD, and cells encapsulated within the patterned regions displayed greater spreading and elongation compared to those within unpatterned regions, showing the robust capability of the 3D platform to promote and study specific cellular outcomes.

2.4.4 SPAAC for tissue engineering

SPAAC has also been used in the design of tunable tissue engineering models. Han *et al.* developed an HA-based injectable scaffold for chondrocyte encapsulation[124]. HA was modified with DBCO-PEG groups via a one-step 1-ethyl-3(3-dimethylaminopropyl)carbodiimide (EDC)/*N*-hydroxysuccinimide (NHS) coupling reaction and mixed with PEG-azide crosslinker to form hydrogels. Varying the crosslinker concentration impacted properties such as stiffness, gelation kinetics, and hydrogel microstructure – to a certain extent, increasing crosslinker concentration correlated with increasing stiffness and decreasing pore size. Chondrocytes encapsulated within the HA hydrogels were found to be uniformly distributed and remain rounded over the 5-day culture period, with observed cell aggregation within stiffer hydrogel groups. Injection of cell-laden hydrogels into mice resulted in regeneration of cartilaginous tissue. Specifically, lower stiffness hydrogels led to host cells migrating into the degraded hydrogels, while intermediate stiffness groups exhibited increased neocartilage formation *in vivo*. Wang *et al.* used azadibenzocyclooctyne-azide SPAAC chemistry to prepare injectable dextran-based hydrogels with varying stiffness (G' ~ 2-6 kPa through increasing polymer concentration and/or polymer

modification) and gelation time (as quick as 1.1 min with increasing polymer modification)[144]. Using a higher polymer concentration (10%) to support cell encapsulation, chondrocytes exhibited high viability and increasing DNA content over the 3-week culture period. In contrast, DNA content of chondrocyte spheroids showed a more stable output, correlating with slower proliferation. Interestingly, normalized ECM production (glycosaminoglycans and collagen) by chondrocyte spheroids was significantly higher. These results prove promising for cartilage tissue engineering.

The incorporation of a photoreactive nitrobenzyl moiety within the azide-functionalized crosslinker allows for UV-mediated degradation after initial SPAAC hydrogel fabrication. McKinnon *et al.* used a dual reaction scheme to fabricate neural networks for studying axon behavior in neuromuscular junctions after injury[145]. Design and formation of hydrogel channels to promote motor neuron axon extension revealed that the speed and extent of outgrowth was independent of channel width. Co-encapsulation of neuron embryoid bodies and C2C12 myotubes within the hydrogel network facilitated significant branching and axon-myotube interactions, indicated by acetylcholine receptor staining for neuromuscular junctions.

Elastin-like proteins (ELPs) are highly modular and can be designed with elastin-like (i.e., VPG*X*G, where the non-proline *X* residue can be used to incorporate chemical functionalities) and bioactive (e.g., adhesion, degradation) domains to regulate cellular behaviors[128]. Madl *et al.* demonstrated functionalization of ELP lysine residues with either azide or BCN groups to permit SPAAC chemistry. Upon mixing, hydrogel formation occurs within seconds and completes within minutes. Stiffness could be increased by either increasing ELP concentration or the molar ratio of

BCN to ELP polymer to yield biologically relevant tissue mechanics (storage modulus, G' ~ 180-1200 Pa). Encapsulation of multiple cell types within RGD-containing SPAAC hydrogels resulted in high viability and maintenance of cell phenotypes; hMSCs displayed actin stress fibers and spread morphologies after two days, HUVECs organized into tubular networks and stained positive for endothelial marker CD31 after one week, and murine neural progenitor cells expressed nestin (neural progenitor marker) and were able to differentiate into neurons and astrocytes following the one week growth period[128,146]. Independent tuning of adhesive sites revealed a correlation between increasing adhesive RGD presentation with hMSC spreading and stress fiber formation to a certain stiffness, agreeing with previous studies[147].

In summary, SPAAC gained momentum as a catalyst-free alternative to CuAAC and has been widely adopted to synthesize hydrogels due to its favorable reaction rate and ability to be combined with other chemistries to produce dual-crosslinked networks. Many of the common cycloalkynes used in SPAAC reactions, including DBCO, support favorable gelation times but more arduous and inefficient syntheses. Fortunately, recent developments in the design of cycloalkynes with increasing strains, such as BCN and DBCO, have led to more rapid gelation times as well as decreased number of synthesis steps and increased overall yield. The utility of the SPAAC reaction extends beyond rapid cell encapsulation and can be demonstrated by its tunability and bioorthogonality. The introduction of secondary crosslinking mechanisms, whether it be between excess cycloalkynes or a reaction mediated by photochemistry, provides endless opportunities to investigate the influence of individual and combined mechanical and biochemical cues on cell behavior and fate. Disease-relevant changes in ECM stiffness, viscoelasticity, degradation, and ligand presentation can all be incorporated within SPAAC hydrogel systems by tuning polymer

concentration, ratio of physical interactions, addition of photodegradable groups, and introduction of pendant adhesive cues or growth factors, respectively. In particular, SPAAC has and will continue to be an attractive method to study cell mechanobiology in 3D cultures.

2.5 Diels-Alder (DA)

The Diels-Alder (DA) reaction is a highly efficient and stereoselective [4 + 2] cycloaddition of a diene and dienophile that can proceed without the use of a catalyst and does not yield any byproducts (**Scheme 2.3A**)[148]. There are several variations of the traditional electron-demand DA reaction, including intramolecular reactions in which the diene and dienophile are on the same molecule[149,150], hetero-DA reactions containing at least one heteroatom (commonly nitrogen or oxygen)[151,152], and inverse electron demand DA reactions (Section 5). Compared to other functional moieties such as thiols, dienes and dienophiles are less reactive and more stable[148,153]. DA reaction kinetics can be accelerated via electron-rich dienes (e.g., alkyls, amines, hydroxyls) and electron-poor dienophiles (e.g., carboxyls, carbonyls, ketones)[148]. Gelation rates are improved in aqueous conditions due to increasing hydrophobicity within the reaction center of the diene and hydrophobic interactions from chosen diene-dienophile substituents, making DA cycloadditions particularly useful for creating cytocompatible hydrogels[81,154,155].

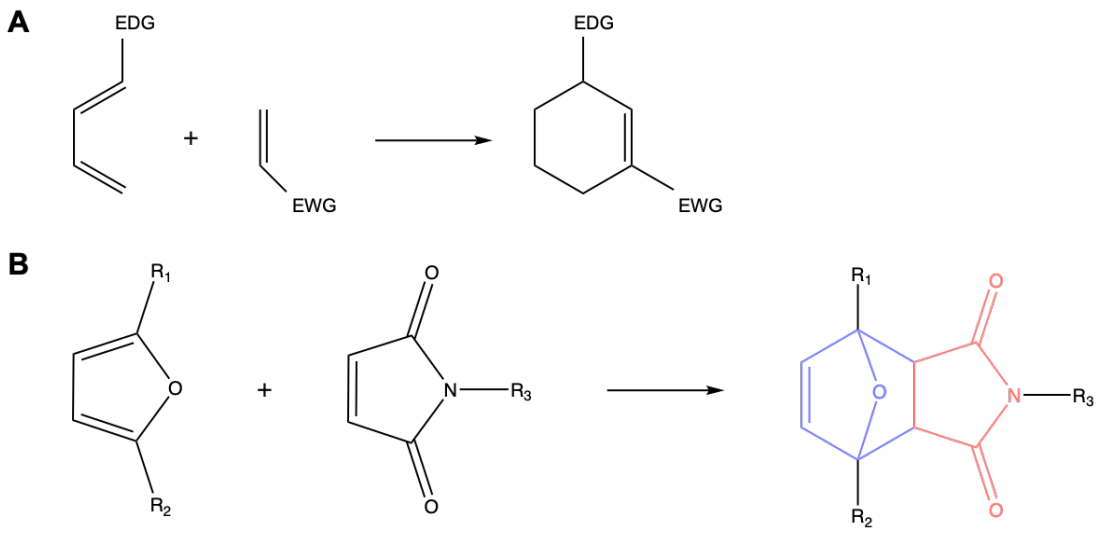

Scheme 2.3. (A) Conventional electron-demand Diels-Alder (DA) cycloaddition of an electron-rich diene with an electron donating group (EDG) and an electron-poor dienophile bearing an electron withdrawing group (EWG). (B) DA reaction between a furan (EDG) and maleimide (EWG) group.

DA reactions are temperature-sensitive and exhibit increased reversibility (via a retro-Diels-Alder reaction) at elevated temperatures (> 100°C). By varying diene and dienophile groups, the thermal equilibrium can be shifted to physiologic conditions, which has facilitated the use of DA hydrogels as tunable biomaterial systems for drug delivery and other applications[156–160]. Several studies have investigated this temperature dependency and have shown variability based on parameters such as chosen diene/dienophile substituent, concentration of diene/dienophile groups, and molecular weight[161–163].

Among the growing number of suitable diene-dienophile pairs, furan and maleimide have become the most established for hydrogel fabrication, predominantly for their rapid reaction rate at physiologic temperatures (**Scheme 2.3B**). Biomimetic hydrogels synthesized by aqueous DA reaction of furan and maleimide groups were initially reported by Wei *et al.*, demonstrating high

stability under mild reaction conditions[164]. Hydrogel formation was shown to be temperature and solvent-dependent, where gelation occurred more rapidly in water (50 min at 37°C and 10 min at 77°C) compared to N,N-dimethylformamide (DMF) over the entire range of studied temperatures. Additionally, Gregoritza *et al*. incorporated various hydrophobic spacers between the polymer backbone and functional groups to enable quicker DA crosslinking[165]. Hydrogels with longer hydrophobic spacers displayed faster gelation, increased crosslinking density and stability, and delayed antibody release profiles. Furan-maleimide DA hydrogels have since been used extensively for tissue engineering and cell culture studies[14,18,166–171].

Due to its thermally-induced reversibility, DA click chemistry has been used for the development of self-healing, injectable hydrogels. Yu *et al.* studied the shear thinning and self-healing properties of DA-based HA/PEG hydrogels in response to 10-30 cycles of applied stress and demonstrated their ability to easily recover with minimal fatigue. Fan *et al.* successfully fabricated biodegradable HA hydrogels with the ability to release dexamethasone, a corticosteroid that induces cell differentiation, in a sustained manner via temperature control[172]. The high tunability afforded by furan-maleimide HA hydrogels, including stiffness through varying polymer concentration and degree of furan modification on HA, porosity via cryogelation, and pore size distribution by tuning thaw temperature, was demonstrated by Owen *et al.*[167]. Additionally, 3D two-photon photopatterning was used to enable spatiotemporal control of protein immobilization within the substrate as well, providing a versatile platform for guiding cell fate[167]. By combining thermoresponsive poloxamines modified with DA-friendly maleimide and furyl moieties, rapid hydrogel formation could be induced at 37°C with controlled stability and triphasic antibody release between 14 and 329 days[173]. Hydrogel stiffness was tuned by varying the ratio of different

armed polymer (e.g., 4-arm and 8-arm poloxamine). Hydrogel swelling and degradation both correlated with stiffness – hydrogels with increased ratio of 8-arm to 4-arm polymer were stiffer and exhibited decreased swelling (quantified by mass) and dissolution in phosphate buffer (pH 7.4) at 37°C.

By encapsulating model proteins within DA hydrogels, Tan *et al.* successfully controlled drug or protein release by taking advantage of the protein charges[169]. Maleimide- and furan-functionalized HA were synthesized via oxidation by sodium periodate and EDC/NHS activation with furan-PEG-NH_2, respectively. Rheological characterization confirmed complete gelation in under an hour, and demonstrated the temperature- and time-dependencies of hydrogel mechanics and swelling behaviors. Negatively-charged insulin and positively-charged lysozyme were encapsulated to enable sustained release. Positively-charged lysozyme demonstrated a slower release profile, perhaps due to electrostatic interactions with negatively-charged HA, compared to the greater burst release profile shown with negatively-charged insulin. Similarly, Koehler *et al*. successfully applied DA chemistry to control the release of dexamethasone toward hMSC osteogenic differentiation[174]. After forming the initial network via Michael addition between thiol and maleimide groups, furan-modified dexamethasone was covalently tethered into the hydrogels. By exploiting the dynamic equilibrium between DA products and reactants, sustained release of the tethered dexamethasone was achieved in a precise manner. Robust hMSC osteogenic differentiation was observed over 14 days as shown via intense alkaline phosphatase staining and mineral deposition.

The reversible nature of DA reactions lends itself to applications requiring degradability, often a desirable feature in biomaterials. In particular, maleimide-based hydrogels fabricated using step-growth polymerization will readily degrade via retro-DA reactions near physiologic temperatures[175]. While gelation is favored at 37°C, a small number of reactants are still likely present, which can react to form a DA pair or hydrolyze into maleamic derivatives that will not participate in DA reactions. Over time, this can shift the dynamic equilibrium until the DA reaction is reversed[162,176]. By varying the polymer molecular weight and branching factors, the degradation rate can be tuned for specific tissue engineering applications. This feature has been used to develop DA-based hydrogel carriers for temporal protein or drug release[177–184]. Several hydrogel systems have combined DA crosslinking with secondary (physical) interactions to create hydrogels with increased toughness, viscoelasticity, self-healing properties, and responsiveness to external stimulants[160,185–190]. Recent studies have also begun to explore other DA-amenable moieties such as furyl[15,162,171,191] and fulvene[159,192] groups as dienes as well as dichloromaleic[159] groups as dienophiles that exhibit decreased degradability. Additional details on Diels-Alder chemistry can be found in the following reviews[148,193–195].

2.5.1 DA hydrogels for 2D and 3D cell cultures

Recently, the ability to control relevant features such as substrate stability, mechanics, and ligand presentation have enabled investigations of DA hydrogel properties on cell behavior. Shoichet and co-workers expanded upon initial reports developing DA-based polymers and introduced a host of furan-maleimide DA hydrogels for soft tissue engineering and regenerative medicine applications. A simple, one-step reaction using 4-(4,6-di-methyoxy-1,3,5-triazin-2-yl)-4-methylmorpholinium (DMTMM), an efficient activator of polysaccharide carboxyl groups in aqueous conditions, allowed furfurylamine coupling to HA carboxylates at a higher yield compared to other methods such as carbodiimide chemistry[18,196]. The addition of bis-maleimide PEG crosslinker enabled DA hydrogel fabrication over a range of soft tissue mechanics (storage modulus, G' ~ 100-1000 Pa). Stiffness was manipulated by varying crosslinker concentration (i.e., furan/maleimide ratio) and degradation was monitored with respect to crosslinker amount; it was noted that varying other properties such as macromer molecular weight could also be used to tune stiffness and degradation. Human epithelial cells seeded atop compliant HA hydrogels attached after 24 hours and spread throughout the two-week culture period.

Although hydrogels requiring a more acidic environment (pH 5.5) for gelation are suitable for 2D cell culture, encapsulation of cells within a 3D environment requires stable hydrogel formation under physiologic conditions. To utilize DA click chemistry for 3D cultures, reaction kinetics can be accelerated by modifying the electronic properties of reaction pair substituents. Smith *et al.* functionalized the HA backbone with methylfuran groups, resulting in more rapid gelation (average gelation of 12 min compared to 32 min with furan-functionalized HA) without affecting bulk mechanics[176]. The ability to rapidly form hydrogels at physiologically-relevant pH was next

demonstrated with multiple cancer cell lines, which exhibited high cell viability over the 7-day culture period as well as characteristic spheroid morphology for the MCF7 breast cancer cell line. Another approach to improve gelation kinetics for cell encapsulation replaced the commonly used furan diene with a more electron-rich group, fulvene[192]. Furan-, methylfuran-, fulvene-, and maleimide-functionalized PEG were synthesized via standard amide coupling chemistries. Compared to furan and methylfuran, gelation kinetics for fulvene-maleimide 4-arm PEG hydrogels improved 10-fold (time to reach critical gelation point: 20 min for fulvene, 10 hours for furan, 7 hours for methylfuran) (**Figure 2.3A-C**). By increasing polymer concentration and the number of reactive sites (i.e., 8-arm PEG), fulvene-based hydrogels were able to cross the critical gelation point in under 30 seconds. The increased gelation kinetics prevented cell settling during encapsulation. Degradable ELPs containing RGD adhesive sequences were functionalized with fulvene groups to enable incorporation into the hydrogels (**Figure 2.3D**). Encapsulated hMSCs exhibited high viability and protrusions into the surrounding environment, indicative of cell-mediated remodeling (**Figure 2.3E-G**).

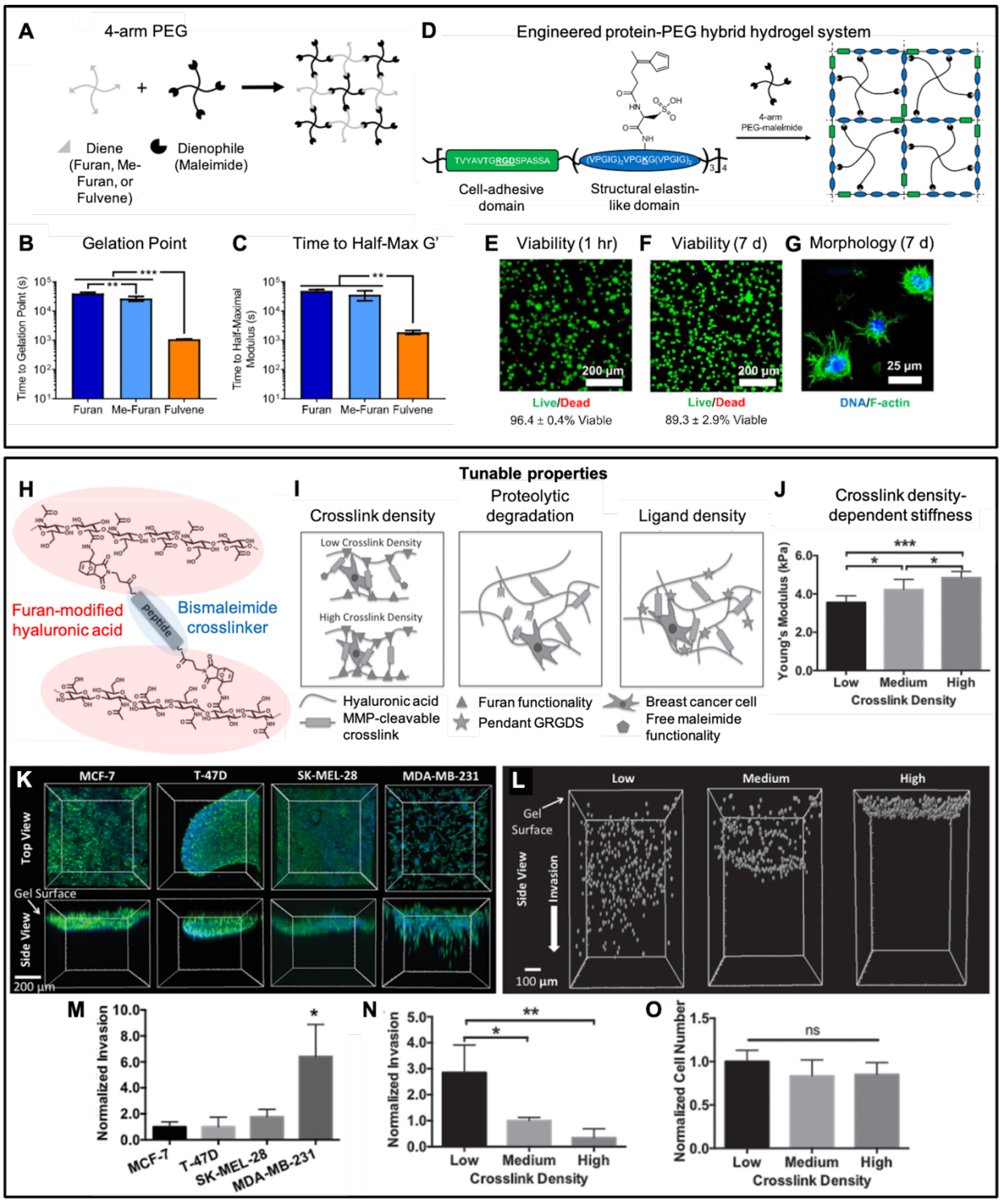

Figure 2.3. Diels Alder (DA) hydrogel tunability can be used to explore the influence of matrix mechanics on cell behaviors. (A) DA hydrogels can be synthesized by mixing a diene (furan, methylfuran, or fulvene) with a dienophile (maleimide). (B,C) The point of gelation and the time it takes to reach half of the maximum storage modulus, G', can be tuned by varying the diene group. Compared to furan and methylfuran, the more electron-rich fulvene demonstrated faster

gelation times. (D) Engineered ELPs functionalized with fulvenes can be used to fabricate hydrogels with cell adhesive and structural domains. (E-G) Encapsulated hMSCs maintained high viability after 7 days and spread. (A-G) adapted with permission from[192]. Copyright 2019, American Chemical Society. (H) DA hydrogels can be fabricated using furan-modified HA and bismaleimide crosslinkers. (I) Several modifications can be made using DA chemistry to tune stiffness (crosslink density), degradation, and bioactive molecule presentation (ligand density). (J) Young's moduli of hydrogels increased as crosslink density increased. (K) Invasion of MCF-7, T-47D, SK-MEL-28, and MDA-MB-231 cancer cell lines in medium crosslinked hydrogels revealed different morphologies and infiltration mechanisms based on cell type. (L-O) MDA-MB-231 invasion was stifled as hydrogel stiffness increased. (H-O) adapted with permission from[14]. Copyright 2015 WILEY-VCH.

DA click chemistry has also been utilized for co-culture systems. Silva *et al.* synthesized furan-modified gellan gum hydrogels using the DMTMM coupling method described previously[18,166]. Maleimide-RGD adhesive peptides were incorporated via the Diels-Alder reaction, and studies showed that neural stem/progenitor cells (NSPCs) migrated and spread with distinctive cytoplasmic extensions in both 2D and 3D cultures. However, without the presence of RGD, increased cell-cell interactions resulted in aggregates of neurospheres. Co-culture of NSPCs and olfactory ensheathing glia (OEG) promoted increased NSPC proliferation in direct and indirect co-culture, indicating that OEG secrete factors that do not require direct cell-cell contact to enhance proliferation.

2.5.2 Thermosensitive DA hydrogels

To address the slower gelation kinetics of the DA reaction that may be unfavorable for injection-based applications, DA hydrogels have been engineered incorporating thermosensitive moieties to enable dual crosslinking. Bi *et al.* explored the use of thermosensitive hydroxypropyl chitin (HPCH) as the backbone polymer for the development of a DA-based injectable hydrogel[191]. The inherent biocompatibility and thermosensitive properties of chitin coupled with furyl-maleimide DA reaction kinetics enabled a dually crosslinked system for both *in vitro* and *in vivo* studies. Even

after HPCH modification with furyl moieties via etherification, the HPCH demonstrated retention of its ability to gel at physiologic conditions. Initial physical crosslinking of chitin at 37°C enabled initial cell incorporation and support prior to the two-hour DA gelation between furyl-modified HPCH and bis-maleimide PEG crosslinker. Manipulation of hydrogel mechanical strength correlated with crosslink density, and encapsulated cancer cells displayed rounded morphologies and formed spheroids with increasing aggregate diameter over time. Abandansari *et al*. combined DA crosslinking between furan-functionalized gelatin and bis-maleimide-PEG crosslinker with thermoresponsive interactions via chitosan grafted with Pluronic F127 (CP), an FDA-approved thermosensitive copolymer, to create a dual crosslinked hydrogel with more robust mechanics and improved cell retention during injection[197]. Compared to the DA- and CP-only hydrogels (G' ~ 0.1-1 kPa and ~ 4-8 kPa, respectively), the dual crosslinked hydrogel exhibited higher stiffness at 37°C (G' > 10 kPa) due to increased crosslinking as well as lower swelling and higher stability while still being injectable. The injected dual hydrogel led to higher hydrogel (70% on day 3) and cardiomyocyte retention (45% after 24 hours) compared to free cells (15% viable cells after 24 hours) or DA hydrogel (15% material retention on day 3 and 20% cells after 24 hours) groups. Additionally, the hybrid hydrogel induced *in vivo* tissue regeneration and preserved the phenotype of the encapsulated cardiac muscle cells.

2.5.3 DA hydrogels to model tumorigenesis

Efforts to create tumor mimetics have also been explored using DA-based hydrogels. Fisher *et al.* exploited the ability to independently tune multiple HA hydrogel properties, including mechanical (e.g., stiffness, degradability) and chemical (e.g., adhesion) cues (**Figure 2.3H,I**)[14]. Similar to previous studies, crosslink density and HA concentration were decoupled by varying the degree of

furan modification on HA while maintaining the same crosslinker concentration for all formulations (**Figure 2.3J**). Hydrogels with a lower crosslink density (Young's modulus, E ~ 3.5 kPa) resulted in greater MDA-MB-231 breast cancer cell invasion into the hydrogels compared with cells within stiffer hydrogels (E ~ 5 kPa) (**Figure 2.3K-O**). Incorporation of MMP-degradable crosslinks also correlated with increased cell invasion independent of stiffness. Interestingly, increased adhesive ligand density led to greater cell proliferation but did not affect the degree of cellular invasion into the hydrogel.

This model was further exploited as a high-throughput metastatic cancer drug screening platform[168]. In addition to the DA chemistry, methylcellulose was covalently incorporated into the matrix to introduce hydrophobic interactions and consequently, tunable stress relaxation properties. The platform was then used to independently assess cell viability and invasion over a range of pharmacological treatments and hydrogel compositions in a lung cancer model, lymphangioleiomyomaosis (LAM). Compared to elastic hydrogel controls, LAM smooth muscle cells displayed increased invasion in 3D viscoelastic substrates due to stress relaxation properties. Drug screening was then tested within a 384-well format to enable higher-throughput analysis, and candidates that showed a decrease in both cell viability and invasion included those that impacted cell cycle (e.g., cyclin-dependent kinase inhibitors) and autophagy (e.g., IRE1 inhibitors). Overall, the hydrogel platform allowed for several physicochemical properties to be varied (e.g., stiffness, viscoelasticity, biochemical composition) with increased throughput to study cell responses to treatments.

In summary, DA chemistry is a highly selective cycloaddition that is easy to synthesize, does not have side reactions or byproducts, and is accelerated in water. While many DA reactions demonstrate slower gelation kinetics compared to other click reactions, this can be overcome by substituting in more hydrolytically stable diene-dienophile pairs[164,198]. The slower DA reaction has also been used in conjunction with secondary assembly mechanisms such as fast-gelling thermosensitive polymers. The DA reaction is also thermosensitive, with higher temperatures resulting in lower gelation times. Under certain conditions such as increased temperature or choice of diene-dienophile pair, the reaction is also reversible, enabling controlled degradation. In the context of mechanobiology, DA chemistry is particularly useful for allowing ligand presentation (e.g., adhesive peptides), mechanics (e.g., stiffness, degradation), and DA-mediated biomolecule release to be tailored within hydrogel systems for studying cell-matrix interactions.

2.6 Inverse electron demand Diels-Alder (IEDDA)

Inverse electron demand Diels-Alder (IEDDA) reactions are fast, chemoselective, and readily proceed at mild conditions without requiring additives such as initiators or catalysts[199,200]. Compared to the normal Diels-Alder (DA) cycloaddition, where an electron-rich diene reacts with an electron-poor dienophile, the IEDDA reaction mechanism involves an electron-poor diene and an electron-rich dienophile (**Scheme 2.4A**). These reactions demonstrate irreversible kinetics on experimental timescales, producing only nitrogen during product formation[201,202]. IEDDA reactions were first discovered through the use of 1,2,4,5-tetrazine, a nitrogen-containing electron-poor diene with electron withdrawing groups (EWG), and demonstrated quicker reaction rates influenced by changes in electronic properties[203]. While other cyclic azines such as pyridazine and triazine have shown suitability as diene candidates, the majority of IEDDA reactions utilize

tetrazine for its increased reactivity and orthogonality with respect to other click chemistries such as CuAAC and thiol-Michael addition, which is particularly valuable within the biomaterials community[10,118,204–209]. However, studies have shown a trade-off between fast reactivity and stability; compared to tetrazines, some less reactive dienes such as 1,2,4-triazines exhibit higher stability under physiologic conditions[118,199,210,211]. Despite this limitation, tetrazine-based reactions have proven stable within characteristic cellular timescales and are a popular route for tissue engineering and hydrogel systems (**Scheme 2.4B,C**)[211–219].

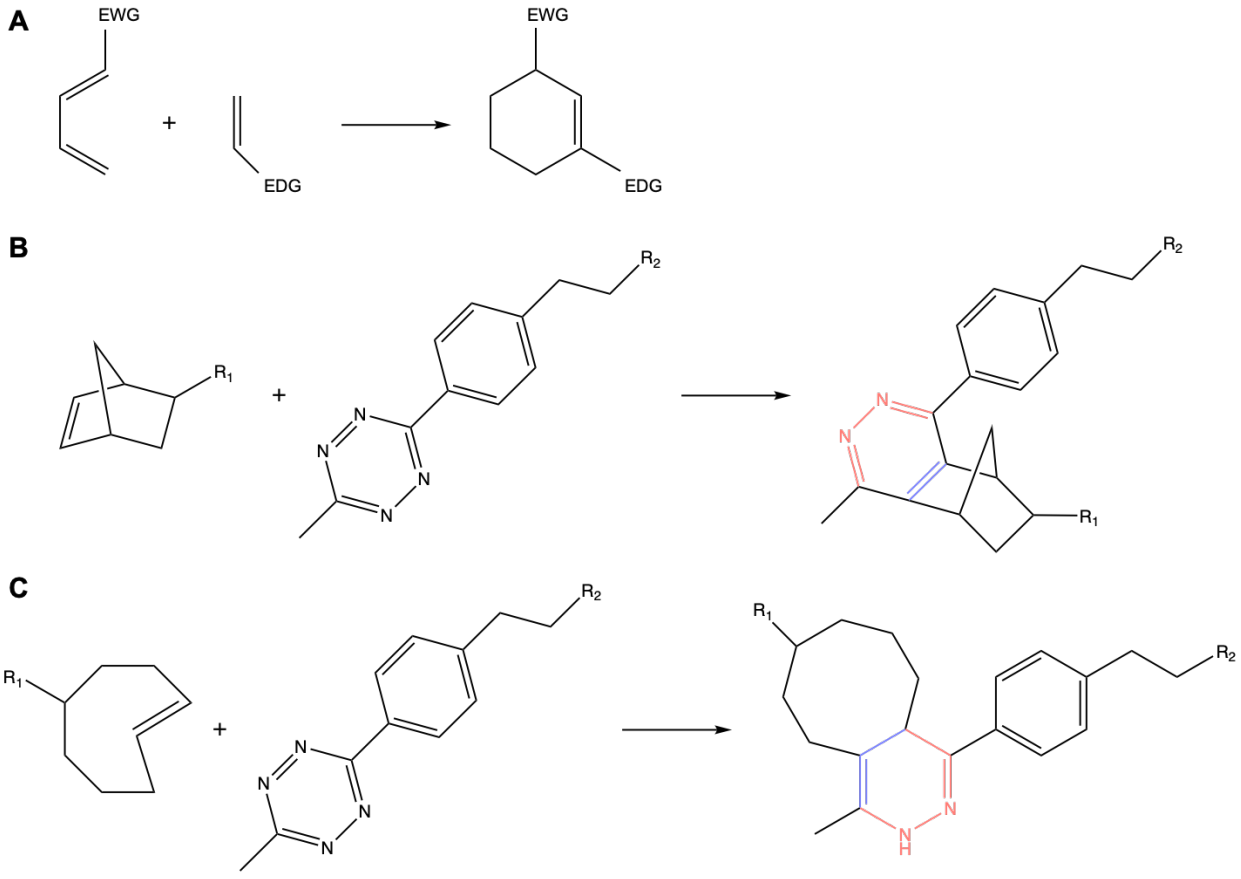

Scheme 2.4. (A) Inverse electron demand Diels-Alder (IEDDA) cycloaddition between an electron-poor diene and an electron-rich dienophile. (B) IEDDA reaction between a norbornene and tetrazine group. (C) IEDDA reaction between a *trans*-cyclooctene (TCO) and tetrazine.

Compared to other common click-based cycloadditions such as CuAAC and SPAAC, IEDDA has a significantly faster reaction rate (IEDDA[83,220,221] second-order rate constant k ~ 1-10^6 $M^{-1}s^{-1}$ versus k ~ 10-100 $M^{-1}s^{-1}$ and k ~ 10^{-2}-1 $M^{-1}s^{-1}$ for CuAAC[79] and SPAAC[80], respectively). Adding electron-withdrawing (i.e., electron-poor) groups such as carboxylates to dienes increases overall reactivity by lowering the energy of the lowest unoccupied molecular orbital (LUMO)[195,222]. Likewise, adding electron-donating (i.e., electron-rich) groups such as olefins and enamines to dienophiles raises the dienophile's highest occupied molecular orbital (HOMO), which greatly impacts kinetic behavior.

IEDDA reaction kinetics can also be controlled by varying substituent features such as dienophile ring strain and solvent type. Decreasing the internal angle of cyclic dienophiles increases ring strain and results in lower distortion energy to reach the transition-state geometry, which correlates with increased reactivity[211,223]. Norbornene groups have become a common dienophile for their low cost and cell encapsulation-friendly gelation kinetics[212,224]. Similarly, the *trans* configuration encourages increased ring strain compared to the *cis* configuration – computational analysis revealed that the 'crown' conformation of *trans*-cyclooctene (TCO) was seven orders of magnitude more reactive than *cis*-cyclooctene toward tetrazines due to a lower activation energy[222,223]. Furthermore, TCO has demonstrated faster reaction rates compared to norbornenes (k ~ 10^3-10^6 M^{-1} s^{-1} for TCO versus k ~ 2 M^{-1} s^{-1} for norbornenes in aqueous solution at room temperature)[83,224,225]. The influence of dienophile stereochemistry on reaction rates is similar to that of the normal DA reaction; *endo*-isomers are typically more thermodynamically favorable and exhibit faster kinetics than *exo*-positioned groups[199,226–228]. However, in some cases, this selectivity can be reversed due to differences in functional group distortions (e.g., norbornenes[224,229]) and

electrostatic repulsions (e.g., cyclopentadiene[230]). Accelerated reaction rates in water have also been observed due to increased hydrophobic interactions and stabilization of the activated complex via hydrogen bonding, which becomes advantageous for cell culture systems[81,211,231,232]. In particular, the influence of protic solvents on reaction rate has mainly centered around the use of tetrazines[201].

In an effort to increase tetrazine stability, Shoichet and co-workers designed an IEDDA-based hydrogel system involving norbornene and methylphenyltetrazine (mpT), where the inclusion of electron-donating groups increased hydrolytic stability while compromising high reactivity[214,215]. Using HA as the polymer backbone, Delplace *et al.* confirmed that gelation time was not significantly affected; depending on polymer and crosslinker concentrations, hydrogel gelation occurred within one hour and could be formed in as little as 5 minutes at high polymer concentrations[214]. Interestingly, at a constant mpT:norbornene ratio, hydrogel swelling was independent of HA-mpT molar mass as well as HA-norbornene concentration. Encapsulated cells maintained high viability over several days, particularly in hydrogels with lower polymer concentrations, and also confirmed the correlation between gelation time and cell sedimentation. Using the same IEDDA click chemistry, Delplace *et al.* also developed a methylcellulose-based hydrogel system for the co-delivery of neural stem cells and chondroitinase ABC (ChABC) enzyme for glial scar degradation[215]. Gelation occurred within 15 minutes with Young's moduli ranging between 0.5-1.5 kPa, similar to that of brain tissue. Using affinity-controlled release, controlled release of ChABC could be extended to 4 days. Interestingly, neurospheres containing neural progenitor cells within degradable IEDDA hydrogels appeared to maintain viability and resulted in increased neurosphere size with the formation of new, smaller neurospheres. Dual-

crosslinked systems have also been used to form robust hydrogels. For example, Truong *et al.* created cytocompatible, tough PEG-based IPNs with compressive stresses of ~ 15 MPa through a one-step fabrication involving IEDDA between tetrazine and norbornene groups and a nucleophilic thiol-yne click reaction[209]. This system provides a structurally supportive hydrogel network with robust mechanical strength that can maintain high cell viability and accommodate ligand functionalization.

2.6.1 Tetrazine-norbornene hydrogels

Many IEDDA hydrogel systems have utilized the high reactivity and bioorthogonality of tetrazine-norbornene interactions. Lueckgen *et al.* fabricated alginate hydrogels using carbodiimide chemistry to modify alginate with norbornene and tetrazine groups[233]. Similar to a previous system developed by Mooney, Joshi, and co-workers, alginate was chosen as the backbone polymer for its degradability via controlled oxidation using sodium periodate[234]. Gelation kinetics and stiffness were tuned by altering the oxidation state of alginate, degree of norbornene modification, and the ratio of norbornene to tetrazine. Hydrogel mechanics were varied from 2-20 kPa, with lower degrees of alginate substitution and oxidation resulting in more compliant hydrogels with slower gelation kinetics. Regulating these parameters enabled control over degradation – increased crosslinking density via backbone modification and norbornene:tetrazine ratio slowed degradation. Compared to degradable substrates, mouse pre-osteoblasts seeded atop hydrogels proliferated more on non-degradable hydrogels. The stability of IEDDA reactions at physiologic conditions lends favorably to 3D culture applications as well. Lueckgen *et al.* expanded their previous alginate 2D cell culture model into a 3D system, and encapsulated mouse pre-osteoblasts retained a more rounded morphology over all hydrogel groups without significant proliferation[233]. Finally, *in vivo*

hydrogel implantation revealed that the degradable, oxidized substrates promoted cell infiltration after 8 weeks compared to non-degradable controls.

Alge *et al.* successfully fabricated tunable 3D PEG hydrogels for cell encapsulation and protein patterning using tetrazine-norbornene chemistry[212]. 4-arm PEG was functionalized with tetrazine groups via acid amine conjugation between PEG-amines and carboxylic acid-bearing tetrazines. Di-norbornene MMP-degradable crosslinker and mono-norbornene adhesion peptides were incorporated for hydrogel fabrication and introduction of adhesive sites, respectively. Varying polymer concentration and norbornene-functionalized pendant peptides enabled control of parameters such as stiffness and adhesive ligand density. Under physiologic conditions initial gelation occurred in a few minutes and plateaued within 15 minutes. Encapsulated hMSCs showed high viability but a low degree of spreading, suggesting the need for optimizing hydrogel parameters (e.g., stiffness, degradability, adhesion presentation). Koshy *et al.* used the natural adhesivity and degradability of gelatin to fabricate "click gelatin hydrogels" (ClickGel) to support increased cell spreading[216]. The addition of norbornene and tetrazine functional groups resulted in decreased gelation temperature and viscosity, making the hydrogel precursors easier to pipet and mix at room temperature. Similar to previous studies, gelation occurred spontaneously and rapidly within minutes, and gelation rate correlated with increased polymer concentration. Encapsulation of enhanced green fluorescent protein (EGFP)-expressing NIH3T3 fibroblasts in 5 and 10 wt% hydrogels revealed the influence of polymer concentration on cell behavior. Cells within the softer 5% ClickGel groups displayed elongated morphologies after a 3 day culture period and remained spherical after treatment with MMP-inhibitor Marimastat, suggesting that cell spreading was largely mediated by enzymatic degradation. Similarly, encapsulated hMSCs within the 5%

ClickGels elongated extensively and displayed organized actin stress fibers due to matrix remodeling, and *in vivo* injection of the hydrogel led to almost complete degradation over 120 days.

2.6.2 Dual-crosslinked hydrogels

Similar to DA-based reactions, several groups have exploited the orthogonal nature of IEDDA chemistry toward the rational design of dual-crosslinked systems. By combining IEDDA chemistry with photoinduced thiol-ene addition, Lueckgen *et al*. demonstrated spatial control over hydrogel biophysical and biochemical properties to study and guide wound healing responses[235]. The IEDDA crosslinks enabled compliant hydrogel formation prior to thiol-ene patterning regions of higher stiffness via non-degradable crosslinkers (**Figure 2.4A,B**), degradation via incorporation of degradable crosslinkers, or biomolecules through immobilization of cell adhesive peptides. Interestingly, for initially IEDDA-crosslinked hydrogels, later UV exposure resulted in stiffer patterned regions by almost an order of magnitude (E ~ 1-2 kPa with early secondary crosslinking vs 9-10 kPa for later crosslinking), enabling spatiotemporal control over stiffness. On regions of patterned stiffness (9-10 kPa), fibroblasts aligned in the direction of the striped pattern, covered more surface area, and displayed both increased cell area and significantly decreased circularity (**Figure 2.4C**). Similarly, patterned regions of cell adhesive RGD and degradable crosslinker led to preferential attachment and lower stiffness respectively compared to non-patterned control regions. As expected, on stiffness-patterned substrates, adipogenic and osteogenic differentiation increased on soft and stiff regions, respectively (**Figure 2.4D**). These trends were quantified by cell attachment as well as oil droplet area (adipogenic) and mineralized area (osteogenic).

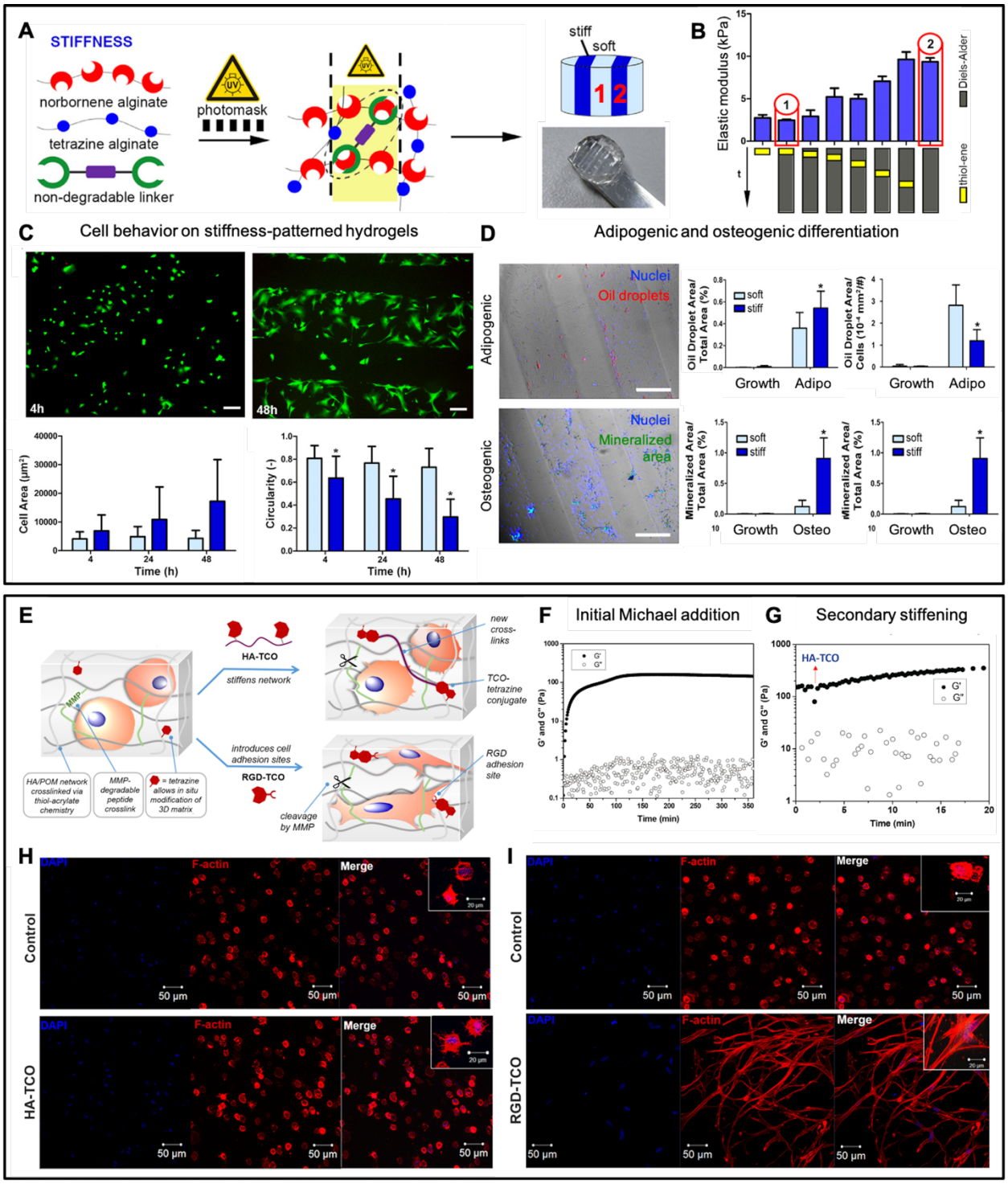

Figure 2.4. Inverse electron demand Diels-Alder (IEDDA) can be used on its own or with secondary crosslinking mechanisms to rapidly and precisely control hydrogel mechanical properties for studying cell mechanobiology. (A) Additional modifications, such as stiffness (*shown*), biomolecule presentation, and degradation sites, can be photopatterned within IEDDA-based alginate hydrogels. (B) Elastic moduli of dual-crosslinked hydrogels were measured by compression testing, showing increased stiffness in regions exposed to UV-mediated thiol-ene

addition. (C) Fibroblast attachment, spread area, and circularity on stiffness-patterned 2D cultures show distinct behaviors based on mechanics. Scale bar = 200 μm. (D) Adipogenic and osteogenic differentiation increased on unpatterned (compliant) and patterned (stiff) regions, respectively. Lineage specification was measured by oil droplet and mineralized area. Scale bar = 500 μm. (A-D) adapted with permission from[235]. Copyright 2020 Elsevier Ltd. (E) IEDDA can facilitate *in situ* stiffening and adhesive ligand presentation without external triggers. (F,G) After initial hydrogel formation, diffusion-controlled secondary crosslinking results in IEDDA-mediated stiffening. (H) Matrix stiffening (*bottom*) led to rounded hMSCs with distinct cortical actin. Scale bars = 50 μm. (I) The addition of RGD-TCO adhesive cues resulted in hMSC elongation with F-actin (red) stress fiber bundles. Scale bars = 50 μm. (E-I) adapted with permission from[236]. Copyright 2018, American Chemical Society.

In addition to varying stiffness, Vining *et al.* varied ionic (between alginate and calcium) and covalent (between norbornene and tetrazine) crosslinking ratios to tune hydrogel viscoelasticity[237]. The viscoelastic properties of the hydrogels, measured by loss angle, were achieved without altering the microscale architecture of the hydrogel network by maintaining constant alginate concentration. To study the impact of physical properties on cell function, MSCs were encapsulated within hydrogels of varying stiffness (storage moduli, G' ~ 0.5 kPa and 2.5 kPa) and viscoelasticity (loss moduli, G" ~ 50 Pa and 250 Pa, respectively). Interestingly, after 72 hours, MSCs exhibited increased cell cross-sectional area in the stiffer more elastic hydrogels containing the covalent IEDDA network. Immunomodulatory markers such as cyclo-oxygenase-2 and TNFα-stimulated gene-6 were upregulated to varying degrees based on hydrogel stiffness and viscoelasticity, with gene expression increasing as both stiffness and viscoelasticity increased.

While IEDDA reactions can occur spontaneously in aqueous conditions without an initiator or catalyst, the addition of a catalyst can be used to both increase stability and trigger gelation. Carthew *et al.* demonstrated the use of horseradish peroxidase (HRP) to increase material stability via oxidation and activate faster crosslinking[238]. To bypass the limitation of tetrazine oxidation

over time, synthesis of dihydrogen tetrazine-functionalized PEG (dHTz-PEG) via carbodiimide coupling provided precursor stability, where mild oxidation to tetrazine could easily occur using a low concentration of HRP. Mixing norbornene-functionalized gelatin, which was synthesized through the same coupling method, dHTz-PEG, and HRP quickly formed a hydrogel within 5 minutes. Encapsulated hMSCs over a 32 day culture period displayed extended filopodia, particularly in the more compliant hydrogel group (G' ~ 1.2 kPa) where star-shaped cellular morphologies were seen. As hydrogel stiffness increased (G' ~ 3.8 kPa), cells remained more rounded with decreased spreading. Overall, the facile synthesis method and ability for the hydrogels to remain stable over a month-long culture are highly attractive for long-term mechanobiology studies.

2.6.3 TCO-tetrazine hydrogels

While norbornenes offer greater stability, TCO-tetrazine reactions demonstrate faster reaction rates, providing an alternative dienophile for rapid hydrogel fabrication. Strategies involving TCO have taken advantage of the increased reactivity to uniquely study cell-matrix interactions in 3D hydrogels. Zhang *et al.* synthesized liquid microspheres composed of an outer HA shell fabricated via IEDDA click chemistry capable of 3D biomolecule patterning and cell culture[239]. Microspheres were created by adding HA-tetrazine droplets to a solution of bis-TCO, triggering nearly instant TCO-tetrazine crosslinking at the droplet surface, where subsequent crosslinking occurred through bis-TCO crosslinker diffusion into the hydrogel. The diffusion-driven crosslinking mechanism enabled biomolecule patterning by switching the solution to generate multilayer structures within the microsphere without an initiator or catalyst. Applying the hydrogel system to mimic an *in vitro* tumor microenvironment, homogeneously encapsulated prostate cancer cells continuously

proliferated within the compliant microspheres (G' ~ 135 Pa) and formed rounded cell clusters with cells displaying cortical actin filaments.

TCO-tetrazine interactions also enable temporal hydrogel stiffening and introduction of tethered biomolecules[236]. Following initial Michael-type addition between thiolated HA, a hydrophilic co-polymer with acrylate and methyltetrazine groups at mildly basic conditions, and MMP-degradable crosslinker, secondary stiffening of the primary network was achieved via incorporation of HA-TCO (through solution diffusion into the hydrogel) to introduce TCO-tetrazine interactions (**Figure 2.4E-G**). Incorporation of cell adhesive sites through the addition of pendant RGD-TCO groups was achieved in a similar manner. The 9 day cell culture revealed the influence of secondary stiffening, where hMSCs displayed more pronounced actin-rich processes from the generally rounded encapsulated cells (**Figure 2.4H**). However, introduction of cell adhesive sites resulted in significant hMSC spreading and elongation, creating a mesh-like cellular network with distinct stress fiber bundles (**Figure 2.4I**). In the absence of degradable crosslinkers, spreading was inhibited even with the addition of RGD sequences, again highlighting the importance of degradation in supporting 3D cell spreading.

In summary, the IEDDA click reaction has been gaining recognition as a bioorthogonal crosslinking mechanism that exhibits rapid gelation at physiologic conditions. Similar to Diels-Alder, varying the diene and dienophile pairs can influence gelation rate. For example, the use of dienophiles with greater strain (e.g., TCO) increases reaction rates by several orders of magnitude compared to their *cis*- counterparts. For this reason, IEDDA reactions are highly advantageous for cell encapsulation studies. Hydrogel properties, including stiffness, viscoelasticity, and

biomolecule presentation, can be efficiently tuned with precise control. More recently, the fast encapsulation properties of IEDDA reactions have been used in hydrogels containing dual crosslinking modes to engineer complex mechanics for studying cellular responses while maintaining a high level of user control. One limitation with IEDDA chemistry is the trade-off between reactivity and stability, with less reactive dienophiles demonstrating higher stability in aqueous conditions. However, the majority of reactions involving tetrazine, a highly reactive but slightly less stable diene, maintain stability within relevant cellular timescales. Continued optimization of reaction pairs to increase stability for longer cell culture studies will only add to the beneficial properties of IEDDA hydrogels to study mechanobiology.

2.7 Imine-derivatives (oximes and hydrazones)

Imines are formed through the dehydration reaction of a primary amine with an aldehyde or ketone. In general, the mechanism involves a proton-catalyzed attack of the α-nucleophile on the carbonyl carbon atom, followed by proton transfer and dehydration of the hydroxyl group to yield an imine or imine-derivative (e.g., oxime, hydrazone)[240–242]. Imines are considered covalent bonds that are reversible within experimental timescales, termed dynamic covalent chemistry (DCC)[242]. In general, the carbonyl reaction can be accelerated under acidic conditions (especially between pH values of 3-7), enabling control over gelation time and mechanical properties via pH.

Hydrazones and oximes share structural similarities with imines with nitrogen and oxygen neighboring the carbon-nitrogen double bond, respectively. Under aqueous conditions, more electronegative heteroatoms (O, oxime > NH, hydrazone > CH_2, imine) create a negative inductive effect and provide addition stability at physiologic pH to oximes and hydrazones compared to

imines[243]. As a result, hydrazone and oxime bonds have become particularly appealing bioorthogonal approaches for tunable biomaterial synthesis and cell behavior studies[244–249].

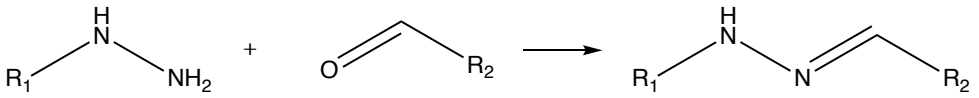

Scheme 2.5. Oxime bond formation between an aminooxy and an aldehyde.

Oxime bond formation (**Scheme 2.5**) is a highly efficient and chemoselective reaction that occurs between either an aldehyde or ketone and an alkoxyamine (typically a hydroxylamine)[250]. Compared to hydrazones, oximes have a higher stability owing to steric and electronic differences. While oxime bioconjugation reactions were studied as early as 1882, previously complex hydroxylamine synthesis techniques limited its utility[250,251]. The development of more facile hydroxylamine syntheses such as the Mitsunobu reaction and BOC deprotection coupled with the increased stability and stimulus-responsiveness of oximes has allowed researchers to exploit the dynamic covalent reaction for both minimally invasive *in vivo* experiments and longer-term cell culture studies[249,250]. In particular, pH has been widely used as a method to alter bond reversibility while maintaining tissue-relevant stiffnesses[252–257].

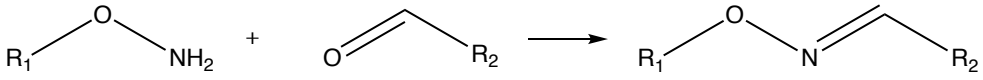

Scheme 2.6. Hydrazone bond formation between a hydrazine and an aldehyde.

Similar to oximes, hydrazones are dynamic covalent bonds that form between a hydrazine and a carbonyl, usually an aldehyde or ketone (**Scheme 2.6**). While they are more stable than imines,

they are more likely to undergo hydrolysis compared to oximes; the rate constant for oxime hydrolysis is nearly 1,000-fold lower than for hydrazones[242,243,258,259]. The degree of acid lability is dependent on the carbonyl group selected; hydrazone bonds formed with ketones exhibit slower reaction rates and are less labile compared to aldehydes. However, aromatic aldehydes have shown more stability than aliphatic aldehydes[245,259–261]. These subtle differences in chemistry have been shown to greatly impact stress relaxation timescales for hydrogel systems[61,262,263]. Notably, many systems have taken advantage of hydrazone tunability and reversibility via alterations in pH, temperature, and/or polymer groups to develop hydrogels with dynamic covalent properties and/or shear-thinning and self-healing capabilities[264,265,274–279,266–273]. Recent approaches utilizing bioorthogonal mechanisms, such as secondary photocrosslinking or photocleavage, have also enabled the design of systems with spatiotemporal control over mechanical and biochemical cues[280,281]. For more in-depth discussion of oxime and hydrazone bioconjugation techniques, readers are referred to the following reviews[86,245,250,257].

2.7.1 Viscoelastic oxime hydrogels

Maynard and co-workers first reported the use of oxime click chemistry as a method of hydrogel fabrication[256]. Eight-armed aminooxy PEG (AO-PEG) was crosslinked with glutaraldehyde and functionalized with a ketone-modified RGD adhesive peptide to support cell culture. By varying AO-PEG concentration or crosslinker density, hydrogel stiffness could be tuned from storage moduli G’ of about 250 Pa to over 4 kPa. Subsequently, viscoelastic properties were also altered by increasing stiffness (loss modulus, G” ~ 10 Pa to around 50 Pa, respectively). Hydrogel gelation was also pH-dependent, with more acidic solutions resulting in quicker gelation. At a more physiologic pH of 7.2, oxime formation occurred in 30 minutes (compared to 5 minutes at a pH of

6) without compromising stiffness to allow 3D encapsulation of MSCs. MSCs were metabolically active and proliferated over the 7 day culture period, demonstrating material cytocompatibility. In the absence of any enzymatically-degradable crosslinkers, encapsulated cells remained rounded during the 7 day culture, indicative of oxime bond stability and non-degradability. Grover *et al.* also demonstrated the ability to tune gelation and stiffness using oxime conjugation. By altering either the concentration of AO-PEG and aldehyde-PEG (ald-PEG) or ald/AO ratios, gelation rate (2-400 seconds) or hydrogel stiffness (G' ~ 450 Pa to 1.4 kPa) could be manipulated, respectively[282]. Interestingly, while the PEG-functionalized hydrogel inhibited 3T3 fibroblast adhesion regardless of the degree of polymer modification, verified by rounded cell morphologies in 2D cultures, functionalization enabled hydrogel adherence to *ex vivo* cardiac tissues to improve material retention for future *in vivo* studies.

The pH-responsive nature of oxime bonds has also been used to incorporate time-dependent properties into hydrogels. Toward this approach, Sánchez-Morán *et al.* synthesized aldehyde-containing oxidized alginate (NaAlg-Ald) by oxidizing alginate diols using sodium metaperiodate ($NaIO_4$), where the diol/$NaIO_4$ ratio could be tuned to control oxidation and subsequently, degree of modification[283]. Alkoxyamine alginate (NaAlg-AA) was synthesized via a Mitsunobu reaction followed by a hydrazinolysis to yield an alkoxyamine group. Stiffness and viscoelasticity were controlled by varying polymer concentrations, Ald/AA ratio, and the degree of NaAld-Ald oxidation – as Ald/AA decreased, both storage and loss moduli increased (G' ~ 0.1-12 kPa and G" ~ 1-30 Pa). Gelation studies demonstrated the dependence of oxime bond formation on pH and temperature; more rapid gelation occurred in mildly acidic conditions (pH 4-6) and at higher temperatures. However, the addition of a nucleophilic aniline catalyst, which has been previously

shown to improve gelation kinetics and mechanical properties, enabled gelation across the entire spectrum[283–285]. Mean relaxation times, $\langle\tau\rangle$, were fitted to experimental stress relaxation profiles. As the Ald/AA ratio increased, faster stress relaxation occurred – for a hydrogel with an Ald/AA ratio of 9, $\langle\tau\rangle \sim 4$ h compared to ~ 27 h for a hydrogel with an Ald/AA ratio of 0.3. Increasing oxidation levels also led to faster stress relaxation ($\langle\tau\rangle \sim 13$ h versus ~ 56 h for 100% and 25% oxidation, respectively). Encapsulation of murine B lymphoma cell line 2PK-3 in oxime hydrogels with faster stress relaxation resulted in increased cell size, proliferation, and migration.

Oximes can also be used to trigger cell adhesion and influence cell mechanobiology. Criado-Gonzalez *et al.* explored this approach by combining stable oxime-based PEG networks with enzyme-assisted peptide self-assemblies[286]. Poly(dimethylacrylamide-*co*-diacetoneacrylamide) (poly(DMA-*co*-DAAM), PDD) was synthesized via reversible addition-fragmentation chain-transfer (RAFT) polymerization and varying polymer concentrations were crosslinked with bis-aminooxy PEG (AOP) at a pH of 7.4 to create hydrogel networks with mechanics ranging from G' ~ 0.3 kPa (G" ~ 4 Pa) to G' ~ 1.8 kPa (G" ~ 8 Pa) (**Figure 2.5A-C**). Embedding alkaline phosphatase within the bulk PDD-AOP hydrogel prior to diffusion of Fmoc-FFpY peptides led to enzyme-assisted peptide dephosphorylation and intercalated Fmoc-FFY self-assemblies without affecting hydrogel stiffness. The presence of self-assembled Fmoc-FFY also allowed incorporation of Fmoc-F-RGD to provide additional adhesion sites. After confirmation of peptide supramolecular self-assembly via circular dichroism spectroscopy, the influence of self-assembled peptides and adhesion was studied using NIH3T3 fibroblasts. A combinatorial study demonstrated that fibroblast area, spreading, and formation of vinculin spots at the tips of actin microfilaments only occurred in the presence of the self-assembled Fmoc-FFY, and these cell metrics were

enhanced with the addition of RGD (**Figure 2.5D-F**). Thus, this hydrogel platform allowed decoupled investigation of the influence of mechanical and adhesive cues on fibroblast behavior.

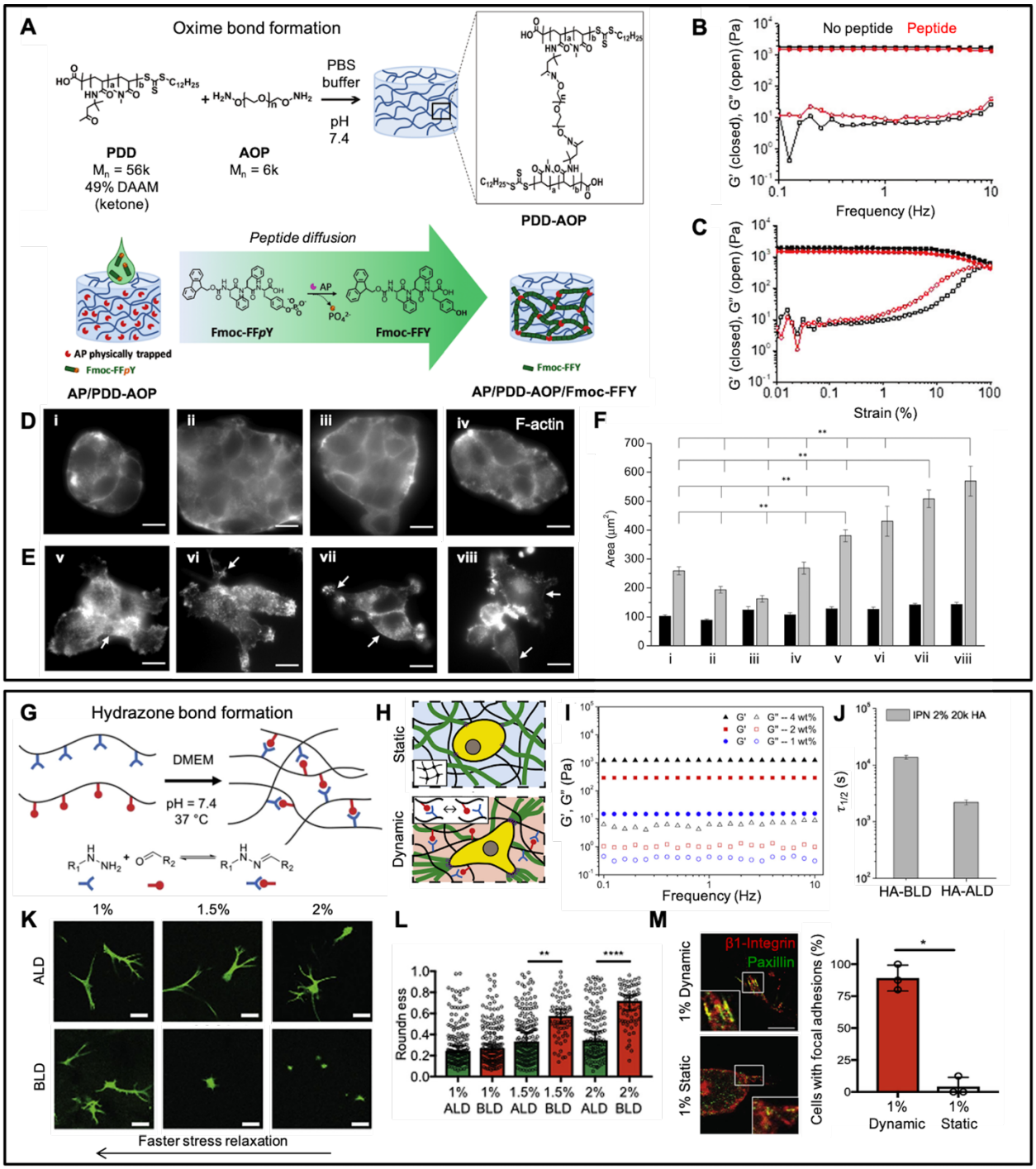

Figure 2.5. Viscoelastic oxime and hydrazone hydrogels can be employed to study the influence of dynamic mechanics on cell behaviors. (A) An oxime-based PEG network containing embedded enzyme alkaline phosphatase enables peptide supramolecular self-assemblies when infused with a peptide solution. (B,C) Storage (G') and loss (G") moduli showing negligible differences in stiffness before and after peptide incorporation. (D-F) F-actin staining revealed distinct increases in cell protrusions and spreading on hydrogels with peptide self-assemblies (*v-viii*), compared to more rounded morphologies without distinct F-actin fibers when peptide self-assembly was absent (*i-iv*). Scale bars = 10 μm. (A-F) adapted from[286] with permission from The Royal Society of Chemistry 2020. (G) Hydrazone interactions occur at physiologically-relevant conditions and are reversible. (H) Dynamic hydrazone bonds introduce stress relaxation behaviors that are commonly displayed in natural tissues. (I) Frequency sweep of hydrogels with varying polymer concentrations demonstrates ability to modulate stiffness and viscoelasticity. (J) HA hydrogels modified with either aliphatic aldehydes (HA-ALD) or benzyl aldehydes (HA-BLD) were formed to tune stress relaxation profiles with HA-ALD hydrogels displaying faster relaxation. (K,L) Cell spreading is influenced by stress relaxation timescale, with increasing MSC spreading in fast relaxing HA-ALD compared to slower relaxing HA-BLD hydrogels. Increasing HA concentration also resulted in decreased cell spreading. Scale bars = 50 μm. (M) Focal adhesion formation increased significantly in viscoelastic substrates capable of stress relaxing. Scale bar = 10 μm. (G-M) adapted with permission from[61]. Copyright 2017 Elsevier Ltd.

2.7.2 Oxime hydrogels to mimic the tumor microenvironment

Oxime chemistry can be combinatorially leveraged with secondary crosslinking methods to enable independent control of mechanical and biochemical properties. By modifying HA with aldehyde and methyl furan groups, Baker and co-workers designed a system allowing initial oxime ligation between HA-aldehyde and bis(oxyamine)-PEG, followed by Diels-Alder click chemistry to facilitate presentation of biochemical cues[287]. Through rational design of hydrogel parameters, they were able to optimize long-term breast cancer epithelial cell growth in spheroids. Cells cultured on optimally compliant matrices (E ~ 0.6 kPa) formed acinar-like spheroids compared to a flattened morphology on tissue culture polystyrene. Similarly, breast cancer cells on stiffer hydrogels (E ~ 2.3 kPa) also deviated from the optimal spheroid morphology in favor of flat monolayers. Increasing concentrations of the laminin-derived IKVAV peptide on the 0.6 kPa substrates also led to cell flattening, highlighting the combined effects of mechanical and adhesive cues in regulating disease-relevant cell behaviors.

2.7.3 Oxime and hydrazone hydrogels for in vivo applications

The dynamic covalent interactions of oxime bonds can also be manipulated for *in vivo* studies that favor minimally invasive approaches. Hardy *et al.* demonstrated the clinical relevance of a hydrogel composed of oxime-crosslinked HA, PEG, and collagen for central or peripheral nervous system applications[288]. Aldehyde-functionalized HA (HA-ALD) was crosslinked with linear aminooxy-terminated PEG to rapidly form oximes at a pH of 7.4, and mechanical properties such as stiffness and degradability were adjusted by tuning the ratios of PEG and HA derivatives. Cell adhesion was mediated by incorporating various amounts of α-1-type collagen. hMSCs seeded atop hydrogels displayed spread morphologies, with increased viability on stiffer substrates.

Within the regenerative medicine field, *in situ* formation and sutureless implantation are ideal characteristics for drug and cell delivery. The Skottman group developed an implantable tissue adhesive hydrogel for corneal regeneration based on a HA hydrogel system enabling corneal cell attachment and high viability of encapsulated human adipose stem cells (hASCs)[289,290]. Koivusalo *et al*. applied this model toward the design of a tissue adhesive scaffold containing distinctly compartmentalized cells to promote regeneration after implantation[290]. Dopamine was functionalized onto hydrazone-crosslinked HA hydrogels (HA-DOPA) to enable adhesion of the scaffold to the defect site. Advantageously, the introduction of dopamine allowed for thiolated collagen IV (col IV-SH) cell adhesive peptide to be conjugated to the hydrogel surface via Michael addition. Compared to DOPA-free HA hydrogels (HA-HA), limbal epithelial stem cells (LESCs) on col IV-SH-conjugated HA-DOPA hydrogels displayed greater adhesion and long-term viability. Interestingly, LESC attachment was observed on unmodified col IV-coated HA-DOPA

groups, owing to the adhesive properties of DOPA. On HA-DOPA, LESCs retained their progenitor-like phenotype via expression of the limbal stem cell marker ΔNp63α (indicated by p63α and p40 nuclear co-localization) in combination with low expression of epithelial maturation marker cytokeratin 12. Covalent attachment of col IV was also necessary for continued cell growth and maintenance of LESCs. Encapsulated hASCs displayed increased elongation within HA-DOPA hydrogels compared to a more rounded phenotype in HA-HA hydrogels, potentially due to DOPA residues promoting the retention of ECM proteins deposited by cells.

2.7.4 Viscoelastic hydrazone hydrogels

Hydrazone-based hydrogels have been used most extensively for their unique dynamically covalent crosslinks, imparting viscoelasticity and rapid shear-thinning and self-healing capabilities at physiologic conditions. Recent efforts by the Anseth group have utilized dynamic covalent hydrazone bonds to provide a stable crosslinked network for cell culture and with tunable stress relaxation profiles. McKinnon *et al.* formed hydrogels composed of aliphatic hydrazine- and aldehyde-functionalized 4-arm PEG at a pH of 7.4 to allow for cell encapsulation[262]. Stress relaxation timescales were tuned by varying the ratio of aliphatic (AA) and aryl (BA) aldehyde crosslinker; AA hydrazone bonds were shown to relax 100% of the imposed stress within a minute, whereas BA hydrazone bonds only relaxed about 75% of the total stress over the course of 14 hours. Encapsulated C2C12 myoblasts remained morphologically rounded in BA hydrazone networks but displayed filopodia and lamellipodia with extended processes in faster stress relaxing substrates with increased AA/BA ratio. Additionally, viscoelastic hydrogels with AA hydrazone linkages supported myoblast fusion into multinucleated myotube-like structures, demonstrating the ability for the dynamic network to permit cell behaviors necessary for myotube maturation. A

subsequent study demonstrated the compatibility of the hydrogel system with sensitive cell types and the ability to characterize how biophysical signals influenced the level of cellular force involved in adhesion and motor neurite extension[291]. Increasing the stoichiometric ratio of PEG-hydrazine to PEG-aldehyde (2:1) resulted in lower cell toxicity and neurite extension from embryoid bodies in a 3D scaffold compared to 1:1 hydrazine-aldehyde hydrogels. This finding is supported by the fact that excess reactive aldehydes can potentially contribute to neurodegenerative diseases[292].

Similarly, by varying the percentage of alkyl aldehyde (aHz) and benzylaldehyde (bHz) in a hydrazone-crosslinked hydrogel, Richardson *et al*. achieved stress relaxation times ranging from one hour to one month ($\langle\tau\rangle \sim 4 \times 10^3$ s to $\sim 3 \times 10^6$ s, respectively)[293]. Hydrogels were fabricated by reacting nucleophilic PEG-hydrazine with either alkyl- or benzylaldehyde-modified PEG; rheological characterization demonstrated that increased bHz crosslinking corresponded with slower relaxation times. While both primarily elastic (100% bHz, slow relaxing) and highly stress relaxing (> 88% aHz, fast relaxing) hydrogels suppressed chondrocyte proliferation and cellularity, hydrazone hydrogels with a combination of aHz and bHz crosslinks supported cellular proliferation. In particular, a significant increase in proliferation, glycosaminoglycan deposition, and collagen deposition was observed in the 22% bHz hydrogels (stress relaxation ~ 3 days). These results suggest that an average stress relaxation timescale of ~ 3 days is relevant for dense chondrocyte growth and formation of high quality neocartilaginous tissue. This hydrogel system was then used to understand how mechanical deformation, similar to a load-bearing joint, would influence chondrocyte morphology[294]. Chondrocytes were encapsulated in elastic (0% aHz), viscoelastic (100% aHz), and mixed (78% aHz, 22% bHz) hydrogels and exposed to 20% uniaxial

compressive strain for 10 hours. Chondrocytes in the elastic hydrogels retained an ellipsoidal morphology over the strain period and only recovered once the strain was removed. Conversely, chondrocytes in viscoelastic hydrogels were able to recover to their unstrained rounded morphology during deformation due to creep compliance behavior of the hydrogel network. The optimized mixed viscoelastic hydrogel resulted in a slower recovery of the rounded morphology, indicating that the network is composed of elastic and viscoelastic interactions. The viscoelastic hydrogel groups (100% and 78% aHz) also showed greater distribution of nascent ECM protein deposition and subsequently, decreased cellular deformation when subjected to compressive strain.

2.7.5 Hydrazone hydrogels incorporating protein cues

The stress relaxation properties of hydrazone bonds can also be exploited to recapitulate fibrillar ECM. Lou and co-workers designed a HA-based IPN consisting of hydrazone bonds and type I collagen with tunable viscoelastic regimes (**Figure 2.5G-I**)[61]. Instead of using oxidation to modify the HA backbone with aldehydes (a common and quick method that can potentially compromise the molecular weight distribution of the polymer backbone), aldehyde functionalization was added to HA by first modifying HA carboxyl groups with alkynes (via carbodiimide coupling), followed by a copper-catalyzed reaction to attach azide-functionalized hydrazines, aliphatic aldehydes (HA-ALD), and benzyl aldehydes (HA-BLD). Consistent with previous findings, the hydrogels containing hydrazine-aliphatic aldehyde hydrazone bonds displayed faster relaxation kinetics compared to hydrazone bonds with benzyl aldehydes (**Figure 2.5J**). MSCs encapsulated within faster relaxing dynamic substrates supported increased cell spreading (**Figure 2.5K**), reduced roundness (**Figure 2.5L**), protrusions up to 100 μm in length, collagen fiber alignment, and focal

adhesion formation indicative of robust integrin binding (IPN with HA-BLD > IPN with HA-ALD) (**Figure 2.5M**)[61,262].

Recent interest in independent tuning of mechanical and biochemical cues has led to the design of hydrogels containing engineered elastin-like proteins (ELPs)[276,295]. Zhu and co-workers designed a hydrazine-functionalized ELP (ELP-HYD) with modular repeats of structural and cell adhesive sequences[295]. When combined with aldehyde-modified HA (HA-ALD) at room temperature, gelation rapidly occurred and stabilized within one minute. Hydrogel stiffness was varied by controlling the crosslinking ratio between hydrazines and aldehydes as well as through polymer concentrations. In general, higher polymer concentrations resulted in increasing stiffness, and this was more sensitive to changes in ELP concentration. To minimize thermally-induced stiffening effects and produce a group of hydrogels with similar storage moduli (G'), a lower concentration of ELP was fixed (1.8 wt%) while HA concentration was varied (1.5, 3, or 5 wt%). Interestingly, increasing HA caused a dose-dependent increase in gene expression of cartilage markers by encapsulated chondrocytes, including aggrecan (*Acan*), SRY (sex determining region Y)-box 9 (*Sox9*), and type II collagen (*Col2a1*). In addition, markers related to the undesirable fibrocartilage phenotype, type I and type X collagens, were downregulated. Matrix metalloproteinase-13 (MMP-13), a marker of cartilage remodeling, increased as HA concentration decreased – this suggests that lower levels of HA enable greater degradation and matrix remodeling. Similarly, decreasing HA concentration led to increased chondrocyte proliferation. Deposition of cartilage-specific matrix (sulfated GAGs) correlated with cartilage marker expression trends, and these observations were consistent with previous reports showing increased matrix deposition resulting in decreased

cell proliferation. Overall, this study highlighted the importance of decoupling mechanical and biochemical cues to probe cell-matrix interactions.

2.7.6 Disease-mimetic hydrazone systems

Several groups have also exploited the cytocompatible nature of hydrazone reactions toward the design of relevant disease models. Dahlmann *et al.* designed an alginate- and HA-based hydrogel system mimicking contractile myocardial tissue with hydrazone crosslinking capabilities to enable a wide range of mechanophysical properties[296]. Gelation kinetics, stiffness, and viscoelasticity were adjustable via the chosen polymer backbone, degree of polymer functionalization, and temperature. Interestingly, incorporation of type I collagen into HA-containing substrates led to increased active contraction force compared to collagen alone; passive forces were also dependent on the substrate material properties (alg-alg > HA-alg > HA-HA > collagen). Finally, cardiomyocytes on all hydrazone-based constructs exhibited elongated, aligned morphologies with cross-striations and expression of the gap junction protein connexin 43, comparable to native myocardium.

One important aspect in the design of pathologically-relevant disease models is the influence of culture dimensionality on cell behaviors, particularly because of their differences in cell-cell and cell-matrix interactions. Toward this objective, Suo *et al*. developed degradable hydrazone hydrogels to compare cell morphology and growth factor expression as a function of culture dimensionality[297]. Increasing the ratio of aldehyde-modified HA (oxidized HA, AHA) to hydrazide-modified HA (glycidyl methacrylated 3,3'-dithiobis(propionic hydrazide), GHHA) resulted in increased hydrogel stiffness. To control degradation, hyaluronidase and glutathione

concentrations were varied, demonstrating that the hydrogels were susceptible to enzymatic hydrolysis and reduction. Human breast cancer MCF-7 cell morphologies differed between 2D and 3D cultures, displaying more polygonal spreading in 2D compared to more rounded and spherical morphologies throughout the 3D culture, similar to those seen in tumors. Interestingly, cells in 3D hydrogels also proliferated at a greater rate due to increased area to grow. Expression of breast cancer-relevant cytokines – vascular endothelial growth factor (VEGF), interleukin 8 (IL-8), and basic fibroblast growth factor (bFGF) – as well as cell migration and invasion were all significantly increased in 3D cultures. This suggests that the 3D microenvironment, which is more hypoxic compared to 2D cultures, potentially provides increased tumorigenic capacity by supporting more disease-relevant cell-cell and cell-matrix interactions.

In summary, dynamic covalent chemistries such as oximes and hydrazones have become particularly attractive for the development of dynamic and mechanically compliant hydrogel systems. The reactions proceed at physiologic conditions and tissue-relevant properties such as viscoelasticity can be easily tuned. For this reason, both oxime and hydrazone chemistries have been utilized in applications requiring shear-thinning and self-healing properties as well as for studies focusing on the impact of material stress relaxation timescales on cell mechanobiology. While oxime bonds are more stable than hydrazone bonds, hydrazone-based hydrogels have been explored more in the biomaterials space because of their increased stress relaxation capabilities. Additionally, imine bond formation is pH- and temperature-sensitive. Not surprisingly, one drawback to these mechanisms is the slow gelation kinetics. However, recent approaches combining imine reactions with secondary crosslinking mechanisms have generated rapidly gelling hydrogels that are structurally stable and viscoelastic.

2.8 Thiols

Thiol-based click hydrogel formation typically occurs under one of two mechanisms: the radical thiol-ene/-yne reaction and the thiol-Michael addition[16]. Both mechanisms meet the criteria for click chemistry with fast reaction kinetics, high yields of one regioselective product, requiring only a small amount of catalyst, taking place in mild solvents, and reacting in air or water. Since the thiol itself, which contains a sulfhydryl group attached to a carbon, is what distinguishes these reactions from other click chemistries it is worth discussing key characteristics of this chemical species. There are a few commonly used thiols including alkyl thiols, aromatic thiols, thiolpropionates, and thiol glycolates[298]. A number of biomaterials researchers have also taken advantage of the sulfhydryl group in cysteine to incorporate peptide-based pendant groups and crosslinkers in hydrogels[299–305]. The high nucleophilicity allows for greater selectivity during crosslinking. Further, as outlined by Fairbanks *et al.*, thiol-based click photopolymerization offers an advantage over some other click chemistries in that it allows precise spatiotemporal control over the reaction, which they demonstrated by toggling light exposure on and off to illustrate modulus increase and stagnation, respectively[306]. A comprehensive discussion of thiols with respect to pK_a, nucleophilicity, and electrophilicity characteristics is covered in Hoyle *et al.*[307].

2.8.1 Radical thiol-ene/-yne chemistry

Thiol-ene addition reactions function by a radical-mediated crosslinking mechanism where a thiol attaches to an alkene. Thiol-yne photopolymerization reactions are similar to thiol-ene, with the substitution of an alkyne for an alkene. While the thiol-ene mechanism follows a 1:1 stoichiometric ratio of the two groups, the thiol-yne utilizes a 2:1 thiol-alkyne ratio[308]. This reaction mechanism

results in greater crosslink density and conversion rates compared to the thiol-ene reaction[309]. Thiol-ene/-yne reactions are most commonly done using light and a photoinitiator to produce radicals[306,310], as opposed to other methods like temperature[311]. This mechanism is efficient, with crosslinking occurring on time scales of seconds to several minutes, is useful for several different alkene functional groups, and results in high yields[306]. Photoinitiators like lithium phenyl(2,4,6-trimethylbenzoyl)phosphinate (LAP) and Irgacure 2959 (I2959) are used to generate the initial radicals that propagate through thiols upon light exposure. Briefly, once thiyl radicals are formed, they follow an addition reaction across the double bond in the -ene, which in turn results in a radical centered on a carbon that attaches to a thiol, producing another thiyl radical (**Scheme 2.7**). This reaction follows a step-growth mechanism which includes initiation, propagation, and termination steps. The termination step depends on the amount of thiol initially added, the number of available -enes, the amount of photoinitiator, and/or the removal of the light source generating the radicals.

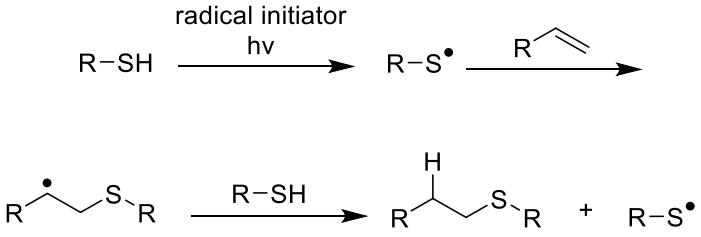

Scheme 2.7. Mechanism for radical initiated thiol-ene addition.

This reaction mechanism has been widely used in the field of macromolecules, with exemplary work in the early 2000s by Bowman who studied the reaction kinetics[312–314] as well as its potential use in biomaterials applications[315]. While this mechanism enables facile regulation of the crosslinking density and spatiotemporal control of the hydrogel formation, the use of toxic

photoinitiators which produce reactive radicals and light within the UV range may be harmful in certain cell culture applications. However, highly sensitive pancreatic β-cells remained viable following encapsulation in UV (365 nm) photopolymerized PEG-norbornene hydrogels, and resulted in higher cell viability compared to chain growth PEG-diacrylate polymerization mechanisms[316]. This result is just one of many examples highlighting the tunability of the functional group presentation and polymerization factors that can accommodate a variety of cell types.

2.8.2 Thiol-Michael chemistry

Since the first publication of the thiol-Michael reaction in 1964, this mechanism has been widely applied in the area of polymer chemistry, and more specifically biomaterial design[317]. By the early 2000s, the thiol-Michael reaction was being used to synthesize PEG hydrogels which paved the way for developing thiol-Michael fabricated hydrogels for cell culture[318,319]. The thiol-Michael addition reaction is a specific class of thiol-ene chemistry that occurs by crosslinking a thiol with a double bond such as those found in commonly used functional groups for hydrogel design like maleimides, vinyl sulfones[318,320–322], and (meth)acrylates[320]. This reaction typically proceeds more rapidly under basic conditions. The more electron-deficient the double carbon bond is, the more readily it will undergo the thiol-Michael reaction[315].

The base-catalyzed Michael addition leads to a thiolate anion which directly adds to the β-carbon of a double bond, producing a carbanion (**Scheme 2.8**). The carbanion obtains a proton from another thiol or the conjugate acid and continues to completion. The yield as well as the kinetics

rely on the base strength and amount, the pKa and steric accessibility the thiol. In biomaterials applications, commonly used bases are triethylamine or triethanolamine[323] mixed in PBS.

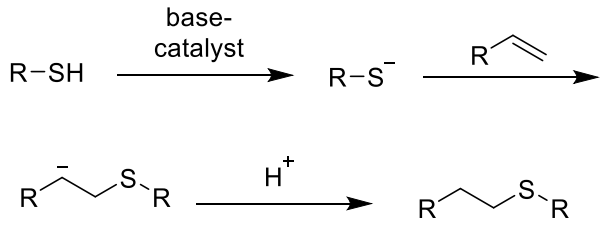

Scheme 2.8. Mechanism for the base-catalyzed thiol-Michael addition.

The Michael addition reaction does not require an especially strong base to produce a high yield of crosslinks and does not generate reactive radicals like the thiol photopolymerization reactions, enabling the formation of hydrogels with Young's moduli ranging from 1 kPa[324] to 300 kPa[320]. Along with the light-mediated thiol-yne reaction, there exists a non-radical mechanism that occurs at a physiologic pH[325]. This has advantages over the photopolymerization mechanism, namely by not producing radicals or requiring light sources which may be detrimental to cells and sensitive therapeutic payloads. For more rapid thiol-Michael reactions, such as thiol-maleimide, nonuniform crosslinking can result in more heterogeneous network formation[326–328]. The Peyton laboratory designed a set of experiments exploring how the buffer concentration and pH, as well as polymer concentration, changed the rate of the polymerization and subsequently investigated cancer cell cytocompatibility within these systems[326]. Using a slightly acidic pH of ~ 6.0 and a lower strength catalytic buffer afforded more optimal hydrogel properties with increased network homogeneity, as measured by visual inspection and small particle diffusion experiments using fluorescent beads. Darling *et al.* further examined how heterogeneous network formation of thiol-maleimide PEG

hydrogels led to a broader distribution of human dermal fibroblast spreading compared to those encapsulated within hydrogels with more homogeneous network crosslinks[327].

2.8.3 Ligand-decorated thiol-based hydrogels

Kasko's group studied the effects of material stiffness and adhesive peptide presentation on lung fibroblast activation by transforming growth factor β (TGF-β)[329]. The thiol-ene mechanism enabled facile crosslinking of PEG-diacrylate to thiol-functionalized peptides of different concentrations. By tuning the molecular weight of the monomer and the concentration of the peptide, hydrogels were fabricated with storage moduli ranging from 10 kPa to 1 MPa. Additionally, the type and concentration of the adhesive peptide could be tuned to control ligand presentation. The authors chose an arginine-glycine-aspartic acid-serine (RGDS) sequence since it is found in numerous ECM components like type I collagen, fibronectin, fibrinogen, and vitronectin. They also examined aspartic acid-glycine-glutamic acid-alanine (DGEA) and IKVAV sequences, which are found in type I collagen and laminin, respectively. Fibroblasts adhered to both RGDS and DGEA-functionalized hydrogels, though the latter required extreme concentrations. While it was demonstrated that stiffness alone did not activate fibroblasts, the RGDS-incorporated hydrogels altered actin cytoskeletal organization and focal adhesion formation. Further, expression of the myofibroblast marker α-smooth muscle actin (α-SMA) increased over time for cells on the stiffer materials, indicating that stiffness progressively drives fibroblast activation.

In addition to investigating cell-matrix interactions, recent work has used thiol-Michael chemistry to understand the combined effects of cell-cell and cell-matrix cues on MSC mechanobiology[330].

Methacrylated HA hydrogels were functionalized via thiol-Michael addition with thiolated HAVDI and RGD peptides to investigate cell-cell N-cadherin interactions and cell-matrix integrin-mediated adhesion respectively. The presence of HAVDI decreased cell contractility as well as YAP/TAZ nuclear translocation in MSCs at intermediate stiffnesses (E ~ 10 kPa) through reduction of Rac1 activity, indicating that cell-cell N-cadherin interactions can alter how cells sense and interpret the mechanics of their environment.

2.8.4 Degradable thiol-crosslinked hydrogels

Recent work using thiol-ene chemistries to design cell-degradable hydrogels has advanced our understanding of how cells sense their surrounding dynamic environments[302,331]. Caliari *et al.* studied how hydrogel stiffness and degradability influenced hMSC behavior in both 2D and 3D cultures using norbornene-modified HA (NorHA) crosslinked with dithiol peptides via thiol-ene photopolymerization (**Figure 2.6A,B**)[331]. While hMSCs demonstrated more spreading and YAP/TAZ nuclear translocation as hydrogel stiffness increased from 1 kPa to 20 kPa on 2D cultures (**Figure 2.6C**), encapsulated cells showed opposite trends with more spreading and YAP/TAZ nuclear localization in lower stiffness (E < 5 kPa) proteolytically-degradable 3D hydrogels (**Figure 2.6D**). Importantly, hMSCs encapsulated in mechanically equivalent but non-degradable 3D hydrogels spread less and had reduced YAP/TAZ in the nucleus. These results indicate that mechanosensing, specifically through YAP/TAZ, depends on hydrogel stiffness as well as culture dimensionality and degradability.

It is critical to consider matrix degradation in 3D hydrogel cultures since cells are encapsulated and sterically hindered within crosslinked networks, as opposed to 2D cultures where cells can

more easily spread and migrate. With this in mind, Lutolf *et al.* developed a multi-arm PEG hydrogel containing vinyl sulfone moieties that underwent thiol-Michael addition with cysteine-containing RGD integrin-binding domains and MMP-degradable peptides for cell adhesion and enzymatic degradation, respectively (**Figure 2.6E-G**)[321]. They investigated human fibroblast invasion from within fibrin clots encapsulated in the hydrogel network, where peptides with increased MMP sensitivity enhanced cell invasion rates compared to less sensitive and insensitive peptides. The results also indicated an optimal RGD concentration, with a peak in the extent of fibroblast outgrowth occurring in the median range of concentrations investigated (42.5 and 85 μM, with a range from 2.5 to 340 μM). Crosslink structure within the 3D PEG hydrogels was found to influence cell migration, with significantly lower invasion rates with increasing crosslink density. Interestingly, the authors used the information gained from this *in vitro* study to implant MMP-degradable hydrogels loaded with BMP-2 within rat cranial defects and found cells permeated throughout the entire hydrogel within 4 weeks of implantation. Notably, the enhanced healing response and bone regeneration depended on the increased sensitivity of the MMP-degradable peptide, corroborating the *in vitro* results. Recently, Lutolf and coworkers improved upon this design by successfully decreasing the network defects often found in thiol-Michael hydrogels. With this system, they reported robust mouse intestinal organoid development that was similar to those formed by the gold standard Matrigel (**Figure 2.6H,I**)[332].

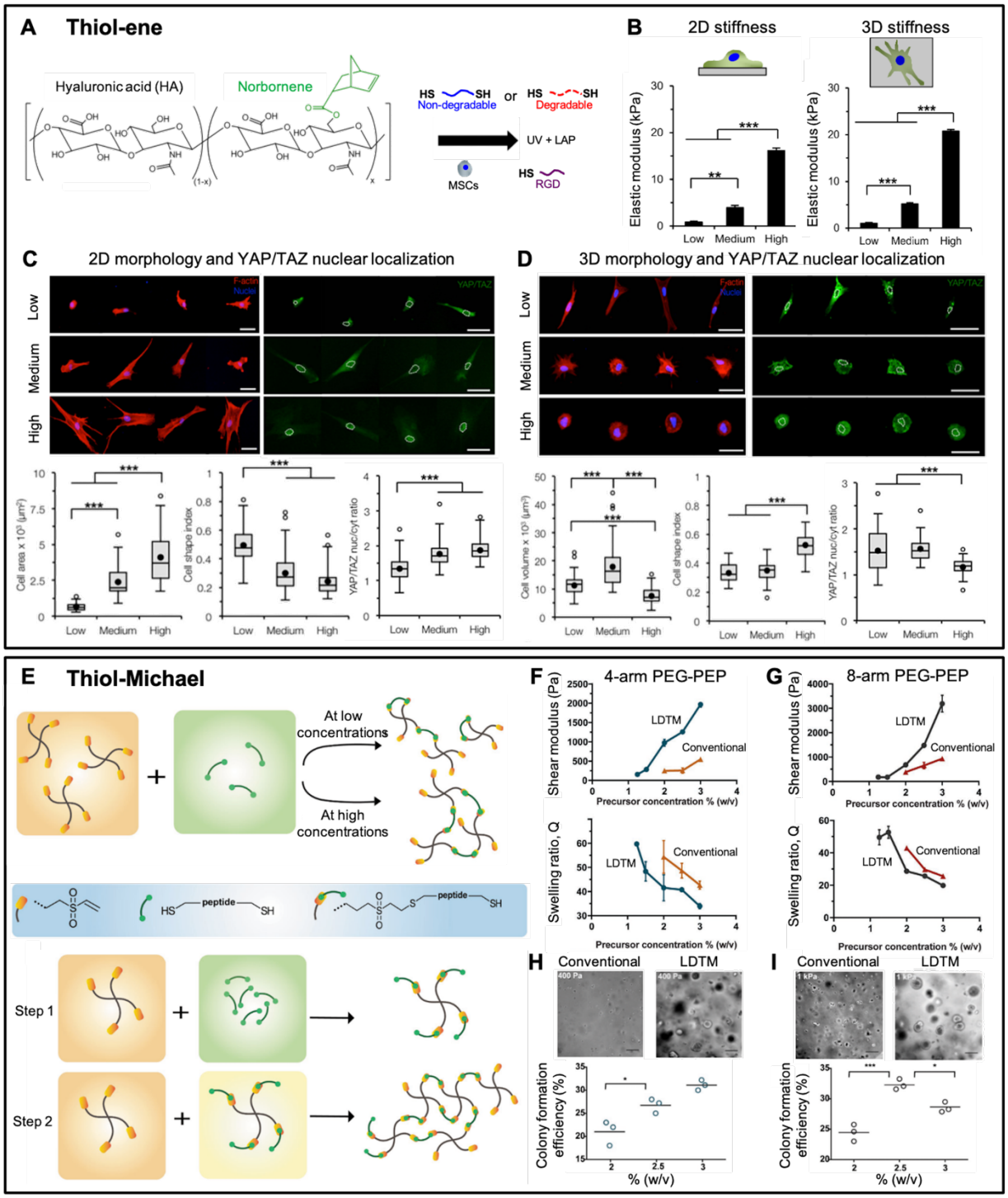

Figure 2.6. Thiol click mechanisms are useful to explore cell behaviors in a variety of contexts. (A) Norbornene-functionalized hyaluronic acid (NorHA) hydrogels were fabricated using UV light-mediated thiol-ene addition with either non-degradable or MMP-degradable peptide crosslinkers. (B) 4 wt% hydrogels with variable crosslinking densities were formed for 2D and 3D hMSC cultures to present a range of mechanical cues. (C) Representative images and quantification show that for 2D cultures, increased stiffness led to increased MSC spreading,

reduced circularity, and greater YAP/TAZ nuclear translocation. (D) In 3D culture, cell volume, circularity, and YAP/TAZ nuclear localization trends were reversed from 2D cultures as stiffness increased. Scale bars = 50 μm. (A-D) adapted with permission from[331]. Copyright 2016 Elsevier Ltd. (E) Thiol-Michael gelation was used to create 4-arm PEG macromers containing bi-functional peptides, either at low or high polymer concentrations in which the hydrogels were formed through stepwise co-polymerization with 4-arm PEG-vinyl sulfone and tetra-thiol peptide-functionalized PEG macromers. (F) 4-arm and (G) 8-arm low defect thiol Michael (LDTM) hydrogels showed higher shear moduli and lower swelling ratios compared to conventional peptide-containing PEG hydrogels. (H) In both 4-arm and (I) 8-arm LDTM hydrogels of 2.5% w/v, $1x10^{-3}$ M RGD, mouse intestinal stem cells formed colonies within 4 days of culture. Scale bars = 100 μm. (E-I) adapted with permission from[332]. Copyright 2020 WILEY-VCH.

Griffith's group utilized the thiol-vinyl sulfone Michael addition to couple PEG-vinyl sulfone with a variety of matrix-binding peptides, such as collagen I-derived, RGD, laminin 5-derived, basement membrane binding, and MMP-sensitive peptides[300]. Epithelial cells and stromal fibroblasts co-cultured within these hydrogels remained biologically active for two weeks of culture as indicated by production of various cytokines and growth factors. The cell behavior depended on hydrogel properties, including incorporation of an adhesive ligand recognized by both cell types, cell-specific peptides that stabilize the secreted ECM, as well as a proteolytically degradable peptide linker that allowed the cells to remodel the hydrogel networks. In an extension of this work, crosslinkers susceptible to a sortase A (SrtA)-mediated transpeptidase reaction were produced to enable user-directed and cell-independent hydrogel degradation to retrieve the co-cultured cells for further downstream analyses[333]. While the control group involving typical protease degradation damaged roughly half of the cytokines and growth factors secreted by the cells that the authors tested, the SrtA treatment only affected the IL-15 protein. These results provide a method for recovering cells from within hydrogels with minimal damage to investigate transcriptional and proteomic changes over time as the cells interact with each other and their surrounding matrix.

Fairbanks *et al.* also reported on the ability to biochemically control a PEG-norbornene hydrogel crosslinked by incorporating MMP-degradable dithiol peptides[306]. In comparison to the previously discussed thiol-Michael hydrogels from Lutholf and Hubbell, PEG-norbornene thiol-ene polymerized hydrogels displayed higher moduli even at similar molecular weights, likely caused by an increased conversion of the functional groups in the radical photopolymerization. RGDS functionalization was necessary for encapsulated MSC spreading; without RGDS the cells remained rounded for all of the degradable peptides studied. The degree of cell spreading at constant RGDS density depended on the structure of the MMP-cleavable peptide, where MMP-tryptophan and MMP-alanine resulted in the highest and lowest cell spreading, respectively. In a similar system, the Anseth group investigated the effects of neuronal axon outgrowth when exposed to different cysteine-functionalized biochemical cues, RGDS and YIGSR[334]. Within 12 hours of encapsulation in peptide-modified hydrogels, motor axons exhibited outgrowth and shapes typical of native motor neurons compared to unmodified PEG hydrogels or PEG hydrogels without the MMP-degradable crosslinker.

Lin's group also used thiol-ene photopolymerization to study the encapsulation of pancreatic ductal epithelial cells (PDEC) in an MMP-degradable PEG-norbornene hydrogel[335]. Within just 4 days, the PDECs arranged into clusters, but their growth was limited by MMP sensitivity, adhesion ligand presentation, and hydrogel mechanical properties. Notably, the authors found that the laminin-derived YIGSR adhesive peptide promoted increased epithelial cell marker expression, like β-catenin and E-cadherin, but less cell growth compared to RGDS presentation. The RGDS ligand also enhanced cyst-like morphologies in the PDECs, owing to how different ECM-mimetic ligands produce different cell behaviors. In another study, the same group incorporated cysteine-

containing SrtA-sensitive peptides for user-controlled matrix degradation and found that hydrogel softening increased encapsulated hMSC spread area[318,336]. Notably, SrtA was incorporated into a bis-cysteine peptide which allowed the authors to cyclically stiffen and soften the PEG-norbornene hydrogel[337]. Pancreatic cancer cells displayed either a decrease or increase in spheroid size upon hydrogel stiffening or softening, respectively. Encapsulating Huh7 or HepG2 liver cells into PEG-norbornene hydrogels resulted in increased urea secretion, CYP3A4 – an important enzyme responsible for toxin removal – and mRNA of hepatocyte genes CYP3A4, BESP, and NTCP, which helped elucidate mechanisms of hepatitis B virology *in vitro*[338]. Huh7 cells encapsulated within thiol-norbornene hydrogels comprised of gelatin with varying stiffness or gelatin concentration showed no significantly altered CYP3A4 activity or urea secretion[339]. However, the immobilization of heparin – a sulfated glycosaminoglycan commonly found in the liver – onto the hydrogel network led to Huh7s displaying greater urea secretion and CYP3A4 activity compared to the hydrogels without heparin, which was likely caused by modified cell signaling due to isolated growth factors in the media or released from cells[340]. In a similar study, Lin *et al.* studied the effects of matrix crosslinking and degradability on YAP regulation in encapsulated Huh7 cells[341] using a modified PEG system containing acrylate groups that could undergo cytocompatible visible light photocrosslinking with thiol moieties[342,343]. YAP expression was suppressed in 3D versus 2D cultures and also in hydrogels that did not contain RGD.

2.8.5 Mechanically dynamic and viscoelastic thiol-crosslinked hydrogels

To better model the dynamic mechanical properties of native ECM during development, wound repair, and disease, sequential crosslinking reactions allow control of hydrogel stiffness in the presence of cells to probe the resulting cell-matrix interactions. Hydrogels formed using

methacrylated HA (MeHA) crosslinked through base-catalyzed thiol-Michael addition displayed initial stiffnesses (E) of ~ 3 to 100 kPa, dependent on the thiol crosslinker concentration[344]. hMSCs exhibited either rounded or elongated morphologies when cultured atop soft or stiff hydrogels, respectively. Following *in situ* chain-growth UV photopolymerization of the remaining methacrylates, which stiffened initially compliant hydrogels from 3 to 30 kPa, hMSC morphology changed to more closely match that of cells initially seeded on the stiffer 30 kPa matrix. Long-term culture on these hydrogels illustrated the effects of stiffening on differentiation, where earlier or later stiffening promoted preferential adipogenic or osteogenic differentiation, respectively.

As a model for liver fibrosis progression, which results in gradual tissue stiffening, hepatic stellate cells seeded on a similar hydrogel system displayed markers of myofibroblast activation including more spreading, YAP/TAZ nuclear translocation, and α-SMA stress fiber organization when stiffening under more cytocompatible blue light occurred at later timepoints[46]. Interestingly, the authors suggested that the decreased cell spreading and myofibroblast marker expression seen in earlier stiffening may be due to a lag in cell mechanosensing following enzymatic primary cell isolation, an important consideration for mechanobiology studies using freshly isolated cells. To mimic fibrosis resolution, incorporation of a thiol crosslinker containing hydrolytically labile ester groups (combined with a non-degradable thiolated crosslinker) resulted in gradual softening, but not complete hydrolysis, of the MeHA hydrogel[345]. Stellate cells seeded on the softening hydrogel demonstrated a reduction in myofibroblast activation with decreased cell spreading as well as YAP/TAZ and α-SMA expression, but assumed an intermediate phenotype and did not completely return to baseline behaviors exhibited on static soft hydrogels. Notably, re-stiffening through blue light photopolymerization resulted in markedly rapid myofibroblast re-activation. The authors

suggested that this mimics *in vivo* hepatic stellate cell behavior following fibrosis resolution and subsequent re-insult.

Groups have also looked at exploiting thiol-based click chemistries in multiple steps to investigate the role of stiffness[324], ligand presentation[346], and ECM deposition[347,348] on the mechanoregulation of cell behavior. Petrou *et al.* leveraged the thiol-Michael and subsequent thiol-ene photopolymerizations to investigate the effects of hydrogel mechanical cues on PDGFRα+ fibroblast behavior[349]. They found that fibroblasts cultured on the stiff as well as temporally stiffened PEG α-methacrylate hydrogels showed greater cell activation, as measured by α-SMA and Col1a1 expression, than those on the soft PEG. A previously developed labeling method[350] using SPAAC was implemented to visualize nascent protein deposition by cells encapsulated in a variety of hydrogels, including Michael addition-formed MeHA and thiol-ene photopolymerized NorHA substrates[347,348]. MSCs displayed spreading, preferential osteogenic differentiation, and YAP/TAZ nuclear localization within either MMP-sensitive covalently crosslinked or dynamic viscoelastic HA hydrogels. However, when nascent protein secretion or remodeling was inhibited, the cells exhibited opposite trends, including preferential adipogenic differentiation, indicating that cellular interactions with nascent proteins in 3D hydrogels are critical to mechanosensing.

Anseth's group is well-known for their work involving PEG-based click reactions to study cell behavior. Valvular interstitial cells (VICs) encapsulated within thiol-ene photopolymerized PEG-norbornene hydrogels displayed more elongation and α-SMA expression, which decreased following *in situ* secondary thiol-ene photocrosslinking[351]. This study also highlighted the opposing trends seen between 2D and 3D cultures, underscoring that culture dimensionality is a

key factor to consider when investigating cell behavior. More recently, the researchers explored VIC contractility within this hydrogel system[352]. Through a combinatorial modeling and experimental approach, they discovered that VIC contraction resulted in an increase in the effective shear modulus of the 3D system, and that this contractility depended on the hydrogel mechanics as well as the concentration of adhesion ligands.

Aside from PEG, researchers have investigated these click reactions in a variety of other polymeric materials. Naturally-derived gelatin hydrogels provide adhesive ligands and enzymatic degradation as opposed to unmodified synthetic systems like PEG. Lin's group utilized thiol-ene photocrosslinking of gelatin-based systems[353] to create mechanically static soft or tyrosine-induced stiffening hydrogels[354] either with or without HA to investigate encapsulated pancreatic ductal adenocarcinoma (PDAC) cell morphology. They found that either a stiffening hydrogel without HA or a soft HA-containing hydrogel reduced PDAC growth, but HA-containing stiffening hydrogels resulted in significantly increased spreading. The authors suggest this is due to upregulation of Rac1, Rac2, RhoA, and Raf1 mRNAs, which are all involved in Ras/MAPK signaling. Notably, they also found upregulated genes involved in fibrosis, specifically TGF-β2, EGFR, and TGFβR1 for cells encapsulated in HA-containing stiffening hydrogels[355].

Recently, a 4D hydrogel developed by Zheng *et al.* allowed control of biochemical and mechanical cues in 3D culture through an initial thiol-Michael addition with methacrylated dextran and dicysteine-containing MMP-sensitive peptides[304]. At the same time, cysteine-bearing cyclo[RGD(DMNPB)fC] also attached to the methacrylates where subsequent UV light cleaved the DMNPB group to activate the RGD peptide, allowing for control of cell adhesion in a

spatiotemporal manner. Under visible light and in the presence of a photoinitiator, the remaining methacrylate groups underwent chain growth polymerization to further stiffen the hydrogel. Fibroblasts encapsulated as embedded spheroids remained confined and did not migrate within the initial hydrogel; however, when RGD was activated the fibroblasts migrated out of the spheroid and into the surrounding dextran hydrogel. When the RGD-activated hydrogel underwent secondary blue light stiffening, fibroblasts stopped migrating due to the increased crosslinks within the hydrogel network. These results highlight the incredible tunability afforded with click-based chemistries in hydrogel design as well as the competing effects of biochemical and biophysical hydrogel properties on regulating cell behaviors such as migration.

Others have even leveraged photopatterning techniques to enable spatiotemporal control of biochemical and biophysical hydrogel properties. Thiol-ene photopolymerization offers an advantage in being relatively mild and quick which helps maintain the stability and function of added signaling moieties. The Burdick group is most noted for their efforts in photopatterning HA-based materials[323,356,357]. Khetan *et al.* developed acrylate-modified HA to investigate cell morphology when encapsulated in hydrogels crosslinked by either thiol-Michael addition, chain growth photopolymerization, or sequential addition and photopolymerization in the presence of RGD, MMP-degradable dithiol crosslinker, or both peptides[323]. In the sequential method, photomasks were used to spatially control the secondary crosslinking reaction, where cells exposed to the additional non-degradable crosslinks displayed rounded morphologies while the hydrogel areas only containing MMP-degradable crosslinks exhibited spindle-like shapes. This system was then applied to investigate aortic arch growth and MSC differentiation[358]. Encapsulated arches as well as MSCs in MMP-degradable hydrogels demonstrated robust outgrowth, while those in the

non-degradable photopolymerized hydrogels did not; the same results occurred for arches and MSCs within hydrogels patterned with regions of the secondary photopolymerization, underscoring the importance of degradability for creating 3D hydrogels permissive to normal mechanical signaling. Gramlich *et al.* made use of the thiol-ene photoclick reaction to first create a norbornene-modified HA hydrogel that could undergo secondary thiol-mediated photocrosslinking to pattern regions of increased crosslinking and/or pendant thiolated peptides like RGD[357].

Numerous recent studies have highlighted the importance of designing hydrogels mimicking the viscoelasticity of native tissue to study mechanobiology[57,61,359,360]. For example, dynamic PDMS substrates, which are inherently viscoelastic, could be stiffened using thiol-ene chemistry to promote increased cardiac fibroblast activation compared to softer PDMS matrices[361]. Noting that many native tissues are viscoelastic and display time-dependent stress relaxation, Hui *et al.* developed NorHA hydrogels photopolymerized with dithiol crosslinkers while also containing β-cyclodextrin-functionalized HA and thiolated adamantane-modified peptides to create a hybrid hydrogel network combining stable covalent crosslinks and guest-host supramolecular interactions to impart viscoelasticity[57]. Human hepatic stellate cells (LX-2s) seeded atop the viscoelastic hydrogels exhibited reduced spreading, actin stress fiber organization, and MRTF-A nuclear localization compared to elastic hydrogels. Additionally, thiol-ene photochemistry was leveraged to spatially pattern stiffer more elastic hydrogel regions interspersed within more compliant and viscoelastic non-patterned regions to mimic the heterogeneous emergence of fibrotic nodules in liver fibrosis. Stellate cells responded to the patterned mechanical properties in a spatially selective manner with cells more spread in the stiffer elastic photopatterned regions.

2.8.6 Structured thiol-based hydrogels

Thiol-ene photopolymerizations also afforded the ability to create hydrogels with hierarchical structures by tethering self-assembling collagen-mimicking peptide fibrils to tetra-thiol PEG[362]. hMSCs displayed more elongation as the concentration of the collagen peptide mimic increased, with the authors describing notable "hole" regions where the cells seem to form donut clusters, in stark contrast to typical cell behavior in PEG hydrogels crosslinked with non-assembling peptides. In a similar study, Reynolds *et al.* formed an initial cell-laden fibrillar collagen structure that was later reinforced with photocrosslinked PEG -norbornenes and -dithiols to create an IPN mimicking *in vivo* collagen microarchitecture[363]. By confining metastatic breast cancer cells to increasingly stiff IPNs, the cells expressed less malignant behavior such as proliferation, therefore impeding tumorigenesis.

Along with incorporating fibrillar architecture into hydrogel networks, researchers also have taken advantage of microgels to engineer microscale porosity into 3D culture systems. Xin *et al.* packed PEG-norbornene microgels together and photocrosslinked them with the addition of PEG-dithiol[301]. hMSCs proliferated around the microgels and into the surrounding micropores within 24 h following encapsulation, but this behavior depended on the concentration of the crosslinker and the photoinitiator; cell proliferation increased for microgels made with lower PEG concentrations, even though the microgel porosity decreased. Cells displayed greater YAP nuclear localization in microgels of increasing stiffness, indicating that mechanical properties of the microgel scaffold influence cell mechanosensing in a similar manner to 2D cell culture. Using this same system, cell response was evaluated to either fast tryptophan-functionalized or slow proline-

containing degradable crosslinks incorporated within the microgels[364]. hMSCs proliferated more in both degradable groups, especially in the fast degrading group, compared to non-degradable microgels after 2 days of culture, suggesting that the degradability allowed for enhanced cell proliferation. Further, cells secreted OPG, a marker of osteogenic differentiation, in the fast degrading group with either the α5β1 peptide c(RRETAWA) – which induces osteogenesis – or RGDS modification. Segura's group also explored the design of microporous annealed particle scaffolds to study human dermal fibroblast mechanobiology[365]. HA-norbornene microgels were formed through photocrosslinking with dithiothreitol before annealing with a PEG-tetrazine crosslinker that was synthesized through base-catalyzed thiol-Michael addition. Fibroblasts displayed increased spreading and proliferation when cultured within scaffolds made with a lower degree of annealing since they could more easily remodel the scaffold network.

In summary, significant advantages of thiol-based click reactions over other click chemistries include the versatile range of groups that can undergo click reactions with thiols and the ability to typically perform these reactions under mild conditions. This has led to a wide breadth of hydrogel designs with reaction kinetics that are often faster than other click chemistries. However, because thiols are so highly reactive in both radical or catalyzed conditions, these mechanisms may not be as selective as other chemistries since they can undergo both reactions simultaneously, which may complicate therapeutic delivery if the payload contains reactive thiols or -ene groups, for example[366,367]. For more information regarding thiols, the complete chemistry of the thiol-ene/-yne and Michael-type reactions, and other applications of thiol-based reactions, the reader is referred to more extensive reviews on these mechanisms[16,298,307,308,366,368].

2.9 Conclusions and future directions

Native tissues are highly dynamic and intricate systems containing hierarchical levels of physical and biochemical cues spanning multiple length and time scales. As researchers endeavor to uncover important details about the cell-cell and cell-matrix interactions governing cell behavior in both normal and diseased tissue states, the development of advanced multi-responsive biomaterial models of tissue becomes increasingly important. Click chemistry is a powerful tool to guide the design of tunable biomaterials for studying cell mechanobiology. Several classes of click reactions have been identified and are continuously being refined to meet various design criteria of cell culture systems. Importantly, click-based hydrogels allow simple, independent manipulation of critical cell-instructive cues such as stiffness, viscoelasticity, degradability, adhesion, and growth factor presentation.

The diversity in click chemistries and reaction pairs, from initial efforts applying CuAAC chemistry to achieve fast and efficient kinetics with limited side product formation, is ideal for the development of a suite of hydrogel systems covering multivariate applications (**Table 2.2**). Hydrogel mechanics and gelation kinetics can easily be tuned by varying polymer concentration (stiffness), click pair reactivity (reaction rate), ratio of reagents (stiffness, viscoelasticity), crosslinking density and type (stiffness, viscoelasticity), and biomolecule ligand presentation. Rational selection of click reaction pairs –using electron-rich dienes or electron-poor dienophiles for Diels-Alder hydrogels, increasing SPAAC cycloalkyne strains, or substituting in more electron-withdrawing groups in an IEDDA system – has enabled more efficient gelation rates. Increasing reaction kinetics can allow more rapid cell encapsulation for 3D cultures. Slower gelation via Diels-Alder, hydrazone, and oxime chemistries, has shown utility for creating cell-

laden injectable and self-healing platforms. Varying hydrazone and oxime reactive group ratios allows for modulation of time-dependent, viscoelastic properties like stress relaxation. External stimuli such as temperature, pH, initiators, or catalysts can also aid in primary and secondary chemistries to enable spatiotemporal control over physical and biochemical cues. Radical- and light-mediated thiol-ene and thiol-yne additions yield systems with high levels of spatiotemporal control, useful for studying the impact of multiple cues on cell behaviors.

Click chemistry	**Common applications/uses**	**Future directions**
CuAAC	2D cell cultures[106,107] Biomolecule conjugation[369–372] Patterned hydrogels via photochemical Cu(II) reduction[103]	Non-toxic catalyst for 3D cultures[115,373]
SPAAC	3D cell cultures[122,123] pH-mediated degradation[136] Biomolecule conjugation[129,142] Stress relaxing hydrogels[125,127]	Dual-crosslinked hydrogels[126,143] Tissue regeneration applications[124,144]
Diels-Alder	Shear thinning and self-healing (injectable) materials[172] Controlled degradation via temperature or pH[172,173,191] Drug/protein delivery[169,174] Tumor models[14,168]	Biomolecule presentation and release[167] Thermosensitive hydrogels for controlled degradation[162,175,176] Tissue regeneration applications[170,171]
IEDDA	3D cell cultures[212,233] Biomolecule bioconjugation[236,239] Dual-crosslinked hydrogels[235]	Multilayer hydrogel microsphere formation[239] Cancer cell spheroid encapsulation[215]
Oxime	pH- and temperature-mediated viscoelastic hydrogels[256,283]	Dual-crosslinked hydrogels[287] Photo-mediated oxime ligation[247]
Hydrazone	Viscoelastic hydrogels[262,293,294] Sutureless tissue implantation[289,290] Biomolecule conjugation[295]	Interpenetrating network (IPN) hydrogels[61] 3D bioprinting of cell-laden scaffolds[279]
Thiol-based	3D cell cultures[306,321,338,352] Biomolecule conjugation[300,329,330] Dual-crosslinked hydrogels (in combination with other click chemistries)[103,123,174,209,235,236] Structured hydrogels (e.g., fibrillar architecture)[362,363]	Spatially patterned hydrogels[57,304,323,357] 3D bioprinting of cell-laden scaffolds[279,374,375] Dynamic platforms with temporal control over mechanical and chemical instructive cues[46,344,345,349,351,354]

Table 2.2. Summary of current and future applications for each click chemistry reaction.

The simplicity of click reactions allows for a more in-depth perspective into how particular mechanisms, such as stress relaxation timescales, can influence cell morphology, nuclear localization of transcriptional mechanoregulators, migration, and differentiation in both 2D and 3D cell culture systems. Several click chemistries can be spatiotemporally combined within a single system, creating an array of dynamic materials in which cell-instructive cues can be added to coincide with disease progression. For instance, a simple yet effective approach that has been applied to several systems is to introduce a secondary photomediated thiol-ene reaction for spatiotemporal presentation of stiffness, viscoelastic, or adhesive cues as well as tethered biomolecules. Dynamic chemistries utilizing dual crosslinking schemes have been used to influence subsequent mechanical properties in the presence of cells (e.g., using orthogonal wavelengths of light to trigger hydrogel stiffening or softening). These multi-factorial systems have enhanced our understanding of the complex mechanisms governing biological processes. Although current studies have already begun to demonstrate the power of click chemistry to design and tune biomaterials for cell culture, further research is needed to improve our understanding of how physical cues individually contribute to tissue regeneration and disease processes, as well as how we can exploit the specific and quick nature of click reactions to repair, replace, and treat diseased tissue.

Continued development toward integrating multiple mechanical and chemical cues in a user-controlled manner will be essential to mimic the complex behaviors of tissues, particularly during disease processes. Fortunately, there are several emerging areas that click-assembled cell culture models could specifically help address. Advancements toward spatiotemporally patterned biomaterials that capture the heterogeneity of healthy and disease tissues will help establish models

that can be used to study pathological cell behaviors. For example, photoclick chemistries such as radical-mediated thiol-ene addition have already shown promise toward achieving this objective because there is a high degree of control of when and where the reaction will take place. Dynamic materials, such as those involving dual-crosslinking approaches, allow cell-instructive cues (e.g., stiffness, viscoelasticity, ligand presentation) to be added to coincide with disease progression, furthering our understanding of how temporally presented signals regulate cell phenotype. Another promising avenue is multi-stimuli responsive hydrogels that can respond to various triggers such as light, pH, temperature, and redox state to independently manipulate physical, chemical, and mechanical properties. Utilizing click chemistry, development of these techniques will continue to expand the field toward the rational design of dynamic yet well-controlled hydrogel platforms. Looking ahead, click reactions should provide accessibility toward investigating complex combinatorial microenvironments. High-throughput arrays that can easily introduce physical cues and bioactive molecules in a single step can help address challenges in trying to increase clinical relevance of biomaterial systems without sacrificing user control or convenience[376].

2.10 Acknowledgements

The authors thank Ivan Basurto, Beverly Miller, and Mackenzie Grubb for helpful discussions. This work was supported by the NIH (R35GM138187, T32GM008715) and NSF (CAREER DMR/BMAT 2046592). The content is solely the responsibility of the authors and does not necessarily represent the official views of the National Institutes of Health.

2.11 References

(1) Bonnans, C.; Chou, J.; Werb, Z. Remodelling the Extracellular Matrix in Development and Disease. *Nat. Rev. Mol. Cell Biol.* **2014**, *15* (12), 786–801. https://doi.org/10.1038/nrm3904.

(2) Midwood, K. S.; Williams, L. V.; Schwarzbauer, J. E. Tissue Repair and the Dynamics of the Extracellular Matrix. *Int. J. Biochem. Cell Biol.* **2004**, *36* (6), 1031–1037. https://doi.org/10.1016/j.biocel.2003.12.003.

(3) Jansen, K. A.; Donato, D. M.; Balcioglu, H. E.; Schmidt, T.; Danen, E. H. J.; Koenderink, G. H. A Guide to Mechanobiology: Where Biology and Physics Meet. *Biochim. Biophys. Acta - Mol. Cell Res.* **2015**, *1853* (11), 3043–3052. https://doi.org/10.1016/j.bbamcr.2015.05.007.

(4) Lim, C. T.; Bershadsky, A.; Sheetz, M. P. Mechanobiology. *J. R. Soc. Interface* **2010**, *7*, S291–S293. https://doi.org/10.1098/rsif.2010.0150.focus.

(5) Mohammed, D.; Versaevel, M.; Bruyère, C.; Alaimo, L.; Luciano, M.; Vercruysse, E.; Procès, A.; Gabriele, S. Innovative Tools for Mechanobiology: Unraveling Outside-In and Inside-Out Mechanotransduction. *Frontiers in Bioengineering and Biotechnology*. 2019.

(6) Eyckmans, J.; Boudou, T.; Yu, X.; Chen, C. S. A Hitchhiker's Guide to Mechanobiology. *Dev. Cell* **2011**, *21* (1), 35–47. https://doi.org/10.1016/j.devcel.2011.06.015.

(7) Caliari, S. R.; Burdick, J. A. A Practical Guide to Hydrogels for Cell Culture. *Nat. Methods* **2016**, *13* (5), 405–414. https://doi.org/10.1038/nmeth.3839.

(8) Song, H. H. G.; Park, K. M.; Gerecht, S. Hydrogels to Model 3D in Vitro Microenvironment of Tumor Vascularization. *Adv. Drug Deliv. Rev.* **2014**, *79*, 19–29. https://doi.org/10.1016/j.addr.2014.06.002.

(9) Lee, J. H.; Kim, H. W. Emerging Properties of Hydrogels in Tissue Engineering. *J. Tissue Eng.* **2018**, *9*, 0–3. https://doi.org/10.1177/2041731418768285.

(10) Jiang, Y.; Chen, J.; Deng, C.; Suuronen, E. J.; Zhong, Z. Click Hydrogels, Microgels and Nanogels: Emerging Platforms for Drug Delivery and Tissue Engineering. *Biomaterials* **2014**, *35* (18), 4969–4985. https://doi.org/10.1016/j.biomaterials.2014.03.001.

(11) Kolb, H. C.; Finn, M. G.; Sharpless, K. B. Click Chemistry: Diverse Chemical Function from a Few Good Reactions. *Angew. Chemie - Int. Ed.* **2001**, *40* (11), 2004–2021. https://doi.org/10.1002/1521-3773(20010601)40:11<2004::AID-ANIE2004>3.0.CO;2-5.

(12) Madl, C. M.; Heilshorn, S. C. Bioorthogonal Strategies for Engineering Extracellular Matrices. *Adv. Funct. Mater.* **2018**, *28* (11), 1–21. https://doi.org/10.1002/adfm.201706046.

(13) Zhan, H.; De Jong, H.; Löwik, D. W. P. M. Comparison of Bioorthogonally Cross-Linked Hydrogels for in Situ Cell Encapsulation. *ACS Appl. Bio Mater.* **2019**, *2* (7), 2862–2871. https://doi.org/10.1021/acsabm.9b00253.

(14) Fisher, S. A.; Anandakumaran, P. N.; Owen, S. C.; Shoichet, M. S. Tuning the Microenvironment: Click-Crosslinked Hyaluronic Acid-Based Hydrogels Provide a Platform for Studying Breast Cancer Cell Invasion. *Adv. Funct. Mater.* **2015**, *25* (46), 7163–7172. https://doi.org/10.1002/adfm.201502778.

(15) Yu, F.; Cao, X.; Li, Y.; Chen, X. Diels-Alder Click-Based Hydrogels for Direct Spatiotemporal Postpatterning via Photoclick Chemistry. *ACS Macro Lett.* **2015**, *4* (3), 289–292. https://doi.org/10.1021/mz5007427.

(16) Nair, D. P.; Podgórski, M.; Chatani, S.; Gong, T.; Xi, W.; Fenoli, C. R.; Bowman, C. N. The Thiol-Michael Addition Click Reaction: A Powerful and Widely Used Tool in Materials Chemistry. *Chem. Mater.* **2014**, *26* (1), 724–744. https://doi.org/10.1021/cm402180t.

(17) Yigit, S.; Sanyal, R.; Sanyal, A. Fabrication and Functionalization of Hydrogels through "Click" Chemistry. *Chem. - An Asian J.* **2011**, *6* (10), 2648–2659. https://doi.org/10.1002/asia.201100440.

(18) Nimmo, C. M.; Owen, S. C.; Shoichet, M. S. Diels-Alder Click Cross-Linked Hyaluronic Acid Hydrogels for Tissue Engineering. *Biomacromolecules* **2011**, *12* (3), 824–830. https://doi.org/10.1021/bm101446k.

(19) Gopinathan, J.; Noh, I. Click Chemistry-Based Injectable Hydrogels and Bioprinting Inks for Tissue Engineering Applications. *Tissue Eng. Regen. Med.* **2018**, *15* (5), 531–546. https://doi.org/10.1007/s13770-018-0152-8.

(20) Jansen, K. A.; Atherton, P.; Ballestrem, C. Mechanotransduction at the Cell-Matrix Interface. *Semin. Cell Dev. Biol.* **2017**, *71*, 75–83. https://doi.org/10.1016/j.semcdb.2017.07.027.

(21) Martino, F.; Perestrelo, A. R.; Vinarský, V.; Pagliari, S.; Forte, G. Cellular Mechanotransduction: From Tension to Function. *Front. Physiol.* **2018**, *9* (JUL), 1–21. https://doi.org/10.3389/fphys.2018.00824.

(22) Humphrey, J. D.; Dufresne, E. R.; Schwartz, M. A. Mechanotransduction and Extracellular Matrix Homeostasis. *Nat. Rev. Mol. Cell Biol.* **2014**, *15* (12), 802–812. https://doi.org/10.1038/nrm3896.

(23) Wang, N.; Tytell, J. D.; Ingber, D. E. Mechanotransduction at a Distance: Mechanically Coupling the Extracellular Matrix with the Nucleus. *Nat. Rev. Mol. Cell Biol.* **2009**, *10* (1), 75–82. https://doi.org/10.1038/nrm2594.

(24) Urbanczyk, M.; Layland, S. L.; Schenke-Layland, K. The Role of Extracellular Matrix in Biomechanics and Its Impact on Bioengineering of Cells and 3D Tissues. *Matrix Biol.* **2020**, *85–86*, 1–14. https://doi.org/10.1016/j.matbio.2019.11.005.

(25) Nakayama, K. H.; Hou, L.; Huang, N. F. Role of Extracellular Matrix Signaling Cues in Modulating Cell Fate Commitment for Cardiovascular Tissue Engineering. *Adv. Healthc. Mater.* **2014**, *3* (5), 628–641. https://doi.org/10.1002/adhm.201300620.

(26) Changede, R.; Sheetz, M. Integrin and Cadherin Clusters: A Robust Way to Organize Adhesions for Cell Mechanics. *BioEssays* **2017**, *39* (1), 1–12. https://doi.org/10.1002/bies.201600123.

(27) Wang, N. Instant Integrin Mechanosensing. *Nat. Mater.* **2017**, *16* (12), 1173–1174. https://doi.org/10.1038/nmat5041.

(28) Wells, R. G.; Discher, D. E. Matrix Elasticity, Cytoskeletal Tension, and TGF-B : The Insoluble and Soluble Meet. *Sci. Signal.* **2008**, *1* (10), 1–4. https://doi.org/10.1126/stke.110pe13.

(29) Roberts, A. B.; McCune, B. K.; Sporn, M. B. TGF-β: Regulation of Extracellular Matrix. *Kidney Int.* **1992**, *41* (3), 557–559. https://doi.org/10.1038/ki.1992.81.

(30) Leight, J. L.; Wozniak, M. A.; Chen, S.; Lynch, M. L.; Chen, C. S.; Wang, Y. Matrix Rigidity Regulates a Switch between TGF-. *Mol. Biol. Cell* **2012**, *23*, 1–11.

(31) Lodyga, M.; Hinz, B. TGF-B1 - A Truly Transforming Growth Factor in Fibrosis and Immunity. *Semin. Cell Dev. Biol.* **2020**, *101*, 123–139. https://doi.org/10.1016/j.semcdb.2019.12.010.

(32) Cox, T. R.; Erler, J. T. Remodeling and Homeostasis of the Extracellular Matrix: Implications for Fibrotic Diseases and Cancer. *DMM Dis. Model. Mech.* **2011**, *4* (2), 165–178. https://doi.org/10.1242/dmm.004077.

(33) Furler, R. L.; Nixon, D. F.; Brantner, C. A.; Popratiloff, A.; Uittenbogaart, C. H. TGF-β

Sustains Tumor Progression through Biochemical and Mechanical Signal Transduction. *Cancers*. 2018, pp 1–18. https://doi.org/10.3390/cancers10060199.

(34) Noskovičová, N.; Petřek, M.; Eickelberg, O.; Heinzelmann, K. Platelet-Derived Growth Factor Signaling in the Lung: From Lung Development and Disease to Clinical Studies. *Am. J. Respir. Cell Mol. Biol.* **2015**, *52* (3), 263–284. https://doi.org/10.1165/rcmb.2014-0294TR.

(35) Li, R.; Bernau, K.; Sandbo, N.; Gu, J.; Preissl, S.; Sun, X. Pdgfra Marks a Cellular Lineage with Distinct Contributions to Myofibroblasts in Lung Maturation and Injury Response. *Elife* **2018**, *7*, 1–20. https://doi.org/10.7554/eLife.36865.

(36) Gouveia, L.; Betsholtz, C.; Andrae, J. PDGF-A Signaling Is Required for Secondary Alveolar Septation and Controls Epithelial Proliferation in the Developing Lung. *Dev.* **2018**, *145* (7), 1–9. https://doi.org/10.1242/dev.161976.

(37) Endale, M.; Ahlfeld, S.; Bao, E.; Chen, X.; Green, J.; Bess, Z.; Weirauch, M. T.; Xu, Y.; Perl, A. K. Temporal, Spatial, and Phenotypical Changes of PDGFRα Expressing Fibroblasts during Late Lung Development. *Dev. Biol.* **2017**, *425* (2), 161–175. https://doi.org/10.1016/j.ydbio.2017.03.020.

(38) Mih, J. D.; Marinkovic, A.; Liu, F.; Sharif, A. S.; Tschumperlin, D. J. Matrix Stiffness Reverses the Effect of Actomyosin Tension on Cell Proliferation. *J. Cell Sci.* **2012**, *125* (24), 5974–5983. https://doi.org/10.1242/jcs.108886.

(39) Kshitiz; Afzal, J.; Chang, H.; Goyal, R.; Levchenko, A. Mechanics of Microenvironment as Instructive Cues Guiding Stem Cell Behavior. *Curr. Stem Cell Reports* **2016**, *2* (1), 62–72. https://doi.org/10.1007/s40778-016-0033-9.

(40) Asano, S.; Ito, S.; Takahashi, K.; Furuya, K.; Kondo, M.; Sokabe, M.; Hasegawa, Y. Matrix Stiffness Regulates Migration of Human Lung Fibroblasts. *Physiol. Rep.* **2017**, *5* (9), 1–11. https://doi.org/10.14814/phy2.13281.

(41) Santos, A.; Lagares, D. Matrix Stiffness: The Conductor of Organ Fibrosis. *Current Rheumatology Reports*. Current Rheumatology Reports 2018. https://doi.org/10.1007/s11926-018-0710-z.

(42) Janmey, P. A.; Fletcher, D. A.; Reinhart-King, C. A. Stiffness Sensing by Cells. *Physiol. Rev.* **2020**, *100* (2), 695–724. https://doi.org/10.1152/physrev.00013.2019.

(43) Handorf, A. M.; Zhou, Y.; Halanski, M. A.; Li, W. J. Tissue Stiffness Dictates

Development, Homeostasis, and Disease Progression. *Organogenesis* **2015**, *11* (1), 1–15. https://doi.org/10.1080/15476278.2015.1019687.

(44) Discher, D. E.; Janmey, P.; Wang, Y. L. Tissue Cells Feel and Respond to the Stiffness of Their Substrate. *Science (80-.).* **2005**, *310* (5751), 1139–1143.

(45) Guimarães, C. F.; Gasperini, L.; Marques, A. P.; Reis, R. L. The Stiffness of Living Tissues and Its Implications for Tissue Engineering. *Nat. Rev. Mater.* **2020**, *5* (5), 351–370. https://doi.org/10.1038/s41578-019-0169-1.

(46) Caliari, S. R.; Perepelyuk, M.; Cosgrove, B. D.; Tsai, S. J.; Lee, G. Y.; Mauck, R. L.; Wells, R. G.; Burdick, J. A. Stiffening Hydrogels for Investigating the Dynamics of Hepatic Stellate Cell Mechanotransduction during Myofibroblast Activation. *Sci. Rep.* **2016**, *6*, 1–10. https://doi.org/10.1038/srep21387.

(47) Parandakh, A.; Anbarlou, A.; Tafazzoli-Shadpour, M.; Ardeshirylajimi, A.; Khani, M. M. Substrate Topography Interacts with Substrate Stiffness and Culture Time to Regulate Mechanical Properties and Smooth Muscle Differentiation of Mesenchymal Stem Cells. *Colloids Surfaces B Biointerfaces* **2019**, *173* (September 2018), 194–201. https://doi.org/10.1016/j.colsurfb.2018.09.066.

(48) Chang, Y. R.; Raghunathan, V. K.; Garland, S. P.; Morgan, J. T.; Russell, P.; Murphy, C. J. Automated AFM Force Curve Analysis for Determining Elastic Modulus of Biomaterials and Biological Samples. *J. Mech. Behav. Biomed. Mater.* **2014**, *37*, 209–218. https://doi.org/10.1016/j.jmbbm.2014.05.027.

(49) Abdellatef, S. A.; Ohi, A.; Nabatame, T.; Taniguchi, A. The Effect of Physical and Chemical Cues on Hepatocellular Function and Morphology. *Int. J. Mol. Sci.* **2014**, *15* (3), 4299–4317. https://doi.org/10.3390/ijms15034299.

(50) Baker, B. M.; Chen, C. S. Deconstructing the Third Dimension-How 3D Culture Microenvironments Alter Cellular Cues. *J. Cell Sci.* **2012**, *125* (13), 3015–3024. https://doi.org/10.1242/jcs.079509.

(51) Davidson, M. D.; Song, K. H.; Lee, M. H.; Llewellyn, J.; Du, Y.; Baker, B. M.; Wells, R. G.; Burdick, J. A. Engineered Fibrous Networks to Investigate the Influence of Fiber Mechanics on Myofibroblast Differentiation. *ACS Biomater. Sci. Eng.* **2019**, *5* (8), 3899–3908. https://doi.org/10.1021/acsbiomaterials.8b01276.

(52) Song, K. H.; Heo, S. J.; Peredo, A. P.; Davidson, M. D.; Mauck, R. L.; Burdick, J. A.

Influence of Fiber Stiffness on Meniscal Cell Migration into Dense Fibrous Networks. *Adv. Healthc. Mater.* **2020**, *9* (8), 1–10. https://doi.org/10.1002/adhm.201901228.

(53) Cacopardo, L.; Guazzelli, N.; Nossa, R.; Mattei, G.; Ahluwalia, A. Engineering Hydrogel Viscoelasticity. *J. Mech. Behav. Biomed. Mater.* **2019**, *89* (May 2018), 162–167. https://doi.org/10.1016/j.jmbbm.2018.09.031.

(54) Efremov, Y. M.; Okajima, T.; Raman, A. Measuring Viscoelasticity of Soft Biological Samples Using Atomic Force Microscopy. *Soft Matter* **2019**, *16* (1), 64–81. https://doi.org/10.1039/c9sm01020c.

(55) Hemshekhar, M.; Thushara, R. M.; Chandranayaka, S.; Sherman, L. S.; Kemparaju, K.; Girish, K. S. Emerging Roles of Hyaluronic Acid Bioscaffolds in Tissue Engineering and Regenerative Medicine. *Int. J. Biol. Macromol.* **2016**, *86*, 917–928. https://doi.org/10.1016/j.ijbiomac.2016.02.032.

(56) Charrier, E. E.; Pogoda, K.; Wells, R. G.; Janmey, P. A. Control of Cell Morphology and Differentiation by Substrates with Independently Tunable Elasticity and Viscous Dissipation. *Nat. Commun.* **2018**, *9* (1), 1–13. https://doi.org/10.1038/s41467-018-02906-9.

(57) Hui, E.; Gimeno, K. I.; Guan, G.; Caliari, S. R. Spatiotemporal Control of Viscoelasticity in Phototunable Hyaluronic Acid Hydrogels. *Biomacromolecules* **2019**, *20* (11), 4126–4134. https://doi.org/10.1021/acs.biomac.9b00965.

(58) Gong, Z.; Szczesny, S. E.; Caliari, S. R.; Charrier, E. E.; Chaudhuri, O.; Cao, X.; Lin, Y.; Mauck, R. L.; Janmey, P. A.; Burdick, J. A.; et al. Matching Material and Cellular Timescales Maximizes Cell Spreading on Viscoelastic Substrates. *Proc. Natl. Acad. Sci. U. S. A.* **2018**, *115* (12), E2686–E2695. https://doi.org/10.1073/pnas.1716620115.

(59) Chaudhuri, O.; Gu, L.; Klumpers, D.; Darnell, M.; Bencherif, S. A.; Weaver, J. C.; Huebsch, N.; Lee, H. P.; Lippens, E.; Duda, G. N.; et al. Hydrogels with Tunable Stress Relaxation Regulate Stem Cell Fate and Activity. *Nat. Mater.* **2016**, *15* (3), 326–334. https://doi.org/10.1038/nmat4489.

(60) Chaudhuri, O.; Gu, L.; Darnell, M.; Klumpers, D.; Bencherif, S. A.; Weaver, J. C.; Huebsch, N.; Mooney, D. J. Substrate Stress Relaxation Regulates Cell Spreading. *Nat. Commun.* **2015**, *6*, 1–7. https://doi.org/10.1038/ncomms7365.

(61) Lou, J.; Stowers, R.; Nam, S.; Xia, Y.; Chaudhuri, O. Stress Relaxing Hyaluronic Acid-

Collagen Hydrogels Promote Cell Spreading, Fiber Remodeling, and Focal Adhesion Formation in 3D Cell Culture. *Biomaterials* **2018**, *154*, 213–222. https://doi.org/10.1016/j.biomaterials.2017.11.004.

(62) Balestrini, J. L.; Chaudhry, S.; Sarrazy, V.; Koehler, A.; Hinz, B. The Mechanical Memory of Lung Myofibroblasts. *Integr. Biol.* **2012**, *4* (4), 410–421. https://doi.org/10.1039/c2ib00149g.

(63) Klingberg, F.; Hinz, B.; White, E. S. The Myofibroblast Matrix: Implications for Tissue Repair and Fibrosis. *Journal of Pathology*. 2013, pp 298–309. https://doi.org/10.1002/path.4104.

(64) Wynn, T. A.; Ramalingam, T. R. Mechanisms of Fibrosis: Therapeutic Translation for Fibrotic Disease. *Nat. Med.* **2012**, *18* (7), 1028–1040. https://doi.org/10.1038/nm.2807.

(65) Pakshir, P.; Hinz, B. The Big Five in Fibrosis: Macrophages, Myofibroblasts, Matrix, Mechanics, and Miscommunication. *Matrix Biol.* **2018**, *68–69* (2017), 81–93. https://doi.org/10.1016/j.matbio.2018.01.019.

(66) Varney, S. D.; Betts, C. B.; Zheng, R.; Wu, L.; Hinz, B.; Zhou, J.; Van De Water, L. Hic-5 Is Required for Myofibroblast Differentiation by Regulating Mechanically Dependent MRTF-A Nuclear Accumulation. *J. Cell Sci.* **2016**, *129* (4), 774–787. https://doi.org/10.1242/jcs.170589.

(67) Halder, G.; Dupont, S.; Piccolo, S. Transduction of Mechanical and Cytoskeletal Cues by YAP and TAZ. *Nat. Rev. Mol. Cell Biol.* **2012**, *13* (9), 591–600. https://doi.org/10.1038/nrm3416.

(68) Jang, M.; An, J.; Oh, S. W.; Lim, J. Y.; Kim, J.; Choi, J. K.; Cheong, J. H.; Kim, P. Matrix Stiffness Epigenetically Regulates the Oncogenic Activation of the Yes-Associated Protein in Gastric Cancer. *Nat. Biomed. Eng.* **2021**, *5* (1), 114–123. https://doi.org/10.1038/s41551-020-00657-x.

(69) Liu, F.; Mih, J. D.; Shea, B. S.; Kho, A. T.; Sharif, A. S.; Tager, A. M.; Tschumperlin, D. J. Feedback Amplification of Fibrosis through Matrix Stiffening and COX-2 Suppression. *J. Cell Biol.* **2010**, *190* (4), 693–706. https://doi.org/10.1083/jcb.201004082.

(70) Wells, R. G. Tissue Mechanics and Fibrosis. *Biochim. Biophys. Acta - Mol. Basis Dis.* **2013**, *1832* (7), 884–890. https://doi.org/10.1016/j.bbadis.2013.02.007.

(71) Zhao, X. H.; Laschinger, C.; Arora, P.; Szászi, K.; Kapus, A.; McCulloch, C. A. Force

Activates Smooth Muscle α-Actin Promoter Activity through the Rho Signaling Pathway. *J. Cell Sci.* **2007**, *120* (10), 1801–1809. https://doi.org/10.1242/jcs.001586.

(72) Engler, A. J.; Sen, S.; Sweeney, H. L.; Discher, D. E. Matrix Elasticity Directs Stem Cell Lineage Specification. *Cell* **2006**, *126* (4), 677–689. https://doi.org/10.1016/j.cell.2006.06.044.

(73) Bauer, A.; Gu, L.; Kwee, B.; Li, W. A.; Dellacherie, M.; Celiz, A. D.; Mooney, D. J. Hydrogel Substrate Stress-Relaxation Regulates the Spreading and Proliferation of Mouse Myoblasts. *Acta Biomater.* **2017**, *62*, 82–90. https://doi.org/10.1016/j.actbio.2017.08.041.

(74) Gardel, M. L.; Schneider, I. C.; Aratyn-Schaus, Y.; Waterman, C. M. Mechanical Integration of Actin and Adhesion Dynamics in Cell Migration. *Annu. Rev. Cell Dev. Biol.* **2010**, *26* (1), 315–333. https://doi.org/10.1146/annurev.cellbio.011209.122036.

(75) Hadden, W. J.; Young, J. L.; Holle, A. W.; McFetridge, M. L.; Kim, D. Y.; Wijesinghe, P.; Taylor-Weiner, H.; Wen, J. H.; Lee, A. R.; Bieback, K.; et al. Stem Cell Migration and Mechanotransduction on Linear Stiffness Gradient Hydrogels. *Proc. Natl. Acad. Sci. U. S. A.* **2017**, *114* (22), 5647–5652. https://doi.org/10.1073/pnas.1618239114.

(76) Burridge, K.; Guilluy, C. Focal Adhesions, Stress Fibers and Mechanical Tension. *Exp. Cell Res.* **2016**, *343* (1), 14–20. https://doi.org/10.1016/j.yexcr.2015.10.029.

(77) Rowlands, A. S.; George, P. A.; Cooper-White, J. J. Directing Osteogenic and Myogenic Differentiation of MSCs: Interplay of Stiffness and Adhesive Ligand Presentation. *Am. J. Physiol. - Cell Physiol.* **2008**, *295* (4), C1037–C1044. https://doi.org/10.1152/ajpcell.67.2008.

(78) Wen, J. H.; Vincent, L. G.; Fuhrmann, A.; Choi, Y. S.; Hribar, K. C.; Taylor-Weiner, H.; Chen, S.; Engler, A. J. Interplay of Matrix Stiffness and Protein Tethering in Stem Cell Differentiation. *Nat. Mater.* **2014**, *13* (10), 979–987. https://doi.org/10.1038/nmat4051.

(79) Presolski, S. I.; Hong, V.; Cho, S. H.; Finn, M. G. Tailored Ligand Acceleration of the Cu-Catalyzed Azide-Alkyne Cycloaddition Reaction: Practical and Mechanistic Implications. *J. Am. Chem. Soc.* **2010**, *132* (41), 14570–14576. https://doi.org/10.1021/ja105743g.

(80) Dommerholt, J.; Rutjes, F. P. J. T.; van Delft, F. L. Strain-Promoted 1,3-Dipolar Cycloaddition of Cycloalkynes and Organic Azides. *Top. Curr. Chem.* **2016**, *374* (2), 1–20. https://doi.org/10.1007/s41061-016-0016-4.

(81) Meijer, A.; Otto, S.; Engberts, J. B. F. N. Effects of the Hydrophobicity of the Reactants on

Dieis-Alder Reactions in Water. *J. Org. Chem.* **1998**, *63* (24), 8989–8994. https://doi.org/10.1021/jo981359x.

(82) Vauthier, M.; Jierry, L.; Martinez Mendez, M. L.; Durst, Y. M.; Kelber, J.; Roucoules, V.; Bally-Le Gall, F. Interfacial Diels-Alder Reaction between Furan-Functionalized Polymer Coatings and Maleimide-Terminated Poly(Ethylene Glycol). *J. Phys. Chem. C* **2019**, *123* (7), 4125–4132. https://doi.org/10.1021/acs.jpcc.8b10533.

(83) Darko, A.; Wallace, S.; Dmitrenko, O.; Machovina, M. M.; Mehl, R. A.; Chin, J. W.; Fox, J. M. Conformationally Strained Trans-Cyclooctene with Improved Stability and Excellent Reactivity in Tetrazine Ligation. *Chem. Sci.* **2014**, *5* (10), 3770–3776. https://doi.org/10.1039/c4sc01348d.

(84) Larsen, D.; Kietrys, A. M.; Clark, S. A.; Park, H. S.; Ekebergh, A.; Kool, E. T. Exceptionally Rapid Oxime and Hydrazone Formation Promoted by Catalytic Amine Buffers with Low Toxicity. *Chem. Sci.* **2018**, *9* (23), 5252–5259. https://doi.org/10.1039/c8sc01082j.

(85) Dirksen, A.; Dirksen, S.; Hackeng, T. M.; Dawson, P. E. Nucleophilic Catalysis of Hydrazone Formation and Transimination: Implications for Dynamic Covalent Chemistry. *J. Am. Chem. Soc.* **2006**, *128* (49), 15602–15603. https://doi.org/10.1021/ja067189k.

(86) Kool, E. T.; Park, D. H.; Crisalli, P. Fast Hydrazone Reactants: Electronic and Acid/Base Effects Strongly Influence Rate at Biological PH. *J. Am. Chem. Soc.* **2013**, *135* (47), 17663–17666. https://doi.org/10.1021/ja407407h.

(87) Saito, F.; Noda, H.; Bode, J. W. Critical Evaluation and Rate Constants of Chemoselective Ligation Reactions for Stoichiometric Conjugations in Water. *ACS Chem. Biol.* **2015**, *10* (4), 1026–1033. https://doi.org/10.1021/cb5006728.

(88) Schelté, P.; Boeckler, C.; Frisch, B.; Schuber, F. Differential Reactivity of Maleimide and Bromoacetyl Functions with Thiols: Application to the Preparation of Liposomal Diepitope Constructs. *Bioconjug. Chem.* **2000**, *11* (1), 118–123. https://doi.org/10.1021/bc990122k.

(89) Tornøe, C. W.; Christensen, C.; Meldal, M. Peptidotriazoles on Solid Phase: [1,2,3]-Triazoles by Regiospecific Copper(I)-Catalyzed 1,3-Dipolar Cycloadditions of Terminal Alkynes to Azides. *J. Org. Chem.* **2002**, *67* (9), 3057–3064. https://doi.org/10.1021/jo011148j.

(90) Rostovtsev, V. V.; Green, L. G.; Fokin, V. V.; Sharpless, K. B. A Stepwise Huisgen Cycloaddition Process: Copper(I)-Catalyzed Regioselective "Ligation" of Azides and

Terminal Alkynes. *Angew. Chemie - Int. Ed.* **2002**, *41* (14), 2596–2599. https://doi.org/10.1002/1521-3773(20020715)41:14<2596::AID-ANIE2596>3.0.CO;2-4.

(91) Lutz, J. F.; Zarafshani, Z. Efficient Construction of Therapeutics, Bioconjugates, Biomaterials and Bioactive Surfaces Using Azide-Alkyne "Click" Chemistry. *Adv. Drug Deliv. Rev.* **2008**, *60* (9), 958–970. https://doi.org/10.1016/j.addr.2008.02.004.

(92) Ossipov, D. A.; Hilborn, J. Poly(Vinyl Alcohol)-Based Hydrogels Formed by "Click Chemistry." *Macromolecules* **2006**, *39* (5), 1709–1718. https://doi.org/10.1021/ma052545p.

(93) Malkoch, M.; Vestberg, R.; Gupta, N.; Mespouille, L.; Dubois, P.; Mason, A. F.; Hedrick, J. L.; Liao, Q.; Frank, C. W.; Kingsbury, K.; et al. Synthesis of Well-Defined Hydrogel Networks Using Click Chemistry. *Chem. Commun.* **2006**, No. 26, 2774–2776. https://doi.org/10.1039/b603438a.

(94) Crescenzi, V.; Cornelio, L.; Di Meo, C.; Nardecchia, S.; Lamanna, R. Novel Hydrogels via Click Chemistry: Synthesis and Potential Biomedical Applications. *Biomacromolecules* **2007**, *8* (6), 1844–1850. https://doi.org/10.1021/bm0700800.

(95) Liu, S. Q.; Rachel Ee, P. L.; Ke, C. Y.; Hedrick, J. L.; Yang, Y. Y. Biodegradable Poly(Ethylene Glycol)-Peptide Hydrogels with Well-Defined Structure and Properties for Cell Delivery. *Biomaterials* **2009**, *30* (8), 1453–1461. https://doi.org/10.1016/j.biomaterials.2008.11.023.

(96) Lallana, E.; Riguera, R.; Fernandez-Megia, E. Reliable and Efficient Procedures for the Conjugation of Biomolecules through Huisgen Azide-Alkyne Cycloadditions. *Angew. Chemie - Int. Ed.* **2011**, *50* (38), 8794–8804. https://doi.org/10.1002/anie.201101019.

(97) Lutz, J. F. 1,3-Dipolar Cycloadditions of Azides and Alkynes: A Universal Ligation Tool in Polymer and Materials Science. *Angew. Chemie - Int. Ed.* **2007**, *46* (7), 1018–1025. https://doi.org/10.1002/anie.200604050.

(98) Bock, V. D.; Hiemstra, H.; Van Maarseveen, J. H. Cu I-Catalyzed Alkyne-Azide "Click" Cycloadditions from a Mechanistic and Synthetic Perspective. *European J. Org. Chem.* **2006**, No. 1, 51–68. https://doi.org/10.1002/ejoc.200500483.

(99) Binder, W. H.; Sachsenhofer, R. "Click" Chemistry in Polymer and Material Science: An Update. *Macromol. Rapid Commun.* **2008**, *29* (12–13), 952–981. https://doi.org/10.1002/marc.200800089.

(100) Evans, R. A. The Rise of Azide-Alkyne 1,3-Dipolar "click" Cycloaddition and Its Application to Polymer Science and Surface Modification. *Aust. J. Chem.* **2007**, *60* (6), 384–395. https://doi.org/10.1071/CH06457.

(101) Moses, J. E.; Moorhouse, A. D. The Growing Applications of Click Chemistry. *Chem. Soc. Rev.* **2007**, *36* (8), 1249–1262. https://doi.org/10.1039/b613014n.

(102) Nandivada, H.; Jiang, X.; Lahann, J. Click Chemistry: Versatility and Control in the Hands of Materials Scientists. *Adv. Mater.* **2007**, *19* (17), 2197–2208. https://doi.org/10.1002/adma.200602739.

(103) Adzima, B. J.; Tao, Y.; Kloxin, C. J.; DeForest, C. A.; Anseth, K. S.; Bowman, C. N. Spatial and Temporal Control of the Alkyne-Azide Cycloaddition by Photoinitiated Cu(II) Reduction. *Nat. Chem.* **2011**, *3* (3), 256–259. https://doi.org/10.1038/nchem.980.

(104) Van Dijk, M.; Van Nostrum, C. F.; Hennink, W. E.; Rijkers, D. T. S.; Liskamp, R. M. J. Synthesis and Characterization of Enzymatically Biodegradable Peg and Peptide-Based Hydrogels Prepared by Click Chemistry. *Biomacromolecules* **2010**, *11* (6), 1608–1614. https://doi.org/10.1021/bm1002637.

(105) Azagarsamy, M. A.; McKinnon, D. D.; Alge, D. L.; Anseth, K. S. Coumarin-Based Photodegradable Hydrogel: Design, Synthesis, Gelation, and Degradation Kinetics. *ACS Macro Lett.* **2014**, *3* (6), 515–519. https://doi.org/10.1021/mz500230p.

(106) Huerta-Angeles, G.; Němcová, M.; Příkopová, E.; Šmejkalová, D.; Pravda, M.; Kučera, L.; Velebný, V. Reductive Alkylation of Hyaluronic Acid for the Synthesis of Biocompatible Hydrogels by Click Chemistry. *Carbohydr. Polym.* **2012**, *90* (4), 1704–1711. https://doi.org/10.1016/j.carbpol.2012.07.054.

(107) Testera, A. M.; Girotti, A.; de Torre, I. G.; Quintanilla, L.; Santos, M.; Alonso, M.; Rodríguez-Cabello, J. C. Biocompatible Elastin-like Click Gels: Design, Synthesis and Characterization. *J. Mater. Sci. Mater. Med.* **2015**, *26* (2), 1–13. https://doi.org/10.1007/s10856-015-5435-1.

(108) Hu, X.; Li, D.; Zhou, F.; Gao, C. Biological Hydrogel Synthesized from Hyaluronic Acid, Gelatin and Chondroitin Sulfate by Click Chemistry. *Acta Biomater.* **2011**, *7* (4), 1618–1626. https://doi.org/10.1016/j.actbio.2010.12.005.

(109) Seelbach, R. J.; Fransen, P.; Peroglio, M.; Pulido, D.; Lopez-Chicon, P.; Duttenhoefer, F.; Sauerbier, S.; Freiman, T.; Niemeyer, P.; Semino, C.; et al. Multivalent Dendrimers

Presenting Spatially Controlled Clusters of Binding Epitopes in Thermoresponsive Hyaluronan Hydrogels. *Acta Biomater.* **2014**, *10* (10), 4340–4350. https://doi.org/10.1016/j.actbio.2014.06.028.

(110) Chen, R. T.; Marchesan, S.; Evans, R. A.; Styan, K. E.; Such, G. K.; Postma, A.; McLean, K. M.; Muir, B. W.; Caruso, F. Photoinitiated Alkyne-Azide Click and Radical Cross-Linking Reactions for the Patterning of PEG Hydrogels. *Biomacromolecules* **2012**, *13* (3), 889–895. https://doi.org/10.1021/bm201802w.

(111) Gallant, N. D.; Lavery, K. A.; Amis, E. J.; Becker, M. L. Universal Gradient Substrates for "Click" Biofunctionalization. *Adv. Mater.* **2007**, *19* (7), 965–969. https://doi.org/10.1002/adma.200602221.

(112) Lu, J.; Shi, M.; Shoichet, M. S. Click Chemistry Functionalized Polymeric Nanoparticles Target Corneal Epithelial Cells through RGD-Cell Surface Receptors. *Bioconjug. Chem.* **2009**, *20* (1), 87–94. https://doi.org/10.1021/bc8003167.

(113) Hudalla, G. A.; Murphy, W. L. Using "Click" Chemistry to Prepare SAM Substrates to Study Stem Cell Adhesion. *Langmuir* **2009**, *25* (10), 5737–5746. https://doi.org/10.1021/la804077t.

(114) Moore, N. M.; Lin, N. J.; Gallant, N. D.; Becker, M. L. The Use of Immobilized Osteogenic Growth Peptide on Gradient Substrates Synthesized via Click Chemistry to Enhance MC3T3-E1 Osteoblast Proliferation. *Biomaterials* **2010**, *31* (7), 1604–1611. https://doi.org/10.1016/j.biomaterials.2009.11.011.

(115) Soriano Del Amo, D.; Wang, W.; Jiang, H.; Besanceney, C.; Yan, A. C.; Levy, M.; Liu, Y.; Marlow, F. L.; Wu, P. Biocompatible Copper(I) Catalysts for in Vivo Imaging of Glycans. *J. Am. Chem. Soc.* **2010**, *132* (47), 16893–16899. https://doi.org/10.1021/ja106553e.

(116) Agard, N. J.; Prescher, J. A.; Bertozzi, C. R. A Strain-Promoted [3 + 2] Azide-Alkyne Cycloaddition for Covalent Modification of Biomolecules in Living Systems. *J. Am. Chem. Soc.* **2004**, *126* (46), 15046–15047. https://doi.org/10.1021/ja044996f.

(117) Debets, M. F.; Van Berkel, S. S.; Dommerholt, J.; Dirks, A. J.; Rutjes, F. P. J. T.; Van Delft, F. L. Bioconjugation with Strained Alkenes and Alkynes. *Acc. Chem. Res.* **2011**, *44* (9), 805–815. https://doi.org/10.1021/ar200059z.

(118) Kim, E.; Koo, H. Biomedical Applications of Copper-Free Click Chemistry:: In Vitro, in Vivo, and Ex Vivo. *Chem. Sci.* **2019**, *10* (34), 7835–7851.

https://doi.org/10.1039/c9sc03368h.

(119) Pickens, C. J.; Johnson, S. N.; Pressnall, M. M.; Leon, M. A.; Berkland, C. J. Practical Considerations, Challenges, and Limitations of Bioconjugation via Azide-Alkyne Cycloaddition. *Bioconjug. Chem.* **2018**, *29* (3), 686–701. https://doi.org/10.1021/acs.bioconjchem.7b00633.

(120) Hodgson, S. M.; Bakaic, E.; Stewart, S. A.; Hoare, T.; Adronov, A. Properties of Poly(Ethylene Glycol) Hydrogels Cross-Linked via Strain-Promoted Alkyne-Azide Cycloaddition (SPAAC). *Biomacromolecules* **2016**, *17* (3), 1093–1100. https://doi.org/10.1021/acs.biomac.5b01711.

(121) Xu, J.; Filion, T. M.; Prifti, F.; Song, J. Cytocompatible Poly(Ethylene Glycol)-Co-Polycarbonate Hydrogels Cross-Linked by Copper-Free, Strain-Promoted Click Chemistry. *Chem. - An Asian J.* **2011**, *6* (10), 2730–2737. https://doi.org/10.1002/asia.201100411.

(122) DeForest, C. A.; Anseth, K. S. Cytocompatible Click-Based Hydrogels with Dynamically Tunable Properties through Orthogonal Photoconjugation and Photocleavage Reactions. *Nat. Chem.* **2011**, *3* (12), 925–931. https://doi.org/10.1038/nchem.1174.

(123) Deforest, C. A.; Polizzotti, B. D.; Anseth, K. S. Sequential Click Reactions for Synthesizing and Patterning Three-Dimensional Cell Microenvironments. *Nat. Mater.* **2009**, *8* (8), 659–664. https://doi.org/10.1038/nmat2473.

(124) Han, S. S.; Yoon, H. Y.; Yhee, J. Y.; Cho, M. O.; Shim, H. E.; Jeong, J. E.; Lee, D. E.; Kim, K.; Guim, H.; Lee, J. H.; et al. In Situ Cross-Linkable Hyaluronic Acid Hydrogels Using Copper Free Click Chemistry for Cartilage Tissue Engineering. *Polym. Chem.* **2018**, *9* (1), 20–27. https://doi.org/10.1039/c7py01654a.

(125) Tan, Y.; Huang, H.; Ayers, D. C.; Song, J. Modulating Viscoelasticity, Stiffness, and Degradation of Synthetic Cellular Niches via Stoichiometric Tuning of Covalent versus Dynamic Noncovalent Cross-Linking. *ACS Cent. Sci.* **2018**, *4* (8), 971–981. https://doi.org/10.1021/acscentsci.8b00170.

(126) Brown, T. E.; Silver, J. S.; Worrell, B. T.; Marozas, I. A.; Yavitt, F. M.; Günay, K. A.; Bowman, C. N.; Anseth, K. S. Secondary Photocrosslinking of Click Hydrogels to Probe Myoblast Mechanotransduction in Three Dimensions. *J. Am. Chem. Soc.* **2018**, *140* (37), 11585–11588. https://doi.org/10.1021/jacs.8b07551.

(127) Tang, S.; Ma, H.; Tu, H. C.; Wang, H. R.; Lin, P. C.; Anseth, K. S. Adaptable Fast Relaxing

Boronate-Based Hydrogels for Probing Cell–Matrix Interactions. *Adv. Sci.* **2018**, *5* (9), 1800638. https://doi.org/10.1002/advs.201800638.

(128) Madl, C. M.; Heilshorn, S. C. Tyrosine-Selective Functionalization for Bio-Orthogonal Cross-Linking of Engineered Protein Hydrogels. *Bioconjug. Chem.* **2017**, *28* (3), 724–730. https://doi.org/10.1021/acs.bioconjchem.6b00720.

(129) Shadish, J. A.; Strange, A. C.; Deforest, C. A. Genetically Encoded Photocleavable Linkers for Patterned Protein Release from Biomaterials. *J. Am. Chem. Soc.* **2019**, *141* (39), 15619–15625. https://doi.org/10.1021/jacs.9b07239.

(130) Arakawa, C. K.; Badeau, B. A.; Zheng, Y.; DeForest, C. A. Multicellular Vascularized Engineered Tissues through User-Programmable Biomaterial Photodegradation. *Adv. Mater.* **2017**, *29* (37), 1–9. https://doi.org/10.1002/adma.201703156.

(131) Dommerholt, J.; Schmidt, S.; Temming, R.; Hendriks, L. J. A.; Rutjes, F. P. J. T.; Van Hest, J. C. M.; Lefeber, D. J.; Friedl, P.; Van Delft, F. L. Readily Accessible Bicyclononynes for Bioorthogonal Labeling and Three-Dimensional Imaging of Living Cells. *Angew. Chemie - Int. Ed.* **2010**, *49* (49), 9422–9425. https://doi.org/10.1002/anie.201003761.

(132) Dommerholt, J.; Van Rooijen, O.; Borrmann, A.; Guerra, C. F.; Bickelhaupt, F. M.; Van Delft, F. L. Highly Accelerated Inverse Electron-Demand Cycloaddition of Electron-Deficient Azides with Aliphatic Cyclooctynes. *Nat. Commun.* **2014**, *5*, 1–7. https://doi.org/10.1038/ncomms6378.

(133) Zimmerman, E. S.; Heibeck, T. H.; Gill, A.; Li, X.; Murray, C. J.; Madlansacay, M. R.; Tran, C.; Uter, N. T.; Yin, G.; Rivers, P. J.; et al. Production of Site-Specific Antibody-Drug Conjugates Using Optimized Non-Natural Amino Acids in a Cell-Free Expression System. *Bioconjug. Chem.* **2014**, *25* (2), 351–361. https://doi.org/10.1021/bc400490z.

(134) Hermann, C. D.; Wilson, D. S.; Lawrence, K. A.; Ning, X.; Olivares-Navarrete, R.; Williams, J. K.; Guldberg, R. E.; Murthy, N.; Schwartz, Z.; Boyan, B. D. Rapidly Polymerizing Injectable Click Hydrogel Therapy to Delay Bone Growth in a Murine Re-Synostosis Model. *Biomaterials* **2014**, *35* (36), 9698–9708. https://doi.org/10.1016/j.biomaterials.2014.07.065.

(135) Deforest, C. A.; Sims, E. A.; Anseth, K. S. Peptide-Functionalized Click Hydrogels with Independently Tunable Mechanics and Chemical Functionality for 3D Cell Culture. *Chem. Mater.* **2010**, *22* (16), 4783–4790. https://doi.org/10.1021/cm101391y.

(136) Jiang, H.; Qin, S.; Dong, H.; Lei, Q.; Su, X.; Zhuo, R.; Zhong, Z. An Injectable and Fast-Degradable Poly(Ethylene Glycol) Hydrogel Fabricated via Bioorthogonal Strain-Promoted Azide-Alkyne Cycloaddition Click Chemistry. *Soft Matter* **2015**, *11* (30), 6029–6036. https://doi.org/10.1039/c5sm00508f.

(137) Grim, J. C.; Brown, T. E.; Aguado, B. A.; Chapnick, D. A.; Viert, A. L.; Liu, X.; Anseth, K. S. A Reversible and Repeatable Thiol-Ene Bioconjugation for Dynamic Patterning of Signaling Proteins in Hydrogels. *ACS Cent. Sci.* **2018**, *4* (7), 909–916. https://doi.org/10.1021/acscentsci.8b00325.

(138) Li, H.; Zheng, J.; Wang, H.; Becker, M. L.; Leipzig, N. D. Neural Stem Cell Encapsulation and Differentiation in Strain Promoted Crosslinked Polyethylene Glycol-Based Hydrogels. *J. Biomater. Appl.* **2018**, *32* (9), 1222–1230. https://doi.org/10.1177/0885328218755711.

(139) Deforest, C. A.; Tirrell, D. A. A Photoreversible Protein-Patterning Approach for Guiding Stem Cell Fate in Three-Dimensional Gels. *Nat. Mater.* **2015**, *14* (5), 523–531. https://doi.org/10.1038/nmat4219.

(140) Truong, V. X.; Tsang, K. M.; Simon, G. P.; Boyd, R. L.; Evans, R. A.; Thissen, H.; Forsythe, J. S. Photodegradable Gelatin-Based Hydrogels Prepared by Bioorthogonal Click Chemistry for Cell Encapsulation and Release. *Biomacromolecules* **2015**, *16* (7), 2246–2253. https://doi.org/10.1021/acs.biomac.5b00706.

(141) Truong, V. X.; Ablett, M. P.; Gilbert, H. T. J.; Bowen, J.; Richardson, S. M.; Hoyland, J. A.; Dove, A. P. In Situ-Forming Robust Chitosan-Poly(Ethylene Glycol) Hydrogels Prepared by Copper-Free Azide-Alkyne Click Reaction for Tissue Engineering. *Biomater. Sci.* **2014**, *2* (2), 167–175. https://doi.org/10.1039/c3bm60159e.

(142) Guo, J. L.; Li, A.; Kim, Y. S.; Xie, V. Y.; Smith, B. T.; Watson, E.; Bao, G.; Mikos, A. G. Click Functionalized, Tissue-Specific Hydrogels for Osteochondral Tissue Engineering. *J. Biomed. Mater. Res. - Part A* **2020**, *108* (3), 684–693. https://doi.org/10.1002/jbm.a.36848.

(143) Killaars, A. R.; Walker, C. J.; Anseth, K. S. Nuclear Mechanosensing Controls MSC Osteogenic Potential through HDAC Epigenetic Remodeling. *Proc. Natl. Acad. Sci. U. S. A.* **2020**, *117* (35), 21258–21266. https://doi.org/10.1073/pnas.2006765117.

(144) Wang, X.; Li, Z.; Shi, T.; Zhao, P.; An, K.; Lin, C.; Liu, H. Injectable Dextran Hydrogels Fabricated by Metal-Free Click Chemistry for Cartilage Tissue Engineering. *Mater. Sci. Eng. C* **2017**, *73*, 21–30. https://doi.org/10.1016/j.msec.2016.12.053.

(145) McKinnon, D. D.; Brown, T. E.; Kyburz, K. A.; Kiyotake, E.; Anseth, K. S. Design and Characterization of a Synthetically Accessible, Photodegradable Hydrogel for User-Directed Formation of Neural Networks. *Biomacromolecules* **2014**, *15* (7), 2808–2816. https://doi.org/10.1021/bm500731b.

(146) Madl, C. M.; Katz, L. M.; Heilshorn, S. C. Bio-Orthogonally Crosslinked, Engineered Protein Hydrogels with Tunable Mechanics and Biochemistry for Cell Encapsulation. *Adv. Funct. Mater.* **2016**, *26* (21), 3612–3620. https://doi.org/10.1002/adfm.201505329.

(147) Huebsch, N.; Arany, P. R.; Mao, A. S.; Shvartsman, D.; Ali, O. A.; Bencherif, S. A.; Rivera-Feliciano, J.; Mooney, D. J. Harnessing Traction-Mediated Manipulation of the Cell/Matrix Interface to Control Stem-Cell Fate. *Nat. Mater.* **2010**, *9* (6), 518–526. https://doi.org/10.1038/nmat2732.

(148) Gregoritza, M.; Brandl, F. P. The Diels-Alder Reaction: A Powerful Tool for the Design of Drug Delivery Systems and Biomaterials. *Eur. J. Pharm. Biopharm.* **2015**, *97*, 438–453. https://doi.org/10.1016/j.ejpb.2015.06.007.

(149) Heravi, M. M.; Vavsari, V. F. Recent Applications of Intramolecular Diels-Alder Reaction in Total Synthesis of Natural Products. *RSC Adv.* **2015**, *5* (63), 50890–50912. https://doi.org/10.1039/c5ra08306k.

(150) Duan, A.; Yu, P.; Liu, F.; Qiu, H.; Gu, F. L.; Doyle, M. P.; Houk, K. N. Diazo Esters as Dienophiles in Intramolecular (4 + 2) Cycloadditions: Computational Explorations of Mechanism. *J. Am. Chem. Soc.* **2017**, *139* (7), 2766–2770. https://doi.org/10.1021/jacs.6b12371.

(151) Heravi, M. M.; Ahmadi, T.; Ghavidel, M.; Heidari, B.; Hamidi, H. Recent Applications of the Hetero Diels-Alder Reaction in the Total Synthesis of Natural Products. *RSC Adv.* **2015**, *5* (123), 101999–102075. https://doi.org/10.1039/c5ra17488k.

(152) Grosso, C.; Liber, M.; Brigas, A. F.; Pinho E Melo, T. M. V. D.; Lemos, A. Regioselectivity in Hetero Diels-Alder Reactions. *J. Chem. Educ.* **2019**, *96* (1), 148–152. https://doi.org/10.1021/acs.jchemed.7b00933.

(153) Altinbasak, I.; Sanyal, R.; Sanyal, A. Best of Both Worlds: Diels-Alder Chemistry towards Fabrication of Redox-Responsive Degradable Hydrogels for Protein Release. *RSC Adv.* **2016**, *6* (78), 74757–74764. https://doi.org/10.1039/c6ra16126j.

(154) Blokzijl, W.; Blandamer, M. J.; Engberts, J. B. F. N. Diels-Alder Reactions in Aqueous

Solutions. Enforced Hydrophobie Interactions Between Diene and Dienophile. *J. Am. Chem. Soc.* **1991**, *113* (11), 4241–4246. https://doi.org/10.1021/ja00011a029.

(155) Rideout, D. C.; Breslow, R. Hydrophobic Acceleration of Diels-AIder Reactions. *J. Am. Chem. Soc.* **1980**, *102* (26), 7816–7817. https://doi.org/10.1021/ja00546a048.

(156) Chujo, Y.; Sada, K.; Saegusa, T. Reversible Gelation of Polyoxazoline by Means of Diels-Alder Reaction. *Macromolecules* **1990**, *23* (10), 2636–2641. https://doi.org/10.1021/ma00212a007.

(157) Jung, S.; Kim, S. Y.; Kim, J. C.; Noh, S. M.; Oh, J. K. Ambient Temperature Induced Diels-Alder Crosslinked Networks Based on Controlled Methacrylate Copolymers for Enhanced Thermoreversibility and Self-Healability. *RSC Adv.* **2017**, *7* (42), 26496–26506. https://doi.org/10.1039/c7ra04222a.

(158) Reutenauer, P.; Buhler, E.; Boul, P. J.; Candau, S. J.; Lehn, J. M. Room Temperature Dynamic Polymers Based on Diels-Alder Chemistry. *Chem. - A Eur. J.* **2009**, *15* (8), 1893–1900. https://doi.org/10.1002/chem.200802145.

(159) Wei, Z.; Yang, J. H.; Du, X. J.; Xu, F.; Zrinyi, M.; Osada, Y.; Li, F.; Chen, Y. M. Dextran-Based Self-Healing Hydrogels Formed by Reversible Diels-Alder Reaction under Physiological Conditions. *Macromol. Rapid Commun.* **2013**, *34* (18), 1464–1470. https://doi.org/10.1002/marc.201300494.

(160) Kramer, R. K.; Belgacem, M. N.; Carvalho, A. J. F.; Gandini, A. Thermally Reversible Nanocellulose Hydrogels Synthesized via the Furan/Maleimide Diels-Alder Click Reaction in Water. *Int. J. Biol. Macromol.* **2019**, *141*, 493–498. https://doi.org/10.1016/j.ijbiomac.2019.09.027.

(161) Wang, G. F.; Chu, H. J.; Wei, H. L.; Liu, X. Q.; Zhao, Z. X.; Zhu, J. Click Synthesis by Diels-Alder Reaction and Characterisation of Hydroxypropyl Methylcellulose-Based Hydrogels. *Chem. Pap.* **2014**, *68* (10), 1390–1399. https://doi.org/10.2478/s11696-014-0574-2.

(162) Kirchhof, S.; Brandl, F. P.; Hammer, N.; Goepferich, A. M. Investigation of the Diels-Alder Reaction as a Cross-Linking Mechanism for Degradable Poly(Ethylene Glycol) Based Hydrogels. *J. Mater. Chem. B* **2013**, *1* (37), 4855–4864. https://doi.org/10.1039/c3tb20831a.

(163) Froidevaux, V.; Borne, M.; Laborbe, E.; Auvergne, R.; Gandini, A.; Boutevin, B. Study of

the Diels-Alder and Retro-Diels-Alder Reaction between Furan Derivatives and Maleimide for the Creation of New Materials. *RSC Adv.* **2015**, *5* (47), 37742–37754. https://doi.org/10.1039/c5ra01185j.

(164) Wei, H. L.; Yang, Z.; Zheng, L. M.; Shen, Y. M. Thermosensitive Hydrogels Synthesized by Fast Diels-Alder Reaction in Water. *Polymer (Guildf).* **2009**, *50* (13), 2836–2840. https://doi.org/10.1016/j.polymer.2009.04.032.

(165) Gregoritza, M.; Messmann, V.; Goepferich, A. M.; Brandl, F. P. Design of Hydrogels for Delayed Antibody Release Utilizing Hydrophobic Association and Diels-Alder Chemistry in Tandem. *J. Mater. Chem. B* **2016**, *4* (19), 3398–3408. https://doi.org/10.1039/c6tb00223d.

(166) Silva, N. A.; Cooke, M. J.; Tam, R. Y.; Sousa, N.; Salgado, A. J.; Reis, R. L.; Shoichet, M. S. The Effects of Peptide Modified Gellan Gum and Olfactory Ensheathing Glia Cells on Neural Stem/Progenitor Cell Fate. *Biomaterials* **2012**, *33* (27), 6345–6354. https://doi.org/10.1016/j.biomaterials.2012.05.050.

(167) Owen, S. C.; Fisher, S. A.; Tam, R. Y.; Nimmo, C. M.; Shoichet, M. S. Hyaluronic Acid Click Hydrogels Emulate the Extracellular Matrix. *Langmuir* **2013**, *29* (24), 7393–7400. https://doi.org/10.1021/la305000w.

(168) Tam, R. Y.; Yockell-Lelièvre, J.; Smith, L. J.; Julian, L. M.; Baker, A. E. G.; Choey, C.; Hasim, M. S.; Dimitroulakos, J.; Stanford, W. L.; Shoichet, M. S. Rationally Designed 3D Hydrogels Model Invasive Lung Diseases Enabling High-Content Drug Screening. *Adv. Mater.* **2019**, *31* (7), 1–9. https://doi.org/10.1002/adma.201806214.

(169) Tan, H.; Rubin, J. P.; Marra, K. G. Direct Synthesis of Biodegradable Polysaccharide Derivative Hydrogels through Aqueous Diels-Alder Chemistry. *Macromol. Rapid Commun.* **2011**, *32* (12), 905–911. https://doi.org/10.1002/marc.201100125.

(170) Xing, D.; Ma, L.; Gao, C. A Bioactive Hyaluronic Acid-Based Hydrogel Cross-Linked by Diels-Alder Reaction for Promoting Neurite Outgrowth of PC12 Cells. *J. Bioact. Compat. Polym.* **2017**, *32* (4), 382–396. https://doi.org/10.1177/0883911516684654.

(171) Yu, F.; Cao, X.; Zeng, L.; Zhang, Q.; Chen, X. An Interpenetrating HA/G/CS Biomimic Hydrogel via Diels-Alder Click Chemistry for Cartilage Tissue Engineering. *Carbohydr. Polym.* **2013**, *97* (1), 188–195. https://doi.org/10.1016/j.carbpol.2013.04.046.

(172) Fan, M.; Ma, Y.; Zhang, Z.; Mao, J.; Tan, H.; Hu, X. Biodegradable Hyaluronic Acid

Hydrogels to Control Release of Dexamethasone through Aqueous Diels-Alder Chemistry for Adipose Tissue Engineering. *Mater. Sci. Eng. C* **2015**, *56*, 311–317. https://doi.org/10.1016/j.msec.2015.04.004.

(173) Gregoritza, M.; Messmann, V.; Abstiens, K.; Brandl, F. P.; Goepferich, A. M. Controlled Antibody Release from Degradable Thermoresponsive Hydrogels Cross-Linked by Diels-Alder Chemistry. *Biomacromolecules* **2017**, *18* (8), 2410–2418. https://doi.org/10.1021/acs.biomac.7b00587.

(174) Koehler, K. C.; Alge, D. L.; Anseth, K. S.; Bowman, C. N. A Diels-Alder Modulated Approach to Control and Sustain the Release of Dexamethasone and Induce Osteogenic Differentiation of Human Mesenchymal Stem Cells. *Biomaterials* **2013**, *34* (16), 4150–4158. https://doi.org/10.1016/j.biomaterials.2013.02.020.

(175) Kirchhof, S.; Strasser, A.; Wittmann, H. J.; Messmann, V.; Hammer, N.; Goepferich, A. M.; Brandl, F. P. New Insights into the Cross-Linking and Degradation Mechanism of Diels-Alder Hydrogels. *J. Mater. Chem. B* **2015**, *3* (3), 449–457. https://doi.org/10.1039/c4tb01680g.

(176) Smith, L. J.; Taimoory, S. M.; Tam, R. Y.; Baker, A. E. G.; Binth Mohammad, N.; Trant, J. F.; Shoichet, M. S. Diels-Alder Click-Cross-Linked Hydrogels with Increased Reactivity Enable 3D Cell Encapsulation. *Biomacromolecules* **2018**, *19* (3), 926–935. https://doi.org/10.1021/acs.biomac.7b01715.

(177) García-Astrain, C.; Avérous, L. Synthesis and Behavior of Click Cross-Linked Alginate Hydrogels: Effect of Cross-Linker Length and Functionality. *Int. J. Biol. Macromol.* **2019**, *137*, 612–619. https://doi.org/10.1016/j.ijbiomac.2019.07.010.

(178) Montiel-Herrera, M.; Gandini, A.; Goycoolea, F. M.; Jacobsen, N. E.; Lizardi-Mendoza, J.; Recillas-Mota, M.; Argüelles-Monal, W. M. N-(Furfural) Chitosan Hydrogels Based on Diels-Alder Cycloadditions and Application as Microspheres for Controlled Drug Release. *Carbohydr. Polym.* **2015**, *128*, 6–12. https://doi.org/10.1016/j.carbpol.2015.03.052.

(179) Kirchhof, S.; Gregoritza, M.; Messmann, V.; Hammer, N.; Goepferich, A. M.; Brandl, F. P. Diels-Alder Hydrogels with Enhanced Stability: First Step toward Controlled Release of Bevacizumab. *Eur. J. Pharm. Biopharm.* **2015**, *96*, 217–225. https://doi.org/10.1016/j.ejpb.2015.07.024.

(180) Stewart, S. A.; Backholm, M.; Burke, N. A. D.; Stöver, H. D. H. Cross-Linked Hydrogels

Formed through Diels-Alder Coupling of Furan- and Maleimide-Modified Poly(Methyl Vinyl Ether- Alt -Maleic Acid). *Langmuir* **2016**, *32* (7), 1863–1870. https://doi.org/10.1021/acs.langmuir.5b04450.

(181) Zhang, M.; Wang, J.; Jin, Z. Supramolecular Hydrogel Formation between Chitosan and Hydroxypropyl β-Cyclodextrin via Diels-Alder Reaction and Its Drug Delivery. *Int. J. Biol. Macromol.* **2018**, *114*, 381–391. https://doi.org/10.1016/j.ijbiomac.2018.03.106.

(182) Guaresti, O.; García-Astrain, C.; Aguirresarobe, R. H.; Eceiza, A.; Gabilondo, N. Synthesis of Stimuli–Responsive Chitosan–Based Hydrogels by Diels–Alder Cross–Linking `click´ Reaction as Potential Carriers for Drug Administration. *Carbohydr. Polym.* **2018**, *183* (June 2017), 278–286. https://doi.org/10.1016/j.carbpol.2017.12.034.

(183) Cengiz, N.; Gevrek, T. N.; Sanyal, R.; Sanyal, R.; Sanyal, A.; Sanyal, A. Fabrication of Patterned Hydrogel Interfaces: Exploiting the Maleimide Group as a Dual Purpose Handle for Cross-Linking and Bioconjugation. *Bioconjug. Chem.* **2020**, *31* (5), 1382–1391. https://doi.org/10.1021/acs.bioconjchem.0c00108.

(184) Park, E. J.; Gevrek, T. N.; Sanyal, R.; Sanyal, A. Indispensable Platforms for Bioimmobilization: Maleimide-Based Thiol Reactive Hydrogels. *Bioconjug. Chem.* **2014**, *25* (11), 2004–2011. https://doi.org/10.1021/bc500375r.

(185) Ghanian, M. H.; Mirzadeh, H.; Baharvand, H. In Situ Forming, Cytocompatible, and Self-Recoverable Tough Hydrogels Based on Dual Ionic and Click Cross-Linked Alginate. *Biomacromolecules* **2018**, *19* (5), 1646–1662. https://doi.org/10.1021/acs.biomac.8b00140.

(186) Yu, F.; Cao, X.; Du, J.; Wang, G.; Chen, X. Multifunctional Hydrogel with Good Structure Integrity, Self-Healing, and Tissue-Adhesive Property Formed by Combining Diels-Alder Click Reaction and Acylhydrazone Bond. *ACS Appl. Mater. Interfaces* **2015**, *7* (43), 24023–24031. https://doi.org/10.1021/acsami.5b06896.

(187) Koehler, K. C.; Anseth, K. S.; Bowman, C. N. Diels-Alder Mediated Controlled Release from a Poly(Ethylene Glycol) Based Hydrogel. *Biomacromolecules* **2013**, *14* (2), 538–547. https://doi.org/10.1021/bm301789d.

(188) Wang, G.; Cao, X.; Dong, H.; Zeng, L.; Yu, C.; Chen, X. A Hyaluronic Acid Based Injectable Hydrogel Formed via Photo-Crosslinking Reaction and Thermal-Induced Diels-Alder Reaction for Cartilage Tissue Engineering. *Polymers*. 2018.

(189) Bai, X.; Lü, S.; Cao, Z.; Ni, B.; Wang, X.; Ning, P.; Ma, D.; Wei, H.; Liu, M. Dual

Crosslinked Chondroitin Sulfate Injectable Hydrogel Formed via Continuous Diels-Alder (DA) Click Chemistry for Bone Repair. *Carbohydr. Polym.* **2017**, *166*, 123–130. https://doi.org/10.1016/j.carbpol.2017.02.062.

(190) Li, S.; Wang, L.; Yu, X.; Wang, C.; Wang, Z. Synthesis and Characterization of a Novel Double Cross-Linked Hydrogel Based on Diels-Alder Click Reaction and Coordination Bonding. *Mater. Sci. Eng. C* **2018**, *82* (May 2017), 299–309. https://doi.org/10.1016/j.msec.2017.08.031.

(191) Bi, B.; Ma, M.; Lv, S.; Zhuo, R.; Jiang, X. In-Situ Forming Thermosensitive Hydroxypropyl Chitin-Based Hydrogel Crosslinked by Diels-Alder Reaction for Three Dimensional Cell Culture. *Carbohydr. Polym.* **2019**, *212* (February), 368–377. https://doi.org/10.1016/j.carbpol.2019.02.058.

(192) Madl, C. M.; Heilshorn, S. C. Rapid Diels-Alder Cross-Linking of Cell Encapsulating Hydrogels. *Chem. Mater.* **2019**, *31* (19), 8035–8043. https://doi.org/10.1021/acs.chemmater.9b02485.

(193) Gandini, A. The Furan/Maleimide Diels-Alder Reaction: A Versatile Click-Unclick Tool in Macromolecular Synthesis. *Prog. Polym. Sci.* **2013**, *38* (1), 1–29. https://doi.org/10.1016/j.progpolymsci.2012.04.002.

(194) Elschner, T.; Obst, F.; Heinze, T. Furfuryl- and Maleimido Polysaccharides: Synthetic Strategies Toward Functional Biomaterials. *Macromolecular Bioscience*. 2018.

(195) Nicolaou, K. C.; Snyder, S. A.; Montagnon, T.; Vassilikogiannakis, G. The Diels-Alder Reaction in Total Synthesis. *Angew. Chemie - Int. Ed.* **2002**, *41* (10), 1668–1698. https://doi.org/10.1002/1521-3773(20020517)41:10<1668::AID-ANIE1668>3.0.CO;2-Z.

(196) Farkaš, P.; Bystrický, S. Efficient Activation of Carboxyl Polysaccharides for the Preparation of Conjugates. *Carbohydr. Polym.* **2007**, *68* (1), 187–190. https://doi.org/10.1016/j.carbpol.2006.07.013.

(197) Abandansari, H. S.; Ghanian, M. H.; Varzideh, F.; Mahmoudi, E.; Rajabi, S.; Taheri, P.; Nabid, M. R.; Baharvand, H. In Situ Formation of Interpenetrating Polymer Network Using Sequential Thermal and Click Crosslinking for Enhanced Retention of Transplanted Cells. *Biomaterials* **2018**, *170*, 12–25. https://doi.org/10.1016/j.biomaterials.2018.04.007.

(198) Cuvellier, A.; Verhelle, R.; Brancart, J.; Vanderborght, B.; Van Assche, G.; Rahier, H. The Influence of Stereochemistry on the Reactivity of the Diels-Alder Cycloaddition and the

Implications for Reversible Network Polymerization. *Polym. Chem.* **2019**, *10* (4), 473–485. https://doi.org/10.1039/c8py01216d.

(199) Oliveira, B. L.; Guo, Z.; Bernardes, G. J. L. Inverse Electron Demand Diels-Alder Reactions in Chemical Biology. *Chem. Soc. Rev.* **2017**, *46* (16), 4895–4950. https://doi.org/10.1039/c7cs00184c.

(200) Pagel, M. Inverse Electron Demand Diels–Alder (IEDDA) Reactions in Peptide Chemistry. *J. Pept. Sci.* **2019**, *25* (1), 1–9. https://doi.org/10.1002/psc.3141.

(201) Blackman, M. L.; Royzen, M.; Fox, J. M. Tetrazine Ligation: Fast Bioconjugation Based on Inverse-Electron-Demand Diels-Alder Reactivity. *J. Am. Chem. Soc.* **2008**, *130* (41), 13518–13519. https://doi.org/10.1021/ja8053805.

(202) Reiner, T.; Zeglis, B. M. The Inverse Electron Demand Diels-Alder Click Reaction in Radiochemistry. *J. Label. Compd. Radiopharm.* **2014**, *57* (4), 285–290. https://doi.org/10.1002/jlcr.3149.

(203) Carboni, R. A.; Lindsey, R. V. Reactions of Tetrazines with Unsaturated Compounds. A New Synthesis of Pyridazines. *J. Am. Chem. Soc.* **1959**, *81* (16), 4342–4346. https://doi.org/10.1021/ja01525a060.

(204) Balcar, J.; Chrisam, G.; Huber, F. X.; Sauer, J. Reaktivität von Stickstoff-Heterocyclen Genenüber Cyclooctin Als Dienophil. *Tetrahedron Lett.* **1983**, *24* (14), 1481–1484. https://doi.org/10.1016/S0040-4039(00)81687-1.

(205) Schoch, J.; Staudt, M.; Samanta, A.; Wiessler, M.; Jäschke, A. Site-Specific One-Pot Dual Labeling of DNA by Orthogonal Cycloaddition Chemistry. *Bioconjug. Chem.* **2012**, *23* (7), 1382–1386. https://doi.org/10.1021/bc300181n.

(206) Rutz, A. L.; Gargus, E. S.; Hyland, K. E.; Lewis, P. L.; Setty, A.; Burghardt, W. R.; Shah, R. N. Employing PEG Crosslinkers to Optimize Cell Viability in Gel Phase Bioinks and Tailor Post Printing Mechanical Properties. *Acta Biomater.* **2019**, *99*, 121–132. https://doi.org/10.1016/j.actbio.2019.09.007.

(207) Knall, A. C.; Hollauf, M.; Saf, R.; Slugovc, C. A Trifunctional Linker Suitable for Conducting Three Orthogonal Click Chemistries in One Pot. *Org. Biomol. Chem.* **2016**, *14* (45), 10576–10580. https://doi.org/10.1039/c6ob02182d.

(208) Jivan, F.; Fabela, N.; Davis, Z.; Alge, D. L. Orthogonal Click Reactions Enable the Synthesis of ECM-Mimetic PEG Hydrogels without Multi-Arm Precursors. *J. Mater.*

Chem. B **2018**, *6* (30), 4929–4936. https://doi.org/10.1039/c8tb01399c.

(209) Truong, V. X.; Ablett, M. P.; Richardson, S. M.; Hoyland, J. A.; Dove, A. P. Simultaneous Orthogonal Dual-Click Approach to Tough, in-Situ -Forming Hydrogels for Cell Encapsulation. *J. Am. Chem. Soc.* **2015**, *137* (4), 1618–1622. https://doi.org/10.1021/ja511681s.

(210) Kamber, D. N.; Liang, Y.; Blizzard, R. J.; Liu, F.; Mehl, R. A.; Houk, K. N.; Prescher, J. A. 1,2,4-Triazines Are Versatile Bioorthogonal Reagents. *J. Am. Chem. Soc.* **2015**, *137* (26), 8388–8391. https://doi.org/10.1021/jacs.5b05100.

(211) Knall, A. C.; Hollauf, M.; Slugovc, C. Kinetic Studies of Inverse Electron Demand Diels-Alder Reactions (IEDDA) of Norbornenes and 3,6-Dipyridin-2-Yl-1,2,4,5-Tetrazine. *Tetrahedron Lett.* **2014**, *55* (34), 4763–4766. https://doi.org/10.1016/j.tetlet.2014.07.002.

(212) Alge, D. L.; Azagarsamy, M. A.; Donohue, D. F.; Anseth, K. S. Synthetically Tractable Click Hydrogels for Three-Dimensional Cell Culture Formed Using Tetrazine-Norbornene Chemistry. *Biomacromolecules* **2013**, *14* (4), 949–953. https://doi.org/10.1021/bm4000508.

(213) Kang, K.; Park, J.; Kim, E. Tetrazine Ligation for Chemical Proteomics. *Proteome Sci.* **2017**, *15* (1), 1–13. https://doi.org/10.1186/s12953-017-0121-5.

(214) Delplace, V.; Nickerson, P. E. B.; Ortin-Martinez, A.; Baker, A. E. G.; Wallace, V. A.; Shoichet, M. S. Nonswelling, Ultralow Content Inverse Electron-Demand Diels–Alder Hyaluronan Hydrogels with Tunable Gelation Time: Synthesis and In Vitro Evaluation. *Adv. Funct. Mater.* **2020**, *30* (14), 1–11. https://doi.org/10.1002/adfm.201903978.

(215) Delplace, V.; Pickering, A. J.; Hettiaratchi, M. H.; Zhao, S.; Kivijärvi, T.; Shoichet, M. S. Inverse Electron-Demand Diels-Alder Methylcellulose Hydrogels Enable the Co-Delivery of Chondroitinase ABC and Neural Progenitor Cells. *Biomacromolecules* **2020**, *21* (6), 2421–2431. https://doi.org/10.1021/acs.biomac.0c00357.

(216) Koshy, S. T.; Desai, R. M.; Joly, P.; Li, J.; Bagrodia, R. K.; Lewin, S. A.; Joshi, N. S.; Mooney, D. J. Click-Crosslinked Injectable Gelatin Hydrogels. *Adv. Healthc. Mater.* **2016**, *5* (5), 541–547. https://doi.org/10.1002/adhm.201500757.

(217) Zhang, Z.; He, C.; Chen, X. Injectable Click Polypeptide Hydrogels via Tetrazine-Norbornene Chemistry for Localized Cisplatin Release. *Polymers*. 2020.

(218) Anugrah, D. S. B.; Ramesh, K.; Kim, M.; Hyun, K.; Lim, K. T. Near-Infrared Light-

Responsive Alginate Hydrogels Based on Diselenide-Containing Cross-Linkage for on Demand Degradation and Drug Release. *Carbohydr. Polym.* **2019**, *223* (June), 115070. https://doi.org/10.1016/j.carbpol.2019.115070.

(219) Zhang, Y.; Chen, H.; Zhang, T.; Zan, Y.; Ni, T.; Liu, M.; Pei, R. Fast-Forming BMSC-Encapsulating Hydrogels through Bioorthogonal Reaction for Osteogenic Differentiation. *Biomater. Sci.* **2018**, *6* (10), 2578–2581. https://doi.org/10.1039/c8bm00689j.

(220) Takayama, Y.; Kusamori, K.; Nishikawa, M. Click Chemistry as a Tool for Cell Engineering and Drug Delivery. *Molecules*. 2019.

(221) Wu, H.; Devaraj, N. K. Inverse Electron-Demand Diels–Alder Bioorthogonal Reactions. *Top. Curr. Chem.* **2016**, *374* (1), 1–22. https://doi.org/10.1007/s41061-015-0005-z.

(222) Liu, F.; Liang, Y.; Houk, K. N. Theoretical Elucidation of the Origins of Substituent and Strain Effects on the Rates of Diels-Alder Reactions of 1,2,4,5-Tetrazines. *J. Am. Chem. Soc.* **2014**, *136* (32), 11483–11493. https://doi.org/10.1021/ja505569a.

(223) Liu, F.; Paton, R. S.; Kim, S.; Liang, Y.; Houk, K. N. Diels-Alder Reactivities of Strained and Unstrained Cycloalkenes with Normal and Inverse-Electron-Demand Dienes: Activation Barriers and Distortion/Interaction Analysis. *J. Am. Chem. Soc.* **2013**, *135* (41), 15642–15649. https://doi.org/10.1021/ja408437u.

(224) Vrabel, M.; Kölle, P.; Brunner, K. M.; Gattner, M. J.; Lõpez-Carrillo, V.; De Vivie-Riedle, R.; Carell, T. Norbornenes in Inverse Electron-Demand Diels-Alder Reactions. *Chem. - A Eur. J.* **2013**, *19* (40), 13309–13312. https://doi.org/10.1002/chem.201301838.

(225) Selvaraj, R.; Fox, J. M. Trans-Cyclooctene-a Stable, Voracious Dienophile for Bioorthogonal Labeling. *Curr. Opin. Chem. Biol.* **2013**, *17* (5), 753–760. https://doi.org/10.1016/j.cbpa.2013.07.031.

(226) Wiessler, M.; Waldeck, W.; Kliem, C.; Pipkorn, R.; Braun, K. Ijmsv07P0019. *Int. J. Med. Sci.* **2010**, *7* (1), 19–28.

(227) Knall, A. C.; Slugovc, C. Inverse Electron Demand Diels-Alder (IEDDA)-Initiated Conjugation: A (High) Potential Click Chemistry Scheme. *Chem. Soc. Rev.* **2013**, *42* (12), 5131–5142. https://doi.org/10.1039/c3cs60049a.

(228) Bodwell, G. J.; Pi, Z. Electron Deficient Dienes I. Normal and Inverse Electron Demand Diels-Alder Reactions of the Same Carbon Skeleton. *Tetrahedron Lett.* **1997**, *38* (3), 309–312. https://doi.org/10.1016/S0040-4039(96)02340-4.

(229) Agopcan Cinar, S.; Ercan, S.; Erol Gunal, S.; Dogan, I.; Aviyente, V. The Origin of Exo-Stereoselectivity of Norbornene in Hetero Diels-Alder Reactions. *Org. Biomol. Chem.* **2014**, *12* (40), 8079–8086. https://doi.org/10.1039/c4ob01217h.

(230) Tamilmani, V.; Daul, C. A.; Venuvanalingam, P. Electrostatic Control on Endo/Exo Selectivity in Ionic Cycloaddition. *Chem. Phys. Lett.* **2005**, *416* (4–6), 354–357. https://doi.org/10.1016/j.cplett.2005.09.120.

(231) Wijnen, J. W.; Zavarise, S.; Engberts, J. B. F. N.; Charton, M. Substituent Effects on an Inverse Electron Demand Hetero Diels-Alder Reaction in Aqueous Solution and Organic Solvents: Cycloaddition of Substituted Styrenes to Di(2-Pyridyl)-1,2,4,5-Tetrazine. *J. Org. Chem.* **1996**, *61* (6), 2001–2005. https://doi.org/10.1021/jo9518563.

(232) Taylor, M. T.; Blackman, M. L.; Dmitrenko, O.; Fox, J. M. Design and Synthesis of Highly Reactive Dienophiles for the Tetrazine-Trans-Cyclooctene Ligation. *J. Am. Chem. Soc.* **2011**, *133* (25), 9646–9649. https://doi.org/10.1021/ja201844c.

(233) Lueckgen, A.; Garske, D. S.; Ellinghaus, A.; Desai, R. M.; Stafford, A. G.; Mooney, D. J.; Duda, G. N.; Cipitria, A. Hydrolytically-Degradable Click-Crosslinked Alginate Hydrogels. *Biomaterials* **2018**, *181*, 189–198. https://doi.org/10.1016/j.biomaterials.2018.07.031.

(234) Desai, R. M.; Koshy, S. T.; Hilderbrand, S. A.; Mooney, D. J.; Joshi, N. S. Versatile Click Alginate Hydrogels Crosslinked via Tetrazine-Norbornene Chemistry. *Biomaterials* **2015**, *50* (1), 30–37. https://doi.org/10.1016/j.biomaterials.2015.01.048.

(235) Lueckgen, A.; Garske, D. S.; Ellinghaus, A.; Mooney, D. J.; Duda, G. N.; Cipitria, A. Dual Alginate Crosslinking for Local Patterning of Biophysical and Biochemical Properties. *Acta Biomater.* **2020**, *115*, 185–196. https://doi.org/10.1016/j.actbio.2020.07.047.

(236) Hao, Y.; Song, J.; Ravikrishnan, A.; Dicker, K. T.; Fowler, E. W.; Zerdoum, A. B.; Li, Y.; Zhang, H.; Rajasekaran, A. K.; Fox, J. M.; et al. Rapid Bioorthogonal Chemistry Enables in Situ Modulation of the Stem Cell Behavior in 3D without External Triggers. *ACS Appl. Mater. Interfaces* **2018**, *10* (31), 26016–26027. https://doi.org/10.1021/acsami.8b07632.

(237) Vining, K. H.; Stafford, A.; Mooney, D. J. Sequential Modes of Crosslinking Tune Viscoelasticity of Cell-Instructive Hydrogels. *Biomaterials* **2019**, *188* (April 2018), 187–197. https://doi.org/10.1016/j.biomaterials.2018.10.013.

(238) Carthew, J.; Frith, J. E.; Forsythe, J. S.; Truong, V. X. Polyethylene Glycol-Gelatin Hydrogels with Tuneable Stiffness Prepared by Horseradish Peroxidase-Activated

Tetrazine-Norbornene Ligation. *J. Mater. Chem. B* **2018**, *6* (9), 1394–1401. https://doi.org/10.1039/c7tb02764h.

(239) Zhang, H.; Dicker, K. T.; Xu, X.; Jia, X.; Fox, J. M. Interfacial Bioorthogonal Cross-Linking. *ACS Macro Lett.* **2014**, *3* (8), 727–731. https://doi.org/10.1021/mz5002993.

(240) Conant, J. B.; Bartlett, P. D. A Quantitative Study of Semicarbazone Formation. *J. Am. Chem. Soc.* **1932**, *54* (7), 2881–2899. https://doi.org/10.1021/ja01346a030.

(241) Crisalli, P.; Kool, E. T. Water-Soluble Organocatalysts for Hydrazone and Oxime Formation. *J. Org. Chem.* **2013**, *78* (3), 1184–1189. https://doi.org/10.1021/jo302746p.

(242) Dirksen, A.; Dawson, P. E. Rapid Oxime and Hydrazone Ligations with Aromatic Aldehydes for Biomolecular Labeling. *Bioconjug. Chem.* **2008**, *19* (12), 2543–2548. https://doi.org/10.1021/bc800310p.

(243) Kalia, J.; Raines, R. T. Hydrolytic Stability of Hydrazones and Oximes. *Angew. Chemie - Int. Ed.* **2008**, *47* (39), 7523–7526. https://doi.org/10.1002/anie.200802651.

(244) Moroni, L.; Burdick, J. A.; Highley, C.; Lee, S. J.; Morimoto, Y.; Takeuchi, S.; Yoo, J. J. Biofabrication Strategies for 3D in Vitro Models and Regenerative Medicine. *Nat. Rev. Mater.* **2018**, *3* (5), 21–37. https://doi.org/10.1038/s41578-018-0006-y.

(245) Kölmel, D. K.; Kool, E. T. Oximes and Hydrazones in Bioconjugation: Mechanism and Catalysis. *Chem. Rev.* **2017**, *117* (15), 10358–10376. https://doi.org/10.1021/acs.chemrev.7b00090.

(246) Hafeez, S.; Ooi, H.; Morgan, F.; Mota, C.; Dettin, M.; van Blitterswijk, C.; Moroni, L.; Baker, M. Viscoelastic Oxidized Alginates with Reversible Imine Type Crosslinks: Self-Healing, Injectable, and Bioprintable Hydrogels. *Gels* **2018**, *4* (4), 85. https://doi.org/10.3390/gels4040085.

(247) Farahani, P. E.; Adelmund, S. M.; Shadish, J. A.; DeForest, C. A. Photomediated Oxime Ligation as a Bioorthogonal Tool for Spatiotemporally-Controlled Hydrogel Formation and Modification. *J. Mater. Chem. B* **2017**, *5* (23), 4435–4442. https://doi.org/10.1039/c6tb03400d.

(248) Poolman, J. M.; Maity, C.; Boekhoven, J.; Van Der Mee, L.; Le Sage, V. A. A.; Groenewold, G. J. M.; Van Kasteren, S. I.; Versluis, F.; Van Esch, J. H.; Eelkema, R. A Toolbox for Controlling the Properties and Functionalisation of Hydrazone-Based Supramolecular Hydrogels. *J. Mater. Chem. B* **2016**, *4* (5), 852–858.

https://doi.org/10.1039/c5tb01870f.

(249) Boehnke, N.; Cam, C.; Bat, E.; Segura, T.; Maynard, H. D. Imine Hydrogels with Tunable Degradability for Tissue Engineering. *Biomacromolecules* **2015**, *16* (7), 2101–2108. https://doi.org/10.1021/acs.biomac.5b00519.

(250) Collins, J.; Xiao, Z.; Müllner, M.; Connal, L. A. The Emergence of Oxime Click Chemistry and Its Utility in Polymer Science. *Polym. Chem.* **2016**, *7* (23), 3812–3826. https://doi.org/10.1039/c6py00635c.

(251) Meyer, V.; Janny, A. Ueber Stickstoffhaltige Acetonderivate. *Berichte der Dtsch. Chem. Gesellschaft* **1882**, *15* (1), 1164–1167. https://doi.org/10.1002/cber.188201501257.

(252) Grover, G. N.; Braden, R. L.; Christman, K. L. Oxime Cross-Linked Injectable Hydrogels for Catheter Delivery. *Adv. Mater.* **2013**, *25* (21), 2937–2942. https://doi.org/10.1002/adma.201205234.

(253) Mukherjee, S.; Hill, M. R.; Sumerlin, B. S. Self-Healing Hydrogels Containing Reversible Oxime Crosslinks. *Soft Matter* **2015**, *11* (30), 6152–6161. https://doi.org/10.1039/c5sm00865d.

(254) Dilla, R. A.; Motta, C. M. M.; Xu, Y.; Zander, Z. K.; Bernard, N.; Wiener, C. G.; Vogt, B. D.; Becker, M. L. Mechanically Tunable, Human Mesenchymal Stem Cell Viable Poly(Ethylene Glycol)–Oxime Hydrogels with Invariant Precursor Composition, Concentration, and Stoichiometry. *Mater. Today Chem.* **2019**, *11*, 244–252. https://doi.org/10.1016/j.mtchem.2018.11.003.

(255) Baker, A. E. G.; Bahlmann, L. C.; Tam, R. Y.; Liu, J. C.; Ganesh, A. N.; Mitrousis, N.; Marcellus, R.; Spears, M.; Bartlett, J. M. S.; Cescon, D. W.; et al. Benchmarking to the Gold Standard: Hyaluronan-Oxime Hydrogels Recapitulate Xenograft Models with In Vitro Breast Cancer Spheroid Culture. *Adv. Mater.* **2019**, *31* (36), 1–11. https://doi.org/10.1002/adma.201901166.

(256) Grover, G. N.; Lam, J.; Nguyen, T. H.; Segura, T.; Maynard, H. D. Biocompatible Hydrogels by Oxime Click Chemistry. *Biomacromolecules* **2012**, *13* (10), 3013–3017. https://doi.org/10.1021/bm301346e.

(257) Zhang, Z.; He, C.; Chen, X. Hydrogels Based on PH-Responsive Reversible Carbon-Nitrogen Double-Bond Linkages for Biomedical Applications. *Mater. Chem. Front.* **2018**, *2* (10), 1765–1778. https://doi.org/10.1039/c8qm00317c.

(258) Yang, C.; Tang, D. Patient-Specific Carotid Plaque Progression Simulation. *C. Model. Eng. Sci.* **2000**, *1* (2), 119–131. https://doi.org/10.1016/j.biotechadv.2011.08.021.Secreted.

(259) Kale, A. A.; Torchilin, V. P. Design, Synthesis, and Characterization of PH-Sensitive PEG-PE Conjugates for Stimuli-Sensitive Pharmaceutical Nanocarriers: The Effect of Substitutes at the Hydrazone Linkage on the PH Stability of PEG-PE Conjugates. *Bioconjug. Chem.* **2007**, *18* (2), 363–370. https://doi.org/10.1021/bc060228x.

(260) Yildiz, I. A DFT Approach to the Mechanistic Study of Hydrozone Hydrolysis. *J. Phys. Chem. A* **2016**, *120* (20), 3683–3692. https://doi.org/10.1021/acs.jpca.6b02882.

(261) Nguyen, R. Optimizing the Reversibility of Hydrazone Formation for Dynamic Combinatorial Chemistry. *Chem. Commun.* **2003**, *8*, 942–943. https://doi.org/10.1039/b211645f.

(262) McKinnon, D. D.; Domaille, D. W.; Cha, J. N.; Anseth, K. S. Biophysically Defined and Cytocompatible Covalently Adaptable Networks as Viscoelastic 3d Cell Culture Systems. *Adv. Mater.* **2014**, *26* (6), 865–872. https://doi.org/10.1002/adma.201303680.

(263) McKinnon, D. D.; Domaille, D. W.; Cha, J. N.; Anseth, K. S. Bis-Aliphatic Hydrazone-Linked Hydrogels Form Most Rapidly at Physiological PH: Identifying the Origin of Hydrogel Properties with Small Molecule Kinetic Studies. *Chem. Mater.* **2014**, *26* (7), 2382–2387. https://doi.org/10.1021/cm5007789.

(264) Karvinen, J.; Koivisto, J. T.; Jönkkäri, I.; Kellomäki, M. The Production of Injectable Hydrazone Crosslinked Gellan Gum-Hyaluronan-Hydrogels with Tunable Mechanical and Physical Properties. *J. Mech. Behav. Biomed. Mater.* **2017**, *71* (April), 383–391. https://doi.org/10.1016/j.jmbbm.2017.04.006.

(265) Patenaude, M.; Hoare, T. Injectable, Mixed Natural-Synthetic Polymer Hydrogels with Modular Properties. *Biomacromolecules* **2012**, *13* (2), 369–378. https://doi.org/10.1021/bm2013982.

(266) Wei, Z.; Yang, J. H.; Liu, Z. Q.; Xu, F.; Zhou, J. X.; Zrínyi, M.; Osada, Y.; Chen, Y. M. Novel Biocompatible Polysaccharide-Based Self-Healing Hydrogel. *Adv. Funct. Mater.* **2015**, *25* (9), 1352–1359. https://doi.org/10.1002/adfm.201401502.

(267) Huang, W.; Wang, Y.; Chen, Y.; Zhao, Y.; Zhang, Q.; Zheng, X.; Chen, L.; Zhang, L. Strong and Rapidly Self-Healing Hydrogels: Potential Hemostatic Materials. *Adv. Healthc. Mater.* **2016**, *5* (21), 2813–2822. https://doi.org/10.1002/adhm.201600720.

(268) Yeo, Y.; Ito, T.; Bellas, E.; Highley, C. B.; Marini, R.; Kohane, D. S. In Situ Cross-Linkable Hyaluronan Hydrogels Containing Polymeric Nanoparticles for Preventing Postsurgical Adhesions. *Ann. Surg.* **2007**, *245* (5), 819–824. https://doi.org/10.1097/01.sla.0000251519.49405.55.

(269) Patenaude, M.; Hoare, T. Injectable, Degradable Thermoresponsive Poly(Nisopropylacrylamide) Hydrogels. *ACS Macro Lett.* **2012**, *1* (3), 409–413. https://doi.org/10.1021/mz200121k.

(270) Chang, R.; Wang, X.; Li, X.; An, H.; Qin, J. Self-Activated Healable Hydrogels with Reversible Temperature Responsiveness. *ACS Appl. Mater. Interfaces* **2016**, *8* (38), 25544–25551. https://doi.org/10.1021/acsami.6b08279.

(271) Qian, H.; Aprahamian, I. An Emissive and PH Switchable Hydrazone-Based Hydrogel. *Chem. Commun.* **2015**, *51* (56), 11158–11161. https://doi.org/10.1039/c5cc03007b.

(272) Xiao, G.; Wang, Y.; Zhang, H.; Chen, L.; Fu, S. Facile Strategy to Construct a Self-Healing and Biocompatible Cellulose Nanocomposite Hydrogel via Reversible Acylhydrazone. *Carbohydr. Polym.* **2019**, *218* (April), 68–77. https://doi.org/10.1016/j.carbpol.2019.04.080.

(273) Xu, F.; Corbett, B.; Bell, S.; Zhang, C.; Budi Hartono, M.; Farsangi, Z. J.; MacGregor, J.; Hoare, T. High-Throughput Synthesis, Analysis, and Optimization of Injectable Hydrogels for Protein Delivery. *Biomacromolecules* **2020**, *21* (1), 214–229. https://doi.org/10.1021/acs.biomac.9b01132.

(274) Chen, F.; Ni, Y.; Liu, B.; Zhou, T.; Yu, C.; Su, Y.; Zhu, X.; Yu, X.; Zhou, Y. Self-Crosslinking and Injectable Hyaluronic Acid/RGD-Functionalized Pectin Hydrogel for Cartilage Tissue Engineering. *Carbohydr. Polym.* **2017**, *166*, 31–44. https://doi.org/10.1016/j.carbpol.2017.02.059.

(275) Sharma, P. K.; Singh, Y. Glyoxylic Hydrazone Linkage-Based PEG Hydrogels for Covalent Entrapment and Controlled Delivery of Doxorubicin. *Biomacromolecules* **2019**, *20* (6), 2174–2184. https://doi.org/10.1021/acs.biomac.9b00020.

(276) Wang, H.; Zhu, D.; Paul, A.; Cai, L.; Enejder, A.; Yang, F.; Heilshorn, S. C. Covalently Adaptable Elastin-Like Protein–Hyaluronic Acid (ELP–HA) Hybrid Hydrogels with Secondary Thermoresponsive Crosslinking for Injectable Stem Cell Delivery. *Adv. Funct. Mater.* **2017**, *27* (28), 1–11. https://doi.org/10.1002/adfm.201605609.

(277) Xu, F.; Lam, A.; Pan, Z.; Randhawa, G.; Lamb, M.; Sheardown, H.; Hoare, T. Fast Thermoresponsive Poly(Oligoethylene Glycol Methacrylate) (POEGMA)-Based Nanostructured Hydrogels for Reversible Tuning of Cell Interactions. *ACS Biomaterials Science and Engineering*. 2021.

(278) Kageyama, T.; Kakegawa, T.; Osaki, T.; Enomoto, J.; Ito, T.; Nittami, T.; Fukuda, J. Rapid Engineering of Endothelial Cell-Lined Vascular-like Structures in in Situ Crosslinkable Hydrogels. *Biofabrication*. 2014.

(279) Wang, L. L.; Highley, C. B.; Yeh, Y. C.; Galarraga, J. H.; Uman, S.; Burdick, J. A. Three-Dimensional Extrusion Bioprinting of Single- and Double-Network Hydrogels Containing Dynamic Covalent Crosslinks. *J. Biomed. Mater. Res. - Part A* **2018**, *106* (4), 865–875. https://doi.org/10.1002/jbm.a.36323.

(280) Azagarsamy, M. A.; Marozas, I. A.; Spaans, S.; Anseth, K. S. Photoregulated Hydrazone-Based Hydrogel Formation for Biochemically Patterning 3D Cellular Microenvironments. *ACS Macro Lett.* **2016**, *5* (1), 19–23. https://doi.org/10.1021/acsmacrolett.5b00682.

(281) Ma, H.; Caldwell, A. S.; Azagarsamy, M. A.; Gonzalez Rodriguez, A.; Anseth, K. S. Bioorthogonal Click Chemistries Enable Simultaneous Spatial Patterning of Multiple Proteins to Probe Synergistic Protein Effects on Fibroblast Function. *Biomaterials* **2020**, *255* (February), 120205. https://doi.org/10.1016/j.biomaterials.2020.120205.

(282) Grover, G. N.; Garcia, J.; Nguyen, M. M.; Zanotelli, M.; Madani, M. M.; Christman, K. L. Binding of Anticell Adhesive Oxime-Crosslinked PEG Hydrogels to Cardiac Tissues. *Adv. Healthc. Mater.* **2015**, *4* (9), 1327–1331. https://doi.org/10.1002/adhm.201500167.

(283) Sánchez-Morán, H.; Ahmadi, A.; Vogler, B.; Roh, K. H. Oxime Cross-Linked Alginate Hydrogels with Tunable Stress Relaxation. *Biomacromolecules* **2019**, *20* (12), 4419–4429. https://doi.org/10.1021/acs.biomac.9b01100.

(284) Lin, F.; Yu, J.; Tang, W.; Zheng, J.; Defante, A.; Guo, K.; Wesdemiotis, C.; Becker, M. L. Peptide-Functionalized Oxime Hydrogels with Tunable Mechanical Properties and Gelation Behavior. *Biomacromolecules* **2013**, *14* (10), 3749–3758. https://doi.org/10.1021/bm401133r.

(285) Trausel, F.; Fan, B.; van Rossum, S. A. P.; van Esch, J. H.; Eelkema, R. Aniline Catalysed Hydrazone Formation Reactions Show a Large Variation in Reaction Rates and Catalytic Effects. *Adv. Synth. Catal.* **2018**, *360* (13), 2571–2576.

https://doi.org/10.1002/adsc.201800342.

(286) Criado-Gonzalez, M.; Loftin, B.; Rodon Fores, J.; Vautier, D.; Kocgozlu, L.; Jierry, L.; Schaaf, P.; Boulmedais, F.; Harth, E. Enzyme Assisted Peptide Self-Assemblies Trigger Cell Adhesion in High Density Oxime Based Host Gels. *J. Mater. Chem. B* **2020**, *8* (20), 4419–4427. https://doi.org/10.1039/d0tb00456a.

(287) Baker, A. E. G.; Tam, R. Y.; Shoichet, M. S. Independently Tuning the Biochemical and Mechanical Properties of 3D Hyaluronan-Based Hydrogels with Oxime and Diels-Alder Chemistry to Culture Breast Cancer Spheroids. *Biomacromolecules* **2017**, *18* (12), 4373–4384. https://doi.org/10.1021/acs.biomac.7b01422.

(288) Hardy, J. G.; Lin, P.; Schmidt, C. E. Biodegradable Hydrogels Composed of Oxime Crosslinked Poly(Ethylene Glycol), Hyaluronic Acid and Collagen: A Tunable Platform for Soft Tissue Engineering. *J. Biomater. Sci. Polym. Ed.* **2015**, *26* (3), 143–161. https://doi.org/10.1080/09205063.2014.975393.

(289) Koivusalo, L.; Karvinen, J.; Sorsa, E.; Jönkkäri, I.; Väliaho, J.; Kallio, P.; Ilmarinen, T.; Miettinen, S.; Skottman, H.; Kellomäki, M. Hydrazone Crosslinked Hyaluronan-Based Hydrogels for Therapeutic Delivery of Adipose Stem Cells to Treat Corneal Defects. *Mater. Sci. Eng. C* **2018**, *85* (July 2017), 68–78. https://doi.org/10.1016/j.msec.2017.12.013.

(290) Koivusalo, L.; Kauppila, M.; Samanta, S.; Parihar, V. S.; Ilmarinen, T.; Miettinen, S.; Oommen, O. P.; Skottman, H. Tissue Adhesive Hyaluronic Acid Hydrogels for Sutureless Stem Cell Delivery and Regeneration of Corneal Epithelium and Stroma. *Biomaterials* **2019**, *225* (September), 119516. https://doi.org/10.1016/j.biomaterials.2019.119516.

(291) McKinnon, D. D.; Domaille, D. W.; Brown, T. E.; Kyburz, K. A.; Kiyotake, E.; Cha, J. N.; Anseth, K. S. Measuring Cellular Forces Using Bis-Aliphatic Hydrazone Crosslinked Stress-Relaxing Hydrogels. *Soft Matter* **2014**, *10* (46), 9230–9236. https://doi.org/10.1039/c4sm01365d.

(292) Marchitti, S. A.; Deitrich, R. A.; Vasiliou, V. Neurotoxicity and Metabolism of the Catecholamine-Derived 3,4-Dihydroxyphenylacetaldehyde and 3,4-Dihydroxyphenylglycolaldehyde: The Role of Aldehyde Dehydrogenase. *Pharmacol. Rev.* **2007**, *59* (2), 125–150. https://doi.org/10.1124/pr.59.2.1.

(293) Richardson, B. M.; Wilcox, D. G.; Randolph, M. A.; Anseth, K. S. Hydrazone Covalent Adaptable Networks Modulate Extracellular Matrix Deposition for Cartilage Tissue

Engineering. *Acta Biomater.* **2019**, *83*, 71–82. https://doi.org/10.1016/j.actbio.2018.11.014.

(294) Richardson, B. M.; Walker, C. J.; MacDougall, L. J.; Hoye, J. W.; Randolph, M. A.; Bryant, S. J.; Anseth, K. S. Viscoelasticity of Hydrazone Crosslinked Poly(Ethylene Glycol) Hydrogels Directs Chondrocyte Morphology during Mechanical Deformation. *Biomater. Sci.* **2020**, *8* (14), 3804–3811. https://doi.org/10.1039/d0bm00860e.

(295) Zhu, D.; Wang, H.; Trinh, P.; Heilshorn, S. C.; Yang, F. Elastin-like Protein-Hyaluronic Acid (ELP-HA) Hydrogels with Decoupled Mechanical and Biochemical Cues for Cartilage Regeneration. *Biomaterials* **2017**, *127*, 132–140. https://doi.org/10.1016/j.biomaterials.2017.02.010.

(296) Dahlmann, J.; Krause, A.; Möller, L.; Kensah, G.; Möwes, M.; Diekmann, A.; Martin, U.; Kirschning, A.; Gruh, I.; Dräger, G. Fully Defined in Situ Cross-Linkable Alginate and Hyaluronic Acid Hydrogels for Myocardial Tissue Engineering. *Biomaterials* **2013**, *34* (4), 940–951. https://doi.org/10.1016/j.biomaterials.2012.10.008.

(297) Suo, A.; Xu, W.; Wang, Y.; Sun, T.; Ji, L.; Qian, J. Dual-Degradable and Injectable Hyaluronic Acid Hydrogel Mimicking Extracellular Matrix for 3D Culture of Breast Cancer MCF-7 Cells. *Carbohydr. Polym.* **2019**, *211* (October 2018), 336–348. https://doi.org/10.1016/j.carbpol.2019.01.115.

(298) Hoyle, C. E.; Bowman, C. N. Thiol-Ene Click Chemistry. *Angew. Chemie - Int. Ed.* **2010**, *49* (9), 1540–1573. https://doi.org/10.1002/anie.200903924.

(299) Huang, S.; Wang, C.; Xu, J.; Ma, L.; Gao, C. In Situ Assembly of Fibrinogen/Hyaluronic Acid Hydrogel via Knob-Hole Interaction for 3D Cellular Engineering. *Bioact. Mater.* **2017**, *2* (4), 253–259. https://doi.org/10.1016/j.bioactmat.2017.09.002.

(300) Cook, C. D.; Hill, A. S.; Guo, M.; Stockdale, L.; Papps, J. P.; Isaacson, K. B.; Lauffenburger, D. A.; Griffith, L. G. Local Remodeling of Synthetic Extracellular Matrix Microenvironments by Co-Cultured Endometrial Epithelial and Stromal Cells Enables Long-Term Dynamic Physiological Function. *Integr. Biol.* **2017**, *9* (4), 271–289. https://doi.org/10.1039/c6ib00245e.

(301) Xin, S.; Wyman, O. M.; Alge, D. L. Assembly of PEG Microgels into Porous Cell-Instructive 3D Scaffolds via Thiol-Ene Click Chemistry. *Adv. Healthc. Mater.* **2018**, *7* (11), 1–7. https://doi.org/10.1002/adhm.201800160.

(302) Lueckgen, A.; Garske, D. S.; Ellinghaus, A.; Mooney, D. J.; Duda, G. N.; Cipitria, A.

Enzymatically-Degradable Alginate Hydrogels Promote Cell Spreading and in Vivo Tissue Infiltration. *Biomaterials* **2019**, *217* (May), 119294. https://doi.org/10.1016/j.biomaterials.2019.119294.

(303) Tirella, A.; Mattei, G.; La Marca, M.; Ahluwalia, A.; Tirelli, N. Functionalized Enzyme-Responsive Biomaterials to Model Tissue Stiffening in Vitro. *Front. Bioeng. Biotechnol.* **2020**, *8* (April), 1–14. https://doi.org/10.3389/fbioe.2020.00208.

(304) Zheng, Y.; Liong Han, M. K.; Jiang, Q.; Li, B.; Feng, J.; Del Campo, A. 4D Hydrogel for Dynamic Cell Culture with Orthogonal, Wavelength-Dependent Mechanical and Biochemical Cues. *Mater. Horizons* **2020**, *7* (1), 111–116. https://doi.org/10.1039/c9mh00665f.

(305) Hui, E.; Moretti, L.; Barker, T. H.; Caliari, S. R. The Combined Influence of Viscoelastic and Adhesive Cues on Fibroblast Spreading and Focal Adhesion Organization. *Cell. Mol. Bioeng.* **2021**. https://doi.org/10.1007/s12195-021-00672-1.

(306) Fairbanks, B. D.; Schwartz, M. P.; Halevi, A. E.; Nuttelman, C. R.; Bowman, C. N.; Anseth, K. S. A Versatile Synthetic Extracellular Matrix Mimic via Thiol-Norbornene Photopolymerization. *Adv. Mater.* **2009**, *21* (48), 5005–5010. https://doi.org/10.1002/adma.200901808.

(307) Hoyle, C. E.; Lowe, A. B.; Bowman, C. N. Thiol-Click Chemistry: A Multifaceted Toolbox for Small Molecule and Polymer Synthesis. *Chem. Soc. Rev.* **2010**, *39* (4), 1355–1387. https://doi.org/10.1039/b901979k.

(308) Lowe, A. B.; Hoyle, C. E.; Bowman, C. N. Thiol-Yne Click Chemistry: A Powerful and Versatile Methodology for Materials Synthesis. *J. Mater. Chem.* **2010**, *20* (23), 4745–4750. https://doi.org/10.1039/b917102a.

(309) Fairbanks, B. D.; Scott, T. F.; Kloxin, C. J.; Anseth, K. S.; Bowman, C. N. Thiol-Yne Photopolymerizations: Novel Mechanism, Kinetics, and Step-Growth Formation of Highly Cross-Linked Networks. *Macromolecules* **2009**, *42* (1), 211–217.

(310) Fairbanks, B. D.; Schwartz, M. P.; Bowman, C. N.; Anseth, K. S. Photoinitiated Polymerization of PEG-Diacrylate with Lithium Phenyl-2,4,6-Trimethylbenzoylphosphinate: Polymerization Rate and Cytocompatibility. *Biomaterials* **2009**, *30* (35), 6702–6707. https://doi.org/10.1016/j.biomaterials.2009.08.055.

(311) Ekerdt, B. L.; Fuentes, C. M.; Lei, Y.; Adil, M. M.; Ramasubramanian, A.; Segalman, R.

A.; Schaffer, D. V. Thermoreversible Hyaluronic Acid-PNIPAAm Hydrogel Systems for 3D Stem Cell Culture. *Adv. Healthc. Mater.* **2018**, *7* (12), e1800225. https://doi.org/10.1002/adhm.201800225.

(312) Reddy, S. K.; Cramer, N. B.; Bowman, C. N. Thiol-Vinyl Mechanisms. 1. Termination and Propagation Kinetics in Thiol-Ene Photopolymerizations. *Macromolecules* **2006**, *39* (10), 3673–3680. https://doi.org/10.1021/ma060008e.

(313) Reddy, S. K.; Cramer, N. B.; Bowman, C. N. Thiol-Vinyl Mechanisms. 2. Kinetic Modeling of Ternary Thiol-Vinyl Photopolymerizations. *Macromolecules* **2006**, *39* (10), 3681–3687. https://doi.org/10.1021/ma0600097.

(314) Johnson, P. M.; Stansbury, J. W.; Bowman, C. N. High-Throughput Kinetic Analysis of Acrylate and Thiol-Ene Photopolymerization Using Temperature and Exposure Time Gradients. *J. Polym. Sci. Part A Polym. Chem.* **2008**, *46* (4), 1502–1509. https://doi.org/10.1002/pola.22491.

(315) Carioscia, J. A.; Lu, H.; Stanbury, J. W.; Bowman, C. N. Thiol-Ene Oligomers as Dental Restorative Materials. *Dent. Mater.* **2005**, *21* (12), 1137–1143. https://doi.org/10.1016/j.dental.2005.04.002.

(316) Lin, C. C.; Raza, A.; Shih, H. PEG Hydrogels Formed by Thiol-Ene Photo-Click Chemistry and Their Effect on the Formation and Recovery of Insulin-Secreting Cell Spheroids. *Biomaterials* **2011**, *32* (36), 9685–9695. https://doi.org/10.1016/j.biomaterials.2011.08.083.

(317) Allen, C. F. H.; Humphlett, W. J. The Thermal Reversibility of the Michael Reaction: V. the Effect of the Structure of Certain Thiol Adducts on Cleavage. *Can. J. Chem.* **1966**, *44* (19), 2315–2321. https://doi.org/10.1139/v66-347.

(318) Elbert, D. L.; Pratt, A. B.; Lutolf, M. P.; Halstenberg, S.; Hubbell, J. A. Protein Delivery from Materials Formed by Self-Selective Conjugate Addition Reactions. *J. Control. Release* **2001**, *76* (1–2), 11–25. https://doi.org/10.1016/S0168-3659(01)00398-4.

(319) Metters, A.; Hubbell, J. Network Formation and Degradation Behavior of Hydrogels Formed by Michael-Type Addition Reactions. *Biomacromolecules* **2005**, *6* (1), 290–301. https://doi.org/10.1021/bm049607o.

(320) Hiemstra, C.; van der Aa, L. J.; Zhong, Z.; Dijkstra, P. J.; Feijen, J. Rapidly in Situ-Forming Degradable Hydrogels from Dextram Triols through Michael Addition. *Biomacromolecules*

2007, *8* (5), 1548–1556. https://doi.org/10.1021/bm061191m.

(321) Lutolf, M. P.; Lauer-Fields, J. L.; Schmoekel, H. G.; Metters, A. T.; Weber, F. E.; Fields, G. B.; Hubbell, J. A. Synthetic Matrix Metalloproteinase-Sensitive Hydrogels for the Conduction of Tissue Regeneration: Engineering Cell-Invasion Characteristics. *Proc. Natl. Acad. Sci. U. S. A.* **2003**, *100* (9), 5413–5418. https://doi.org/10.1073/pnas.0737381100.

(322) Lutolf, M. P.; Hubbell, J. A. Synthetic Biomaterials as Instructive Extracellular Microenvironments for Morphogenesis in Tissue Engineering. *Nat. Biotechnol.* **2005**, *23* (1), 47–55. https://doi.org/10.1038/nbt1055.

(323) Khetan, S.; Katz, J. S.; Burdick, J. A. Sequential Crosslinking to Control Cellular Spreading in 3-Dimensional Hydrogels. *Soft Matter* **2009**, *5* (8), 1601–1606. https://doi.org/10.1039/b820385g.

(324) Rosales, A. M.; Vega, S. L.; DelRio, F. W.; Burdick, J. A.; Anseth, K. S. Hydrogels with Reversible Mechanics to Probe Dynamic Cell Microenvironments. *Angew. Chemie - Int. Ed.* **2017**, *56* (40), 12132–12136. https://doi.org/10.1002/anie.201705684.

(325) Macdougall, L. J.; Wiley, K. L.; Kloxin, A. M.; Dove, A. P. Design of Synthetic Extracellular Matrices for Probing Breast Cancer Cell Growth Using Robust Cyctocompatible Nucleophilic Thiol-Yne Addition Chemistry. *Biomaterials* **2018**, *178*, 435–447. https://doi.org/10.1016/j.biomaterials.2018.04.046.

(326) Jansen, L. E.; Negrón-Piñeiro, L. J.; Galarza, S.; Peyton, S. R. Control of Thiol-Maleimide Reaction Kinetics in PEG Hydrogel Networks. *Acta Biomater.* **2018**, *70*, 120–128. https://doi.org/10.1016/j.actbio.2018.01.043.

(327) Darling, N. J.; Hung, Y. S.; Sharma, S.; Segura, T. Controlling the Kinetics of Thiol-Maleimide Michael-Type Addition Gelation Kinetics for the Generation of Homogenous Poly(Ethylene Glycol) Hydrogels. *Biomaterials* **2016**, *101*, 199–206. https://doi.org/10.1016/j.biomaterials.2016.05.053.

(328) Phelps, E. A.; Enemchukwu, N. O.; Fiore, V. F.; Sy, J. C.; Murthy, N.; Sulchek, T. A.; Barker, T. H.; García, A. J. Maleimide Cross-Linked Bioactive PEG Hydrogel Exhibits Improved Reaction Kinetics and Cross-Linking for Cell Encapsulation and in Situ Delivery. *Adv. Mater.* **2012**, *24* (1), 64–70. https://doi.org/10.1002/adma.201103574.

(329) Chia, H. N.; Vigen, M.; Kasko, A. M. Effect of Substrate Stiffness on Pulmonary Fibroblast Activation by TGF-β. *Acta Biomater.* **2012**, *8* (7), 2602–2611.

https://doi.org/10.1016/j.actbio.2012.03.027.

(330) Cosgrove, B. D.; Mui, K. L.; Driscoll, T. P.; Caliari, S. R.; Mehta, K. D.; Assoian, R. K.; Burdick, J. A.; Mauck, R. L. N-Cadherin Adhesive Interactions Modulate Matrix Mechanosensing and Fate Commitment of Mesenchymal Stem Cells. *Nat. Mater.* **2016**, *15* (12), 1297–1306. https://doi.org/10.1038/nmat4725.

(331) Caliari, S. R.; Vega, S. L.; Kwon, M.; Soulas, E. M.; Burdick, J. A. Dimensionality and Spreading Influence MSC YAP/TAZ Signaling in Hydrogel Environments. *Biomaterials* **2016**, *103*, 314–323. https://doi.org/10.1016/j.biomaterials.2016.06.061.

(332) Rezakhani, S.; Gjorevski, N.; Lutolf, M. P. Low-Defect Thiol-Michael Addition Hydrogels as Matrigel Substitutes for Epithelial Organoid Derivation. *Adv. Funct. Mater.* **2020**, *30* (48), 1–12. https://doi.org/10.1002/adfm.202000761.

(333) Valdez, J.; Cook, C. D.; Ahrens, C. C.; Wang, A. J.; Brown, A.; Kumar, M.; Stockdale, L.; Rothenberg, D.; Renggli, K.; Gordon, E.; et al. On-Demand Dissolution of Modular, Synthetic Extracellular Matrix Reveals Local Epithelial-Stromal Communication Networks. *Biomaterials* **2017**, *130*, 90–103. https://doi.org/10.1016/j.biomaterials.2017.03.030.

(334) McKinnon, D. D.; Kloxin, A. M.; Anseth, K. S. Synthetic Hydrogel Platform for Three-Dimensional Culture of Embryonic Stem Cell-Derived Motor Neurons. *Biomater. Sci.* **2013**, *1* (5), 460–469. https://doi.org/10.1039/c3bm00166k.

(335) Raza, A.; Ki, C. S.; Lin, C. C. The Influence of Matrix Properties on Growth and Morphogenesis Ofhuman Pancreatic Ductal Epithelial Cells in 3D. *Biomaterials* **2013**, *34* (21), 5117–5127. https://doi.org/10.1016/j.biomaterials.2013.03.086.

(336) Cambria, E.; Renggli, K.; Ahrens, C. C.; Cook, C. D.; Kroll, C.; Krueger, A. T.; Imperiali, B.; Griffith, L. G. Covalent Modification of Synthetic Hydrogels with Bioactive Proteins via Sortase-Mediated Ligation. *Biomacromolecules* **2015**, *16* (8), 2316–2326. https://doi.org/10.1021/acs.biomac.5b00549.

(337) Arkenberg, M. R.; Moore, D. M.; Lin, C. C. Dynamic Control of Hydrogel Crosslinking via Sortase-Mediated Reversible Transpeptidation. *Acta Biomater.* **2019**, *83* (xxxx), 83–95. https://doi.org/10.1016/j.actbio.2018.11.011.

(338) Lin, T. Y.; Ki, C. S.; Lin, C. C. Manipulating Hepatocellular Carcinoma Cell Fate in Orthogonally Cross-Linked Hydrogels. *Biomaterials* **2014**, *35* (25), 6898–6906.

https://doi.org/10.1016/j.biomaterials.2014.04.118.

(339) Mũnoz, Z.; Shih, H.; Lin, C. C. Gelatin Hydrogels Formed by Orthogonal Thiol-Norbornene Photochemistry for Cell Encapsulation. *Biomater. Sci.* **2014**, *2* (8), 1063–1072. https://doi.org/10.1039/c4bm00070f.

(340) Greene, T.; Lin, C. C. Modular Cross-Linking of Gelatin-Based Thiol-Norbornene Hydrogels for in Vitro 3D Culture of Hepatocellular Carcinoma Cells. *ACS Biomater. Sci. Eng.* **2015**, *1* (12), 1314–1323. https://doi.org/10.1021/acsbiomaterials.5b00436.

(341) Lin, T. Y.; Bragg, J. C.; Lin, C. C. Designing Visible Light-Cured Thiol-Acrylate Hydrogels for Studying the HIPPO Pathway Activation in Hepatocellular Carcinoma Cells. *Macromol. Biosci.* **2016**, *16* (4), 496–507. https://doi.org/10.1002/mabi.201500361.

(342) Hao, Y.; Lin, C. C. Degradable Thiol-Acrylate Hydrogels as Tunable Matrices for Three-Dimensional Hepatic Culture. *J. Biomed. Mater. Res. - Part A* **2014**, *102* (11), 3813–3827. https://doi.org/10.1002/jbm.a.35044.

(343) Hao, Y.; Shih, H.; Muňoz, Z.; Kemp, A.; Lin, C. C. Visible Light Cured Thiol-Vinyl Hydrogels with Tunable Degradation for 3D Cell Culture. *Acta Biomater.* **2014**, *10* (1), 104–114. https://doi.org/10.1016/j.actbio.2013.08.044.

(344) Guvendiren, M.; Burdick, J. A. Stiffening Hydrogels to Probe Short- and Long-Term Cellular Responses to Dynamic Mechanics. *Nat. Commun.* **2012**, *3*, 792–799. https://doi.org/10.1038/ncomms1792.

(345) Caliari, S. R.; Perepelyuk, M.; Soulas, E. M.; Lee, G. Y.; Wells, R. G.; Burdick, J. A. Gradually Softening Hydrogels for Modeling Hepatic Stellate Cell Behavior during Fibrosis Regression. *Integr. Biol.* **2016**, *8* (6), 720–728. https://doi.org/10.1039/c6ib00027d.

(346) Mosiewicz, K. A.; Kolb, L.; Van Der Vlies, A. J.; Martino, M. M.; Lienemann, P. S.; Hubbell, J. A.; Ehrbar, M.; Lutolf, M. P. In Situ Cell Manipulation through Enzymatic Hydrogel Photopatterning. *Nat. Mater.* **2013**, *12* (11), 1072–1078. https://doi.org/10.1038/nmat3766.

(347) Mcleod, C. M.; Mauck, R. L. High Fidelity Visualization of Cell-to-Cell Variation and Temporal Dynamics in Nascent Extracellular Matrix Formation. *Sci. Rep.* **2016**, *6* (August), 1–12. https://doi.org/10.1038/srep38852.

(348) Loebel, C.; Mauck, R. L.; Burdick, J. A. Local Nascent Protein Deposition and Remodelling Guide Mesenchymal Stromal Cell Mechanosensing and Fate in Three-Dimensional

Hydrogels. *Nat. Mater.* **2019**, *18* (8), 883–891. https://doi.org/10.1038/s41563-019-0307-6.

(349) Zhao, J.; Ullah, I.; Gao, B.; Guo, J.; Ren, X. K.; Xia, S.; Zhang, W.; Feng, Y. Agmatine-Grafted Bioreducible Poly(l-Lysine) for Gene Delivery with Low Cytotoxicity and High Efficiency. *J. Mater. Chem. B* **2020**, *8* (12), 2418–2430. https://doi.org/10.1039/c9tb02641j.

(350) Dieterich, D. C.; Lee, J. J.; Link, A. J.; Graumann, J.; Tirrell, D. A.; Schuman, E. M. Labeling, Detection and Identification of Newly Synthesized Proteomes with Bioorthogonal Non-Canonical Amino-Acid Tagging. *Nat. Protoc.* **2007**, *2* (3), 532–540. https://doi.org/10.1038/nprot.2007.52.

(351) Mabry, K. M.; Lawrence, R. L.; Anseth, K. S. Dynamic Stiffening of Poly(Ethylene Glycol)-Based Hydrogels to Direct Valvular Interstitial Cell Phenotype in a Three-Dimensional Environment. *Biomaterials* **2015**, *49*, 47–56. https://doi.org/10.1016/j.biomaterials.2015.01.047.

(352) Khang, A.; Gonzalez Rodriguez, A.; Schroeder, M. E.; Sansom, J.; Lejeune, E.; Anseth, K. S.; Sacks, M. S. Quantifying Heart Valve Interstitial Cell Contractile State Using Highly Tunable Poly(Ethylene Glycol) Hydrogels. *Acta Biomater.* **2019**, *96*, 354–367. https://doi.org/10.1016/j.actbio.2019.07.010.

(353) Shih, H.; Greene, T.; Korc, M.; Lin, C. C. Modular and Adaptable Tumor Niche Prepared from Visible Light Initiated Thiol-Norbornene Photopolymerization. *Biomacromolecules* **2016**, *17* (12), 3872–3882. https://doi.org/10.1021/acs.biomac.6b00931.

(354) Liu, H. Y.; Greene, T.; Lin, T. Y.; Dawes, C. S.; Korc, M.; Lin, C. C. Enzyme-Mediated Stiffening Hydrogels for Probing Activation of Pancreatic Stellate Cells. *Acta Biomater.* **2017**, *48*, 258–269. https://doi.org/10.1016/j.actbio.2016.10.027.

(355) Liu, H. Y.; Korc, M.; Lin, C. C. Biomimetic and Enzyme-Responsive Dynamic Hydrogels for Studying Cell-Matrix Interactions in Pancreatic Ductal Adenocarcinoma. *Biomaterials* **2018**, *160*, 24–36. https://doi.org/10.1016/j.biomaterials.2018.01.012.

(356) Wade, R. J.; Bassin, E. J.; Gramlich, W. M.; Burdick, J. A. Nanofibrous Hydrogels with Spatially Patterned Biochemical Signals to Control Cell Behavior. *Adv. Mater.* **2015**, *27* (8), 1356–1362. https://doi.org/10.1002/adma.201404993.

(357) Gramlich, W. M.; Kim, I. L.; Burdick, J. A. Synthesis and Orthogonal Photopatterning of Hyaluronic Acid Hydrogels with Thiol-Norbornene Chemistry. *Biomaterials* **2013**, *34* (38), 9803–9811. https://doi.org/10.1016/j.biomaterials.2013.08.089.

(358) Khetan, S.; Burdick, J. A. Patterning Network Structure to Spatially Control Cellular Remodeling and Stem Cell Fate within 3-Dimensional Hydrogels. *Biomaterials* **2010**, *31* (32), 8228–8234. https://doi.org/10.1016/j.biomaterials.2010.07.035.

(359) Daniele, M. A.; Adams, A. A.; Naciri, J.; North, S. H.; Ligler, F. S. Interpenetrating Networks Based on Gelatin Methacrylamide and PEG Formed Using Concurrent Thiol Click Chemistries for Hydrogel Tissue Engineering Scaffolds. *Biomaterials* **2014**, *35* (6), 1845–1856. https://doi.org/10.1016/j.biomaterials.2013.11.009.

(360) Brown, T. E.; Carberry, B. J.; Worrell, B. T.; Dudaryeva, O. Y.; McBride, M. K.; Bowman, C. N.; Anseth, K. S. Photopolymerized Dynamic Hydrogels with Tunable Viscoelastic Properties through Thioester Exchange. *Biomaterials* **2018**, *178*, 496–503. https://doi.org/10.1016/j.biomaterials.2018.03.060.

(361) Yeh, Y. C.; Corbin, E. A.; Caliari, S. R.; Ouyang, L.; Vega, S. L.; Truitt, R.; Han, L.; Margulies, K. B.; Burdick, J. A. Mechanically Dynamic PDMS Substrates to Investigate Changing Cell Environments. *Biomaterials* **2017**, *145*, 23–32. https://doi.org/10.1016/j.biomaterials.2017.08.033.

(362) Lee, D.; Park, J. P.; Koh, M. Y.; Kim, P.; Lee, J.; Shin, M.; Lee, H. Chitosan-Catechol: A Writable Bioink under Serum Culture Media. *Biomater. Sci.* **2018**, *6* (5), 1040–1047. https://doi.org/10.1039/c8bm00174j.

(363) Reynolds, D. S.; Bougher, K. M.; Letendre, J. H.; Fitzgerald, S. F.; Gisladottir, U. O.; Grinstaff, M. W.; Zaman, M. H. Mechanical Confinement via a PEG/Collagen Interpenetrating Network Inhibits Behavior Characteristic of Malignant Cells in the Triple Negative Breast Cancer Cell Line MDA.MB.231. *Acta Biomater.* **2018**, *77*, 85–95. https://doi.org/10.1016/j.actbio.2018.07.032.

(364) Xin, S.; Gregory, C. A.; Alge, D. L. Interplay between Degradability and Integrin Signaling on Mesenchymal Stem Cell Function within Poly(Ethylene Glycol) Based Microporous Annealed Particle Hydrogels. *Acta Biomater.* **2020**, *101*, 227–236. https://doi.org/10.1016/j.actbio.2019.11.009.

(365) Darling, N. J.; Xi, W.; Sideris, E.; Anderson, A. R.; Pong, C.; Carmichael, S. T.; Segura, T. Click by Click Microporous Annealed Particle (MAP) Scaffolds. *Adv. Healthc. Mater.* **2020**, *9* (10), 1–10. https://doi.org/10.1002/adhm.201901391.

(366) Lowe, A. B. Thiol-Ene "Click" Reactions and Recent Applications in Polymer and

Materials Synthesis. *Polym. Chem.* **2010**, *1* (1), 17–36. https://doi.org/10.1039/b9py00216b.

(367) Kharkar, P. M.; Rehmann, M. S.; Skeens, K. M.; Maverakis, E.; Kloxin, A. M. Thiol-Ene Click Hydrogels for Therapeutic Delivery. *ACS Biomater. Sci. Eng.* **2016**, *2* (2), 165–179. https://doi.org/10.1021/acsbiomaterials.5b00420.

(368) Lowe, A. B.; Harvison, M. A. Thiol-Based Click Chemistries in Polymer: Synthesis and Modification. *Aust. J. Chem.* **2010**, *63* (8), 1251–1266. https://doi.org/10.1071/CH10214.

(369) Song, N.; Ding, M.; Pan, Z.; Li, J.; Zhou, L.; Tan, H.; Fu, Q. Construction of Targeting-Clickable and Tumor-Cleavable Polyurethane Nanomicelles for Multifunctional Intracellular Drug Delivery. *Biomacromolecules* **2013**, *14* (12), 4407–4419. https://doi.org/10.1021/bm401342t.

(370) Parrish, B.; Breitenkamp, R. B.; Emrick, T. PEG- and Peptide-Grafted Aliphatic Polyesters by Click Chemistry. *J. Am. Chem. Soc.* **2005**, *127* (20), 7404–7410. https://doi.org/10.1021/ja050310n.

(371) Chen, Y.; Guan, Z. Bioinspired Modular Synthesis of Elastin-Mimic Polymers to Probe the Mechanism of Elastin Elasticity. *J. Am. Chem. Soc.* **2010**, *132* (13), 4577–4579. https://doi.org/10.1021/ja9104446.

(372) Presolski, S. I.; Hong, V. P.; Finn, M. G. Copper-Catalyzed Azide–Alkyne Click Chemistry for Bioconjugation. *Curr. Protoc. Chem. Biol.* **2011**, *3* (4), 153–162. https://doi.org/10.1002/9780470559277.ch110148.

(373) Li, L.; Zhang, Z. Development and Applications of the Copper-Catalyzed Azide-Alkyne Cycloaddition (CuAAC) as a Bioorthogonal Reaction. *Molecules* **2016**, *21* (10), 1–22. https://doi.org/10.3390/molecules21101393.

(374) Highley, C. B.; Rodell, C. B.; Burdick, J. A. Direct 3D Printing of Shear-Thinning Hydrogels into Self-Healing Hydrogels. *Adv. Mater.* **2015**, *27* (34), 5075–5079. https://doi.org/10.1002/adma.201501234.

(375) Ding, Y.; Xu, X.; Sharma, S.; Floren, M.; Stenmark, K.; Bryant, S. J.; Neu, C. P.; Tan, W. Biomimetic Soft Fibrous Hydrogels for Contractile and Pharmacologically Responsive Smooth Muscle. *Acta Biomater.* **2018**, *74*, 121–130. https://doi.org/10.1016/j.actbio.2018.05.015.

(376) Grubb, M. L.; Caliari, S. R. Fabrication Approaches for High-Throughput and Biomimetic

Disease Modeling. *Acta Biomater.* **2021**, *132*, 52–82. https://doi.org/10.1016/j.actbio.2021.03.006.

CHAPTER 3: MICROMECHANICAL CHARACTERIZATION OF VISCOELASTIC CUES IN EX VIVO RAT LUNG TISSUES TO DIRECT BIOMATERIAL DESIGN

3.1 Abstract

The mechanical properties of biological tissues play important roles in physiological and pathological processes. In particular, the spatial variability of time-dependent viscoelasticity has been recognized as a critical regulator of such processes. However, common characterization approaches such as rheology are limited by their ability to probe local time-dependent properties and identify mechanical heterogeneity of a substrate. Nanoindentation offers microscale mechanical characterization in a spatially-dependent manner. In this work, we characterized the viscoelastic properties of normal rat lung tissue using nanoindentation. The Young's modulus, or stiffness, of the lung lobes averaged around 1.5 kPa. Viscoelasticity was quantified via frequency sweeps and force relaxation tests performed using the dynamic mechanical analysis (DMA)-like capabilities of the nanoindenter. Frequency-dependent behaviors were observed and loss tangent values revealed a greater increase in loss modulus as frequency increased compared to storage modulus. Relaxation profiles showed rapid decreases in force within the first 10 seconds and 20-50% relaxation occurred for all lung lobes. Heterogeneity was evident among all lung lobes with Young's modulus values ranging from 0.1-8 kPa. Soft viscoelastic hydrogels mimicking the mechanics of normal lung tissue were fabricated and demonstrated frequency-dependent behavior. Overall, the results here provide valuable parameters toward understanding time-dependent mechanical properties of tissues and can be further applied in tissue engineering applications such as modeling healthy and diseased tissues.

3.2 Introduction

The unique mechanical and chemical composition of various biological tissues not only dictates structure but also influences cellular processes essential to development, wound healing, and homeostasis[1–5]. Importantly, cells sense and respond to these intrinsic cues through several means, including force-mediated matrix rearrangements, accumulation and breakdown of extracellular matrix (ECM) proteins, and recruitment of cells, which all ultimately impact tissue properties[6–8]. In general, it is well understood that the majority of soft tissues display viscoelastic behaviors, characterized by their ability undergo stress relaxation over time and dissipate energy after deformation[9–12]. However, during fibrosis progression, increasing deposition of ECM components such as collagen type I results in a decrease in viscoelasticity and an increase in overall elasticity and stiffness mediated by LOX-mediated crosslinking[12–15]. While the majority of mechanical measurements of soft tissues have focused on bulk stiffness properties, time-dependent mechanics such as viscoelasticity, which plays an important role during normal physiological functioning and tissue remodeling, have been severely understated and understudied.

Shear rheology is a common method to measure material properties at the macroscale and has shown previous success in characterizing viscoelastic properties of soft tissues[16–20] and *in vitro* hydrogel models. By applying a constant strain, the resulting stress can be measured over time to determine the timescale and extent of relaxation for a given material. An elastic substrate will exhibit minimal to no stress relaxation compared to viscoelastic materials such as soft tissues, which will display relaxation on the order of seconds to minutes[9,11]. Alternately, frequency sweeps can be performed on a material to show frequency-dependent behavior of tissues; viscoelastic

substrates have shown increasing loss modulus as frequency increases due to dynamic viscous associations[21,22]. However, a limitation of rheological characterization is that only bulk time-dependent properties can be measured and cannot be decoupled from spatial variations in mechanics. Tissue structure and organization are inherently heterogeneous in physiological and pathological conditions at both the macro- and micro-scales, and changes in tissue properties occur over multiple length- and time-scales[10,23–25]. Nanoindentation has recently emerged as a powerful tool to spatially characterize local, rather than bulk, mechanical properties[10,12,26–29]. This technique enables spatial mapping of heterogeneous substrates at the micro- and nano-scale with control over several parameters, including the force of the probe applied onto the substrate. While nanoindentation has become recognized as a method to quantify substrate stiffness, studies reporting time-dependent properties such as viscoelasticity have been limited.

This work begins to address the current disparity in complementary mechanical measurement techniques that can directly compare native tissue viscoelastic properties to engineered hydrogel systems and facilitate translatable, biomimetic biomaterial design. Here, we illustrate the application of measuring microscale viscoelastic properties using nanoindentation of *ex vivo* lung tissue. Force relaxation, stiffness (Young's modulus, E), and frequency-dependent storage (E') and loss (E") modulus were measured to quantify tissue viscoelasticity. Strong viscoelastic properties were observed from all lung lobes, including force relaxation of 30-60% and frequency-dependent mechanical responses. Heterogeneous mechanics were also seen among all samples, where the Young's modulus varied from 0.1-8 kPa. Finally, soft viscoelastic hydrogels with stiffness and viscoelasticity matching normal rat lung tissue were successfully fabricated. Overall, the work here demonstrates a robust method to characterize tissue properties such as stiffness,

viscoelasticity, and spatial heterogeneity on a microscale level and can be directly associated to conventional characterization techniques to inform the design of biomaterials for potential therapeutic evaluations.

3.3 Materials and Methods

3.3.1 Tissue sample preparation

Fresh tissue samples were harvested from 24-week old male Lewis rats and 26-week old female Lewis rats (retired breeders) shortly after each anesthetized animal was euthanized via carbon dioxide asphyxiation, with secondary confirmation of death by cervical dislocation. The five lobes of the lung (four right lung lobes and one left lung lobe) were separated; the left lung lobe was subsequently cut into 3-5 sections for mechanical testing. The tissue samples were stored in 50 mL Falcon tubes filled with phosphate-buffered saline (PBS) after harvest and kept at 4°C until testing. Tissue sections were lightly patted with a Kimwipe to remove excess PBS, glued to Petri dishes to prevent sliding (clear silicone waterproof sealant, Loctite), and submerged in PBS for testing. All measurements were performed within 72 hours of tissue harvest.

3.3.2 Polymer and peptide synthesis

Norbornene-modified hyaluronic acid (NorHA)[30], β-cyclodextrin modified HA (CD-HA)[31], and thiolated adamantane (Ad) peptide[21] were synthesized for hydrogel synthesis as previously described. For NorHA, a hyaluronic acid tert-butyl ammonium salt intermediate (HA-TBA) was synthesized by reacting sodium hyaluronate (Lifecore, 62 kDa) with Dowex 50W proton-exchange resin, neutralized to pH 7.05, filtered, frozen, and lyophilized. HA-TBA was then reacted with 5-norbornene-2-methylamine and benzotriazole-1-yloxytris-(dimethylamino)phosphonium

hexafluorophosphate (BOP) in anhydrous dimethylsulfoxide (DMSO) for 2 hours at 25°C, quenched with cold water, dialyzed (molecular weight cutoff: 6-8 kDa) for 5 days, filtered, dialyzed for another 5 days, frozen, and lyophilized. Using proton nuclear magnetic resonance (^{1}H NMR, 500 MHz Varian Inova 500), the degree of modification was determined to be 31% (**Figure S3.1**). CD-HA was synthesized by reacting HA-TBA with 6-(6-amino-hexyl)amino-6-deoxy-β-cyclodextrin (β-CD-HDA) and BOP in anhydrous DMSO for 3 hours at 25°C, quenched with cold water, dialyzed for 5 days, filtered, dialyzed for 5 more days, frozen, and lyophilized. Using ^{1}H NMR, the degree of modification was determined to be 28% (**Figure S3.2**). Thiolated Ad peptide (Ad-KKKCG) was synthesized on Rink Amide MBHA high-loaded resin (0.78 mmol/g) using a Gyros Protein Technologies Tribute peptide synthesizer via Fmoc-protected methods as previously described. The peptide was cleaved in 95% trifluoroacetic acid, 2.5% triisopropylsilane, and 2.5% water for 2-3 hours, precipitated in cold ethyl ether, dried, resuspended in water, frozen, and lyophilized. Synthesis was confirmed through matrix-assisted laser desorption/ionization (MALDI) mass spectrometry (**Figure S3.3**).

3.3.3 Hydrogel fabrication

Hydrogel thin films (50 μL precursor solution, 18 x 18 mm, ~ 100 μm thickness) were fabricated on thiolated coverslips using ultraviolet (UV) light-mediated thiol-ene addition as previously described[21,32]. Soft viscoelastic hydrogels (2 wt% NorHA-CDHA) were produced via a combination of covalent crosslinking (NorHA and dithiothreitol, thiol-norbornene ratio of 0.35) and supramolecular interactions (CD-HA and Ad peptide, 1:1 molar ratio of CD to Ad). Hydrogels were photopolymerized (365 nm, 5 mW/cm^2) in the presence of 1 mM lithium acylphosphinate

(LAP) photoinitiator for 2 minutes and swelled in PBS overnight at 37°C prior to mechanical characterization.

3.3.4 Nanoindentation measurements

Nanoindentation measurements were performed using an Optics11 Piuma nanoindenter. A spherical borosilicate glass probe (radius between 47-51.5 μm, probe stiffness between 0.45-0.49 N/m) was used for indentation tests. Each indentation was made at a constant depth (δ = 4 μm) using a constant ramp time (t_r = 2 s). The indentation depth was determined based on the probe used and did not exceed 16% of the tip radius in order to meet Hertzian contact model criteria (assuming a Poisson's ratio of 0.5)[10,33]. The load relaxation response of the substrates was made by bringing the probe to a fixed depth and holding the probe for 30 s. Viscoelastic properties (E' and E") were also quantified via frequency sweeps (δ = 4 μm, 0.1-10 Hz) using the dynamic mechanical analysis (DMA) mode, which allows mechanical oscillations during indentation. Matrix scans were performed with 200 μm between each measurement and the surface was re-located prior to each indentation to account for any heterogeneity in substrate topography.

3.3.5 Data analysis

Force vs. indentation depth curves were generated from each indentation, and the loading curve was used to determine the effective Young's modulus, E_{eff}, by fitting the Hertzian contact mechanics model:

$$E_{eff} = \frac{3F}{4d^{3/2}\sqrt{R_i}}$$

where F is the applied force, d is the indentation depth, and R_i is the radius of the spherical tip of the probe. E_{eff} was then used to calculate Young's modulus, E, by accounting for the Poisson's ratio, *v* (0.5 was used for all analyses):

$$E = E_{eff}(1 - v^2)$$

Frequency-dependent storage and loss moduli, E'(f) and E"(f), respectively, were obtained using the DMA-like capabilities of the nanoindenter enabling user-controlled indentation depth and load. E' and E" were calculated using the formulas:

$$E'(f) = \frac{1}{2}\frac{F_0}{d_0}\cos(\delta)\frac{1}{\sqrt{dR}}(1 - v^2)$$

$$E''(f) = \frac{1}{2}\frac{F_0}{d_0}\sin(\delta)\frac{1}{\sqrt{dR}}(1 - v^2)$$

where F_0 is the load amplitude, d_0 is the displacement amplitude, δ is the phase lag between the sinusoidal indentation and loading oscillations, d is the indentation depth, R is the probe radius, and *v* is the Poisson's ratio.

3.3.6 Statistical analysis

For the rat lung tissue, all mechanical characterization tests included between 3-6 whole rat lung lobes (n = 3-6). One-way ANOVA with Tukey's HSD post hoc analysis was performed for all data sets for statistical comparison between rat lung lobes. Box and whisker plots of indentation data illustrated mean, median, quartiles, and error bars corresponding to the lower value of either the minimum/maximum value or 1.5*interquartile range; outlier data points were shown as open circles. Unless otherwise stated, data presented as bar graphs or single data points show the mean ± standard deviation with data points indicating average data from a whole lung lobe. For hydrogel

experiments, at least 3 hydrogels were used per test. Significance was designated by *, **, or *** corresponding to $P < 0.05$, 0.01, or 0.001, respectively.

3.4 Results and Discussion

3.4.1 Nanoindentation set-up and tissue sample testing

Lung tissue from Lewis rats were collected and used for micromechanical quantification via nanoindentation. Whole lung tissues (**Figure 3.1A**) were rinsed in PBS and cut into sections depending on lobe – the left lobe was cut into 3-5 sections (**Figure 3.1B**) and the four right lobes, superior, middle, inferior, and post caval, were separated (**Figure 3.1C**). The tissue samples were glued to a Petri dish to prevent sample movement, submerged in PBS to maintain tissue hydration during testing, and positioned directly under the nanoindenter probe for indentations (**Figure 3.1D, E**).

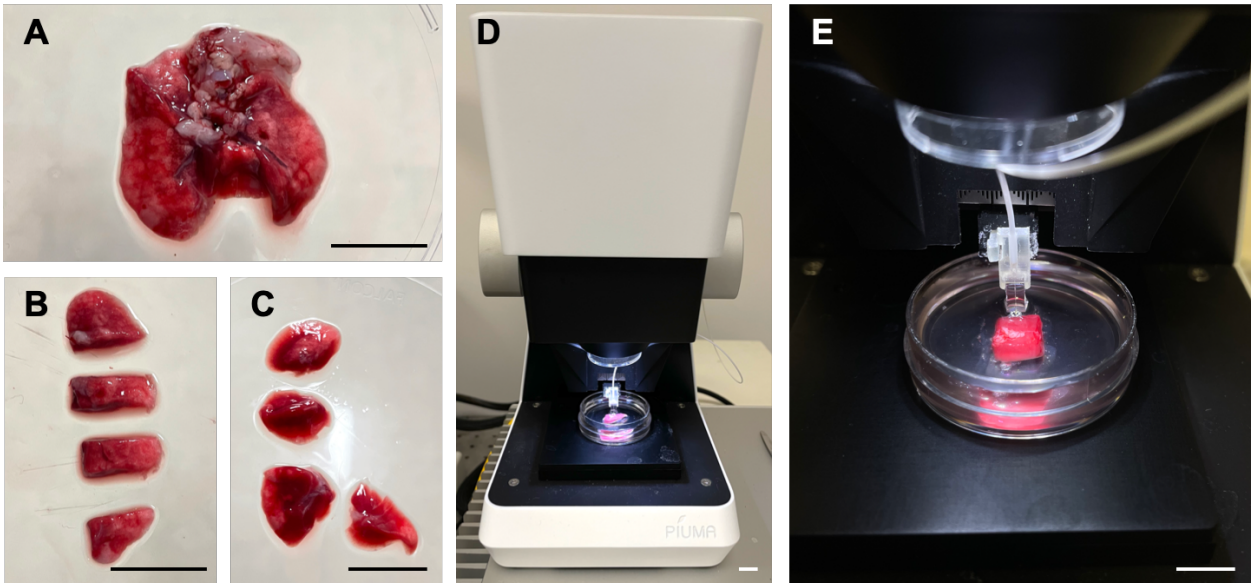

Figure 3.1. Experimental set-up of tissue mechanical characterization. (A) Image of an intact rat lung on a Petri dish. (B) Sectioned left lobe of a lung. (C) Right lung lobes. From top to bottom: Right superior lobe, right middle lobe, right inferior lobe, right post caval lobe (*bottom right*). (D) Image of the nanoindentation set-up. Lung sections were glued to a small Petri dish, submerged in PBS, and positioned under the probe for characterization. (E) Close up image of the nanoindentation set-up. Scale bars = 10 mm.

Each measurement resulted in a load-depth curve that was fit to the Hertzian contact model, and a constant indentation depth was used to ensure consistent measurements and to decouple that parameter from stiffness and viscoelasticity. Spatial mapping of tissue mechanics, including topography and stiffness, were conducted via automated matrix scans to evaluate tissue heterogeneity of normal lung tissue. To quantify viscoelastic properties, the dynamic mechanical analysis (DMA) operational mode was used. In this capacity, adjustable mechanical oscillation parameters (amplitude, period, frequency) were used to determine frequency-dependent behavior over cell-relevant frequencies. In general, the technique used here was reproducible over multiple tissue samples and measurement parameters could be directly related to common biomaterials mechanical characterization techniques such as rheology and nanoindentation to guide the design of tissue mimicking biomaterials.

3.4.2 Stiffness and viscoelasticity of normal lung tissue were characterized via nanoindentation

Young's modulus (E), a measure of stiffness, of normal lung tissue was determined by fitting the loading portion of the indentation curve to the Hertzian contact model and assuming a Poisson's ratio of 0.5 (**Figure 3.2A**). The loading curves for the majority of the lung lobes showed similar profiles, which yielded comparable Young's moduli. In contrast, the right inferior lobe displayed increased loading behavior at the same indentation depth and greater Young's modulus values (average E for the left, right superior, right middle, and right post caval lobes ~ 1.2 kPa vs. average E for the right inferior lobe ~ 2 kPa). Regardless, the Young's modulus values for all the lung lobes still align with previously reported values for normal lung tissue[34,35].

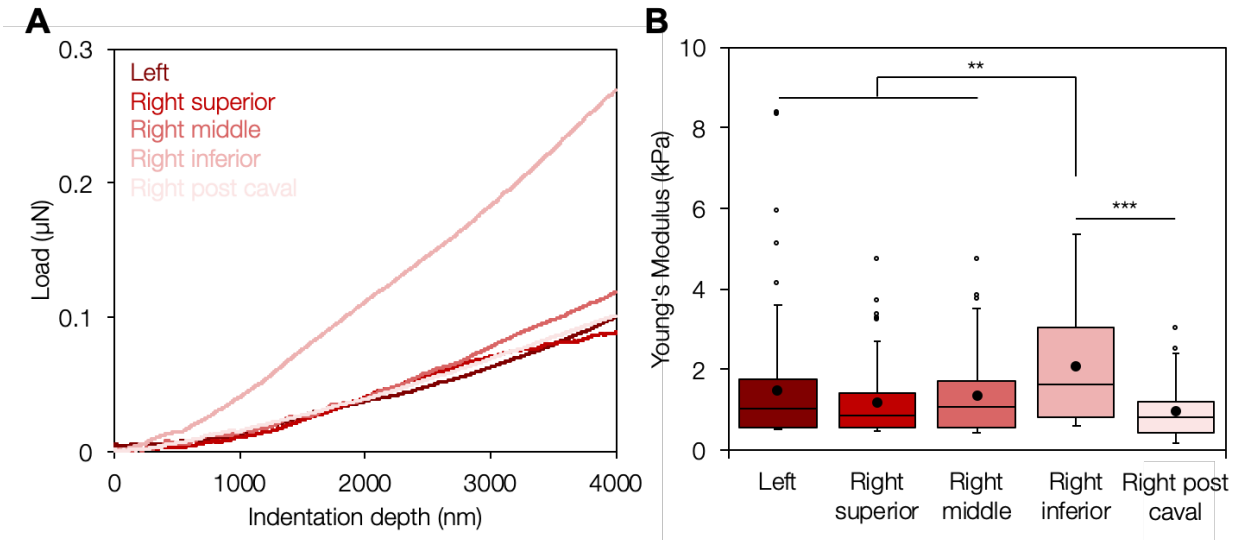

Figure 3.2. Loading behavior of tissue lobes during indentation and corresponding tissue stiffness. (A) The loading curves of load vs. indentation depth profiles of representative tissue lobes were used to determine Young's modulus (E) using the Hertzian contact model (assuming a Poisson's ratio of 0.5). (B) Box and whisker plots of tissue lobe stiffness demonstrate a slight increase in Young's modulus for the right inferior lobe, but similar Young's moduli for the remainder of the lung lobes. Box plots show the mean (black filled circle), median (line), first and third quartiles, error bars denoting either the minimum/maximum value or 1.5*interquartile range (whichever is lower), and outliers (black outlined open circles). At least 50 data points were used for each group. 3-6 whole lung lobes were tested for each group (50-340 data points total). **: $P < 0.01$, ***: $P < 0.001$.

We next measured tissue viscoelasticity using the DMA-like operational capabilities of the nanoindenter. Cyclic oscillations at a set displacement and load enabled frequency-dependent storage (E') and loss (E") moduli to be calculated. Storage and loss moduli were similar for the left, right superior, right middle, and right post caval lobes (E' ~ 1.5-2.5 kPa, E" ~ 0.5-0.7 kPa) at a frequency of 1 Hz (**Figure 3.3A, B**). In comparison, the right inferior lobes showed significantly higher storage and loss moduli (E' ~ 3.5 kPa, E" ~ 0.9 kPa) as well as increased variance in stiffness, which could be attributed to an increase in mechanical heterogeneity. Notably, the E" values for all groups were all around 25% of the E' values owing to their viscoelastic properties.

Similar trends were seen at frequencies of 0.1 Hz (**Figure S3.4A, B**) and 0.5 Hz (**Figure S3.4C, D**).

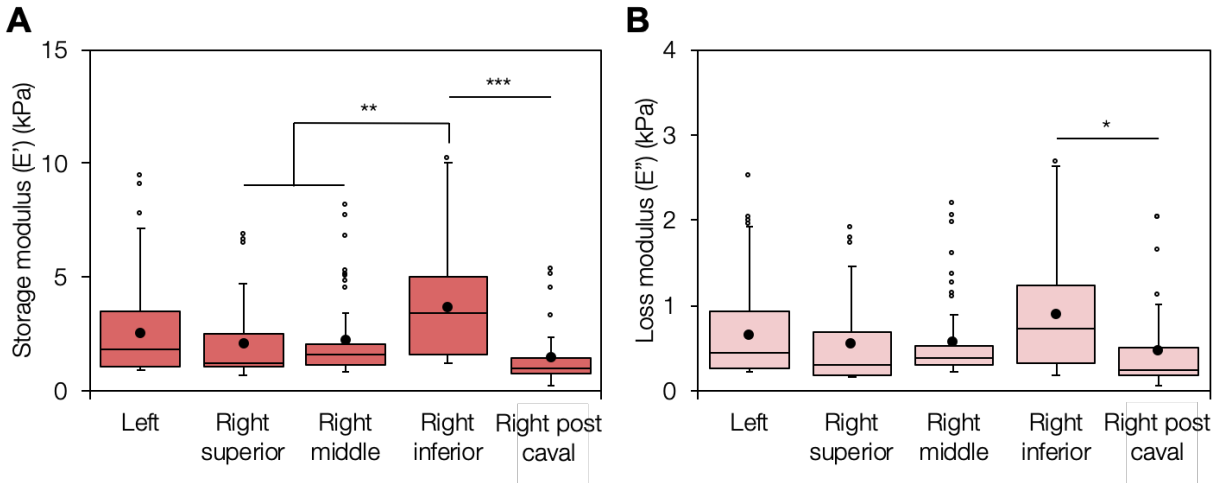

Figure 3.3. Mechanical characterization of normal rat lung tissue. (A) Box and whisker plots of storage modulus (E') measured at a frequency of 1 Hz. (B) Box plots of loss modulus (E") measured at a frequency of 1 Hz. 3-6 whole lung lobes were tested for each group (30-190 data points total). *: $P < 0.05$, **: $P < 0.01$, ***: $P < 0.001$.

3.4.3 Lung tissue samples demonstrated frequency-dependent behavior

Frequency sweeps were performed to investigate the time-dependent mechanical responses of normal lung tissue. All lung lobes showed pronounced frequency-dependent behavior over a range of physiologically-relevant frequencies (0.1-10 Hz). As frequency increased, both E' and E" increased (**Figure 3.4A**). Interestingly, at higher frequencies (shorter time scales), E" increased at a greater extent compared to E', which is also corroborated by the increasing loss tangent values from around 0.2 to 0.3-0.5 (**Figure 3.4B**). The dynamic mechanical responses observed within this time scale represent how tissue properties can rapidly change based on cell behaviors such as traction force exertion and morphological changes, responding to force oscillations, and motility[9,36–38]. Similar frequency-dependent behavior was also observed for other tissues[17,19,29,39].

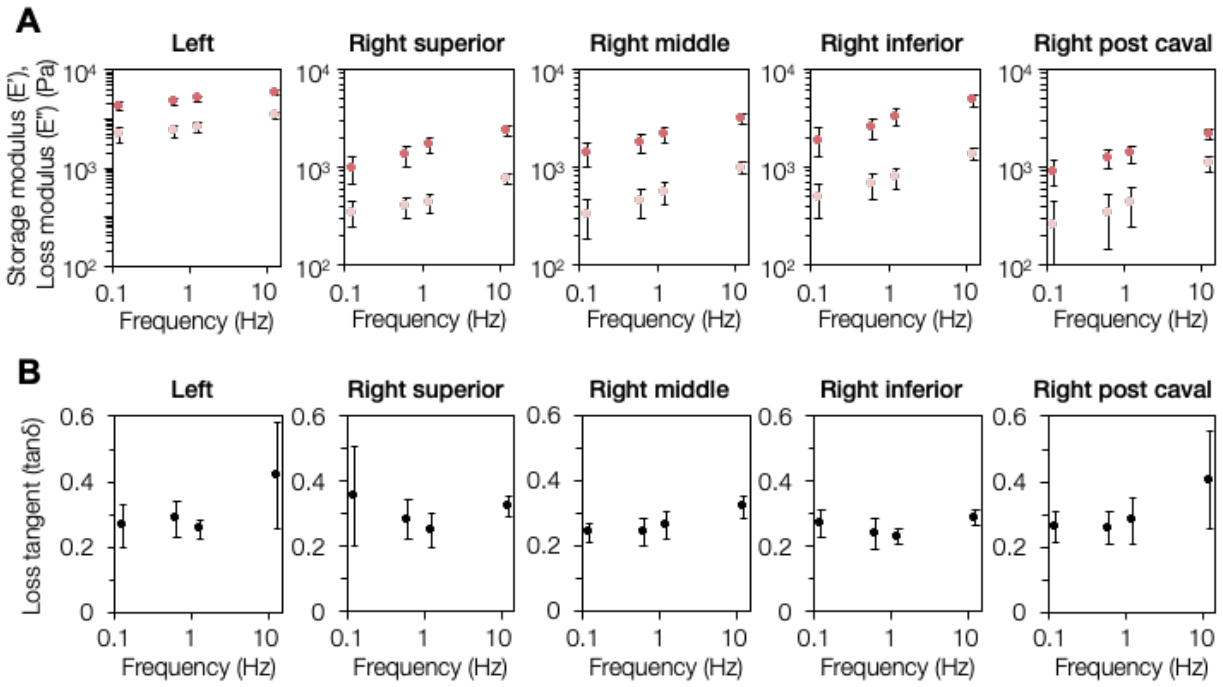

Figure 3.4. Frequency-dependent behavior of normal lung tissue. (A) Frequency sweeps from 0.1-10 Hz demonstrated increasing storage (E', filled circles) and loss (E", open circles) moduli as frequency increased. (B) Loss tangent (tanδ), or E"/E', is indicative of the viscoelastic behavior of the tissue. For all lung lobes, tanδ at low frequencies was at least 0.25 and increased at increasing frequencies. 3-6 whole lung lobes were tested for each group (30-190 data points total).

3.4.4 Stress relaxation was observed for all lung tissue samples regardless of region

Tissue samples were subjected to force relaxation tests in which the probe was indented in the tissue sample at a prescribed depth (δ = 4 μm for all measurements) and held for 30 seconds. To compare relaxation profiles and degree of relaxation, the time-dependent Young's modulus values were normalized to the instantaneous modulus, or the maximum value. All lung lobes demonstrated rapid stress relaxation with the majority of the response occurring within the first 10 seconds (**Figure 3.5A**). The average extent of relaxation was between 20-50% of the initial force for all lung lobes, which is in agreement with previously observed trends[35,40–42]. Comparable relaxation profiles for other soft tissues such as liver, kidney, heart, breast, and adipose have also been reported[10,18,43–45]. These results provide a quantitative measure of tissue viscoelasticity and

provides insight toward understanding cell-matrix interactions and how tissues store and dissipate cell-generated forces during homeostasis, wound healing, and disease processes.

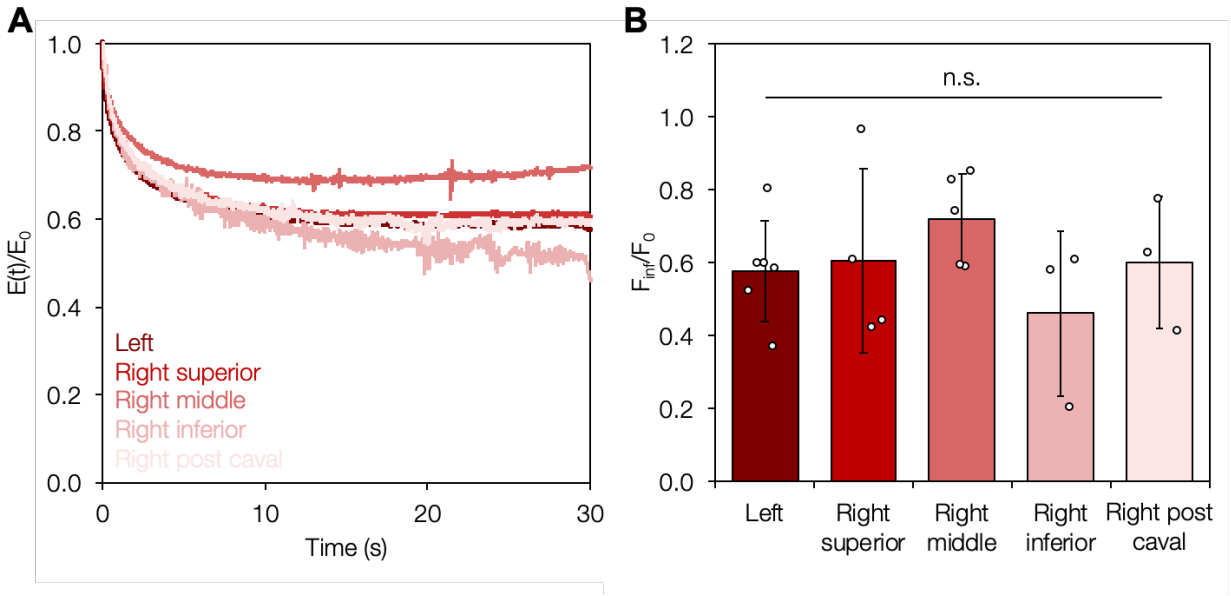

Figure 3.5. Force relaxation showed characteristic viscoelasticity of normal lung tissue. (A) Force relaxation tests of the left and right lobes, measured by the time-dependent Young's modulus E(t) normalized to the initial instantaneous modulus E_0, showed between 30-50% average relaxation in original mechanics. (B) Quantification of the ratio of the equilibrium force (F_{inf}) to the initial force (F_0). Each scatter point represents averaged measurements from a tissue section. 3-6 whole lung lobes were tested for each group (9-36 data points total).

3.4.5 Nanoindentation enables spatial mapping of stiffness and viscoelastic tissue properties

Due to its small probe size, nanoindentation can also be used to characterize local mechanical properties of heterogeneous substrates. Mechanical properties were mapped across lung tissue sample surfaces to investigate spatial heterogeneity of lung lobes. Spatial heterogeneity was seen for all lung lobes and Young's modulus values ranged from 0.1-8 kPa. Lobe mechanics showed high variability depending on the region of indentation (**Figure 3.6A, B**); areas that included differences in thickness, such as the right superior lobe, correlated with increased heterogeneity compared to more uniformly thick left lobes (**Figure 3.6C, D**).

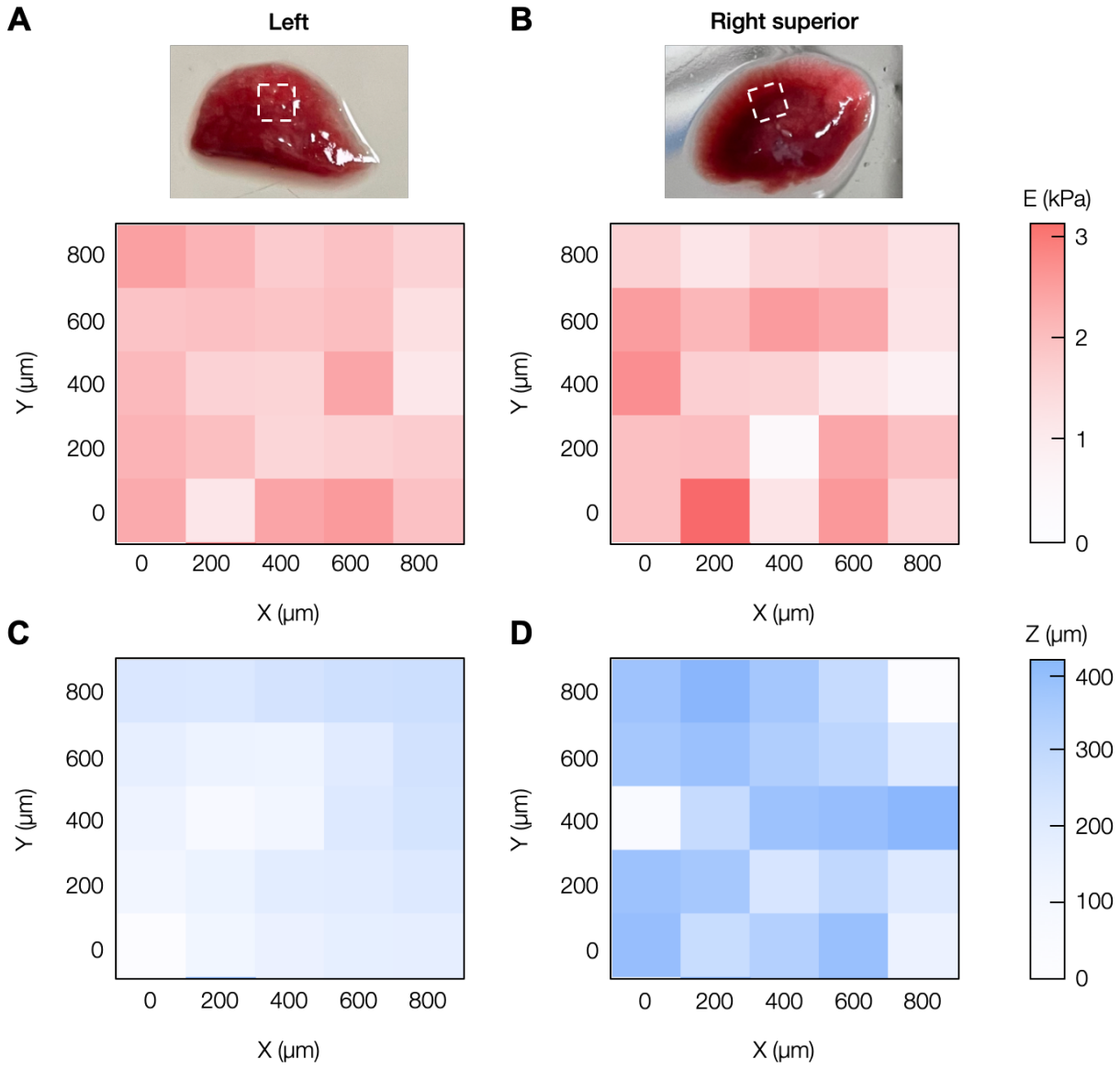

Figure 3.6. Spatial heterogeneity in stiffness of normal rat lung tissue. (A) Representative Young's modulus map of a left lung lobe section where the dotted square corresponds to the region where mechanical characterization occurred. Mechanical properties were mapped over 800 µm in the X and Y directions with a step size of 200 µm (5x5 matrix). (B) Representative Young's modulus map of a right superior lobe with increased variability in tissue thickness, resulting in increased tissue heterogeneity. The bar on the right shows the scale of Young's modulus values; for these samples, the Young's modulus ranged from 0.1-3.1 kPa. (C) Surface map of a left lung lobe section showing minimal differences in topography in the measured region. (D) Topographical heterogeneity was more evident for the right superior lobe section. Lung samples in this figure are from 26-week-old female Lewis rats.

3.4.6 Soft viscoelastic hydrogels can be fabricated with mechanics matching normal lung tissue

By mechanically characterizing rat lung tissue using nanoindentation, we were able to direct correlate viscoelastic parameters toward the design of *in vitro* hydrogel systems. Soft viscoelastic hyaluronic acid (HA) hydrogels containing a combination of covalent crosslinks and physical interactions were fabricated to match the mechanics of healthy rat lung tissue (**Figure 3.7A**). Previous work by our lab and others[21,31,32,46] has shown the ability for this HA-based system to achieve a range of stiffness and viscoelastic properties. Specifically, stiffness was tuned through HA polymer concentration and crosslinker density (ratio of dithiol crosslinker to norbornene groups. Viscous characteristics were incorporated through dynamic supramolecular guest-host interactions between thiolated adamantane (Ad) peptides and CD-HA, where the hydrophobic Ad guest molecule has a high affinity for the CD host group. Hydrogels were rapidly fabricated via UV light-mediated thiol-ene addition (365 nm, 5 mW/cm^2, 2 minute light irradiation) and mechanics were characterized using nanoindentation. As expected, the incorporation of viscous characteristics from the supramolecular interactions resulted in frequency-dependent behavior equivalent to healthy rat lung tissue and loss tangent values between 0.3-0.5 were achieved, demonstrating the ability to design tissue-relevant hydrogel models (**Figure 3.7B, C**).

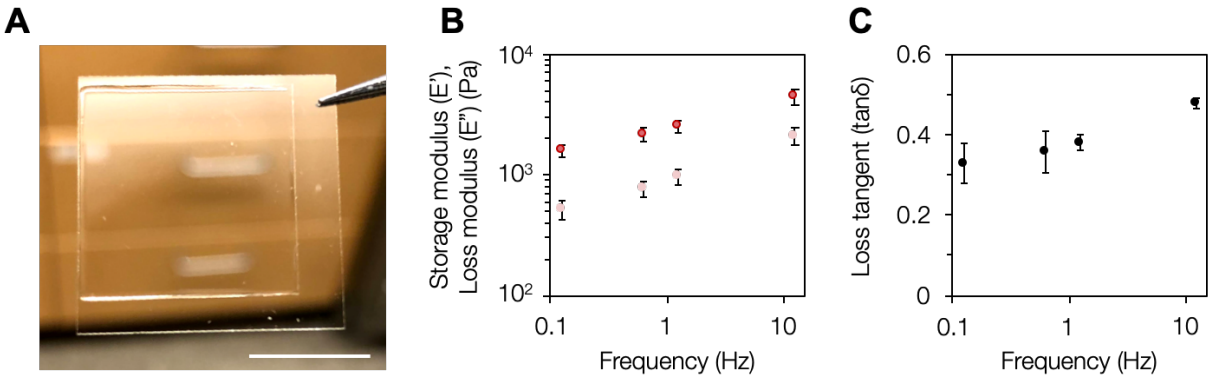

Figure 3.7. Soft viscoelastic hydrogels match mechanical properties of normal rat lung tissue. (A) Representative soft viscoelastic hydrogel thin film fabricated for nanoindentation measurements.

Scale bar = 10 mm. (B) Frequency sweep of hydrogels using the nanoindenter show equivalent frequency-dependent behavior observed in normal lung tissue. (C) Hydrogels demonstrate viscoelastic behavior in line with normal lung tissue, as measured by the loss tangent (tanδ) values. 3 hydrogels were tested (27 measurements total).

3.5 Conclusions

This work illustrates the capabilities of nanoindentation for measuring soft tissue viscoelastic responses in a reproducible manner. Stiffness, time-dependent viscoelastic behaviors, and spatial heterogeneity can be characterized using parameters that can be translated to developing *in vitro* tissue-like test systems. We showed that normal rat lung tissue is heterogeneous in stiffness and topography depending on lobe. Frequency-dependent behaviors were also observed, with loss tangent values increasing with increasing frequency. We also characterized force relaxing behaviors of lung tissue and found that for normal, healthy lung sections, around 20-50% relaxation occurs within 10-30 seconds. Finally, soft viscoelastic hydrogels replicating the mechanics of healthy lung tissue were fabricated, demonstrating the successful utility and application of tissue nanoindentation. Moving forward, we expect nanoindentation to be applied to other soft biological tissues and compared to their diseased tissue counterparts for a more accurate evaluation of changing mechanics. We also believe that this characterization can be directly correlated to the design of biomaterial systems for future therapeutic applications.

3.6 References

(1) Martino, F.; Perestrelo, A. R.; Vinarský, V.; Pagliari, S.; Forte, G. Cellular Mechanotransduction: From Tension to Function. *Front. Physiol.* **2018**, *9* (JUL), 1–21. https://doi.org/10.3389/fphys.2018.00824.

(2) Wells, R. G. The Role of Matrix Stiffness in Regulating Cell Behavior. *Hepatology* **2008**, *47* (4), 1394–1400. https://doi.org/10.1002/hep.22193.

(3) Lu, P.; Takai, K.; Weaver, V. M.; Werb, Z. Extracellular Matrix Degradation and Remodeling in Development and Disease. *Cold Spring Harb. Perspect. Biol.* **2011**, *3* (12), 1–24. https://doi.org/10.1101/cshperspect.a005058.

(4) Guimarães, C. F.; Gasperini, L.; Marques, A. P.; Reis, R. L. The Stiffness of Living Tissues and Its Implications for Tissue Engineering. *Nat. Rev. Mater.* **2020**, *5* (5), 351–370. https://doi.org/10.1038/s41578-019-0169-1.

(5) Humphrey, J. D.; Dufresne, E. R.; Schwartz, M. A. Mechanotransduction and Extracellular Matrix Homeostasis. *Nat. Rev. Mol. Cell Biol.* **2014**, *15* (12), 802–812. https://doi.org/10.1038/nrm3896.

(6) Jansen, K. A.; Donato, D. M.; Balcioglu, H. E.; Schmidt, T.; Danen, E. H. J.; Koenderink, G. H. A Guide to Mechanobiology: Where Biology and Physics Meet. *Biochim. Biophys. Acta - Mol. Cell Res.* **2015**, *1853* (11), 3043–3052. https://doi.org/10.1016/j.bbamcr.2015.05.007.

(7) Ingber, D. E. Cellular Mechanotransduction: Putting All the Pieces Together Again. *FASEB J.* **2006**, *20* (7), 811–827. https://doi.org/10.1096/fj.05-5424rev.

(8) Bonnans, C.; Chou, J.; Werb, Z. Remodelling the Extracellular Matrix in Development and Disease. *Nat. Rev. Mol. Cell Biol.* **2014**, *15* (12), 786–801. https://doi.org/10.1038/nrm3904.

(9) Chaudhuri, O.; Gu, L.; Klumpers, D.; Darnell, M.; Bencherif, S. A.; Weaver, J. C.; Huebsch, N.; Lee, H. P.; Lippens, E.; Duda, G. N.; et al. Hydrogels with Tunable Stress Relaxation Regulate Stem Cell Fate and Activity. *Nat. Mater.* **2016**, *15* (3), 326–334. https://doi.org/10.1038/nmat4489.

(10) Islam, M. R.; Virag, J.; Oyen, M. L. Micromechanical Poroelastic and Viscoelastic Properties of Ex-Vivo Soft Tissues. *J. Biomech.* **2020**, *113*, 110090. https://doi.org/10.1016/j.jbiomech.2020.110090.

(11) Chaudhuri, O.; Cooper-White, J.; Janmey, P. A.; Mooney, D. J.; Shenoy, V. B. Effects of Extracellular Matrix Viscoelasticity on Cellular Behaviour. *Nature* **2020**, *584* (7822), 535–546. https://doi.org/10.1038/s41586-020-2612-2.

(12) Fiore, V. F.; Wong, S. S.; Tran, C.; Tan, C.; Xu, W.; Sulchek, T.; White, E. S.; Hagood, J. S.; Barker, T. H. Avβ3 Integrin Drives Fibroblast Contraction and Strain Stiffening of Soft Provisional Matrix during Progressive Fibrosis. *JCI insight* **2018**, *3* (20), 1–35. https://doi.org/10.1172/jci.insight.97597.

(13) Liu, F.; Mih, J. D.; Shea, B. S.; Kho, A. T.; Sharif, A. S.; Tager, A. M.; Tschumperlin, D. J. Feedback Amplification of Fibrosis through Matrix Stiffening and COX-2 Suppression. *J. Cell Biol.* **2010**, *190* (4), 693–706. https://doi.org/10.1083/jcb.201004082.

(14) Cheng, T.; Liu, Q.; Zhang, R.; Zhang, Y.; Chen, J.; Yu, R.; Ge, G. Lysyl Oxidase Promotes Bleomycin-Induced Lung Fibrosis through Modulating Inflammation. *J. Mol. Cell Biol.* **2014**, *6* (6), 506–515. https://doi.org/10.1093/jmcb/mju039.

(15) Yang, N.; Cao, D. F.; Yin, X. X.; Zhou, H. H.; Mao, X. Y. Lysyl Oxidases: Emerging Biomarkers and Therapeutic Targets for Various Diseases. *Biomed. Pharmacother.* **2020**, *131* (August), 110791. https://doi.org/10.1016/j.biopha.2020.110791.

(16) Verdier, C.; Etienne, J.; Duperray, A.; Preziosi, L. Review: Rheological Properties of Biological Materials. *Comptes Rendus Phys.* **2009**, *10* (8), 790–811. https://doi.org/10.1016/j.crhy.2009.10.003.

(17) Perni, S.; Prokopovich, P. Rheometer Enabled Study of Cartilage Frequency-Dependent Properties. *Sci. Rep.* **2020**, *10* (1), 1–11. https://doi.org/10.1038/s41598-020-77758-9.

(18) Geerligs, M.; Peters, G. W. M.; Ackermans, P. A. J.; Oomens, C. W. J.; Baaijens, F. P. T. Linear Viscoelastic Behavior of Subcutaneous Adipose Tissue. *Biorheology* **2008**, *45* (6), 677–688. https://doi.org/10.3233/BIR-2008-0517.

(19) Lu, Y. B.; Franze, K.; Seifert, G.; Steinhäuser, C.; Kirchhoff, F.; Wolburg, H.; Guck, J.; Janmey, P.; Wei, E. Q.; Käs, J.; et al. Viscoelastic Properties of Individual Glial Cells and Neurons in the CNS. *Proc. Natl. Acad. Sci. U. S. A.* **2006**, *103* (47), 17759–17764. https://doi.org/10.1073/pnas.0606150103.

(20) Maccabi, A.; Shin, A.; Namiri, N. K.; Bajwa, N.; John, M. S.; Taylor, Z. D.; Grundfest, W.; Saddik, G. N. Quantitative Characterization of Viscoelastic Behavior in Tissue-Mimicking Phantoms and Ex Vivo Animal Tissues. *PLoS One* **2018**, *13* (1), 1–18.

https://doi.org/10.1371/journal.pone.0191919.

(21) Hui, E.; Gimeno, K. I.; Guan, G.; Caliari, S. R. Spatiotemporal Control of Viscoelasticity in Phototunable Hyaluronic Acid Hydrogels. *Biomacromolecules* **2019**, *20* (11), 4126–4134. https://doi.org/10.1021/acs.biomac.9b00965.

(22) Charrier, E. E.; Pogoda, K.; Wells, R. G.; Janmey, P. A. Control of Cell Morphology and Differentiation by Substrates with Independently Tunable Elasticity and Viscous Dissipation. *Nat. Commun.* **2018**, *9* (1), 1–13. https://doi.org/10.1038/s41467-018-02906-9.

(23) Akhtar, R.; Sherratt, M. J.; Cruickshank, J. K.; Derby, B. Characterizing the Elastic Properties of Tissues. *Mater Today* **2011**, *14* (3), 96–105. https://doi.org/10.1016/S1369-7021(11)70059-1.Characterizing.

(24) Gurtner, G. C.; Werner, S.; Barrandon, Y.; Longaker, M. T. Wound Repair and Regeneration. *Nature* **2008**, *453* (7193), 314–321. https://doi.org/10.1038/nature07039.

(25) Zhu, M.; Tao, H.; Samani, M.; Luo, M.; Wang, X.; Hopyan, S.; Sun, Y. Spatial Mapping of Tissue Properties in Vivo Reveals a 3D Stiffness Gradient in the Mouse Limb Bud. *Proc. Natl. Acad. Sci. U. S. A.* **2020**, *117* (9), 4781–4791. https://doi.org/10.1073/pnas.1912656117.

(26) Ebenstein, D. M.; Pruitt, L. A. Nanoindentation of Biological Materials. *Nano Today* **2006**, *1* (3), 26–33. https://doi.org/10.1016/S1748-0132(06)70077-9.

(27) Efremov, Y. M.; Okajima, T.; Raman, A. Measuring Viscoelasticity of Soft Biological Samples Using Atomic Force Microscopy. *Soft Matter* **2019**, *16* (1), 64–81. https://doi.org/10.1039/c9sm01020c.

(28) Jorba, I.; Uriarte, J. J.; Campillo, N.; Farré, R.; Navajas, D. Probing Micromechanical Properties of the Extracellular Matrix of Soft Tissues by Atomic Force Microscopy. *J. Cell. Physiol.* **2017**, *232* (1), 19–26. https://doi.org/10.1002/jcp.25420.

(29) Grant, C. A.; Twigg, P. C.; Tobin, D. J. Static and Dynamic Nanomechanical Properties of Human Skin Tissue Using Atomic Force Microscopy: Effect of Scarring in the Upper Dermis. *Acta Biomater.* **2012**, *8* (11), 4123–4129. https://doi.org/10.1016/j.actbio.2012.06.042.

(30) Gramlich, W. M.; Kim, I. L.; Burdick, J. A. Synthesis and Orthogonal Photopatterning of Hyaluronic Acid Hydrogels with Thiol-Norbornene Chemistry. *Biomaterials* **2013**, *34* (38),

9803–9811. https://doi.org/10.1016/j.biomaterials.2013.08.089.

(31) Rodell, C. B.; Kaminski, A. L.; Burdick, J. A. Rational Design of Network Properties in Guest-Host Assembled and Shear-Thinning Hyaluronic Acid Hydrogels. *Biomacromolecules* **2013**, *14* (11), 4125–4134. https://doi.org/10.1021/bm401280z.

(32) Hui, E.; Moretti, L.; Barker, T. H.; Caliari, S. R. The Combined Influence of Viscoelastic and Adhesive Cues on Fibroblast Spreading and Focal Adhesion Organization. *Cell. Mol. Bioeng.* **2021**. https://doi.org/10.1007/s12195-021-00672-1.

(33) Lin, D. C.; Shreiber, D. I.; Dimitriadis, E. K.; Horkay, F. Spherical Indentation of Soft Matter beyond the Hertzian Regime: Numerical and Experimental Validation of Hyperelastic Models. *Biomech. Model. Mechanobiol.* **2009**, *8* (5), 345–358. https://doi.org/10.1007/s10237-008-0139-9.

(34) Booth, A. J.; Hadley, R.; Cornett, A. M.; Dreffs, A. A.; Matthes, S. A.; Tsui, J. L.; Weiss, K.; Horowitz, J. C.; Fiore, V. F.; Barker, T. H.; et al. Acellular Normal and Fibrotic Human Lung Matrices as a Culture System for in Vitro Investigation. *Am. J. Respir. Crit. Care Med.* **2012**, *186* (9), 866–876. https://doi.org/10.1164/rccm.201204-0754OC.

(35) De Hilster, R. H. J.; Sharma, P. K.; Jonker, M. R.; White, E. S.; Gercama, E. A.; Roobeek, M.; Timens, W.; Harmsen, M. C.; Hylkema, M. N.; Burgess, J. K. Human Lung Extracellular Matrix Hydrogels Resemble the Stiffness and Viscoelasticity of Native Lung Tissue. *Am. J. Physiol. - Lung Cell. Mol. Physiol.* **2020**, *318* (4), L698–L704. https://doi.org/10.1152/AJPLUNG.00451.2019.

(36) Cameron, A. R.; Frith, J. E.; Cooper-White, J. J. The Influence of Substrate Creep on Mesenchymal Stem Cell Behaviour and Phenotype. *Biomaterials* **2011**, *32* (26), 5979–5993. https://doi.org/10.1016/j.biomaterials.2011.04.003.

(37) Chaubet, L.; Chaudhary, A. R.; Heris, H. K.; Ehrlicher, A. J.; Hendricks, A. G. Dynamic Actin Cross-Linking Governs the Cytoplasm's Transition to Fluid-like Behavior. *Mol. Biol. Cell* **2020**, *31* (16), 1744–1752. https://doi.org/10.1091/mbc.E19-09-0504.

(38) Stamenović, D.; Rosenblatt, N.; Montoya-Zavala, M.; Matthews, B. D.; Hu, S.; Suki, B.; Wang, N.; Ingber, D. E. Rheological Behavior of Living Cells Is Timescale-Dependent. *Biophys. J.* **2007**, *93* (8), 39–41. https://doi.org/10.1529/biophysj.107.116582.

(39) Li, W.; Shepherd, D. E. T.; Espino, D. M. Frequency Dependent Viscoelastic Properties of Porcine Brain Tissue. *J. Mech. Behav. Biomed. Mater.* **2020**, *102* (September 2019),

103460. https://doi.org/10.1016/j.jmbbm.2019.103460.

(40) Dai, Z.; Peng, Y.; Mansy, H. A.; Sandler, R. H.; Royston, T. J. A Model of Lung Parenchyma Stress Relaxation Using Fractional Viscoelasticity. *Med. Eng. Phys.* **2015**, *37* (8), 752–758. https://doi.org/10.1016/j.medengphy.2015.05.003.

(41) Sattari, S.; Eskandari, M. Characterizing the Viscoelasticity of Extra- and Intra-Parenchymal Lung Bronchi. *J. Mech. Behav. Biomed. Mater.* **2020**, *110*, 103824. https://doi.org/10.1016/j.jmbbm.2020.103824.

(42) Eskandari, M.; Arvayo, A. L.; Levenston, M. E. Mechanical Properties of the Airway Tree: Heterogeneous and Anisotropic Pseudoelastic and Viscoelastic Tissue Responses. *J. Appl. Physiol.* **2018**, *125* (3), 878–888. https://doi.org/10.1152/japplphysiol.00090.2018.

(43) Perepelyuk, M.; Chin, L.; Cao, X.; Van Oosten, A.; Shenoy, V. B.; Janmey, P. A.; Wells, R. G. Normal and Fibrotic Rat Livers Demonstrate Shear Strain Softening and Compression Stiffening: A Model for Soft Tissue Mechanics. *PLoS One* **2016**, *11* (1), 1–18. https://doi.org/10.1371/journal.pone.0146588.

(44) Liu, Z.; Bilston, L. On the Viscoelastic Character of Liver Tissue: Experiments and Modelling of the Linear Behaviour. *Biorheology* **2000**, *37* (3), 191–201.

(45) Qiu, S.; Zhao, X.; Chen, J.; Zeng, J.; Chen, S.; Chen, L.; Meng, Y.; Liu, B.; Shan, H.; Gao, M.; et al. Characterizing Viscoelastic Properties of Breast Cancer Tissue in a Mouse Model Using Indentation. *J. Biomech.* **2018**, *69*, 81–89. https://doi.org/10.1016/j.jbiomech.2018.01.007.

(46) Caliari, S. R.; Vega, S. L.; Kwon, M.; Soulas, E. M.; Burdick, J. A. Dimensionality and Spreading Influence MSC YAP/TAZ Signaling in Hydrogel Environments. *Biomaterials* **2016**, *103*, 314–323. https://doi.org/10.1016/j.biomaterials.2016.06.061.

3.7 Supplementary Figures

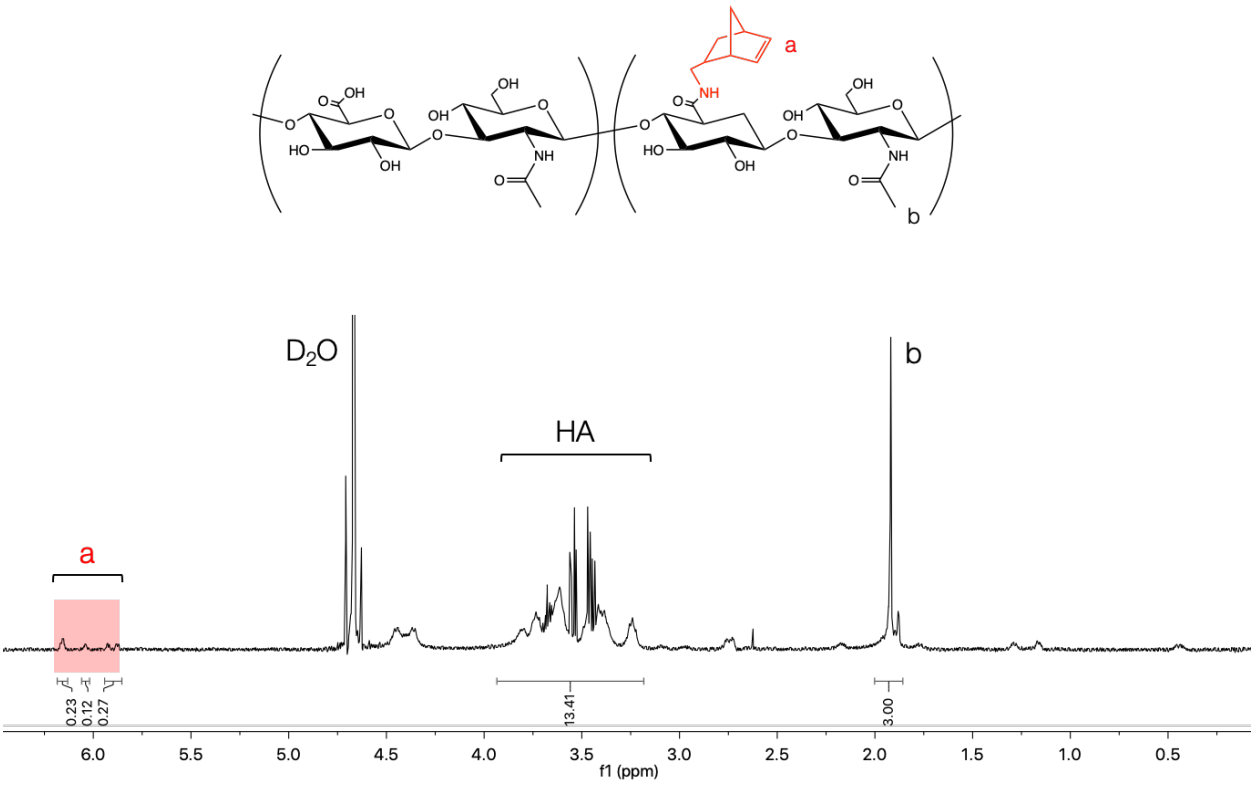

Figure S3.1. ^{1}H NMR spectrum of norbornene-modified hyaluronic acid (NorHA). The degree of modification was determined to be 31% based on the norbornene peaks, labeled 'a,' relative to the methyl peak, labeled 'b.'

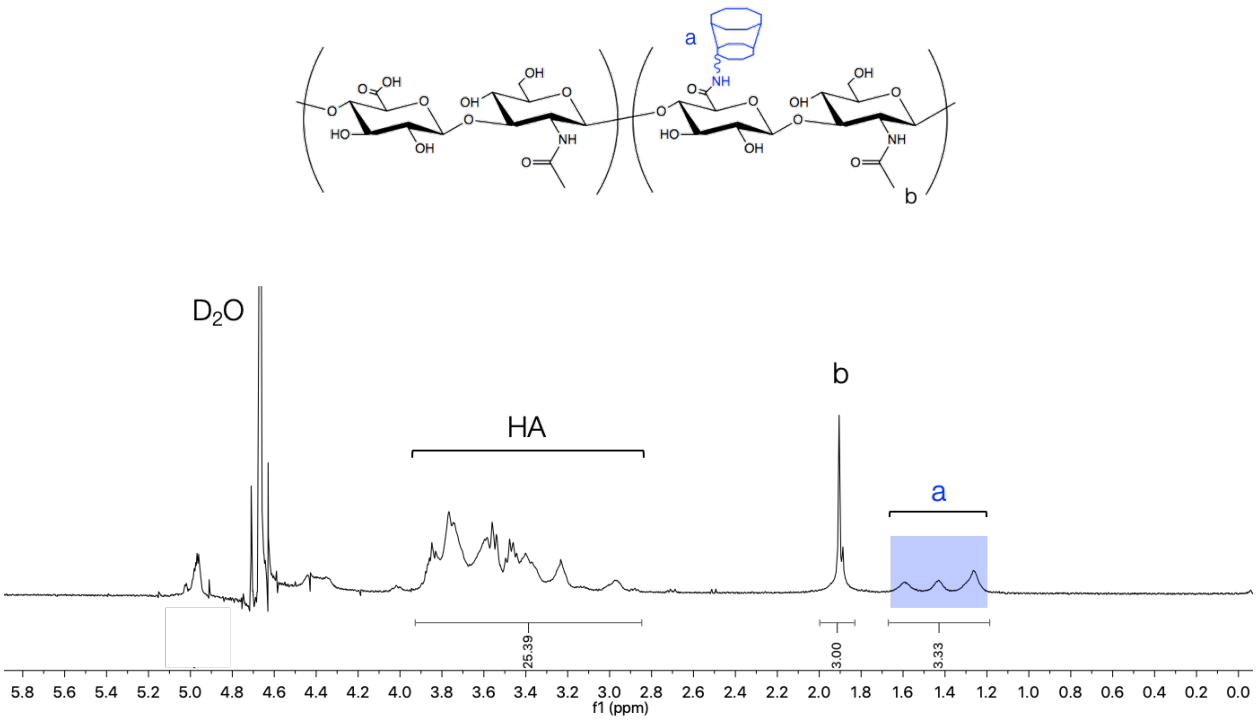

Figure S3.2. ^{1}H NMR spectrum of β-cyclodextrin modified HA (CD-HA). The degree of modification was determined to be 28% based on the β-CD peaks, labeled 'a,' relative to the methyl peak, labeled 'b.'

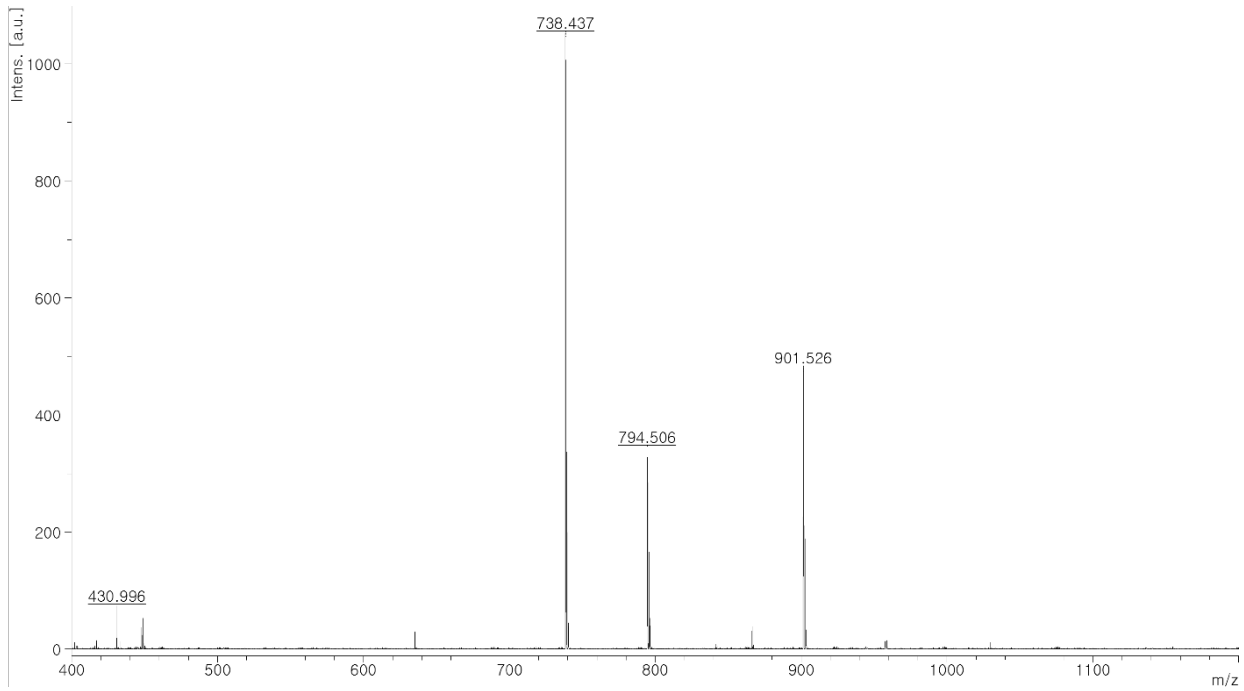

Figure S3.3. MALDI spectrum of thiolated adamantane (Ad) peptide. Expected mass: 738.6 g/mol. Actual mass: 738.4 g/mol.

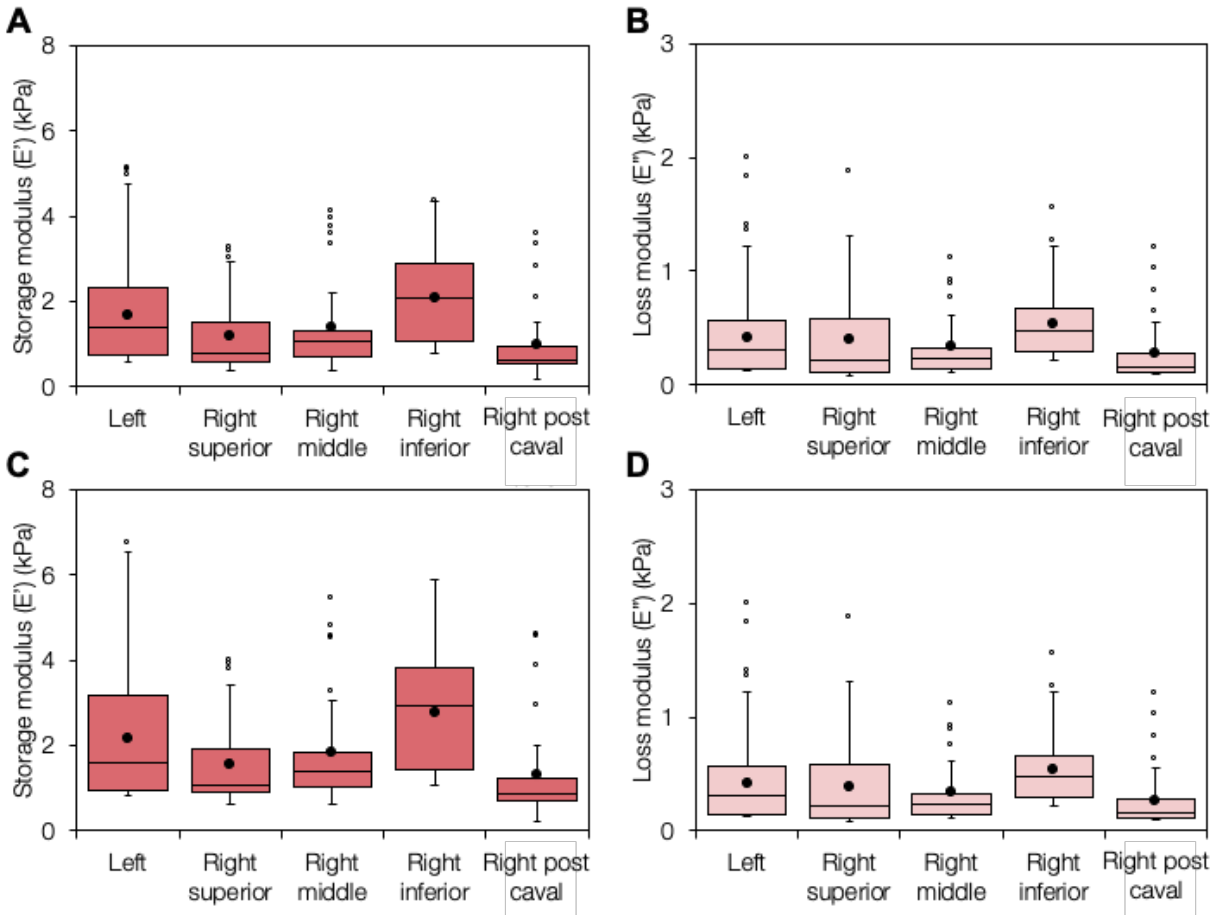

Figure S3.4. Mechanical characterization of normal rat lung tissue. (A) Box and whisker plots of storage modulus (E') measured at a frequency of 0.1 Hz. (B) Box plots of loss modulus (E") measured at a frequency of 0.1 Hz. (C) Box and whisker plots of storage modulus (E') measured at a frequency of 0.5 Hz. (D) Box plots of loss modulus (E") measured at a frequency of 0.5 Hz. 3-6 lobes were tested for each group (30-190 data points total).

CHAPTER 4: SPATIOTEMPORAL CONTROL OF VISCOELASTICITY IN PHOTOTUNABLE HYALURONIC ACID HYDROGELS

This chapter has been adapted from the following publication: Hui, E., Gimeno, K.I., Guan, G., Caliari, S.R. "Spatiotemporal Control of Viscoelasticity in Phototunable Hyaluronic Acid Hydrogels." *Biomacromolecules* **2019**, 20, 4126-4134.

4.1 Abstract

Viscoelasticity has emerged as a critical regulator of cell behavior. However, there is an unmet need to develop biomaterials where viscoelasticity can be spatiotemporally controlled to mimic the dynamic and heterogeneous nature of tissue microenvironments. Toward this objective, we developed a modular hyaluronic acid hydrogel combining light-mediated covalent and supramolecular cross-linking to afford spatiotemporal control of network viscoelastic properties. Covalently cross-linked elastic hydrogels or viscoelastic hydrogels combining covalent and supramolecular interactions were fabricated to match healthy and fibrotic liver mechanics. LX-2 human hepatic stellate cells cultured on viscoelastic hydrogels displayed reductions in spreading, actin stress fiber organization, and myocardin-related transcription factor A (MRTF-A) nuclear localization compared to cells on elastic hydrogels. We further demonstrated the dynamic capabilities of our hydrogel system through photo-mediated secondary incorporation of either covalent or supramolecular cross-links to modulate viscoelastic properties. We used photopatterning to create hydrogels with well-controlled patterned regions of stiff elastic mechanics representing fibrotic tissue nodules surrounded by regions of soft viscoelastic hydrogel mimicking healthy tissue. Cells responded to the local mechanics of the patterned substrates with increased spreading in fibrosis-mimicking regions. Together, this work represents an important

step forward toward the creation of hydrogel models with spatiotemporal control of both stiffness and viscoelastic cell-instructive cues.

4.2 Introduction

The interplay between cells and their surrounding extracellular matrix (ECM) plays a critical role in regulating development, wound healing, and disease progression[1–3]. Through mechanisms including mechanotransduction, a process in which mechanical forces are converted into biochemical signals, cells are constantly probing and responding to their evolving microenvironment[4]. Cell−ECM interactions are especially important in pathologies such as fibrosis, a heterogeneous pathological scarring process that can lead to irreversible loss of tissue function and organ failure. During fibrosis progression, healthy tissue mechanics transition from softer and viscoelastic to stiffer and less viscous[5,6]. Moreover, fibrosis progresses in a heterogeneous manner, leading to microscale spatial heterogeneity in the form of patchy, stiff fibrotic nodules surrounded by areas of softer, less-affected tissue where nodule size often directly correlates with the severity of fibrosis[7–9]. The presence of a stiff microenvironment can guide mechanotransduction by providing necessary biophysical cues for the activation of resident cells into fibrosis-promoting myofibroblasts[10], and elevated stiffness alone has been shown to drive progression of both fibrosis[11] and cancer[12].

Hydrogels have become valuable model systems to better understand the complex roles that matrix biophysical properties play in regulating cell behaviors through their ability to mimic salient properties of natural tissue, including soft tissue mechanics and high water content[13,14], and numerous systems have already investigated the influence of hydrogel mechanics on cell

behavior[3,9,15–21]. In particular, many groups have shown a direct correlation between increasing hydrogel Young's modulus (stiffness) and elevated cell spreading in two-dimensional (2D) cultures[10,22–25]. Although many studies have developed homogenous substrates to study cell−ECM interactions, healthy and especially diseased tissues are inherently heterogeneous. During pathologies such as fibrosis, changes in the physical environment have direct implications on cell mechanotransduction, where activated cell patches begin depositing excessive amounts of ECM proteins, resulting in nodules of nonfunctional scar tissue[7]. Therefore, it is necessary to develop methods to recapitulate tissue heterogeneity in hydrogel models. Recent work using light-based chemistries to spatially pattern elastic substrates has shown that cells will exhibit behavior correlating to their local mechanics such as increased spreading on stiffer areas[9,26,27].

Although these findings are informative, they typically involve covalently cross-linked hydrogels that primarily behave as elastic solids and do not display time-dependent tissue-relevant mechanical properties. The majority of native tissues exhibits viscoelastic behaviors including stress relaxation[6,28], which can occur through both external and cell-mediated forces exerted onto the matrix. For this reason, viscoelasticity has recently emerged as a critical parameter for probing cell behaviors and functions. Viscoelastic hydrogels have been developed using ionic[15,16], supramolecular[29], and dynamic covalent crosslinking[30] mechanisms. Viscoelastic hydrogels with stress relaxation properties similar to native tissues have been shown to affect cell spreading, focal adhesion organization, proliferation, and differentiation in comparison with elastic hydrogels[15–18,31,32]. This can be attributed in part to cell-mediated reorganization and/or relaxation of the energy-dissipative viscoelastic hydrogel network. Recent work from Charrier *et al.*[18] showed changes in the behavior of hepatic stellate cells, the primary cellular source of hepatic

myofibroblasts, when cultured on viscoelastic hydrogels. Stellate cells displayed lower spread area and reduced expression of α-smooth muscle actin (α-SMA), a hallmark of myofibroblast activation, with increasing hydrogel loss modulus[18]. This study highlighted the importance of hydrogel viscoelasticity in regulating disease-relevant cellular behaviors.

Although the importance of incorporating viscoelasticity into hydrogel cellular microenvironments is clearly established, an approach to spatially control viscoelastic properties in a manner that mimics heterogeneous tissue has not been developed. The ability to pattern regions of hydrogel stiffness and/or viscoelasticity in a manner that captures both the dynamic stiffening that occurs during fibrosis progression and the overall heterogeneity of fibrotic tissue would help establish more robust disease models to study pathological cell behaviors. Here, we designed a phototunable viscoelastic hydrogel system where stiffness and viscoelasticity can be independently tuned through control of network covalent and supramolecular interactions. Using this modular approach, we developed photopatterned substrates where stiffness and viscoelasticity could be spatiotemporally controlled and investigated the role that matrix mechanical properties played in regulating cell behavior in an in vitro model of fibrosis.

4.3 Materials and Methods

4.3.1 NorHA synthesis

Norbornene-modified HA was synthesized similar to previous methods[33]. Briefly, sodium hyaluronate (Lifecore, 74 kDa) was reacted with Dowex 50W proton-exchange resin, filtered, titrated to pH 7.05, frozen, and lyophilized to yield hyaluronic acid tertbutyl ammonium salt (HA-TBA). HA-TBA was then reacted with 5-norbornene-2-methylamine and benzotriazole-1-

yloxytris-(dimethylamino)phosphonium hexafluorophosphate (BOP) in dimethylsulfoxide (DMSO) for 2 h at 25 °C. The reaction was quenched with cold water, dialyzed (molecular weight cutoff: 6−8 kDa) for 5 days, filtered, dialyzed for 5 more days, frozen, and lyophilized. The degree of modification was 22% as determined by ^{1}H NMR (500 MHz Varian Inova 500, **Figure S4.1**).

4.3.2 β-CD-HDA synthesis

The synthesis of β-cyclodextrin hexamethylene diamine (β-CD-HDA) followed the procedure outlined previously[34]. p-Toluenesulfonyl chloride (TosCl) was dissolved in acetonitrile and added dropwise to an aqueous β-cyclodextrin (CD) suspension (5:4 molar ratio of TosCl to CD) at 25 °C. After 2 h, the solution was cooled on ice and an aqueous NaOH solution was added dropwise (3.1:1 molar ratio of NaOH to CD). The solution was reacted for 30 min at 25 °C before adding ammonium chloride to reach a pH of 8.5. The solution was cooled on ice, precipitated using cold water and acetone, and dried overnight. The CD-Tos product was then charged with hexamethylene diamine (HDA) (4 g/g CD-Tos) and dimethylformamide (DMF) (5 mL/g CD-Tos), and the reaction was carried out under nitrogen at 80 °C for 12 h before being precipitated with cold acetone (5 × 50 mL/g CD-Tos), washed with cold diethyl ether (3 × 100 mL), and dried. The degree of modification was 61% as determined by ^{1}H NMR (**Figure S4.2**).

4.3.3 β-CD-HA synthesis

β-Cyclodextrin-modified hyaluronic acid (CD-HA) was prepared through coupling of β-CD-HDA to HA-TBA. A reaction containing HA-TBA, 6-(6-aminohexyl)amino-6-deoxy-βcyclodextrin (β-CD-HDA), and BOP in DMSO was carried out at 25°C for 3 h. The reaction was quenched with

cold water, dialyzed for 5 days, filtered, dialyzed for 5 more days, frozen, and lyophilized. The degree of modification was 27% as determined by ^{1}H NMR (**Figure S4.3**).

4.3.4 Peptide synthesis

Solid-phase peptide synthesis was performed on a Gyros Protein Technologies Tribute peptide synthesizer. A thiolated adamantane (Ad) peptide (Ad-KKKCG) and a fluorescently-labeled thiolated peptide (Fluorescein-KKCG) were synthesized on either Rink Amide MBHA high-loaded (0.78 mmol/g) or Wang (1 mmol/g) resins using standard solid-supported Fmoc-protected peptide synthesis. The resin was swelled with 20% (v/v) piperidine in DMF, and the amino acids were activated using HBTU and 0.4 N-methyl morpholine in DMF (5:1 excess). Peptides were cleaved in a solution of 95% trifluoroacetic acid, 2.5% triisopropylsilane, and 2.5% H2O for 2−3 h, precipitated in cold ethyl ether, and dried overnight. The peptide products were resuspended in H2O, frozen, and lyophilized. Synthesis was confirmed by matrix-assisted laser desorption/ionization (MALDI) (**Figures S4.4 and S4.5**).

4.3.5 HA hydrogel fabrication

2D hydrogel thin films were made between untreated and thiolated coverslips (50 μL, 18 × 18 mm). Elastic NorHA hydrogels were fabricated using ultraviolet (UV) light-mediated thiol−ene addition. Soft (2 wt % NorHA) and stiff (6 wt % NorHA) hydrogel precursor solutions containing 1 mM thiolated RGD peptide (GCGYGRGDSPG, Genscript) and dithiothreitol (DTT, thiol−norbornene ratios of 0.35 for both groups) were photopolymerized (365 nm, 5 mW/cm^2) in the presence of 1 mM lithium acylphosphinate (LAP) photoinitiator for 2 min. Soft (2 wt % NorHA-CD-HA) and stiff (6 wt % NorHA-CD-HA) viscoelastic NorHA-CD-HA hydrogels were

fabricated by first mixing CD-HA (5 and 8 wt % stock solutions for soft and stiff viscoelastic groups, respectively) with the thiolated adamantane peptide (1:1 molar ratio of CD to Ad) to introduce Ad−CD guest−host interactions before mixing in RGD, DTT (thiol-norbornene ratios of 0.45 and 0.55 for soft and stiff viscoelastic groups, respectively), and 8 wt % NorHA stock solution. The 2 and 6 wt % NorHA-CD-HA precursor solutions were then photopolymerized using the same conditions as elastic hydrogels. Hydrogels were swelled in phosphate-buffered saline (PBS) overnight at 37 °C before subsequent cell-seeding procedures.

4.3.6 Rheological characterization

All rheological measurements were performed at 25 °C on an Anton Paar MCR 302 rheometer using a cone-plate geometry (25 mm diameter, 0.5°, 25 μm gap). Rheological properties were tested using oscillatory time sweeps (1 Hz, 1% strain) with a 2 min UV irradiation (365 nm, 5 mW/cm^2), oscillatory frequency sweeps (0.001−10 Hz, 1% strain), cyclic stress relaxation and recovery tests alternating between 0.1 and 5% strain (1 Hz), and creep tests where a constant stress of 100 Pa was applied to the sample for 50 s.[18]

4.3.7 Cell culture

Human hepatic stellate cells (LX-2s[35], Millipore Sigma) were used between passages 6−8 for all experiments. Culture media contained Dulbecco's modified Eagle's medium supplemented with 10 v/v% fetal bovine serum (Gibco) and 1 v/v% penicillin/streptomycin/amphotericin B (1000 U/mL, 1000 μg/mL, and 0.25 μg/mL final concentrations, respectively, Gibco). For cell seeding, swelled thin film hydrogels (18 × 18 mm) were sterilized using germicidal UV irradiation for 2 h and incubated in culture media for at least 30 min prior to cell seeding. Cultures were treated with

5−10 μg/mL mitomycin C (Sigma-Aldrich) in serum-free media for 2 h, washed thrice with PBS, and incubated in complete culture media for at least 1 h prior to cell seeding. Cells were seeded atop hydrogels placed in untreated 6-well plates at a density of 2×10^4 cells per hydrogel. For all experiments, media was replaced every 2−3 days for 7 day cultures.

4.3.8 Immunocytochemistry, imaging, and analysis

For immunostaining, cell-seeded hydrogels were fixed in 10% buffered formalin for 15 min, permeabilized in 0.1% Triton X-100 for 10 min, and blocked in 3% bovine serum albumin (BSA) in PBS for at least 1 h at room temperature. Hydrogels were then incubated overnight at 4 °C with primary antibodies against myocardin-related transcription factor A (MRTF-A, rabbit polyclonal anti-Mk11 antibody, 1:600, Abcam) and either α-SMA (mouse monoclonal anti-α-SMA clone 1A4, 1:400, Sigma-Aldrich) or rhodamine phalloidin to visualize F-actin (1:600, Invitrogen). The hydrogels were washed three times in PBS and incubated with secondary antibodies (AlexaFluor 488 goat anti-rabbit IgG, 1:800; AlexaFluor 555 goat anti-mouse, 1:800) for 2 h in the dark at room temperature. The hydrogels were then rinsed three times with PBS and stained with a DAPI nuclear stain (1:10,000) for 1 min before rinsing twice with 3% BSA. Stained hydrogels were stored in the dark at 4 °C until imaging. Microscopy was performed on a Zeiss AxioObserver 7 inverted microscope. 2D hydrogels were covered with an 18 × 18 mm glass coverslip and inverted for imaging. Exposure time and other image settings for each respective channel were held constant while imaging. Cell spread area, cell shape index (CSI), and MRTF-A nuclear localization were determined using a CellProfiler (Broad Institute, Harvard/MIT) pipeline modified to include adaptive thresholding. CSI determines the circularity of the cell, where a line and a circle have values of 0 and 1, respectively, and was calculated using the formula

$$CSI = \frac{4\pi A}{P^2}$$

where A is the cell area and P is the cell perimeter. MRTF-A nuclear/ cytosolic ratio was determined using the formula

$$Nuclear\ MRTF = \frac{nuclear\ MRTF - signal/area\ of\ nucleus}{cytosolic\ MRTF - signal/area\ of\ nucleus}$$

where the signal intensities were taken and normalized to their respective areas.

4.3.9 Photopatterning HA hydrogels

NorHA hydrogels (6 wt %) with low amounts of DTT (thiol−norbornene ratio = 0.12 for initially soft viscoelastic, 0.2 for initially soft elastic, 0.45 for initially stiff elastic) were fabricated and swelled overnight in PBS at 37 °C. The hydrogels were first swelled in a 2 wt % BSA in PBS solution for 2 h before being swelled in a 500 μL PBS solution containing 1 wt % BSA, LAP, DTT, and fluorescent-thiolated peptide for 1 h at 37 °C before irradiation with a patterned photomask transparency (CAD/Art Services, Inc) for 2 min (5 mW/cm^2). The resulting patterned hydrogels were washed with PBS several times prior to cell seeding and imaging.

4.3.10 Atomic force microscopy characterization and analysis

Atomic force microscopy (AFM) force spectroscopy was performed using an Asylum Research MFP 3D AFM. A silicon nitride cantilever (MLCT-O10/Tipless/Ti−Au, cantilever C, Bruker) with

a nominal spring constant of 0.1 N/m was functionalized with a 25 μm diameter polystyrene bead at the tip. The spring constant of the cantilever was calibrated via thermal resonance curves prior to data collection. Nanoindentation tests (indentation rate, ν = 5−10 μm/s) were performed on photopatterned hydrogels in PBS to determine the mechanics of the patterned and nonpatterned regions. Force versus distance curves were generated, and the instantaneous Young's modulus (E(0)) at each indentation was calculated using the initial loading portion of the indentation curve by applying the Hertzian contact mechanics model and assuming a Poisson's ratio of 0.5. Force relaxation tests were performed to study viscoelasticity of patterned substrates. Following indentation, the tip was held at a constant indentation depth for 10−30 s at a 500 Hz sampling rate. Indentation force and depth were recorded as a function of time[36,37]. Temporal relaxation tests measuring time-dependent Young's modulus (E(t)) normalized to the instantaneous modulus (E(0)) were used to assess viscoelasticity.

4.3.11 Statistical analysis

Student's t-tests (two experimental groups) or one-way ANOVA with Tukey's HSD post hoc tests (more than two experimental groups) were performed for all quantitative data sets. All experiments included at least 3 hydrogels and/or 20 individual cells quantified per experimental group. Box plots of single cell data had error bars that were the lower value of either 1.5 × interquartile range or the maximum/minimum value, with data points between 1.5 × interquartile range and the maximum/minimum indicated as open circles. Significance was indicated by *, **, or *** corresponding to $P < 0.05$, 0.01, or 0.001, respectively.

4.4 Results and Discussion

4.4.1 Viscoelastic hydrogels were synthesized with a combination of covalent and supramolecular cross-links

Hyaluronic acid was functionalized with norbornene groups (NorHA) to produce hydrogels containing a high degree of reactive sites (~ 20% of repeat units). Compared to common functional groups such as (meth)acrylates, which can react with each other to form kinetic chains, norbornene groups have high reactivity to thiyl radicals and low reactivity to themselves, allowing rapid and controllable thiol−ene click addition of both pendant and multifunctional thiolated groups[33]. This biorthogonal system was also chosen for its ability to easily synthesize hydrogels with a wide range of tissue-relevant mechanics by a simple tuning of parameters such as cross-linker concentration or light intensity. In this study, soft (G' ~ 0.5 kPa) and stiff (G' ~ 5 kPa) hydrogels were fabricated to represent healthy and fibrotic liver tissue, respectively[10,11]. Elastic NorHA hydrogels were fabricated via ultraviolet (UV) light-mediated thiol−ene addition between norbornenes on HA and thiols on DTT to create stable covalently cross-linked networks.

Viscoelasticity was introduced to the system by incorporating reversible guest−host interactions between adamantane (guest) and β-cyclodextrin (host) groups. The adamantane (Ad) guest moiety has a high affinity to the hydrophobic cavity of β-cyclodextrin ($K_a \sim 10^5\ M^{-1}$), and has previously been exploited to make viscoelastic, shear-thinning hydrogels[34,38,39]. For viscoelastic hydrogel groups, β-cyclodextrin HA (CD-HA) and thiolated Ad peptide were mixed in solution (1:1 molar ratio of CD to Ad) to introduce supramolecular guest−host interactions, followed by the addition of NorHA and DTT, where the ratio of DTT to norbornene groups provided control over hydrogel modulus (**Figure 4.1**). This particular methodology involving Ad peptides allowed for a more modular approach to fabricate hydrogels because of its detachment from the HA backbone prior

to the thiol-ene addition, making the hydrogel precursors less viscous and easier to pipet and mix. Following mixing of the Ad peptide, CD-HA, NorHA, and DTT, the thiols on the cysteine residues of the CD-associated Ad peptide reacted with the norbornenes to form stable supramolecular connections between HA chains, whereas the DTT formed covalent cross-links, creating a viscoelastic hydrogel network with both covalent and supramolecular cross-links.

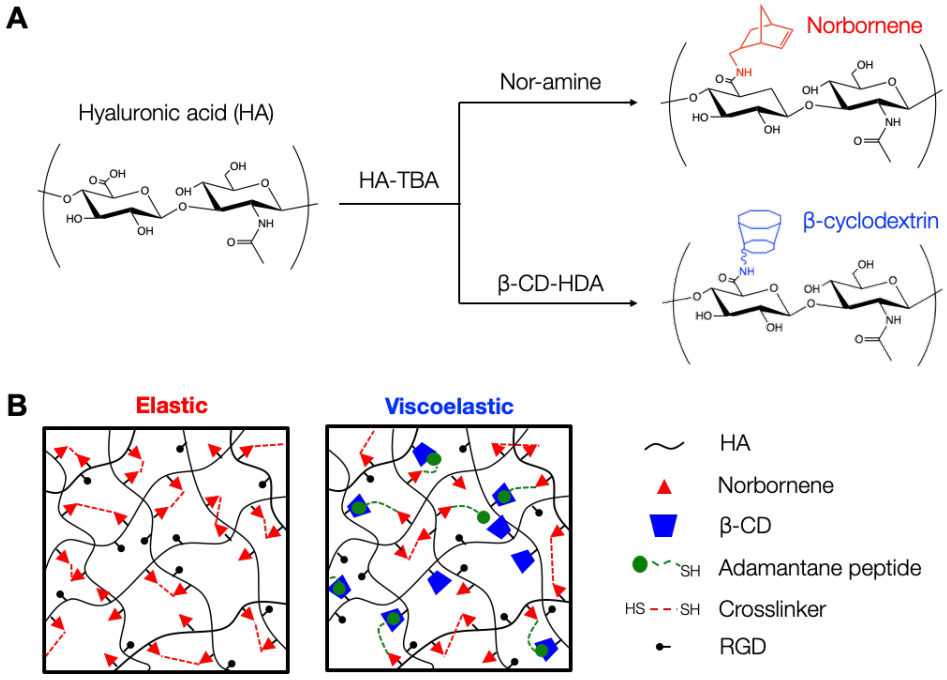

Figure 4.1. Overview of hydrogel synthesis and cross-linking. (A) Hyaluronic acid was first converted to HA-TBA salt before modification with norbornene or β-cyclodextrin groups using BOP coupling chemistry to synthesize NorHA and CD-HA. (B) For the elastic hydrogel system, covalent cross-links between the norbornene groups were introduced using di-thiol cross-linkers via light-mediated thiol−ene addition. For the viscoelastic hydrogel system, thiol−ene photochemistry was used to introduce supramolecular interactions between CD-HA and Ad groups on thiolated peptides in addition to dithiol-mediated covalent cross-links between the norbornenes.

4.4.2 Viscoelastic hydrogels display stress relaxation and frequency-dependent behavior

Hydrogel mechanical properties were characterized through shear oscillatory rheology (**Figure 4.2**). *In situ* gelation of hydrogel precursor solutions demonstrated rapid gelation kinetics controlled by light exposure, resulting in a nearly immediate plateau in storage and loss moduli

once light irradiation was stopped (**Figure 4.2A, B**). Similar storage moduli at 1 Hz were observed for the soft (elastic: G' = 0.51 ± 0.08 kPa, viscoelastic: G' = 0.46 ± 0.07 kPa) and stiff (elastic: G' = 4.59 ± 0.24 kPa, viscoelastic: G' = 4.93 ± 0.77 kPa) hydrogel groups corresponding to healthy and fibrotic liver tissues, respectively. However, as expected, the viscoelastic hydrogels had significantly higher loss moduli at 1 Hz (soft viscoelastic: G" = 67.2 ± 2.44 Pa, stiff viscoelastic: G" = 330 ± 45.5 Pa) compared to elastic groups (soft elastic: G" = 0.99 ± 0.89 Pa, stiff elastic: G" = 2.78 ± 2.21 Pa). Notably, the G" values for the viscoelastic hydrogels were within an order of magnitude of the G', similar to the ratios observed in native viscoelastic tissue[18,40]. Hydrogel frequency sweeps revealed relatively constant storage and loss moduli for the elastic groups (**Figure 4.2C**). However, the viscoelastic hydrogels showed frequency-dependent behavior; at higher frequencies, the loss modulus increased, demonstrating that guest−host interactions were being disrupted with less time to reassociate. Although there were no statistically significant differences in G' between the elastic and viscoelastic groups over the range of frequencies tested (0.001−10 Hz), the strong frequency-dependent behavior shown by the viscoelastic hydrogels for G″ is similar to trends seen in other comparable viscoelastic systems[18,34]. Stress relaxation and recovery tests showed that at a constant applied strain of 5%, the elastic hydrogels showed no stress relaxation over time because of their stable covalently crosslinked network (**Figure 4.2D**). In contrast, the viscoelastic hydrogel groups showed cyclic stress relaxation in which high stress was observed, followed by a plateau to a final stress value equal to the corresponding elastic groups. The ability of the hydrogels to fully recover their mechanical properties upon repeated bouts of applied strain highlighted their viscoelasticity as opposed to viscoplasticity.

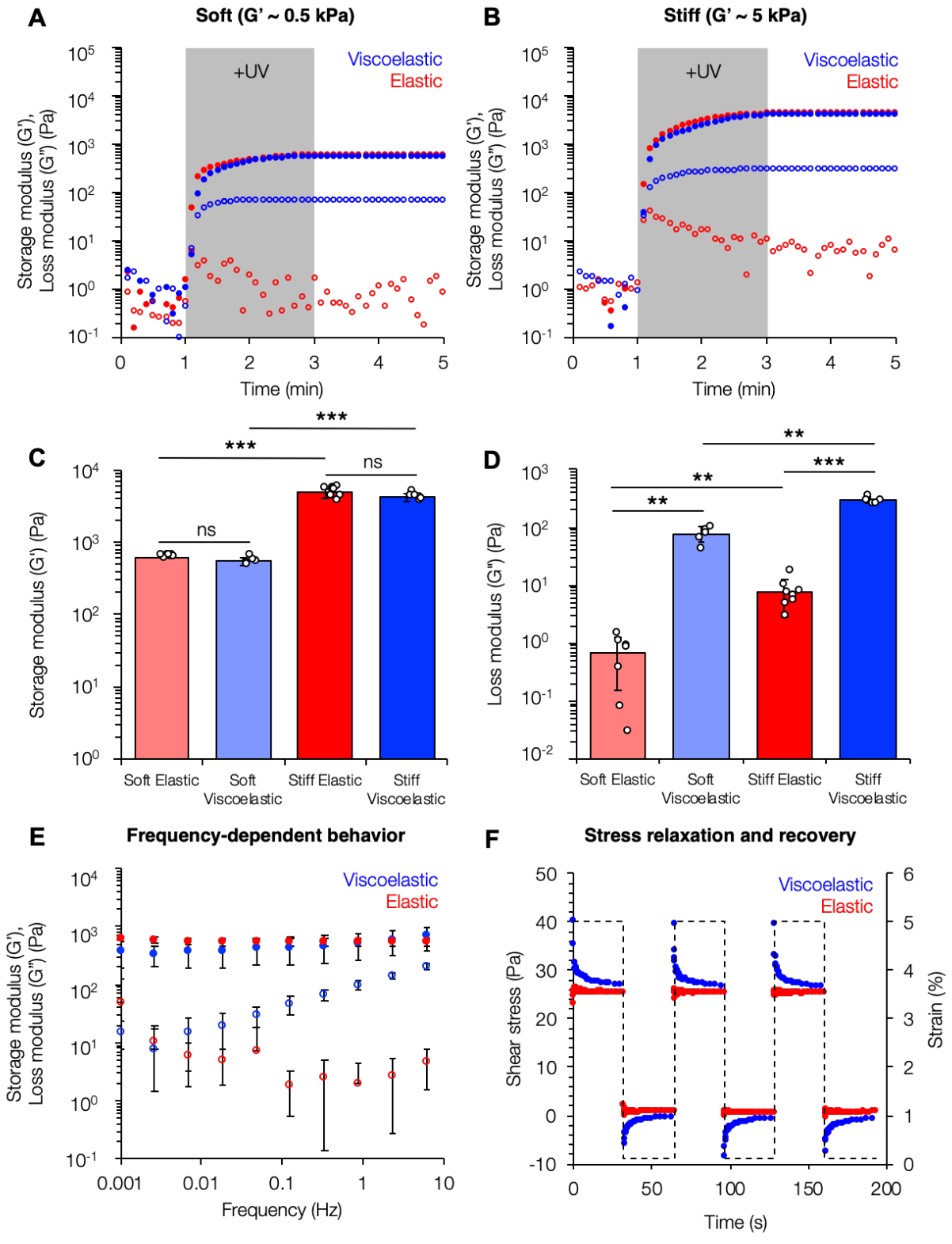

Figure 4.2. Rheological characterization of viscoelastic hydrogels. Viscoelastic hydrogels (blue) of equivalent storage moduli (closed circles) to their elastic counterparts (red) showed loss moduli

(open circles) within an order of magnitude for both (A) "soft" (G′ ≈ 0.5 kPa) and (B) "stiff" (G′ ≈ 5 kPa) hydrogel formulations corresponding to healthy and fibrotic tissue, respectively. (C) Average values of storage moduli (G′) measured at a constant frequency (1 Hz) and strain (1%). (D) Average values of loss moduli (G″) measured at a constant frequency (1 Hz) and strain (1%). (E) Viscoelastic hydrogels also showed frequency-dependent behavior with increasing loss moduli as frequency was increased, whereas the elastic hydrogel properties remained relatively constant. (F) Stress relaxation and recovery tests showed full recovery of the mechanical properties of the viscoelastic hydrogels. For the frequency and stress relaxation tests, the soft groups are shown; similar trends were seen for the stiff groups (Figure S4.6). **: $P < 0.01$, ***: $P < 0.001$.

4.4.3 Cell spreading is modulated by both hydrogel stiffness and viscoelasticity

After rheological characterization highlighted the tunable viscoelastic nature of our hydrogel design, we investigated the behavior of LX-2s, a human hepatic stellate cell line, when cultured on four hydrogel groups: soft elastic, stiff elastic, soft viscoelastic, and stiff viscoelastic. Cells on stiff elastic substrates showed increased spreading compared to cells on soft elastic substrates, similar to what has previously been reported for elastic substrates of increasing stiffness (**Figure 4.3**). In comparison the viscoelastic hydrogels, which had the same storage moduli as the corresponding elastic groups but higher loss moduli, supported decreased cell spreading and more rounded morphologies as measured by CSI compared to the corresponding elastic substrates for both the soft and stiff groups. The differences in cell spreading and circularity were the greatest between cells cultured on the stiff elastic hydrogels, which became more elongated and extended protrusions (average spread area: 6600 μm^2, CSI: 0.17), and cells cultured on the soft viscoelastic hydrogels, which showed smaller, more rounded morphologies (average spread area: 3000 μm^2, CSI: 0.26). The reduction in stellate cell spreading is similar to observations from a recent study where stellate cells showed reduced spreading and reduced expression of α-SMA, a marker of myofibroblast activation, when cultured on polyacrylamide substrates with higher loss moduli[18]. Similarly, although cells on our viscoelastic hydrogels showed positive α-SMA staining, we also observed reduction in the organization of α-SMA stress fibers that is typical of activated

myofibroblasts[18,41,42]. Although around 85% of cells on stiff elastic hydrogels displayed at least some organized α-SMA stress fibers, only 6 and 22% of cells on soft and stiff viscoelastic hydrogels, respectively, displayed well-organized α-SMA stress fibers (**Figure S4.7**).

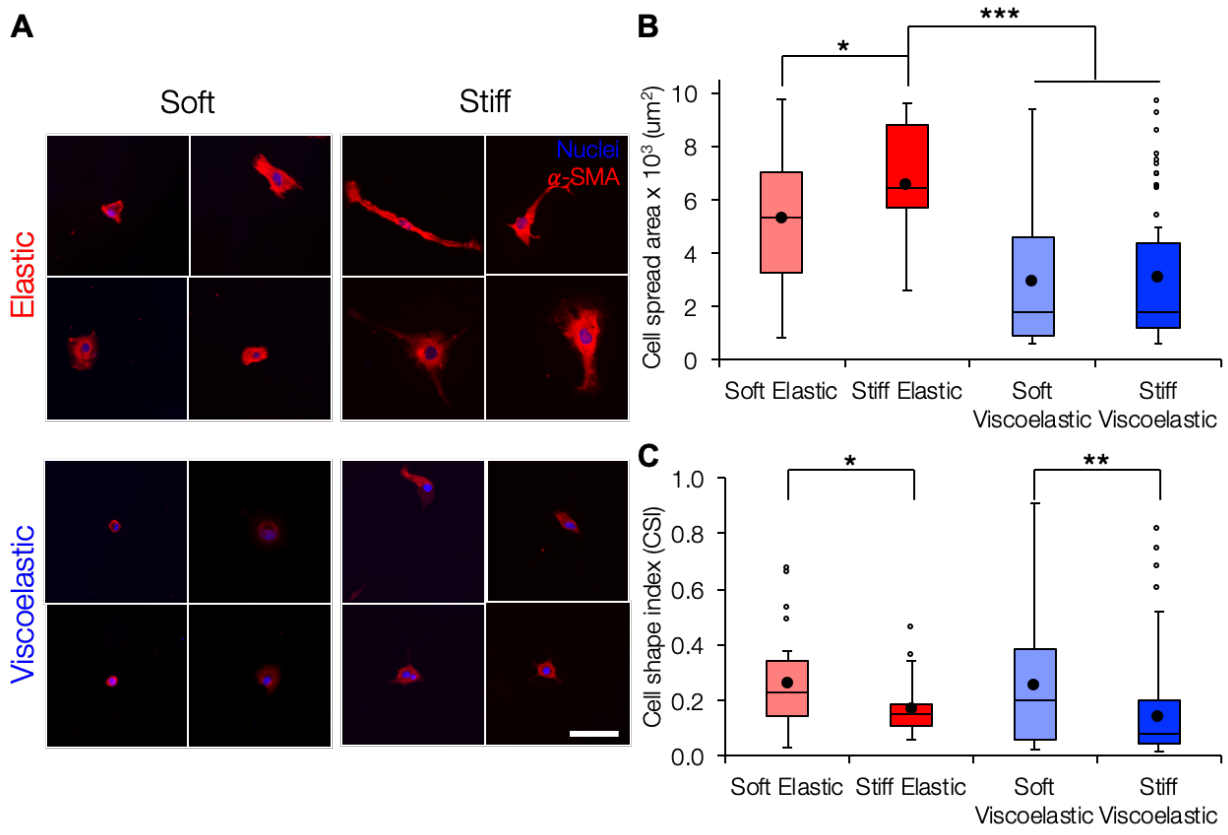

Figure 4.3. Cell spreading is modulated by both stiffness and viscoelasticity. (A) Representative images of LX-2 hepatic stellate cells stained for α-SMA (red) and nuclei (blue) after 7 days of culture. Scale bar 100 μm. (B) Although cell spreading was increased on stiff elastic compared to soft elastic hydrogels, spreading was significantly reduced on both soft and stiff viscoelastic hydrogels compared to the stiff elastic group. (C) CSI was significantly higher for cells on soft hydrogels compared to their respective stiff counterparts, indicating that the cells displayed more rounded morphologies. *: $P < 0.05$, **: $P < 0.01$, and ***: $P < 0.001$.

Because α-SMA expression is a relatively late marker of myofibroblast activation, we also investigated earlier markers of fibrogenic mechanotransduction. MRTF-A, a transcriptional coactivator implicated in the regulation and progression of fibrosis, which has been shown to drive

α-SMA expression and subsequent myofibroblast activation[43–45]. Specifically, activation of mechanotransduction pathways through cell−matrix interactions can promote RhoA/ROCK signaling, actin polymerization, and subsequent MRTF-A nuclear translocation. MRTF-A then interacts with serum response factor, the transcription factor that promotes upregulation of the Acta2 gene encoding for α-SMA[44,46–48]. We measured the ratio of MRTF-A nuclear to cytosolic signaling intensity and found elevated MRTF-A nuclear localization for cells on stiff compared to soft elastic hydrogels (**Figure S4.8**). However, cells cultured on the viscoelastic hydrogel groups showed reduced MRTF-A nuclear localization compared to the stiff elastic group. Overall, both soft and stiff viscoelastic hydrogels promoted reduced stellate cell spreading, α-SMA stress fiber organization, and MRTF-A nuclear localization. A possible explanation for these results could be that the higher loss moduli and rapid viscous dissipation of cell-generated traction forces into the matrix prevented spreading and the activation of the mechanoresponsive signaling pathways was investigated here[49]. Differences in cell spreading and MRTF-A nuclear localization between elastic and viscoelastic groups could also be attributed to differences in relaxation timescales and initial moduli.

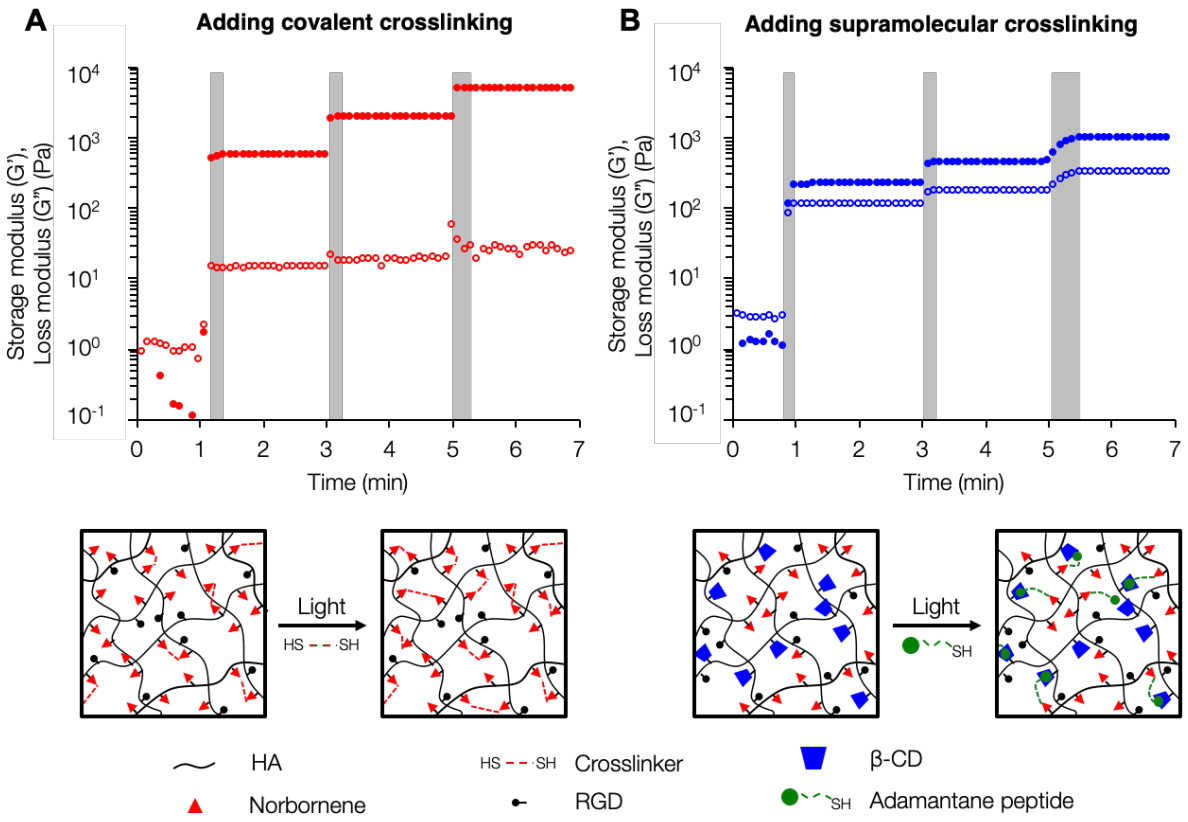

Figure 4.4. Secondary introduction of covalent or supramolecular cross-links to modulate viscoelastic properties. (A) When incorporating new covalent cross-links through DTT addition, each subsequent UV light exposure (gray bars) results in an increased storage modulus but minor changes in loss modulus. (B) Following initial formation of a viscoelastic hydrogel, incorporating new supramolecular guest−host cross-links leads to increases in both the storage and loss moduli with each UV light exposure.

4.4.4 Light-mediated thiol-ene addition enables secondary incorporation of covalent or supramolecular cross-links

Following the evaluation of cell behavior on static elastic and viscoelastic hydrogels, we next demonstrated the dynamic capabilities of our viscoelastic hydrogel system through specific secondary introduction of either covalent or supramolecular interactions. First, we fabricated elastic hydrogels with increasing covalent cross-linking density controlled by sequential bouts of light exposure, permitting further thiol−ene crosslinking. Rheological analysis indicated that each

additional irradiation corresponded with increasing storage modulus but relatively little change in loss modulus as expected for an elastic network (**Figure 4.4A**). Next, we made initially soft viscoelastic hydrogels containing unreacted norbornene and β-cyclodextrin groups and introduced additional supramolecular cross-links through sequential thiol−ene addition of thiolated adamantane peptide. Each additional light irradiation led to increases in both the storage and loss moduli as the hydrogel maintained its viscoelastic nature (**Figure 4.4B**). We observed that incorporating additional supramolecular cross-linking required progressively longer irradiation times, which is likely because of the difficulty of new incorporated supramolecular cross-links (via the Ad peptide) in finding both a free cyclodextrin group and neighboring norbornene group to associate with in the already cross-linked network. However, this change in irradiation time does not significantly impact the tunability of the system. Overall, the unique amenability of our system to the light-mediated introduction of either new covalent or supramolecular cross-links sets the stage for the creation of dynamic, heterogeneous viscoelastic hydrogels.

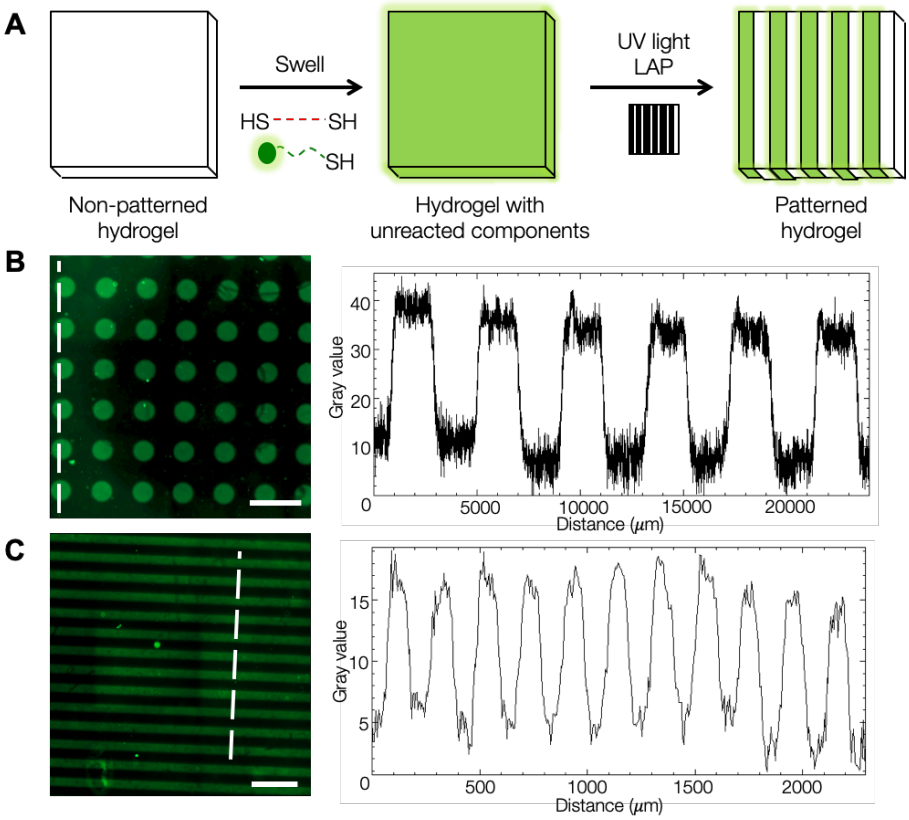

Figure 4.5. Photopatterning of hydrogels to introduce heterogeneous properties. (A) Schematic of the photopatterning process. NorHA hydrogels were swollen with thiolated molecules, covered with a photomask, and exposed to UV light, resulting in regions that underwent secondary cross-linking via light-mediated thiol−ene addition. A model of thiolated fluorescent peptide was used to demonstrate patterning capabilities. Color intensity profiles showed high pattern fidelity across pattern features for (B) 200 μm diameter circles and (C) 200 μm stripe patterns; signal intensity profiles were quantified along the white-dotted lines. Scale bars: 500 μm.

4.4.5 Photopatterning enables presentation of dynamic, heterogeneous, and cell-instructive viscoelastic hydrogel cues

After developing our viscoelastic hydrogel system and demonstrating its amenability to secondary cross-linking reactions, we explored the use of photopatterning to recapitulate the heterogeneity of matrix mechanical properties during fibrogenesis in a well-defined manner (**Figure 4.5**). Using photomasks to control light penetration into the hydrogel during secondary cross-linking enabled spatial control over the thiol−ene addition reactions. Soft NorHA hydrogels were swelled in a

solution containing 1 wt % BSA, LAP photoinitiator, DTT cross-linker or adamantane peptide, and thiolated fluorescent peptide for pattern visualization. Fluorescence microscopy confirmed pattern fidelity, with alternating fluorescent and nonfluorescent regions present in the hydrogel (**Figure 4.5B**).

After establishing the photopatterning approach, we wanted to develop a patterned hydrogel model of fibrotic tissue. During the heterogeneous progression of fibrosis, the aberrant shift in healthy tissue mechanics from soft and viscoelastic to stiff and more elastic highlights the need for in vitro models enabling independent spatiotemporal control of both stiffness and viscoelasticity. Given the ability for multiple light-mediated thiol−ene click reactions to occur in series, our hydrogel system can model both the heterogeneity of fibrosis through photopatterning and the induction of fibrosis progression through the introduction of new cross-links to stiffen the hydrogel. Starting from an initial soft viscoelastic hydrogel, we photopatterned additional covalent cross-links to create stiff, less viscoelastic hydrogel regions mimicking fibrotic nodules. AFM was used to characterize the elastic and viscoelastic properties of the patterned substrates. AFM nanoindentation tests demonstrated that patterned hydrogel regions undergoing secondary covalent cross-linking displayed higher Young's moduli (16.5 ± 0.23 kPa) compared to nonpatterned regions (1.78 ± 0.22 kPa) (**Figure 4.6A**). The viscoelasticity of the patterned hydrogel regions was characterized using a nanoindentation test, followed by a dwell period in which the AFM tip was held at a constant indentation depth to measure force as a function of time. The nonpatterned soft viscoelastic regions showed ∼20% force relaxation over a period of 10 s, whereas the patterned stiff elastic regions showed negligible relaxation (**Figure 4.6B, C**), similar to bulk rheological measurements for homogeneous hydrogels. Importantly, this novel method for

patterning viscoelasticity can be decoupled from changing the stiffness. As a demonstration of this, viscoelasticity can be patterned into a stiff elastic substrate through the introduction of supramolecular cross-links to produce regions of patterned, stiff viscoelasticity, as shown by force relaxation data without changing the overall Young's modulus under the measuring conditions of the AFM (initial stiff elastic = 10.6 ± 0.38 kPa, patterned stiff viscoelastic = 10.7 ± 0.49 kPa) (**Figure S4.9**).

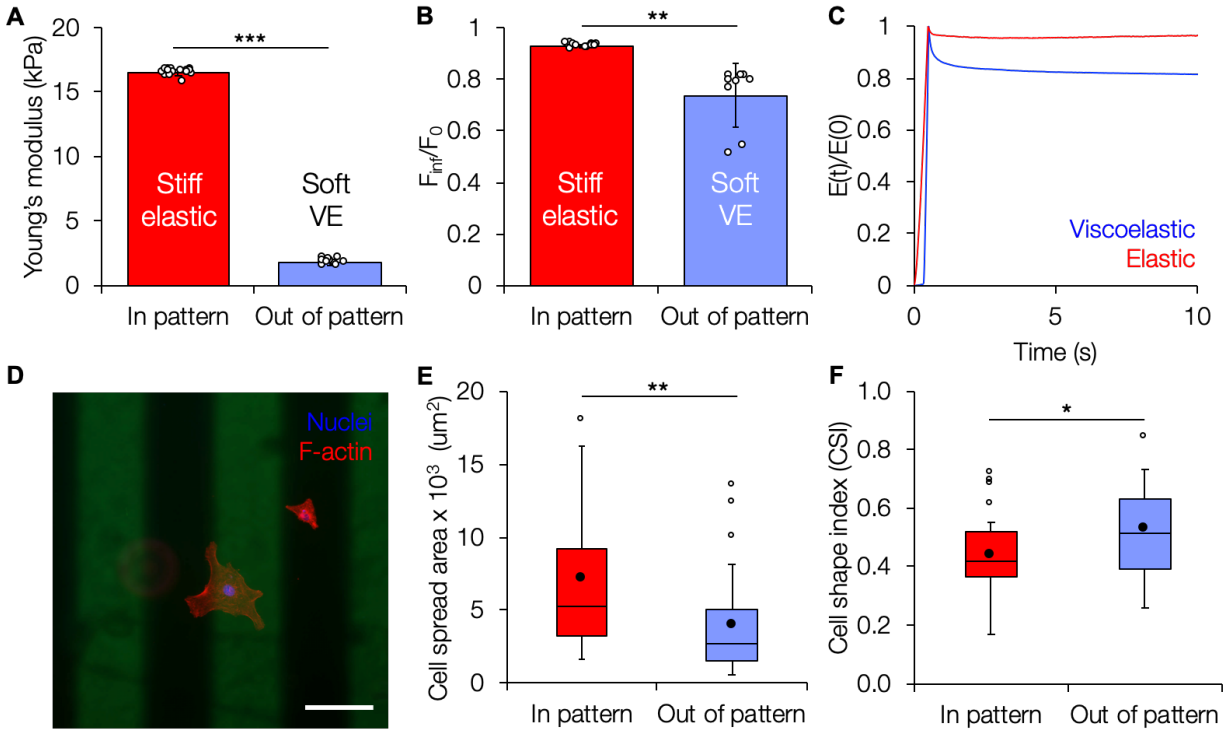

Figure 4.6. Mechanical characterization and cell response on patterned viscoelastic hydrogels. (A) Patterned (stiff elastic) and nonpatterned (soft viscoelastic) regions showed differences in Young's moduli similar to homogeneous substrates. (B) Quantification of the ratio of equilibrium force (F_{inf}) to initial indentation force (F_0) of patterned hydrogels indicates significantly greater levels of stress relaxation in the nonpatterned (soft viscoelastic) regions. (C) Time-dependent Young's modulus E(t) normalized to the initial instantaneous modulus E(0) showed ~20% relaxation in the nonpatterned soft viscoelastic regions compared to negligible relaxation for the stiff elastic patterned regions. (D) Representative fluorescent image of LX-2 stellate cells (red: F-actin, blue: nuclei) cultured for 7 days on a patterned hydrogel (200 μm wide stripes, green). Scale bar: 200 μm. (E) Cells on the patterned (stiff elastic) region showed significantly increased spread area compared to those in the nonpatterned (soft viscoelastic) regions. (F) Cells in the patterned regions

also showed significantly lower CSI, indicating a more elongated morphology, compared to more rounded cells in the nonpatterned regions. *: $P < 0.05$, **: $P < 0.01$, and ***: $P < 0.001$.

Next, we seeded LX-2 stellate cells onto soft viscoelastic hydrogels with patterned regions of stiff elastic mechanics (**Figure 4.6D**). Cells responded to the local mechanics of the patterned substrate and showed significantly increased spreading (Figure 6E) and significantly lower CSI (Figure 6F) on stiffer patterned regions. Although photopatterning was performed prior to cell seeding in these experiments, the reagents used are cytocompatible; therefore, we anticipate that these results will inform the future development of hydrogel models of heterogeneous tissue mechanics via in situ photopatterning in the presence of cells.

4.5 Conclusions

This work developed an approach to make viscoelastic hydrogels via light-mediated thiol−ene addition of both covalent and supramolecular cross-links. The use of light as a trigger for crosslinking enabled secondary modification of the hydrogel network to increase stiffness (mimicking initiation of fibrosis) and/or modulate viscoelasticity (through the introduction of covalent and/or supramolecular cross-links). We showed that LX-2 human hepatic stellate cells responded to the viscoelastic hydrogels by displaying reductions in spread area, MRTF-A nuclear translocation, and organization of actin stress fibers. We also used photopatterning to create hydrogels with stiff, elastic areas surrounded by soft, viscoelastic regions to mimic a heterogeneous fibrotic environment and showed that cells spread more in the stiffer patterned regions. Moving forward, we expect that this hydrogel system affording spatiotemporal control of stiffness and viscoelasticity will be useful to model a range of healthy and diseased cellular microenvironments.

4.6 Acknowledgements

The authors would like to thank Dr. Tom Barker and Dr. Wei Li for providing training and use of AFM, and Dr. Lin Han and Biao Han for providing the initial MATLAB code for AFM analysis. This work was supported by the University of Virginia and the Biotechnology Training Program NIGMS 5T32 GM008715.

4.7 References

(1) Wang, N.; Tytell, J. D.; Ingber, D. E. Mechanotransduction at a Distance: Mechanically Coupling the Extracellular Matrix with the Nucleus. *Nat. Rev. Mol. Cell Biol.* **2009**, *10* (1), 75–82. https://doi.org/10.1038/nrm2594.

(2) Dupont, S.; Morsut, L.; Aragona, M.; Enzo, E.; Giulitti, S.; Cordenonsi, M.; Zanconato, F.; Le Digabel, J.; Forcato, M.; Bicciato, S.; et al. Role of YAP/TAZ in Mechanotransduction. *Nature* **2011**, *474* (7350), 179–184. https://doi.org/10.1038/nature10137.

(3) Engler, A. J.; Sen, S.; Sweeney, H. L.; Discher, D. E. Matrix Elasticity Directs Stem Cell Lineage Specification. *Cell* **2006**, *126* (4), 677–689. https://doi.org/10.1016/j.cell.2006.06.044.

(4) Ingber, D. E. Cellular Mechanotransduction: Putting All the Pieces Together Again. *FASEB J. Off. Publ. Fed. Am. Soc. Exp. Biol.* **2006**, *20* (7), 811–827. https://doi.org/10.1096/fj.05-5424rev.

(5) Wells, R. G. Tissue Mechanics and Fibrosis. *Biochim. Biophys. Acta* **2014**, *1832* (7), 884–890. https://doi.org/10.1016/j.bbadis.2013.02.007.Tissue.

(6) Fiore, V. F.; Wong, S. S.; Tran, C.; Tan, C.; Xu, W.; Sulchek, T.; White, E. S.; Hagood, J. S.; Barker, T. H. Avβ3 Integrin Drives Fibroblast Contraction and Strain Stiffening of Soft Provisional Matrix during Progressive Fibrosis. *JCI Insight* **2018**, *3* (20). https://doi.org/10.1172/jci.insight.97597.

(7) Gurtner, G. C.; Werner, S.; Barrandon, Y.; Longaker, M. T. Wound Repair and Regeneration. *Nature* **2008**, *453* (7193), 314–321. https://doi.org/10.1038/nature07039.

(8) Wynn, T. A. Integrating Mechanisms of Pulmonary Fibrosis. *J. Exp. Med.* **2011**, *208* (7), 1339–1350. https://doi.org/10.1084/jem.20110551.

(9) Guvendiren, M.; Perepelyuk, M.; Wells, R. G.; Burdick, J. A. Hydrogels with Differential and Patterned Mechanics to Study Stiffness-Mediated Myofibroblastic Differentiation of Hepatic Stellate Cells. *J. Mech. Behav. Biomed. Mater.* **2014**, *38*, 198–208. https://doi.org/10.1016/j.jmbbm.2013.11.008.

(10) Olsen, A. L.; Bloomer, S. A.; Chan, E. P.; Gaça, M. D. A.; Georges, P. C.; Sackey, B.; Uemura, M.; Janmey, P. A.; Wells, R. G. Hepatic Stellate Cells Require a Stiff Environment for Myofibroblastic Differentiation. *Am J Physiol Gastroinstest Liver Physiol* **2011**, *301*, 110–118. https://doi.org/10.1152/ajpgi.00412.2010.

(11) Georges, P. C.; Hui, J.-J.; Gombos, Z.; McCormick, M. E.; Wang, A. Y.; Uemura, M.; Mick, R.; Janmey, P. A.; Furth, E. E.; Wells, R. G. Increased Stiffness of the Rat Liver Precedes Matrix Deposition: Implications for Fibrosis. *AJP Gastrointest. Liver Physiol.* **2007**, *293* (6), G1147–G1154. https://doi.org/10.1152/ajpgi.00032.2007.

(12) Levental, K. R.; Yu, H.; Kass, L.; Lakins, J. N.; Egeblad, M.; Erler, J. T.; Fong, S. F. T.; Csiszar, K.; Giaccia, A.; Weninger, W.; et al. Matrix Crosslinking Forces Tumor Progression by Enhancing Integrin Signaling. *Cell* **2009**, *139* (5), 891–906. https://doi.org/10.1016/j.cell.2009.10.027.

(13) Caliari, S. R.; Burdick, J. A. A Practical Guide to Hydrogels for Cell Culture. *Nat. Methods* **2016**, *13* (5), 405–414.

(14) Baker, B. M.; Chen, C. S. Deconstructing the Third Dimension – How 3D Culture Microenvironments Alter Cellular Cues. *J. Cell Sci.* **2012**, *125* (13), 3015–3024. https://doi.org/10.1242/jcs.079509.

(15) Chaudhuri, O.; Gu, L.; Klumpers, D.; Darnell, M.; Bencherif, S. A.; Weaver, J. C.; Huebsch, N.; Lee, H. P.; Lippens, E.; Duda, G. N.; et al. Hydrogels with Tunable Stress Relaxation Regulate Stem Cell Fate and Activity. *Nat. Mater.* **2016**, *15* (3), 326–334. https://doi.org/10.1038/nmat4489.

(16) Chaudhuri, O.; Gu, L.; Darnell, M.; Klumpers, D.; Bencherif, S. A.; Weaver, J. C.; Huebsch, N.; Mooney, D. J. Substrate Stress Relaxation Regulates Cell Spreading. *Nat. Commun.* **2015**, *6*, 1–7. https://doi.org/10.1038/ncomms7365.

(17) Cameron, A. R.; Frith, J. E.; Cooper-White, J. J. The Influence of Substrate Creep on Mesenchymal Stem Cell Behaviour and Phenotype. *Biomaterials* **2011**, *32* (26), 5979–5993. https://doi.org/10.1016/j.biomaterials.2011.04.003.

(18) Charrier, E. E.; Pogoda, K.; Wells, R. G.; Janmey, P. A. Control of Cell Morphology and Differentiation by Substrates with Independently Tunable Elasticity and Viscous Dissipation. *Nat. Commun.* **2018**, 1–13. https://doi.org/10.1038/s41467-018-02906-9.

(19) Pelham, R. J.; Wang, Y. Cell Locomotion and Focal Adhesions Are Regulated by Substrate Flexibility. *Proc. Natl. Acad. Sci.* **1997**, *94*, 13661–13665.

(20) Mcbeath, R.; Pirone, D. M.; Nelson, C. M.; Bhadriraju, K.; Chen, C. S. Cell Shape , Cytoskeletal Tension , and RhoA Regulate Stem Cell Lineage Commitment. *Dev. Cell* **2004**, *6*, 483–495.

(21) Wen, J. H.; Vincent, L. G.; Fuhrmann, A.; Choi, Y. S.; Hribar, K. C.; Taylor-Weiner, H.; Chen, S. C.; Engler, A. J. Interplay of Matrix Stiffness and Protein Tethering in Stem Cell Differentiation. *Nat. Mater.* **2014**, *13* (10), 979–987. https://doi.org/10.1038/Nmat4051.

(22) Yeh, Y. C.; Corbin, E. A.; Caliari, S. R.; Ouyang, L.; Vega, S. L.; Truitt, R.; Han, L.; Margulies, K. B.; Burdick, J. A. Mechanically Dynamic PDMS Substrates to Investigate Changing Cell Environments. *Biomaterials* **2017**, *145*, 23–32. https://doi.org/10.1016/j.biomaterials.2017.08.033.

(23) Mih, J. D.; Marinkovic, A.; Liu, F.; Sharif, A. S.; Tschumperlin, D. J. Matrix Stiffness Reverses the Effect of Actomyosin Tension on Cell Proliferation. *J. Cell Sci.* **2012**, *125* (24), 5974–5983. https://doi.org/10.1242/jcs.108886.

(24) Guvendiren, M.; Burdick, J. A. Stiffening Hydrogels to Probe Short- and Long-Term Cellular Responses to Dynamic Mechanics. *Nat. Commun.* **2012**, *3*, 792–799. https://doi.org/10.1038/ncomms1792.

(25) Wells, R. G. The Role of Matrix Stiffness in Regulating Cell Behavior. *Hepatology* **2008**, *47* (4), 1394–1400. https://doi.org/10.1002/hep.22193.

(26) Yang, C.; DelRio, F. W.; Ma, H.; Killaars, A. R.; Basta, L. P.; Kyburz, K. A.; Anseth, K. S. Spatially Patterned Matrix Elasticity Directs Stem Cell Fate. *Proc. Natl. Acad. Sci.* **2016**, *113* (31), E4439–E4445. https://doi.org/10.1073/pnas.1609731113.

(27) Marklein, R. A.; Burdick, J. A. Spatially Controlled Hydrogel Mechanics to Modulate Stem Cell Interactions. *Soft Matter* **2010**, *6* (1), 136–143. https://doi.org/10.1039/b916933d.

(28) Verdier, C.; Etienne, J.; Duperray, A.; Preziosi, L. Review: Rheological Properties of Biological Materials. *Comptes Rendus Phys.* **2009**, *10* (8), 790–811. https://doi.org/10.1016/j.crhy.2009.10.003.

(29) Rodell, C. B.; Dusaj, N. N.; Highley, C. B.; Burdick, J. A. Injectable and Cytocompatible Tough Double-Network Hydrogels through Tandem Supramolecular and Covalent Crosslinking. **2016**, 8419–8424. https://doi.org/10.1002/adma.201602268.

(30) McKinnon, D. D.; Domaille, D. W.; Cha, J. N.; Anseth, K. S. Biophysically Defined and Cytocompatible Covalently Adaptable Networks as Viscoelastic 3d Cell Culture Systems. *Adv. Mater.* **2014**, *26* (6), 865–872. https://doi.org/10.1002/adma.201303680.

(31) Gong, Z.; Szczesny, S. E.; Caliari, S. R.; Charrier, E. E.; Chaudhuri, O.; Cao, X.; Lin, Y.; Mauck, R. L.; Janmey, P. A.; Burdick, J. A.; et al. Matching Material and Cellular

Timescales Maximizes Cell Spreading on Viscoelastic Substrates. *Proc. Natl. Acad. Sci.* **2018**, *115* (12), E2686–E2695. https://doi.org/10.1073/pnas.1716620115.

(32) Tang, S.; Ma, H.; Tu, H.-C.; Wang, H.-R.; Lin, P.-C.; Anseth, K. S. Adaptable Fast Relaxing Boronate-Based Hydrogels for Probing Cell-Matrix Interactions. *Adv. Sci.* **2018**, *1800638* (9), 1800638. https://doi.org/10.1002/advs.201800638.

(33) Gramlich, W. M.; Kim, I. L.; Burdick, J. A. Synthesis and Orthogonal Photopatterning of Hyaluronic Acid Hydrogels with Thiol-Norbornene Chemistry. *Biomaterials* **2013**, *34* (38), 9803–9811. https://doi.org/10.1016/j.biomaterials.2013.08.089.

(34) Rodell, C. B.; Kaminski, A. L.; Burdick, J. A. Rational Design of Network Properties in Guest-Host Assembled and Shear-Thinning Hyaluronic Acid Hydrogels. *Biomacromolecules* **2013**, *14* (11), 4125–4134. https://doi.org/10.1021/bm401280z.

(35) Xu, L.; Hui, A. Y.; Albanis, E.; Arthur, M. J.; Blaner, W. S.; Mukherjee, P.; Friedman, S. L.; Eng, F. J. Human Hepatic Stellate Cell Lines, LX-1 and LX-2: New Tools for Analysis of Hepatic Fibrosis. **2005**, 142–151. https://doi.org/10.1136/gut.2004.042127.

(36) Han, B.; Chery, D. R.; Yin, J.; Lu, X. L.; Lee, D.; Han, L. Nanomechanics of Layer-by-Layer Polyelectrolyte Complexes: A Manifestation of Ionic Cross-Links and Fixed Charges. *Soft Matter* **2016**, *12* (4), 1158–1169. https://doi.org/10.1039/c5sm01430a.

(37) Li, Q.; Qu, F.; Han, B.; Wang, C.; Li, H.; Mauck, R. L.; Han, L. Micromechanical Anisotropy and Heterogeneity of the Meniscus Extracellular Matrix. *Acta Biomater.* **2017**, *54*, 356–366. https://doi.org/10.1016/j.actbio.2017.02.043.

(38) Rodell, C. B.; Jr, J. W. M.; Dorsey, S. M.; Wade, R. J.; Wang, L. L.; Woo, Y. J.; Burdick, J. A. Shear-Thinning Supramolecular Hydrogels with Secondary Autonomous Covalent Crosslinking to Modulate Viscoelastic Properties In Vivo. *Adv. Funct. Mater.* **2015**, *25*, 636–644. https://doi.org/10.1002/adfm.201403550.

(39) Hörning, M.; Nakahata, M.; Linke, P.; Yamamoto, A.; Veschgini, M.; Kaufmann, S.; Takashima, Y.; Harada, A.; Tanaka, M. Dynamic Mechano-Regulation of Myoblast Cells on Supramolecular Hydrogels Cross-Linked by Reversible Host-Guest Interactions. *Sci. Rep.* **2017**, *7* (1), 1–3. https://doi.org/10.1038/s41598-017-07934-x.

(40) Perepelyuk, M.; Chin, L.; Cao, X.; Van Oosten, A.; Shenoy, V. B.; Janmey, P. A.; Wells, R. G. Normal and Fibrotic Rat Livers Demonstrate Shear Strain Softening and Compression Stiffening: A Model for Soft Tissue Mechanics. *PLoS One* **2016**, *11* (1), 1–18.

https://doi.org/10.1371/journal.pone.0146588.

(41) Balestrini, J. L.; Chaudhry, S.; Sarrazy, V.; Koehler, A.; Hinz, B. The Mechanical Memory of Lung Myofibroblasts. *Integr. Biol.* **2012**, *4* (4), 410. https://doi.org/10.1039/c2ib00149g.

(42) Caliari, S. R.; Perepelyuk, M.; Cosgrove, B. D.; Tsai, S. J.; Lee, G. Y.; Mauck, R. L.; Wells, R. G.; Burdick, J. A. Stiffening Hydrogels for Investigating the Dynamics of Hepatic Stellate Cell Mechanotransduction during Myofibroblast Activation. *Sci. Rep.* **2016**, *6*, 1–10. https://doi.org/10.1038/srep21387.

(43) Parmacek, M. S. Myocardin-Related Transcription Factors: Critical Coactivators Regulating Cardiovascular Development and Adaptation. *Circ. Res.* **2007**, *100* (5), 633–644. https://doi.org/10.1161/01.RES.0000259563.61091.e8.

(44) Zhao, X.-H.; Laschinger, C.; Arora, P.; Szaszi, K.; Kapus, A.; McCulloch, C. A. Force Activates Smooth Muscle -Actin Promoter Activity through the Rho Signaling Pathway. *J. Cell Sci.* **2007**, *120* (10), 1801–1809. https://doi.org/10.1242/jcs.001586.

(45) O'Connor, J. W.; Gomez, E. W. Cell Adhesion and Shape Regulate TGF-Beta1-Induced Epithelial-Myofibroblast Transition via MRTF-A Signaling. *PLoS One* **2013**, *8* (12), 1–11. https://doi.org/10.1371/journal.pone.0083188.

(46) Hinson, J. S.; Medlin, M. D.; Lockman, K.; Taylor, J. M.; Mack, C. P. Smooth Muscle Cell-Specific Transcription Is Regulated by Nuclear Localization of the Myocardin-Related Transcription Factors. *AJP Hear. Circ. Physiol.* **2006**, *292* (2), H1170–H1180. https://doi.org/10.1152/ajpheart.00864.2006.

(47) Gupta, M.; Korol, A.; West-Mays, J. a. Nuclear Translocation of Myocardin-Related Transcription Factor-A during Transforming Growth Factor Beta-Induced Epithelial to Mesenchymal Transition of Lens Epithelial Cells. *Mol. Vis.* **2013**, *19* (May), 1017–1028.

(48) Marjoram, R. J.; Lessey, E. C.; Burridge, K. Regulation of RhoA Activity by Adhesion Molecules and Mechanotransduction. *Curr. Mol. Med.* **2014**, *14* (2), 199–208. https://doi.org/10.2174/1566524014666140128104541.

(49) Goffin, J. M.; Pittet, P.; Csucs, G.; Lussi, J. W.; Meister, J.-J.; Hinz, B. Focal Adhesion Size Controls Tension-Dependent Recruitment of α-Smooth Muscle Actin to Stress Fibers. *J. Cell Biol.* **2006**, *172* (2), 259. https://doi.org/10.1083/jcb.200506179.

4.8 Supplementary Figures

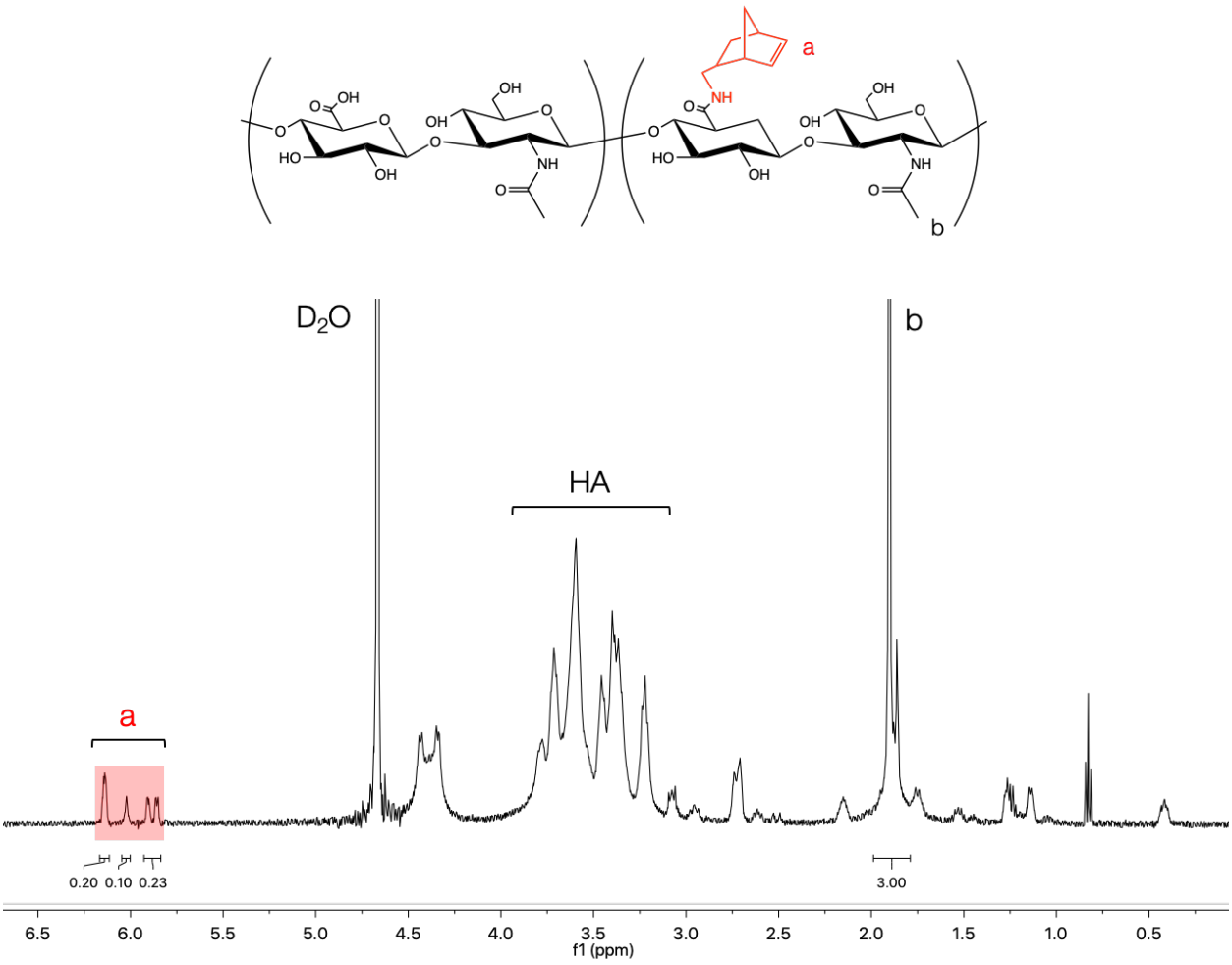

Figure S4.1. ^{1}H NMR spectrum of norbornene-modified hyaluronic acid (NorHA). The degree of modification was determined to be 22%.

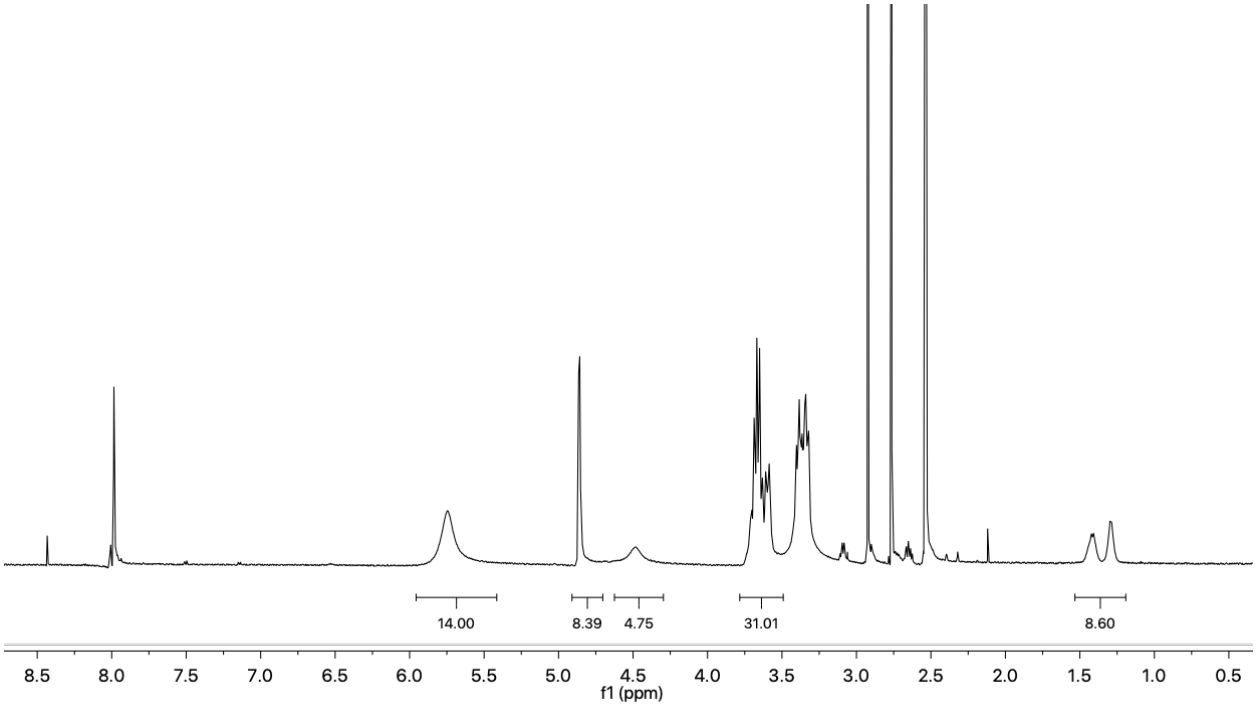

Figure S4.2. ^{1}H NMR spectrum of β-cyclodextrin hexamethylene diamine (β-CD-HDA). The degree of modification was determined to be 61%.

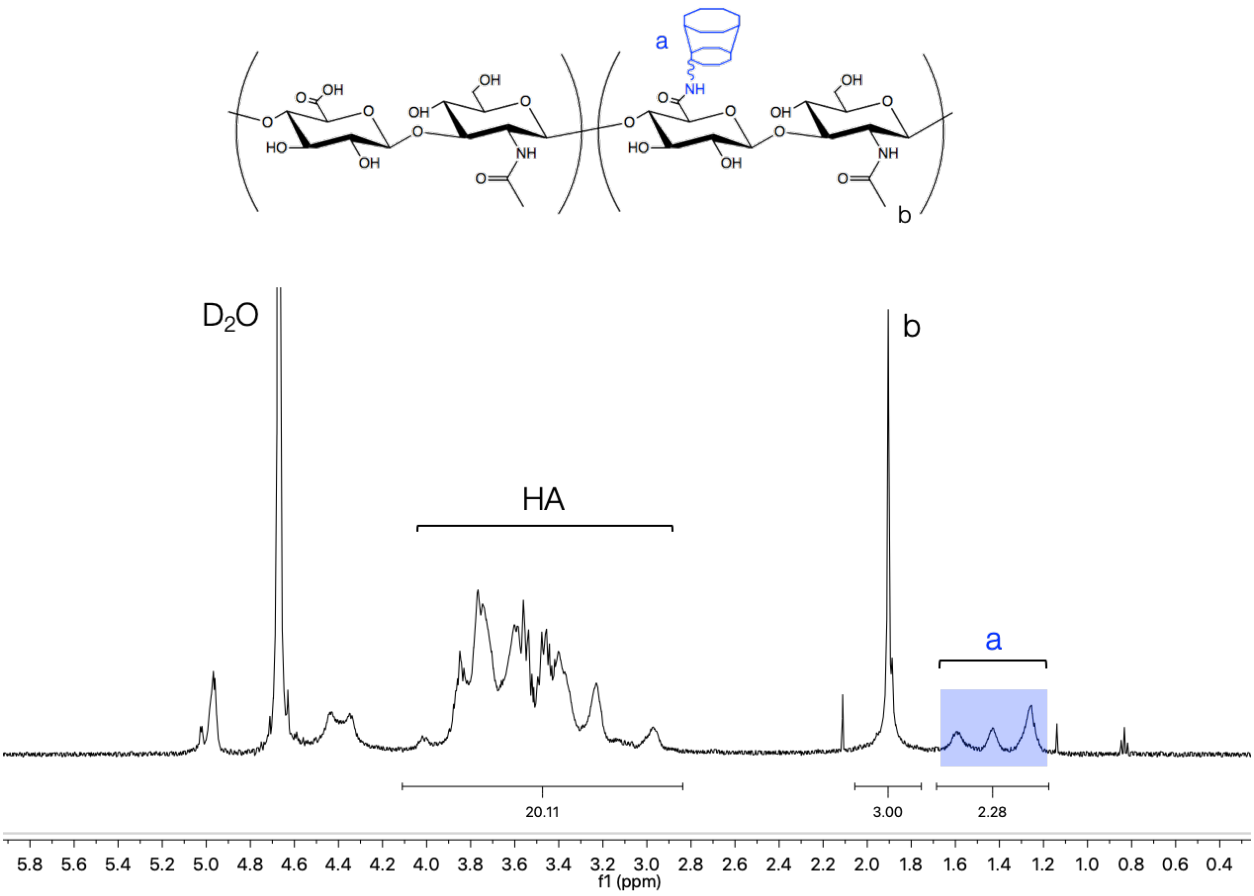

Figure S4.3. ^{1}H NMR spectrum of β-cyclodextrin-modified hyaluronic acid (CD-HA). The degree of modification was determined to be 27%.

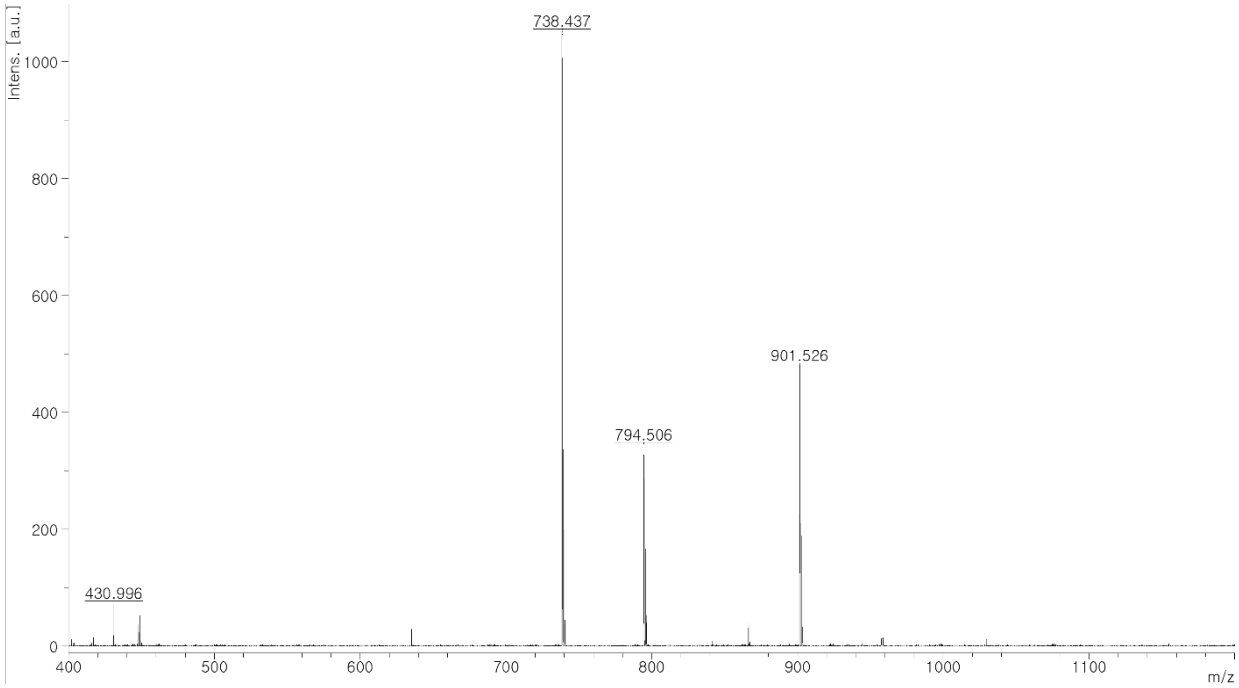

Figure S4.4. MALDI spectrum of adamantane peptide with the sequence 1-adamantaneacetic acid-KKKCG. Expected mass: 738.6 g/mol. Actual mass: 738.4 g/mol.

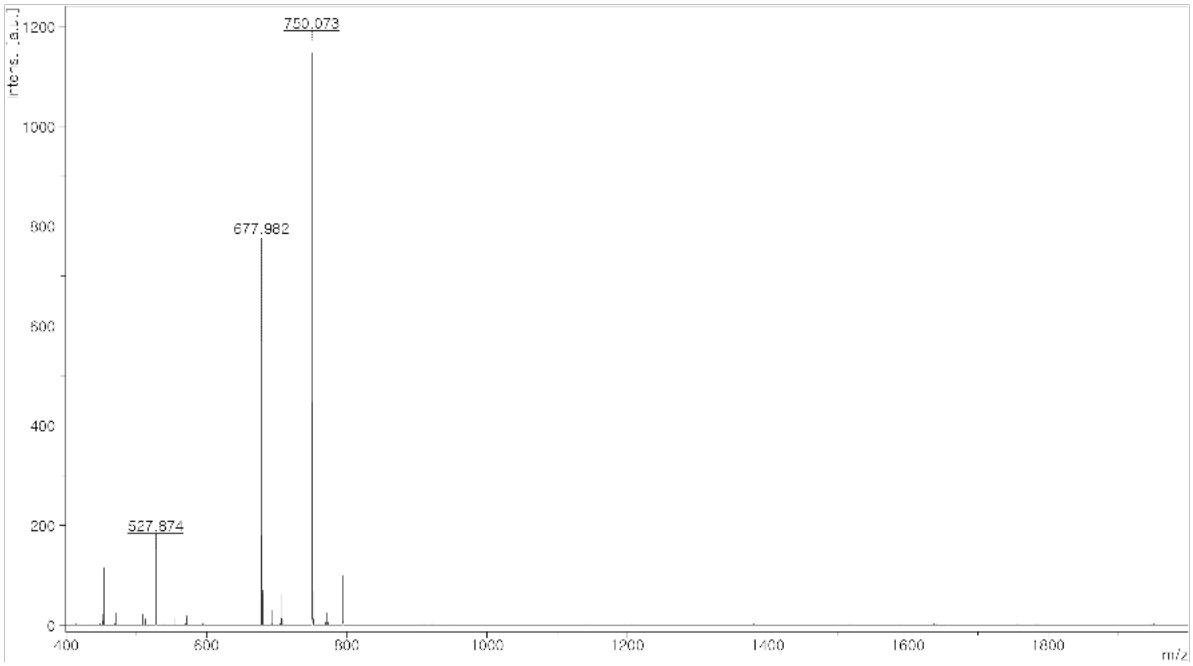

Figure S4.5. MALDI spectra of fluorescent peptide. Fluorescent peptide with the sequence Fluorescein-KKCG. Expected mass: 749 g/mol. Actual mass: 750 g/mol.

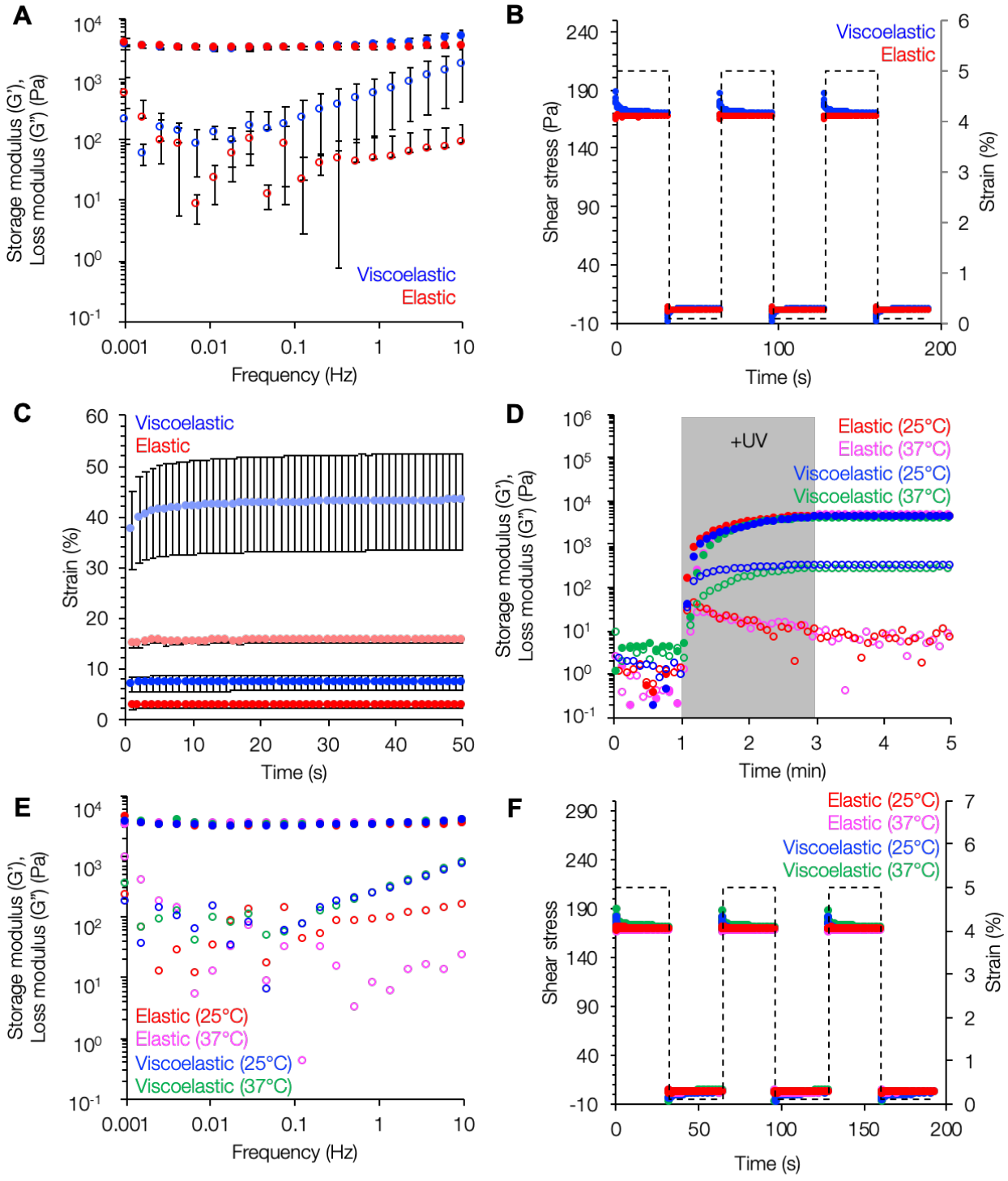

Figure S4.6. Additional rheological characterization of hydrogel groups. (A) Stiff viscoelastic hydrogels also showed frequency-dependent behavior with increasing loss moduli as frequency was increased, whereas the elastic hydrogel properties remained relatively constant. (B) Stress relaxation and recovery tests showed the full recovery of the mechanical properties of the

viscoelastic hydrogels. For the frequency and stress relaxation tests, the stiff hydrogel groups are shown; the soft hydrogel groups can be found in Figure 2. (C) Creep test for the viscoelastic hydrogels showed a modest increase in strain as a constant stress of 100 Pa was applied for soft viscoelastic groups but minimal change for stiff viscoelastic substrates. Rheological tests were performed at both 25°C and 37°C and compared for all groups (stiff elastic and viscoelastic groups shown). (D) In situ time sweeps, (E) frequency-dependent behavior, and (F) stress relaxation and recovery tests all showed similar behavior between the two temperatures.

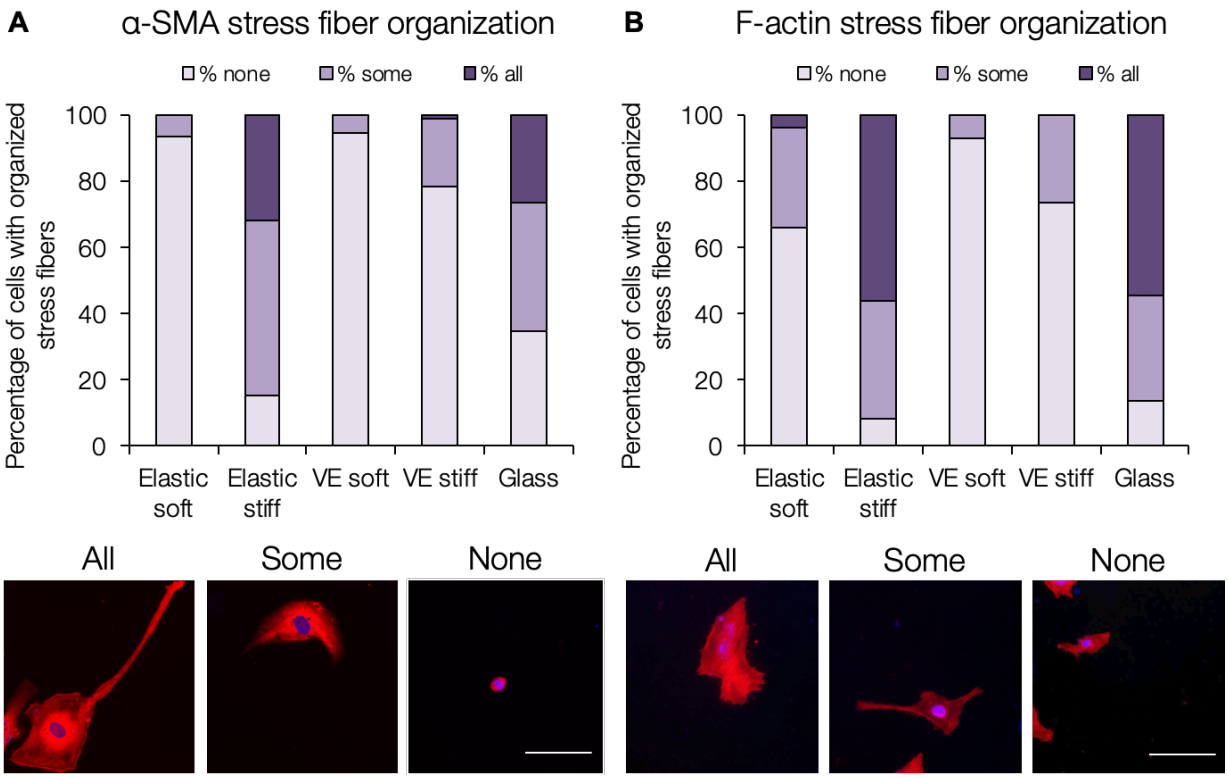

Figure S4.7. Characterization of stress fiber organization. Percentage of LX-2 hepatic stellate cells showing distinct stress fiber formation and representative cell images showing all, some, or no stress fiber organization. 50-120 cells were assessed per group. Scale bars 100 μm.

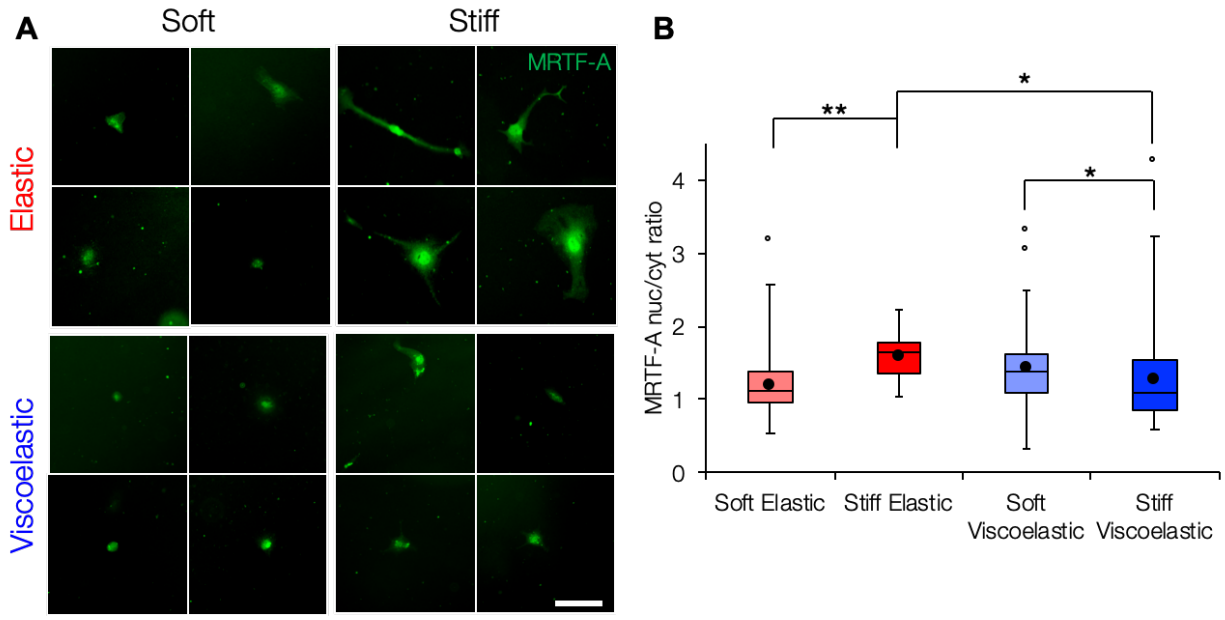

Figure S4.8. Quantification of MRTF-A nuclear localization. (A) Representative images of MRTF-A nuclear localization (green) in LX-2 hepatic stellate cells. (B) Quantification of the nuclear to cytosolic ratio of MRTF-A staining showed increased nuclear localization in the stiff elastic versus soft elastic groups (nuclear/cytosolic ratios of 1.61 and 1.20 respectively) while nuclear localization was similar between soft and stiff viscoelastic groups. Scale bar 100 μm. *: $P < 0.05$, **: $P < 0.01$.

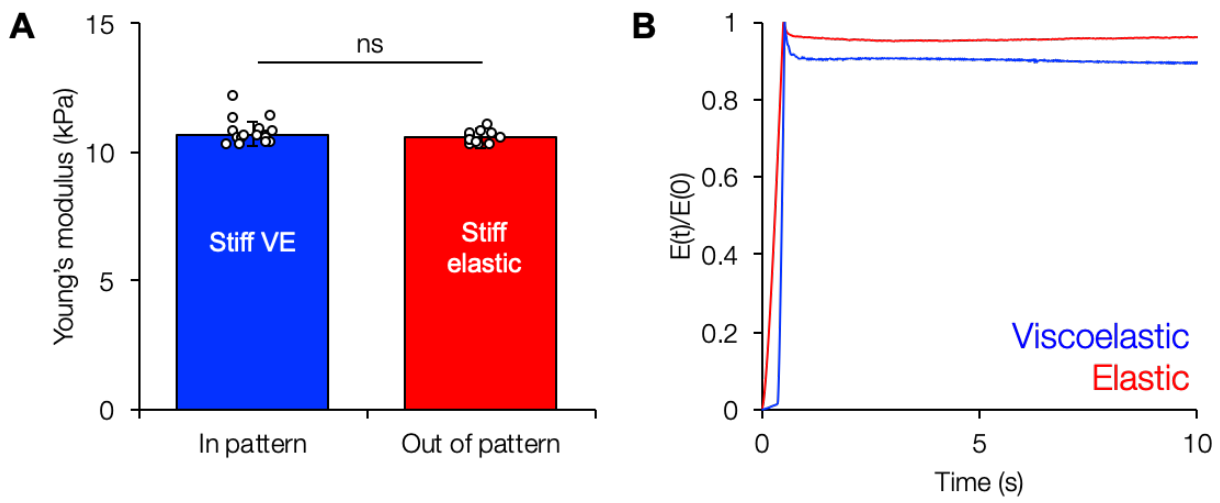

Figure S4.9. Patterning viscoelasticity without changing hydrogel Young's modulus. (A) Atomic force microscope (AFM) mechanical characterization of patterned (stiff viscoelastic) and non-patterned (stiff elastic) regions showed comparable Young's moduli. (B) Time-dependent Young's modulus E(t) normalized to the initial instantaneous modulus E(0) showed ~ 10% relaxation in the patterned stiff viscoelastic regions.

CHAPTER 5: THE COMBINED INFLUENCE OF VISCOELASTIC AND ADHESIVE CUES ON FIBROBLAST SPREADING AND FOCAL ADHESION ORGANIZATION

This chapter has been adapted from the following publication: Hui, E., Moretti, L., Barker, T.B., Caliari, S.R. "The Combined Influence of Viscoelastic and Adhesive Cues on Fibroblast Spreading and Focal Adhesion Organization" *Cellular and Molecular Bioengineering* **2021** (2021 CMBE Young Innovators Special Issue).

5.1 Abstract

Tissue fibrosis is characterized by progressive extracellular matrix (ECM) stiffening and loss of viscoelasticity that ultimately impairs organ functionality. Cells bind to the ECM through integrins, where αv integrin engagement in particular has been correlated with fibroblast activation into contractile myofibroblasts that drive fibrosis progression. There is a significant unmet need for *in vitro* hydrogel systems that deconstruct the complexity of native tissues to better understand the individual and combined effects of stiffness, viscoelasticity, and integrin engagement on fibroblast behavior. We developed hyaluronic acid hydrogels with independently tunable cell-instructive properties (stiffness, viscoelasticity, ligand presentation) to address this challenge. Hydrogels with mechanics matching normal or fibrotic lung tissue were synthesized using a combination of covalent crosslinks and supramolecular interactions to tune viscoelasticity. Cell adhesion was mediated through incorporation of either RGD peptide or engineered fibronectin fragments promoting preferential integrin engagement via αvβ3 or α5β1. On fibrosis-mimicking stiff elastic hydrogels, preferential αvβ3 engagement promoted increased spreading, actin stress fiber organization, and focal adhesion maturation as indicated by paxillin organization in human

lung fibroblasts. In contrast, preferential α5β1 binding suppressed these metrics. Viscoelasticity, mimicking the mechanics of healthy tissue, largely curtailed fibroblast spreading and focal adhesion organization independent of adhesive ligand type, highlighting its role in reducing fibroblast-activating behaviors. Together, these results provide new insights into how mechanical and adhesive cues collectively guide disease-relevant cell behaviors.

5.2 Introduction

Tissue fibrosis is a pathological scarring process characterized by the excessive deposition of crosslinked extracellular matrix (ECM) proteins leading to progressive matrix stiffening and decreased viscoelasticity[1–6]. These aberrant changes in tissue mechanics detrimentally impact organ function, contributing to the role fibrosis plays in nearly half of all deaths in the developed world[7–9]. Reciprocal interactions between fibroblasts and their surrounding extracellular microenvironment actively drive a cascade of biochemical and biophysical signaling events to direct both normal and fibrogenic behaviors including adhesion, spreading, focal adhesion organization, and activation into fibrosis-promoting myofibroblasts[10–15]. However, delineating the specific environmental regulators of fibroblast behavior is difficult in multifaceted tissue milieus.

Numerous in vitro studies have used hydrogel biomaterials to deconstruct complex in vivo cellular microenvironments to better understand the individual and combined influence of biophysical factors such as stiffness and viscoelasticity on driving fibrogenic cell behaviors[16–23]. It is well understood that stiffer microenvironments guide mechanotransduction by providing biophysical cues for fibroblast activation. Culturing cells atop substrates of increasing stiffness promotes increased spreading, actin stress fiber organization, and nuclear localization of transcriptional

cofactors regulating the expression of fibrogenic genes encoding α-smooth muscle actin (α-SMA) and type I collagen[23–30]. While many studies of mechanotransduction use covalently-crosslinked hydrogels that behave as linearly elastic solids, tissues are viscoelastic, meaning they exhibit both elastic solid and viscous liquidlike behaviors such as stress relaxation[1,31,32]. Seminal studies incorporating viscoelasticity into hydrogels showed that, compared to stiffness-matched elastic controls, cells displayed reduced spreading and expression of disease-relevant markers such as α-SMA with increasing loss modulus (viscoelasticity) due to reduced cellular contractility as a result of viscous dissipation[20,33], highlighting the importance of viscoelasticity in disease mechanobiology.

While stiffness and viscoelasticity are well-established regulators of cell behavior, comparatively little attention has been paid to engineering hydrogels that can control cell adhesive interactions through preferential integrin engagement. Integrins are transmembrane proteins composed of a and b subunits that bind to the ECM and serve as conduits for biochemical and mechanical signaling between cells and the ECM[34,35]. Importantly, integrin-based adhesions enable the conversion of complex biophysical cues, such as matrix mechanics and viscoelasticity, into chemical signals through mechanotransduction[36–40]. Integrin engagement and clustering facilitates the recruitment and formation of force dependent focal adhesions (FAs) composed of proteins including paxillin, which play an important role in regulating cell behaviors such as spreading, contraction, migration, and differentiation[11,13–15,41,42]. As nascent cell–matrix adhesions (< 0.25 μm) mature into stable and larger FAs (1–5 μm), this strengthens integrin-FA-cytoskeletal linkages, facilitating actin polymerization and stress fiber organization, nuclear localization of transcriptional mechanoregulators, and the transcription of fibrogenic genes that ultimately results in dysregulated

ECM production and organ failure[13,39,43–47]. While many synthetic hydrogels are engineered to support integrin-mediated cell attachment by incorporating the fibronectin-derived RGD peptide, this may inadvertently convolute mechanobiology studies due to its inefficient cell binding affinity compared to longer peptide or protein domains as well as its ability to non-specifically bind multiple integrin heterodimers[48]. Recent work has shown that provisional matrix proteins such as fibronectin (Fn) are upregulated during early stages of tissue remodeling and that preferential engagement of specific Fn-associated integrins (e.g., αvβ3 vs. α5β1) caused by tension-stimulated conformational changes can influence fibrosis mechanoregulation[1,37,39,49]. In particular, engagement of the αv integrin has been shown to promote integrin-mediated myofibroblast contractility[1,41,45,50], mechanoactivation of latent transforming growth factor-beta 1 (TGF-β1)[38,51,52], and expression and organization of α-SMA stress fibers, a hallmark of myofibroblast activation[24,53,54].

While several studies, including from our group[33], have highlighted the importance of stiffness and viscoelasticity in directing cell behavior, an approach to independently manipulate stiffness, viscoelasticity, and integrin engagement in a single system has not been developed. To address this challenge, we designed a phototunable viscoelastic hydrogel platform to deconstruct the complexity of native tissue toward understanding the individual and combined roles of cell-instructive cues including stiffness, viscoelasticity, and integrin-binding ligand presentation. We then used this system to determine how multiple mechanoregulatory cues work together to guide cellular behavior in the context of fibroblast activation.

5.3 Materials and Methods

5.3.1 NorHA synthesis

HA was functionalized with norbornene groups as previously described[33,55]. Sodium hyaluronate (Lifecore, 62 kDa) was converted to hyaluronic acid tertbutyl ammonium salt (HA-TBA) via proton exchange with Dowex 50W resin prior to being filtered, titrated to pH 7.05, frozen, and lyophilized. 5-norbornene-2-methylamine and benzotriazole-1-yloxytris(dimethylamino)-phosphonium hexafluorophosphate (BOP) were added dropwise to HA-TBA in dimethylsulfoxide (DMSO) and reacted for 2 h at 25°C, quenched with cold water, dialyzed (molecular weight cutoff: 6– 8 kDa) for 5 days, filtered, dialyzed for 5 more days, frozen, and lyophilized. The degree of modification was 31% as determined via proton nuclear magnetic resonance (^{1}H NMR, 500 MHz Varian Inova 500, **Figure S5.1**).

5.3.2 β-CD-HA synthesis

β-cyclodextrin modified hyaluronic acid (CD-HA) was synthesized by coupling synthesized 6-(6-aminohexyl)amino-6-deoxy-β-cyclodextrin (β-CD-HDA) to HA-TBA in anhydrous DMSO in the presence of BOP[33,56]. The amidation reaction was carried out at 25°C for 3 h, quenched with cold water, dialyzed for 5 days, filtered, dialyzed for 5 more days, frozen, and lyophilized. The degree of modification was 28% as determined by ^{1}H NMR (**Figure S5.2**).

5.3.3 Peptide synthesis

Thiolated adamantane peptide (Ad-KKKCG) was synthesized on Rink Amide MBHA high-loaded (0.78 mmol/g) resin using solid phase peptide synthesis as previously described[33]. The peptide was cleaved in 95% trifluoroacetic acid, 2.5% triisopropylsilane, and 2.5% H2O for 2–3 h, precipitated

in cold ether, dried, resuspended in water, frozen, and lyophilized. Synthesis was confirmed via matrix-assisted laser desorption/ionization (MALDI) mass spectrometry (**Figure S5.3**).

5.3.4 Recombinant fibronectin fragments

Recombinant fibronectin fragments of the ninth and tenth type III repeat units (FnIII9 and FnIII10) were designed to preferentially bind α5β1 or αvβ3 integrin heterodimers as previously described[1,57,58]. Fibronectin fragments were separately expressed in E. coli and purified via a Strep-Tag II column in house. Briefly, to promote α5β1 binding, FnIII9 was thermodynamically stabilized through a leucine to proline point mutation at position 1408, which has demonstrated stabilization of the spatial orientation of the RGD motif on FnIII10 and the synergy site PHSRN on FnIII9, increasing selectivity to β1 integrins[59]. While this fragment still supports αvβ3 binding, it has greater α5β1 integrin-binding affinity (KD ~ 12 nM for α5β1 vs. ~ 40 nM for αvβ3)[59]. We have referred to this fragment as 'Fn9*10' throughout the manuscript. For preferential αvβ3 integrin binding, four glycine residues were inserted into the liner region between FnIII9 and FnIII10 to disrupt α5β1 binding by increasing the separation between the RGD and PHSRN sites. This fragment is denoted 'Fn4G'. Both fibronectin fragments contained N-terminal cysteine residues to enable thiol-ene coupling to the HA hydrogels. Fragment quality was validated using ELISA. The thiolated fragments were first covalently bound to maleimide-activated plates (Thermo Fisher Scientific, 15150, 20 μg/mL). Bound fragments were then detected using the single chain fragment antibody H5 engineered to recognize both Fn9*10 and Fn4G as described previously[59].

5.3.5 HA hydrogel fabrication

Thin film hydrogels (18 x 18 mm, ~ 100 μm thickness) were fabricated on thiolated coverslips via ultraviolet (UV)-light mediated thiol-ene addition, similar to previously established methods[33]. 'Soft' and 'stiff' hydrogel formulations were designed to match normal (Young's modulus or stiffness ~ 1 kPa) and fibrotic (~ 15 kPa) stiffnesses respectively[1,3,5,60]. Covalently-crosslinked soft (2 wt% NorHA) and stiff (6 wt% NorHA) elastic hydrogels formulations were crosslinked with dithiothreitol (DTT, thiol-norbornene ratios of 0.22 and 0.35 for soft and stiff groups, respectively). Soft (2 wt% NorHA-CDHA) and stiff (6 wt% NorHA-CDHA) viscoelastic hydrogels were fabricated through a combination of covalent and physical crosslinking. NorHA and DTT (covalent crosslinks, thiol-norbornene ratios of 0.35 and 0.55 for soft and stiff groups, respectively) were combined with CD-HA and thiolated adamantane (Ad) peptides (supramolecular guest–host interactions between CD and Ad, 1:1 molar ratio of CD to Ad). Cell adhesion was enabled in all hydrogel groups through incorporation of either 1 mM RGD peptide (GCGYGRGDSPG, Genscript) or 2 μM thiolated Fn fragments (Fn9*10 or Fn4G). Hydrogel solutions were photopolymerized (365 nm, 5 mW/cm^2) between coverslips in the presence of 1 mM lithium acylphosphinate (LAP) photoinitiator for 2 min and swelled in PBS overnight at 37°C before subsequent experiments.

5.3.6 Mechanical characterization

Hydrogel rheological properties were quantified on an Anton Paar MCR 302 rheometer using a cone-plate geometry (25 mm diameter, 0.5°, 25 μm gap). *In situ* gelation via 2 min UV light irradiation (5 mW/cm^2) was tracked using oscillatory time sweeps (1 Hz, 1% strain) followed by oscillatory frequency sweeps (0.001–10 Hz, 1% strain) and cyclic stress relaxation and recovery tests alternating between 0.1 and 5% strain. Nanoindentation tests were performed using Optics11

Piuma and Chiaro nanoindenters on hydrogels swollen in PBS for at least 24 h to determine hydrogel mechanical characteristics. A 25 μm diameter spherical borosilicate glass probe attached to a cantilever with a spring constant of 0.5 N/m was used during testing. For each indentation, the loading portion of the generated force versus distance indentation curve was used to determine the Young's modulus by applying the Hertzian contact mechanics model and assuming a Poisson's ratio of 0.5. The Optics11 nanoindenter software also features a dynamic operational mode to enable dynamic mechanical analysis (DMA)-like measurements through mechanical oscillations. DMA measurements were performed to quantify viscoelasticity (G' and G") of swollen hydrogels via frequency sweeps (0.1–10 Hz) and force relaxation tests.

5.3.7 Cell culture

Human lung fibroblasts (hTERT T1015, abmgood) were used between passages 7–12 and culture medium was changed every 2–3 days (Gibco Dulbecco's Modified Eagle Medium (DMEM) supplemented with 10 v/v% fetal bovine serum (FBS) and 1 v/v% antibiotic antimycotic (1000 U/mL penicillin, 1000 μg/mL streptomycin, and 0.25 μg/mL amphotericin B)). Normal human lung fibroblasts (CC-2512, Lonza) were used between passages 3–5 for paxillin experiments and culture medium was changed every 2– 3 days (Lonza FBM Basal Medium supplemented with 2 v/v% fetal bovine serum (FBS), 0.1 v/v% human recombinant insulin (1–20 μg/mL), 0.1 v/v% recombinant human fibroblast growth factor-B (rhFGF-B, 0.5–5 ng/mL), and 0.1 v/v% gentamicin sulfate amphotericin B (GA-1000, 30 μg/mL gentamicin and 15 ng/mL amphotericin)). Swelled hydrogels were sterilized in non-TC-treated 6-well plates via germicidal UV irradiation for at least 2 h and incubated in culture medium for at least 30 min prior to cell seeding. Cells were seeded at 2 x 10^4 cells/hydrogel (18 x 18 mm).

5.3.8 Immunostaining, imaging, and analysis

Cell-seeded hydrogels were fixed in 10% neutral buffered formalin for 15 min, permeabilized in PBST (0.1% Triton X-100 in PBS) for 10 min, and blocked in 3% bovine serum albumin (BSA) in PBS for at least 1 h at 25°C. To visualize focal adhesions (FAs), cells were fixed using a microtubule stabilization buffer for 10 min at 37°C before blocking. Hydrogels were then incubated overnight at 4°C with primary antibodies. Primary antibodies used in this work included paxillin (mouse monoclonal anti-paxillin B-2, Santa Cruz Biotechnology, sc-365379, 1:500) to visualize FA formation and α-smooth muscle actin (α-SMA, mouse monoclonal anti-α-SMA clone 1A4, Sigma-Aldrich, A2547, 1:400). Hydrogels were washed three times using PBS and incubated with secondary antibodies (AlexaFluor 488 goat anti-mouse IgG or AlexaFluor 555 goat anti-mouse IgG, Invitrogen, 1:600–800) and/or rhodamine phalloidin (Invitrogen, R415 1:600) to visualize F-actin for 2 h in the dark at 25°C. Hydrogels were rinsed three times with PBS and incubated with a DAPI nuclear stain (Invitrogen, D1306, 1:10000) for 1 min before washing with PBS. Images were taken on a Zeiss AxioObserver 7 inverted microscope. Cell spread area and cell shape index were determined using a CellProfiler (Broad Institute, Harvard/MIT) pipeline modified to include adaptive thresholding. Cell shape index determines the circularity of the cell, where a line and a circle have values of 0 and 1, respectively, and was calculated using the formula:

$$CSI = \frac{4\pi A}{P^2}$$

where A is the cell area and P is the cell perimeter. For qualitative analysis of actin stress fiber organization, cells were binned into three categories – "mostly stress fibers" showed stress fibers in over 60% of the cell area, "some stress fibers" constituted those with roughly 15-60% stress fibers, and "no stress fibers" showed only diffuse actin staining. For FA analysis, cells stained with

paxillin were imaged using a 40x oil objective. FA count, area, and fluorescence intensity were quantified via the Focal Adhesion Analysis Server (FAAS)[61] automated imaging processing pipeline using a 4.5 threshold and minimum pixel size of 25.

5.3.9 Statistical analysis

For mechanical characterization, at least three technical replicates were performed and the data were presented as mean ± standard deviation. For statistical comparisons between hydrogel groups, two-way ANOVA with Tukey's HSD post hoc analysis (more than two experimental groups) were performed. All experiments included at least 3 replicate hydrogels per experimental group. Box plots of single cell data include median/mean indicators as well as error bars corresponding to the lower value of either the 1.5*interquartile range or the maximum/minimum value, with data points outside the 1.5*interquartile range shown as open circles. Statistically significant differences are indicated by *, **, or *** corresponding to $P < 0.05$, 0.01, or 0.001 respectively.

5.4 Results and Discussion

5.4.1 Hydrogels were designed to independently control stiffness, viscoelasticity, and presentation of integrin-binding adhesive sites

Hyaluronic acid (HA) hydrogels representing normal (G' ~ 0.5 kPa) and fibrotic (G' ~ 5 kPa) lung tissue mechanics were fabricated with a combination of covalent crosslinks and supramolecular guest–host interactions to impart viscous properties (**Figure 5.1**)[33,56,62]. HA was chosen as the hydrogel backbone for its ability to be chemically modified with various functional groups to achieve a range of viscoelastic properties covering healthy and diseased soft tissue, as shown in

previous work by our lab and others[33,55,63–66]. Stiffness was controlled primarily through adjusting the concentration of HA and the ratio of dithiol crosslinker to norbornene groups on HA. Several methods to incorporate viscoelasticity into material systems have been developed, including the addition of sterically entrapped high molecular weight linear polymers to introduce viscosity[20,67], covalent adaptable networks[68–70], physical crosslinking of natural polymers (e.g., alginate[71,72], collagen[73,74]) for modulation of stress relaxation properties, and supramolecular crosslinking chemistries (e.g., host–guest complexes[33,56,75,76]). In this work, the addition of supramolecular guest–host interactions between β-cyclodextrin HA (CD-HA) and thiolated adamantane (Ad) peptides (1:1 molar ratio of CD to Ad), where the hydrophobic Ad guest moiety has a high affinity for the hydrophobic interior of CD, introduced viscous characteristics into the system[33,56]. Elastic hydrogel substrates contained only covalent crosslinks, while viscoelastic substrates included a combination of covalent and supramolecular interactions.

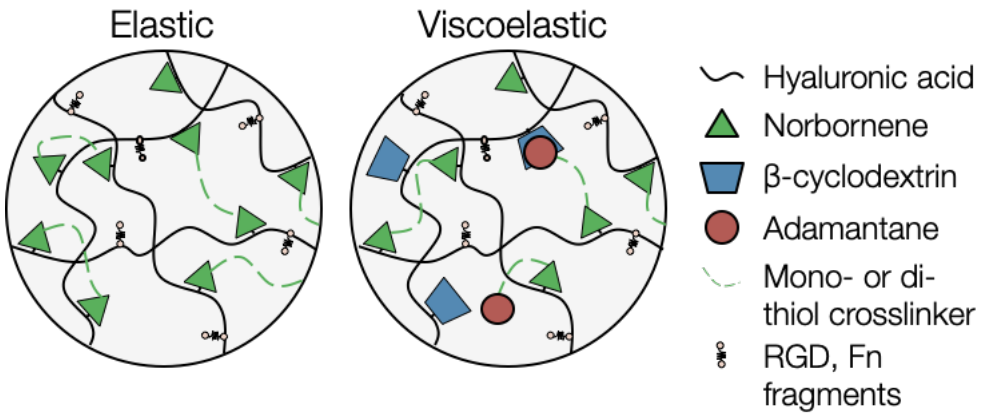

Figure 5.1. Schematic of elastic and viscoelastic hyaluronic acid hydrogel design. Covalent crosslinks between norbornenes and di-thiol crosslinkers are formed via light-mediated thiol-ene addition to create elastic hydrogel networks. A combination of covalent crosslinking and supramolecular guest–host interactions between cyclodextrins and thiolated adamantane groups confer viscous characteristics to the viscoelastic system. Thiolated adhesive ligands (RGD or Fn fragments) were also incorporated during hydrogel formation.

While HA is a natural ECM component and interacts with cell surface receptors including CD44 and RHAMM in its unmodified forms, it does not support integrin binding, allowing customization of these interactions in our hydrogel design[17,77]. In addition to controlling hydrogel stiffness and viscoelasticity by modulating crosslinking as described above, we hypothesized that we could also dictate cellular adhesion through the incorporation of either thiolated RGD peptide or Fn fragments designed to preferentially bind αvβ3 (Fn4G) or α5β1 (Fn9*10) integrins[1,57,58]. Preferential α5β1 engagement in Fn9*10 is engineered by stabilizing the spatial proximity of the PHSRN synergy site on FnIII9 with the RGD on FnIII10, although Fn9*10 can also bind αvβ3[59]. Insertion of a four glycine spacer between FnIII9 and FnIII10 in Fn4G abrogates simultaneous binding to both the PHSRN and RGD sequences necessary for α5β1 engagement, leading to preferential αvβ3 binding[59]. Since the RGD peptide does not contain the PHSRN synergy sequence, we anticipate that it would also preferentially engage αvβ3 over α5β1. Overall, the modular hydrogel design allows independent control of HA content, crosslinking type and density, and adhesive ligand incorporation to enable simultaneous tuning of stiffness, viscoelasticity, and integrin engagement.

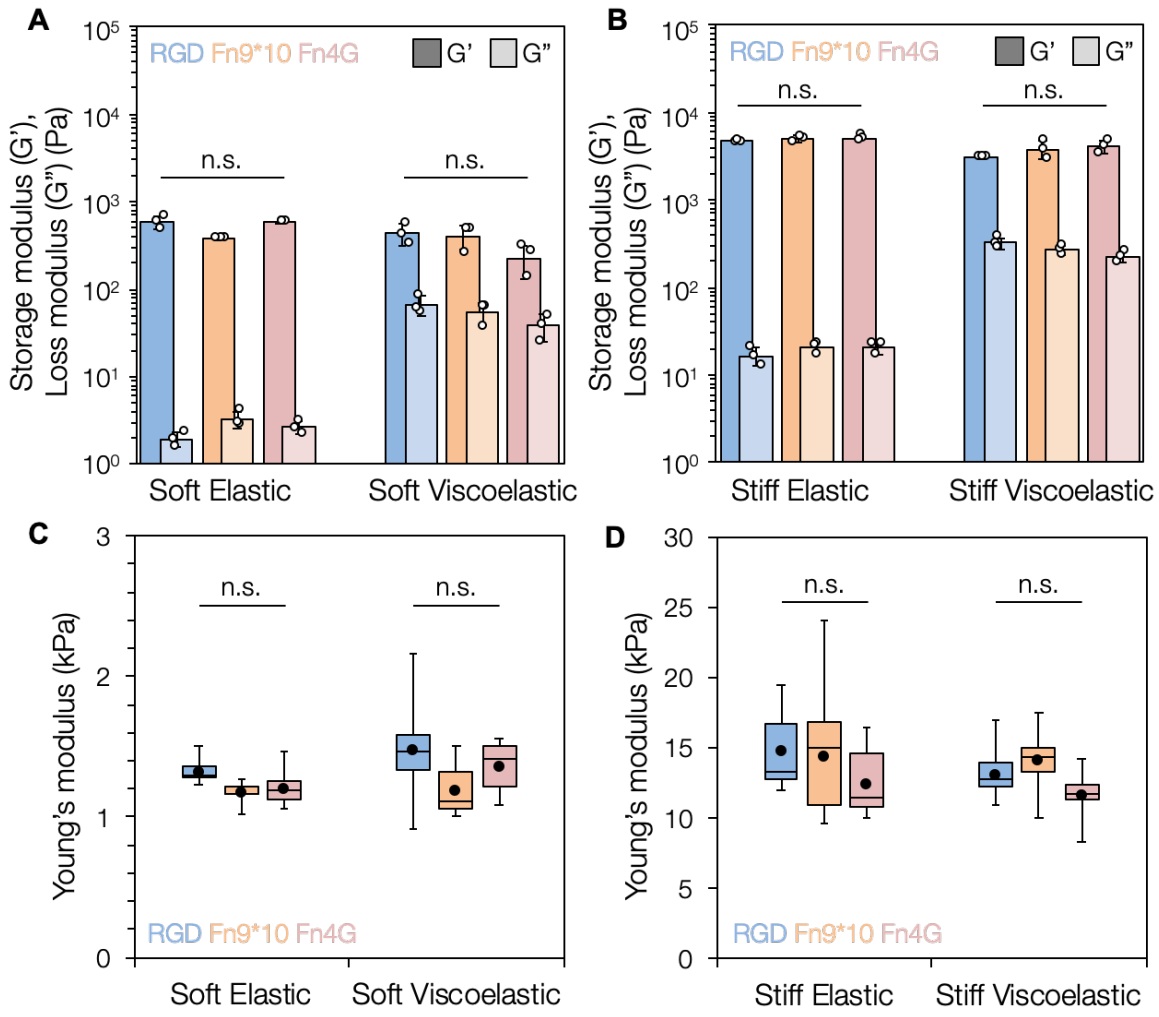

Figure 5.2. Mechanical characterization of viscoelastic hydrogels. (a) Average values of soft elastic and soft viscoelastic storage (*G', darker bars*) and loss (*G", lighter bars*) moduli measured at a constant frequency (1 Hz) and strain (1%), characterized by oscillatory shear rheology, show clear differences in loss moduli between elastic and viscoelastic groups but no significant differences as a function of adhesive ligand type (RGD, Fn9*10, Fn4G). (b) Average values of stiff elastic and stiff viscoelastic storage (*G', darker bars*) and loss (*G", lighter bars*) moduli measured at a constant frequency (1 Hz) and strain (1%), characterized by oscillatory shear rheology, show similar trends to the soft hydrogel groups. (c) Box and whisker plots of soft elastic and soft viscoelastic Young's moduli (E) of swollen hydrogels, characterized via nanoindentation, demonstrate equivalent Young's moduli (stiffnesses) for all groups. (d) Box and whisker plots of stiff elastic and stiff viscoelastic Young's moduli (E) of swollen hydrogels, characterized via nanoindentation, show similar trends to the soft hydrogel groups. Box plots of indentation data show median (*line*), mean (*filled black circle*), and have error bars corresponding to the lower value of either 1.5*interquartile range or the maximum/minimum value. At least 3 hydrogels were tested per experimental group.

5.4.2 Incorporation of fibronectin-related adhesive ligands did not impact hydrogel mechanics

We next wanted to determine if incorporating different adhesive ligands would impact the ability to independently control hydrogel stiffness and viscoelasticity. Hydrogel mechanics were examined through in situ oscillatory shear rheology (**Figure 5.2A, B**) and nanoindentation of PBS-swollen hydrogels (**Figure 5.2C, D**). Rapid *in situ* gelation for all hydrogel experimental groups was confirmed via rheology (**Figure S5.4**). The introduction of fibronectin-based adhesive ligands did not affect overall mechanics; similar storage and loss moduli were observed for all groups compared to RGD-containing hydrogels. Target mechanical values for 'soft' and 'stiff' groups corresponding to normal (elastic modulus, E ~ 1 kPa) and fibrotic (E ~ 15 kPa) lung tissue were successfully reached. As expected, the viscoelastic hydrogel design led to increased viscous properties as evidenced by higher loss moduli (G") that were within an order of magnitude of the storage moduli (G'), analogous to normal soft tissue like lung and liver[4].

Viscoelastic substrates also displayed tissue-relevant frequency-dependent mechanical responses as measured by both rheology (**Figure 5.3, S5.5**) and DMA-like nanoindentation measurements (**Figure S5.6**); at lower frequencies (longer time scales), the ability for guest–host interactions to re-organize and re-associate resulted in more solid-like behavior, whereas at higher frequencies (shorter time scales) guest–host interactions were disrupted with less time for complex reformation[33,56]. Stress relaxation, a key feature of viscoelastic materials, was demonstrated by observation of time-dependent decreases in storage moduli only in viscoelastic substrates when constant strain (5%) was applied (**Figure S5.7).** The frequency-dependent relaxation behavior observed for the viscoelastic groups relates to cell-relevant time scales; cells are able to respond

to force oscillations and exert traction forces on the order of seconds to minutes at a frequency of around 0.1– 1 Hz[19,20,71]. Elastic hydrogels consisting of only stable covalent crosslinks did not display stress relaxation over time.

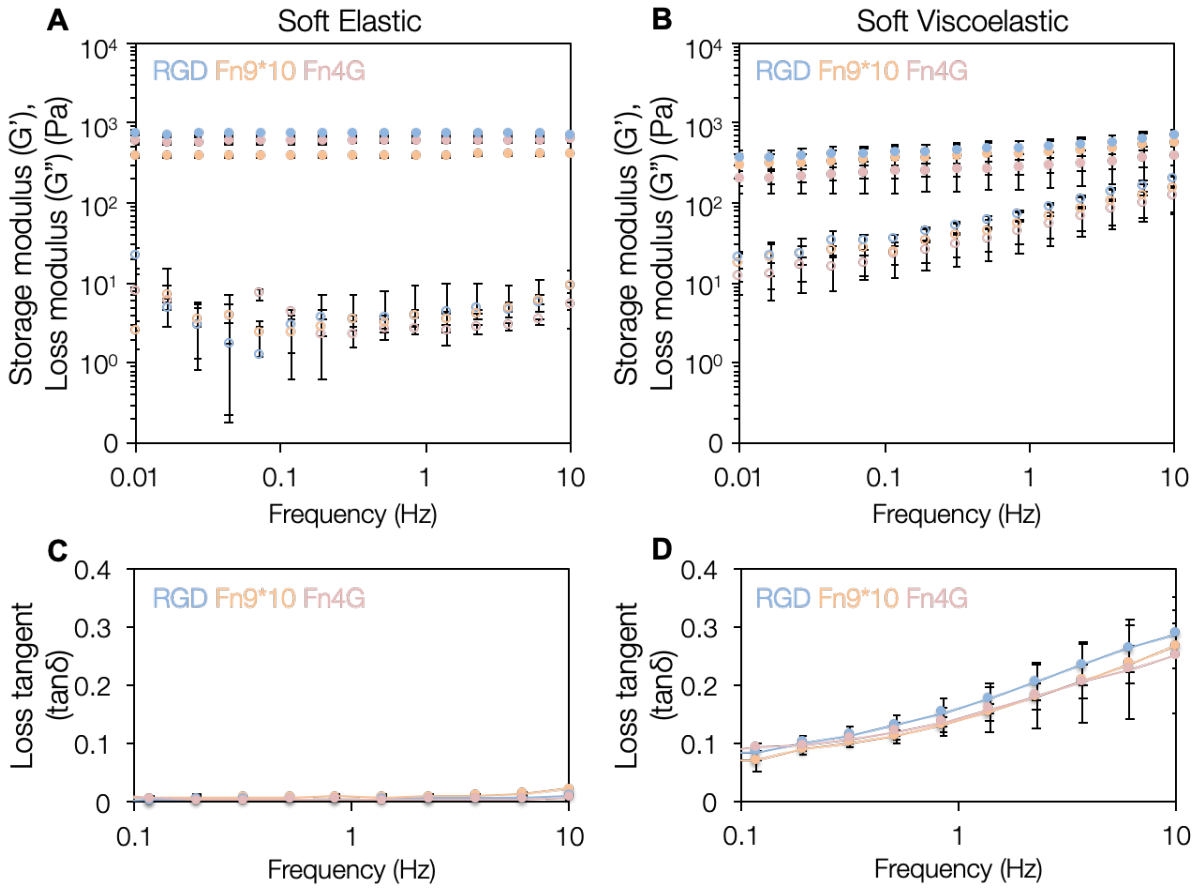

Figure 5.3. Frequency-dependent behavior of viscoelastic hydrogels. (a) Elastic hydrogels showed frequency-independent behavior, with storage (*G', closed circles*) and loss moduli (*G", open circles*) remaining relatively constant. (b) In contrast, viscoelastic hydrogels displayed frequency-dependent behavior with increasing loss moduli (*open circles*) at increasing frequencies. (c) Loss tangent (tanδ) values, which represent the ratio of viscous to elastic mechanical properties (*G"/G'*), remained relatively constant and close to 0 for all elastic hydrogels. (d) In contrast, loss tangent values were elevated for viscoelastic groups across all frequencies tested and increased at higher frequencies. Similar trends were seen for the stiff groups (**Figure S5.5**). Similar results for swollen hydrogel samples were measured using dynamic mechanical analysis (DMA)-like nanoindentation (**Figure S5.6**). 3 hydrogels were tested per experimental group.

5.4.3 Fibroblast spreading is influenced by both viscoelasticity and adhesive ligand type

After validating that hydrogels incorporating different adhesive ligands could be synthesized in both elastic and viscoelastic forms with overall stiffness matching normal and fibrotic tissue, we sought to confirm that our hydrogel formulations would support equivalent cell adhesion. We quantified the number of human lung fibroblasts attached to the hydrogels after 1 day and confirmed that all formulations supported similar levels of adhesion (**Figure S5.8**). Notably, hydrogels containing only 2 μM Fn fragments allowed equivalent fibroblast attachment to hydrogels with 1 mM RGD peptide. Previous work using these fragments has also shown robust cell attachment using concentrations of this magnitude[57,59]. In contrast, short linear RGD peptides have previously been shown to be around 1000 times less effective in cell attachment compared to fibronectin[78].

We next investigated the combined influence of stiffness, viscoelasticity, and adhesive ligand presentation on fibroblast spread area and shape. We used increased spreading as a proxy for increased cell contractility and myofibroblast-like activation as previously observed in many in vitro systems[20,23,24,79,80]. Human lung fibroblasts were seeded atop hydrogels and cultured for three days. We then quantified fibroblast spread area and cell shape index, a measure of cell circularity between 0 and 1, where 0 is a line and 1 is a circle (**Figure 5.4**). For the RGD-presenting hydrogels, cells showed greater spreading (2590 ± 670 μm^2) on stiff elastic groups compared to smaller morphologies on soft (1210 ± 650 μm^2) and stiff (1110 ± 510 μm^2) viscoelastic groups, similar to results observed in previous studies[33]. The promotion of α5β1 engagement largely blunted the stiffness-dependent spreading response with fibroblasts showing reduced spreading and more rounded morphologies across all hydrogel groups regardless of stiffness or viscoelasticity (average spread area on Fn9*10 hydrogels: 780 ± 490 μm^2), similar to previous findings with alveolar

epithelial cell spreading[10,81]. Hydrogels supporting preferential αvβ3 integrin engagement promoted similar levels of spreading to RGD-modified substrates, although increased spreading was observed even on soft elastic substrates (2060 ± 640 μm^2). However, cells displayed decreased spreading and remained rounded on viscoelastic hydrogels regardless of stiffness. Additionally, we used nanoindentation to measure apical fibroblast stiffness on the different hydrogel formulations and found that fibroblasts were significantly stiffer on stiff elastic hydrogels where they preferentially engaged αvβ3 (RGD, Fn4G groups), but not on Fn9*10-modified hydrogels (**Figure S5.9**).

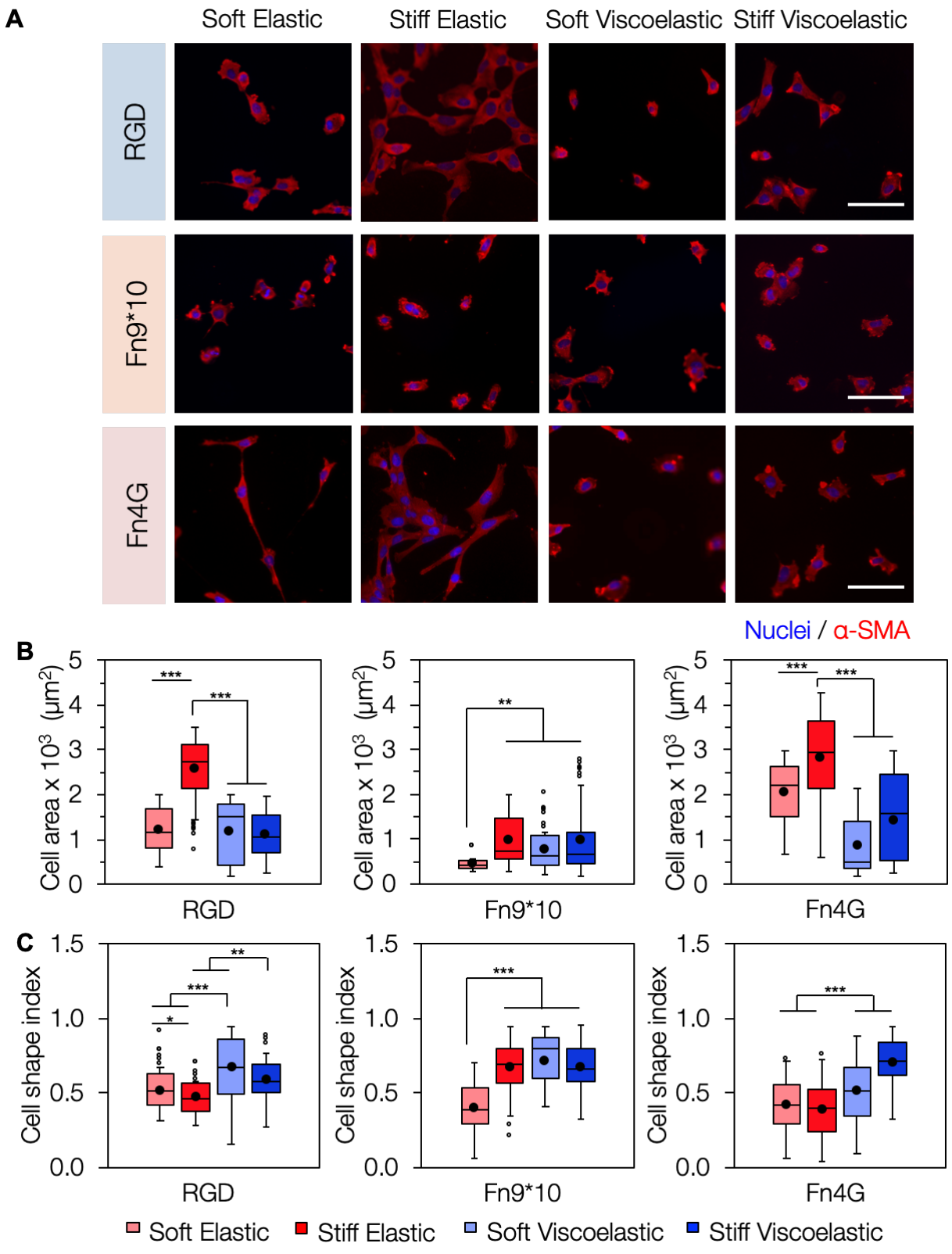
A
Soft Elastic
Stiff Elastic
Soft Viscoelastic
Stiff Viscoelastic
RGD
Fn9*10
Fn4G
Nuclei / α-SMA
B
Cell area x 10³ (μm²)
RGD
Fn9*10
Fn4G
C
Cell shape index
RGD
Fn9*10
Fn4G
Soft Elastic
Stiff Elastic
Soft Viscoelastic
Stiff Viscoelastic

Figure 5.4. Fibroblast spreading is influenced by both viscoelastic mechanics and adhesive ligand type. (a) Human lung fibroblasts were cultured for 3 days on soft or stiff elastic and viscoelastic hydrogel groups modified with either RGD or fibronectin fragments preferentially engaging α5β1 or αvβ3. (b) Fibroblasts preferentially binding αvβ3 (RGD, Fn4G) displayed increased spread area on elastic groups regardless of stiffness, but viscoelasticity suppressed spreading on all groups. (c) Cell shape index showed correlative results with spreading as smaller fibroblasts remained elongated (lower cell shape index) while larger fibroblasts assumed a more spread, activated morphology. Box plots of single cell data show median (*line*), mean (*filled black circle*), and have error bars corresponding to the lower value of either 1.5*interquartile range or the maximum/minimum value, with data points outside the 1.5*interquartile range shown as open circles. Scale bars: 100 μm, *: $P < 0.05$, **: $P < 0.01$, ***: $P < 0.001$. 3 hydrogels were tested per experimental group (50-600 cells total).

Similar to previous experimental and theoretical results, we observed reduced cell spreading on stiffer viscoelastic substrates compared to their elastic counterparts[22,82]. However, in contrast to these findings, we also observed decreased spreading on softer viscoelastic substrates. This can likely be attributed to differences in the viscoelastic hydrogel design; ionically-crosslinked viscoelastic hydrogels enable plastic deformation and adhesive ligand clustering to support increased cell spreading at lower stiffnesses[82]. In contrast, our viscoelastic hydrogel contains both covalent and supramolecular crosslinks and does not undergo plastic deformation (see stress relaxation and recovery tests in **Figure S5.7**).

5.4.4 Preferential αvβ3 integrin engagement promotes actin stress fiber organization and larger focal adhesion formation

The differences in fibroblast spreading observed as a function of stiffness, viscoelasticity, and adhesive ligand motivated us to more completely understand potential differences in cytoskeletal organization, particularly actin stress fiber formation and focal adhesion maturation. First, we qualitatively evaluated the level of actin stress fiber organization as well as the organization of paxillin, a prominent focal adhesion (FA) adaptor protein that has been implicated in regulating

cytoskeletal organization[83–86], in fibroblasts seeded on hydrogels (**Figure 5.5**). We found that F-actin organization was strongly correlated to spread area, with significantly more fibroblasts on both stiff elastic RGD and stiff elastic Fn4G hydrogels engaging primarily αvβ3 displaying organized stress fibers. In contrast, fibroblasts on Fn9*10 hydrogels showed few organized stress fibers, even on stiff elastic hydrogels mimicking fibrotic tissue. Notably, F-actin stress fiber organization was absent in the vast majority of fibroblasts cultured on soft or stiff viscoelastic hydrogels regardless of adhesive ligand functionalization. Qualitative analysis of α-SMA, a later marker of the myofibroblast phenotype[25,33,87,88], showed relatively low levels of stress fiber organization across all hydrogel groups (**Figure S5.10**). This was expected due to the shorter culture time used in this study. Nevertheless, we still observed significantly more fibroblasts displaying organized α-SMA stress fibers on stiff elastic RGD substrates.

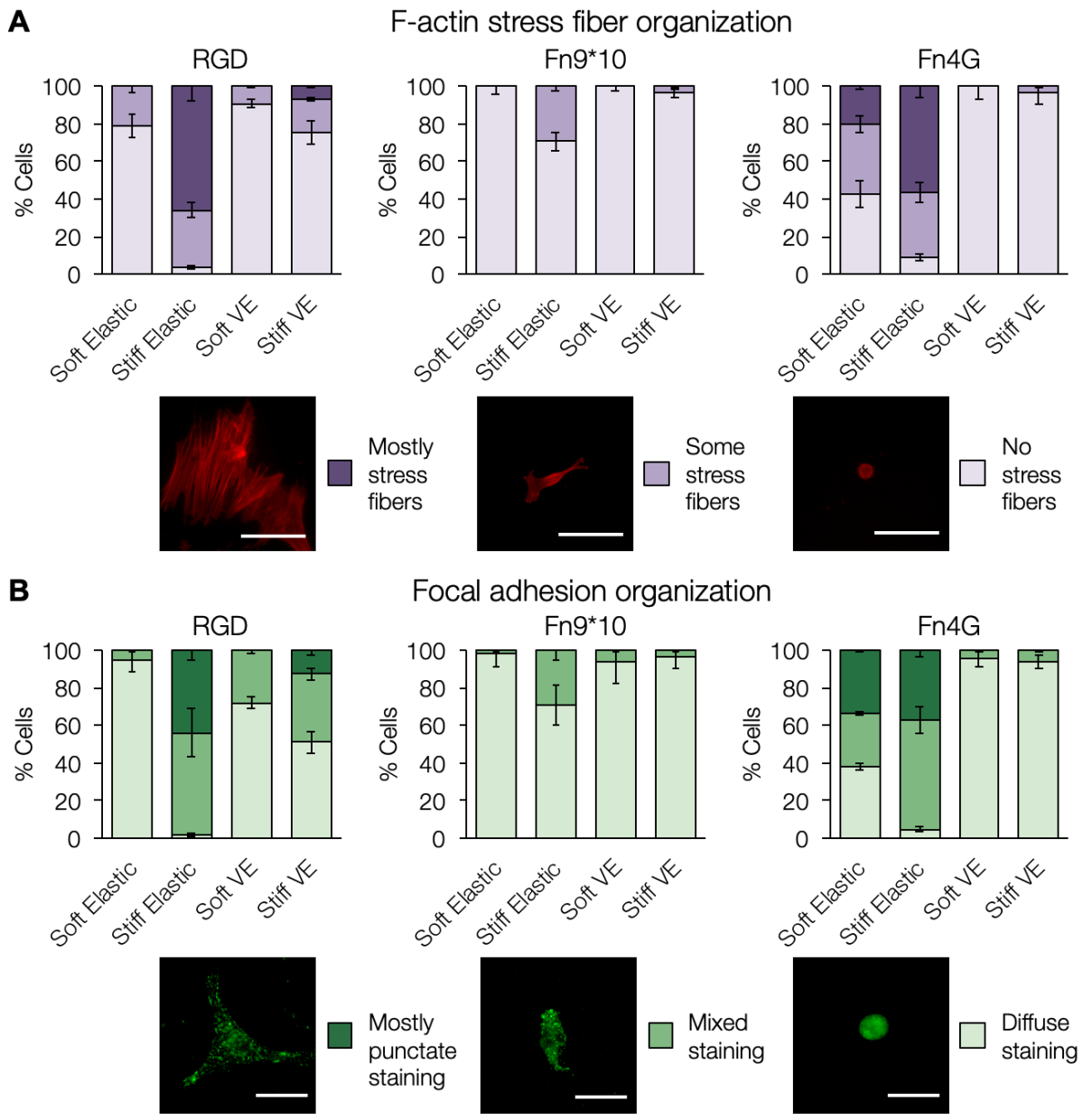

Figure 5.5. Qualitative analysis of F-actin stress fiber and focal adhesion organization. (a) Percentage of human lung fibroblasts showing various levels of F-actin stress fiber organization as indicated by the representative images. More F-actin stress fibers were observed in fibroblasts on stiff elastic hydrogels, especially for groups preferentially binding αvβ3 (RGD, Fn4G) while viscoelasticity suppressed stress fiber formation across all ligand groups. Scale bars: 100 μm. 3 hydrogels were tested per experimental group (60–110 cells total). (b) Percentage of human lung fibroblasts showing various levels of paxillin organization as indicated by the representative images. Similarly to the results in (a), more punctate paxillin staining was observed in fibroblasts on stiff elastic hydrogels, especially for groups preferentially binding αvβ3 (RGD, Fn4G) while viscoelasticity suppressed focal adhesion maturation across all ligand groups. Scale bars: 50 μm. 3 hydrogels were tested per experimental group (40-130 cells total).

On RGD-containing hydrogels punctate focal adhesion organization, as measured by paxillin staining, was observed near the periphery of the majority of cells on stiff elastic substrates (**Figure 5.5B, 6**). In contrast, fibroblasts on soft viscoelastic substrates, more reminiscent of normal healthy soft tissue, contained little to no punctate localization of paxillin, which can be attributed to the increase in viscous character (loss modulus) preventing spreading and the formation of larger FAs. Fibroblasts on soft elastic and stiff viscoelastic substrates displayed a mix of punctate paxillin staining and diffuse staining. Cells on Fn9*10 hydrogels, which typically remained rounded regardless of stiffness or viscoelasticity, showed mainly diffuse paxillin staining. Fibroblasts on Fn4G αvβ3- engaging elastic hydrogels also led to a mix of punctate paxillin structures and diffuse staining, similar to those seen with RGD groups. Again, viscoelasticity played a role in suppressing the formation of larger focal adhesions. These findings were also observed quantitatively with fibroblasts on αvβ3-engaging hydrogels (RGD, Fn4G) displaying increased focal adhesion area (**Figure S5.11**). However, some large, mature FAs were observed for fibroblasts seeded on soft elastic Fn4G hydrogels. Together, these results suggest that preferential αvβ3 binding may facilitate focal adhesion maturation and subsequent actin stress fiber organization and spreading even on soft hydrogels that are more linearly elastic, perhaps mimicking the soft but less viscoelastic mechanical environment observed in active fibroblastic foci in progressive pulmonary fibrosis[1].

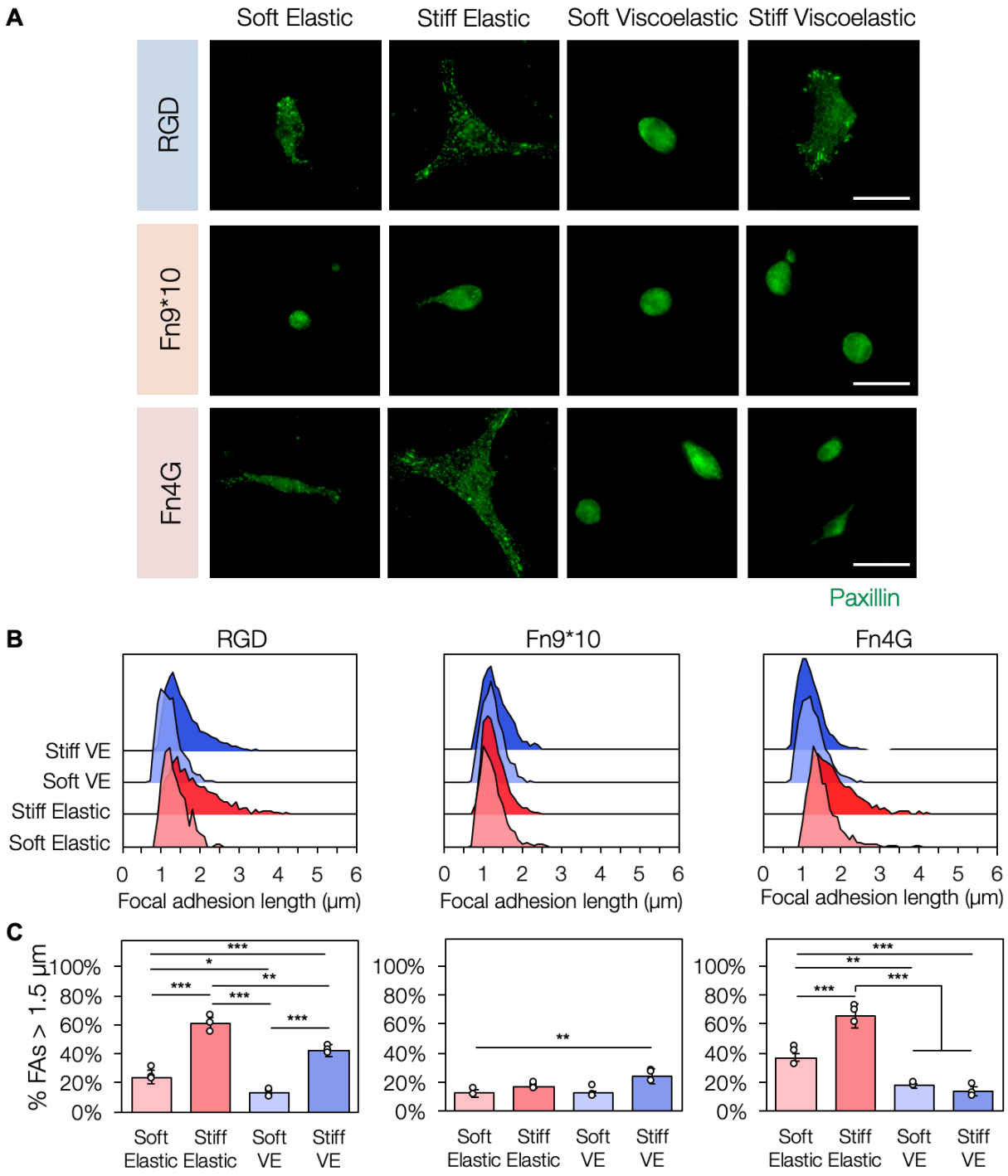

Figure 5.6. Preferential αvβ3 integrin engagement promotes larger focal adhesion formation. (a) Human lung fibroblasts seeded on hydrogels preferentially binding αvβ3 displayed more punctate paxillin staining on stiff elastic substrates, but viscoelasticity suppressed focal adhesion organization and maturation. Scale bars: 50 μm. (b) Ridgeline plots of focal adhesion length (determined via quantification of paxillin staining) for fibroblasts cultured on hydrogels for 1 day. Plots are grouped by ligand and superimposed to show variance as a function of stiffness and

viscoelasticity. (c) The percentages of focal adhesion lengths over 1.5 μm for each hydrogel group. Fibroblasts on Fn9*10-functionalized α5β1-engaging hydrogels had smaller focal adhesions regardless of stiffness and viscoelasticity. *: $P < 0.05$, **: $P < 0.01$, ***: $P < 0.001$; $n > 180$ adhesions from at least 3 hydrogels per experimental group.

5.5 Conclusions

We have described the successful design and implementation of a modular hydrogel platform enabling independent control of covalent crosslinking, incorporation of supramolecular guest–host interactions, and functionalization with cell adhesive groups differentially engaging integrin heterodimers. Hydrogels with stiffnesses approximating normal and fibrotic lung tissue were synthesized in both elastic and viscoelastic forms presenting either RGD or Fn fragments promoting preferential α5β1 or αvβ3 binding. We then showed that fibroblasts seeded on hydrogels preferentially engaging αvβ3 (RGD, Fn4G) generally showed increased spreading, actin stress fiber formation, and focal adhesion size on stiffer elastic hydrogels, but viscoelasticity played a role in suppressing spreading and focal adhesion maturation regardless of adhesive ligand presentation. In particular, fibrosis-associated αvβ3 engagement on Fn4G-modified hydrogels promoted increased spread area and focal adhesion size, even on softer elastic materials. Together, these results highlight the importance of understanding the combinatorial role that viscoelastic and adhesive cues play in regulating fibroblast mechanobiology.

5.6 Acknowledgements

This work was supported by the UVA Fibrosis Initiative and the NIH (R35GM138187, T32GM008715). The content is solely the responsibility of the authors and does not necessarily represent the official views of the National Institutes of Health.

5.7 References

(1) Fiore, V. F.; Wong, S. S.; Tran, C.; Tan, C.; Xu, W.; Sulchek, T.; White, E. S.; Hagood, J. S.; Barker, T. H. Avβ3 Integrin Drives Fibroblast Contraction and Strain Stiffening of Soft Provisional Matrix during Progressive Fibrosis. *JCI insight* **2018**, *3* (20), 1–35. https://doi.org/10.1172/jci.insight.97597.

(2) De Hilster, R. H. J.; Sharma, P. K.; Jonker, M. R.; White, E. S.; Gercama, E. A.; Roobeek, M.; Timens, W.; Harmsen, M. C.; Hylkema, M. N.; Burgess, J. K. Human Lung Extracellular Matrix Hydrogels Resemble the Stiffness and Viscoelasticity of Native Lung Tissue. *Am. J. Physiol. - Lung Cell. Mol. Physiol.* **2020**, *318* (4), L698–L704. https://doi.org/10.1152/AJPLUNG.00451.2019.

(3) Liu, F.; Mih, J. D.; Shea, B. S.; Kho, A. T.; Sharif, A. S.; Tager, A. M.; Tschumperlin, D. J. Feedback Amplification of Fibrosis through Matrix Stiffening and COX-2 Suppression. *J. Cell Biol.* **2010**, *190* (4), 693–706. https://doi.org/10.1083/jcb.201004082.

(4) Perepelyuk, M.; Chin, L.; Cao, X.; Van Oosten, A.; Shenoy, V. B.; Janmey, P. A.; Wells, R. G. Normal and Fibrotic Rat Livers Demonstrate Shear Strain Softening and Compression Stiffening: A Model for Soft Tissue Mechanics. *PLoS One* **2016**, *11* (1), 1–18. https://doi.org/10.1371/journal.pone.0146588.

(5) Wells, R. G. Tissue Mechanics and Fibrosis. *Biochim. Biophys. Acta - Mol. Basis Dis.* **2013**, *1832* (7), 884–890. https://doi.org/10.1016/j.bbadis.2013.02.007.

(6) Wynn, T. A.; Ramalingam, T. R. Mechanisms of Fibrosis: Therapeutic Translation for Fibrotic Disease. *Nat. Med.* **2012**, *18* (7), 1028–1040. https://doi.org/10.1038/nm.2807.

(7) Henderson, N. C.; Rieder, F.; Wynn, T. A. Fibrosis: From Mechanisms to Medicines. *Nature* **2020**, *587* (7835), 555–566. https://doi.org/10.1038/s41586-020-2938-9.

(8) Martinez, F. J.; Collard, H. R.; Pardo, A.; Raghu, G.; Richeldi, L.; Selman, M.; Swigris, J. J.; Taniguchi, H.; Wells, A. U. Idiopathic Pulmonary Fibrosis. *Nat. Rev. Dis. Prim.* **2017**, *3*. https://doi.org/10.1038/nrdp.2017.74.

(9) Wynn, T. Cellular and Molecular Mechanisms of Fibrosis. *J. Pathol.* **2008**, *214*, 199–210.

(10) Brown, A. C.; Rowe, J. A.; Barker, T. H. Guiding Epithelial Cell Phenotypes with Engineered Integrin-Specific Recombinant Fibronectin Fragments. *Tissue Eng. - Part A* **2011**, *17* (1–2), 139–150. https://doi.org/10.1089/ten.tea.2010.0199.

(11) Duscher, D.; Maan, Z. N.; Wong, V. W.; Rennert, R. C.; Januszyk, M.; Rodrigues, M.; Hu,

M.; Whitmore, A. J.; Whittam, A. J.; Longaker, M. T.; et al. Mechanotransduction and Fibrosis. *J. Biomech.* **2014**, *47* (9), 1997–2005. https://doi.org/10.1016/j.jbiomech.2014.03.031.

(12) Hinz, B.; Gabbiani, G. Mechanisms of Force Generation and Transmission by Myofibroblasts. *Curr. Opin. Biotechnol.* **2003**, *14* (5), 538–546. https://doi.org/10.1016/j.copbio.2003.08.006.

(13) Humphrey, J. D.; Dufresne, E. R.; Schwartz, M. A. Mechanotransduction and Extracellular Matrix Homeostasis. *Nat. Rev. Mol. Cell Biol.* **2014**, *15* (12), 802–812. https://doi.org/10.1038/nrm3896.

(14) Ingber, D. E. Cellular Mechanotransduction: Putting All the Pieces Together Again. *FASEB J.* **2006**, *20* (7), 811–827. https://doi.org/10.1096/fj.05-5424rev.

(15) Jansen, K. A.; Atherton, P.; Ballestrem, C. Mechanotransduction at the Cell-Matrix Interface. *Semin. Cell Dev. Biol.* **2017**, *71*, 75–83. https://doi.org/10.1016/j.semcdb.2017.07.027.

(16) Baker, B. M.; Chen, C. S. Deconstructing the Third Dimension-How 3D Culture Microenvironments Alter Cellular Cues. *J. Cell Sci.* **2012**, *125* (13), 3015–3024. https://doi.org/10.1242/jcs.079509.

(17) Caliari, S. R.; Burdick, J. A. A Practical Guide to Hydrogels for Cell Culture. *Nat. Methods* **2016**, *13* (5), 405–414. https://doi.org/10.1038/nmeth.3839.

(18) Caliari, S. R.; Perepelyuk, M.; Soulas, E. M.; Lee, G. Y.; Wells, R. G.; Burdick, J. A. Gradually Softening Hydrogels for Modeling Hepatic Stellate Cell Behavior during Fibrosis Regression. *Integr. Biol.* **2016**, *8* (6), 720–728. https://doi.org/10.1039/c6ib00027d.

(19) Cameron, A. R.; Frith, J. E.; Cooper-White, J. J. The Influence of Substrate Creep on Mesenchymal Stem Cell Behaviour and Phenotype. *Biomaterials* **2011**, *32* (26), 5979–5993. https://doi.org/10.1016/j.biomaterials.2011.04.003.

(20) Charrier, E. E.; Pogoda, K.; Wells, R. G.; Janmey, P. A. Control of Cell Morphology and Differentiation by Substrates with Independently Tunable Elasticity and Viscous Dissipation. *Nat. Commun.* **2018**, *9* (1), 1–13. https://doi.org/10.1038/s41467-018-02906-9.

(21) Chaudhuri, O.; Cooper-White, J.; Janmey, P. A.; Mooney, D. J.; Shenoy, V. B. Effects of Extracellular Matrix Viscoelasticity on Cellular Behaviour. *Nature* **2020**, *584* (7822), 535–

546. https://doi.org/10.1038/s41586-020-2612-2.

(22) Gong, Z.; Szczesny, S. E.; Caliari, S. R.; Charrier, E. E.; Chaudhuri, O.; Cao, X.; Lin, Y.; Mauck, R. L.; Janmey, P. A.; Burdick, J. A.; et al. Matching Material and Cellular Timescales Maximizes Cell Spreading on Viscoelastic Substrates. *Proc. Natl. Acad. Sci. U. S. A.* **2018**, *115* (12), E2686–E2695. https://doi.org/10.1073/pnas.1716620115.

(23) Yeh, Y. C.; Corbin, E. A.; Caliari, S. R.; Ouyang, L.; Vega, S. L.; Truitt, R.; Han, L.; Margulies, K. B.; Burdick, J. A. Mechanically Dynamic PDMS Substrates to Investigate Changing Cell Environments. *Biomaterials* **2017**, *145*, 23–32. https://doi.org/10.1016/j.biomaterials.2017.08.033.

(24) Balestrini, J. L.; Chaudhry, S.; Sarrazy, V.; Koehler, A.; Hinz, B. The Mechanical Memory of Lung Myofibroblasts. *Integr. Biol.* **2012**, *4* (4), 410–421. https://doi.org/10.1039/c2ib00149g.

(25) Caliari, S. R.; Perepelyuk, M.; Cosgrove, B. D.; Tsai, S. J.; Lee, G. Y.; Mauck, R. L.; Wells, R. G.; Burdick, J. A. Stiffening Hydrogels for Investigating the Dynamics of Hepatic Stellate Cell Mechanotransduction during Myofibroblast Activation. *Sci. Rep.* **2016**, *6*, 1–10. https://doi.org/10.1038/srep21387.

(26) Kloxin, A. M.; Benton, J. A.; Anseth, K. S. In Situ Elasticity Modulation with Dynamic Substrates to Direct Cell Phenotype. *Biomaterials* **2010**, *31* (1), 1–8. https://doi.org/10.1016/j.biomaterials.2009.09.025.

(27) Olsen, A. L.; Bloomer, S. A.; Chan, E. P.; Gaça, M. D. A.; Georges, P. C.; Sackey, B.; Uemura, M.; Janmey, P. A.; Wells, R. G. Hepatic Stellate Cells Require a Stiff Environment for Myofibroblastic Differentiation. *Am. J. Physiol. - Gastrointest. Liver Physiol.* **2011**, *301* (1), 110–118. https://doi.org/10.1152/ajpgi.00412.2010.

(28) Travers, J. G.; Kamal, F. A.; Robbins, J.; Yutzey, K. E.; Blaxall, B. C. Cardiac Fibrosis: The Fibroblast Awakens. *Circ. Res.* **2016**, *118* (6), 1021–1040. https://doi.org/10.1161/CIRCRESAHA.115.306565.

(29) Wells, R. G. The Role of Matrix Stiffness in Regulating Cell Behavior. *Hepatology* **2008**, *47* (4), 1394–1400. https://doi.org/10.1002/hep.22193.

(30) Wen, J. H.; Vincent, L. G.; Fuhrmann, A.; Choi, Y. S.; Hribar, K. C.; Taylor-Weiner, H.; Chen, S.; Engler, A. J. Interplay of Matrix Stiffness and Protein Tethering in Stem Cell Differentiation. *Nat. Mater.* **2014**, *13* (10), 979–987. https://doi.org/10.1038/nmat4051.

(31) Islam, M. R.; Virag, J.; Oyen, M. L. Micromechanical Poroelastic and Viscoelastic Properties of Ex-Vivo Soft Tissues. *J. Biomech.* **2020**, *113*, 110090. https://doi.org/10.1016/j.jbiomech.2020.110090.

(32) Zhu, M.; Tao, H.; Samani, M.; Luo, M.; Wang, X.; Hopyan, S.; Sun, Y. Spatial Mapping of Tissue Properties in Vivo Reveals a 3D Stiffness Gradient in the Mouse Limb Bud. *Proc. Natl. Acad. Sci. U. S. A.* **2020**, *117* (9), 4781–4791. https://doi.org/10.1073/pnas.1912656117.

(33) Hui, E.; Gimeno, K. I.; Guan, G.; Caliari, S. R. Spatiotemporal Control of Viscoelasticity in Phototunable Hyaluronic Acid Hydrogels. *Biomacromolecules* **2019**, *20* (11), 4126–4134. https://doi.org/10.1021/acs.biomac.9b00965.

(34) Kechagia, J. Z.; Ivaska, J.; Roca-Cusachs, P. Integrins as Biomechanical Sensors of the Microenvironment. *Nat. Rev. Mol. Cell Biol.* **2019**, *20* (8), 457–473. https://doi.org/10.1038/s41580-019-0134-2.

(35) Rustad, K. C.; Wong, V. W.; Gurtner, G. C. The Role of Focal Adhesion Complexes in Fibroblast Mechanotransduction during Scar Formation. *Differentiation* **2013**, *86* (3), 87–91. https://doi.org/10.1016/j.diff.2013.02.003.

(36) Asano, S.; Ito, S.; Takahashi, K.; Furuya, K.; Kondo, M.; Sokabe, M.; Hasegawa, Y. Matrix Stiffness Regulates Migration of Human Lung Fibroblasts. *Physiol. Rep.* **2017**, *5* (9), 1–11. https://doi.org/10.14814/phy2.13281.

(37) Conroy, K. P.; Kitto, L. J.; Henderson, N. C. Av Integrins: Key Regulators of Tissue Fibrosis. *Cell Tissue Res.* **2016**, *365* (3), 511–519. https://doi.org/10.1007/s00441-016-2407-9.

(38) Henderson, N. C.; Sheppard, D. Integrin-Mediated Regulation of TGFβ in Fibrosis. *Biochim. Biophys. Acta - Mol. Basis Dis.* **2013**, *1832* (7), 891–896. https://doi.org/10.1016/j.bbadis.2012.10.005.

(39) Roca-Cusachs, P.; Iskratsch, T.; Sheetz, M. P. Finding the Weakest Link-Exploring Integrin-Mediated Mechanical Molecular Pathways. *J. Cell Sci.* **2012**, *125* (13), 3025–3038. https://doi.org/10.1242/jcs.095794.

(40) Sun, Z.; Guo, S. S.; Fässler, R. Integrin-Mediated Mechanotransduction. **2016**, *215* (4).

(41) Paszek, M. J.; Boettiger, D.; Weaver, V. M.; Hammer, D. A. Integrin Clustering Is Driven by Mechanical Resistance from the Glycocalyx and the Substrate. *PLoS Comput. Biol.*

2009, *5* (12). https://doi.org/10.1371/journal.pcbi.1000604.

(42) Seong, J.; Wang, N.; Wang, Y. Mechanotransduction at Focal Adhesions: From Physiology to Cancer Development. *J. Cell. Mol. Med.* **2013**, *17* (5), 597–604. https://doi.org/10.1111/jcmm.12045.

(43) Driscoll, T. P.; Ahn, S. J.; Huang, B.; Kumar, A.; Schwartz, M. A. Actin Flow-Dependent and -Independent Force Transmission through Integrins. *Proc. Natl. Acad. Sci. U. S. A.* **2020**, *117* (51), 32413–32422. https://doi.org/10.1073/pnas.2010292117.

(44) Gardel, M. L.; Schneider, I. C.; Aratyn-Schaus, Y.; Waterman, C. M. Mechanical Integration of Actin and Adhesion Dynamics in Cell Migration. *Annu. Rev. Cell Dev. Biol.* **2010**, *26* (1), 315–333. https://doi.org/10.1146/annurev.cellbio.011209.122036.

(45) Harjanto, D.; Zaman, M. H. Matrix Mechanics and Receptor-Ligand Interactions in Cell Adhesion. *Org. Biomol. Chem.* **2010**, *8* (2), 299–304. https://doi.org/10.1039/b913064k.

(46) Kishi, T.; Mayanagi, T.; Iwabuchi, S.; Akasaka, T.; Sobue, K. Myocardin-Related Transcription Factor A (MRTF-A) Activitydependent Cell Adhesion Is Correlated to Focal Adhesion Kinase (FAK) Activity. *Oncotarget* **2016**, *7* (44), 72113–72130. https://doi.org/10.18632/oncotarget.12350.

(47) Panciera, T.; Azzolin, L.; Cordenonsi, M.; Piccolo, S. Mechanobiology of YAP and TAZ in Physiology and Disease. *Nat. Rev. Mol. Cell Biol.* **2017**, *18* (12), 758–770. https://doi.org/10.1038/nrm.2017.87.

(48) Ruoslahti, E. RGD and Other Recognition Sequences for Integrins. *Annu. Rev. Cell Dev. Biol.* **1996**, *12* (1), 697–715. https://doi.org/10.1146/annurev.cellbio.12.1.697.

(49) Leiphart, R. J.; Chen, D.; Peredo, A. P.; Loneker, A. E.; Janmey, P. A. Mechanosensing at Cellular Interfaces. *Langmuir* **2019**, *35* (23), 7509–7519. https://doi.org/10.1021/acs.langmuir.8b02841.

(50) Henderson, N. C.; Arnold, T. D.; Katamura, Y.; Giacomini, M. M.; Rodriguez, J. D.; McCarty, J. H.; Pellicoro, A.; Raschperger, E.; Betsholtz, C.; Ruminski, P. G.; et al. Targeting of Av Integrin Identifies a Core Molecular Pathway That Regulates Fibrosis in Several Organs. *Nat. Med.* **2013**, *19* (12), 1617–1624. https://doi.org/10.1038/nm.3282.

(51) Arora, P. D.; Narani, N.; McCulloch, C. A. G. The Compliance of Collagen Gels Regulates Transforming Growth Factor-β Induction of α-Smooth Muscle Actin in Fibroblasts. *Am. J. Pathol.* **1999**, *154* (3), 871–882. https://doi.org/10.1016/S0002-9440(10)65334-5.

(52) Fernandez, I. E.; Eickelberg, O. The Impact of TGF-β on Lung Fibrosis: From Targeting to Biomarkers. *Proc. Am. Thorac. Soc.* **2012**, *9* (3), 111–116. https://doi.org/10.1513/pats.201203-023AW.

(53) Deng, X.; Jin, K.; Li, Y.; Gu, W.; Liu, M.; Zhou, L. Platelet-Derived Growth Factor and Transforming Growth Factor B1 Regulate ARDS-Associated Lung Fibrosis Through Distinct Signaling Pathways. *Cell. Physiol. Biochem.* **2015**, *36* (3), 937–946. https://doi.org/10.1159/000430268.

(54) Scaffidi, A. K.; Moodley, Y. P.; Weichselbaum, M.; Thompson, P. J.; Knight, D. A. Regulation of Human Lung Fibroblast Phenotype and Function by Vitronectin and Vitronectin Integrins. *J. Cell Sci.* **2001**, *114* (19), 3507–3516. https://doi.org/10.1242/jcs.114.19.3507.

(55) Gramlich, W. M.; Kim, I. L.; Burdick, J. A. Synthesis and Orthogonal Photopatterning of Hyaluronic Acid Hydrogels with Thiol-Norbornene Chemistry. *Biomaterials* **2013**, *34* (38), 9803–9811. https://doi.org/10.1016/j.biomaterials.2013.08.089.

(56) Rodell, C. B.; Kaminski, A. L.; Burdick, J. A. Rational Design of Network Properties in Guest-Host Assembled and Shear-Thinning Hyaluronic Acid Hydrogels. *Biomacromolecules* **2013**, *14* (11), 4125–4134. https://doi.org/10.1021/bm401280z.

(57) Li, S.; Nih, L. R.; Bachman, H.; Fei, P.; Li, Y.; Nam, E.; Dimatteo, R.; Carmichael, S. T.; Barker, T. H.; Segura, T. Hydrogels with Precisely Controlled Integrin Activation Dictate Vascular Patterning and Permeability. *Nat. Mater.* **2017**, *16* (9), 953–961. https://doi.org/10.1038/nmat4954.

(58) Martino, M. M.; Mochizuki, M.; Rothenfluh, D. A.; Rempel, S. A.; Hubbell, J. A.; Barker, T. H. Controlling Integrin Specificity and Stem Cell Differentiation in 2D and 3D Environments through Regulation of Fibronectin Domain Stability. *Biomaterials* **2009**, *30* (6), 1089–1097. https://doi.org/10.1016/j.biomaterials.2008.10.047.

(59) Cao, L.; Nicosia, J.; Larouche, J.; Zhang, Y.; Bachman, H.; Brown, A. C.; Holmgren, L.; Barker, T. H. Detection of an Integrin-Binding Mechanoswitch within Fibronectin during Tissue Formation and Fibrosis. *ACS Nano* **2017**, *11* (7), 7110–7117. https://doi.org/10.1021/acsnano.7b02755.

(60) Booth, A. J.; Hadley, R.; Cornett, A. M.; Dreffs, A. A.; Matthes, S. A.; Tsui, J. L.; Weiss, K.; Horowitz, J. C.; Fiore, V. F.; Barker, T. H.; et al. Acellular Normal and Fibrotic Human

Lung Matrices as a Culture System for in Vitro Investigation. *Am. J. Respir. Crit. Care Med.* **2012**, *186* (9), 866–876. https://doi.org/10.1164/rccm.201204-0754OC.

(61) Berginski, M. E.; Gomez, S. M. The Focal Adhesion Analysis Server: A Web Tool for Analyzing Focal Adhesion Dynamics. *F1000Research* **2013**, *2*, 68. https://doi.org/10.12688/f1000research.2-68.v1.

(62) Rodell, C. B.; Dusaj, N. N.; Highley, C. B.; Burdick, J. A. Injectable and Cytocompatible Tough Double-Network Hydrogels through Tandem Supramolecular and Covalent Crosslinking. *Adv. Mater.* **2016**, *28* (38), 8419–8424. https://doi.org/10.1002/adma.201602268.

(63) Burdick, J. A.; Prestwich, G. D. Hyaluronic Acid Hydrogels for Biomedical Applications. *Adv. Mater.* **2011**, *23* (12), H41–H56. https://doi.org/10.1002/adma.201003963.

(64) Caliari, S. R.; Vega, S. L.; Kwon, M.; Soulas, E. M.; Burdick, J. A. Dimensionality and Spreading Influence MSC YAP/TAZ Signaling in Hydrogel Environments. *Biomaterials* **2016**, *103*, 314–323. https://doi.org/10.1016/j.biomaterials.2016.06.061.

(65) Kwon, M. Y.; Wang, C.; Galarraga, J. H.; Puré, E.; Han, L.; Burdick, J. A. Influence of Hyaluronic Acid Modification on CD44 Binding towards the Design of Hydrogel Biomaterials. *Biomaterials* **2019**, *222* (August). https://doi.org/10.1016/j.biomaterials.2019.119451.

(66) Schanté, C. E.; Zuber, G.; Herlin, C.; Vandamme, T. F. Chemical Modifications of Hyaluronic Acid for the Synthesis of Derivatives for a Broad Range of Biomedical Applications. *Carbohydr. Polym.* **2011**, *85* (3), 469–489. https://doi.org/10.1016/j.carbpol.2011.03.019.

(67) Aida, T.; Meijer, E. W.; Stupp, S. I. Functional Supramolecular Polymers. *Science (80-.).* **2012**, *335* (6070), 813–817. https://doi.org/10.1126/science.1205962.

(68) Marozas, I. A.; Anseth, K. S.; Cooper-White, J. J. Adaptable Boronate Ester Hydrogels with Tunable Viscoelastic Spectra to Probe Timescale Dependent Mechanotransduction. *Biomaterials* **2019**, *223* (August), 119430. https://doi.org/10.1016/j.biomaterials.2019.119430.

(69) McKinnon, D. D.; Domaille, D. W.; Cha, J. N.; Anseth, K. S. Biophysically Defined and Cytocompatible Covalently Adaptable Networks as Viscoelastic 3d Cell Culture Systems. *Adv. Mater.* **2014**, *26* (6), 865–872. https://doi.org/10.1002/adma.201303680.

(70) Tang, S.; Ma, H.; Tu, H. C.; Wang, H. R.; Lin, P. C.; Anseth, K. S. Adaptable Fast Relaxing Boronate-Based Hydrogels for Probing Cell–Matrix Interactions. *Adv. Sci.* **2018**, *5* (9), 1800638. https://doi.org/10.1002/advs.201800638.

(71) Chaudhuri, O.; Gu, L.; Klumpers, D.; Darnell, M.; Bencherif, S. A.; Weaver, J. C.; Huebsch, N.; Lee, H. P.; Lippens, E.; Duda, G. N.; et al. Hydrogels with Tunable Stress Relaxation Regulate Stem Cell Fate and Activity. *Nat. Mater.* **2016**, *15* (3), 326–334. https://doi.org/10.1038/nmat4489.

(72) Zhao, X.; Huebsch, N.; Mooney, D. J.; Suo, Z. Stress-Relaxation Behavior in Gels with Ionic and Covalent Crosslinks. *J. Appl. Phys.* **2010**, *107* (6), 1–5. https://doi.org/10.1063/1.3343265.

(73) Mohammadi, H.; Arora, P. D.; Simmons, C. A.; Janmey, P. A.; McCulloch, C. A. Inelastic Behaviour of Collagen Networks in Cell-Matrix Interactions and Mechanosensation. *J. R. Soc. Interface* **2015**, *12* (102). https://doi.org/10.1098/rsif.2014.1074.

(74) Nam, S.; Hu, K. H.; Butte, M. J.; Chaudhuri, O. Strain-Enhanced Stress Relaxation Impacts Nonlinear Elasticity in Collagen Gels. *Proc. Natl. Acad. Sci. U. S. A.* **2016**, *113* (20), 5492–5497. https://doi.org/10.1073/pnas.1523906113.

(75) Rodell, C. B.; MacArthur, J. W.; Dorsey, S. M.; Wade, R. J.; Wang, L. L.; Woo, Y. J.; Burdick, J. A. Shear-Thinning Supramolecular Hydrogels with Secondary Autonomous Covalent Crosslinking to Modulate Viscoelastic Properties in Vivo. *Adv. Funct. Mater.* **2015**, *25* (4), 636–644. https://doi.org/10.1002/adfm.201403550.

(76) Van De Manakker, F.; Kroon-Batenburg, L. M. J.; Vermonden, T.; Van Nostrum, C. F.; Hennink, W. E. Supramolecular Hydrogels Formed by β-Cyclodextrin Self-Association and Host-Guest Inclusion Complexes. *Soft Matter* **2009**, *6* (1), 187–194. https://doi.org/10.1039/b916378f.

(77) Dicker, K. T.; Gurski, L. A.; Pradhan-Bhatt, S.; Witt, R. L.; Farach-Carson, M. C.; Jia, X. Hyaluronan: A Simple Polysaccharide with Diverse Biological Functions. *Acta Biomater.* **2014**, *10* (4), 1558–1570. https://doi.org/10.1016/j.actbio.2013.12.019.

(78) Hautanen, A.; Gailit, J.; Mann, D. M.; Ruoslahti, E. Effects of Modifications of the RGD Sequence and Its Context on Recognition by the Fibronectin Receptor. *J. Biol. Chem.* **1989**, *264* (3), 1437–1442. https://doi.org/10.1016/s0021-9258(18)94206-7.

(79) Guvendiren, M.; Perepelyuk, M.; Wells, R. G.; Burdick, J. A. Hydrogels with Differential

and Patterned Mechanics to Study Stiffness-Mediated Myofibroblastic Differentiation of Hepatic Stellate Cells. *J. Mech. Behav. Biomed. Mater.* **2014**, *38*, 198–208. https://doi.org/10.1016/j.jmbbm.2013.11.008.

(80) McBeath, R.; Pirone, D. M.; Nelson, C. M.; Bhadriraju, K.; Chen, C. S. Cell Shape, Cytoskeletal Tension, and RhoA Regulate Stem Cell Lineage Commitment. *Dev. Cell* **2004**, *6*, 483–495.

(81) Markowski, M. C.; Brown, A. C.; Barker, T. H. Directing Epithelial to Mesenchymal Transition through Engineered Microenvironments Displaying Orthogonal Adhesive and Mechanical Cues. *J. Biomed. Mater. Res. - Part A* **2012**, *100 A* (8), 2119–2127. https://doi.org/10.1002/jbm.a.34068.

(82) Chaudhuri, O.; Gu, L.; Darnell, M.; Klumpers, D.; Bencherif, S. A.; Weaver, J. C.; Huebsch, N.; Mooney, D. J. Substrate Stress Relaxation Regulates Cell Spreading. *Nat. Commun.* **2015**, *6*, 1–7. https://doi.org/10.1038/ncomms7365.

(83) López-Colomé, A. M.; Lee-Rivera, I.; Benavides-Hidalgo, R.; López, E. Paxillin: A Crossroad in Pathological Cell Migration. *J. Hematol. Oncol.* **2017**, *10* (1), 1–15. https://doi.org/10.1186/s13045-017-0418-y.

(84) Sero, J. E.; German, A. E.; Mammoto, A.; Ingber, D. E. Paxillin Controls Directional Cell Motility in Response to Physical Cues. *Cell Adhes. Migr.* **2012**, *6* (6), 502–508. https://doi.org/10.4161/cam.21672.

(85) Turner, C. E. Paxillin Interactions. *J. Cell Sci.* **2000**, *113* (23), 4139–4140. https://doi.org/10.1242/jcs.113.23.4139.

(86) Turner, C. E. Paxillin and Focal Adhesion Signalling. *Nat. Cell Biol.* **2000**, *2* (12), 231–236. https://doi.org/10.1038/35046659.

(87) Shinde, A. V.; Humeres, C.; Frangogiannis, N. G. The Role of α-Smooth Muscle Actin in Fibroblast-Mediated Matrix Contraction and Remodeling. *Biochim. Biophys. Acta - Mol. Basis Dis.* **2017**, *1863* (1), 298–309. https://doi.org/10.1016/j.bbadis.2016.11.006.

(88) Waisberg, D. R.; Parra, E. R.; Barbas-Filho, J. V.; Fernezlian, S.; Capelozzi, V. L. Increased Fibroblast Telomerase Expression Precedes Myofibroblastα-Smooth Muscle Actin Expression in Idiopathic Pulmonary Fibrosis. *Clinics* **2012**, *67* (9), 1039–1046. https://doi.org/10.6061/clinics/2012(09)10.

5.8 Supplementary Figures

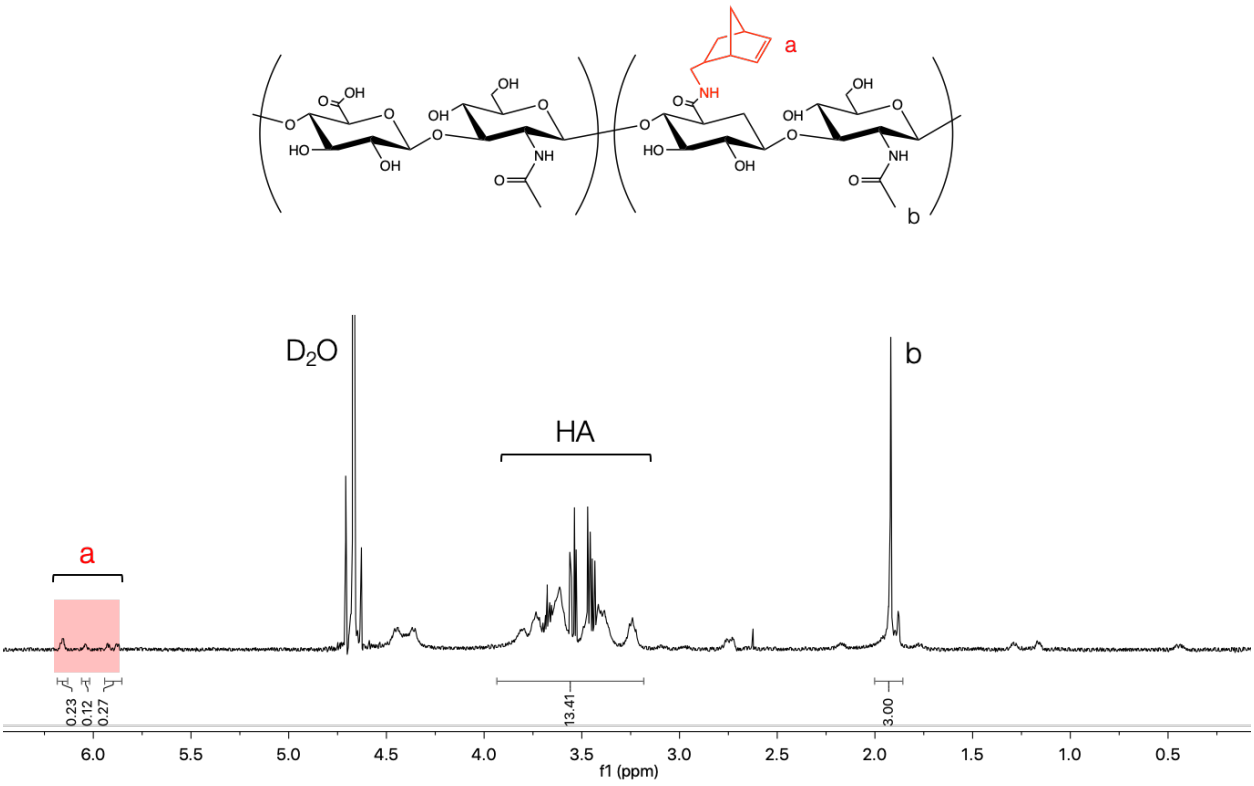

Figure S5.1. ^{1}H NMR spectrum of norbornene-functionalized hyaluronic acid (NorHA). The degree of modification, based on norbornene peaks ('a') relative to the methyl peak ('b'), was determined to be 31%.

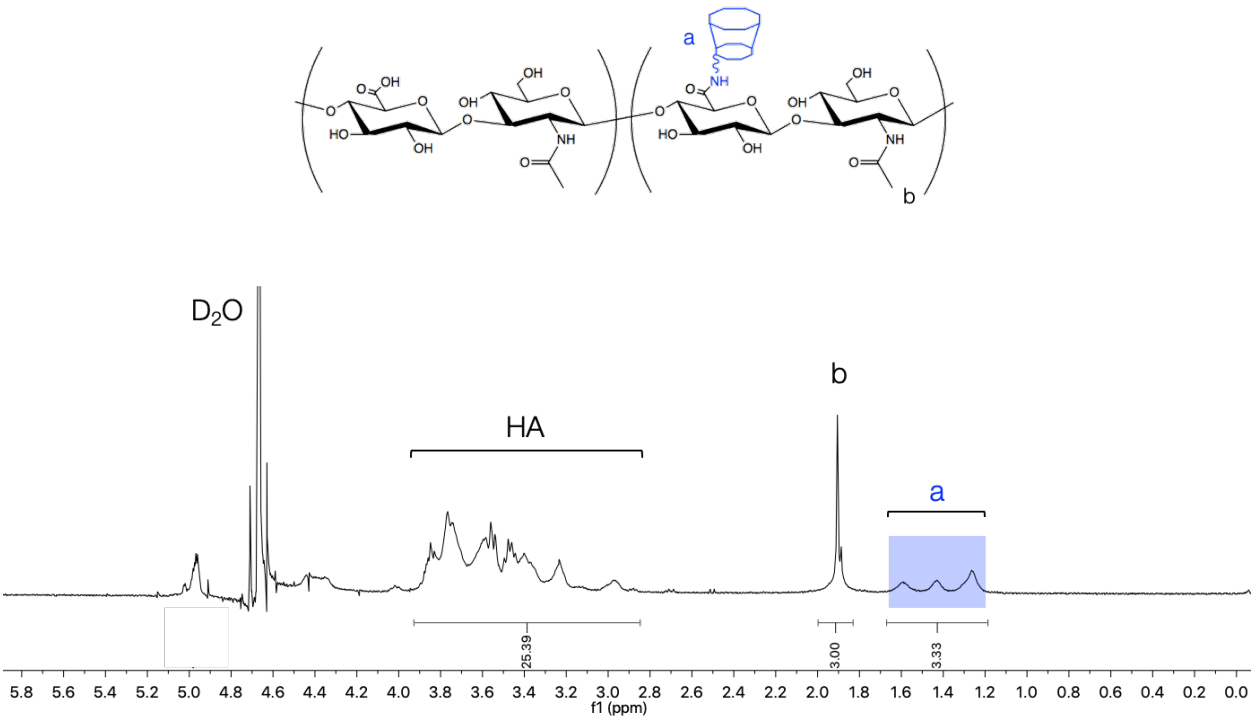

Figure S5.2. ^{1}H NMR spectrum of β-cyclodextrin-functionalized hyaluronic acid (CD-HA). The degree of modification was determined to be 28%.

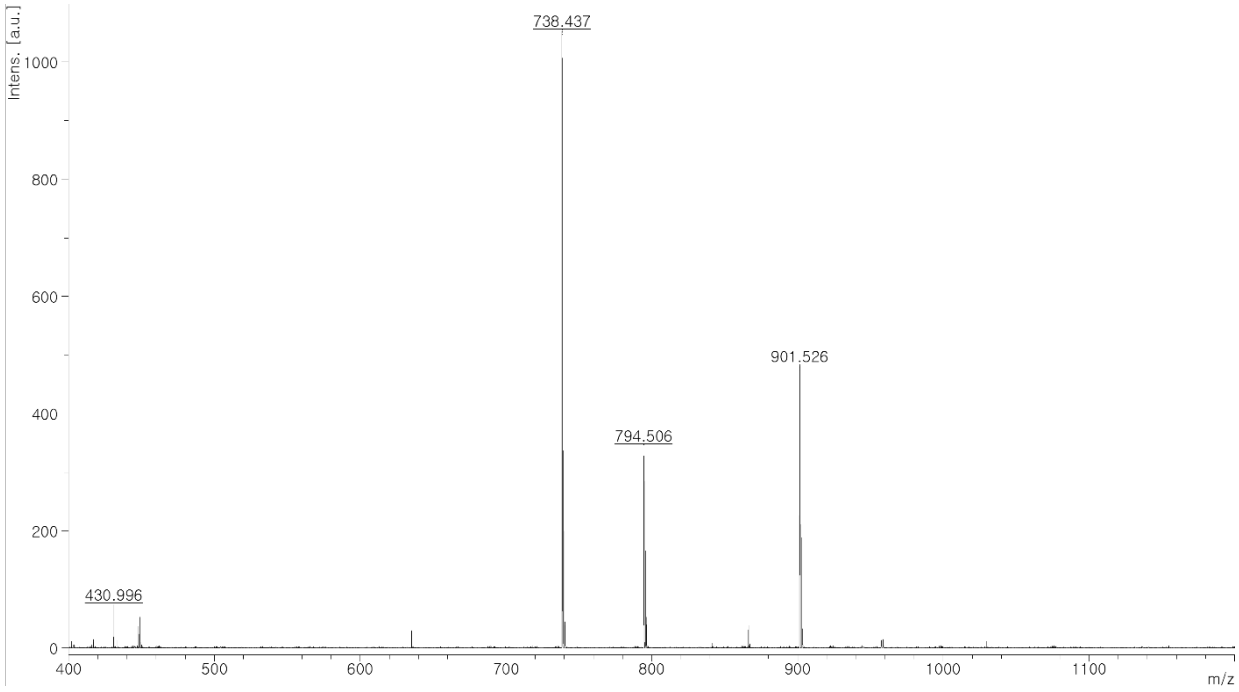

Figure S5.3. MALDI spectrum of adamantane (Ad) peptide with the sequence 1-adamantaneacetic acid-KKKCG. Expected mass: 738.6 g/mol. Actual mass: 738.4 g/mol.

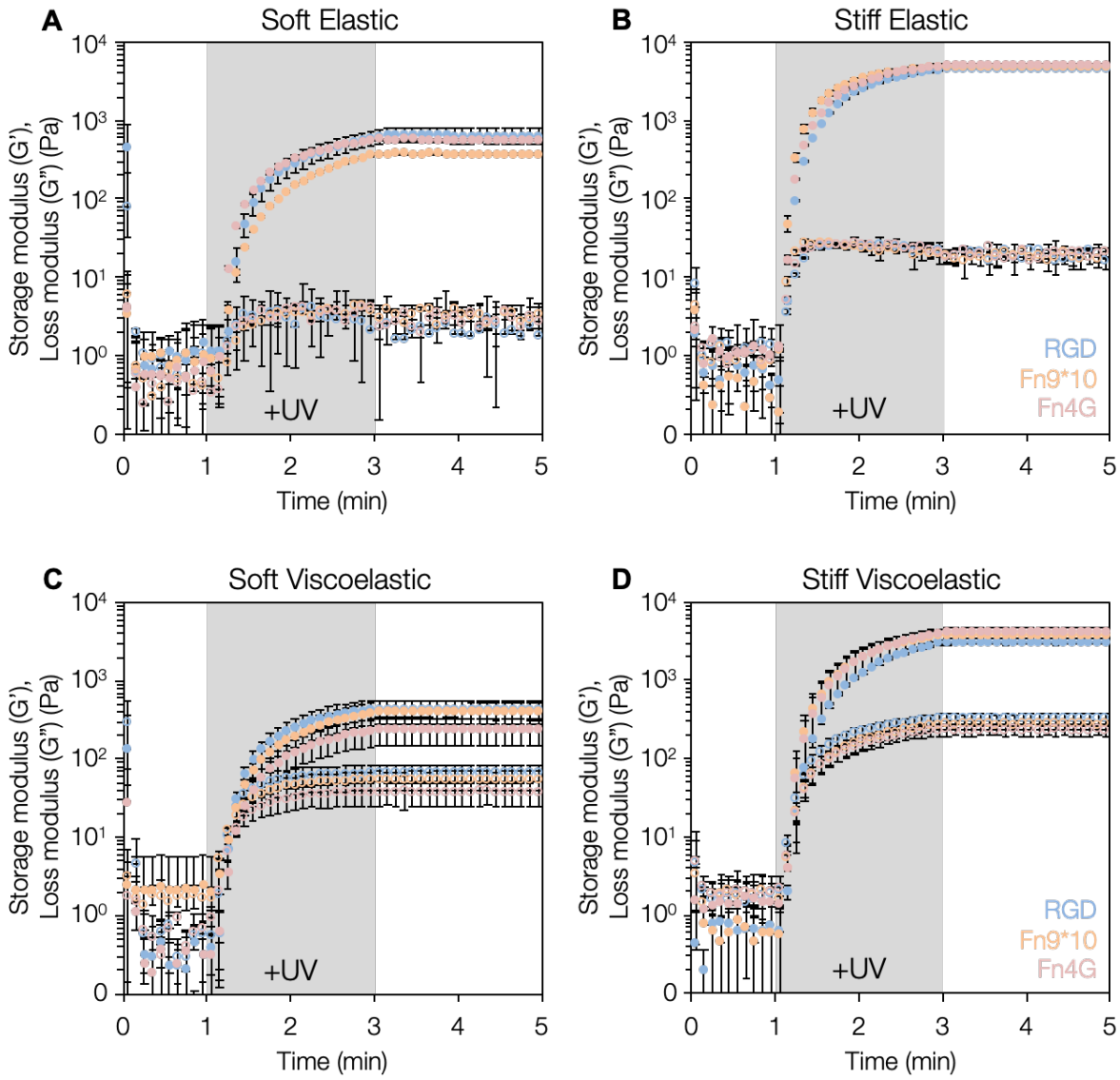

Figure S5.4. *In situ* gelation of hydrogel groups. Rheological characterization of elastic and viscoelastic hydrogels representing normal (G' ~ 0.5 kPa, 'soft') and fibrotic (G' ~ 5 kPa, 'stiff') tissue. Viscoelastic groups displayed loss moduli (*G", open circles*) within an order of magnitude of the storage moduli (*G', filled circles*). The gray shaded regions show the 2 minute UV light exposures during gelation. 3 hydrogels were tested per experimental group.

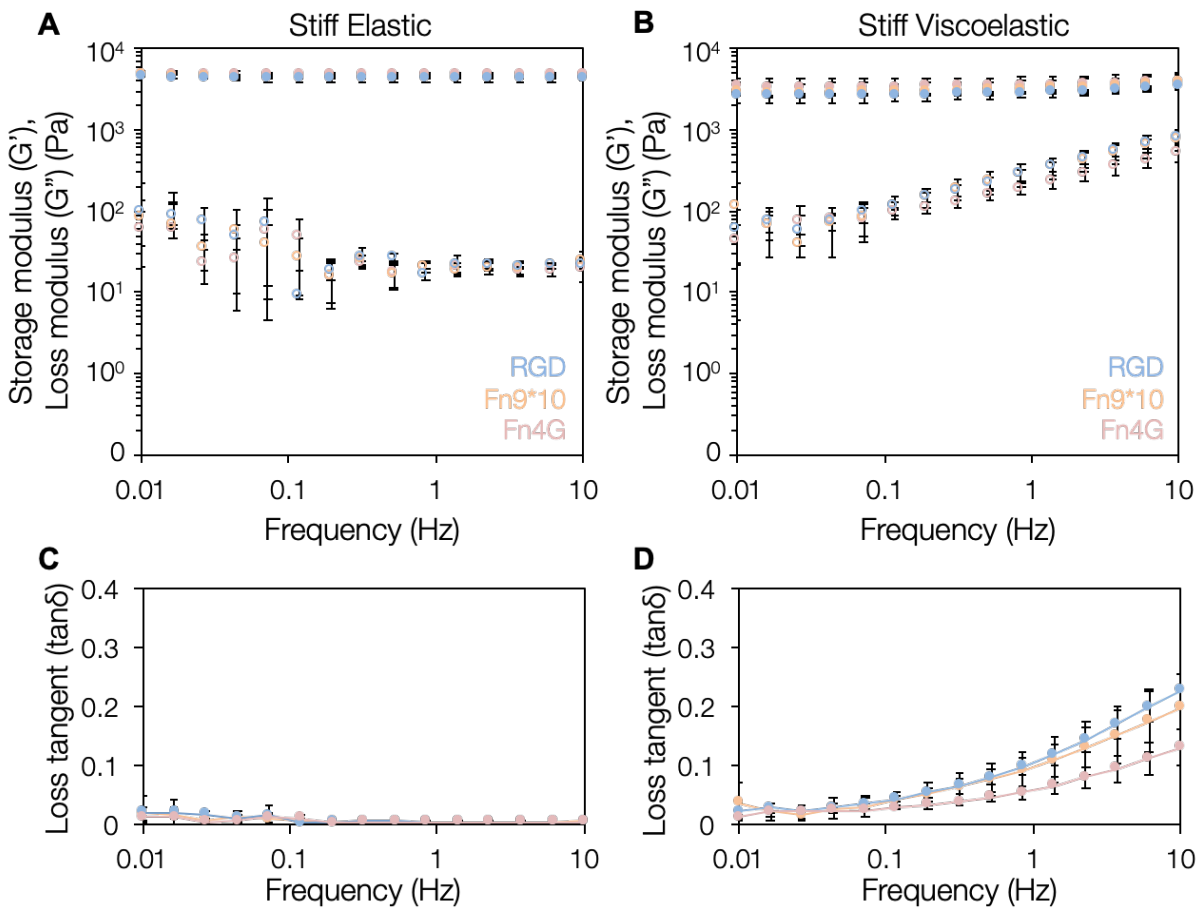

Figure S5.5. Rheological behavior of stiff hydrogel groups. (A) Stiff elastic hydrogels showed frequency-independent behavior with constant loss moduli relative to frequency. (B) Viscoelastic hydrogels displayed frequency-dependent behavior with increasing loss moduli at increasing frequencies. (C) Loss tangent (tanδ, *G"/G'*) values remained relatively constant for all stiff elastic hydrogels. (D) In contrast, loss tangent values were elevated for viscoelastic groups across all frequencies tested and increased at higher frequencies. The soft hydrogel groups can be found in Figure 3.

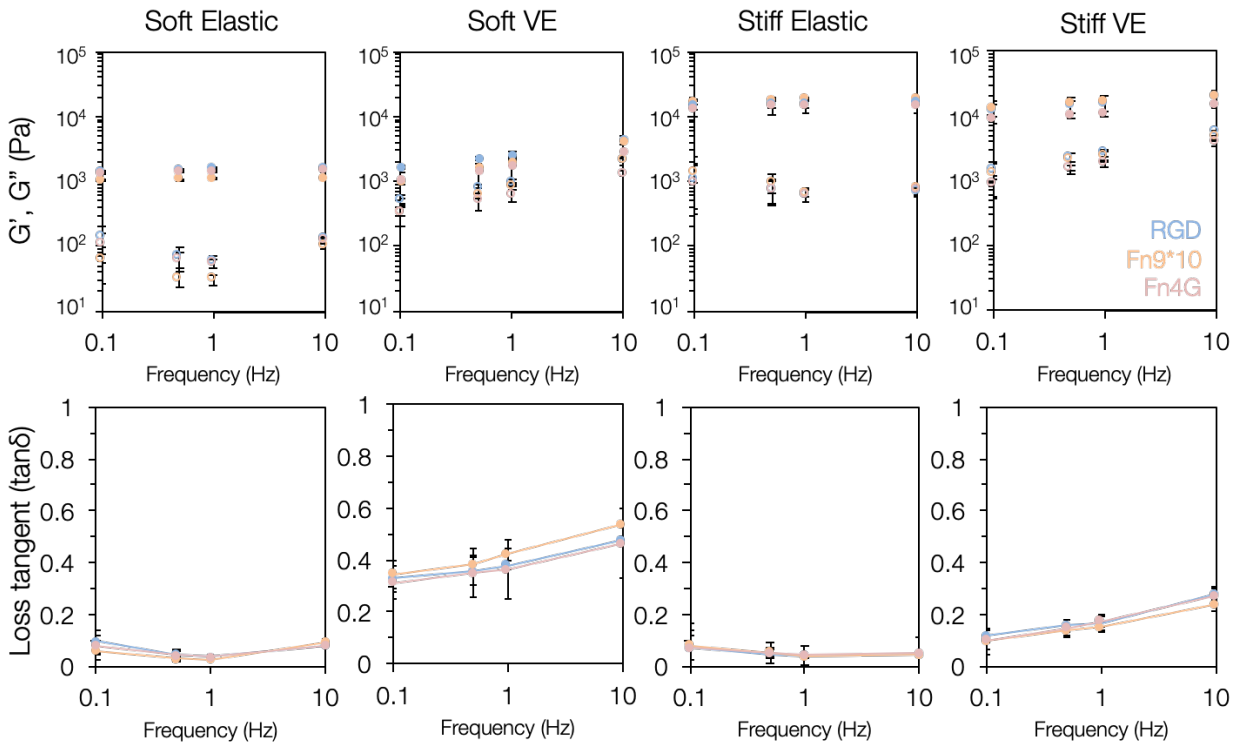

Figure S5.6. Mechanical characterization of swollen hydrogels via nanoindentation. Dynamic mechanical analysis (DMA)-like analysis of PBS-swollen hydrogel groups showed similar frequency-dependent behavior for viscoelastic groups and relatively constant trends for elastic hydrogels.

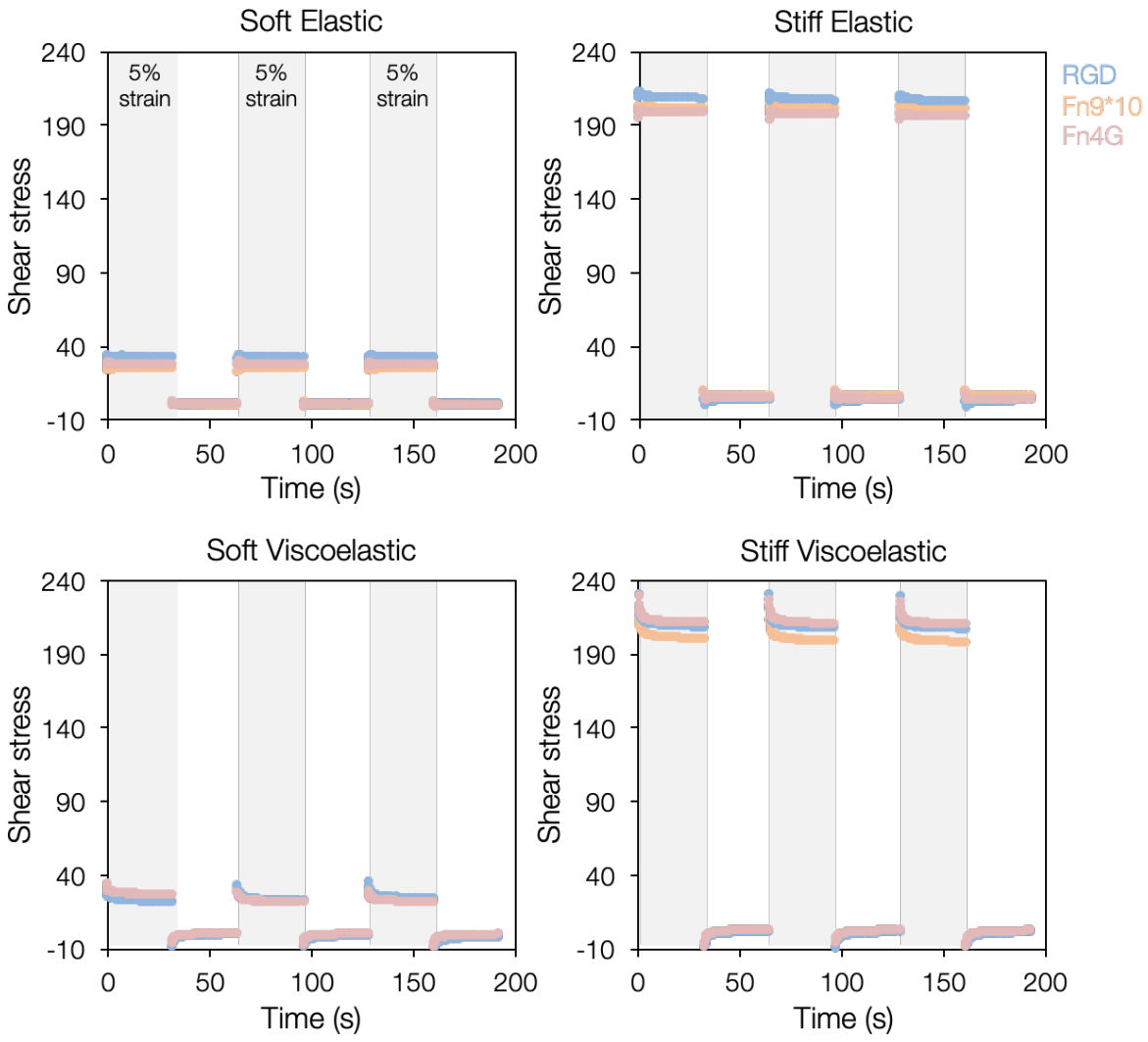

Figure S5.7. Stress relaxation and recovery tests. Cyclic stress relaxation and recovery tests showed full recovery of mechanical properties of hydrogel groups with stress relaxation only occurring in the viscoelastic groups for all ligand types. Strain cycled between 5% (*gray bars*) and 0.1% (*white areas*).

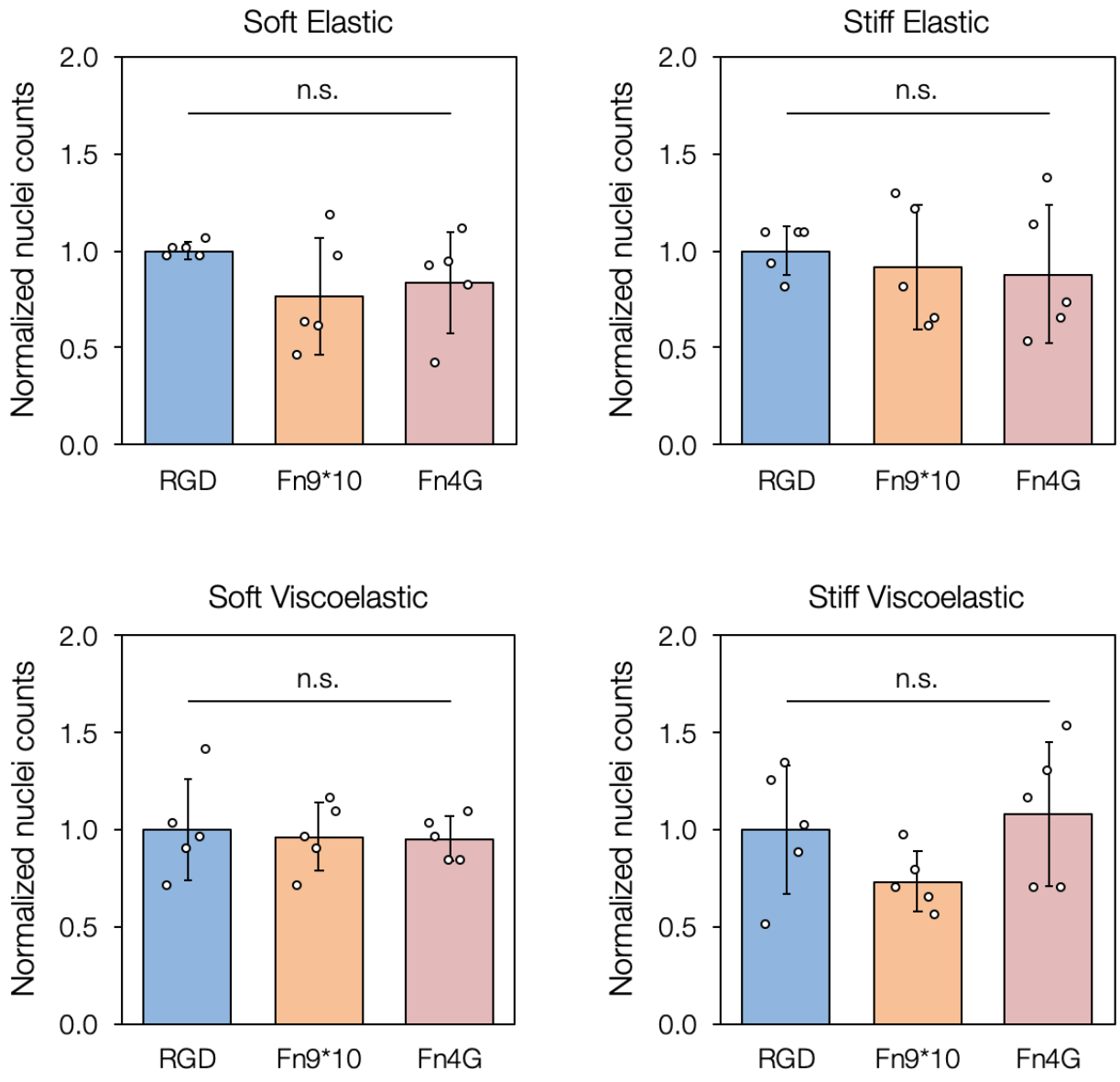

Figure S5.8. Fibronectin fragment-functionalized hydrogels support equivalent fibroblast attachment to RGD-modified hydrogels. Nuclei counts of fibroblasts adhered to all hydrogel experimental groups after one day showed no significant differences between RGD (1 mM) and Fn fragment (2 μM) groups. Nuclei counts were normalized to the RGD groups for each graph. 5 hydrogels were tested per experimental group.

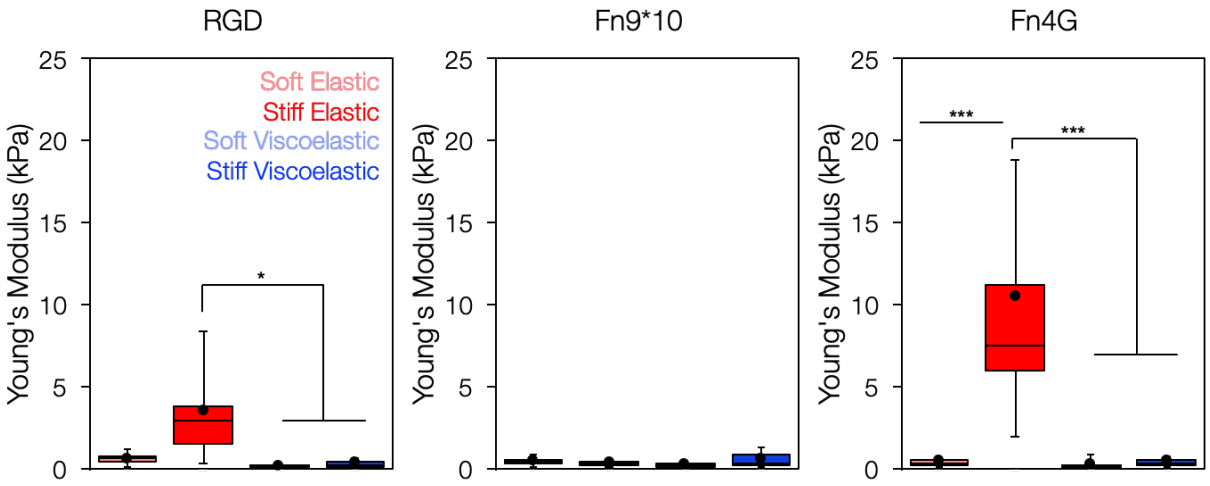

Figure S5.9. Nanoindentation measurements of cell stiffness. Fibroblasts are stiffer on hydrogels promoting αvβ3 engagement on stiff elastic substrates.*: $P < 0.05$, ***: $P < 0.001$; n = 9-19 cells from 3 hydrogels per experimental group.

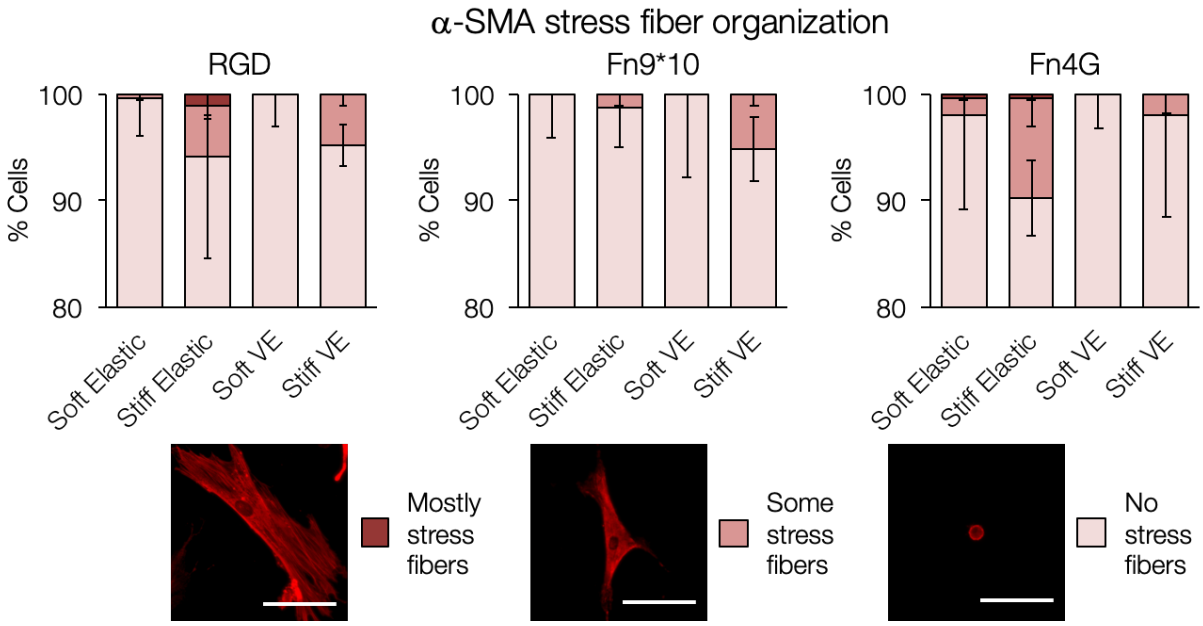

Figure S5.10. Qualitative analysis of α-SMA stress fiber organization. Percentage of human lung fibroblasts showing various levels of α-SMA stress fiber organization as indicated by the representative images. Scale bars: 100 μm. 3 hydrogels were tested per experimental group (60-450 cells total).

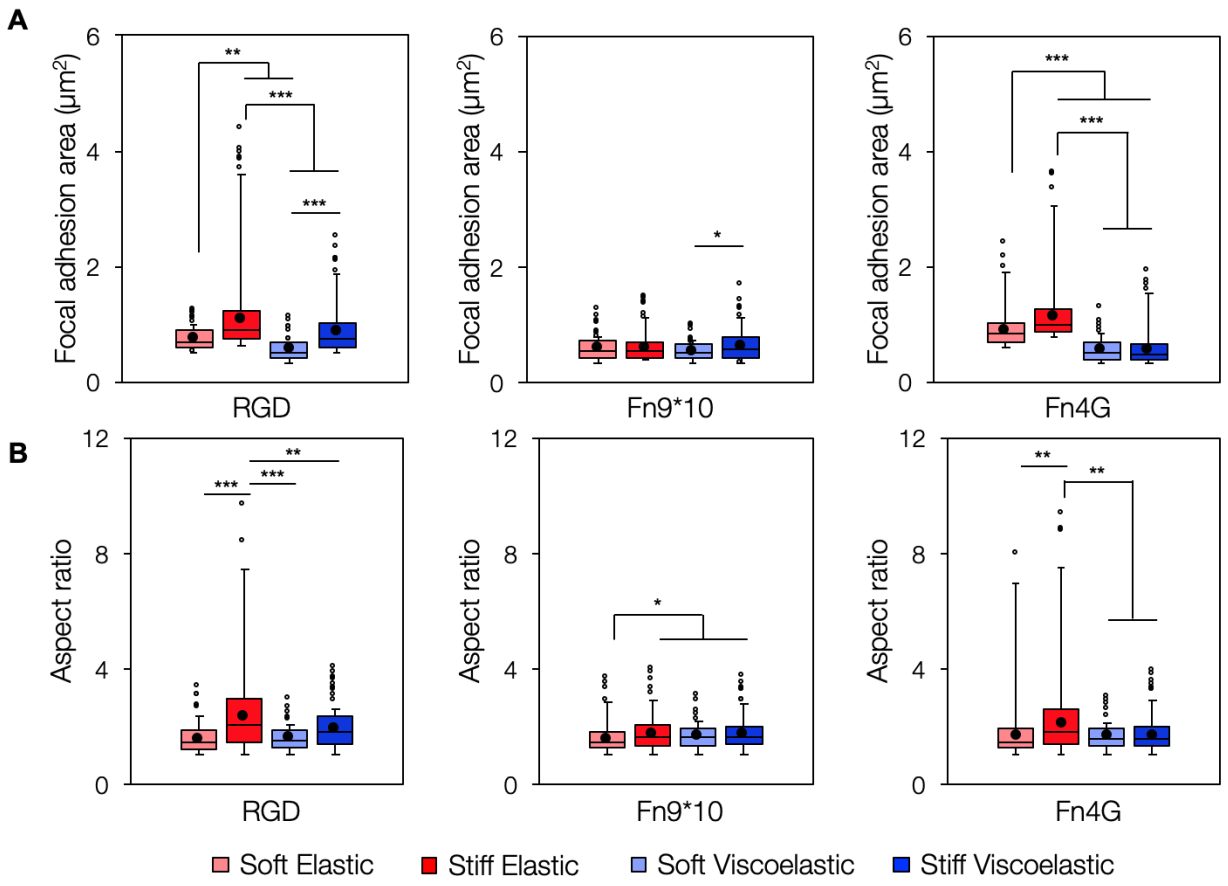

Figure S5.11. Focal adhesion area quantification. (A) Human lung fibroblasts on hydrogels preferentially engaging αvβ3 (RGD, Fn4G) displayed increased focal adhesion area as measured by paxillin staining on stiffer, more elastic substrates while fibroblasts on Fn9*10 show reduced focal adhesion size regardless of substrate stiffness or viscoelasticity. (B) Focal adhesion aspect ratio quantification showed similar trends to area measurements. Box plots of single cell data show median (*line*), mean (*filled black circle*), and have error bars corresponding to the lower value of either 1.5*interquartile range or the maximum/minimum value, with data points outside the 1.5*interquartile range shown as open circles. *: $P < 0.05$, **: $P < 0.01$, ***: $P < 0.001$; $n > 180$ adhesions from at least 3 hydrogels per experimental group.

CHAPTER 6: IMPACT OF VISCOELASTICITY ON FIBROBLAST AND MESENCHYMAL STEM CELL BEHAVIOR IN 3D PHOTOTUNABLE HYDROGELS

6.1 Abstract

Cell-matrix interactions play a key role in regulating biological processes. Changes in substrate mechanical properties such as stiffness and viscoelasticity during disease progression influence cell fate. However, the mechanisms underlying how cells interpret these signals in 3D is not well understood. In this study, we developed a 3D viscoelastic hydrogel system in which stiffness, viscoelasticity, and degradability were decoupled to study their role in cell volume expansion, spreading, stress fiber organization, and YAP nuclear localization. Human lung fibroblasts (HLFs) displayed protrusions within soft elastic hydrogels but remained rounded in stiff elastic and viscoelastic substrates. Similarly, human mesenchymal stem cells (hMSCs) demonstrated increased spreading within soft elastic hydrogels but showed rounded morphologies in stiff elastic substrates. Viscoelasticity suppressed spreading behaviors overall, but moderate hMSC spreading was observed in stiff viscoelastic substrates, highlighting the combined role of instructive cues. Increasing viscoelasticity of via increasing loss moduli (G”), comparable to compliant healthy tissue mechanics, resulted in reduced stress fiber formation and YAP nuclear localization. Overall, this work demonstrates the influence of dimensionality and time-dependent parameters on differential cell behaviors.

6.2 Introduction

The relationship between cells and their microenvironment is multifaceted and intricate. Cell-matrix interactions are critical for regulating cell spreading, contraction, migration, and ultimately, cell fate[1,2]. The interplay between cells and their surrounding extracellular matrix (ECM) is well orchestrated, and disruptions in homeostasis can result in aberrant signaling and disease pathologies. In particular, changes in the local microenvironment during fibrosis, a scarring outcome of many disease processes, can impact cell-mediated ECM remodeling and downstream signaling pathways[3–7]. Hydrogels are versatile polymer systems that can exhibit a wide range of relevant biophysical and chemical properties such as stiffness, degradability, and adhesion to mimic soft biological tissues[8,9]. Improving our understanding of these behaviors is important to inform the development of biomimetic biomaterials for future therapeutic applications.

While the mechanisms regulating cell phenotype on 2D substrates are becoming increasingly understood, cell behaviors within 3D cultures are less familiar. Many 2D cell culture systems have demonstrated correlative behaviors between physical microenvironmental cues and cell shape and phenotypic behavior. Increased elasticity and stiffness of 2D hydrogels, corresponding to fibrosis progression, typically results in greater cell spreading and elongation, more actin stress fiber formation and organization, and nuclear localization of disease-relevant transcriptional co-activators[3,10–16]. However, current 3D models have shown conflicting cell behaviors to those in 2D cultures[9,17]. The mechanical cues often associated with profibrotic behavior in 2D, such as increased matrix stiffness, actually hinder cell spreading in 3D – in some covalently crosslinked hydrogels, the increase in crosslinking density restricts cell spreading and contractility, leading to more rounded morphologies that have been previously coupled with normal, healthy tissue

behavior[18–22]. These counterintuitive trends emphasize the need to develop more tissue-relevant 3D hydrogel systems to study cell behaviors during the progression of fibrosis and disease.

The incorporation of stress relaxing materials, a characteristic feature of soft viscoelastic tissue, has enabled more nuanced studies focusing on the role of mechanics on cell behaviors, particularly during disease processes where soft viscoelastic tissue transitions into a stiffer and more elastic state[23–26]. The introduction of viscoelastic cues alters cell responses and highlights the importance of studying how multiple mechanical inputs contribute to cellular outcomes and tissue homeostasis. Seminal work by Charrier *et al*. demonstrated reduced fibroblast spread area on viscoelastic substrates with increasing loss modulus (G") due to substrate energy dissipation[27]. The degree and speed of stress relaxation, a key characteristic of viscoelastic substrates, also influences cell fate. Previous work by our lab has also illustrated that cells on viscoelastic hydrogels are more rounded and less spread due to viscous interactions preventing mature focal adhesion formation compared to elastic counterparts[28,29]. In 3D culture, Chaudhuri *et al*. tuned stress relaxation timescales, in which the stress relaxed to half its original value, of viscoplastic alginate hydrogels from 3300 seconds to 70 seconds and showed extensive fibroblast spreading and proliferation due to plastic deformation of the matrix[30]. Recent work has also revealed cell spreading and volume expansion in 3D may occur simultaneously in alginate hydrogels with faster stress relaxation[31].

In this study, we developed a 3D hydrogel system in which stiffness, viscoelasticity, and degradability could be independently controlled. In this system, a combination of covalent bonds and supramolecular interactions were incorporated to produce a viscoelastic system that cannot undergo plastic deformation. We chose to compare changes in cell behaviors by encapsulating

either human lung fibroblasts (HLFs), which are primary mediators of fibrosis, or human mesenchymal stem cells (hMSCs), whose cell mechanobiology is well characterized. We then used immunofluorescence and confocal microscopy to explore how these biophysical properties influenced cell morphology. We hypothesized that increasing viscoelasticity would facilitate more viscous dissipation of cell-generated forces into the matrix and lead to behaviors reminiscent of healthy tissue, but that elevations in matrix stiffness in combination with viscoelastic cues would promote cell spreading and elongation in 3D systems.

6.3 Materials and Methods

6.3.1 NorHA synthesis

Hyaluronic acid (HA) was functionalized with norbornene groups (NorHA), similar to previous methods[32]. Hyaluronic acid tertbutyl ammonium salt (HA-TBA) was first synthesized by reacting sodium hyaluronate (Lifecore, 62 kDa) with Dowex 50W proton-exchange resin. The reaction solution was then filtered, titrated to pH 7.05, frozen, and lyophilized. HA-TBA was then dissolved in dimethylsulfoxide (DMSO) with benzotriazole-1-yloxytris-(dimethylamino)phosphonium hexafluorophosphate (BOP) for 2 hours at 25°C before being quenched with cold water and dialyzed (molecular weight cutoff: 6−8 kDa) for 10 days. The solution was filtered after 5 days to remove any unreacted components. The product was frozen and lyophilized, and the degree of modification was 31% as determined by ^{1}H NMR (500 MHz Varian Inova 500, **Figure S6.1**).

6.3.2 β-CD-HA synthesis

β-cyclodextrin-modified hyaluronic acid (CD-HA) was synthesized by dissolving HA-TBA and 6-(6-aminohexyl)amino-6-deoxy-βcyclodextrin (β-CD-HDA) in DMSO with BOP and stirring for

3 hours at 25°C[33]. The reaction was then quenched with cold water and dialyzed for 10 days. The solution was filtered after 5 days to remove any unreacted components. The product was frozen and lyophilized before use. The degree of modification was 28%, determined via ^{1}H NMR (**Figure S6.2**).

6.3.3 Peptide synthesis

Solid-phase peptide synthesis of a thiolated adamantane (Ad) peptide (Ad-KKKCG) was performed on a Gyros Protein Technologies Tribute peptide synthesizer via Fmoc-protected methods as previously reported[28,29]. Rink Amide MBHA high-loaded (0.78 mmol/g) resin was swelled with 20% (v/v) piperidine in DMF and the amino acids were activated using N,N,N',N'-tetramethyl-O-(1H-benzotriazol-1-yl)uronium hexafluorophosphate (HBTU) and 0.4 M N-methyl morpholine in DMF. MMP-degradable di-thiol peptides (GCRD**PQG**↓IWGQDRCG, GCNS**VPMS**↓MRGGSNCG, abbreviated as PQG and VPMS) were synthesized on a Liberty Blue (CEM) microwave-assisted solid-phase peptide synthesizer via Fmoc-protected methods. Similarly, Rink Amide MBHA high-loaded resin was swelled with 20% (v/v) piperidine in DMF. The amino acids were coupled using 1 M diisopropylcarbodiimide (DIC) in DMF and 1 M Oxyma Pure (Advanced ChemTech) in DMF at 90°C. All peptides were cleaved from the resin using a solution of 92.5% trifluoroacetic acid, 2.5% triisopropylsilane, 2.5% 2,2'-(ethylenedioxy) diethanethiol (DODT), and 2.5% DI water for 2-3 hours, precipitated in cold ethyl ether and centrifuged thrice, and dried overnight. Peptides were resuspended in DI water, frozen, and lyophilized. Syntheses were confirmed via matrix-assisted laser desorption/ionization (MALDI) (**Figure S6.3**).

6.3.4 Three-dimensional (3D) HA hydrogel fabrication

3D hydrogels were fabricated via ultraviolet (UV) light-mediated thiol-ene addition. Soft (2 wt%) and stiff (6 wt%) elastic hydrogel precursor solutions containing 2 mM thiolated RGD peptide (GCGYGRGDSPG, Genscript) and degradable di-thiol peptide (either PQG or VPMS) were polymerized in the presence of UV light (365 nm, 5 mW/cm^2) and 1 mM lithium acylphosphinate (LAP) photoinitiator for 4 minutes. Soft (3 wt% NorHA-CDHA) and stiff (7 wt% NorHA-CDHA) viscoelastic hydrogels were fabricated by mixing CDHA with thiolated adamantane peptides (1:1 molar ratio of CD to Ad) to introduce physical interactions before adding in the degradable peptide (thiol-norbornene ratios of 0.5, 0.6, 0.7, 0.8 for soft elastic, stiff elastic, soft viscoelastic, and stiff viscoelastic, respectively), RGD, and NorHA. The viscoelastic hydrogel precursor solutions were photopolymerized using the same conditions as the elastic hydrogels. 3D hydrogel plugs (50 μL, ~ 4.7 mm diameter × 2 mm thick for unswollen hydrogels) were formed in 1 mL syringes in which the tips were cut off at the 0.1 mL mark using a razor blade. Hydrogels were swelled in either phosphate-buffered saline (PBS) or cell culture media at 37°C.

6.3.5 Hydrogel photopatterning

NorHA hydrogels (6 wt %) with an initially low crosslinking density (0.3 thiol-norbornene ratio) were fabricated via UV-mediated thiol-ene addition (4 min, 5 mW/cm^2) and swelled overnight in PBS at 37 °C. The hydrogels were swelled in a 2 wt% BSA in PBS solution for 2 hours before being swelled in a photopatterning solution containing 1 wt% BSA, LAP, di-thiol crosslinker, and fluorescently-labeled thiolated peptide for 1 hour at 37 °C. A patterned photomask transparency (CAD/Art Services, Inc) was then placed on top of the hydrogel and irradiated with a secondary

bout of UV light (2 min, 5 mW/cm^2). The hydrogels were then washed with PBS several times before imaging.

6.3.6 Mechanical characterization

Hydrogel rheological measurements were taken on an Anton Paar MCR 302 rheometer using either a cone-plate geometry (CP25-0.5, 25 mm diameter, 0.5°, 25 μm gap) to validate pre-fabricated hydrogel mechanics *in situ* or parallel plate geometry (PP08/S, 8 mm diameter) for swollen 3D hydrogels. *In situ* gelation was measured via oscillatory time sweeps (1 Hz, 1% strain) with a 2 min UV irradiation (365 nm, 5 mW/cm^2), oscillatory frequency sweeps (0.01-10 Hz, 1% strain), and stress relaxation and recovery tests cycling between 0.1 and 5% strain (1 Hz). Rheological characterization was also performed on 3D hydrogels that were swollen in PBS for at least 24 h to determine post-fabrication bulk mechanics. 3D hydrogel plugs were sandwiched between a fixed bottom rheometer plate and a top parallel plate until a 0.2 N force was obtained. Frequency sweeps (0.01-10 Hz, 1% strain) were performed to measure viscoelastic properties post-fabrication. Nanoindentation measurements of swollen 3D hydrogels were done using an Optics11 Piuma nanoindenter. A 47 μm diameter spherical borosilicate glass probe attached to a cantilever with a spring constant of 0.49 N/m was used during testing. The Young's modulus (E) was determined after each indentation (6 μm indentation depth) by taking the resulting loading portions of the force versus distance curve and applying the Hertzian contact mechanics model (Poisson's ratio of 0.5). Frequency-dependent properties were also quantified using the dynamic mechanical analysis (DMA)-like operational mode. DMA tests of swollen 3D hydrogels were used to measure viscoelastic properties (G' and G") via frequency sweeps (6 μm indentation depth, 1-10 Hz).

6.3.7 Cell culture

Human lung fibroblasts (HLFs) and human mesenchymal stem cells (hMSCs) were used for all experiments. HLFs (hTERT T1015, abmgood) were used between passages 2-10 and culture medium was changed every 2-3 days (Gibco Dulbecco's Modified Eagle's Medium (DMEM), 10 v/v% fetal bovine serum (FBS), and 1 v/v% antibiotic antimycotic (1000 U/mL penicillin, 1000 μg/mL streptomycin, 0.25 μg/mL amphotericin B)). hMSCs (PT-2501, Lonza) were used at passage 5 and culture medium was changed every 2-3 days (Gibco Minimal Essential Media α (MEM α), 20 v/v% FBS, and 1 v/v% antibiotic antimycotic). Prior to cell encapsulation, all polymer, peptide, and cell culture reagents were either sterile filtered or re-lyophilized and sterilized using germicidal UV irradiation for 2 h before adding sterile PBS. Cells were encapsulated within hydrogel plugs at a density of 1-3 million cells/mL. Culture medium was replaced every 2 days for 7-day cultures.

6.3.8 Live/Dead assay

Cell viability after hydrogel encapsulation was determined using a Live/Dead cell viability assay (Invitrogen) per the manufacturer's instructions. Fluorescent images were taken on a Leica SP8 confocal laser scanning microscope. 3D hydrogels were placed in a Nunc glass bottom dish and z-stack fluorescent images (400 μm thickness, 10 μm step size) were taken. Viability was quantified via Fiji image analysis software as the percentage of live (green-fluorescent calcein-AM stain) cells.

6.3.9 Immunocytochemistry and imaging

For immunostaining, cell-encapsulated hydrogels were fixed in 10% buffered formalin overnight, permeabilized in 0.1% Triton X-100 for 45 min, and blocked in 3% bovine serum albumin (BSA) in PBS for 1-2 h at room temperature. Hydrogels were then incubated overnight at 4°C with primary antibodies, which included Yes-associated protein (YAP, mouse monoclonal antibody, 1:200, Santa Cruz) and α-SMA (mouse monoclonal anti-α-SMA clone 1A4, 1:400, Sigma-Aldrich). The hydrogels were rinsed three times in PBS and incubated with secondary antibodies (AlexaFluor 488 goat anti-rabbit IgG, 1:400; AlexaFluor 555 goat anti-mouse, 1:400) and/or rhodamine phalloidin to visualize F-actin (1:200, Invitrogen) for 2 h in the dark at room temperature. The hydrogels were then rinsed and stained with a DAPI nuclear stain (1:5,000) for 30 min, rinsed again, and stored in the dark at 4°C. Fluorescent z-stack images (400 μm thickness, 10 μm step size) were acquired using a Leica SP8 confocal laser scanning microscope.

6.3.10 Image analysis

Image analysis was done via Fiji image analysis software. Cell volume, cell shape index (CSI), and aspect ratio (AR) were quantified from fluorescent images. Each 3D z-stack image was converted to 8-bit grayscale and then analyzed using Fiji's "3D Object Counter" module, which enables semi-automated intensity-based thresholding to determine cell metrics including volume (V), surface area (A_0), and bounding box. CSI, a measure of circularity (line = 0, sphere = 1), was calculated using the following formula:

$$CSI = \frac{\pi^{\frac{1}{3}}(6V)^{\frac{2}{3}}}{A_0}$$

AR was calculated as the ratio of the largest and smallest side of a bounding box surrounding each cell.

6.3.11 Statistical analysis

All experiment groups included at least 3 hydrogels. Data points represent average values from one hydrogel. Error bars represent standard deviation unless otherwise stated. One-way ANOVA with Tukey's HSD post hoc tests were performed for all quantitative data sets. Significance was indicated by *, **, or *** corresponding to $P < 0.05$, 0.01, or 0.001, respectively.

6.4 Results and Discussion

6.4.1 Three-dimensional (3D) viscoelastic hydrogels were successfully fabricated with a combination of covalent crosslinks and supramolecular interactions

To investigate the influence of viscoelasticity on cell behavior, we adapted a previously designed phototunable hydrogel system with independent control over stiffness, viscoelasticity, and ligand presentation for 3D cell culture (**Figure 6.1A**)[28,29]. Viscoelastic hyaluronic acid (HA) hydrogels were fabricated to represent normal (G' ~ 0.5 kPa) and fibrotic (G' ~ 3 kPa) tissue mechanics. Stiffness was controlled by adjusting HA polymer concentration and the ratio of dithiol crosslinker to norbornene-modified HA (NorHA) for ultraviolet (UV) light-mediated thiol-ene addition between thiols and norbornenes. Presentation of time-dependent viscoelastic properties occurred through incorporation of supramolecular guest-host interactions between thiolated adamantane (Ad) peptides and β-cyclodextrin modified HA (CDHA). In addition, cell-mediated degradation was also tested using two MMP-sensitive crosslinkers, GCRD**PQG**↓IWGQDRCG and GCNS**VPMS**↓MRGGSNCG (abbreviated as PQG and VPMS).

Hydrogel bulk mechanics of post-fabricated swollen hydrogels were assessed via oscillatory shear rheology. While the storage modulus of the soft and stiff groups remained equivalent between

elastic and viscoelastic counterparts (soft: G' ~ 0.5 kPa, stiff: G' ~ 3 kPa), the introduction of viscous character resulted in loss modulus values within an order of magnitude of G' values for the viscoelastic groups (G" ~ 0.13 kPa for soft hydrogels) compared to elastic counterparts (G" ~ 0.02 kPa for soft hydrogels), which corresponds to native tissue mechanics (**Figure 6.1B, S6.4**).

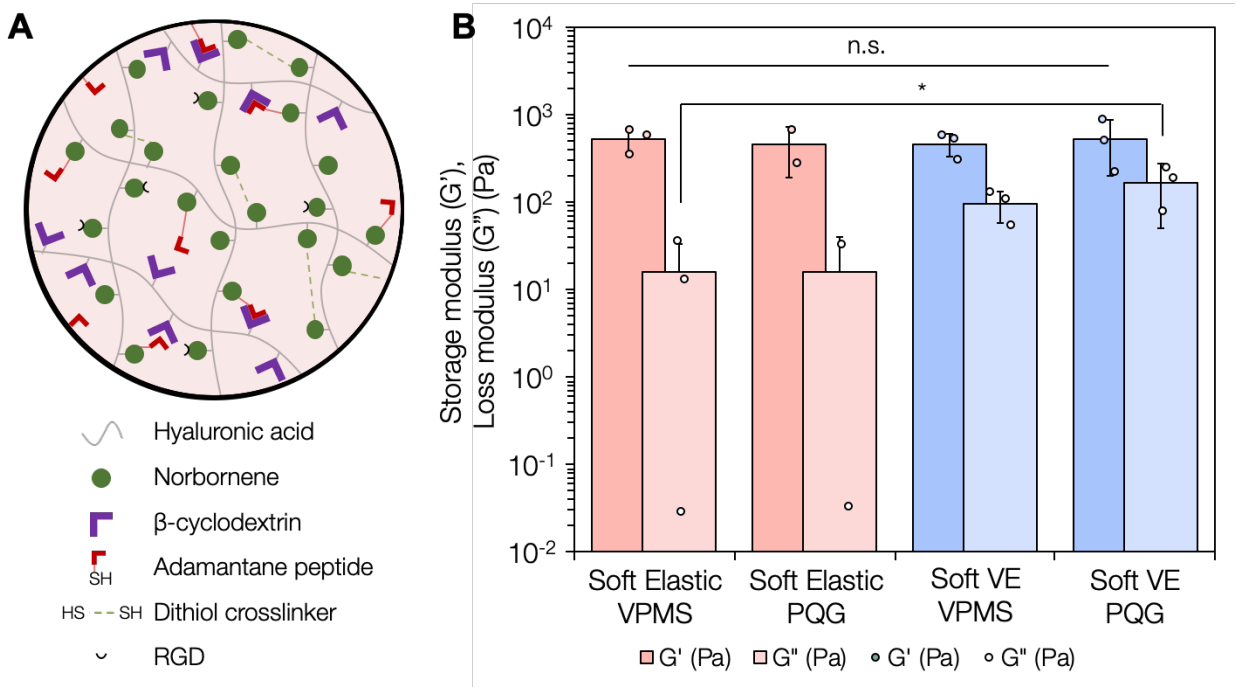

Figure 6.1. Viscoelastic hydrogel design and mechanical characterization. (A) Schematic illustrating components in a viscoelastic hydrogel. Covalent crosslinks between norbornenes (green circles) and thiols (-SH) via light-mediated thiol-ene addition enables elastic hydrogel formation (with dithiol crosslinker) or tethering of thiolated peptides such as adamantane (Ad) peptides. Viscoelastic properties are incorporated through guest-host interactions between Ad groups (guest, red L-shape) and β-cyclodextrin (host, purple L-shape). Adhesive ligands such as RGD are also included to support cell attachment. (B) Rheological characterization of storage (G') and loss (G") moduli of soft hydrogel groups with either the VPMS or PQG dithiol crosslinker. G' is maintained across the soft groups but G" is within an order of magnitude for the viscoelastic hydrogels with both covalent crosslinks and supramolecular guest-host interactions.

6.4.2 Engineered degradability via MMP-degradable dithiol crosslinkers enabled cell spreading after 14 days

Following mechanical characterization of the hydrogel groups, we next encapsulated either human lung fibroblasts (HLFs) or human mesenchymal stem cells (hMSCs) within hydrogels to assess cell viability and changes in volume and spread area over a 14-day culture period (**Figure 6.2A**). In addition, two crosslinkers with MMP-sensitive sequences, VPMS and PQG, were used to investigate their influence on cell spreading[34,35]. The first sequence, VPMSMRGG, has been utilized in several hydrogel systems due to its sensitivity to cleavage by MMPs known to play a major role in ECM remodeling such as MMP-1 (collagenase 1), MMP-2 (gelatinase A), MMP-7 (matrilysin), and MMP-9 (gelatinase B)[36,37]. In addition to MMP-1, MMP-2, and MMP-9, the PQGIWGQ sequence is also sensitive to MMP-3 (stromelysin-1) and MMP-8 (neutrophil collagenase)[38–40]. Notably, the PQG sequence is a mutated version of the native collagen type I α1 chain moiety PQGIAGQ and the substitution of alanine (A) for tryptophan (W) results in an increased rate constant[37,41]. For example, kinetic rate constant k_{cat} values reported in literature for MMP-1 are 0.31 ± 0.25 s^{-1} and 0.65 ± 0.13 s^{-1} for PQGIAGQ and PQGIWGQ, respectively, and for MMP-2, are 1.50 ± 0.25 s^{-1} and 2.17 ± 0.16 s^{-1} for PQGIAGQ and PQGIWGQ, respectively[37].

High cell viability was maintained in all hydrogel groups for both cell types, as determined by live/dead staining (**Figure 6.2B**). Both HLFs and hMSCs showed at least 80% viability on day 1 (HLFs: 93.8 ± 5.96%, hMSCs: 98.9 ± 1.46%). Over the 14-day period, HLFs showed a decline in viability but remained over 70% viable for all hydrogel groups (average viability ~ 88% on day 7, ~ 79% on day 14). High hMSC viability was maintained, with at least 90% viability for all hydrogel groups on days 7 (average viability ~ 97%) and 14 (average viability ~ 96%), regardless of stiffness and viscoelasticity.

After confirming that encapsulation within the viscoelastic hydrogels did not significantly impact cell viability, we next investigated the influence of stiffness, viscoelasticity, and degradability on cell volume and shape. Overall, HLF volumes significantly increased during the first 7 days of culture and then plateaued in the second week (**Figure 6.2C**). Interestingly, cell volume expansion occurred while maintaining similar aspect ratios throughout the culture period (**Figure 6.2D**). In addition, in all the hydrogel groups, cell clustering was seen. HLFs displayed protrusions within soft elastic hydrogels, especially containing the PQG crosslinker, after 14 days. This behavior could be attributed to the lower crosslinking density. While greater cell volume was seen for HLFs in viscoelastic hydrogels, minimal protrusions were exhibited, potentially owing to the physical, supramolecular interactions giving way to viscous dissipation and decreased ability for stable spreading mechanisms to take place. In contrast, while lower hMSC volumes were observed, hMSCs demonstrated increased spreading and elongation after 14 days compared to HLFs, particularly within soft elastic substrates. This behavior was more pronounced within PQG-containing hydrogels. In stiff elastic hydrogels with higher crosslinker density and HA polymer concentration, hMSCs remained smaller and more rounded. Interestingly, hMSC spreading was greater in stiff viscoelastic groups than in soft viscoelastic hydrogels, and elongation was more pronounced in hydrogels containing the MMP-degradable PQG crosslinker. Decreased hMSC volumes within viscoelastic substrates could be due to the viscous contributions from the supramolecular interactions. Nonetheless, hMSC spreading and elongation displayed greater responsiveness to hydrogel mechanical properties compared to HLFs.

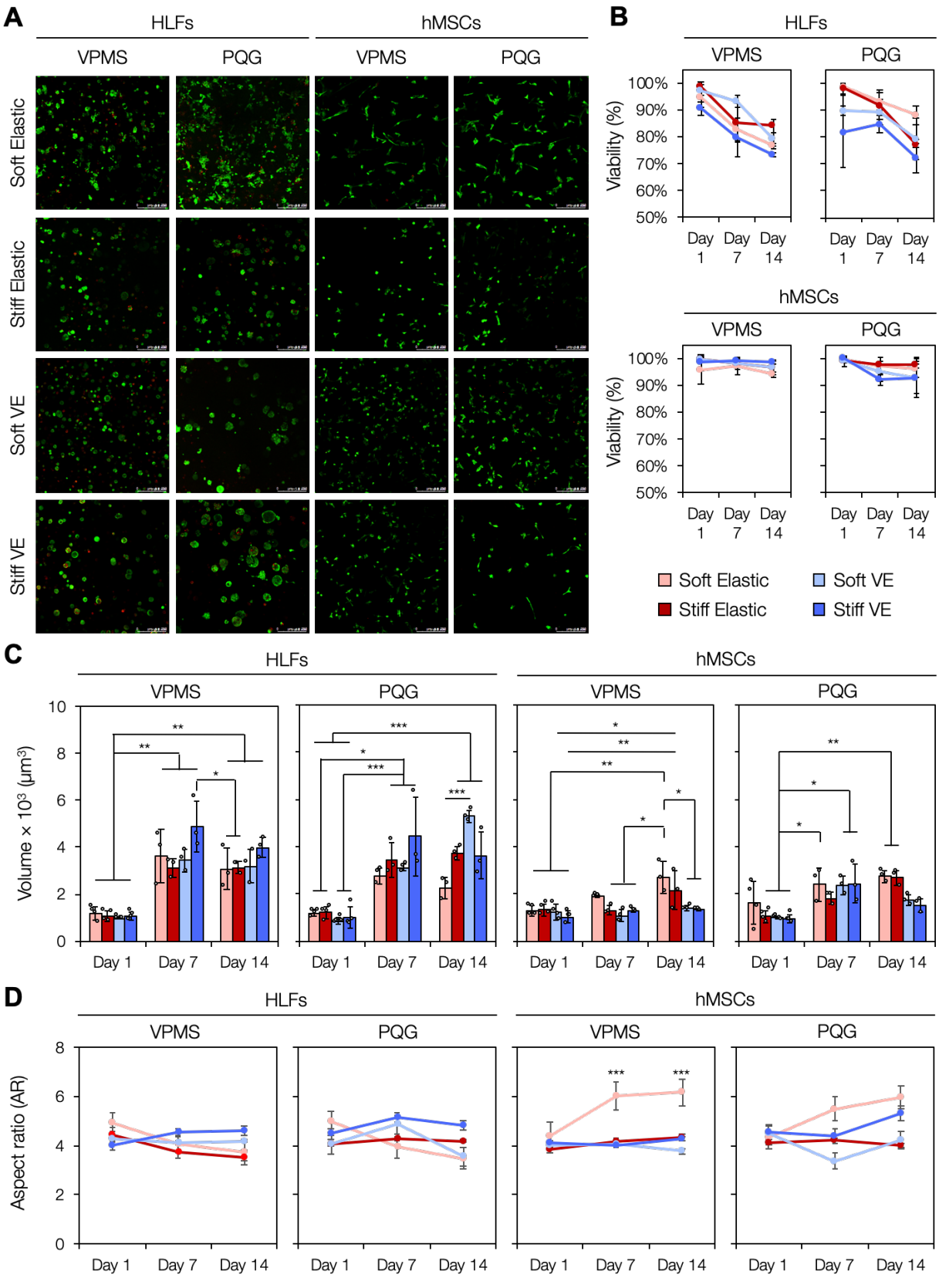
A
HLFs
hMSCs
VPMS
PQG
VPMS
PQG
Soft Elastic
Stiff Elastic
Soft VE
Stiff VE
B
HLFs
VPMS
PQG
Viability (%)
100%
90%
80%
70%
60%
50%
Day 1
Day 7
Day 14
hMSCs
Soft Elastic
Stiff Elastic
Soft VE
Stiff VE
C
HLFs
hMSCs
VPMS
PQG
Volume × 10³ (μm³)
0
2
4
6
8
10
Day 1
Day 7
Day 14
D
Aspect ratio (AR)
0
2
4
6
8

Figure 6.2. Cell behaviors as a function of stiffness and viscoelasticity over a 14-day culture period. (A) Human lung fibroblasts (HLFs) and human mesenchymal stem cells (hMSCs) were encapsulated within soft or stiff elastic and viscoelastic hydrogels. Images shown are maximum projection live/dead images from day 14 (400 μm thickness, 10 μm step size). Scale bars: 250 μm. (B) Cell viability remained high for both HLFs and hMSCs regardless of hydrogel group. (C) Cell volume increased significantly for HLFs compared to hMSCs and plateaued in the second week in both cases. (D) Aspect ratio (AR) did not significantly change for HLFs, which demonstrated volume expansion while maintaining rounded morphologies. In contrast, hMSCs displayed increased spreading after 14 days and became more elongated, particularly within soft elastic substrates. *: $P < 0.05$, **: $P < 0.01$, ***: $P < 0.001$.

6.4.3 Cell spreading was influenced by the degree of hydrogel viscoelasticity

After observing differences in cell volume, spreading, and elongation as a function of multiple microenvironmental cues, we were interested in understanding the influence of increasing viscoelasticity on cell behaviors and in particular, cell spreading. We first used *in situ* oscillatory shear rheology to mechanical characterize our hydrogel groups, in which we increased the ratio of supramolecular interactions to covalent crosslinks by increasing both the concentration of Ad peptides and CD-HA while maintaining a 1:1 Ad:CD ratio. Our formulations resulted in a soft elastic control group and three soft viscoelastic groups with 3 v/v% Ad peptide, 5 v/v% Ad peptide, and 7 v/v% Ad peptide. While the storage modulus (G') remained the same for all hydrogel groups (G' ~ 0.45 kPa), the loss modulus (G") increased as supramolecular interactions increased (G" ~ 25, 35, and 50 Pa for 3 v/v%, 5 v/v%, and 7 v/v%, respectively) (**Figure 6.3A**). Frequency-dependent behavior was observed for all soft viscoelastic groups, G" increased as frequency increased. In contrast, frequency did not significantly influence G' or G" for soft elastic hydrogels (**Figure 6.3B**). Loss tangent, indicative of viscoelasticity, ranged from 0.01 for soft elastic hydrogels to 0.32 for 7 v/v% hydrogels at a frequency of 10 Hz (**Figure 6.3C**), demonstrating control over viscoelastic properties. Time-dependent stress relaxation, a key characteristic of viscoelastic materials, was also demonstrated in viscoelastic hydrogels. At a constant strain (5%),

the relaxation profiles of the viscoelastic hydrogel groups showed an immediate stress relaxation within the first 10 seconds (**Figure 6.3D**).

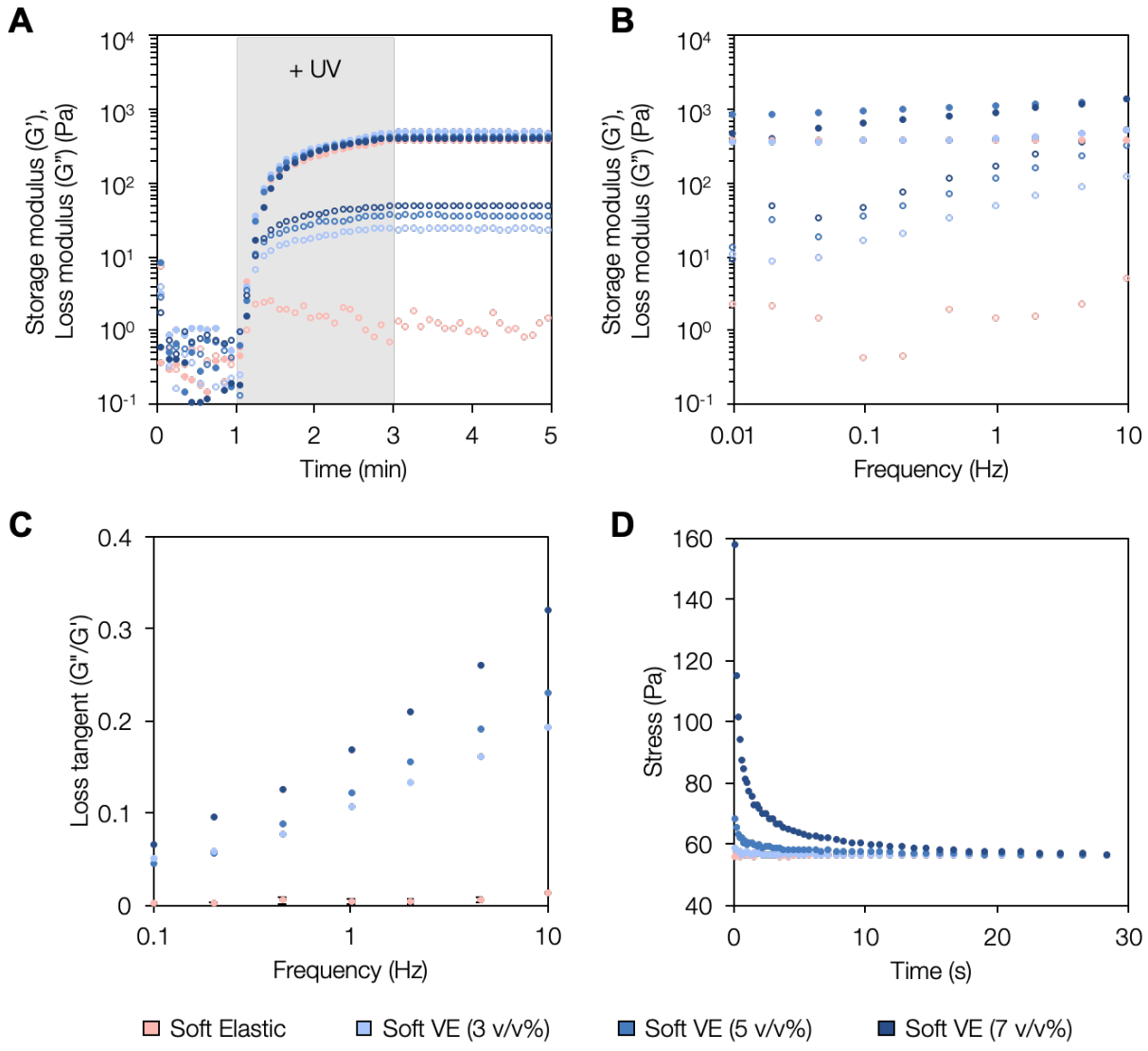

Figure 6.3. Rheological characterization of hydrogels with increasing loss moduli (G"). (A) Soft viscoelastic hydrogels with equivalent storage moduli (G', filled circles) show increasing loss moduli (G", open circles) as the concentration of supramolecular interactions (indicated on the legend as 3 v/v%, 5 v/v%, and 7 v/v% Ad peptide) increases. (B) Frequency-dependent behavior is demonstrated for viscoelastic hydrogels at a constant frequency (1 Hz) and strain (1%), as shown by increasing G" as frequency increases. (C) Loss tangent, or G"/G', increases significantly with increasing frequency for viscoelastic groups. (D) Viscoelastic hydrogels show rapid stress relaxation within the first 10 seconds compared to elastic counterparts.

After confirming mechanical properties, we encapsulated HLFs and hMSCs within hydrogels of increasing viscoelasticity for 7 days and measured cell viability, volume, aspect ratio (AR), a measure of elongation, and cell shape index (CSI), a measure of circularity (**Figure 6.4A**). Both HLFs and hMSCs showed high levels of viability that were retained over 7 days, with the lowest viability at 88% at day 7 (**Figure 6.4B**). Compared to hMSCs, which showed minimal volume increases over the culture period, HLFs demonstrated greater volume expansion and growth among all hydrogel groups (**Figure 6.4C, D**). Aspect ratio and cell shape index did not significantly change as a function of viscoelasticity for either cell type. HLF elongation was not seen in within any hydrogel group after 7 days. Increasing G" seemed to suppress hMSC elongation, which could be attributed to the increase in viscous dissipation preventing cell spreading within a viscoelastic environment. While other groups have observed increased spreading in hydrogels with greater stress relaxation, those typically involved viscoelastic liquid, or viscoplastic, hydrogel systems that enabled complete plastic deformation by cells[30,42,43]. In contrast, this viscoelastic solid system introduced time-dependent behavior while preventing irrecoverable deformation, suggesting differential cell sensing from viscous cues. Additionally, the subtle morphological changes may be related to the relatively narrow range of G" investigated.

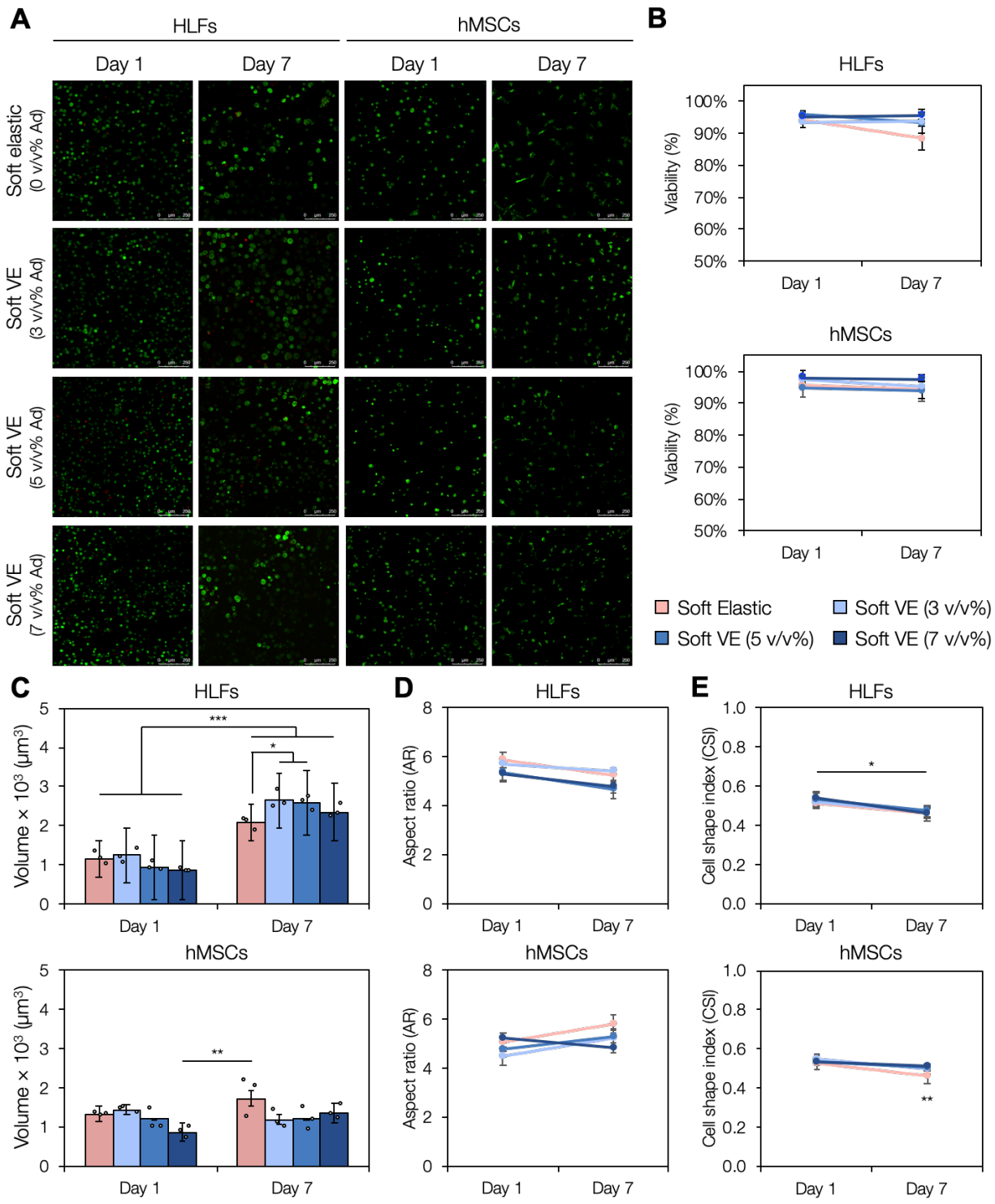

Figure 6.4. Influence of increasing loss modulus (G") on cell volume and spreading. (A) Live/dead maximum projections of HLFs and hMSCs on days 1 and 7 in hydrogels with increasing G". Scale bars: 250 μm. (B) High HLF and hMSC viability was demonstrated for all hydrogel groups. (C) HLF volumes increased significantly over 7 days compared to hMSCs, which exhibited minimal volume increases. HLFs maintained rounded morphologies regardless of viscoelasticity as

measured by (D) aspect ratio (AR) and (E) cell shape index (CSI). Spreading was observed for hMSCs in soft elastic hydrogels. *: $P < 0.05$, **: $P < 0.01$, ***: $P < 0.001$.

Finally, to further explore the impact of biophysical factors on spreading and cell behaviors, we analyzed F-actin stress fiber organization and nuclear translocation of YAP/TAZ, a mechanosensing transcriptional co-activator involved in disease processes (**Figure 6.5A**)[44]. In general, F-actin stress fibers were not prominent in HLFs across all hydrogel groups, showing more diffuse actin staining (**Figure 6.5B**). However, YAP nuclear localization was heightened in all groups, especially within cell clusters. More pronounced trends were demonstrated in hMSCs. Stress fiber organization decreased as substrate viscoelasticity increased, with more diffuse actin staining and rounded hMSC morphologies compared to more spread with distinct stress fiber formation and organization within soft elastic hydrogels. Nuclear localization of YAP showed similar trends, with greater localization in soft elastic substrates compared to soft viscoelastic groups.

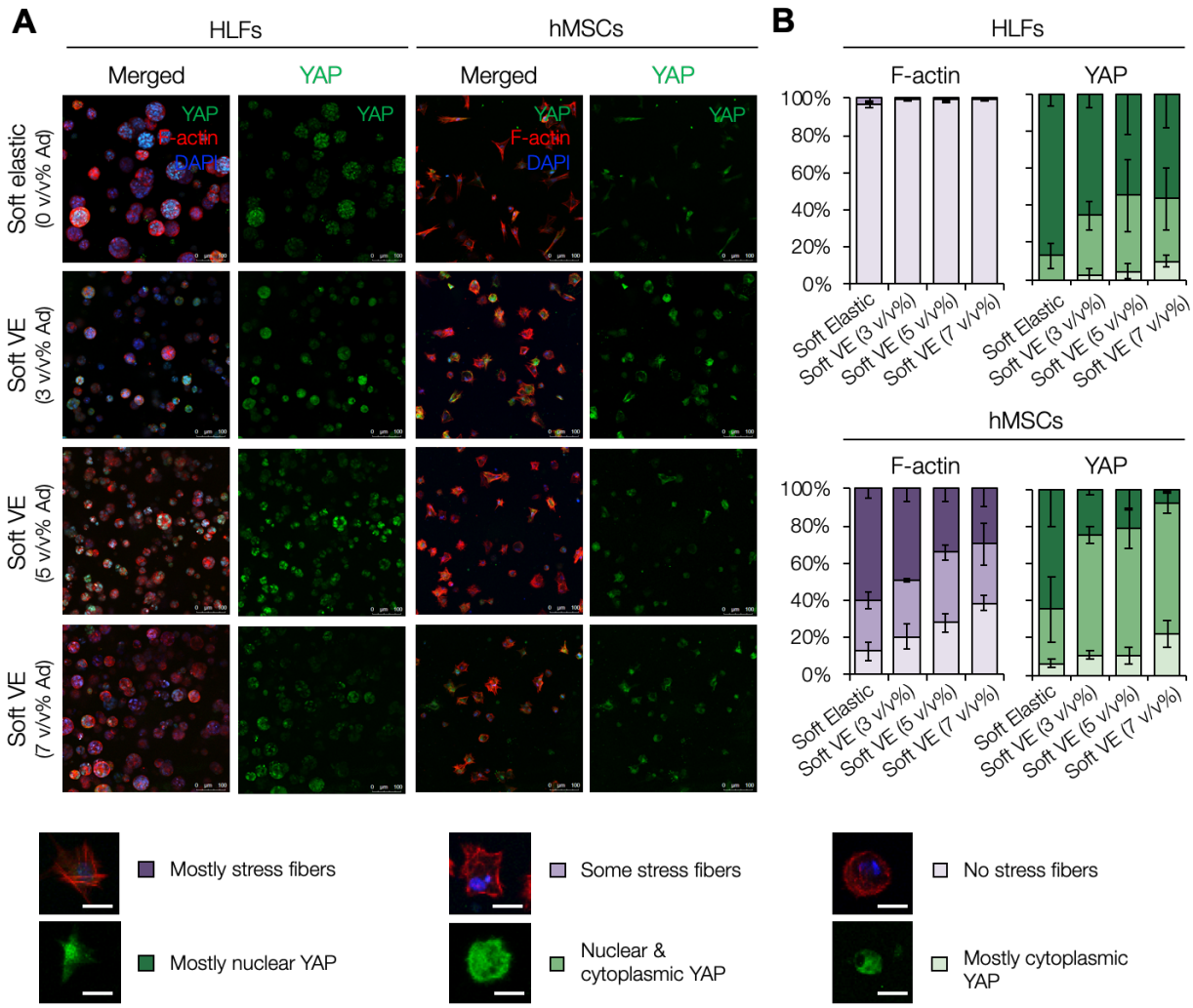

Figure 6.5. Qualitative analysis of F-actin stress fiber organization and YAP nuclear localization. (A) HLFs and hMSCs encapsulated in soft elastic and soft viscoelastic hydrogels of increasing G" were fixed and stained for F-actin and YAP. Scale bars: 100 μm. (B) Percentage of HLFs and hMSCs showing different degrees of F-actin stress fiber organization and YAP nuclear localization. As viscoelasticity increased, both stress fiber organization and nuclear YAP decreased. 3 hydrogels were tested per experimental group (150-550 cells total). Legend scale bars: 25 μm.

6.4.4 Heterogeneous mechanics were photopatterned via secondary light-mediated thiol-ene addition

Finally, we explored the use of photopatterning to introduce heterogeneous mechanics within a 3D hydrogel model. After fabricating an initial hydrogel with a low crosslinker density (thiol-

norbornene ratio of 0.3), the swollen hydrogel was then incubated in a secondary photopatterning solution containing dithiol crosslinker, photoinitiator, and thiolated fluorescent peptides for pattern visualization. A photomask transparency was then placed over the hydrogel and irradiated with UV light (365 nm) for 2 minutes to enable secondary thiol-ene addition to occur in the regions exposed to light, resulting in patterned regions of increased stiffness alternating with more compliant, non-patterned regions, mimicking heterogeneous tissue with fibrotic regions alternating with normal, healthier tissue areas (**Figure 6.6A**). Successful hydrogel photopatterning was confirmed via fluorescence microscopy (**Figure 6.6B**). To examine the pattern depth within the hydrogel, images were taken to a depth of 400 μm and the side profile was analyzed in 3D, demonstrating minimal decreases in fluorescence intensity through the depth of the hydrogel. Compared to other patterning approaches, the use of a photomask is simple, cost-effective, and can spatiotemporally introduce mechanical cues in a 3D hydrogel model.

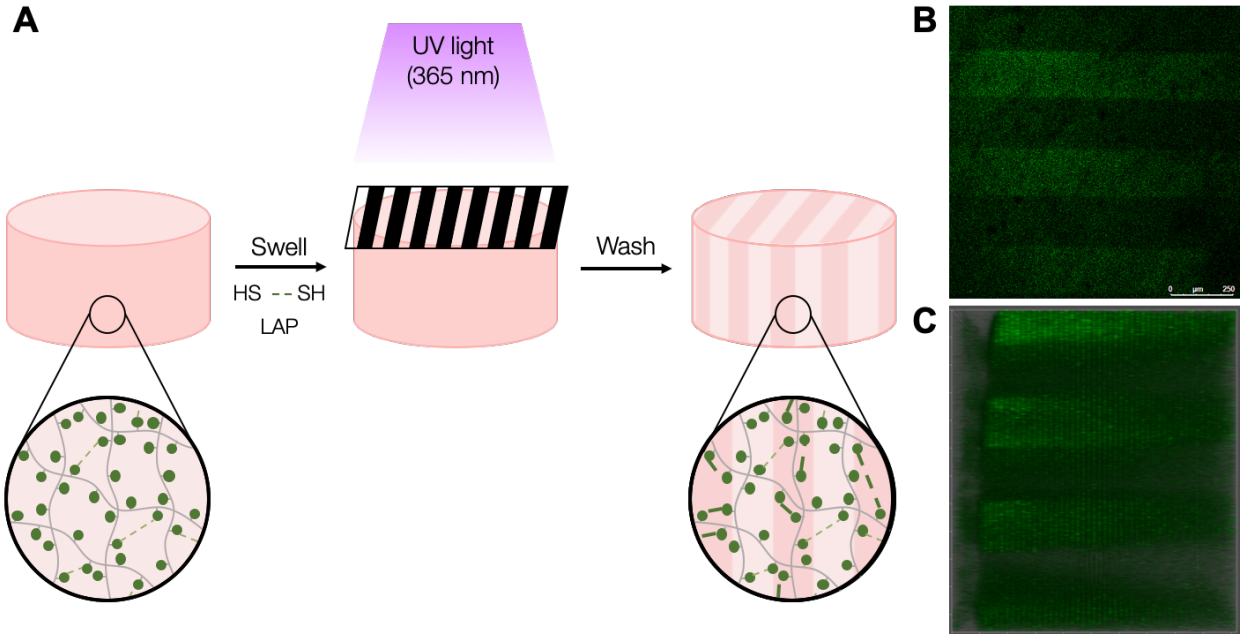

Figure 6.6. Hydrogel photopatterning to introduce heterogeneous mechanics. (A) Schematic of photopatterning process. An initially soft 3D hydrogel is formed via UV light-mediated thiol-ene

addition between dithiol crosslinker and norbornenes, leaving the majority of norbornenes available for secondary crosslinking. After swelling in PBS overnight, the hydrogel is swelled in a photopatterning solution containing dithiol crosslinker, LAP photoinitiator, and thiolated fluorophore for visualization. The hydrogel is then covered with a photomask transparency and irradiated with a second bout of UV light for 2 minutes to enable the formation of additional crosslinks in the exposed regions. The photopatterned hydrogel is then washed to remove unreacted components. (B) Maximum projection of a 3D photopatterned hydrogel with 200 µm stripes. Scale bar: 250 µm. (C) Side profile of a photopatterned hydrogel showing pattern fidelity throughout the depth of the substrate; left side is the top of the hydrogel and right is the bottom.

To further characterize the heterogeneous mechanical properties patterned into the hydrogels, nanoindentation was performed. Photopatterned hydrogels were horizontally sectioned in half and the cut surfaces were indented to measure stiffness. Matrix scans (8 x 8, 200 µm indentation spacing) were used to map the hydrogel surface and measure Young's moduli. Hydrogel stiffness ranged from 0.7 kPa to around 5 kPa and also aligned with the striped photomask (200 µm diameter stripes) used during the patterning process (**Figure 6.7**). We anticipate this spatiotemporally tunable photopatterning approach will be useful in the design of 3D heterogeneous disease models requiring control over microenvironmental cues.

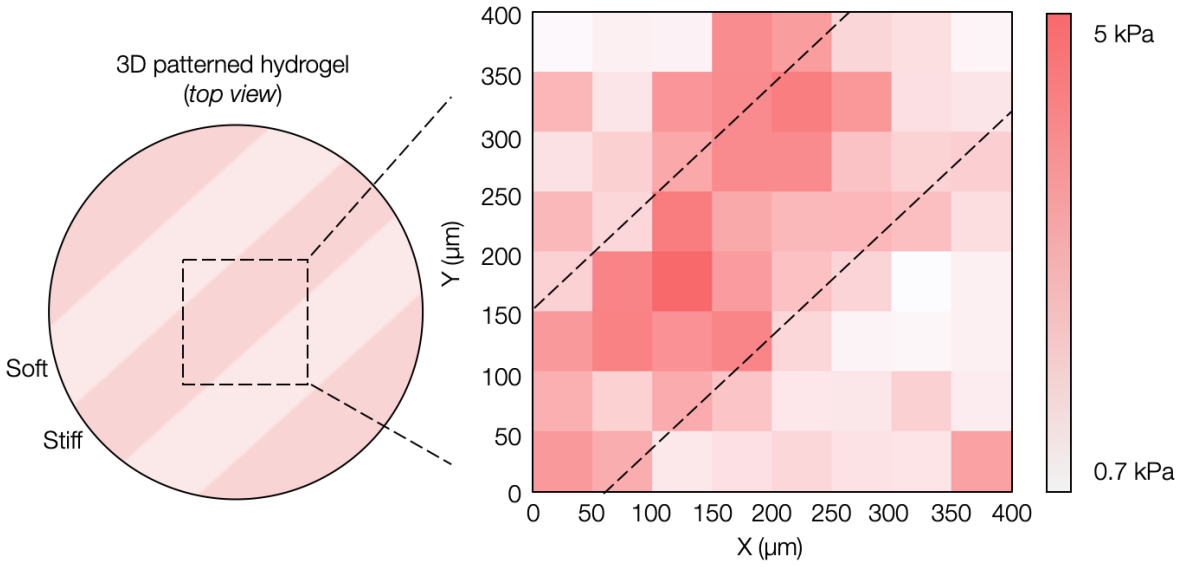

Figure 6.7. Mechanical characterization of photopatterned hydrogels via nanoindentation. 3D hydrogel plugs were cut in half horizontally for nanoindentation and matrix scans (8 x 8 with 200

μm indentation spacing) of the cut hydrogel surface were conducted to determine Young's modulus values. Young's moduli correlated with the 200 μm photomask used to diagonally pattern the 3D hydrogel. Dashed lines on the heat map represent the photopatterned region.

6.5 Conclusions

This work explored the influence of stiffness, viscoelasticity, and degradability cell volume and spreading in a 3D hydrogel system. We showed that for elastic hydrogel groups, cell spreading and elongation was seen in soft hydrogels but restricted for stiff groups. However, cells in viscoelastic substrates demonstrated reduced spreading and cell expansion for hMSCs and HLFs, respectively, due to energy dissipation of viscous contributions into the matrix. Trends were more prominent in hydrogels containing the PQG crosslinker sequence, suggesting that differences in cell-secreted MMPs impacted hydrogel permissibility. Increasing loss moduli (G") led to reduced F-actin stress fiber organization and YAP nuclear localization as well. Surprisingly, these behaviors seen in soft viscoelastic 3D hydrogels are more reminiscent of normal healthy tissue and corroborate with well-understood mechanisms on 2D cultures, in contrast to cell morphologies seen in traditional 3D elastic substrates (e.g., increased cell spreading in soft elastic substrates mimicking normal tissue versus more rounded morphologies in stiff elastic substrates mimicking fibrotic tissue). Successful photopatterning of mechanical cues was also highlighted, showing relevance in designing 3D hydrogel systems for studying cell fate during disease progression.

6.6 References

(1) Duscher, D.; Maan, Z. N.; Wong, V. W.; Rennert, R. C.; Januszyk, M.; Rodrigues, M.; Hu, M.; Whitmore, A. J.; Whittam, A. J.; Longaker, M. T.; et al. Mechanotransduction and Fibrosis. *J. Biomech.* **2014**, *47* (9), 1997–2005. https://doi.org/10.1016/j.jbiomech.2014.03.031.

(2) Wang, N.; Tytell, J. D.; Ingber, D. E. Mechanotransduction at a Distance: Mechanically Coupling the Extracellular Matrix with the Nucleus. *Nat. Rev. Mol. Cell Biol.* **2009**, *10* (1), 75–82. https://doi.org/10.1038/nrm2594.

(3) Wells, R. G. The Role of Matrix Stiffness in Regulating Cell Behavior. *Hepatology* **2008**, *47* (4), 1394–1400. https://doi.org/10.1002/hep.22193.

(4) Burridge, K.; Guilluy, C. Focal Adhesions, Stress Fibers and Mechanical Tension. *Exp. Cell Res.* **2016**, *343* (1), 14–20. https://doi.org/10.1016/j.yexcr.2015.10.029.

(5) Hinz, B.; Lagares, D. *Myofibroblasts*; 2021.

(6) Lu, P.; Takai, K.; Weaver, V. M.; Werb, Z. Extracellular Matrix Degradation and Remodeling in Development and Disease. *Cold Spring Harb. Perspect. Biol.* **2011**, *3* (12), 1–24. https://doi.org/10.1101/cshperspect.a005058.

(7) Wan, S.; Fu, X.; Ji, Y.; Li, M.; Shi, X.; Wang, Y. FAK- and YAP/TAZ Dependent Mechanotransduction Pathways Are Required for Enhanced Immunomodulatory Properties of Adipose-Derived Mesenchymal Stem Cells Induced by Aligned Fibrous Scaffolds. *Biomaterials* **2018**, *171*, 107–117. https://doi.org/10.1016/j.biomaterials.2018.04.035.

(8) Caliari, S. R.; Burdick, J. A. A Practical Guide to Hydrogels for Cell Culture. *Nat. Methods* **2016**, *13* (5), 405–414. https://doi.org/10.1038/nmeth.3839.

(9) Baker, B. M.; Chen, C. S. Deconstructing the Third Dimension-How 3D Culture Microenvironments Alter Cellular Cues. *J. Cell Sci.* **2012**, *125* (13), 3015–3024. https://doi.org/10.1242/jcs.079509.

(10) Guvendiren, M.; Burdick, J. A. Stiffening Hydrogels to Probe Short- and Long-Term Cellular Responses to Dynamic Mechanics. *Nat. Commun.* **2012**, *3*, 792–799. https://doi.org/10.1038/ncomms1792.

(11) Rosales, A. M.; Vega, S. L.; DelRio, F. W.; Burdick, J. A.; Anseth, K. S. Hydrogels with Reversible Mechanics to Probe Dynamic Cell Microenvironments. *Angew. Chemie - Int. Ed.* **2017**, *56* (40), 12132–12136. https://doi.org/10.1002/anie.201705684.

(12) Mih, J. D.; Marinkovic, A.; Liu, F.; Sharif, A. S.; Tschumperlin, D. J. Matrix Stiffness Reverses the Effect of Actomyosin Tension on Cell Proliferation. *J. Cell Sci.* **2012**, *125* (24), 5974–5983. https://doi.org/10.1242/jcs.108886.

(13) Asano, S.; Ito, S.; Takahashi, K.; Furuya, K.; Kondo, M.; Sokabe, M.; Hasegawa, Y. Matrix Stiffness Regulates Migration of Human Lung Fibroblasts. *Physiol. Rep.* **2017**, *5* (9), 1–11. https://doi.org/10.14814/phy2.13281.

(14) Santos, A.; Lagares, D. Matrix Stiffness: The Conductor of Organ Fibrosis. *Current Rheumatology Reports*. Current Rheumatology Reports 2018. https://doi.org/10.1007/s11926-018-0710-z.

(15) Caliari, S. R.; Perepelyuk, M.; Cosgrove, B. D.; Tsai, S. J.; Lee, G. Y.; Mauck, R. L.; Wells, R. G.; Burdick, J. A. Stiffening Hydrogels for Investigating the Dynamics of Hepatic Stellate Cell Mechanotransduction during Myofibroblast Activation. *Sci. Rep.* **2016**, *6*, 1–10. https://doi.org/10.1038/srep21387.

(16) Discher, D. E.; Janmey, P.; Wang, Y. L. Tissue Cells Feel and Respond to the Stiffness of Their Substrate. *Science (80-.).* **2005**, *310* (5751), 1139–1143.

(17) Tibbitt, M. W.; Anseth, K. S. Hydrogels as Extracellular Matrix Mimics for 3D Cell Culture. *Biotechnol. Bioeng.* **2009**, *103* (4), 655–663. https://doi.org/10.1002/bit.22361.

(18) Caliari, S. R.; Vega, S. L.; Kwon, M.; Soulas, E. M.; Burdick, J. A. Dimensionality and Spreading Influence MSC YAP/TAZ Signaling in Hydrogel Environments. *Biomaterials* **2016**, *103*, 314–323. https://doi.org/10.1016/j.biomaterials.2016.06.061.

(19) Stowers, R. S.; Allen, S. C.; Suggs, L. J.; Anseth, K. S. Dynamic Phototuning of 3D Hydrogel Stiffness. *Proc. Natl. Acad. Sci. U. S. A.* **2015**, *112* (7), 1953–1958. https://doi.org/10.1073/pnas.1421897112.

(20) Wade, R. J.; Burdick, J. A. Engineering ECM Signals into Biomaterials. *Mater. Today* **2012**, *15* (10), 454–459. https://doi.org/10.1016/S1369-7021(12)70197-9.

(21) Truong, V. X.; Ablett, M. P.; Gilbert, H. T. J.; Bowen, J.; Richardson, S. M.; Hoyland, J. A.; Dove, A. P. In Situ-Forming Robust Chitosan-Poly(Ethylene Glycol) Hydrogels Prepared by Copper-Free Azide-Alkyne Click Reaction for Tissue Engineering. *Biomater. Sci.* **2014**, *2* (2), 167–175. https://doi.org/10.1039/c3bm60159e.

(22) Alge, D. L.; Azagarsamy, M. A.; Donohue, D. F.; Anseth, K. S. Synthetically Tractable Click Hydrogels for Three-Dimensional Cell Culture Formed Using Tetrazine-Norbornene

Chemistry. *Biomacromolecules* **2013**, *14* (4), 949–953. https://doi.org/10.1021/bm4000508.

(23) Fiore, V. F.; Wong, S. S.; Tran, C.; Tan, C.; Xu, W.; Sulchek, T.; White, E. S.; Hagood, J. S.; Barker, T. H. Avβ3 Integrin Drives Fibroblast Contraction and Strain Stiffening of Soft Provisional Matrix during Progressive Fibrosis. *JCI insight* **2018**, *3* (20), 1–35. https://doi.org/10.1172/jci.insight.97597.

(24) De Hilster, R. H. J.; Sharma, P. K.; Jonker, M. R.; White, E. S.; Gercama, E. A.; Roobeek, M.; Timens, W.; Harmsen, M. C.; Hylkema, M. N.; Burgess, J. K. Human Lung Extracellular Matrix Hydrogels Resemble the Stiffness and Viscoelasticity of Native Lung Tissue. *Am. J. Physiol. - Lung Cell. Mol. Physiol.* **2020**, *318* (4), L698–L704. https://doi.org/10.1152/AJPLUNG.00451.2019.

(25) Liu, F.; Mih, J. D.; Shea, B. S.; Kho, A. T.; Sharif, A. S.; Tager, A. M.; Tschumperlin, D. J. Feedback Amplification of Fibrosis through Matrix Stiffening and COX-2 Suppression. *J. Cell Biol.* **2010**, *190* (4), 693–706. https://doi.org/10.1083/jcb.201004082.

(26) Wynn, T. A.; Ramalingam, T. R. Mechanisms of Fibrosis: Therapeutic Translation for Fibrotic Disease. *Nat. Med.* **2012**, *18* (7), 1028–1040. https://doi.org/10.1038/nm.2807.

(27) Charrier, E. E.; Pogoda, K.; Wells, R. G.; Janmey, P. A. Control of Cell Morphology and Differentiation by Substrates with Independently Tunable Elasticity and Viscous Dissipation. *Nat. Commun.* **2018**, *9* (1), 1–13. https://doi.org/10.1038/s41467-018-02906-9.

(28) Hui, E.; Gimeno, K. I.; Guan, G.; Caliari, S. R. Spatiotemporal Control of Viscoelasticity in Phototunable Hyaluronic Acid Hydrogels. *Biomacromolecules* **2019**, *20* (11), 4126–4134. https://doi.org/10.1021/acs.biomac.9b00965.

(29) Hui, E.; Moretti, L.; Barker, T. H.; Caliari, S. R. The Combined Influence of Viscoelastic and Adhesive Cues on Fibroblast Spreading and Focal Adhesion Organization. *Cell. Mol. Bioeng.* **2021**. https://doi.org/10.1007/s12195-021-00672-1.

(30) Chaudhuri, O.; Gu, L.; Klumpers, D.; Darnell, M.; Bencherif, S. A.; Weaver, J. C.; Huebsch, N.; Lee, H. P.; Lippens, E.; Duda, G. N.; et al. Hydrogels with Tunable Stress Relaxation Regulate Stem Cell Fate and Activity. *Nat. Mater.* **2016**, *15* (3), 326–334. https://doi.org/10.1038/nmat4489.

(31) Lee, H. pyo; Stowers, R.; Chaudhuri, O. Volume Expansion and TRPV4 Activation

Regulate Stem Cell Fate in Three-Dimensional Microenvironments. *Nat. Commun.* **2019**, *10* (1). https://doi.org/10.1038/s41467-019-08465-x.

(32) Gramlich, W. M.; Kim, I. L.; Burdick, J. A. Synthesis and Orthogonal Photopatterning of Hyaluronic Acid Hydrogels with Thiol-Norbornene Chemistry. *Biomaterials* **2013**, *34* (38), 9803–9811. https://doi.org/10.1016/j.biomaterials.2013.08.089.

(33) Rodell, C. B.; Kaminski, A. L.; Burdick, J. A. Rational Design of Network Properties in Guest-Host Assembled and Shear-Thinning Hyaluronic Acid Hydrogels. *Biomacromolecules* **2013**, *14* (11), 4125–4134. https://doi.org/10.1021/bm401280z.

(34) Lueckgen, A.; Garske, D. S.; Ellinghaus, A.; Mooney, D. J.; Duda, G. N.; Cipitria, A. Enzymatically-Degradable Alginate Hydrogels Promote Cell Spreading and in Vivo Tissue Infiltration. *Biomaterials* **2019**, *217* (May), 119294. https://doi.org/10.1016/j.biomaterials.2019.119294.

(35) Lin, L.; Marchant, R. E.; Zhu, J.; Kottke-Marchant, K. Extracellular Matrix-Mimetic Poly(Ethylene Glycol) Hydrogels Engineered to Regulate Smooth Muscle Cell Proliferation in 3-D. *Acta Biomater.* **2014**, *10* (12), 5106–5115. https://doi.org/10.1016/j.actbio.2014.08.025.

(36) Turturro, M. V.; Christenson, M. C.; Larson, J. C.; Young, D. A.; Brey, E. M.; Papavasiliou, G. MMP-Sensitive PEG Diacrylate Hydrogels with Spatial Variations in Matrix Properties Stimulate Directional Vascular Sprout Formation. *PLoS One* **2013**, *8* (3). https://doi.org/10.1371/journal.pone.0058897.

(37) Patterson, J.; Hubbell, J. A. Enhanced Proteolytic Degradation of Molecularly Engineered PEG Hydrogels in Response to MMP-1 and MMP-2. *Biomaterials* **2010**, *31* (30), 7836–7845. https://doi.org/10.1016/j.biomaterials.2010.06.061.

(38) Patterson, J.; Hubbell, J. A. SPARC-Derived Protease Substrates to Enhance the Plasmin Sensitivity of Molecularly Engineered PEG Hydrogels. *Biomaterials* **2011**, *32* (5), 1301–1310. https://doi.org/10.1016/j.biomaterials.2010.10.016.

(39) Lei, Y.; Gojgini, S.; Lam, J.; Segura, T. The Spreading, Migration and Proliferation of Mouse Mesenchymal Stem Cells Cultured inside Hyaluronic Acid Hydrogels. *Biomaterials* **2011**, *32* (1), 39–47. https://doi.org/10.1016/j.biomaterials.2010.08.103.

(40) Lutolf, M. P.; Raeber, G. P.; Zisch, A. H.; Tirelli, N.; Hubbell, J. A. Cell-Responsive Synthetic Hydrogels. *Adv. Mater.* **2003**, *15* (11), 888–892.

https://doi.org/10.1002/adma.200304621.

(41) Zerdoum, A. B.; Fowler, E. W.; Jia, X. Induction of Fibrogenic Phenotype in Human Mesenchymal Stem Cells by Connective Tissue Growth Factor in a Hydrogel Model of Soft Connective Tissue. *ACS Biomater. Sci. Eng.* **2019**, *5* (9), 4531–4541. https://doi.org/10.1021/acsbiomaterials.9b00425.

(42) Chaudhuri, O. Viscoelastic Hydrogels for 3D Cell Culture. *Biomater. Sci.* **2017**, *5* (8), 1480–1490. https://doi.org/10.1039/c7bm00261k.

(43) Chaudhuri, O.; Cooper-White, J.; Janmey, P. A.; Mooney, D. J.; Shenoy, V. B. Effects of Extracellular Matrix Viscoelasticity on Cellular Behaviour. *Nature* **2020**, *584* (7822), 535–546. https://doi.org/10.1038/s41586-020-2612-2.

(44) Dupont, S.; Morsut, L.; Aragona, M.; Enzo, E.; Giulitti, S.; Cordenonsi, M.; Zanconato, F.; Le Digabel, J.; Forcato, M.; Bicciato, S.; et al. Role of YAP/TAZ in Mechanotransduction. *Nature* **2011**, *474* (7350), 179–184. https://doi.org/10.1038/nature10137.

6.7 Supplementary Figures

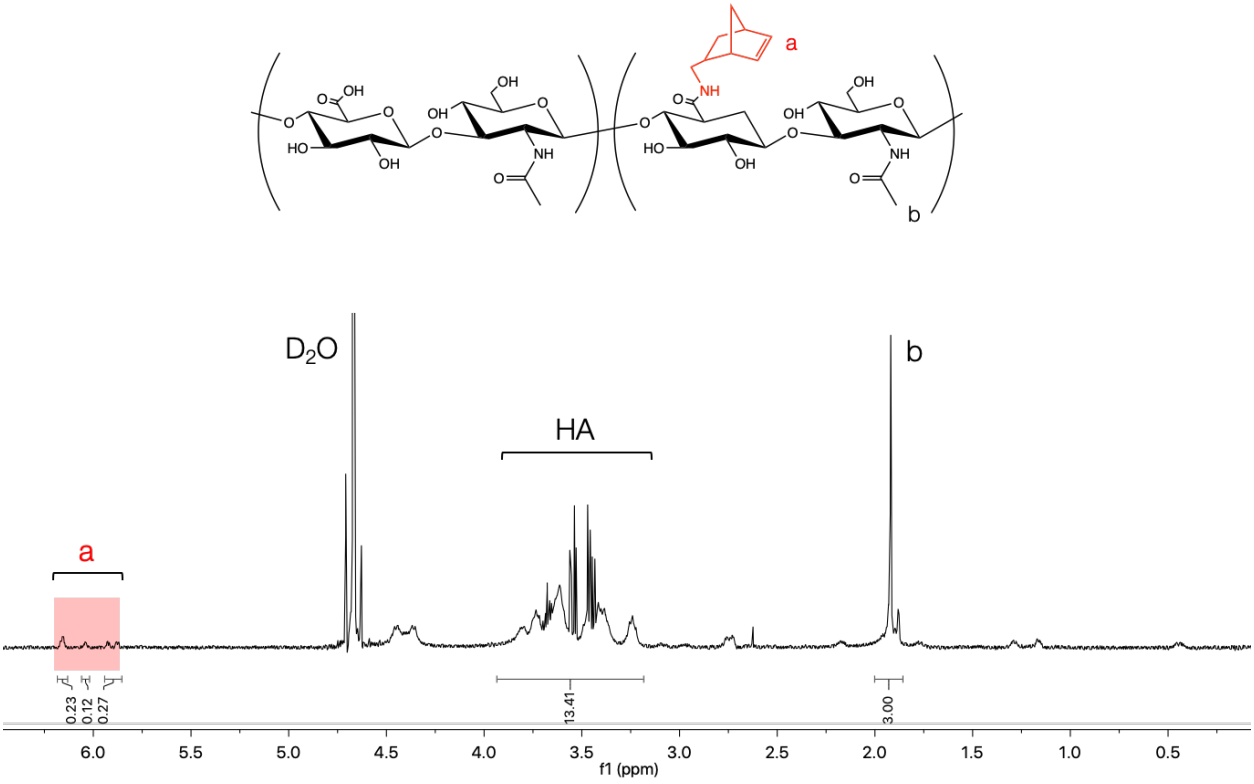

Figure S6.1. ^{1}H NMR spectrum of NorHA. The degree of modification was calculated to be 31% based on the ratio of the norbornene peaks (a) to the methyl peak (b).

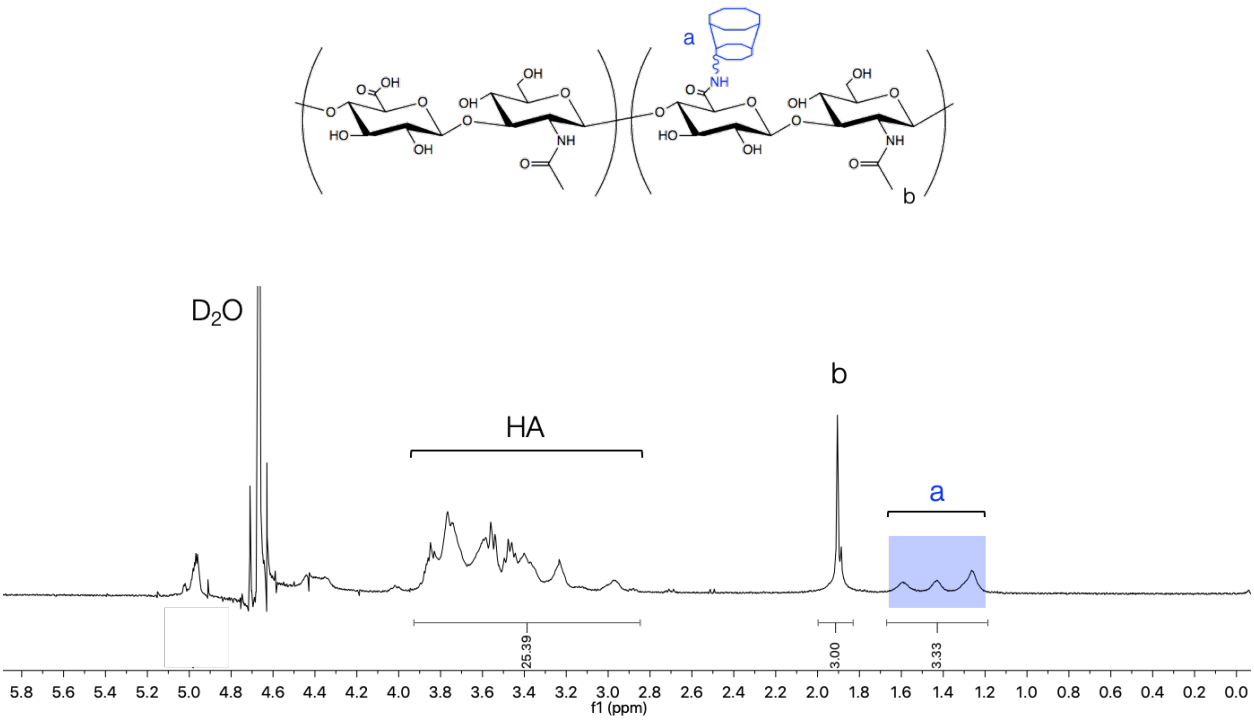

Figure S6.2. ^{1}H NMR spectrum of CD-HA. The degree of modification was calculated to be 28% based on the ratio of the cyclodextrin peaks (a) to the methyl peak (b).

A

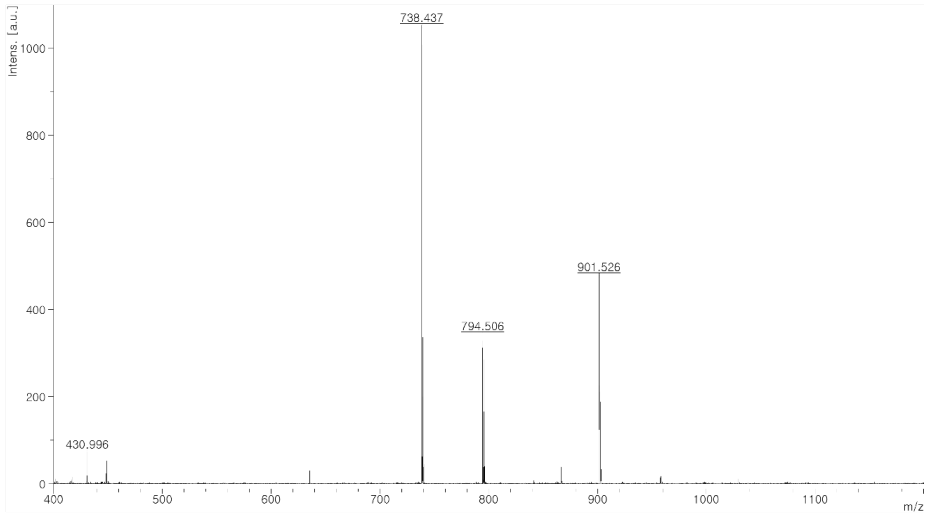
Intens. [a.u.]
738.437
901.526
794.506
430.996
m/z

B

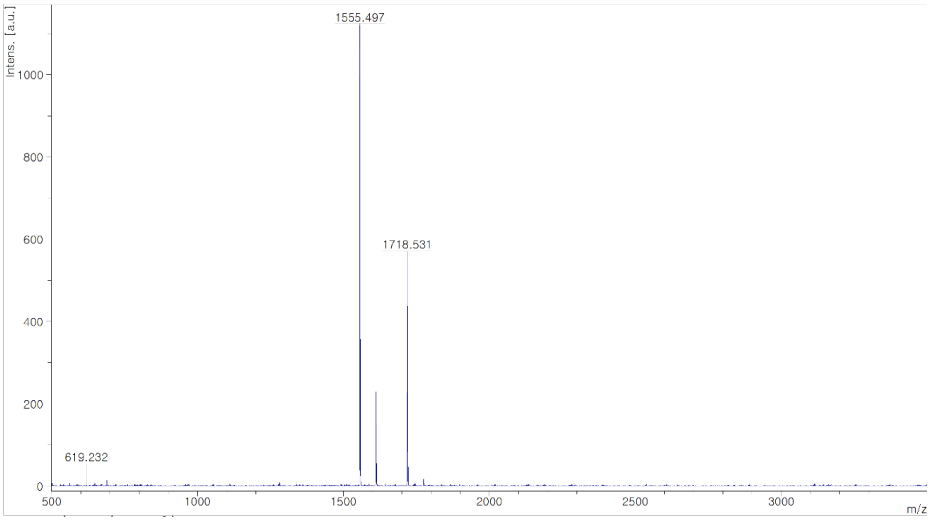
Intens. [a.u.]
1555.497
1718.531
619.232
m/z

C

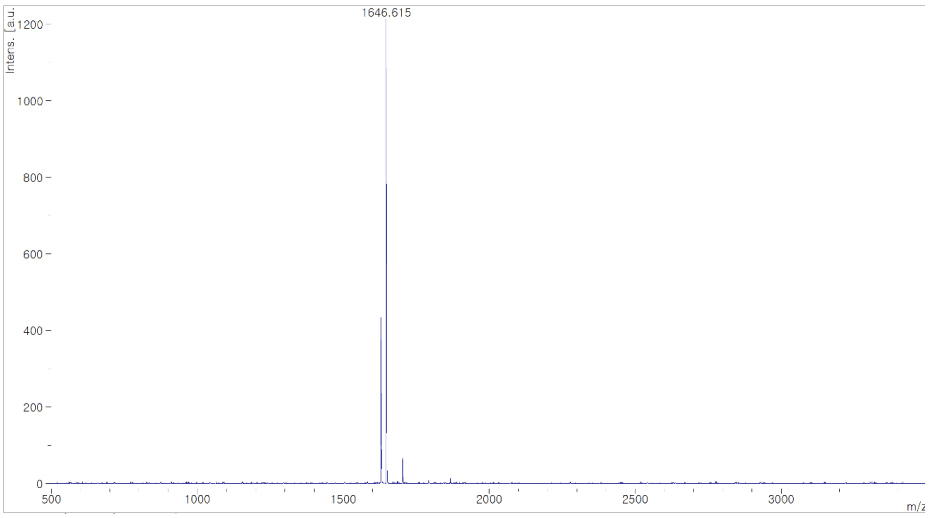
Intens. [a.u.]
1646.615
m/z

Figure S6.3. Peptide characterization via MALDI. (A) Spectrum of adamantane peptide Ad-KKKCG. Expected mass: 738.6 g/mol. Actual mass: 738.4 g/mol. (B) Spectrum of VPMS peptide with the sequence GCNSVPMSMRGGSNCG. Expected mass: 1555.6 g/mol. Actual mass: 1555.5 g/mol. (C) Spectrum of PQG peptide with the sequence GCRDPQGIWGQDRCG. Expected mass: 1646.7 g/mol. Actual mass: 1646.6 g/mol.

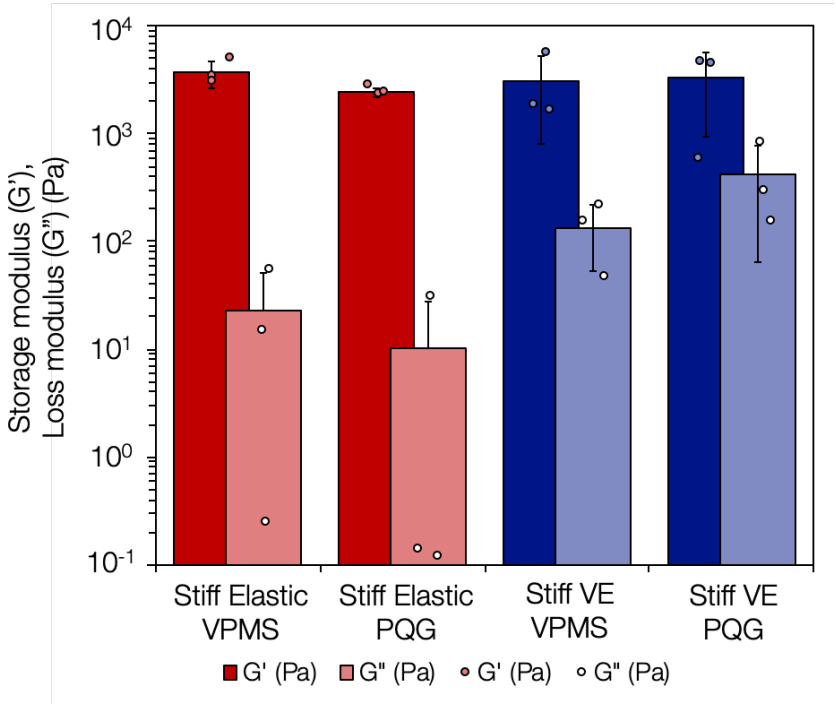

Figure S6.4. Rheological characterization of stiff hydrogels. Storage (G') and loss (G") moduli of stiff hydrogel groups with either the VPMS or PQG dithiol crosslinker.

CHAPTER 7: CONCLUSIONS AND FUTURE DIRECTIONS

7.1 Summary

The work presented in this thesis focused on the design and development of phototunable viscoelastic hyaluronic acid (HA) hydrogels to study cell mechanobiology during fibrosis. This approach leveraged the phototunable capabilities of thiol-ene "click" chemistry to facilitate independent control over stiffness, viscoelasticity, ligand presentation in a fibrosis model to better understand the individual and combined roles of microenvironmental cues on cell behavior. While the application of this hydrogel system was designed to mimic liver and lung tissue, it could potentially be cross-applied to many other soft tissues including heart, skin, and muscle.

In Chapter 3, we sought to spatially characterize the time-dependent viscoelastic properties of lung tissue using nanoindentation. Since nanoindentation is already a common technique to mechanically characterize biomaterials, it enables a direct comparison of viscoelastic properties between *ex vivo* tissues and hydrogels to inform tissue-relevant biomaterial design. Normal *ex vivo* rat lung tissue was harvested, cut into sections, and glued to Petri dishes for reproducible measurements. Young's moduli (E), a measure of stiffness, of normal lung tissue was determined using the Hertzian contact model and on average, revealed healthy tissue-relevant stiffnesses (E ~ 1.2 kPa for the left, right superior, right middle, and right post caval lobes; E ~ 2 kPa for the right inferior lobe). Viscoelastic properties were measured using the dynamic mechanical analysis (DMA)-like operational capabilities of the nanoindentation, where cyclic oscillations allowed storage (E') and loss (E") moduli to be determined. The E" values of the normal lung tissue were all within 25% of their respective E' values regardless of oscillation frequency, indicative of tissue viscoelasticity. Frequency-dependent behavior was also observed for all samples, providing

insight into how dynamic tissue properties may be influenced by various cell and external forces. Stress relaxation, a key characteristic of viscoelastic materials, was observed for all normal tissue samples and the extent of relaxation spanned between 20-50% of the initial force, agreeing with previously observed trends and providing a quantitative measure of how the lung tissue matrix accommodates applied strains. Nanoindentation also enabled microscale spatial mapping of stiffness and viscoelastic properties and confirmed significant mechanical heterogeneity spanning orders of magnitude. Finally, the results of this work allowed the fabrication of viscoelastic hyaluronic acid (HA) hydrogels where stiffness and viscoelasticity of normal rat lung tissue were matched, illustrating the capability of nanoindentation to reproducibly measure tissue properties to directly inform biomaterial design.

Chapter 4 describes the development of a phototunable HA hydrogel system where stiffness and viscoelasticity were spatiotemporally controlled to examine pathologically-relevant cell behavior[1]. Elastic or viscoelastic hydrogels were fabricated with soft (G' ~ 0.5 kPa) and stiff (G' ~ 5 kPa) mechanics representing normal and fibrotic liver tissue, respectively. While elastic hydrogels contained only thiol-ene addition-mediated covalent crosslinks between norbornene groups and di-thiol crosslinkers, viscoelastic substrates were designed with a combination of covalent bonds and supramolecular guest-host interactions between thiolated adamantane peptides and β-cyclodextrin that introduced time-dependent properties such as stress relaxation and frequency-dependent behavior. Notably, for viscoelastic hydrogel groups, the loss moduli (G") was within an order of magnitude of the storage moduli (G'), mimicking soft biological tissue mechanics. Hepatic stellate cells (HSCs), the primary mediators of liver fibrosis[2–4], were cultured on hydrogel groups for 7 days. Cell morphology, spread area, α-smooth muscle actin (α-SMA) stress fiber

organization, a key myofibroblast marker, and MRTF-A nuclear localization, a transcriptional co-activator implicated in fibrosis progression, were measured. HSCs on stiff elastic substrates mimicking fibrotic tissue exhibited greater spread areas and more elongated morphologies, as quantified by lower cell shape index (CSI) values, compared to cells on soft elastic hydrogels, more reminiscent of intermediate mechanical stages of fibrosis. The introduction of viscoelastic cues mimicking healthy tissue mechanics led to decreased cell spread areas and more rounded morphologies, with those on soft viscoelastic substrates showing the greatest difference with HSCs on stiff elastic groups. Cells on stiff elastic substrates also showed greater α-SMA stress fiber organization and MRTF-A nuclear translocation compared to all other groups, especially the soft viscoelastic hydrogels.

We further demonstrated the dynamic capabilities of the hydrogel system through photopatterning to introduce additional mechanical cues in a user-controlled manner. Using this approach, we successfully patterned regions of stiffness in soft viscoelastic regions to mimic the presence of fibrotic nodules and showed that cells responded to the local mechanics of the patterned hydrogels. We were also able to introduce regions of viscoelasticity to stiff elastic hydrogels and confirm secondary incorporation of stress relaxation. Overall, the results from Chapter 4 suggest the importance of time-dependent stress relaxation on cell mechanosensing and signal transduction pathways.

In Chapter 5, we expanded upon the hydrogel system developed in Chapter 4 to explore the influence of integrin-specific adhesive ligand presentation on cell behavior in a lung fibrosis model[5]. While most traditional hydrogel systems use a synthetic RGD peptide sequence derived

from fibronectin to mediate cell attachment, its inefficient cell binding affinity and ability to engage multiple integrin heterodimers underscores the need to explore alternate adhesive mechanisms to more directly understand cell-matrix adhesions and subsequent mechanotransduction signaling dynamics. To address this, we used engineered fibronectin (Fn) fragments containing both PHSRN and RGD integrin-binding sequences within the 9th ($FnIII_9$) and 10th ($FnIII_{10}$) type III repeats, respectively, that were designed to preferentially engage $\alpha5\beta1$ and $\alpha v\beta3$[6]. To generate a Fn fragment with preferential $\alpha5\beta1$ binding (Fn9*10), a Leu^{1408}Pro point mutation between $FnIII_9$ and $FnIII_{10}$ was created to stabilize the spatial and angular orientation of the PHSRN synergy site relative to RGD, essential for $\alpha5\beta1$ integrin engagement. The design of a Fn fragment promoting $\alpha v\beta3$ binding (Fn4G) was accomplished by adding a four glycine linker between $FnIII_9$ and $FnIII_{10}$ to increase the distance between PHSRN and RGD and disrupt binding to the PHSRN synergy site, allowing preferential $\alpha v\beta3$ engagement.

Normal and fibrotic lung tissue mechanics were recapitulated during HA hydrogel fabrication. Similar to what was demonstrated in Chapter 4, viscoelastic substrates displayed tissue-relevant frequency-dependent and stress relaxation responses that were not shown for elastic counterparts. Additionally, the incorporation of thiolated Fn fragments did not influence overall mechanics during formation as well as after swelling. Interestingly, hydrogels containing only 2 μM Fn fragments supported equivalent fibroblast attachment as hydrogels with 1 mM RGD, supporting previous work showing that the synthetic RGD peptide had lower cell binding affinity compared to full and fragmented proteins. Human lung fibroblasts (HLFs) cultured on RGD-containing hydrogels displayed similar morphologies as in Chapter 4 with greater spread area on stiff elastic substrates and more rounded cell shapes on viscoelastic groups. The promotion of $\alpha5\beta1$ integrin

engagement via Fn9*10 Fn fragment incorporation minimized cell spreading regardless of stiffness or viscoelasticity and agreed with previous results with alveolar epithelial cell morphologies. Interestingly, while HLFs on Fn4G-containing hydrogels with preferential αvβ3 integrin engagement exhibited similar characteristics to those on RGD hydrogels, increased spreading was observed on soft elastic substrates mimicking an intermediate fibrotic tissue state. These results also correlated with F-actin stress fiber organization and focal adhesion formation and maturation. Altogether, this work highlighted the potential role of preferential αvβ3 engagement in facilitating focal adhesion maturation, actin stress fiber organization, and cell spreading on soft elastic substrates that are reminiscent of active fibroproliferative tissue. In contrast, both viscoelastic cues and preferential α5β1 binding led to reduced cell spreading, stress fiber organization, and focal adhesion formation, highlighting their roles in reducing fibrosis-activating behaviors.

Chapter 6 investigated the impact of viscoelasticity on cell behavior in a 3D hydrogel model. Human mesenchymal stem cells (hMSCs), which have been used in many seminal studies in the field of mechanobiology, and HLFs, which are important in the context of fibrosis progression, were used in this study to compare cell responses to substrate mechanics. Both hMSCs and HLFs exhibited spreading and elongation in soft elastic hydrogels compared to more rounded morphologies in stiff elastic groups. Viscoelasticity led to more rounded HLFs and reduced hMSC spreading, although the aspect ratio of hMSCs in stiff viscoelastic substrates was elevated after 14 days. Increasing the loss moduli (G") of soft viscoelastic hydrogels resulted in decreased actin stress fiber formation and nuclear localization of YAP, a mechanosensitive transcriptional co-activator, and these trends were more prominent in hMSCs. Finally, the development of

mechanically dynamic hydrogels was demonstrated via photopatterning in regions of stiffness, confirming the ability to introduce heterogeneity into 3D hydrogel systems for studying fibrosis progression.

7.2 Future directions

7.2.1 Characterizing viscoelastic properties of normal and fibrotic tissue to direct biomaterial design

Progression of disease outcomes such as fibrosis is associated with changes in extracellular matrix (ECM) mechanics that can be detrimental to tissue structure and function. Importantly, tissue viscoelasticity has shown to influence cell behaviors including spreading, actin stress fiber formation, and the nuclear localization of mechanosensitive transcriptional co-activators[7–11]. Therefore, it is of interest to characterize and understand viscoelastic parameters such as force relaxation and frequency-dependence response and how they differ between normal and diseased states to inform biomaterial design, improve medical diagnoses, and advance the development of future therapies.

Compared to other techniques, nanoindentation provides an approach to locally assess viscoelastic properties, and can be customized to measure a range of substrates depending on probe material, diameter, stiffness, and geometry[12]. The tests can be completed in air or while the sample is submerged in liquid and can be conducted at varying temperatures. Mechanical characterization of *in vitro* models such as hydrogels are also commonly done via nanoindentation, which would enable direct translation of viscoelastic properties from tissue testing to biomaterial design and vice versa. Previous work in this thesis (Chapter 3) and by others[13–15] has used nanoindentation to

characterize microscale mechanical properties of normal animal tissues from the lung, liver, heart, and kidney.

Future work could focus on expanding microscale characterization to early- and late-stage diseased tissues. Commonly, animal models have been used to understand molecular mechanisms behind pathological conditions such as fibrosis. For lung fibrosis, the most frequent model is through bleomycin administration, which can be delivered subcutaneously, intravenously, intratracheally, intraperitoneally, and via inhalation[16–18]. The bleomycin-induced method of lung fibrosis leads to cell injury via DNA strand breaks, cell necrosis and/or apoptosis, inflammation, and fibrosis progression. It can occur in a relatively short period of time (2-4 weeks in an intratracheal model) and repetitive dosing models, or those with more than one bleomycin dose, have shown histopathologic features similar to those seen in human lung fibrosis[19,20]. Other animal models of fibrosis that could be used for tissue harvest and nanoindentation include silica administration, asbestos exposure, fluorescein isothiocyanate (FITC) delivery, age-related models, and models introducing the overexpression of cytokines such as transforming growth factor-β (TGF-β), interleukin-13 (IL-13), and tumor necrosis factor α (TNF-α)[16,21]. Models of liver fibrosis, particularly in rodents, has been commonly induced via carbon tetrachloride, dimethylnitrosamine, thioacetamide, and diethylnitrosamine delivery, which all gets metabolized by hepatocytes in the liver[22–24]. As an alternative to animal tissues, samples from hospital patients or from a tissue repository could also be potential routes for acquiring tissue. While these samples would most directly relate to human pathologies, they may be more difficult to obtain.

Nanoindentation could be used to characterize the spatial heterogeneity of tissue mechanics over the course of fibrosis progression. The degree of stress relaxation, frequency-dependent behavior, and loss tangent (loss modulus over storage modulus, E"/E'), could be measured and would help to highlight the relevant cellular timescales as they respond to dynamic ECM cues during fibrosis. These analyses could then be used to directly inform the design of biomaterial models. For example, mapped tissue stiffnesses could be reproduced on photomask transparencies for subsequent hydrogel photopatterning and introduction of spatial variations in substrate stiffness, analogous to the technique shown in Chapter 4[1]. The design of photomasks for secondary introduction of viscoelastic cues could also be accomplished in the same manner.

7.2.2 Investigating the combined roles of integrin-specific cell adhesion, viscoelasticity, and growth factor presentation on cell mechanobiology

The work in Chapter 5 showed the influence of stiffness, viscoelasticity, and integrin-specific adhesive cues on cell spreading, actin stress fiber formation, and focal adhesion formation[5]. Importantly, it demonstrated the ability of preferential αv engagement to lead to disease-relevant cell behaviors including increased spread area, actin stress fiber organization, and focal adhesion size and maturation. Additionally, the incorporation of viscoelasticity, which mimics normal tissue mechanics, largely suppressed fibrosis-activating behaviors regardless of integrin engagement.

Although it is well accepted that TGF-β1 plays an important role in the profibrotic signaling pathway, the crosstalk that occurs between growth factor signaling and mechanotransduction pathways is not well understood[25,26]. The spatial and temporal presentation of bioactive cues may be linked to numerous cellular processes such as migration and phenotypic maintenance, and

traction forces could release sequestered growth factors such as TGF-β1 that mediate profibrotic processes[27–33]. Recent work has shown that preferential engagement of the αv integrin can promote the myofibroblast phenotype through integrin-mediated fibroblast contractility and mechanoactivation of both latent TGF-β1[34–36] and platelet-derived growth factor (PDGF)[26,37–39]. An outcome of these bonds is the expression and organization of α-SMA, a hallmark of myofibroblast activation[26,40].

Future work could study the role that viscoelasticity, disease-relevant integrin engagement (e.g., using the fibronectin fragments from Chapter 5), and soluble or tethered growth factor presentation play in regulating downstream phenotypic changes such as cell spreading, proliferation, and myofibroblast activation. It would be of interest to observe if the introduction of viscoelastic cues could suppress or override the overexpression of growth factors such as TGF-β1. Relevant metrics such as cell spreading, actin stress fiber formation, and focal adhesion formation could be measured on hydrogels with homogeneously distributed mechanical and biochemical properties as well as patterned cues. Deposition of fibrillar type I collagen could be measured through second harmonic imaging microscopy (SHIM), where the collagen second-harmonic generation (SHG) image signal would be quantified by the mean intensity per pixel[41,42]. Integrin clustering is responsive to chemical and physical cues provided by the ECM, including matrix stiffness and ligand density[43]. The clustering of these transmembrane proteins enhances mechanotransmission of force and can lead to the formation of stress fibers and focal adhesions, which in turn regulates the activity of transcriptional regulators to drive gene expression. The impact of mechanical and biochemical cues on ligand clustering could also be measured via Förster resonance energy transfer (FRET) and confocal microscopy[44,45]. The ability to decouple matrix microenvironmental cues to

understand the fibrotic program has great implications on the future development of *in vitro* hydrogel models and therapeutics.

7.2.3 Synthesis of photo- and enzymatically-cleavable peptides to enable user-directed biomaterial degradation and cell isolation

While the fibrotic program is not fully understood, it is recognized that there is significant tissue heterogeneity due to development and the progression of pathological outcomes (e.g., early- to late-stage fibrosis). Differential changes in ECM mechanics are then exacerbated by emerging fibrotic cell subtypes from structural irregularities found in tissue[3,46,47], crosstalk with different cell types[48–51], and epigenetic modifications[52–54], among others. Several hydrogel models that introduce patterning capabilities have been developed to study how spatial heterogeneity in mechanical properties impacts cell behaviors and the regulation of various signaling pathways[55–59]. Further insight into the complex mechanisms of cell mechanobiology requires a deeper analysis of spatially-selective cell characterization and cell lineage tracing, which demonstrates the need to develop systems capable of isolating cell subtypes from discrete patterned regions to enable high resolution single cell analyses. A more complete understanding of the cellular events that occur during fibrogenesis will aid in developing more accurate models of fibrosis.

In addition to developing a more accurate viscoelastic model to recapitulate the heterogeneous landscape, methods to analyze distinct cell subpopulations from substrates of varying mechanics need to be established to better understand mechanistic pathways underlying pathologies. The ability to control presentation, patterning, and release of biorelevant markers in hydrogel models would allow for more direct cell analyses. Photocleavable groups offer precise spatial control over

the release of bioactive molecules, the breakdown of crosslinkers, and uncaging of growth factors relevant in biological functioning and in tissue dysregulation. Kaplan and co-workers first cross-applied the use of photoremovable protecting groups in biological applications via ATP photorelease[60]. The *o*-nitrobenzyl group, which can undergo selective cleavage upon UV light irradiation, has gained popularity as a photoresponsive method to control cell-matrix interactions[60–62]. The precise spatiotemporal control that photoreactions provide enables the patterning of bioactive molecules and cells to study cell behaviors and subsequent changes in downstream gene expression mediated by physical cues. The ability to combine multiple photochemical reactions that react at orthogonal wavelengths of light permits sequential crosslinking, cleavage, and patterning reactions[63].

Enzymatic strategies have also recently emerged as a powerful reaction method for protein modification, crosslinking, and biomaterial dissolution due to high site specificity, selectivity, and compatibility with a range of chemistries for biomaterial formation and functionalization[64–67]. In particular, the *Staphylococcus aureus* transpeptidase Sortase A (SrtA) has been recognized for its ability to perform a wide range of protein modifications with simple production and reaction robustness[68]. The SrtA enzyme recognizes the 'LP*X*TG' motif (where *X* is any amino acid) and catalyzes an exchange process in which the enzyme removes the C-terminal G to form a thioester intermediate with 'LP*X*T-' before being displaced by the N-terminus of a polyglycine motif[64,65,68,69]. Taking advantage of this selective enzymatic exchange process, an enzymatically cleavable adhesion peptide could be designed for selective cell retrieval. Since SrtA is not commonly expressed in mammalian cells, cleavage can be user-defined and decoupled from local enzymes produced by cells[68].

Incorporation of orthogonal triggers (e.g., light, enzymes) that can permit selective cell release could enable downstream analysis of single cell subtypes from defined patterned regions of interest through techniques such as single cell RNA sequencing[70–73]. This approach could ideally yield information about how specific cells regulate profibrotic signaling pathways contributing to fibrotic diseases like idiopathic pulmonary fibrosis (IPF). The engineered peptides could also be cross-applied to other systems for spatiotemporal control of cell and matrix patterning.

7.3 References

(1) Hui, E.; Gimeno, K. I.; Guan, G.; Caliari, S. R. Spatiotemporal Control of Viscoelasticity in Phototunable Hyaluronic Acid Hydrogels. *Biomacromolecules* **2019**, *20* (11), 4126–4134. https://doi.org/10.1021/acs.biomac.9b00965.

(2) Wells, R. G. Cellular Sources of Extracellular Matrix in Hepatic Fibrosis. *Clin. Liver Dis.* **2008**, *12* (4), 759–768. https://doi.org/10.1016/j.cld.2008.07.008.

(3) Wells, R. G. Tissue Mechanics and Fibrosis. *Biochim. Biophys. Acta - Mol. Basis Dis.* **2013**, *1832* (7), 884–890. https://doi.org/10.1016/j.bbadis.2013.02.007.

(4) Moreira, R. K. Hepatic Stellate Cells and Liver Fibrosis. *Arch. Pathol. Lab. Med.* **2007**, *131*, 1728–1734.

(5) Hui, E.; Moretti, L.; Barker, T. H.; Caliari, S. R. The Combined Influence of Viscoelastic and Adhesive Cues on Fibroblast Spreading and Focal Adhesion Organization. *Cell. Mol. Bioeng.* **2021**. https://doi.org/10.1007/s12195-021-00672-1.

(6) Cao, L.; Nicosia, J.; Larouche, J.; Zhang, Y.; Bachman, H.; Brown, A. C.; Holmgren, L.; Barker, T. H. Detection of an Integrin-Binding Mechanoswitch within Fibronectin during Tissue Formation and Fibrosis. *ACS Nano* **2017**, *11* (7), 7110–7117. https://doi.org/10.1021/acsnano.7b02755.

(7) Liu, F.; Mih, J. D.; Shea, B. S.; Kho, A. T.; Sharif, A. S.; Tager, A. M.; Tschumperlin, D. J. Feedback Amplification of Fibrosis through Matrix Stiffening and COX-2 Suppression. *J. Cell Biol.* **2010**, *190* (4), 693–706. https://doi.org/10.1083/jcb.201004082.

(8) Chaudhuri, O.; Gu, L.; Darnell, M.; Klumpers, D.; Bencherif, S. A.; Weaver, J. C.; Huebsch, N.; Mooney, D. J. Substrate Stress Relaxation Regulates Cell Spreading. *Nat. Commun.* **2015**, *6*, 1–7. https://doi.org/10.1038/ncomms7365.

(9) Charrier, E. E.; Pogoda, K.; Wells, R. G.; Janmey, P. A. Control of Cell Morphology and Differentiation by Substrates with Independently Tunable Elasticity and Viscous Dissipation. *Nat. Commun.* **2018**, *9* (1), 1–13. https://doi.org/10.1038/s41467-018-02906-9.

(10) Gong, Z.; Szczesny, S. E.; Caliari, S. R.; Charrier, E. E.; Chaudhuri, O.; Cao, X.; Lin, Y.; Mauck, R. L.; Janmey, P. A.; Burdick, J. A.; et al. Matching Material and Cellular Timescales Maximizes Cell Spreading on Viscoelastic Substrates. *Proc. Natl. Acad. Sci. U. S. A.* **2018**, *115* (12), E2686–E2695. https://doi.org/10.1073/pnas.1716620115.

(11) Fiore, V. F.; Wong, S. S.; Tran, C.; Tan, C.; Xu, W.; Sulchek, T.; White, E. S.; Hagood, J. S.; Barker, T. H. Avβ3 Integrin Drives Fibroblast Contraction and Strain Stiffening of Soft Provisional Matrix during Progressive Fibrosis. *JCI insight* **2018**, *3* (20), 1–35. https://doi.org/10.1172/jci.insight.97597.

(12) Ebenstein, D. M.; Pruitt, L. A. Nanoindentation of Biological Materials. *Nano Today* **2006**, *1* (3), 26–33. https://doi.org/10.1016/S1748-0132(06)70077-9.

(13) Islam, M. R.; Virag, J.; Oyen, M. L. Micromechanical Poroelastic and Viscoelastic Properties of Ex-Vivo Soft Tissues. *J. Biomech.* **2020**, *113*, 110090. https://doi.org/10.1016/j.jbiomech.2020.110090.

(14) Akhtar, R.; Schwarzer, N.; Sherratt, M. J.; Watson, R. E. B.; Graham, H. K.; Trafford, A. W.; Mummery, P. M.; Derby, B. Nanoindentation of Histological Specimens: Mapping the Elastic Properties of Soft Tissues. *J. Mater. Res.* **2009**, *24* (3), 638–646. https://doi.org/10.1557/jmr.2009.0130.

(15) Ebenstein, D. M.; Pruitt, L. A. Nanoindentation of Soft Hydrated Materials for Application to Vascular Tissues. *J. Biomed. Mater. Res. - Part A* **2004**, *69* (2), 222–232. https://doi.org/10.1002/jbm.a.20096.

(16) Moore, B. B.; Lawson, W. E.; Oury, T. D.; Sisson, T. H.; Raghavendran, K.; Hogaboam, C. M. Animal Models of Fibrotic Lung Disease. *Am. J. Respir. Cell Mol. Biol.* **2013**, *49* (2), 167–179. https://doi.org/10.1165/rcmb.2013-0094TR.

(17) Thrall, R. S.; McCormick, J. R.; Jack, R. M.; McReynolds, R. A.; Ward, P. A. Bleomycin-Induced Pulmonary Fibrosis in the Rat. Inhibition by Indomethacin. *Am. J. Pathol.* **1979**, *95* (1), 117–130.

(18) Moeller, A.; Ask, K.; Warburton, D.; Gauldie, J.; Kolb, M. The Bleomycin Animal Model: A Useful Tool to Investigate Treatment Options for Idiopathic Pulmonary Fibrosis? *Int. J. Biochem. Cell Biol.* **2008**, *40* (3), 362–382. https://doi.org/10.1016/j.biocel.2007.08.011.

(19) Degryse, A. L.; Tanjore, H.; Xu, X. C.; Polosukhin, V. V.; Jones, B. R.; McMahon, F. B.; Gleaves, L. A.; Blackwell, T. S.; Lawson, W. E. Repetitive Intratracheal Bleomycin Models Several Features of Idiopathic Pulmonary Fibrosis. *Am. J. Physiol. - Lung Cell. Mol. Physiol.* **2010**, *299* (4), 442–452. https://doi.org/10.1152/ajplung.00026.2010.

(20) Degryse, A. L.; Lawson, W. E. Progress toward Improving Animal Models for Idiopathic Pulmonary Fibrosis. *Am. J. Med. Sci.* **2011**, *341* (6), 444–449.

https://doi.org/10.1097/MAJ.0b013e31821aa000.

(21) Tashiro, J.; Rubio, G. A.; Limper, A. H.; Williams, K.; Elliot, S. J.; Ninou, I.; Aidinis, V.; Tzouvelekis, A.; Glassberg, M. K. Exploring Animal Models That Resemble Idiopathic Pulmonary Fibrosis. *Front. Med.* **2017**, *4* (JUL), 1–11. https://doi.org/10.3389/fmed.2017.00118.

(22) Delire, B.; Stärkel, P.; Leclercq, I. Animal Models for Fibrotic Liver Diseases: What We Have, What We Need, and What Is under Development. *J. Clin. Transl. Hepatol.* **2015**, *3* (1), 53–66. https://doi.org/10.14218/JCTH.2014.00035.

(23) Bao, Y. L.; Wang, L.; Pan, H. T.; Zhang, T. R.; Chen, Y. H.; Xu, S. J.; Mao, X. L.; Li, S. W. Animal and Organoid Models of Liver Fibrosis. *Front. Physiol.* **2021**, *12* (May). https://doi.org/10.3389/fphys.2021.666138.

(24) Li, L.; Hu, Z.; Li, W.; Hu, M.; Ran, J.; Chen, P.; Sun, Q. Establishment of a Standardized Liver Fibrosis Model with Different Pathological Stages in Rats. *Gastroenterol. Res. Pract.* **2012**, *2012*. https://doi.org/10.1155/2012/560345.

(25) Wernig, G.; Chen, S. Y.; Cui, L.; Van Neste, C.; Tsai, J. M.; Kambham, N.; Vogel, H.; Natkunam, Y.; Gilliland, D. G.; Nolan, G.; et al. Unifying Mechanism for Different Fibrotic Diseases. *Proc. Natl. Acad. Sci. U. S. A.* **2017**, *114* (18), 4757–4762. https://doi.org/10.1073/pnas.1621375114.

(26) Deng, X.; Jin, K.; Li, Y.; Gu, W.; Liu, M.; Zhou, L. Platelet-Derived Growth Factor and Transforming Growth Factor B1 Regulate ARDS-Associated Lung Fibrosis Through Distinct Signaling Pathways. *Cell. Physiol. Biochem.* **2015**, *36* (3), 937–946. https://doi.org/10.1159/000430268.

(27) Baker, B. M.; Chen, C. S. Deconstructing the Third Dimension-How 3D Culture Microenvironments Alter Cellular Cues. *J. Cell Sci.* **2012**, *125* (13), 3015–3024. https://doi.org/10.1242/jcs.079509.

(28) Wipff, P. J.; Rifkin, D. B.; Meister, J. J.; Hinz, B. Myofibroblast Contraction Activates Latent TGF-B1 from the Extracellular Matrix. *J. Cell Biol.* **2007**, *179* (6), 1311–1323. https://doi.org/10.1083/jcb.200704042.

(29) Wells, R. G.; Discher, D. E. Matrix Elasticity, Cytoskeletal Tension, and TGF-B : The Insoluble and Soluble Meet. *Sci. Signal.* **2008**, *1* (10), 1–4. https://doi.org/10.1126/stke.110pe13.

(30) Johnson, C. P.; Tang, H. Y.; Carag, C.; Speicher, D. W.; Discher, D. E. Forced Unfolding of Proteins within Cells. *Science (80-.).* **2007**, *317* (5838), 663–666. https://doi.org/10.1126/science.1139857.

(31) Robertson, I. B.; Rifkin, D. B. Regulation of the Bioavailability of TGF-b and TGF-b-Related Proteins. *Cold Spring Harb. Perspect. Biol.* **2016**, *8*, 1–25.

(32) Hinz, B. The Extracellular Matrix and Transforming Growth Factor-B1: Tale of a Strained Relationship. *Matrix Biol.* **2015**, *47*, 54–65. https://doi.org/10.1016/j.matbio.2015.05.006.

(33) Xu, X.; Zheng, L.; Yuan, Q.; Zhen, G.; Crane, J. L.; Zhou, X.; Cao, X. Transforming Growth Factor-β in Stem Cells and Tissue Homeostasis. *Bone Res.* **2018**, *6* (1). https://doi.org/10.1038/s41413-017-0005-4.

(34) Henderson, N. C.; Sheppard, D. Integrin-Mediated Regulation of TGFβ in Fibrosis. *Biochim. Biophys. Acta - Mol. Basis Dis.* **2013**, *1832* (7), 891–896. https://doi.org/10.1016/j.bbadis.2012.10.005.

(35) Arora, P. D.; Narani, N.; McCulloch, C. A. G. The Compliance of Collagen Gels Regulates Transforming Growth Factor-β Induction of α-Smooth Muscle Actin in Fibroblasts. *Am. J. Pathol.* **1999**, *154* (3), 871–882. https://doi.org/10.1016/S0002-9440(10)65334-5.

(36) Balestrini, J. L.; Chaudhry, S.; Sarrazy, V.; Koehler, A.; Hinz, B. The Mechanical Memory of Lung Myofibroblasts. *Integr. Biol.* **2012**, *4* (4), 410–421. https://doi.org/10.1039/c2ib00149g.

(37) Endale, M.; Ahlfeld, S.; Bao, E.; Chen, X.; Green, J.; Bess, Z.; Weirauch, M. T.; Xu, Y.; Perl, A. K. Temporal, Spatial, and Phenotypical Changes of PDGFRα Expressing Fibroblasts during Late Lung Development. *Dev. Biol.* **2017**, *425* (2), 161–175. https://doi.org/10.1016/j.ydbio.2017.03.020.

(38) Lu, Y. Y.; Zhao, X. K.; Yu, L.; Qi, F.; Zhai, B.; Gao, C. Q.; Ding, Q. Interaction of Src and Alpha-V Integrin Regulates Fibroblast Migration and Modulates Lung Fibrosis in A Preclinical Model of Lung Fibrosis. *Sci. Rep.* **2017**, *7* (March), 1–11. https://doi.org/10.1038/srep46357.

(39) Li, R.; Bernau, K.; Sandbo, N.; Gu, J.; Preissl, S.; Sun, X. Pdgfra Marks a Cellular Lineage with Distinct Contributions to Myofibroblasts in Lung Maturation and Injury Response. *Elife* **2018**, *7*, 1–20. https://doi.org/10.7554/eLife.36865.

(40) Scaffidi, A. K.; Moodley, Y. P.; Weichselbaum, M.; Thompson, P. J.; Knight, D. A.

Regulation of Human Lung Fibroblast Phenotype and Function by Vitronectin and Vitronectin Integrins. *J. Cell Sci.* **2001**, *114* (19), 3507–3516. https://doi.org/10.1242/jcs.114.19.3507.

(41) Chen, X.; Nadiarynkh, O.; Plotnikov, S.; Campagnola, P. J. Second Harmonic Generation Microscopy for Quantitative Analysis of Collagen Fibrillar Structure. *Nat. Protoc.* **2012**, *7* (4), 654–669. https://doi.org/10.1038/nprot.2012.009.

(42) Boddupalli, A.; Bratlie, K. M. Second Harmonic Generation Microscopy of Collagen Organization in Tunable, Environmentally Responsive Alginate Hydrogels. *Biomater. Sci.* **2019**, *7* (3), 1188–1199. https://doi.org/10.1039/c8bm01535j.

(43) Paszek, M. J.; Boettiger, D.; Weaver, V. M.; Hammer, D. A. Integrin Clustering Is Driven by Mechanical Resistance from the Glycocalyx and the Substrate. *PLoS Comput. Biol.* **2009**, *5* (12). https://doi.org/10.1371/journal.pcbi.1000604.

(44) Chaudhuri, O.; Gu, L.; Klumpers, D.; Darnell, M.; Bencherif, S. A.; Weaver, J. C.; Huebsch, N.; Lee, H. P.; Lippens, E.; Duda, G. N.; et al. Hydrogels with Tunable Stress Relaxation Regulate Stem Cell Fate and Activity. *Nat. Mater.* **2016**, *15* (3), 326–334. https://doi.org/10.1038/nmat4489.

(45) Antia, M.; Baneyx, G.; Kubow, K. E.; Vogel, V. Fibronectin in Aging Extracellular Matrix Fibrils Is Progressively Unfolded by Cells and Elicits an Enhanced Rigidity Response. *Faraday Discuss.* **2008**, *139*, 229–249. https://doi.org/10.1039/b718714a.

(46) DePianto, D. J.; Chandriani, S.; Abbas, A. R.; Jia, G.; N'Diaye, E. N.; Caplazi, P.; Kauder, S. E.; Biswas, S.; Karnik, S. K.; Ha, C.; et al. Heterogeneous Gene Expression Signatures Correspond to Distinct Lung Pathologies and Biomarkers of Disease Severity in Idiopathic Pulmonary Fibrosis. *Thorax* **2015**, *70* (1), 48–56. https://doi.org/10.1136/thoraxjnl-2013-204596.

(47) Shaw, T. J.; Rognoni, E. Dissecting Fibroblast Heterogeneity in Health and Fibrotic Disease. *Curr. Rheumatol. Rep.* **2020**, *22* (8). https://doi.org/10.1007/s11926-020-00903-w.

(48) Cohen, M.; Giladi, A.; Gorki, A. D.; Solodkin, D. G.; Zada, M.; Hladik, A.; Miklosi, A.; Salame, T. M.; Halpern, K. B.; David, E.; et al. Lung Single-Cell Signaling Interaction Map Reveals Basophil Role in Macrophage Imprinting. *Cell* **2018**, *175* (4), 1031-1044.e18. https://doi.org/10.1016/j.cell.2018.09.009.

(49) Van Linthout, S.; Miteva, K.; Tschöpe, C. Crosstalk between Fibroblasts and Inflammatory Cells. *Cardiovasc. Res.* **2014**, *102* (2), 258–269. https://doi.org/10.1093/cvr/cvu062.

(50) Matsuda, M.; Seki, E. Hepatic Stellate Cell–Macrophage Crosstalk in Liver Fibrosis and Carcinogenesis. *Semin. Liver Dis.* **2020**, *40* (3), 307–320.

(51) Worrell, J. C.; MacLeod, M. K. L. Stromal–Immune Cell Crosstalk Fundamentally Alters the Lung Microenvironment Following Tissue Insult. *Immunology* **2021**, *163* (3), 239–249. https://doi.org/10.1111/imm.13319.

(52) Rajasekar, P.; Patel, J.; Clifford, R. L. DNA Methylation of Fibroblast Phenotypes and Contributions to Lung Fibrosis. *Cells* **2021**, *10* (8). https://doi.org/10.3390/cells10081977.

(53) Johnson, N. D.; Wu, X.; Still, C. D.; Chu, X.; Petrick, A. T.; Gerhard, G. S.; Conneely, K. N.; DiStefano, J. K. Differential DNA Methylation and Changing Cell-Type Proportions as Fibrotic Stage Progresses in NAFLD. *Clin. Epigenetics* **2021**, *13* (1), 1–14. https://doi.org/10.1186/s13148-021-01129-y.

(54) Killaars, A. R.; Walker, C. J.; Anseth, K. S. Nuclear Mechanosensing Controls MSC Osteogenic Potential through HDAC Epigenetic Remodeling. *Proc. Natl. Acad. Sci. U. S. A.* **2020**, *117* (35), 21258–21266. https://doi.org/10.1073/pnas.2006765117.

(55) Munoz-Robles, B. G.; Kopyeva, I.; DeForest, C. A. Surface Patterning of Hydrogel Biomaterials to Probe and Direct Cell–Matrix Interactions. *Adv. Mater. Interfaces* **2020**, *7* (21), 1–25. https://doi.org/10.1002/admi.202001198.

(56) Guvendiren, M.; Perepelyuk, M.; Wells, R. G.; Burdick, J. A. Hydrogels with Differential and Patterned Mechanics to Study Stiffness-Mediated Myofibroblastic Differentiation of Hepatic Stellate Cells. *J. Mech. Behav. Biomed. Mater.* **2014**, *38*, 198–208. https://doi.org/10.1016/j.jmbbm.2013.11.008.

(57) Yang, C.; DelRio, F. W.; Ma, H.; Killaars, A. R.; Basta, L. P.; Kyburz, K. A.; Anseth, K. S. Spatially Patterned Matrix Elasticity Directs Stem Cell Fate. *Proc. Natl. Acad. Sci. U. S. A.* **2016**, *113* (31), E4439–E4445. https://doi.org/10.1073/pnas.1609731113.

(58) Hadden, W. J.; Young, J. L.; Holle, A. W.; McFetridge, M. L.; Kim, D. Y.; Wijesinghe, P.; Taylor-Weiner, H.; Wen, J. H.; Lee, A. R.; Bieback, K.; et al. Stem Cell Migration and Mechanotransduction on Linear Stiffness Gradient Hydrogels. *Proc. Natl. Acad. Sci. U. S. A.* **2017**, *114* (22), 5647–5652. https://doi.org/10.1073/pnas.1618239114.

(59) Piroli, M. E.; Jabbarzadeh, E. Matrix Stiffness Modulates Mesenchymal Stem Cell

Sensitivity to Geometric Asymmetry Signals. *Ann. Biomed. Eng.* **2018**, *46* (6), 888–898. https://doi.org/10.1007/s10439-018-2008-8.

(60) Klán, P.; Šolomek, T.; Bochet, C. G.; Blanc, A.; Givens, R.; Rubina, M.; Popik, V.; Kostikov, A.; Wirz, J. Photoremovable Protecting Groups in Chemistry and Biology: Reaction Mechanisms and Efficacy. *Chem. Rev.* **2013**, *113* (1), 119–191. https://doi.org/10.1021/cr300177k.

(61) Holmes, C. P. Model Studies for New O-Nitrobenzyl Photolabile Linkers: Substituent Effects on the Rates of Photochemical Cleavage. *J. Org. Chem.* **1997**, *62* (8), 2370–2380. https://doi.org/10.1021/jo961602x.

(62) Sur, S.; Matson, J. B.; Webber, M. J.; Newcomb, C. J.; Stupp, S. I. Photodynamic Control of Bioactivity in a Nanofiber Matrix. *ACS Nano* **2012**, *6* (12), 10776–10785. https://doi.org/10.1021/nn304101x.

(63) Rosales, A. M.; Vega, S. L.; DelRio, F. W.; Burdick, J. A.; Anseth, K. S. Hydrogels with Reversible Mechanics to Probe Dynamic Cell Microenvironments. *Angew. Chemie - Int. Ed.* **2017**, *56* (40), 12132–12136. https://doi.org/10.1002/anie.201705684.

(64) Broguiere, N.; Formica, F.; Barreto, G.; Zenobi-Wong, M. Sortase A as a Cross-Linking Enzyme in Tissue Engineering. *Acta Biomater.* **2018**, *77*, 182–190. https://doi.org/10.1016/j.actbio.2018.07.020.

(65) Valdez, J.; Cook, C. D.; Ahrens, C. C.; Wang, A. J.; Brown, A.; Kumar, M.; Stockdale, L.; Rothenberg, D.; Renggli, K.; Gordon, E.; et al. On-Demand Dissolution of Modular, Synthetic Extracellular Matrix Reveals Local Epithelial-Stromal Communication Networks. *Biomaterials* **2017**, *130*, 90–103. https://doi.org/10.1016/j.biomaterials.2017.03.030.

(66) Shadish, J. A.; Benuska, G. M.; DeForest, C. A. Bioactive Site-Specifically Modified Proteins for 4D Patterning of Gel Biomaterials. *Nat. Mater.* **2019**, *18* (9), 1005–1014. https://doi.org/10.1038/s41563-019-0367-7.

(67) Arkenberg, M. R.; Moore, D. M.; Lin, C. C. Dynamic Control of Hydrogel Crosslinking via Sortase-Mediated Reversible Transpeptidation. *Acta Biomater.* **2019**, *83* (xxxx), 83–95. https://doi.org/10.1016/j.actbio.2018.11.011.

(68) Pishesha, N.; Ingram, J. R.; Ploegh, H. L. Sortase A: A Model for Transpeptidation and Its Biological Applications. *Annu. Rev. Cell Dev. Biol.* **2018**, *34*, 163–188.

https://doi.org/10.1146/annurev-cellbio-100617-062527.

(69) Suree, N.; Liew, C. K.; Villareal, V. A.; Thieu, W.; Fadeev, E. A.; Clemens, J. J.; Jung, M. E.; Clubb, R. T. The Structure of the Staphylococcus Aureus Sortase-Substrate Complex Reveals How the Universally Conserved LPXTG Sorting Signal Is Recognized. *J. Biol. Chem.* **2009**, *284* (36), 24465–24477. https://doi.org/10.1074/jbc.M109.022624.

(70) Xie, T.; Wang, Y.; Deng, N.; Huang, G.; Taghavifar, F.; Geng, Y.; Liu, N.; Kulur, V.; Yao, C.; Chen, P.; et al. Single-Cell Deconvolution of Fibroblast Heterogeneity in Mouse Pulmonary Fibrosis. *Cell Rep.* **2018**, *22* (13), 3625–3640. https://doi.org/10.1016/j.celrep.2018.03.010.

(71) Poczobutt, J. M.; Eickelberg, O. Defining the Cell Types That Drive Idiopathic Pulmonary Fibrosis Using Single-Cell RNA Sequencing. *Am. J. Respir. Crit. Care Med.* **2019**, *199* (12), 1454–1456.

(72) Reyfman, P. A.; Walter, J. M.; Joshi, N.; Anekalla, K. R.; McQuattie-Pimentel, A. C.; Chiu, S.; Fernandez, R.; Akbarpour, M.; Chen, C. I.; Ren, Z.; et al. Single-Cell Transcriptomic Analysis of Human Lung Provides Insights into the Pathobiology of Pulmonary Fibrosis. *Am. J. Respir. Crit. Care Med.* **2019**, *199* (12), 1517–1536. https://doi.org/10.1164/rccm.201712-2410OC.

(73) Chen, G.; Ning, B.; Shi, T. Single-Cell RNA-Seq Technologies and Related Computational Data Analysis. *Front. Genet.* **2019**, *10* (APR), 1–13. https://doi.org/10.3389/fgene.2019.00317.

APPENDIX A: DESIGN OF ENZYMATICALLY-CLEAVABLE ADHESIVE AND CROSSLINKER PEPTIDES FOR USER-CONTROLLED HYDROGEL DEGRADATION AND SPATIALLY-SELECTIVE CELL RELEASE

A.1 Background

The development of ECM mimetic hydrogels that enable independent control of matrix stiffness, viscoelasticity, degradability, cell adhesion, and other properties in a spatially-dependent manner has advanced our understanding of how cell behaviors are influenced by multiple local chemical and biophysical cues. This is especially evident during pathologies where the microenvironment undergoes progressive changes in an uncontrolled manner. An important direction for continuing our knowledge of mechanistic pathways underlying disease outcomes such as fibrosis is being able to explore the changes and variability in gene expression on a single cell level. However, a limitation of *in vitro* hydrogel models, particularly for 3D cultures, is that it is typically difficult to rapidly breakdown the substrate to yield cell populations without degrading surrounding proteins and signaling molecules that could immediately alter relevant parameters. Previously developed systems have incorporation thermal[1,2], chemical[3,4], or photodegradation[5–7] methods and have shown success in hydrogel degradation. However, some drawbacks include slow degradation rates, cell damage during isolation, inability to be used in tissue substrates (e.g., light penetration depth), or lack of spatial control.

An alternative approach is the use of enzymes to facilitate hydrogel formation, degradation, and cell isolation. As highlighted in Chapter 7 (Section 7.2.3), the transpeptidase Sortase A (SrtA) has already been established as a powerful protein engineering tool. SrtA, which is readily expressed

in high yield, catalyzes a transpeptidase reaction which cleaves polypeptides at the highly conserved SrtA recognition sequence, 'LP*X*TG,' and anchors them to a polyglycine[8–11]. This peptide exchange process is highly selective and reversible, enabling spatial control over substrate dissolution. The reaction rate can be tuned from minutes to days depending on enzyme and peptide concentrations[8,12]. Here, we report the synthesis of SrtA-recognizing adhesive and crosslinker peptides for incorporation within a modular hydrogel system capable of user-controlled degradation. We expect this system to permit spatially-selective isolation of specific cell subpopulations for downstream analysis of single cell subtypes from defined patterned regions of interest. Ultimately, this system could yield information about how cell types regulate profibrotic signaling pathways that contribute to the progression of fibrosis and other pathological outcomes.

A.2 Materials and Methods

A.2.1 Purchased reagents

Recombinant SrtA A5 protein (Cat. No. 13101, 1 mg/mL, Active Motif), SrtA Pentamutant (Cat. No. 71086, 1 mg/mL, BPS Bioscience), GGG peptide (Cat. No. 79939, BPS Bioscience), and dithiol crosslinker peptide (GCRDLPRTGPQGIWGQDRCG, GenScript) were purchased for control and troubleshooting experiments. A SrtA Activity Assay Kit (Cat. No. 79937) was purchased from BPS Bioscience.

A.2.2 Peptide synthesis

Thiolated adhesive peptides (GCRDLPRTGGRGDSPG), di-thiol crosslinkers (GCRDLPRTGDRCG, GCRDLPRTGPQGIWGQDRCG), and a triglycine peptide (GGG) were synthesized on Rink Amide MBHA high-loaded (0.78 mmol/g) resin via Fmoc-protected solid-

phase methods. The resin was swelled with 20% (v/v) piperidine in dimethylformamide (DMF) and amino acids were coupled using 1 M diisopropylcarbodiimide (DIC) in DMF and 1 M Oxyma Pure (Advanced ChemTech) in DMF at 90°C. All peptides were cleaved in a solution of 92.5% trifluoroacetic acid, 2.5% triisopropylsilane (TIPS), 2.5% 2,2'-(ethylenedioxy) diethanethiol (DODT), and 2.5% DI water for 2-3 hours, precipitated in cold ethyl ether, centrifuged, and dried overnight. Peptides were then resuspended in DI water, frozen, and lyophilized. Syntheses were confirmed via matrix-assisted laser desorption/ionization (MALDI) or capillary electrophoresis-electrospray ionization-mass spectrometry (CE-ESI-MS) (**Figure SA.1-4**).

A.2.3 Sortase A (SrtA) expression

Sortase A pentamutant (eSrtA) in pET29 (Addgene plasmid 75144; gift from David Liu) were expressed and purified similar to previous methods[8,13]. BL21 *E. coli* transformed with pET29 sortase expression plasmids were cultured at 37°C in 10 mL LB media with 50 μg/mL kanamycin overnight. The tube was then centrifuged at 3000 xg for 5 minutes and the cell pellet was resuspended in an autoclaved baffled flask with 100 mL of fresh LB media and 50 μg/mL kanamycin. The flask was then put on a shaker at 37°C until the optical density of the sample at 600 nm (OD_{600}) reached 0.6. 1 mM isopropyl β-d-1-thiogalactopyranoside (IPTG) was added to induce protein expression overnight at 20°C. Cells were harvested via centrifugation and washed with lysis buffer (50 mM Tris pH 8.0, 300 mM NaCl, 1 mM $MgCl_2$, 2 units/mL DNAseI (NEB), 260 nM aprotinin, 1.2 μM leupeptin, and 1 mM PMSF). Cells were then lysed via sonication and the supernatant was purified with a Ni-NTA agarose column. Elution fractions were checked using SDS-PAGE. Clean elution fractions were consolidated and dialyzed against Tris-buffered saline (25 mM Tris pH 7.5, 150 mM NaCl) in snake skin tubing at 4°C overnight. Aliquots were sterile

filtered using Ultra-15 Centrifugal Filters Units (10 kDa molecular weight cutoff (MWCO), Amicon) and flash frozen for storage at -80°C. Enzyme concentration was calculated from the measured A_{280} using the extinction coefficient of 17,420 M^{-1} cm^{-1} [14].

A.2.4 SrtA activity assay

The inhibitory activity of SrtA was determined via fluorescence measurements using a Sortase A Activity Assay Kit (BPS Bioscience). Briefly, the reactions were performed in a black, low binding 96-well plate. All wells contained 20 µL 1x Sortase assay buffer, 2.5 µL triglycine, and 2.5 uL Abz/Dnp substrate (fluorescent peptide). The positive control contained 5 µL 10% DMSO in water (inhibitor buffer) and 20 µL Sortase A (6.25 ng/µL), the test inhibitor contained 5 µL4-(hydroxymercuri)benzoic acid (test inhibitor) and 20 µL Sortase A, and the blank contained 5 µL 10% DMSO in water and an addition 20 µL assay buffer. Reactions were carried out at 30°C for 30 minutes and analyzed using a plate reader (λ_{ex} = 320 nm, λ_{em} = 420 nm). The blank values were subtracted from all measurements.

A.2.5 NorHA hydrogel synthesis

Norbornene-modified hyaluronic acid (HA) was synthesized as described in Chapters 4, 5, and 6[15,16]. The degree of NorHA modification was 31% as determined by ^{1}H NMR (500 MHz Varian Inova 500). 3D hydrogels were fabricated via ultraviolet (UV) light-mediated thiol-ene addition. Soft (2 wt%) elastic hydrogel precursor solutions containing di-thiol peptides (0.5 thiol-norbornene ratio) were polymerized in the presence of UV light (365 nm, 5 mW/cm^2) and 1 mM lithium acylphosphinate (LAP) photoinitiator for 4 minutes. Hydrogel plugs (50 µL, ~ 4.7 mm diameter × 2 mm thick for unswollen hydrogels) were formed in 1 mL syringes where the syringe

tips were cut off at the 0.1 mL mark. Hydrogels were swelled in phosphate-buffered saline (PBS) or TTC buffer (pH 7.5, 50 mM Tris-HCl, 1 mM $CaCl_2$, and 0.05% Triton X-100) at 37°C.

A.2.6 Hydrogel degradation via collagenase

Hydrogel degradation in response to collagenase (Type II, 100 U/mL, Worthington) was assessed over 7 days, similar to previous methods[17]. 3D NorHA hydrogels were synthesized and swelled in TTC buffer at 37°C with buffer changes (fresh buffer and collagenase) on days 1, 3, 5, and 7. Buffer samples were stored at -80°C until analysis after the last time point. Hydrogels with hyaluronidase (1 mg/mL) or without any enzyme were the positive and negative controls, respectively.

A.2.7 Hydrogel degradation via SrtA

Hydrogel degradation in response to SrtA was assessed. 3D NorHA hydrogels (50 μL) were synthesized and allowed to swell in PBS at 37°C overnight. Hydrogels were then transferred into a multi-well plate with 60 μL SrtA (18 μM), followed by the addition of GGG (18 mM). Incubation of the hydrogels in SrtA alone was varied between 10 and 30 minutes. After the addition of GGG, the well plate was placed on a shaker and mixed at 300 RPM at 37°C. Degradation was assessed qualitatively and via a plate reader (using a covalently bound fluorophore).

A.3 Results and Discussion

A.3.1 Sortase A (SrtA) synthesis

The SrtA pentamutant (eSrtA) was used for its improved catalytic activity compared to the wild type variant (140-fold improvement)[13]. BL21 *E. coli* cells were transformed with the SrtA plasmid

and 1 mM IPTG was used to induce protein expression (**Figure A.1A, B**). After cell harvesting via centrifugation, the cells were lysed via sonication. The supernatant containing the SrtA enzyme was purified using Ni-NTA agarose, a nickel-charged affinity resin that purifies recombinant proteins with a His tag (**Figure A.1C**). The eluent contained Tris buffer (50 mM Tris pH 8.0) and increasing amounts of imidazole. The eluent gradient started with 10 mM imidazole and increased to 500 mM imidazole to ensure complete elution. Elution fractions were checked using SDS-PAGE (**Figure A.1D**). Clean elution fractions were consolidated and dialyzed against Tris buffer. The SrtA enzyme concentration was measured using a Nanodrop and was determined to be 1.35 mg/mL.

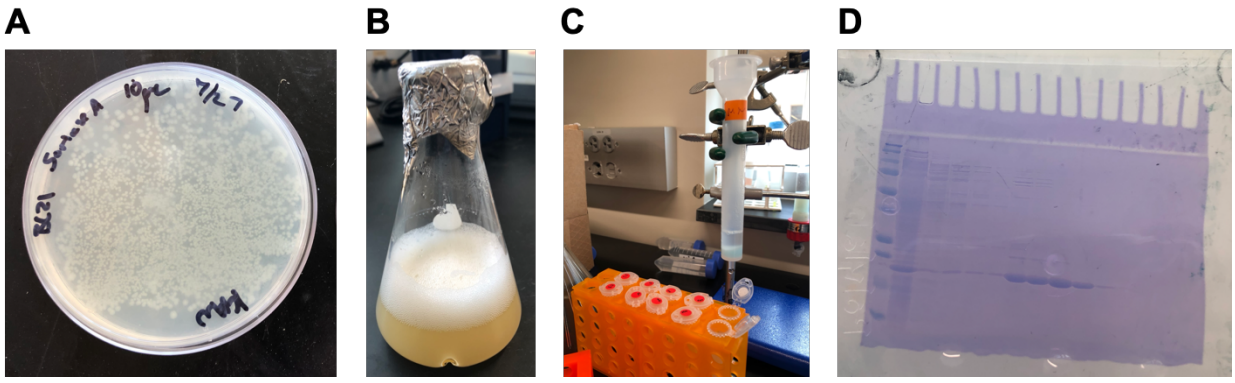

Figure A.1. Sortase A expression and purification. (A) BL21 *E. coli* transformed with the SrtA plasmid. (B) Cell growth in LB media until the OD reached ~ 0.6. (C) After cell harvesting and lysing, the supernatant was purified via a Ni-NTA agarose column. (D) SDS PAGE confirmed elution fractions containing SrtA for subsequent experiments.

We next measured SrtA activity in the presence of a SrtA inhibitor, 4-(hydroxymercuri)benzoic acid. Fluorescence measurements indicated positive SrtA activity trends; activity was around 100% in the absence of the inhibitor and decreased as inhibitor concentration increased (**Figure A.2**), yielding promising results.

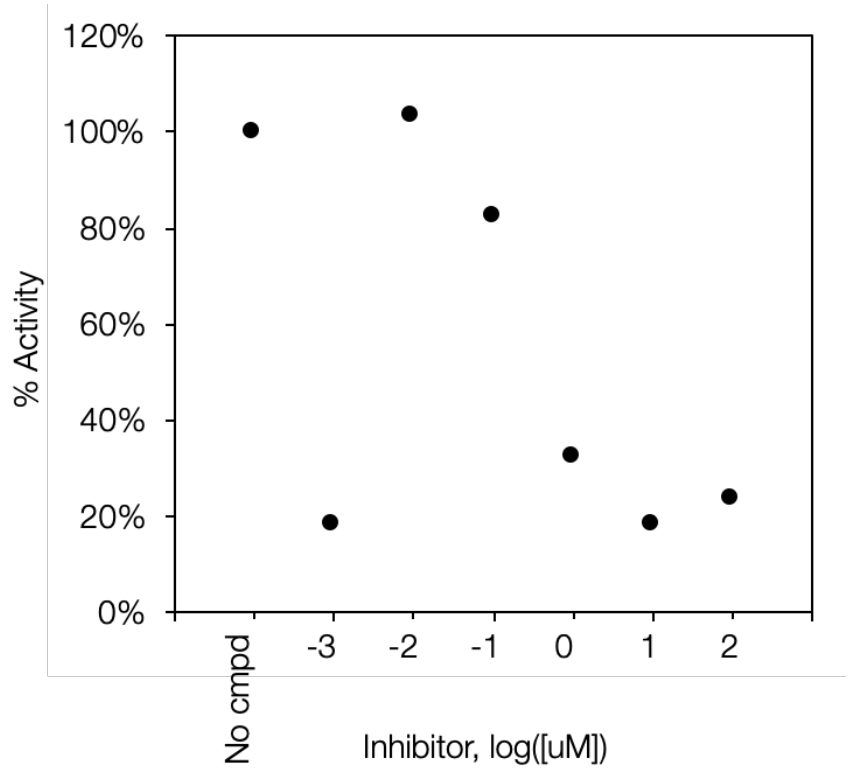

Figure A.2. Sortase A activity. Experimental plate reader results showing activity as a function of a SrtA inhibitor, 4-(hydroymercuri)benzoic acid. SrtA demonstrated high activity without the presence of the inhibitor and decreases as inhibitor concentration increases.

A.3.2 Hydrogel formation

3D soft elastic NorHA hydrogels were successfully fabricated via UV light-mediated thiol-ene addition, similar to Chapter 6. Thiolated adhesive and dithiol crosslinker peptides containing the SrtA-cleavable sequence were synthesized to incorporate SrtA-cleavable cues. Based off of previous work, we chose to use the 'LPRTG' sequence[8,12]. For the adhesive peptides, the sequence contained a thiol on one end and an RGD adhesive motif at the other to enable peptide conjugation to the hydrogel and cell attachment, respectively. Two dithiol crosslinkers were synthesized, one with a MMP-cleavable sequence (PQGIWG) and one without. These were chosen to be able to

explore the influence of both cell-mediated degradability and user-controlled dissolution on cell behaviors, especially for longer cultures. All peptides were successfully incorporated in hydrogels. However, to simplify our initial experiments, we chose to continue with the dithiol crosslinkers only to be able to measure bulk hydrogel degradation without cells. Moving forward, the adhesive peptides could be used for cell attachment and subsequent release upon SrtA incubation.

A.3.2 Hydrogel degradation

We next wanted to test the ability for the hydrogels to degrade in the presence of SrtA. 3D hydrogels were fabricated with SrtA-cleavable dithiol crosslinkers and swelled in PBS overnight. We first measured degradation in response to collagenase and hyaluronidase. Hydrogels were incubated in either collagenase, hyaluronidase (positive control), or neither (negative control) and the solution was replaced every other day for 1 week. Hydrogels in hyaluronidase degraded within 1 day, but those in collagenase did not fully degrade even after 1 week, which was a concern for the ability of these hydrogels to degrade regardless of degradation method. However, we continued on to see if the addition of SrtA would influence dissolution.

Many of the reports on SrtA-mediated degradation first added the SrtA enzyme for a specified period before adding the polyglycine, which acted to catalyze the exchange process. We incubated the hydrogels in 18 μM SrtA enzyme in PBS for 15 minutes before adding 18 mM GGG peptide and placing it on a shaker at room temperature. Previous work by Valdez *et al.* used 10 μM SrtA and incubated for 10 minutes before the addition of 18 mM GGG, demonstrating hydrogel dissolution in around 20 minutes and faster degradation kinetics at higher SrtA concentrations and greater SrtA incubation times[8]. Additionally, degradation kinetics did not seem to be affected by

crosslinking chemistry or density. However, in our case, qualitative observations showed minimal to no degradation after 30 minutes of GGG addition. We next chose to have all the incubation steps on the shaker and in 37°C to explore if temperature or shaking would speed up degradation. Degradation seemed to be minimal in this case as well and only dissolved after several days in the incubator.

We next investigated if one of the synthesized materials affected hydrogel degradation. Dithiol 'LPRTG'-containing crosslinker peptide, SrtA enzyme, and GGG peptide were all purchased commercially and tested. Again, minimal degradation was observed over 1-2 days and only dissolved after several days. Additionally, in several cases, the hydrogels seemed to produce a white precipitate, which later was determined to from the use of phosphate buffers. One major problem that was determined was the absence of Ca^{2+} in the buffers used during incubation – the enzyme is calcium dependent and is initiated via binding of a Ca^{2+} ion[10]. However, the extent of calcium dependency for the SrtA pentamutant is not certain. We next looked at the influence of buffer on hydrogel degradation. Hydrogels were incubated in either PBS, calcium-containing PBS, or calcium-containing TTC buffer. While little to no qualitative degradation was observed after 2 hours, there was more noticeable degradation after 2 days (**Figure A.3A**). In particular, hydrogels that were incubated in the calcium-containing TTC buffer qualitatively demonstrated the greatest hydrogel dissolution compared to the other groups in phosphate-based buffers (**Figure A.3B, C**).

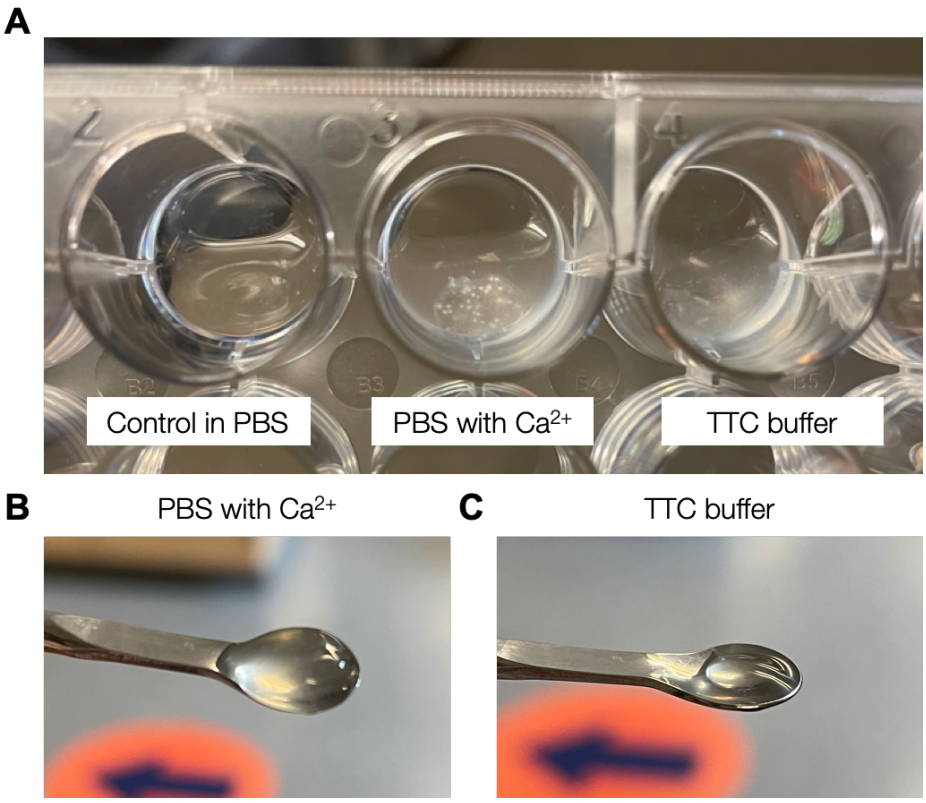

Figure A.3. Hydrogel degradation as a function of buffer makeup. (A) Hydrogels after 2 days. *Left to right*: Hydrogel in PBS without the addition of SrtA, hydrogel in calcium-containing PBS with SrtA and GGG, hydrogel in TTC buffer with SrtA and GGG. (B) Hydrogel after incubation in calcium-containing PBS. (C) Hydrogel after incubation in TTC buffer.

A.3.3 Challenges, alternative approaches, and future directions

The goal of this work is to design an enzymatically-cleavable hydrogel system capable of spatially-selective cell release. This approach enables the design of several systems – the hydrogel can be photopatterned with SrtA-cleavable adhesive and/or crosslinker peptides, photocleavable peptides, or both via secondary photopatterning. The approach can also be combined with spatially diverse mechanics (e.g., stiffness, viscoelasticity) to mimic the heterogeneous tissue microenvironment (**Figure A.4**).

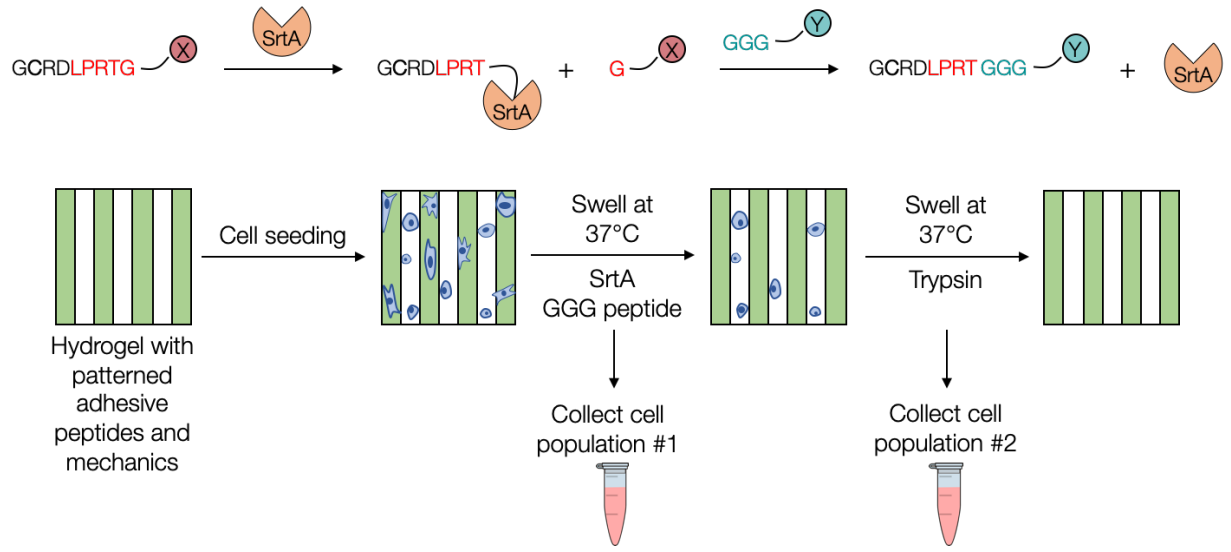

Figure A.4. Schematic of the photopatterning process for sequential collection of cells on patterned regions. Hydrogels patterned with cleavable adhesive peptides and dithiol peptides can be seeded with cells (or encapsulated within hydrogels) and cultured. Hydrogels would then be incubated in SrtA enzyme followed by polyglycine peptides to permit hydrogel degradation (with SrtA-cleavable dithiol crosslinkers) or cell release (with SrtA-cleavable adhesive peptides) from the regions of interest (e.g., patterned regions of stiffness). The remaining regions could then be subjected to secondary photodegradation or trypsinization for complete hydrogel dissolution or cell collection.

Although attempts to rapidly degrade hydrogels using SrtA were unsuccessful in preliminary experiments, there are alternative routes that could alleviate challenges. On the peptide synthesis side, while this work focused on the 'LPRTG' sequence (where R can be any amino acid) based on previous studies, future work could explore varying the middle amino acid. For example, another popular SrtA-recognizable sequence, 'LPETG,' could be investigated[18,19]. Testing the degradability of these sequences was a challenge that was not overcome and alternative methods to validate that these peptides can degrade is essential for this system to work. As mentioned in Section A.3.2, the addition of hyaluronidase was successful in complete hydrogel degradation within 1 day, but full hydrogel degradation did not occur in the presence of high concentrations of collagenase even after 7 days. Testing SrtA-mediated degradation of the 'LP*X*TG' sequence was

difficult due to low amounts of purified SrtA, which was also at lower concentrations than anticipated. For SrtA, a large concern was filtering and long-term storage of the enzyme. For sterile filtering, centrifugal tubes with 10 MWCO filters were used to concentrate the enzyme (~ 20 kDa) but the process was messy and some product and enzyme activity might have been lost and reduced during the long centrifuging process. Additionally, there are differences in long-term storage of enzymes to prolong their activity – while some studies add a glycol solution, others do not add additional solution before freezing. In the future, synthesizing larger batches of SrtA could help in determining the best method of filtering and storing the enzyme. During hydrogel incubations, greater concentrations of SrtA and/or GGG should be tested to determine their efficacy in hydrogel degradation. Finally, testing degradation against increasing levels of Ca^{2+} in a non-phosphate buffer solution could elucidate how calcium dependent the SrtA pentamutant is. While there may be a trade-off on kinetics, an alternative approach could be to use a SrtA variant (e.g., heptamutant SrtA) that is calcium independent[12,20].

Future work could also look at the incorporation of both enzymatic and light-mediated triggers as a method to increase control over hydrogel degradation and selective cell release. For photocleavage, a popular photoresponsive group is *ortho*-nitrobenzyl (*o*-NB), which can undergo spatially selective cleavage[5,21,22]. Since the *o*-NB photocleavage mechanism is most efficient with UV light (365 nm), initial attachment of the peptide thiols to the hydrogel backbone could be done using blue light (400-500 nm). However, any overlap in absorption may cause unwanted initial cleavage of some *o*-NB prior to cell studies. If this is the case, a dental curing lamp (3M ESPE Elipar 2500) with a narrower wavelength range (470 nm) and full width half maximum value could be used. In addition, it may be of interest to synthesize cleavable peptides in combination with

other adhesion sequences that can preferentially engage αvβ3 (e.g., RLD, KRLDGS) or α5β1 (e.g., RGDGW) integrins[23,24]. Fluorescence-activated cell sorting (FACS) could also be initially utilized to validate emerging cell subtypes. As mentioned in Chapter 7 (Section 7.2.3), the isolation of cells from spatially distinct regions could allow for more nuanced gene expression analyses (e.g., single cell RNA sequencing[25]) where substrate mechanics plays a role in cell phenotype and population changes.

A.4 References

(1) Shen, Z.; Bi, J.; Shi, B.; Nguyen, D.; Xian, C. J.; Zhang, H.; Dai, S. Exploring Thermal Reversible Hydrogels for Stem Cell Expansion in Three-Dimensions. *Soft Matter* **2012**, *8* (27), 7250–7257. https://doi.org/10.1039/c2sm25407g.

(2) Klouda, L.; Mikos, A. G. Thermoresponsive Hydrogels in Biomedical Applications - a Review. *Eur J Pharm Biopharm* **2011**, *68* (1), 34–45. https://doi.org/10.1016/j.ejpb.2007.02.025.Thermoresponsive.

(3) Zhang, J.; Skardal, A.; Prestwich, G. D. Engineered Extracellular Matrices with Cleavable Crosslinkers for Cell Expansion and Easy Cell Recovery. *Biomaterials* **2008**, *29* (34), 4521–4531. https://doi.org/10.1016/j.biomaterials.2008.08.008.

(4) Gevrek, T. N.; Cosar, M.; Aydin, D.; Kaga, E.; Arslan, M.; Sanyal, R.; Sanyal, A. Facile Fabrication of a Modular "Catch and Release" Hydrogel Interface: Harnessing Thiol-Disulfide Exchange for Reversible Protein Capture and Cell Attachment. *ACS Appl. Mater. Interfaces* **2018**, *10* (17), 14399–14409. https://doi.org/10.1021/acsami.8b00802.

(5) DeForest, C. A.; Anseth, K. S. Photoreversible Patterning of Biomolecules within Click-Based Hydrogels. *Angew. Chemie - Int. Ed.* **2012**, *51* (8), 1816–1819. https://doi.org/10.1002/anie.201106463.

(6) Brown, T. E.; Marozas, I. A.; Anseth, K. S. Amplified Photodegradation of Cell-Laden Hydrogels via an Addition–Fragmentation Chain Transfer Reaction. *Adv. Mater.* **2017**, *29* (11). https://doi.org/10.1002/adma.201605001.

(7) Griffin, D. R.; Kasko, A. M. Photodegradable Macromers and Hydrogels for Live Cell Encapsulation and Release. *J. Am. Chem. Soc.* **2012**, *134* (31), 13103–13107. https://doi.org/10.1021/ja305280w.

(8) Valdez, J.; Cook, C. D.; Ahrens, C. C.; Wang, A. J.; Brown, A.; Kumar, M.; Stockdale, L.; Rothenberg, D.; Renggli, K.; Gordon, E.; et al. On-Demand Dissolution of Modular, Synthetic Extracellular Matrix Reveals Local Epithelial-Stromal Communication Networks. *Biomaterials* **2017**, *130*, 90–103. https://doi.org/10.1016/j.biomaterials.2017.03.030.

(9) Pishesha, N.; Ingram, J. R.; Ploegh, H. L. Sortase A: A Model for Transpeptidation and Its Biological Applications. *Annu. Rev. Cell Dev. Biol.* **2018**, *34*, 163–188. https://doi.org/10.1146/annurev-cellbio-100617-062527.

(10) Wu, Z.; Hong, H.; Zhao, X.; Wang, X. Efficient Expression of Sortase A from Staphylococcus Aureus in Escherichia Coli and Its Enzymatic Characterizations. *Bioresour. Bioprocess.* **2017**, *4* (1). https://doi.org/10.1186/s40643-017-0143-y.

(11) Suree, N.; Liew, C. K.; Villareal, V. A.; Thieu, W.; Fadeev, E. A.; Clemens, J. J.; Jung, M. E.; Clubb, R. T. The Structure of the Staphylococcus Aureus Sortase-Substrate Complex Reveals How the Universally Conserved LPXTG Sorting Signal Is Recognized. *J. Biol. Chem.* **2009**, *284* (36), 24465–24477. https://doi.org/10.1074/jbc.M109.022624.

(12) Arkenberg, M. R.; Moore, D. M.; Lin, C. C. Dynamic Control of Hydrogel Crosslinking via Sortase-Mediated Reversible Transpeptidation. *Acta Biomater.* **2019**, *83* (xxxx), 83–95. https://doi.org/10.1016/j.actbio.2018.11.011.

(13) Chen, I.; Dorr, B. M.; Liu, D. R. A General Strategy for the Evolution of Bond-Forming Enzymes Using Yeast Display. *Proc. Natl. Acad. Sci. U. S. A.* **2011**, *108* (28), 11399–11404. https://doi.org/10.1073/pnas.1101046108.

(14) Kruger, R. G.; Otvos, B.; Frankel, B. A.; Bentley, M.; Dostal, P.; McCafferty, D. G. Analysis of the Substrate Specificity of the Staphylococcus Aureus Sortase Transpeptidase SrtA. *Biochemistry* **2004**, *43* (6), 1541–1551. https://doi.org/10.1021/bi035920j.

(15) Hui, E.; Gimeno, K. I.; Guan, G.; Caliari, S. R. Spatiotemporal Control of Viscoelasticity in Phototunable Hyaluronic Acid Hydrogels. *Biomacromolecules* **2019**, *20* (11), 4126–4134. https://doi.org/10.1021/acs.biomac.9b00965.

(16) Hui, E.; Moretti, L.; Barker, T. H.; Caliari, S. R. The Combined Influence of Viscoelastic and Adhesive Cues on Fibroblast Spreading and Focal Adhesion Organization. *Cell. Mol. Bioeng.* **2021**. https://doi.org/10.1007/s12195-021-00672-1.

(17) Caliari, S. R.; Vega, S. L.; Kwon, M.; Soulas, E. M.; Burdick, J. A. Dimensionality and Spreading Influence MSC YAP/TAZ Signaling in Hydrogel Environments. *Biomaterials* **2016**, *103*, 314–323. https://doi.org/10.1016/j.biomaterials.2016.06.061.

(18) Broguiere, N.; Formica, F.; Barreto, G.; Zenobi-Wong, M. Sortase A as a Cross-Linking Enzyme in Tissue Engineering. *Acta Biomater.* **2018**, *77*, 182–190. https://doi.org/10.1016/j.actbio.2018.07.020.

(19) Shadish, J. A.; Benuska, G. M.; DeForest, C. A. Bioactive Site-Specifically Modified Proteins for 4D Patterning of Gel Biomaterials. *Nat. Mater.* **2019**, *18* (9), 1005–1014. https://doi.org/10.1038/s41563-019-0367-7.

(20) Guimaraes, C. P.; Witte, M. D.; Theile, C. S.; Bozkurt, G.; Kundrat, L.; Blom, A. E. M.; Ploegh, H. L. Site-Specific C-Terminal and Internal Loop Labeling of Proteins Using Sortase-Mediated Reactions. *Nat. Protoc.* **2013**, *8* (9), 1787–1799. https://doi.org/10.1038/nprot.2013.101.

(21) Truong, V. X.; Tsang, K. M.; Simon, G. P.; Boyd, R. L.; Evans, R. A.; Thissen, H.; Forsythe, J. S. Photodegradable Gelatin-Based Hydrogels Prepared by Bioorthogonal Click Chemistry for Cell Encapsulation and Release. *Biomacromolecules* **2015**, *16* (7), 2246–2253. https://doi.org/10.1021/acs.biomac.5b00706.

(22) Kloxin, A. M.; Tibbitt, M. W.; Anseth, K. S. Synthesis of Photodegradable Hydrogels as Dynamically Tunable Cell Culture Platforms. *Nat. Protoc.* **2010**, *5* (12), 1867–1887. https://doi.org/10.1038/nprot.2010.139.

(23) Ruoslahti, E. RGD and Other Recognition Sequences for Integrins. *Annu. Rev. Cell Dev. Biol.* **1996**, *12* (1), 697–715. https://doi.org/10.1146/annurev.cellbio.12.1.697.

(24) Humphries, J. D.; Askari, J. A.; Zhang, X. P.; Takada, Y.; Humphries, M. J.; Mould, A. P. Molecular Basis of Ligand Recognition by Integrin A5β1. II. Specificity of Arg-Gly-Asp Binding Is Determined by Trp157 of the α Subunit. *J. Biol. Chem.* **2000**, *275* (27), 20337–20345. https://doi.org/10.1074/jbc.M000568200.

(25) Bingham, G. C.; Lee, F.; Naba, A.; Barker, T. H. Spatial-Omics: Novel Approaches to Probe Cell Heterogeneity and Extracellular Matrix Biology. *Matrix Biol.* **2020**, *91–92*, 152–166. https://doi.org/10.1016/j.matbio.2020.04.004.

A.5 Supplementary Figures

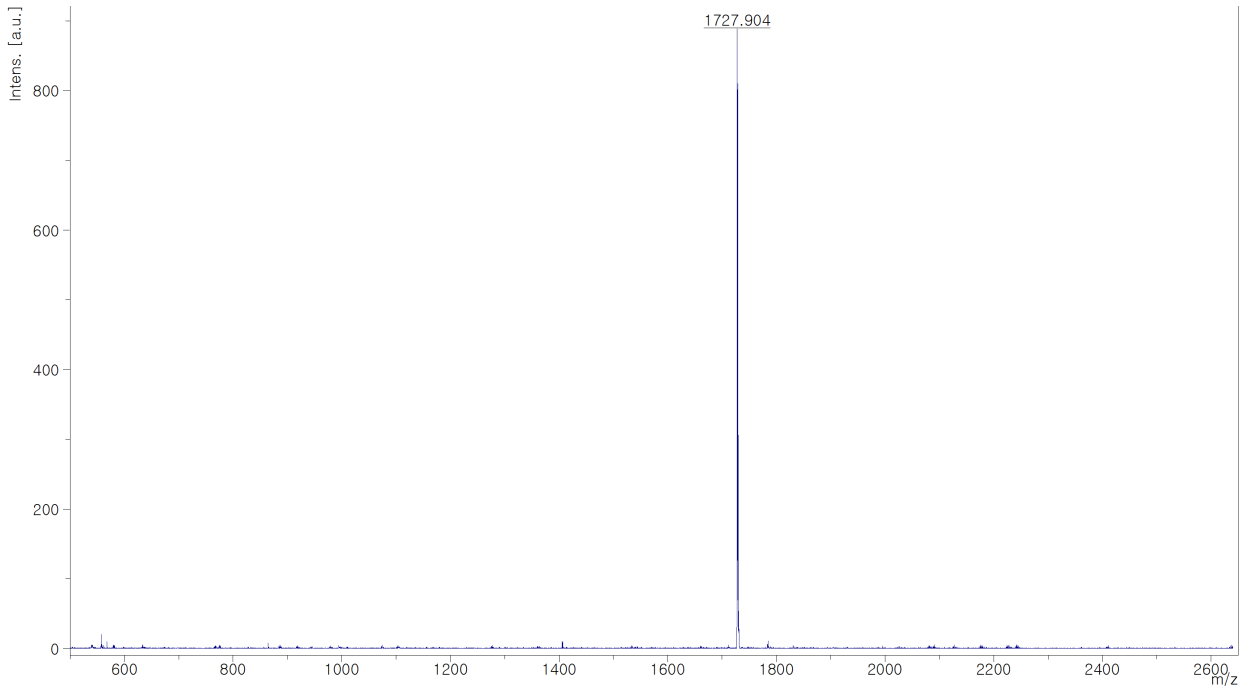

Figure SA.1. **MALDI spectrum of the thiolated adhesive SrtA-cleavable peptide GCRDLPRTGGRGDSPG.** Expected mass: 1727.9 g/mol. Actual mass: 1727.9 g/mol.

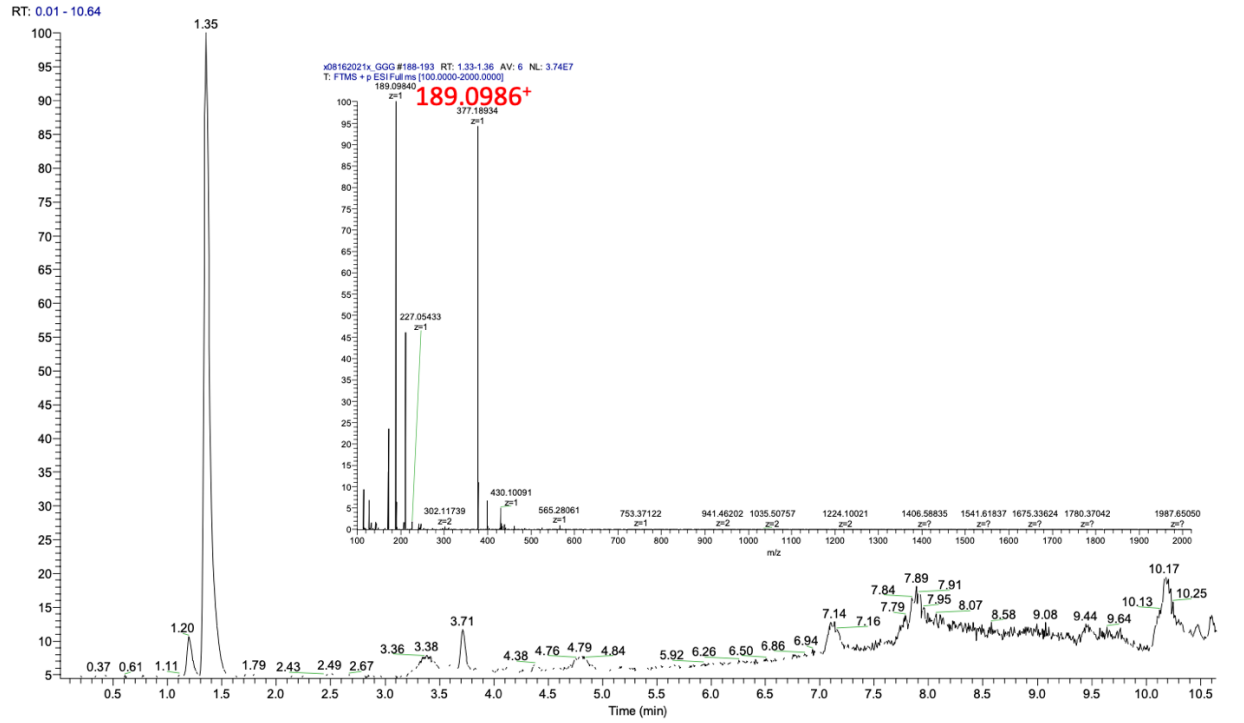

Figure SA.2. **ESI-MS spectrum of the GGG peptide.** Expected mass: 189 g/mol. Actual mass: 189.1 g/mol.

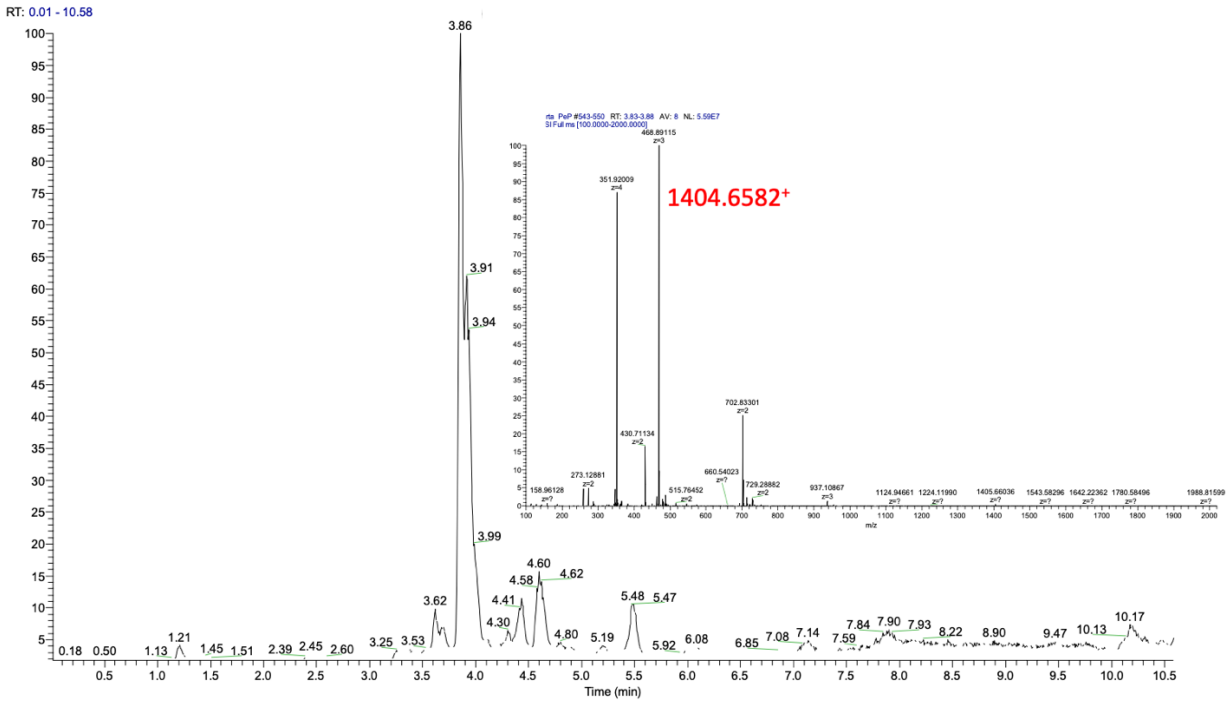

Figure SA.3. ESI-MS spectrum of the dithiol peptide GCRDLPRTGDRCG. Expected mass: 1404.6 g/mol. Actual mass: 1404.7 g/mol.

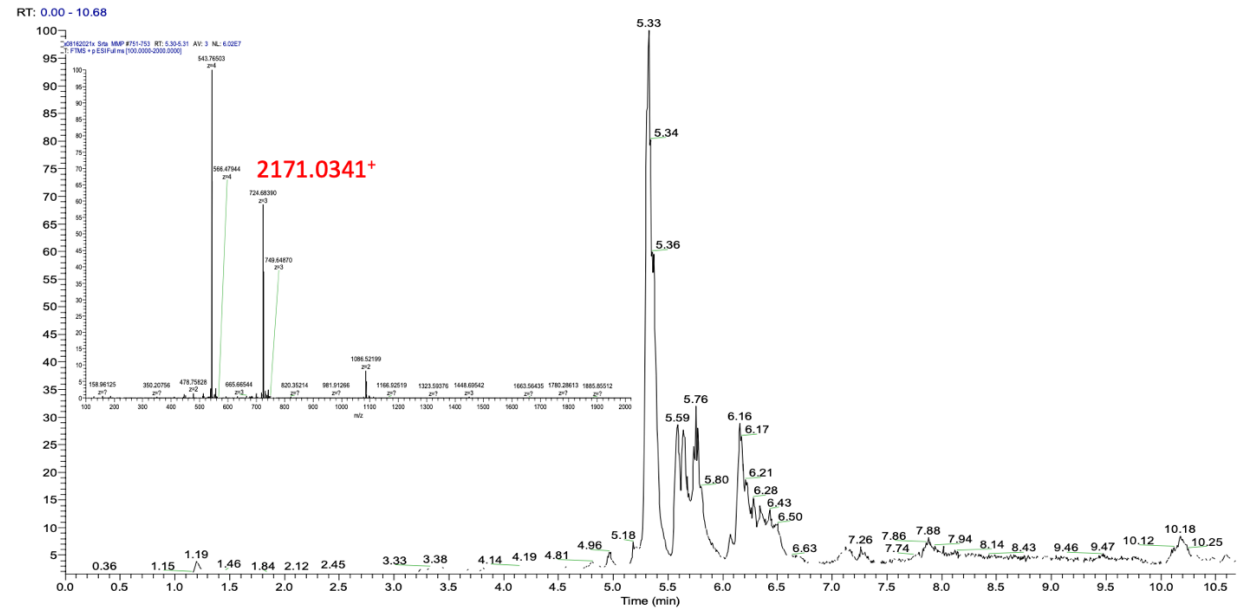

Figure SA.4. **ESI-MS spectrum of the dithiol MMP- and SrtA- cleavable peptide GCRDLPRTGPQGIWGDRCG.** Expected mass: 2171 g/mol. Actual mass: 2171 g/mol.